



HAL
open science

Instabilities, turbulence and heat transfer in confined rotating flows

Sébastien Poncet

► **To cite this version:**

Sébastien Poncet. Instabilities, turbulence and heat transfer in confined rotating flows. Fluids mechanics [physics.class-ph]. Aix-Marseille Université, 2014. tel-01098553

HAL Id: tel-01098553

<https://hal.science/tel-01098553v1>

Submitted on 26 Dec 2014

HAL is a multi-disciplinary open access archive for the deposit and dissemination of scientific research documents, whether they are published or not. The documents may come from teaching and research institutions in France or abroad, or from public or private research centers.

L'archive ouverte pluridisciplinaire **HAL**, est destinée au dépôt et à la diffusion de documents scientifiques de niveau recherche, publiés ou non, émanant des établissements d'enseignement et de recherche français ou étrangers, des laboratoires publics ou privés.



Summary of research works

Habilitation thesis of AIX-MARSEILLE UNIVERSITY

Mention: “Engineering Sciences: Mechanics, Physics, Micro & Nanoelectronics”

to obtain

the accreditation to supervise research

by **Sébastien Poncet**

Assistant Professor at Aix-Marseille University

Laboratoire de Modélisation en Mécanique et Procédés Propres UMR 7340

Instabilities, turbulence and heat transfer in confined rotating flows

Defended on the 5th of February 2014

Committee Members:

Prof. Souad HARMAND (Univ. Valenciennes, TEMPO): examiner

Prof. Hector IACOVIDES (Univ. Manchester, MACE): examiner

Dr. Patrice LE GAL (DR CNRS, IRPHE Marseille): examiner

Prof. Francisco MARQUES (Univ. Politècnica de Catalunya): rapporteur

Prof. Frédéric MOISY (Univ. Paris Sud, FAST): rapporteur

Prof. Caroline NORE (Univ. Paris Sud, LIMSI): rapporteur

Dr. Eric SERRE (DR CNRS, M2P2 Marseille): director

Ces quelques personnes méritent infiniment plus que des remerciements:

À mon cercle familial proche: Célia, Emma, Coline, Séverine et mes parents,

À mes deux "papas scientifiques", Marie-Pierre Chauve et Roland Schiestel, sans qui j'aurais sans doute fait fortune en dimensionnant des risers pour de grands groupes pétroliers.

À méditer:

Pour être performants, les chercheurs doivent s'appuyer sur la dyade compétition-collaboration. Compétition car chacun dans sa catégorie veut être le meilleur; collaboration car les questions posées sont tellement complexes qu'il est indispensable de travailler en équipe, au sein de communautés où chaque chercheur, chaque ingénieur, chaque technicien compte. En ce sens la recherche est un sport d'équipe. Comme dans le sport, il n'y a pas que des champions. Il faut tenir compte de tous, car c'est l'ensemble des sportifs qui fait progresser le sport . . . Comme dans tout acte de création, en peinture, sculpture, architecture, ou en musique, littérature, l'homme se trouve à un moment seul devant le vide qu'il doit remplir. Il ne peut le faire que s'il aiguisé sa pensée au contact de ceux qui lui ressemblent.

Catherine Bréchnac dans N'ayons pas peur de la science: raison et déraison (CNRS Editions, 2009).

Acknowledgements

First of all, I would like to express my heartfelt gratitude to my two mentors, Marie-Pierre Chauve and Roland Schiestel. I could not have asked for better role models, each inspirational, supportive, and patient. In my everyday scientific life, I still remember some of your precious advices, which guide me continuously on the right way, I hope.

I would like to acknowledge Professors Caroline Nore, Souad Harmand, Hector Iacovides, Francisco Marques, Frédéric Moisy and Drs Patrice Le Gal and Eric Serre, who accepted to be members of the present jury. It is really a great honour. I would like also to take this opportunity to apologize for the length of this thesis. I promise not to have included all the results I got since the end of my PhD thesis. But this habilitation thesis will mark a little bit the end of my research activities on rotating flows and I had the wish to deal with all the aspects of rotating flows and write a monograph, which could be helpful for future students.

I am also very grateful to Stéphane Viazzo. Many results obtained in this manuscript are partly owed to your golden hands to develop numerical methods as easily as I play soccer on my Playstation 2. It was nice also to visit Paris and Rome with you and share some time at the IUT GTE. Thanks for all.

I would like to acknowledge Eric Serre for accepting to be my HDR supervisor but also for including me in some of his research programs with Brian for example.

Thanks to Virginie and Michel. You are doubtless the cornerstones of the lab. Your expertise and kindness make the everyday life much easier. I hope that the University of Sherbrooke has at least one “Virginie” and one “Michel”. Thanks also to Guido and Umberto. We have shared the same office and it was for me really a great pleasure to discuss with you about everything except from rotating flows. Thanks also to Julien to make me a “Marseille-Cassis” finisher, I appreciated your support on that occasion but also in many others.

I would like to acknowledge also all my other collaborators: Patrice L.G., Michael L.B., Souad H., Julien P., Riccardo D.S., Cosimo B., Bikash S., Isabelle S.G., Brian L., Laurent M.W., Roger D., Laurie D., Jiri P., Bruno F. I interacted with you with always a great pleasure. Thanks also to all the former or present students: Romain O., Adrien A., Guillaume F., Noele P., Clément M., Sofia H., Hector B., Eric S., Raissa N., Thien N., Fadi A.N., Lyes K., Nabila A.M., who did or still do really a great job. To the staff members of both the IUT GTE and the M2P2 lab, I am grateful for the chance to work with you for 8 years now.

To finish, the financial supports of the Institut Carnot STAR, the LABEX MEC (ANR-11-LABX-0092) through the HYDREX program, the company Liebherr Aerospace Toulouse and the start-up Physio-Assist are also gratefully acknowledged.

Contents

I	Introduction	13
1	Introduction	15
2	Curriculum Vitae	19
II	Numerical modeling	39
3	3D High-order numerical methods	41
3.1	Geometrical modeling	41
3.2	Conservation equations	42
3.3	Projection scheme for time-discretization	43
3.4	Space approximations	44
3.4.1	Pseudospectral method	44
3.4.2	Compact finite-difference schemes	47
3.5	The $r = 0$ -singularity	47
3.6	Multidomain decomposition: the influence matrix technique	50
3.6.1	Multidomain geometry	50
3.6.2	Multidomain decomposition of the solutions	50
3.6.3	The influence matrix technique	51
3.6.4	Singularity of the Poisson-problem	52
3.6.5	Validation of the multidomain approach	52
3.7	Subgrid scale modeling	53
3.7.1	The Spectral vanishing viscosity (SVV) technique	54
3.7.2	Subgrid scale models based on an eddy-viscosity assumption	55
4	Reynolds Stress Model	57
4.1	The differential Reynolds Stress Model (RSM)	57
4.1.1	The transport equations for the Reynolds stress tensor	57
4.1.2	Modeling of the diffusion terms	58
4.1.3	Modeling of the pressure-strain correlation term	58
4.1.4	Modeling of the viscous dissipation term	60
4.1.5	Modeling of the extra terms sensitized to rotation effects	60
4.1.6	Transport equations for the turbulence kinetic energy k and its dissipation rate ε	62
4.1.7	Energy equation	62
4.2	Numerical method	63
4.3	Boundary conditions	63
III	Rotating disk flows	65
5	Bödewadt flow of a non-Newtonian fluid	67
5.1	Introduction	67
5.2	Flow analysis	69
5.3	Numerical solutions of the problem	70
5.3.1	Finite-difference solution	70
5.3.2	The Keller-box method	71
5.3.3	Performances of the two methods	73
5.4	Results and discussion	73
5.4.1	Viscous fluid ($L = 0$)	73
5.4.2	Non-Newtonian fluid ($L \neq 0$)	77
5.5	Conclusion	80

6	Shear-layer instability over a rotating disk	81
6.1	Introduction	81
6.2	Experimental set-up and flow parameters	83
6.2.1	The apparatus	83
6.2.2	The flow global parameters	84
6.2.3	The experimental procedure	84
6.2.4	Shape of the free surface for $\eta = 0$	85
6.3	Results and discussion	86
6.3.1	Structure of the flow for $\eta = 0$	86
6.3.2	Transition diagram for $\eta = 0$	88
6.3.3	Influence of the radius ratio η	94
6.4	Conclusion	95
7	Transition to turbulence of a Batchelor flow in a rotor-stator system	97
7.1	Introduction	97
7.2	Geometrical configuration	98
7.3	Two first bifurcations of Batchelor flows on the stator side	99
7.3.1	Influence of the curvature parameter on the stability of rotor-stator flows	99
7.3.2	Nature of the circular and spiral patterns	100
7.3.2.1	Circular rolls (CR)	101
7.3.2.2	Spiral rolls (SR1)	103
7.4	Transitional flow regime on both rotor and stator sides	106
7.4.1	Boundary layers instabilities and turbulence in the Bödewadt layer	107
7.4.2	Boundary layers instabilities and turbulence in the Ekman layer	107
7.5	Conclusion	110
8	Turbulent enclosed rotor-stator disk flows	113
8.1	Introduction	113
8.1.1	Why studying rotor-stator flows?	113
8.1.2	Regime IV of Daily and Nece [67]	114
8.1.3	Turbulent rotor-stator flows: a challenge for numerical methods	116
8.2	The experimental set-up	117
8.3	Numerical approaches	118
8.4	Turbulent isothermal rotor-stator disk flows	119
8.4.1	Benchmark of two Large Eddy Simulations	119
8.4.2	Influence of the rotational Reynolds number	122
8.4.3	Finite cavity effects	128
8.4.4	Three-dimensional boundary layers	131
8.4.5	Flow structures	132
8.5	Heat transfer in turbulent rotor-stator flows	135
8.5.1	Heat transfer parameters	135
8.5.2	Influence of the heat transfer on the flow structures	135
8.5.3	Mean flow and turbulence statistics	137
8.5.3.1	Flow field	137
8.5.3.2	Temperature field	138
8.5.3.3	Heat fluxes along the disks	140
8.6	3D unsteady large scale vortices in turbulent flows	145
8.6.1	A general feature in rotating flows	145
8.6.2	The MACE rotor-stator facility	146
8.6.3	Flow visualizations of 3D unsteady vortices in turbulent Batchelor rotor-stator flows	147
8.7	Conclusion	149

9	Turbulent Von Kármán flow between counter-rotating disks	151
9.1	Introduction	151
9.2	Geometrical configuration and flow parameters	153
9.2.1	Geometrical configuration	153
9.2.2	Measurement technique	154
9.2.3	Flow parameters	154
9.3	Numerical approach and blade modeling	154
9.4	Smooth disk case: viscous stirring	155
9.4.1	Flow structure in the exact counter-rotating regime	155
9.4.2	Flow structure for $-1 \leq s \leq 0$	158
9.4.3	Turbulence field in the exact counter-rotating regime	160
9.5	Bladed disk case: inertial stirring	160
9.5.1	Flow structure in the exact counter-rotating regime	161
9.5.2	Flow structure for $-1 \leq s \leq 0$	161
9.5.3	Turbulence field in the exact counter-rotating regime	163
9.6	Conclusion	164
IV	Taylor-Couette flows between concentric cylinders	165
10	Influence of a radial temperature gradient on the flow stability	167
10.1	Introduction	167
10.2	Global flow parameters	169
10.3	Numerical details	169
10.4	Base flow	170
10.5	Instability regimes	172
10.5.1	Stability diagram	172
10.5.2	Primary bifurcations at low Taylor numbers	173
10.5.3	Secondary instabilities at higher Taylor numbers	176
10.6	Moment coefficient and heat transfer distributions	179
10.7	Conclusion	182
11	Turbulent flows with endwall effects	183
11.1	Introduction	183
11.2	Details of the geometrical configuration and flow parameters	185
11.3	Numerical modeling	186
11.4	Results	188
11.4.1	Flow structures	188
11.4.2	Mean hydrodynamic field	189
11.4.3	Turbulent statistics	193
11.4.3.1	Cross-correlation coefficient	193
11.4.3.2	Transport of turbulent angular momentum	194
11.5	Conclusion	196
12	Turbulent Taylor-Couette-Poiseuille flows	197
12.1	Introduction	197
12.2	Geometrical configuration and flow global parameters	200
12.3	Preliminary results using the RSM model	201
12.3.1	Benchmark of RANS models in the configuration of Escudier and Gouldson [89]	201
12.3.2	Are second order RANS models suitable for modeling heat transfer in electrical motors?	205
12.3.2.1	Mean and turbulent flow field in the Configuration “Liebherr 1”	205
12.3.2.2	Budgets for the turbulence kinetic energy transport equation	208
12.3.2.3	Distributions of the Nusselt numbers	209
12.4	Towards the LES of Taylor-Couette-Poiseuille in real operating flow conditions	215
12.4.1	Configuration of Nouri and Whitelaw [226]	216
12.4.1.1	Numerical details	216

12.4.1.2	Flow structures	216
12.4.1.3	Mean and turbulent flow fields	217
12.4.2	Configuration of the “Entrefer” project	219
12.4.2.1	Experimental facility developed at IRPHE	219
12.4.2.2	Numerical modeling	220
12.4.2.3	Hydrodynamic field	221
12.4.2.4	Heat transfer coefficient	228
12.5	Conclusion	234
 V Research outlooks		 237
13	Impinging jet flow onto a rotating disk	239
13.1	Motivation	240
13.2	Experimental facility developed at the TEMPO laboratory	241
13.3	Preliminary results	244
13.3.1	Hydrodynamic fields	244
13.3.2	Thermal field	248
13.4	Future works	251
14	Other projects for the next five years	255
14.1	SIMEOX project	255
14.2	Industrial chair CRSNG-Hydro-Québec on energy efficiency	259
14.2.1	Two-phase ejectors	260
14.2.2	Storage and transport of ice slurry coolants	262
14.2.3	Magnetic refrigeration	264

Part I

Introduction

Part I: Introduction

Summary: This first part is divided into two chapters. In Chapter 1, a general introduction presents the main motivations of studying rotating confined flows between disks or cylinders as well as the structure of this habilitation thesis. Chapter 2 is a detailed curriculum vitae listing my research activities in terms of publications, conferences, seminars ... as well as my teaching activities in the Thermal Engineering and Energy department and in the Master 2 on process engineering at Aix-Marseille University.

Introduction

The subject of rotating flows is important for many engineers, mathematicians and physicists. The Earth's weather system is controlled by the combined effects of solar radiation and rotation. The jet stream and ocean circulations occur as a direct result of the Earth's rotation; hurricanes and tornadoes are extreme phenomena that owe their existence to rotation-induced swirl.

There are many examples of flow near rotating machines, the most important of which is the gas turbine. Rotating-disc systems are used to model (theroretically, experimentally and computationally) the flow and heat transfer associated with the internal-air systems of gas turbines, where discs rotate close to a rotating or a stationary surface. The engine designer uses compressed air to cool the turbine discs: too little air could result in catastrophic failure; too much is wasteful and increases the fuel consumption and CO_2 production of the engine. Small improvements to the cooling system can result in significant savings, but the optimum design requires an understanding of the principles of rotating flows and the development and solution of the appropriate solutions. These two paragraphs are the foreword written by the Professor J.M. Owen from the University of Bath in the monograph by Childs [51] on rotating flow. These words sum up perfectly (and without any english mistakes) the motivations and applications of the present works in geophysics (Fig.1.1a), astrophysics (Fig.1.1b) and in the turbomachinery industry (Fig.1.1c) as well as the different approaches (theory, experiment and CFD) used.

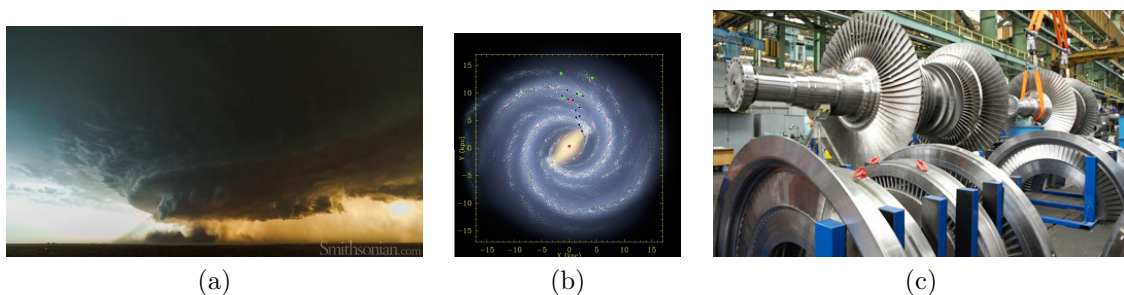


Figure 1.1: (a) Massive supercell in North Texas (Photo by Mike Olbinski, 2013); (b) Artist's conception of the Milky Way galaxy highlighting large scale spiral patterns (courtesy of Harvard-Smithsonian Center for Astrophysics); (c) Example of steam turbine developed by Skoda.

Confined cavity flows between two coaxial disks or cylinders, are both rich in the flow phenomena they create and the range of industrial flows with which they are linked. Figure 1.2 presents only few of the possible geometrical configurations for interdisk flows. The same sketch could be drawn for flows induced by the differential rotation of concentric cylinders and may be found in [51]. Some impression of the variety of flow structures arising in various flow arrangements may be gained from the books by Owen & Rogers [233], Childs [51] or the review papers of Launder *et al.* [170] for enclosed rotor-stator disk flows, of Harmand *et al.* [123] for rotor-stator flows with an impinging jet and of Fénot *et al.* [94] for Taylor-Couette flows between concentric cylinders. All these flows have in common to be quite complex even if most of the time, the geometry considered remains quite simple. There may have indeed a strong competition between rotation effects and the flow due either to an impinging jet or a superimposed throughflow. Wall effects are also quite important in such confined flows as very thin boundary layers, which are sites of various instabilities, develop along the walls. With the presence of enclosed cylinders, curvature effects have also to be taken into account. Thus, global control parameters (such as the rotational Reynolds number, the flowrate coefficient, the aspect ratio of the cavity, the curvature parameter, the Rayleigh and Prandtl numbers ...), while necessary, are not sufficient to describe the transition scenarii but also to simply describe the base

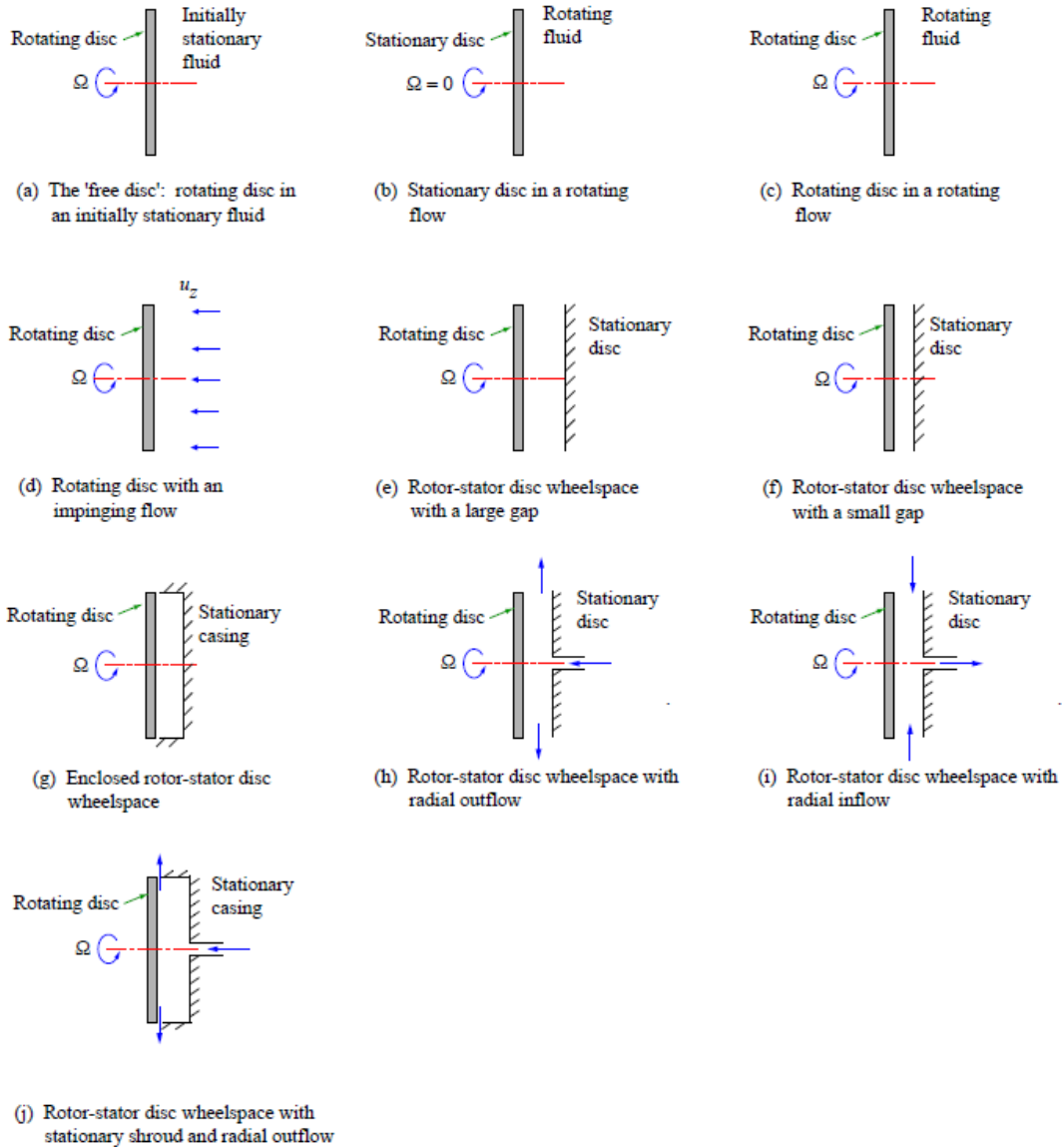


Figure 1.2: Possible disk flow configurations after Childs [51].

flows. In various cases, different flow regimes may indeed coexist for a given set of global parameters. Figure 1.3 presents an example of flow visualization of the Bödewadt problem (rotating fluid at a large distance from a stationary disk) by Savas [294] highlighting the transition from a stable flow regime around the rotation axis to a turbulent regime when moving towards the periphery of the cavity. Local parameters such as the local Reynolds and Rossby numbers (including the spatial location) have then to be introduced to fully understand the transition mechanisms. This multiplicity of flow parameters and the various applications of rotating flows make that it is still an alive topic of research.

This habilitation thesis lies along the lines of my PhD thesis [249] defended in 2005 at IRPHE under the co-supervisions of Dr M.P. Chauve and R. Schiestel (CNRS). I studied both experimentally and numerically the effect of an axial throughflow on the stability and turbulent regime of isothermal rotor-stator disk flows. Velocity and pressure measurements were compared to the predictions of the Reynolds Stress Model (RSM) developed by Elena and Schiestel [85] mainly for flows with unmerged boundary layers. New analytical models have been also developed to predict the core-swirl ratio of the fluid as a function of the interdisk spacing, rotation rate and flowrate in various configurations including smooth or rough disks and both in the laminar and turbulent regimes. It was financially supported by the SNECMA Moteurs group, who uses them now in their codes to evaluate the axial

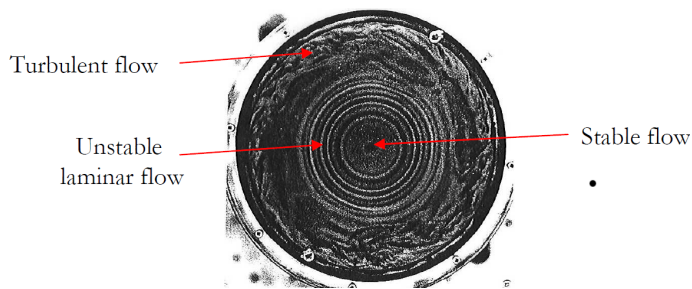


Figure 1.3: Flow visualization of the Bödewadt layer over a stationary finite disk after Savas [294].

thrusts applied on the rotors in the Hydrogen Liquid Turbopump of the Vulcain engine (Ariane V). The influence of an axial throughflow on the stability of interdisk rotor-stator flows has been also investigated from flow visualizations. Among other things, a crossflow instability, generic of rotating flows, appeared under the form of positive spirals located at the periphery of the cavity along the stator boundary layer. After one year as assistant lecturer at IRPHE, I got a position of assistant professor attached to the M2P2 laboratory. By force of circumstance and a little bit despite me, I switch to numerics with only few opportunities to perform other experiments. Rotating flows of Newtonian fluids remain my favored research topic apprehended using various levels of modeling (direct or large eddy simulations and RANS modeling) implemented into three in-house numerical codes:

- two DNS (Direct Numerical Simulation) codes, which solve the incompressible three-dimensional Navier-Stokes equations written in the velocity-pressure formulation, together with the continuity equation and appropriate boundary conditions. For both codes, Fourier series are used in the azimuthal periodic direction. The time scheme is semi-implicit and second-order accurate. It is a combination of an explicit treatment of the convective terms (Adams-Bashforth scheme) and of an implicit treatment for the diffusive terms (second-order backward Euler scheme). The solution method is based on an efficient projection scheme to solve the coupling between velocity and pressure ensuring a divergence-free velocity field at each time step. For each Fourier mode, a full diagonalization technique is used and yields simple matrix products for the solution of successive two-dimensional uncoupled Helmholtz and Poisson equations at each time step. The main difference lies in the spatial discretizations of the continuity and Navier-Stokes in the radial and axial inhomogeneous directions by Chebyshev polynomials for the code 1 and by fourth-order compact schemes for the code 2. Both codes were formerly available in their monodomain version, whereas the multidomain approach has been recently achieved and validated. Code 1 is extended to LES (Large Eddy Simulation) via a SVV (Spectral Vanishing Viscosity) technique [316], whereas in code 2, subgrid scale models like the dynamic Smagorinsky or the WALE models have been introduced.
- the RSM of Elena and Schiestel [85] available in a 2D unsteady finite-volume code. The model is available within a low Reynolds number approach and has been sensitized to rotation effects through the introduction of four additive terms taking into account some implicit effects of rotation on turbulence (spectral jamming, inverse cascade ...).

For non-isothermal flows, temperature is considered as a passive scalar, when heat transfers are mainly piloted by forced convection. When temperature gradients remain small, the Boussinesq approximation is used to solve the flow/heat transfer coupling.

Various flow configurations will be considered in the following chapters and for each problem, the transition scenarii as well as the turbulence itself will be investigated experimentally and numerically by varying most of the flow parameters to get a better insight into the dynamics of these flows and the heat and mass transfer processes. This habilitation thesis is an attempt to summarize what I think to be the main contributions of my research activities, which are at 90% dedicated to the study of rotating flows. After a detailed curriculum vitae and a brief description of the numerical tools, which will be used, the following subjects will be covered including:

- Similarity solutions of the flow of a non-Newtonian fluid over an infinite stationary rough disk;
- Stability of the flow over a finite rotating disk with a free surface;
- Stability and transition to turbulence of enclosed rotor-stator disk flows;
- Fully turbulent regime of enclosed rotor-stator disk flows under isothermal and non-isothermal conditions;
- Turbulent Von Kármán swirling flows between two rotating disks equipped or not with straight blades;
- Stability of Taylor-Couette flows with a radial thermal gradient;
- Transitional and turbulent flows in a Taylor-Couette apparatus with atypical boundary conditions;
- Turbulent Taylor-Couette-Poiseuille flows with or without heat transfer;
- Impinging jet flow over a rotating disk with heat transfer.

These flow configurations are gathered in two main parts: one dedicated to disk flows (Chapters 5 to 9) and the other on flows due to the differential rotation of cylinders (Chapters 10 to 12). This second part was inspired by a collaboration initiated in 2008 with Liebherr Aerospace Toulouse on the cooling of electric motors. The final part will address some overviews, first in similar configurations and especially the turbulent impinging jet flow onto a rotating disk with or without heat transfer (Chapter 13) and then in orthogonal domains related to the simulation of air/mucus/cilia interactions for patients suffering from respiratory diseases and to the combined experimental and numerical approaches of three refrigeration technologies (Chapter 14).

Curriculum Vitae

Civil status

Sébastien Poncet

Born on January 26th 1979 in Feurs (42),

married, 3 daughters,

French nationality

Current Academic Position

Assistant Professor at Aix-Marseille University (section 62) since 2006.

Teaching at the Energy and Thermal Engineering Department (GTE) of the University Institute of Technology (IUT) in Marseilles.

Research in the *Instability and Turbulence* team of the M2P2 laboratory.

Starting date the 1st of September 2006 and permanent position since the 1st of September 2007.

Laboratoire M2P2 (Modélisation en Mécanique et Procédés Propres)

UMR 7340 CNRS - Aix-Marseille University - École Centrale Marseille

IMT La Jetée, Technopôle de Château-Gombert

38 rue F. Joliot-Curie, 13 451 Marseilles, France

poncet@l3m.univ-mrs.fr or sebastien.poncet@univ-amu.fr

Tél : 04.91.11.85.55 - Fax : 04.91.11.85.02

<http://l3mgp.l3m.univ-mrs.fr/site/SitePersoPoncet/>

University education

2005-06: Lecturer at Paul Cézanne University (Aix-Marseille III).

Oct.2005-Feb.2006: Researcher at IRPHE, financially supported by the group SNECMA Moteurs.

2002-05: **PhD thesis** at the Institut de Recherche sur les Phénomènes Hors Equilibre (IRPHE). Study entitled *Rotor-stator flows with superimposed throughflow: from Batchelor to Stewartson*, supervisors M.P. Chauve & R. Schiestel (IRPHE-CNRS), obtained with the highest distinction, Marseilles (Fig.2.1,2.2).

2001-02: Master in marine environnement sciences with distinctions, University of Toulon.

1999-2002: **Engineer** in physical oceanography at the Institut des Sciences de l'Ingénieur de Toulon et du Var (ISITV), Toulon.

Research activities

Project manager

- Project "Entrefer moteur" supported by Liebherr Aerospace Toulouse (235,000 Euros), 2010-2013.
- Project "TCPtherm" supported by ICSTAR (30,000 Euros), 2010-2011.

- Project "Simeox" supported by Physio-Assist (6,000 Euros), 2012-2013.

Member of two other projects: Urabaïla (FUI, 2014-15) and MUCIL (ICSTAR, 2014).

Organization committees

- Member of the organization committee of "Journée franco-italienne sur la recherche et la coopération", École Centrale de Marseille, Marseilles, 19 October 2007.
- Member of the organisation committee of "Congrès Français de Mécanique", Marseilles, 24-28 August 2009.
- Member of the organisation committee of 8th International ERCOFTAC Symposium on Engineering Turbulence Modelling and Measurements (ETMM8), Marseilles, 9-11 June 2010.
- Member of the scientific committee of "Colloque franco-allemand ouvert à l'Europe du Nord: Environnement, Risques et Énergies Renouvelables", École Centrale de Marseille, Marseilles, 3-4 June 2010.
- Member of the scientific committee of "1er Congrès International de Physique Numérique", Oran, 13-15 October 2012.
- Member of the organization committee of "Quels défis énergétiques en région PACA?", IUT GTE, Marseilles, 11 April 2014.

Collective liabilities

- Member of the piloting committee of the thematic group "Écoulements et transferts", Institut Carnot STAR, 2012-.
- Member of two selecting committees at the University of Lyon 1 (Section 62) for two positions of assistant professor (MCF 1314 & 1458), 2012.
- Member of the "Hydrodynamique extrême dans les machines tournantes" action (HYDREX), labex MEC, 2011-.
- Member of the M2P2 laboratory board, 2008-2012.
- Member of the group "Ingénieurs Sans Frontières" (I.S.F. Riviera), 1999-2002.

Honors and Awards

1. PhD prize of AUM (Activités Universitaires en Mécanique) / AFM (Association Française de Mécanique), 2007 (Fig.2.3).
2. Research and doctoral supervision grant (2006-2010).
3. PhD prize of the French Section of the American Society of Mechanical Engineers, 2005.

Supervisions

Post-doctorates

1. Adrien Aubert, Expérimentation des écoulements de type Taylor-Couette-Poiseuille et des transferts de chaleur dans l'entrefer moteur d'une ACM, Post-doctorate, co-supervisor with P. Le Gal (IRPHE), 2011-2012. Financially supported by Liebherr Aerospace.
2. Raphael Guillerm, Simulation et modélisation des écoulements de type Taylor-Couette-Poiseuille et des transferts de chaleur dans l'entrefer moteur d'une ACM, Post-doctorate, co-supervisor with P. Le Gal (IRPHE), 2010-2011. Financially supported by Liebherr Aerospace.

PhD students

1. Romain Oguic, Simulation des grandes échelles d'un jet impactant un disque tournant, PhD thesis supported by the French Ministry of Research, co-supervisor with S. Viazzo (50%), 2012-.
2. Khaoula Hamidi, Modélisation des transferts de chaleur et de masse dans les systèmes de Taylor-Couette-Poiseuille. Application aux machines tournantes en régime extrême, co-supervisor with T. Rezoug (Univ. Blida) (30%), 2011-.
3. Guillaume Fontaine, Développement d'un solveur pseudospectral multidomaine parallèle pour la résolution des équations de Navier-Stokes tridimensionnelles en coordonnées cylindriques, PhD thesis supported by DGA (French Ministry of Army), co-supervisor with E. Serre (50%), 2008-2012 (defended the 17th of December 2012).
4. Noele Baptista Peres, A 3D pseudospectral method for cylindrical coordinates. Application to the simulations of rotating cavity flows, PhD thesis supported by the French Ministry of Research, Aix-Marseille Université, co-supervisor with E. Serre (50%), 2009-2012 (defended the 19th July 2012).

Graduate and undergraduate students

1. Hana Benkoussas, Transport et caractérisation rhéologique du mucus bronchique - Influence du SIMEOX, Master 2, Aix-Marseille Université, February-June 2014. Financially supported by Physio-Assist.
2. Raïssa Ngwong, Étude sur la caractérisation rhéologique du mucus bronchique: simulation numérique de l'écoulement air/mucus dans la trachée, Master 1, Aix-Marseille Université, March-June 2013. Financially supported by Physio-Assist.
3. Valentin Hoarau, Simulation de l'écoulement du mucus dans les bronchioles respirantes et influence du SIMEOX, Master 1, École de l'Air Salon, April-June 2013.
4. Emmanuel Tanti-Hardouin, Simulation numérique directe de la transition vers la turbulence dans un système de Taylor-Couette-Poiseuille avec transferts thermiques et entrefer rainuré, Master 1, June-September 2012. Financially supported by Liebherr Aerospace.
5. Clément Moreau, Bilan carbone du projet Entrefer moteur et étude des conditions d'entrée sur l'écoulement de Taylor-Couette-Poiseuille avec gradients thermiques, 2nd year at IUT GTE, April-June 2011. Financially supported by Liebherr Aerospace.
6. Jeff Ngoma, Benchmark numérique sur les écoulements de type rotor-stator, Master 1, École Polytechnique de Marseille, April-June 2009. Financially supported by CNRS.
7. Sofia Haddadi, Modélisation et simulation des écoulements tournants fortement cisailés, Master 2, ENSIAME, February-July 2008. Financially supported by Liebherr Aerospace.
8. Loic Liotard, Stabilité des écoulements de type Batchelor en cavité rotor-stator fermée: étude expérimentale et numérique, Master 1, ISITV, April-June 2007. Financially supported by CNRS.

Member of PhD committees

1. PhD thesis of Nicolas Hérenger entitled *Étude expérimentale du transitoire de remplissage des cavités d'injection des organes de combustion du moteur VINCI*, defended the 8th of October 2012, LEGI, Grenoble.
2. PhD thesis of Lyes Kahouadji entitled *Analyse de stabilité linéaire d'écoulements tournants en présence de surface libre*, defended the 24th of October 2011, LIMSI, Paris.
3. PhD thesis of Somia Freifer entitled *Contribution aux phénomènes d'interfaces fluide-solide*, defended the 11th of November 2010 at the University of Sciences and Technology (USTO) Mohamed Boudiaf, Oran (Algeria).

Publications

Peer Reviewed Articles (ACL)

Citation metrics: $h = 7$ (7 publications cited at least 7 times) and a sum of the times cited equal to 174 measured using Web of Knowledge and $h = 13$, $i_{10} = 15$ and a sum of the times cited equal to 484 measured using Google Scholar.

1. Sahoo B., Abbasbandy S., **Poncet S.**, A brief note on the computation of the Bödewadt flow with Navier slip boundary conditions, *Computers & Fluids*, **90**, p.133-137, 2014
2. **Poncet S.**, Pellé J., Nguyen T., Harmand S., Da Soghe R., Bianchini C., Viazzo S., Turbulent impinging jet flow into an unshrouded rotor-stator system: hydrodynamics and heat transfer, *Int. J. Heat Fluid Flow*, **44**, p.719-734, 2013
3. **Poncet S.**, Da Soghe R., Bianchini C., Viazzo S., Aubert A., Turbulent Couette-Taylor flows with endwall effects: a numerical benchmark, *Int. J. Heat Fluid Flow*, **44**, p.229-238, 2013
4. Sahoo B., **Poncet S.**, Blasius flow and heat transfer of a fourth grade fluid with slip, to appear in *Appl. Math. Mech.*, **34 (12)**, p.1465-1480, 2013
5. Harmand S., Pellé J., **Poncet S.**, Shevchuk I., Review of fluid flow and convective heat transfer within rotating disk cavities with impinging jet, *Int. J. Therm. Sci.*, **67**, p.1-30, 2013
6. Peres N., **Poncet S.**, Serre E., A 3D pseudo-spectral method for cylindrical coordinates. Application to the simulations of rotating cavity flows, *J. Comp. Phys.*, **231**, p.6290-6305, 2012
7. Nguyen T.D., Pellé J., Harmand S., **Poncet S.**, PIV measurements of a jet impinging to an opened rotor-stator system, sous presse, *Exp. in Fluids*, **53**, p.401-412, 2012
8. Sahoo B., **Poncet S.**, Effects of slip on steady Bödewadt flow of a Reiner-Rivlin fluid, *Communications in Nonlinear Science and Numerical Simulations*, **17**, p.4181-4191, 2012
9. Viazzo S., **Poncet S.**, Serre E., Randriamampianina A., Bontoux P., High-order LES benchmarking of confined rotor-stator flows, *Flow, Turbulence & Combustion*, **88** (1-2), p.63-75, 2012
10. **Poncet S.**, Dahlberg L., The legacy of Henri Victor Regnault in arts and sciences, *Int. J. Arts & Science*, **4** (13), p.377-400, 2011
11. Sahoo B., **Poncet S.**, Flow and heat transfer of a third grade fluid past an exponentially stretching sheet with partial slip boundary condition, *Int. J. Heat Mass Transfer*, **54** (23-24), p.5010-5019, 2011
12. **Poncet S.**, Haddadi S., Viazzo S., Numerical modeling of fluid flow and heat transfer in a narrow Taylor-Couette-Poiseuille system, *Int. J. Heat Fluid Flow*, **32**, p.128-144, 2011
13. **Poncet S.**, Chauve M.P., Curvature effects on the instabilities of Batchelor rotating disk flows, *Int. J. Fluid Mech. Research*, **37 (4)**, p.343-358, 2010
14. Launder B.E., **Poncet S.**, Serre E., Laminar, Transitional and Turbulent Rotating Disk Flows, *Ann. Rev. Fluid Mech.*, Vol.42, p.229-248, 2010
15. Abdel Nour F., **Poncet S.**, Debuchy R., Bois G., A Combined Analytical, Experimental and Numerical Investigation of Turbulent Air Flow Behaviour in a Rotor-Stator Cavity, *Mécanique & Industries*, **10 (3-4)**, p.195-202, 2009
16. **Poncet S.**, Serre E., High-order LES of turbulent heat transfer in a rotor-stator cavity, *Int. J. Heat Fluid Flow*, **30 (4)**, p.590-601, 2009
17. **Poncet S.**, Serre E., Le Gal P., Revisiting the two first instabilities of the flow in an annular rotor-stator cavity, *Phys. Fluids*, **21 (6)**, 064106, 2009

18. Haddadi S., **Poncet S.**, Turbulence modeling of torsional Couette flows, *Int. J. Rotating Machinery*, **Article ID 635138**, 27 pages, 2008
19. **Poncet S.**, Chauve M.-P., Le Gal P., Lois analytiques pour les écoulements en cavité rotor-stator, *Mécanique & Industries*, **9 (3)**, p.227-236, 2008
20. **Poncet S.**, Schiestel R., Monchaux R., Turbulence modeling of the Von Kármán flow: viscous and inertial stirrings, *Int. J. Heat Fluid Flow*, **29 (1)**, p.62-74, 2008
21. **Poncet S.**, Randriamampianina A., Three-dimensional turbulent boundary layer in a shrouded rotating system, *Flow, Turbulence and Combustion*, **80 (1)**, p.107-117, 2008
22. Séverac E., **Poncet S.**, Serre E., Chauve M.-P., Large eddy simulation and measurements of turbulent enclosed rotor-stator flows, *Phys. Fluids*, **19 (8)**, 085113 (17 pages), 2007
23. **Poncet S.**, Chauve M.-P., Shear-layer instability in a rotating system, *J. Flow Visualization and Image Processing*, **14 (1)**, p.85-105, 2007
24. **Poncet S.**, Schiestel R., Numerical modeling of heat transfer and fluid flow in rotor-stator cavities with throughflow, *Int. J. Heat Mass Transfer*, **50 (7-8)**, p.1528-1544, 2007
25. Shew W.L., **Poncet S.**, Pinton J.F., Force measurements on rising bubbles, *J. Fluid Mech.*, **569**, p.51-60, 2006.
26. Randriamampianina A., **Poncet S.**, Turbulence characteristics of the Bödewadt layer in a large enclosed rotor-stator system, *Phys. Fluids*, **18 (5)**, 055104 (16 pages), 2006
27. **Poncet S.**, Chauve M.-P., Seuils d'instabilités des écoulements de type rotor-stator avec flux axial, *C.R. Mécanique*, **334 (2)**, p.123-128, 2006
28. **Poncet S.**, Chauve M.-P., Crossflow instability in a rotor-stator cavity with an axial inward throughflow, *J. Fluid Mech.*, **545**, p.281-289, 2005
29. **Poncet S.**, Randriamampianina A., Écoulement turbulent dans une cavité rotor-stator fermée de grand rapport d'aspect, *C.R. Mécanique*, **333 (10)**, p.783-788, 2005
30. **Poncet S.**, Schiestel R., Chauve M.-P., Centrifugal flow in a rotor-stator cavity, *J. Fluid Eng.*, **127 (4)**, p.687-694, 2005
31. **Poncet S.**, Chauve M.-P., Schiestel R., Batchelor versus Stewartson flow structures in a rotor-stator cavity with throughflow, *Phys. Fluids*, **17 (7)**, 075110 (15 pages), 2005
32. **Poncet S.**, Chauve M.-P., Le Gal P., Turbulent Rotating Disk with Inward Throughflow, *J. Fluid Mech.*, **522**, p.253-262, 2005

Peer Reviewed Papers in International Conferences (ACTI)

1. Friess C., **Poncet S.**, Viazzo S., Taylor-Couette-Poiseuille flows: from RANS to LES, *Int. Symp. on Turbulence & Shear Flow Phenomena TSFP 8*, Poitiers, 28-30 August 2013
2. **Poncet S.**, Nguyen T.D., Harmand S., Pellé J., Viazzo S., Transferts de chaleur et de masse dans un système discoïde de type rotor-stator, *XIeme Colloque Interuniversitaire Franco-Québécois sur la Thermique des Systèmes*, Reims, 3-5 June 2013
3. Oguic R., Viazzo S., **Poncet S.**, Numerical simulations of a middle gap turbulent Taylor-Couette-Poiseuille flow, *Direct and Large-Eddy Simulation 9*, Dresden, 3-5 April 2013
4. Peres N., **Poncet S.**, Serre E., A 3D pseudo-spectral algorithm to simulate turbulent flows in cylindrical rotating cavities, *International Conference on Spectral and High Order Methods ICOSAHOM 2012*, Gammarth (Tunisia), 25-29 June 2012
5. Guillerm R., Da Soghe R., Bianchini C., **Poncet S.**, Viazzo S., Numerical predictions of flow field in closed and opened Taylor-Couette cavities, *European Conference for Aerospace Sciences (EUCASS 4)*, Saint-Petersburg, 4-8 July 2011

6. Da Soghe R., Innocenti L., Andreini A., **Poncet S.**, Numerical Benchmark of Turbulence modelling in Gas Turbine Rotor-Stator System, *Proceedings of ASME TURBO EXPO 2010: Power for Land, Sea & Air*, papier GT2010-22627, Glasgow, 14-18 June 2010
7. Viazzo S., Randriamampianina A., **Poncet S.**, Bontoux P., Serre E., High-order LES benchmarking of confined rotor-stator flows, *Proc. of the 8th Int. ERCOFTAC symposium on Engineering Turbulence Modelling and Measurements (ETMM8)*, Marseilles, 9-11 June 2010
8. Viazzo S., **Poncet S.**, Serre E., Randriamampianina A., Bontoux P., High-order LES benchmarking in confined rotating disk flows, 3rd European Conference for Aerospace Sciences (EU-CASS), Versailles, 6-9 July 2009
9. Barrios H., Viazzo S., Rey C., **Poncet S.**, Simulation numérique d'un écoulement de convection mixte en aval d'une marche, *14èmes Journées Internationales de Thermiques (JITH2009)*, Djerba (Tunisia), 27-29 March 2009
10. Haddadi S., **Poncet S.**, Viazzo S., Modélisation de la turbulence dans un système de Taylor-Couette différentiellement chauffé avec flux axial, *14èmes Journées Internationales de Thermiques (JITH2009)*, Djerba (Tunisia), 27-29 March 2009
11. Debuchy R., **Poncet S.**, Abdel Nour F., Bois G., Experimental and numerical investigation of turbulent air flow behaviour in a rotor-stator cavity, *Proc. of the European Turbomachinery Conference 8 (ETC8)*, Graz (Austria), 23-27 March 2009
12. **Poncet S.**, Serre E., Large Eddy Simulation of Non-Isothermal Turbulent Rotor-Stator Flows, *The Twelfth International Symposium on Transport Phenomena and Dynamics of Rotating Machinery (ISROMAC-12)*, ISROMAC12-2008-20009, Honolulu (USA), 17-22 February 2008
13. Séverac E., **Poncet S.**, Serre E., Chauve M.-P., Large Eddy Simulation and Measurements in a Turbulent Rotor-stator Flow, *Proceedings of the 5th International Symposium on Turbulence and Shear Flow Phenomena (TSFP5)*, Edited by J.A.C. Humphrey, J.K. Eaton, R. Friedrich, N. Kasagi, M.A. Leschziner & T. B. Gatski, Munich, 27-29 August 2007
14. **Poncet S.**, Randriamampianina A., Turbulence characteristics of the Bödewadt layer in a large shrouded rotor-stator system, *Conference on Turbulence and Interactions TI2006*, Porquerolles (France), 29 May - 2 June 2006

Peer Reviewed Papers in National Conferences (ACTN)

1. Aubert A., **Poncet S.**, Le Gal P., Viazzo S., Le Bars M., Thouveny T., Transferts de chaleur et de masse dans des écoulements turbulents de Taylor-Couette avec flux axial, *Congrès Français de Mécanique*, Bordeaux, 24-28 August 2013
2. Aubert A., Thouveny T., Le Bars M., Le Gal P., **Poncet S.**, Viazzo S., Transferts de chaleur et de masse dans des écoulements turbulents de Taylor-Couette avec flux axial, *Congrès Français de Thermique - SFT 2013 Thermique & Contexte incertain*, Gérardmer, 28-31 May 2013
3. Peres N., **Poncet S.**, Serre E., Traitement numérique de la singularité à l'axe pour les écoulements 3D en cavités tournantes, *Actes du XXème Congrès Français de Mécanique*, Ed. D. Chapelle, M. Dahan, P. Picart, Presses universitaires de Franche-Comté, ISBN 978-2-84867-416-2, Besançon, 28 August - 2 September 2011
4. Fontaine G., **Poncet S.**, Serre E., Approche multidomaine pseudospectrale pour la résolution des équations de Navier-Stokes en géométrie cylindrique, *Actes du XXème Congrès Français de Mécanique*, Ed. D. Chapelle, M. Dahan, P. Picart, Presses universitaires de Franche-Comté, ISBN 978-2-84867-416-2, Besançon, 28 August - 2 September 2011
5. Guillerm R., Da Soghe R., **Poncet S.**, Viazzo S., Benchmark numérique des écoulements de Couette-Taylor turbulents, *Actes du XXème Congrès Français de Mécanique*, Ed. D. Chapelle, M. Dahan, P. Picart, Presses universitaires de Franche-Comté, ISBN 978-2-84867-416-2, Besançon, 28 August - 2 September 2011

6. Sahoo B., **Poncet S.**, Effets des conditions de glissement sur l'écoulement de Bödewadt d'un fluide de type Reiner-Rivlin, *Actes du XXème Congrès Français de Mécanique*, Ed. D. Chapelle, M. Dahan, P. Picart, Presses universitaires de Franche-Comté, ISBN 978-2-84867-416-2, Besançon, 28 August - 2 September 2011
7. **Poncet S.**, Chauve M.P., Instabilité d'une couche de cisaillement au-dessus d'un disque en rotation, *Actes du 18^{ème} Congrès Français de Mécanique*, Grenoble, 27-31 August 2007
8. Séverac E., **Poncet S.**, Serre E., Chauve M.-P., Large Eddy Simulation and experimentation in an enclosed rotor-stator flow, *Actes du 18^{ème} Congrès Français de Mécanique*, Grenoble, 27-31 August 2007
9. Serre E., **Poncet S.**, Schiestel R. Launder B., Simulation d'écoulements transitionnels et turbulents en cavités rotor-stator avec transferts de chaleur, *Congrès Français de Thermique SFT07: Thermique et Société*, Ile des Embiez (France), 29 May - 1 June 2007
10. **Poncet S.**, Chauve M.-P., Schiestel R., Écoulements tournants: de Stewartson à Batchelor, *Actes du 17^{ème} Congrès Français de Mécanique*, Troyes, 29 August - 2 September 2005

Oral communications without proceedings in international or national conferences (COM)

1. Sahoo B., Abbasbandy S., **Poncet S.**, Pop I., Labropulu F., Modeling and computation of Bodewadt flow and heat transfer of a viscous fluid near a rough disk, *ISMMACS*, Kanpur (India), 31 December 2013 - 2 January 2014
2. Ait-Moussa N., **Poncet S.**, Ghezal A., Lounis M., Numerical study of the transition in counter-rotating Taylor-Couette flow for a wide gap, *18th International Couette-Taylor Workshop ICTW18*, Twente, 24-26 June 2013
3. **Poncet S.**, Viazzo S., Thermo-hydrodynamic instabilities in a high aspect ratio Couette-Taylor system using Direct Numerical Simulation, *European Fluid Mechanics Conference 9*, Roma, 9-13 September 2012
4. Kahouadji L., Martin-Witkowski L., Peres N., **Poncet S.**, Le Quéré P., Serre E., Primary bifurcation of a thin-layer flow driven by a rotating disk in a fixed open cylindrical cavity: flat free surface, *4th International Symposium Bifurcations and instabilities in fluid dynamics*, Barcelona, 18-21 July 2011
5. Peres N., **Poncet S.**, Serre E., Transition mechanisms to turbulence in a cylindrical rotor-stator cavity by pseudo-spectral simulations of Navier-Stokes equations, *Chaos, Complexity and Transport*, Marseilles, 23-27 May 2011
6. Viazzo S., Randriamampianina A., **Poncet S.**, Serre E., High-order LES benchmarking in confined rotor-stator flows, *Large Eddy Simulation in Turbulence, Aeroacoustic and Combustion (LESTAC 09)*, Marseilles, 24-28 August 2009
7. **Poncet S.**, Serre E., Chauve M.P., Le Gal P., Circular and spiral waves in a Batchelor flow between a rotating and a stationary disk, *EUROMECH Fluid Mechanics Conference 7 (EFMC7)*, Manchester, 14-18 September 2008. Marie Curie funding
8. Serre E., Séverac E., **Poncet S.**, Chauve M.-P., Large Eddy Simulation and Measurements of Turbulent Rotor-Stator Flows, *60th Annual Meeting of the Division of Fluid Dynamics, APS*, Salt Lake City, 18-20 November 2007
9. **Poncet S. et al.**, Sur les Écoulements de Disque Tournant, *Colloque Interdisciplinaire des Écoles Centrale*, Marseilles, 31 Mai - 1 June 2007
10. **Poncet S.**, Chauve M.-P., Crossflow instability in rotor-stator flows with throughflow, *Euromech Fluid Mechanics Conference 6*, Stockholm, 26-30 June 2006

11. **Poncet S.**, Schiestel R., Numerical modeling of heat transfer and fluid flow in rotor-stator cavities with throughflow, *Euromech Fluid Mechanics Conference 6*, Stockholm, 26-30 June 2006
12. **Poncet S.**, Chauve M.-P., Schiestel R., Écoulements tournants: de Batchelor à Stewartson, *Observer, Analyser, Modéliser, dans les milieux fluides complexes*, EGIM (Marseille), 2005

Book chapters (OS)

1. Fontaine G., **Poncet S.**, Serre E., Multidomain extension of a divergence-free pseudo-spectral algorithm for the direct numerical simulation of wall-confined rotating flows, *Lecture Notes in computational Science and Engineering*, M. Azaiez, H. El Fekih, J.S. Hesthaven (Eds), Springer, **95**, p.261-271, 2014
2. **Poncet S.**, Da Soghe R., Facchini B., RANS modeling of flows in rotating cavity systems, *Proceedings of the V European Conference on Computational Fluid Dynamics ECCOMAS CFD 2010*, J.C.F. Pereira, A. Sequeira & J.M.C. Pereira (Eds), ISBN: 978-989-96778-1-4, Lisbon, Portugal, June 14-17, 2010
3. Peres N., **Poncet S.**, Serre E., Numerical treatment of cylindrical coordinate singularity, *Proceedings of the V European Conference on Computational Fluid Dynamics ECCOMAS CFD 2010*, J.C.F. Pereira, A. Sequeira & J.M.C. Pereira (Eds), ISBN: 978-989-96778-1-4, Lisbon, Portugal, June 14-17, 2010
4. **Poncet S.**, Le Gal, P., Serre E., Simulation numérique directe des écoulements rotor-stator en cavité annulaire, *Actes du XIXe Congrès Français de Mécanique*, Marseille, Ed. C. Rey, P. Bontoux, A. Chrysochoos, ISSN 2103 – 6225 paper 594 - S9, 24-28 August 2009
5. Abdel Nour F., Debuchy R., Bois G., **Poncet S.**, A combined Analytical Experimental and Numerical Investigation of Turbulent Air Flow Behaviour in a Rotor-Stator Cavity, *Actes du XIXe Congrès Français de Mécanique*, Marseille, Ed. C. Rey, P. Bontoux, A. Chrysochoos, ISSN 2103 – 6225 paper 222 - S11, 24-28 August 2009
6. Séverac E., **Poncet S.**, Serre E., Chauve M.-P., A coupled numerical / experimental investigation of a turbulent rotor-stator flow, *Conference Proceedings of the 8th International Symposium on Experimental and Computational Aerothermodynamics of Internal Flows*, Ed. X.Ottavy & I. Trébinjac, Volume 2, p.703-712, paper ISAI8-006, Lyon, 2-5 July 2007
7. **Poncet S.**, Schiestel R., Monchaux R., Turbulent Von Kármán flow between two counter-rotating disks, *Conference Proceedings of the 8th International Symposium on Experimental and Computational Aerothermodynamics of Internal Flows*, Ed. X.Ottavy & I. Trébinjac, Volume 1, p.141-150, paper ISAI8-0013, Lyon, 2-5 July 2007
8. **Poncet S.**, Schiestel R., Monchaux R., Turbulent Von Kármán Swirling flows, *Advances in Turbulence XI, Proceedings of the 11th EUROMECH European Turbulence Conference*, Editors: J.M.L.M. Palma and A.Silva Lopes, Springer Proceedings in Physics 117, Springer, Heidelberg, ISBN 978-3-540-72603-6, Porto, Portugal, June 25-28, 2007
9. **Poncet S.**, Chauve M.-P., Le Gal P., Study of the entrainment coefficient of the fluid in a rotor-stator cavity, *Proc. of the 6th European Conference on Turbomachinery - Fluid Dynamics and Thermodynamics Vol.1*, Ed. G. Bois, C. Sierverding, M. Manna, T. Arts, ENSAM (Lille), p.246-256, 2005
10. **Poncet S.**, Schiestel R., Chauve M.-P., Turbulence modelling and measurements in a rotor-stator system with throughflow, *Engineering Turbulence Modelling and Experiments 6*, Ed. W. Rodi & M. Mulas, Elsevier (New-York), p.761-770, 2005
11. **Poncet S.**, Chauve M.-P., Le Gal P., Experimental study of rotor-stator flows with centripetal fluxes, *Mechanics of the 21st Century, Proceedings of the 21st International Congress of Theoretical and Applied Mechanics*, ISBN 1-4020-3559-4, Eds. W. Gutkowski, T.A. Kowalewski, Springer Verlag, 2005 (ICTAM 2004, Warsaw)

Reports of industrial contracts

1. Aubert A., **Poncet S.**, Le Gal P., Viazzo S., Le Bars M., Projet entrefer moteur: Caractérisation des écoulements et des transferts thermiques dans l'entrefer entre un cylindre fixe et un cylindre tournant soumis ou non à un flux axial, *Liebherr Aerospace Toulouse*, **Contract 30017596**, Final report, 2013
2. Seyssiecq-Guarente I., **Poncet S.**, Étude sur la caractérisation rhéologique du mucus bronchique. Premiers résultats sur fluides modèles, *Physio-Assist*, **Contract 080931**, Report 2, 2012
3. **Poncet S.**, Seyssiecq-Guarente I., Étude sur la caractérisation rhéologique du mucus bronchique. Étude bibliographique, *Physio-Assist*, **Contract 080931**, Report 1, 2012
4. Aubert A., **Poncet S.**, Le Gal P., Le Bars M., Viazzo S., Projet entrefer moteur: Caractérisation des écoulements et des transferts thermiques dans l'entrefer entre un cylindre fixe et un cylindre tournant soumis ou non à un flux axial, *Liebherr Aerospace Toulouse*, **Contract 30017596**, Report 2, 2012
5. **Poncet S.**, Le Gal P., Viazzo S., Le Bars M., Guillerm R., Moreau C., Projet entrefer moteur: Caractérisation des écoulements dans l'entrefer entre un cylindre fixe et un cylindre tournant soumis ou non à un flux axial, *Liebherr Aerospace Toulouse*, **Contract 30017596**, Report 1, 2011
6. Chauve M.-P., **Poncet S.**, Le Gal, P., Campagne de caractérisation des écoulements centrifuges et centripètes entre un disque fixe lisse et un disque tournant aileté, *SNECMA Moteurs*, **2005.060.I**, 2005
7. **Poncet S.**, Chauve M.-P., Le Gal, P., Campagne de caractérisation des écoulements centrifuges entre un disque lisse fixe et un disque lisse tournant, *SNECMA Moteurs*, **2004.093.G**, 2005
8. Chauve M.-P., **Poncet S.**, Le Gal, P., Campagne de caractérisation des écoulements centripètes aux travers d'ajutages supérieurs, *SNECMA Moteurs*, **2003.021.G**, 2004

Articles of popular science (OV)

1. Collegiate writing, Activities of the M2P2 laboratory, Report of the South-France Pilot Center by M. Braza, *ERCOfTAC Bulletin 97*, Ed. M. Marek, p.20-24, 2013
2. **Poncet S.**, Bontoux P., Ciralo G., Morvan D., Serre E., Main activities of the MSNM-GP laboratory, in France South Pilot Center by M. Braza, *ERCOfTAC Bulletin 77*, Ed. N. Borhani, p.42-46, 2008

Editorial activities (DO)

- Member of the Editorial Board of the *American Journal of Fluid Mechanics* (SAPUB) since 2011 and then Editor-in-chief since 2012
- Member of the Editorial Board of the *Progress in Computational Fluid Dynamics* (Inderscience, Impact factor: 0.48) since 2013
- Member of the Editorial Board of the *The Scientific World Journal, Mechanical Engineering* (Hindawi, Impact factor: 1.73) since 2013
- Member of the Editorial Board of the *Journal of Nonlinear Dynamics* (Hindawi, journal funded in 2013) since 2013
- Member of the Editorial Board of the *Advances in Chemical Engineering* (Edinwilson, journal funded in 2013) since 2013

Dissertations

- PhD thesis, *Écoulements de type rotor-stator soumis à un flux axial: de Batchelor à Stewartson*, under the supervisions of Marie-Pierre Chauve & Roland Schiestel, IRPHE / University of Aix-Marseille I, 2005
Book format published by the “Éditions Universitaires Européennes”: *Écoulements de type rotor-stator soumis à un flux axial*, ISBN 978-613-1-51686-3, 18 June 2010
- Master’s dissertation, *Détection et suivi de cibles: étude du mouvement d’une bulle par l’effet Doppler ultrasonore*, under the supervision of Jean-François Pinton, Laboratoire de physique - ENS Lyon, 2002

Seminars & Presentations

Invited Seminars

1. Deux exemples de simulation d’écoulements turbulents dans le domaine des turbomachines, *Faculté de Génie*, Sherbrooke, 15 March 2011
2. Simulation et modélisation d’écoulements turbulents dans les turbomachines, *Université des Sciences et de la Technologie (USTO)*, Mohamed Boudiaf, Oran, 11 November 2010
3. High-order LES of confined rotor-stator flows, *Institute of Thermomechanics, Academy of Sciences of Czech Republic*, Prague, 25 May 2010
4. High-order LES of confined rotor-stator flows, *Energy Engineering Department S. Stecco, University of Florence*, Florence, 16 April 2010
5. Approches expérimentale et numérique des écoulements de disque tournant, *ENSAM-LML*, Lille, 27 March 2008
6. “Café” seminar - Revue sur les écoulements de disque(s) tournant(s), *Laboratoire PMMH*, Paris, 4 May 2006
7. “Café” seminar - Revue sur les écoulements de disque(s) tournant(s), *LMFA*, Lyon, 2 May 2006
8. “Café” seminar - Revue sur les écoulements de disque(s) tournant(s), *CEA/SPEC/GIT*, Saclay, 4 January 2006

Presentations in International Conferences

1. Transferts de chaleur et de masse par jet impactant dans un système discoïde rotor-stator, *XI Colloque Interuniversitaire Franco-Québécois sur la Thermique des Systèmes*, Reims, 4 June 2013
2. Thermo-hydrodynamic instabilities in a high aspect ratio Couette-Taylor system using Direct Numerical Simulation, *European Fluid Mechanics Conference 9*, Roma, 13 September 2012
3. Numerical predictions of flow field in closed and opened Taylor-Couette cavities, *European Conference for Aerospace Sciences (EUCASS 4)*, Saint-Petersburg, 7 July 2011
4. The legacy of Henri Victor Regnault in arts and sciences, *IJAS Conference Series*, Aix en Provence, 7 June 2011
5. RANS modeling of flows in rotating cavity systems, *ECCOMAS CFD 2010*, Lisbon, 15 June 2010
6. High-order LES benchmarking in confined rotating disk flows, *3rd European Conference for Aerospace Sciences (EUCASS)*, Versailles, 9 July 2009
7. Circular and spiral waves in a Batchelor flow between a rotating and a stationary disk, *Seventh Euromech Fluid Mechanics Conference*, Manchester, 16 September 2008

8. Large Eddy Simulation of Non-Isothermal Turbulent Rotor-Stator Flows, *ISROMAC12*, Honolulu, 20 February 2008
9. Turbulent Von Kármán flow between two counter-rotating disks, *8th International Symposium on Experimental and Computational Aerothermodynamics of Internal Flows*, Lyon, 2 July 2007
10. Turbulent Von Kármán swirling flows, *11th European Turbulence Conference*, Porto, 27 June 2007
11. Numerical modeling of heat transfer and fluid flow in rotor-stator cavities with throughflow, *Euromech Fluid Mechanics Conference 6*, Stockholm, 27 June 2006
12. Crossflow instability in rotor-stator flows with throughflow, *Euromech Fluid Mechanics Conference 6*, Stockholm, 27 June 2006
13. Turbulence characteristics of the Bödewadt layer in a large shrouded rotor-stator system, *Conference on Turbulence and Interactions TI2006*, Porquerolles, 29 May 2006
14. Turbulence modelling and measurements in a rotor-stator system with throughflow, *6th Int. Symp. on Engng Turbulence Modelling and Measurements*, Villasimius (Italy), 25 May 2005
15. Study of the entrainment coefficient of the fluid in a rotor-stator cavity, *6th European Turbomachinery Conference - Fluid Dynamics and Thermodynamics*, Lille, 8 March 2005

Presentations in National Conferences

1. Effets des conditions de glissement sur l'écoulement de Bödewadt d'un fluide de type Reiner-Rivlin, *20e Congrès Français de Mécanique*, Besançon, 2 September 2011
2. Benchmark numérique des écoulements de Couette-Taylor turbulents, *20e Congrès Français de Mécanique*, Besançon, 30 August 2011
3. Études numériques d'écoulements confinés en rotation, *Journée de la SFT - Groupe "Modes de transfert - Convection"*, Paris, 21 June 2011
4. Simulation numérique directe des écoulements rotor-stator en cavité annulaire, *XIXe Congrès Français de Mécanique*, Marseilles, 26 August 2009
5. Instabilities and turbulence in rotating disk flows, *Journée ERCOFTAC SIG 36 "Swirling flows"*, ENSEEIHT, Toulouse, 23 October 2007
6. Instabilité d'une couche de cisaillement au-dessus d'un disque en rotation, *18^{eme} Congrès Français de Mécanique*, Grenoble, 29 August 2007
7. Sur les écoulements de disque tournant, *Colloque Interdisciplinaire des Écoles Centrale*, Marseilles, 1 June 2007.
8. Simulation des Grandes Échelles d'écoulements en cavité rotor-stator fermée, *GDR "Structure de la Turbulence et Mélange" & DYCOEC*, Marseilles, 21 May 2007
9. Écoulements de type rotor-stator soumis à un flux: de Batchelor à Stewartson, *GDR Structure de la Turbulence et Mélange*, Nantes, 10 November 2005
10. Écoulements tournants: de Batchelor à Stewartson, *17^{eme} Congrès Français de Mécanique*, Troyes, 1 September 2005

Posters

1. Numerical study of the transition in counter-rotating Taylor-Couette flow for a wide gap, *18th International Couette-Taylor Workshop ICTW18*, Twente, 24-26 June 2013 (best poster award)
2. Transferts de chaleur et de masse dans des écoulements turbulents de Taylor-Couette avec flux, *Congrès Français de Thermique SFT 2013*, Gerardmer, 28-31 May 2013
3. Transition mechanisms to turbulence in a cylindrical rotor-stator cavity by pseudo-spectral simulations of Navier-Stokes equations, *Chaos, Complexity and Transport*, Marseilles, 25 May 2011
4. Simulation numérique d'un écoulement de convection mixte en aval d'une marche, *14èmes Journées Internationales de Thermiques (JITH2009)*, Djerba, 28 March 2009
5. Modélisation de la turbulence dans un système de Taylor-Couette différentiellement chauffé avec flux axial, *14e Journées Internationales de Thermiques (JITH2009)*, Djerba, 28 March 2009
6. Écoulements tournants: de Batchelor à Stewartson, *Observer, Analyser, Modéliser, dans les milieux fluides complexes*, EGIM, Marseilles, 31 January 2005
7. Écoulements tournants: de Batchelor à Stewartson, *Journée de l'École Doctorale ED353*, Marseilles, 18 November 2004
8. Experimental study of rotor-stator flows with centripetal fluxes, *XXI International Congress of Theoretical and Applied Mechanics*, Warsaw, 20 August 2004

Consulting experience

- Reviewer for international journals (total of 66 papers): Energy and Buildings (6 articles), Phys. Fluids (5 articles), Int. J. Heat Fluid Flow, Int. J. Thermal Sciences, Progress in Computational Fluid Dynamics, Journal of Fluid Engineering (4 articles), Int. J. Comp. Meth., American Journal of Fluid Dynamics (3), Experiments in Fluids, Computers and Mathematics with Applications, Int. J. Numerical Methods for Heat and Fluid Flow, Int. J. Physical Sciences, Eur. J. Phys. Plus, J. Thermal Sci., The Scientific World Journal (2), Rheologica Acta, Langmuir, J. Porous Media, ZAMM, Mechanics & Industry, J. Taiwan Institute of Chemical Engineers, Int. J. Thermodynamics, Int. J. Numerical Methods in Fluids, J. Zhejiang University-SCIENCE A, Applied Thermal Engineering, Sky J. Mech. Electrical Electronics Eng., Int. J. Fluid Mechanics Research, Chem. Eng. Research & Design, Int. J. Mechanical Sciences, Adv. Chem. Eng., Int. J. Eng. Technology Innovation, Int. J. Phys. Sci., J. Fluid Mech., Chem. Eng. J. (1)
- Reviewer for national or international conferences (total of 7): Congrès Français de Mécanique 2007 (1), 2009 (2), Congrès Français de Thermique SFT 2011 (2), Transactions ASME 2008 (1), 2014 (2)
- "La Recherche" prize (2010), CIFRE fundings (2011), Executive Agency for Higher Education, Research, Development and Innovation Funding (UEFISCDI) of Romania (2 projects in 2011, 8 in 2013), PEERS projects of AIRD (3 projects, 2011-2013), National Science Center of Poland (1 project, 2012), ANR blanche (1 project in 2013)

Trainings

- *Fortran 95*, IDRIS, Orsay, December 2003
- *Carbon balance*, ADEME, Marseilles, 17-18 November 2010
- *Lighting and energy efficiency*, CM3E, Marseilles, 30 March 2011
- *STAR CCM+* software, Marseilles, 31 May 2011

Miscellaneous

- Stay at the University of de Manchester in the “School of Mechanical, Aerospace and Civil Engineering” Department, with the Prof. B.E. Launder, 3D unsteady structures in turbulent rotor-stator flows, November 2007
- Chairman of the “Technology and Science I” session, IJAS Conference, Aix-en-Provence, 7 June 2011

R É P U B L I Q U E F R A N Ç A I S E

Ministère de l'éducation nationale, de l'enseignement supérieur et de la recherche

UNIVERSITÉ AIX-MARSEILLE I

DOCTORAT
GRADE DE DOCTEUR

Vu le code de l'éducation

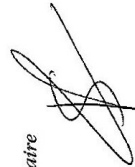
Vu l'arrêté du 25 avril 2002 relatif aux études doctorales

Vu le procès-verbal du jury attestant que l'intéressé a soutenu, le 3 octobre 2005 une thèse portant sur le sujet suivant : ECOULEMENTS DE TYPE ROTOR-STATOR SOUMIS A UN FLUX AXIAL : DE BATCHELOR A STEWARTSON devant un jury présidé par CLAUDE CAMBON, DIRECTEUR DE RECHERCHE et composé de MARIE-PIERRE CHAUVE, DIRECTEUR DE RECHERCHE, GEORGES A. GEROLYMOS, PROFESSEUR DES UNIVERSITES, JEAN-FRANCOIS PINTON, DIRECTEUR DE RECHERCHE, CLAUDE REY, PROFESSEUR DES UNIVERSITES, ROLAND SCHIESTEL, DIRECTEUR DE RECHERCHE

Vu la décision dudit jury prononçant l'admission de l'intéressé avec la mention très honorable avec félicitations

le Doctorat de l'Université SYSTEMES COMPLEXES : PHENOMENES HORS EQUILIBRE ; MICRO ET NANO ELECTRONIQUE est délivré à **M. SEBASTIEN PONCET** né le 26 janvier 1979 à FEURS (042) pour en jouir avec les droits et prérogatives qui y sont attachés et confère le grade de docteur.

Le titulaire



N° A I M A I 5 9 5 0 4 4 1
/2006200401312

Le Président



Paul TORDO

Fait à Aix en Provence, le 3 avril 2006

Le Recteur d'Académie
Chancelier des universités



Jean-Paul de GAUDEMAR

Figure 2.1: Diploma of my PhD thesis from the University of Aix-Marseille I, defended the 3rd of October 2005.



3 Place Victor Hugo
13331 MARSEILLE CEDEX 3

UNIVERSITE DE PROVENCE (AIX-MARSEILLE I)

Ecole Doctorale : Physique, Modélisation et Sciences
pour l'Ingénieur

Discipline : Systèmes Complexes : Phénomènes hors-
équilibre, micro et nano électronique

DIPLÔME Doctorat d'Université
 Doctorat d'Etat

RAPPORT DE SOUTENANCE

Nom et Prénom de l'Etudiant : Monsieur PONCET Sébastien, Pierre-Henry

Date de l'épreuve : le lundi 03 octobre 2005

Sujet : ECOULEMENTS DE TYPE ROTOR-STATOR SOUMIS A UN FLUX AXIAL : DE
BACHELOR A STEWARTSON

Rapport du Jury : M. Sébastien Poncet a présenté un travail d'une très grande
ampleur et qualité, à la fois expérimental et numérique, sur la turbulence et les
instabilités. Ces différents aspects ont tous été très bien maîtrisés et intégrés dans un
travail qui a demandé beaucoup d'autonomie et de dynamisme. L'exposé oral a bien
synthétisé l'étude, qui représente une avancée dans le domaine, tant sur les aspects
fondamentaux que sur les applications. Les réponses aux nombreuses questions du jury ont
confirmé la grande honnêteté du candidat et sa vaste culture scientifique.
En conséquence, la mention avec félicitations a été accordée à l'unanimité, et
le jury propose que ce travail soit soumis pour concourir à un prix de thèse.

Décision du Jury : DIPLOME Accordé.....
(accordé ou refusé)

Mention accordée Très honorable avec félicitations.....
(Pour les Doctorats la mention peut être : Honorable, Très honorable, Très honorable avec Félicitations)

NOMS DES MEMBRES DU JURY ET SIGNATURES


Monsieur SCHIESTEL Roland	<i>R. Schiestel</i>
Monsieur CHAUVE Marie-Pierre	<i>M. Chauve</i>
Monsieur PINTON Jean-François	<i>J. Pinton</i>
Monsieur GEROLYMOS Georges A.	<i>G. Gerolymos</i>
Monsieur CAMBON Claude	<i>C. Cambon</i>
Monsieur REY Claude	<i>C. Rey</i>

Marseille, le 03.10.2005
Le Président du Jury :
(NOM et SIGNATURE)

Claude CAMBON

Figure 2.2: Report of my PhD defence (IRPHE, 2005).

CFM '07
 18 - CONGRES FRANÇAIS DE MECANIQUE
 DU 27 AU 31 JUIN 2007
 DOMAINE UNIVERSITAIRE
 DE GRENOBLE



PRIX de THÈSE

Le Prix de thèse 2007 a été décerné à :

Fabien AMIOT

Pour son mémoire intitulé :

« *Mesure de champ à l'échelle micrométrique pour l'identification d'effets mécaniques surfaciques* »

Soutenu le 14/12/05 à l'ENS Cachan – Spécialité : Mécanique, Génie-mécanique, Génie-civil.
 Directeurs : Jean-Pierre ROGER et François HILD.

Christel METIVIER

Pour son mémoire intitulé :

« *Instabilités thermoconvectives pour des fluides viscoplastiques* »


Soutenu le 08/12/06 à l'INPL – Spécialité : Mécanique.
 Directeur : Chérif NOUAR.

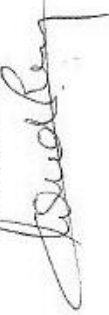
Sébastien PONCET

Pour son mémoire intitulé :

« *Ecoulement de type rotor-stator soumis à un flux axial : de Batchelor à Stewartson* »

Soutenu le 03/12/05 à l'Université de Provence – Spécialité : Physique, Modélisation et SPI
 Directeurs : Marie-Pierre CHAUVE et Roland SCHIESTEL.

Dr. Jacqueline ETAY
 Présidente du CFM'07


Pr. Claude REY
 Président du Jury



Pr Alain CIMETIERE
 Président du Groupe Universitaire de l'AFM


Figure 2.3: PhD prize of the AUM/AFM received after the French Congress of Mechanics held in Grenoble (2007).

Teaching activities

The following section describes my teaching activities from an accounting point of view.

Details of the teaching activities

I am assistant professor since 2006 with most of my teaching activities in the Thermal Engineering and Energy Department (GTE) of the Aix-Marseille University Institute of Technology (IUT). I teach also two courses at the Master 2 level in process engineering at the Aix-Marseille University: one dealing with two-phase flows and one being an introduction course to turbulence. It represents an average of 315.2 HETD (french equivalent of one hour of exercises) per year since 2006.

The distribution in terms of courses, exercises, practical works, internship supervision and administrative responsibilities is shown in Figure 2.4 for each year since 2006.

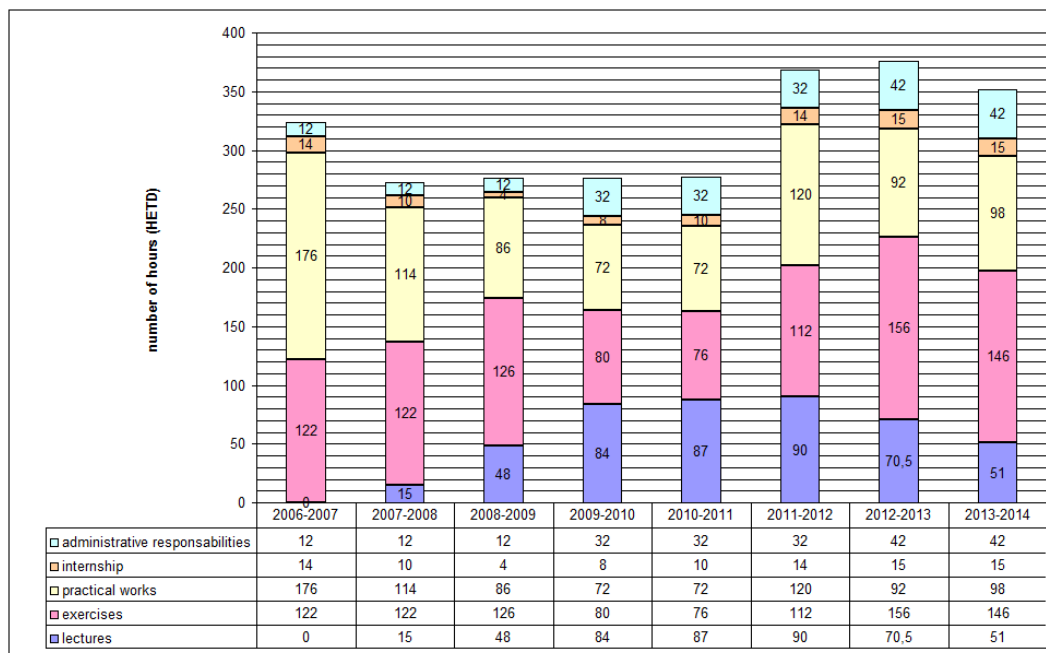


Figure 2.4: Histogram showing the distribution in terms of lectures, exercises and practical works and the total amount of teaching hours converted in HETD (french equivalent of one hour of exercises) since 2006.

These courses are provided mainly at the IUT GTE (L1-L2) as shown on Figure 2.5 with only 5% provided at the Master 2 level for the period 2006-2014. There are two main reasons for that: I started to teach in Master 2 only in 2009 and these two courses are optional and so do not open each year. This distribution changed to 13% of courses in Master 2 and 87% at the IUT GTE for the year 2011-12 as example.

One can also decompose the teaching activities according to the national section (section CNU) to which they can be attached (Fig.2.5b): 56% for the section 62 (thermodynamics, thermal engineering, air treatment), 43% for the section 60 (fluid mechanics, resistance of materials and solid mechanics, acoustics) and 1% for the section 61 (automatism).

The strong spots of my teaching activities can be summed up as follows:

- **Thermodynamics:** course for 1-year students at the IUT GTE (lectures=24h, exercises=28h, practical works=24h). In this course, the basic concepts in thermodynamics are tackled: different forms of energy, concepts of thermodynamic pressure and temperature, perfect gas law ... The first principle is written for closed, open and isolated (calorimetry) systems. Students tackle the concept of thermodynamic cycle thanks to the four elementary transformations (isothermal,

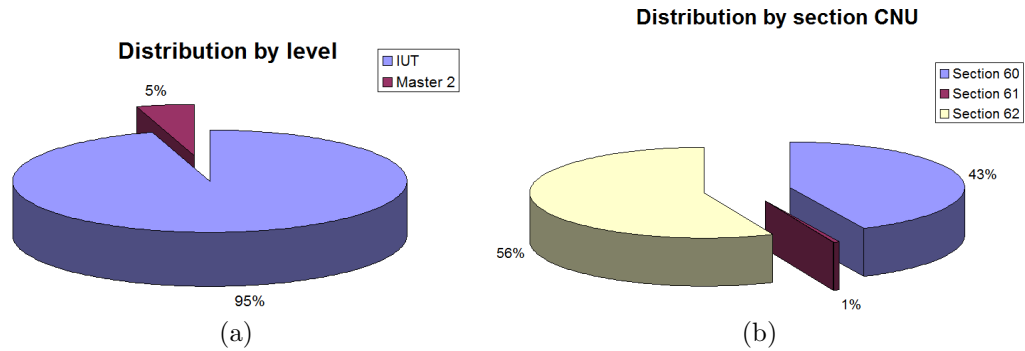


Figure 2.5: Distributions of my teaching activities by (a) level or by (b) section CNU.

isobaric, isovolumetric, adiabatic). The necessity of a second principle of evolution is demonstrated. On that occasion, I wrote lecture course notes (95 pages), a collection of 127 exercises and developed a practical work based on the software CyclePad used to study thermodynamic cycles (Carnot and Beau de Rochas cycles).

- Fluid mechanics:** course for 2-year students at the IUT GTE (lectures=12h, exercises=10h, practical works=12h). This course is divided into two parts: an introduction to rheology and a more detailed part dedicated to compressible fluid flows. In the first part, all types of non-Newtonian fluids are discussed together with the main rheological laws and a description of the main rheometers and experimental techniques (47 slides and 14 exercises). In the second part, various concepts are tackled: speed of sound, the limit of the incompressibility assumption, 1D isentropic flows of compressible perfect fluid (Barré de Saint-Venant equations, Hugoniot theorems), straight and oblique shock waves, flows in nozzles and in wind tunnels (25 pages of lecture notes and 15 exercises). I developed three practical works: one on the rheological characterization of everyday life fluids using a rheometer of Couette type, one on rotating flows where students highlight the different characteristic times, the Taylor-Proudman theorem . . . and one on the hydraulic jump (circular on in a channel with a free surface) for which a strong analogy with compressible fluid flows may be done.
- Two-phase flows:** courses at the Master 2 level in process engineering (lectures=12h, exercises=4h). This course is written for students having a strong background in process engineering and in chemistry but a weak background in fluid mechanics. It is then very phenomenological. Through 103 slides, one presents first some industrial applications including multiphase flows, some reminders on the basic fluid mechanics concepts, all configurations for two-phase flows in vertical and horizontal pipes with or without heat transfer (mainly through flow maps) and then the main experimental techniques dedicated specifically to the study of multiphase flows. In the second part of this course (not available in an electronic format), one introduces the Favre average decomposition and the concept of phase weighted average. It enables to write the continuity, fluid motion and energy equations for the mixture. Two models, the homogeneous model and the separated phase model, are finally discussed in details. A collection of 16 exercises is used to apply the concepts tackled in the course.
- Turbulent flows:** courses at the Master 2 level in process engineering (lectures=12h, exercises=4h). As for the course on “two-phase flows”, this course is very phenomenological. After some concrete examples of turbulent flows and a brief historical overview, the different mechanisms for the transition to turbulence are discussed. One presents then the main properties of turbulence. One introduces the different statistical tools used to analyse turbulent flows before establishing the one-point statistical equations (Reynolds average decomposition). Different flow configurations are then classified according to the nature of turbulence: homogeneous turbulence, open and confined flows. This course ends by a brief description of the main experimental and numerical (DNS, LES, RANS models) approaches used to investigate turbulent flows. The

lecture is based on a presentation composed of 183 slides and is accompanied by a collection of 17 exercises.

All the duplicated notes of the lectures, exercises and practical works I developed as well as all the exams are available online (in French) on my website on the “Teaching” page:

<http://l3mmp.l3m.univ-mrs.fr/site/SitePersoPoncet/teaching.html>

I also wrote lecture course notes about automatism and regulation. I provided this course only one year for 3-year students in the Bachelor’s degree (vocational Bachelor’s degree on management and maintenance of energy systems, L3 pro GMIE). It is not available in an electronic format.

Between 2002 and 2005, I provided some courses during my PhD thesis for a total amount of 242 HETD distributed as follows:

- lectures, exercises and practical works on the finite difference method, 1-year engineer, ISITV (Institut des Sciences de l’Ingénieur de Toulon et du Var, marine engineering option), 2002-05 (90 h). I had the opportunity to develop some practical works on that topic using Matlab;
- exercises in fluid mechanics, 1-year engineer, ISITV (marine engineering), 2002-03 (25 h);
- practical works in solid mechanics and resistance of materials, 1-year IUT GTE, Marseilles, 2004-05 (29 h);
- practical works in fluid mechanics, 1-year IUT GTE, Marseilles, 2004-05 (29 h);
- practical works in heat transfer, 2-year engineer, Ecole Polytechnique Universitaire de Marseille, 2004-05 (36 h);
- practical works in solid mechanics and resistance of materials, 1-year engineer, Ecole Polytechnique Universitaire de Marseille, 2003-04 (36 h);
- exercises in algorithmic in C language, 2-year engineer, Ecole Supérieure de Mécanique de Marseille (ESM2), 2003-04 (10.5 h);
- practical works in fluid mechanics, 1-year engineer, Ecole Généraliste d’Ingénieurs de Marseille (EGIM), 2003-04 (45 h).

I have been then assistant lecturer (demi-ATER in french) between 2005 and 2006 at IUT GTE where I have been in charge of exercises and practical works in thermodynamics, fluid mechanics, solid mechanics and mechanics of materials for the first and second year students for a total amount of 97 HETD.

Administrative responsibilities

- In charge of the Bachelor degree (second year) at the IUT GTE since 2010. It consists in organizing and managing the second year at the IUT GTE in in-house training: to make up of the groups, to organize two jurys, to promote the continuation through higher education . . .
- In charge of the Bachelor degree (indenture) at the IUT GTE since 2010. It consists in organizing and managing (teachers, students, companies) the second year at the IUT GTE in professionalization contract. This vocational training does not open every year.
- In charge of the public relations at the IUT GTE between 2006 and 2009. The main assignments are to promote the department through student forums and to organize the open doors day and the “Rencontres du Futur Bachelier”.

Other activities

- Writing of lecture course notes on Energy and of specific sheets about all forms of energy for the École Nationale des Techniciens de l’Équipement (ENTE), Aix-en-Provence, 2012.
- Recruitment mission DGBS-ADIUT-CNOUS in Gabon, May-June 2009.

Part II

Numerical modeling

Part II: Numerical modeling

Summary: The results presented in this thesis have been obtained most of the time numerically by Direct Numerical Simulation (DNS) for transitional regimes or by Reynolds-Averaged Navier-Stokes modeling (RANS) or Large Eddy Simulation (LES) for turbulent regimes. The numerical methods and the turbulence modeling are presented here briefly to ease the sections dedicated to the flow and heat transfer analysis. The two DNS solvers as well as their extension to LES are described in Chapter 3. Some numerical developments including the treatment of the axis singularity and the extension to a multidomain version made during the PhD theses of N. Peres and G. Fontaine respectively are also briefly presented. Chapter 4 sums up the main ingredients of the innovative Reynolds Stress Model of Elena and Schiestel [85] widely used in the following chapters.

3D High-order numerical methods

For many years now, the M2P2 laboratory develops an highly accurate in-house code dedicated to the direct numerical simulation (DNS) or large eddy simulation (LES) of confined rotating flows [269, 313, 316]. It is based on a pseudospectral method using Chebyshev polynomials in the non homogeneous directions and Fourier series in the tangential direction. It has been widely validated in various rotating flow arrangements including rotor-stator disk flows [260, 261, 266, 309, 310, 311, 312, 314, 315], Taylor-Couette flows [63, 65, 338] or rotating cavities with throughflow [344]. This code in its DNS then LES version as well as the recent developments by Peres [241] and Fontaine [97] during their PhD theses, that I co-supervised with E. Serre, are described briefly below. A second code will also be used in the following chapters. It is an extension of the former version of Abide and Viazzo [3] developed for turbulent flows in a Cartesian frame. Both codes are based on the same methods. They share the same time discretization but not the same spatial ones. The spatial discretizations in the non homogeneous directions are achieved in the second code by compact finite-difference schemes.

3.1 Geometrical modeling

Let's first introduce the parameters of a typical rotor-stator cavity (see in Fig.3.1) between two disks of outer radius b : one rotating at a constant rotation rate Ω , while the other is at rest. They are confined between two cylinders: the inner one of radius a being attached to the rotor and the outer one to the stator. The interdisk spacing is denoted h , so that one can define the following geometrical parameters:

- the curvature parameter: $R_m = (b + a)/(b - a)$, which is usually replaced by the radius ratio $\eta = a/b$ when dealing with Taylor-Couette flows between cylinders;
- the aspect ratio of the cavity defined either as $G = (b - a)/h$ (denoted also L) or as $\Gamma = h/(b - a)$.

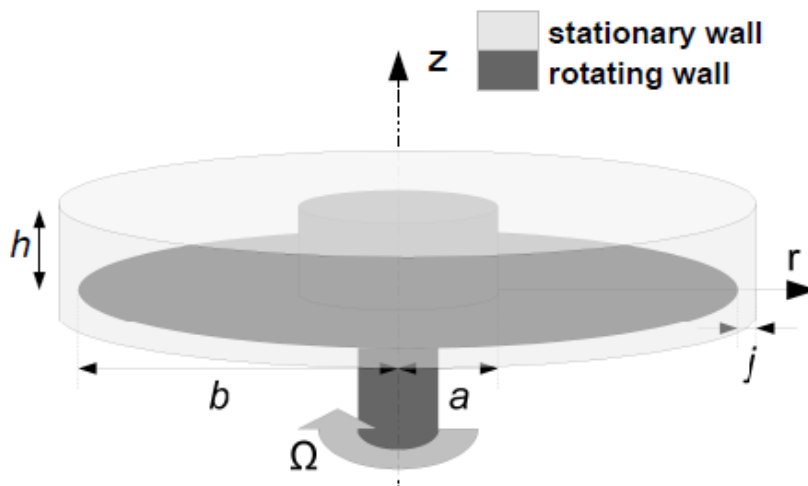


Figure 3.1: Schematic representation of an annular enclosed rotor-stator device with relevant notation.

In an enclosed cavity, the rotational Reynolds number $Re = \Omega b^2/\nu$ based on the maximum velocity Ωb reached within the cavity may be also chosen as a flow control parameter.

3.2 Conservation equations

The flow is governed by the three-dimensional incompressible Navier-Stokes equations written in a fixed frame of reference for the velocity-pressure formulation together with the continuity equation and appropriate boundary conditions. The components of the velocity vector \mathbf{V} are denoted u , v and w in the cylindrical coordinate system (r, θ, z) and P is the static pressure. In the domain D of border ∂D , the equations can be written as:

$$\rho \left(\frac{\partial \mathbf{V}}{\partial t} + (\mathbf{V} \cdot \nabla) \mathbf{V} \right) = -\nabla P + \mu \Delta \mathbf{V} + \mathbf{F} \quad \text{in } D \quad (3.1)$$

$$\nabla \cdot \mathbf{V} = 0 \quad \text{in } D \quad (3.2)$$

where t is time and \mathbf{F} represents a given body force.

Appropriate boundary conditions of Dirichlet type for the velocity vector can be written in a general way:

$$\mathbf{V} = \mathbf{W} \quad \text{on } \partial D \quad (3.3)$$

Δ is the vectorial Laplacian operator written for cylindrical coordinates:

$$(\Delta V)_r = \nabla^2 u - \frac{u}{r^2} - \frac{2}{r^2} \frac{\partial v}{\partial \theta} \quad (3.4)$$

$$(\Delta V)_\theta = \nabla^2 v - \frac{v}{r^2} + \frac{2}{r^2} \frac{\partial u}{\partial \theta} \quad (3.5)$$

$$(\Delta V)_z = \nabla^2 w \quad (3.6)$$

$$\nabla^2 = \frac{\partial^2}{\partial r^2} + \frac{1}{r} \frac{\partial}{\partial r} + \frac{1}{r^2} \frac{\partial^2}{\partial \theta^2} + \frac{\partial^2}{\partial z^2} \quad (3.7)$$

The scales for the dimensionless variables of space, time and velocity are h , Ω^{-1} and ΩR respectively. (\bar{r}, \bar{z}) denote the dimensionless space variables (r, z) mapped into the square $[-1, 1] \times [-1, 1]$ as $\bar{r} = (r/G - R_m)$ and $\bar{z} = z$. It is a requisite for the use of Chebyshev polynomials. Thus, the domain \bar{D} can be defined as $\bar{D} = \{(r, \theta, z) \in [-1, 1] \times [0, 2\pi] \times [-1, 1]\}$. Dimensionless equations for continuity and each velocity components write:

$$\frac{1}{G} \frac{\partial u}{\partial r} + \frac{u}{Gr} + \frac{1}{Gr} \frac{\partial v}{\partial \theta} + \frac{\partial w}{\partial z} = 0 \quad \text{in } D \quad (3.8)$$

$$\frac{Re}{G^2} \frac{\partial u}{\partial t} + \frac{Re}{G} (\mathbf{V} \cdot \nabla) u = -\frac{Re}{2G^2} \frac{\partial p}{\partial r} + \left[\nabla^2 u - \frac{u}{G^2 r^2} - \frac{2}{G^2 r^2} \frac{\partial v}{\partial \theta} \right] \quad \text{in } D \quad (3.9)$$

$$\frac{Re}{G^2} \frac{\partial v}{\partial t} + \frac{Re}{G} (\mathbf{V} \cdot \nabla) v = -\frac{Re}{2G} \frac{\partial p}{\partial \theta} + \left[\nabla^2 v - \frac{v}{G^2 r^2} + \frac{2}{G^2 r^2} \frac{\partial u}{\partial \theta} \right] \quad \text{in } D \quad (3.10)$$

$$\frac{Re}{G^2} \frac{\partial w}{\partial t} + \frac{Re}{G} (\mathbf{V} \cdot \nabla) w = -\frac{Re}{2G} \frac{\partial p}{\partial z} + \nabla^2 w \quad \text{in } D \quad (3.11)$$

The advection terms are given by:

$$(\mathbf{V} \cdot \nabla) u = \frac{1}{G} u \frac{\partial u}{\partial r} + \frac{1}{G} \frac{v}{r} \frac{\partial u}{\partial \theta} + w \frac{\partial u}{\partial z} - \frac{v^2}{Gr} \quad (3.12)$$

$$(\mathbf{V} \cdot \nabla) v = \frac{1}{G} v \frac{\partial v}{\partial r} + \frac{1}{G} \frac{v}{r} \frac{\partial v}{\partial \theta} + w \frac{\partial v}{\partial z} + \frac{vu}{Gr} \quad (3.13)$$

$$(\mathbf{V} \cdot \nabla) w = \frac{1}{G} u \frac{\partial w}{\partial r} + \frac{1}{G} \frac{v}{r} \frac{\partial w}{\partial \theta} + w \frac{\partial w}{\partial z} \quad (3.14)$$

and the Laplacian operator ∇^2 can be rewritten as:

$$\nabla^2 = \frac{1}{G^2} \frac{\partial^2}{\partial r^2} + \frac{1}{G^2 r^2} \frac{\partial}{\partial r} + \frac{1}{G^2 r^2} \frac{\partial^2}{\partial \theta^2} + \frac{\partial^2}{\partial z^2} \quad (3.15)$$

When thermal effects are considered, the following dimensionless energy equation is also solved:

$$\frac{Re}{G^2} \frac{\partial T}{\partial t} + \frac{Re}{G} (\mathbf{V} \cdot \nabla) T = \frac{1}{Pr} \Delta T \quad \text{in } D \quad (3.16)$$

where the temperature normalization has been made with respect to $2(T^* - T_0^*)/\Delta T$ with $\Delta T = T_{max}^* - T_{min}^*$, T_0^* being a reference temperature. $Pr = \nu/\alpha$ is the Prandtl number, with ν the kinematic viscosity and α the thermal diffusivity of the fluid. Buoyancy effect has been modeled using the Boussinesq approximation, assuming linear variations of the density ρ with temperature in the gravity term only such as:

$$\rho = \rho_0 [1 - \beta_0 (T^* - T_0^*)] \quad (3.17)$$

with β_0 the thermal expansion coefficient and ρ_0 the density at T_0 .

This coupling leads to a new force term $F = (RaGT)/(2PrRe)$ in the axial component of the velocity (Eq. 3.11), controlled by the Rayleigh number defined as $Ra = h^3 \Delta T \beta_0 g / (\nu \alpha)$. Centrifugal buoyancy effects are here neglected. This assumption is generally valid for low values of the Froude number $Fr = \Omega^2 b / g$ as in Chapter 10, where the maximum value of the Froude number is around 0.03.

Very recently, Lopez et al. [188] developed a new Boussinesq-type approximation accounting for centrifugal buoyancy effects by keeping the density variations in the advection term of the Navier-Stokes equations. This approximation appears to be relevant in various situations including flows with differential rotation, high Rayleigh numbers, strong vortices ... Taking into account centrifugal buoyancy effects appears necessary, for example, to extend the results presented in Chapter 8 in the case of non-isothermal turbulent rotor-stator flows. The approximation proposed by Lopez et al. [188] could be easily implemented in the present solvers in a close future.

3.3 Projection scheme for time-discretization

The velocity-pressure coupling is solved using the 3D projection algorithm proposed by Raspo et al. [269]. It is based on a semi-implicit second-order scheme that combines an implicit backward Euler scheme for the diffusive terms and an explicit Adams-Bashforth extrapolation for the convective non-linear terms as expressed below:

$$\begin{cases} \frac{3\mathbf{V}^{n+1} - 4\mathbf{V}^n + \mathbf{V}^{n-1}}{2\delta t} + 2(\mathbf{V}^n \cdot \nabla) \mathbf{V}^n - (\mathbf{V}^{n-1} \cdot \nabla) \mathbf{V}^{n-1} = -\nabla P^{n+1} + \frac{1}{Re} \Delta \mathbf{V}^{n+1} + \mathbf{F}^{n+1} & \text{in } D \\ \nabla \cdot \mathbf{V}^{n+1} = 0 & \text{in } D \\ \mathbf{V}^{n+1} = \mathbf{W}^{n+1} & \text{on } \partial D \end{cases} \quad (3.18)$$

Just as in the classical projection scheme, initially proposed by Goda [111] for finite-element approximations, a velocity predictor is calculated from Equation (3.18). But here the projection method introduces a preliminary step computing a preliminary pressure \bar{P}^{n+1} from the Poisson equation, derived from the Equation (3.18) applying the incompressibility condition and associated to Neumann boundary conditions in which the diffusion term $\Delta \mathbf{V}^{n+1}$ is approximated using an Adams-Bashforth scheme as mentioned above. The elliptic problem to solve is therefore:

$$\begin{cases} \nabla^2 \bar{P}^{n+1} = \nabla \cdot [-2(\mathbf{V}^n \cdot \nabla) \mathbf{V}^n + (\mathbf{V}^{n-1} \cdot \nabla) \mathbf{V}^{n-1} + \mathbf{F}^{n+1}] & \text{in } D \\ \frac{\partial \bar{P}^{n+1}}{\partial n} = \vec{n} \cdot \left[\frac{-3\mathbf{W}^{n+1} + 4\mathbf{V}^n - \mathbf{V}^{n-1}}{2\delta t} - 2(\mathbf{V} \cdot \nabla \mathbf{V})^n + (\mathbf{V} \cdot \nabla \mathbf{V})^{n-1} + \frac{1}{Re} (2\Delta \mathbf{V}^n - \Delta \mathbf{V}^{n-1}) + \mathbf{F}^{n+1} \right] & \text{on } \partial D \end{cases} \quad (3.19)$$

However this Poisson problem leads to an unstable algorithm. In order to satisfy the compatibility condition, the diffusion term has been decomposed into a solenoidal and an rotational part as proposed by Karniadakis et al. [147]. Since the velocity fields \mathbf{V}^n and \mathbf{V}^{n-1} are divergence free, the diffusion term is given by:

$$2\Delta \mathbf{V}^n - \Delta \mathbf{V}^{n-1} = -2\nabla \times \nabla \times \mathbf{V}^n + \nabla \times \nabla \times \mathbf{V}^{n-1} \quad (3.20)$$

the preliminary pressure \bar{P}^{n+1} is then used to compute the predicted velocity field \mathbf{V}^* . This velocity field is obtained implicitly from Equation (3.18) in which the pressure gradient at the current time step t_{n+1} is now replaced by the gradient of the preliminary pressure \bar{P}^{n+1} as:

$$\begin{cases} \frac{3\mathbf{V}^* - 4\mathbf{V}^n + \mathbf{V}^{n-1}}{2\delta t} + 2(\mathbf{V}^n \cdot \nabla)\mathbf{V}^n - (\mathbf{V}^{n-1} \cdot \nabla)\mathbf{V}^{n-1} = -\nabla\bar{P}^{n+1} + \frac{1}{Re}\Delta\mathbf{V}^* + \mathbf{F}^{n+1} & \text{in } D \\ \mathbf{V}^* = \mathbf{W}^{n+1} & \text{on } \partial D \end{cases} \quad (3.21)$$

The velocity field \mathbf{V}^* is then corrected taking into account the pressure gradient, $\nabla(P^{n+1})$ at the current time step t_{n+1} . This step, defined as a projection step, makes it possible to obtain a velocity field that respects the incompressibility constraint and is described as:

$$\begin{cases} \frac{3}{2\delta t}(\mathbf{V}^{n+1} - \mathbf{V}^*) = -\nabla(P^{n+1} - \bar{P}^{n+1}) & \text{in } \bar{D} \\ \nabla \cdot (\mathbf{V}^{n+1}) = 0 & \text{in } D \\ \mathbf{V}^{n+1} \cdot \vec{n} = \mathbf{W}^{n+1} \cdot \vec{n} & \text{on } \partial D \end{cases} \quad (3.22)$$

This step is performed by computing a pseudo-pressure $\phi = 2\delta t(P^{n+1} - \bar{P}^{n+1})/3$ from an elliptic problem applying the incompressibility constraint with the respective boundary conditions defined by:

$$\begin{cases} \nabla^2\phi = \nabla \cdot \mathbf{V}^* & \text{in } D \\ \frac{\partial\phi}{\partial n} = 0 & \text{on } \partial D \end{cases} \quad (3.23)$$

Finally, the velocity and pressure fields are obtained from:

$$\begin{cases} \mathbf{V}^{n+1} = \mathbf{V}^* - \nabla\phi & \text{in } \bar{D} \\ P^{n+1} = \bar{P}^{n+1} + \frac{3}{2\delta t}\phi & \text{in } \bar{D} \end{cases} \quad (3.24)$$

Projection schemes induce a spurious slip velocity on the boundary since the tangential boundary conditions on the velocity are not prescribed in the projection step. This slip velocity is expressed in 3D as $\mathbf{V}_s = \mathbf{n} \times ((\mathbf{V}^{n+1} - \mathbf{W}^{n+1}) \times \mathbf{n})$ where \mathbf{n} is the unit normal vector to ∂D . By allowing the correct temporal evolution of the normal pressure gradient at the boundaries during the time integration, numerical results have shown that such calculation significantly improved the accuracy of the scheme by reducing the error of the slip velocity by about one order at the walls to $O(\delta t^3)$ [269].

3.4 Space approximations

3.4.1 Pseudospectral method

All variables $\Psi = (u, v, w, p, \phi)$ are spatially discretized using the collocation-Chebyshev method for both non-homogeneous directions (r, z) and the Fourier-Galerkin approximation in the azimuthal direction θ . In three-dimensions, a numerical solution is thus sought in the form of the following truncated series:

$$\Psi_{NKM}(\bar{r}, \theta, \bar{z}) = \sum_{k=-K/2}^{K/2-1} \sum_{n=0}^N \sum_{m=0}^M \hat{\Psi}_{nkm} T_n(\bar{r}) T_m(\bar{z}) e^{ik\theta} \quad (3.25)$$

where T_n and T_m are Chebyshev polynomials of highest degrees N and M respectively. (\bar{r}, \bar{z}) denote the dimensionless space variables (r, z) mapped into the square $[-1, 1] \times [-1, 1]$. N and M correspond to the number of Gauss-Lobatto collocation points. K is the cut-off frequency of the Fourier series that corresponds to $K/2$ modes. The explicit non-linear terms are calculated using the pseudospectral techniques described in [244] where the derivatives in each space direction are calculated in the spectral space and the products are performed in the physical one. The derivatives of implicit diffusion terms are all performed in the physical space using matrix products.

The coupling between the two first components of the vectorial cylindrical Laplacian (Eqs. (3.4, 3.5)) usually requires to split the operator into an implicit and explicit part that leads to time-step limitations. Therefore, the following variable transformation [230] is introduced:

$$u_+ = u + iv, \quad u_- = u - iv \quad (i^2 = -1) \quad (3.26)$$

that makes the Laplacian diagonal:

$$(\Delta V)_+ = \left(\nabla^2 - \frac{1}{r^2} + \frac{2i}{r^2} \frac{\partial}{\partial \theta} \right) u_+ \quad (3.27)$$

$$(\Delta V)_- = \left(\nabla^2 - \frac{1}{r^2} - \frac{2i}{r^2} \frac{\partial}{\partial \theta} \right) u_- \quad (3.28)$$

$$(\Delta V)_z = \nabla^2 w \quad (3.29)$$

Such a transformation requires the reorganization in the complex plane of the Fourier coefficient matrix $\widehat{\Psi}$ as follows:

$$\widehat{\Psi} = \begin{cases} \left(\widehat{\Psi}_{j, \frac{K}{2}+k} \right), & k = 1, \\ \left(\widehat{\Psi}_{j, \frac{K}{2}+k} + i\widehat{\Psi}_{j, k-1} \right), & k = 2, \dots, K/2 \end{cases} \quad (3.30)$$

for $1 \leq j \leq N \times M$. It must be noted that the Fourier mode $K/2$ has been set to zero [244] as previously mentioned. According to Equation (3.26), the spectral matrices \widehat{u}_+ and \widehat{u}_- are written as:

$$\widehat{u}_+ = \widehat{u} + i\widehat{v}, \quad \widehat{u}_- = \widehat{u} - i\widehat{v}, \quad (3.31)$$

that is to say,

$$\widehat{u}_+ = \begin{cases} \left(\widehat{u}_{j, \frac{K}{2}+k} + i\widehat{v}_{j, \frac{K}{2}+k} \right), & k = 1, \\ \left(\widehat{u}_{j, \frac{K}{2}+k} - \widehat{v}_{j, k-1} \right) + i \left(\widehat{u}_{j, k-1} + \widehat{v}_{j, \frac{K}{2}+k} \right), & k = 2, \dots, K/2 \end{cases} \quad (3.32)$$

$$\widehat{u}_- = \begin{cases} \left(\widehat{u}_{j, \frac{K}{2}+k} + i\widehat{v}_{j, \frac{K}{2}+k} \right), & k = 1, \\ \left(\widehat{u}_{j, \frac{K}{2}+k} + \widehat{v}_{j, k-1} \right) + i \left(\widehat{u}_{j, k-1} - \widehat{v}_{j, \frac{K}{2}+k} \right), & k = 2, \dots, K/2 \end{cases} \quad (3.33)$$

Finally, the coefficients $\widehat{u}_{j, \frac{K}{2}+k}$, $\widehat{u}_{j, k-1}$, $\widehat{v}_{j, \frac{K}{2}+k}$ and $\widehat{v}_{j, k-1}$ can be written for $1 \leq k \leq K/2$:

$$\begin{cases} \widehat{u}_{j, \frac{K}{2}+k} = \operatorname{Re} \left(\frac{\widehat{u}_+ + \widehat{u}_-}{2} \right), & \widehat{u}_{j, k-1} = \operatorname{Im} \left(\frac{\widehat{u}_+ + \widehat{u}_-}{2} \right) \\ \widehat{v}_{j, \frac{K}{2}+k} = \operatorname{Im} \left(\frac{\widehat{u}_+ - \widehat{u}_-}{2} \right), & \widehat{v}_{j, k-1} = \operatorname{Re} \left(\frac{\widehat{u}_+ - \widehat{u}_-}{2} \right) \end{cases} \quad (3.34)$$

The time-discretization and the Fourier-Galerkin approximation described above lead to a set of elliptic equations for each Fourier wave to be solved in a 2D domain depending on the two non-periodic directions (r, z) . Successive 2D Helmholtz and Poisson equations can be written as:

$$\Delta_{rz}^{(\Psi)} \widehat{\Psi}_k - \sigma^{(\Psi)} \widehat{\Psi}_k = \widehat{S}_k \quad (3.35)$$

for $1 \leq k \leq K/2$. $\Delta_{rz}^{(\Psi)}$ and $\sigma^{(\Psi)}$ are given for the different variables by:

$$\Delta_{rz}^{(\Psi)} = \nabla^2 - \frac{1}{r^2} \quad \text{for } \Psi = u_+, u_-, \quad (3.36)$$

$$\Delta_{rz}^{(\Psi)} = \nabla^2 \quad \text{for } \Psi = (w, P, \phi), \quad (3.37)$$

$$\sigma^{(\Psi)}(k, r) = \frac{(k+1)^2}{r^2} + \frac{3Re}{2\delta t} \quad \text{for } \Psi = u_+, \quad (3.38)$$

$$\sigma^{(\Psi)}(k, r) = \frac{(k-1)^2}{r^2} + \frac{3Re}{2\delta t} \quad \text{for } \Psi = u_-, \quad (3.39)$$

$$\sigma^{(\Psi)}(k, r) = \frac{k^2}{r^2} + \frac{3Re}{2\delta t} \quad \text{for } \Psi = w, \quad (3.40)$$

$$\sigma^{(\Psi)}(k, r) = \frac{k^2}{r^2} \quad \text{for } \Psi = (P, \phi) \quad (3.41)$$

The spectral derivatives of $\widehat{\Psi}_k$ in the radial and axial directions are expressed in terms of $\widehat{\Psi}_k(r_i, z_j)$ at the other collocation points with appropriate coefficients $d\bar{r}_{ij}^{(p)}$ and $d\bar{z}_{ji}^{(p)}$ [244] as follows:

$$\frac{\partial^p \widehat{\Psi}_k}{\partial r^p}(r_i, z_j) = \sum_{i=0}^N \left(\frac{1}{G}\right)^p d\bar{r}_{ij}^{(p)} \widehat{\Psi}_k(r_i, z_j), \quad (3.42)$$

$$\frac{\partial^p \widehat{\Psi}_k}{\partial z^p}(r_i, z_j) = \sum_{j=0}^M d\bar{z}_{ji}^{(p)} \widehat{\Psi}_k(r_i, z_j) \quad \text{with } p = 1, 2, \quad (3.43)$$

that can be expressed in matrix notation as:

$$\frac{\partial^p \widehat{\Psi}_k}{\partial r^p}(r_i, z_j) = D_r^{(p)} \Psi \quad (3.44)$$

$$\frac{\partial^p \widehat{\Psi}_k}{\partial z^p}(r_i, z_j) = \Psi \left(D_z^{(p)}\right)^T \quad (3.45)$$

If one denotes S the matrix $\left[\widehat{S}_k(r_i, z_j)\right]$, Equation (3.35) can be written in the matrix form:

$$A\Psi + \Psi B^T = S \quad (3.46)$$

with $A = D_r^{(2)} - \frac{1}{r}D_r^{(1)} - \sigma^{(\Psi)}I$ and $B = D_z^{(2)}$. It is noted that only B does not depend on the harmonic k . The Dirichlet boundary conditions are taken into account in S while the Neumann boundary conditions appear in A or B according to the direction. These 2D algebraic linear systems are solved directly using a fully diagonalization technique for each Fourier mode. This technique used by Raspo *et al.* [269] is summarized below.

If A is diagonalizable, there exists a matrix H_r such that:

$$\begin{cases} A = H_r \Lambda_r H_r^{-1} \\ H_r \Lambda_r H_r^{-1} \Psi + \Psi B = S \\ \Lambda_r \widetilde{\Psi} + \widetilde{\Psi} B = \widetilde{S} \end{cases} \quad (3.47)$$

with $\widetilde{\Psi} = H_r^{-1} \Psi$ and $\widetilde{S} = H_r^{-1} S$. The matrix H_r is formed by the eigenvectors and Λ_r the diagonal matrix of the corresponding eigenvalues $\lambda_{r,i}$. Similarly, if the matrix B is diagonalizable, there exists a matrix H_z such that:

$$\begin{cases} B = H_z \Lambda_z H_z^{-1} \\ \Lambda_r \widetilde{\Psi} + \widetilde{\Psi} H_z \Lambda_z H_z^{-1} = \widetilde{S} \\ \Lambda_r \widetilde{\Psi} + \widetilde{\Psi} \Lambda_z = \widetilde{S} \end{cases} \quad (3.48)$$

with $\bar{\Psi} = \tilde{\Psi}H_z$ and $\bar{S} = \tilde{S}H_z$. The matrix H_z is formed by the eigenvectors and Λ_z the diagonal matrix of the corresponding eigenvalues $\lambda_{z,j}$. The system (3.48) is equivalent to:

$$\bar{\Psi}_{ij} = \frac{\bar{S}_{ij}}{\lambda_{r,i} + \lambda_{z,j}}, \quad \text{for } i = 1, \dots, N-1 \quad \text{and} \quad j = 1, \dots, M-1 \quad (3.49)$$

where $\bar{\Psi}_{ij}$ and \bar{S}_{ij} are the elements of matrices $\bar{\Psi}$ and \bar{S} respectively. Finally knowing $\bar{\Psi}$, one gets Ψ from:

$$\begin{cases} \Psi = H_r \tilde{\Psi} \\ \Psi = H_r \bar{\Psi} H_z^{-1} \end{cases} \quad (3.50)$$

It should be noted that the matrix A may contain several complex eigenvalues on the three-dimensional Fourier modes that are easily taken into account by the formalism introduced in Eq. (3.30). The number of complex eigenvalues is mesh dependent and increases with finer meshes in the radial and azimuthal directions.

3.4.2 Compact finite-difference schemes

The main difference between the two DNS codes lies in the discretization of the equations in the non homogeneous radial and axial directions. This code is the cylindrical extension of the solver developed by Abide and Viazzo [3]. In both codes, Fourier approximations are used in the tangential direction.

The equations in the non homogeneous radial and axial directions are discretized by fourth-order compact finite-difference schemes. Hermitian methods provide compact relations between a given function and its derivatives in several neighboring points of the mesh grid. These relations are deduced from Taylor series expansions of the function and its derivatives. Such numerical schemes are relatively simple and easy to implement using only a reduced number of mesh points, while keeping a high order accuracy close to the one reached by spectral or pseudo-spectral methods [177]. Another advantage is their flexibility regarding the distribution of the mesh points.

Schiestel and Viazzo [300] have previously found that non-staggered grids cannot prevent oscillatory numerical wiggles in the pressure field. In order to circumvent the pressure checkerboarding, a staggered MAC (Marker And Cell) mesh developed by Welch *et al.* [351] is used. Each primitive variable is evaluated on its own grid. The main advantage is to reduce aliasing errors when using pseudo-spectral methods on staggered grids. The mesh is refined close to the walls but also in intense shear flow regions. The mesh point distribution is controlled through *tanh* functions including refinement coefficients. Instead of using a complex spatial approximation on a non-uniform mesh, an analytical coordinate transformation preserving the continuity of the first and second derivatives is introduced. These first and second derivatives are then approximated using a spatial scheme on an uniform mesh. As the pressure and the velocity components are evaluated on different meshes, the first derivatives in the non-linear terms of the Navier-Stokes equation have to be evaluated on the staggered but also on the non-staggered meshes. Some interpolations are then necessary. For the diffusive terms, the second-order derivatives are only evaluated on the non-staggered mesh. All the derivation and interpolation formula as well as the explicit calculation of the derivatives and the Hermitian interpolations and details about the mesh grid may be found in the PhD theses of Beaubert [18] and Abide [2].

Compact finite-difference discretizations, like other centered schemes, are non dissipative and are therefore susceptible to numerical instabilities. Consequently, a sixth-order compact filter is applied to the conserved variable and sequentially in each coordinate non-homogeneous direction [346]. This numerical method has been validated in various Cartesian configurations: turbulent planar impinging jet [19], lid-driven cavity flow, flow over a backward-facing step, flow past a square cylinder [3].

3.5 The $r = 0$ -singularity

This section has been developed in the framework of the pseudo-spectral method based on Chebyshev polynomials during the PhD thesis of Noe Peres [241], that I co-supervised with Eric Serre. This

method has been published in Ref.[242].

As it will be shown in section 3.3, the discretization of Equations (3.1-3.3) leads to a Stokes problem coupling velocity and pressure. The collocation method requires boundary conditions in the physical space that can lead to an indetermination at $r = 0$ when the domain is discretized over the radius for $r \in [0, R]$ as in [313].

To avoid problems arising near the coordinate origin, the computational domain is discretized in the radial direction over the whole diameter between $-R$ and R with an even number of Gauss-Lobatto collocation points, $r_i = \cos(i\pi/N)$, $0 \leq i \leq N$. Thus, no collocation point is located at $r = 0$ and consequently no pole condition is required. However, the discretization over the diameter leads to an overlapping of points in the azimuthal direction that usually requires parity conditions for all variables Ψ such as $\Psi(r, \theta, z) = \Psi(-r, \theta + \pi, z)$.

Here, for a given even number of points K , a shift equal to $\pi/(2K)$ for $\theta > \pi$ is introduced in the angular discretization over $[0, 2\pi]$, as formerly proposed by Heinrichs [125] to solve two-dimensional Poisson equations on an unit disk. According to the angular shift, the following discrete angles θ_j are defined by:

$$\theta_j = \begin{cases} (j-1) \frac{2\pi}{K} & \text{if } j = 1, \dots, \frac{K}{2}, \\ \pi + \frac{\pi}{K} + (j - (\frac{K}{2} + 1)) \frac{2\pi}{K} & \text{if } j = \frac{K}{2} + 1, \dots, K. \end{cases} \quad (3.51)$$

An example is shown on Figure 3.2a for $K = 8$. Such discretization clearly leads to a better resolution in the azimuthal direction with twice the amount of points although the number of Fourier modes remains equal to $K/2$. An example of the 3D grid is shown on Figure 3.2b. The distribution of Gauss-Lobatto collocation points over the diameter tightens the points within the boundary layers along the vertical walls and avoids unnecessary clustering of points around the axis.

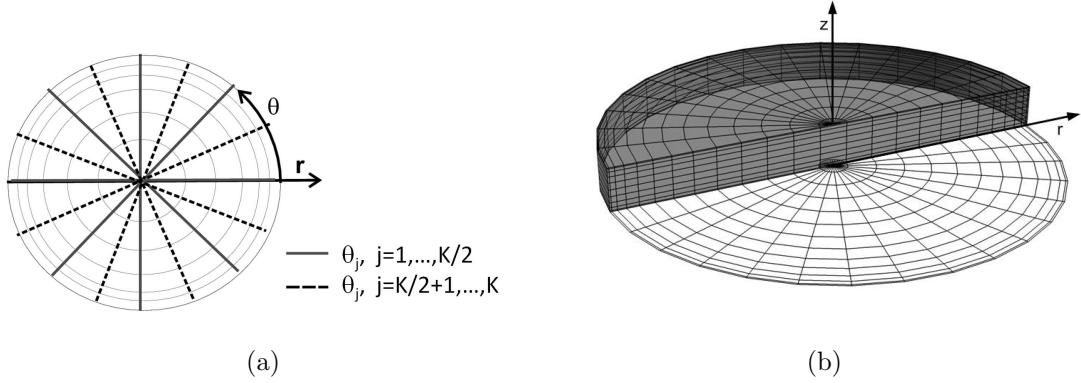


Figure 3.2: Grid structure: (a) Discrete angle θ_j distribution defined by Equation (3.51) in a (θ, z) plane showing the angular shift. Black and dashed diameters correspond to discretization indices $j = 1, \dots, \frac{K}{2}$ and $j = \frac{K}{2} + 1, \dots, K$, respectively. Grey circles show the radial mesh distribution; (b) Example of 3D mesh discretization in a thin interdisk cavity.

According to this angular discretization, the following real Fourier basis can be introduced:

$$\Phi_k(\theta) = \begin{cases} \sin(k\theta) & \text{if } k = 1, \dots, \frac{K}{2} - 1, \\ \cos(k\theta) + \sin(k\theta) & \text{if } k = \frac{K}{2}, \\ \cos((k - (\frac{K}{2} + 1))\theta) & \text{if } k = \frac{K}{2} + 1, \dots, K. \end{cases} \quad (3.52)$$

that corresponds to the following $K \times K$ transformation matrix in the spectral space:

$$P_\theta = (\Phi_k(\theta_j)), \quad j, k = 1, \dots, K \quad (3.53)$$

According to this basis, calculations of the first and second-order derivative operators in the azimuthal direction are straightforward both in the physical and spectral spaces. The first derivation of any variable is given by the matrix product $D_\theta P_\theta^{-1} \Psi$, where D_θ is the following $K \times K$ full matrix:

$$D_\theta = \left(\Phi'_k(\theta_j) \right)_{1 \leq j, k \leq K} \quad (3.54)$$

and for $1 \leq j \leq K$:

$$\Phi'_k(\theta_j) = \begin{cases} k \cos(k\theta_j), & k = 1, \dots, \frac{K}{2} - 1, \\ -k \sin(k\theta_j) + k \cos(k\theta_j), & k = \frac{K}{2}, \\ -(k - (\frac{K}{2} + 1)) \sin((k - (\frac{K}{2} + 1))\theta_j), & k = \frac{K}{2} + 1, \dots, K. \end{cases}$$

As referred by Peyret [244], numerical experiments have shown that the presence of the term at $k = K/2$ may lead to instabilities in time-dependent problems mainly because the first derivative cannot be represented in this basis. Therefore the mode $K/2$ must be filtered. The second-order derivative in Fourier space is written as:

$$\hat{D}_\theta^2 = \begin{cases} -diag(k^2) & \text{if } k = 1, \dots, \frac{K}{2}, \\ -diag\left(\left(k - \left(\frac{K}{2} + 1\right)\right)^2\right) & \text{if } k = \frac{K}{2} + 1, \dots, K. \end{cases} \quad (3.55)$$

The fast Fourier transform algorithm (FFT) based on Equation (3.52) is not yet available. Consequently, the Fourier transform in the azimuthal direction is performed here by matrix products using the subroutine *DGEMM* of the Blas (Basic Linear Algebra Subprograms) library. Additional cost is expected since for the matrix multiplication transform the cost behaves as N^2 with respect to $O(N \log_2 N)$ for FFT. However, as mentioned in Boyd [36], the actual costs must be significantly different since it is known that they are strongly grid and hardware dependents [36]. The performance study is presented in [241] using the NEC-SX8 supercomputer of IDRIS.

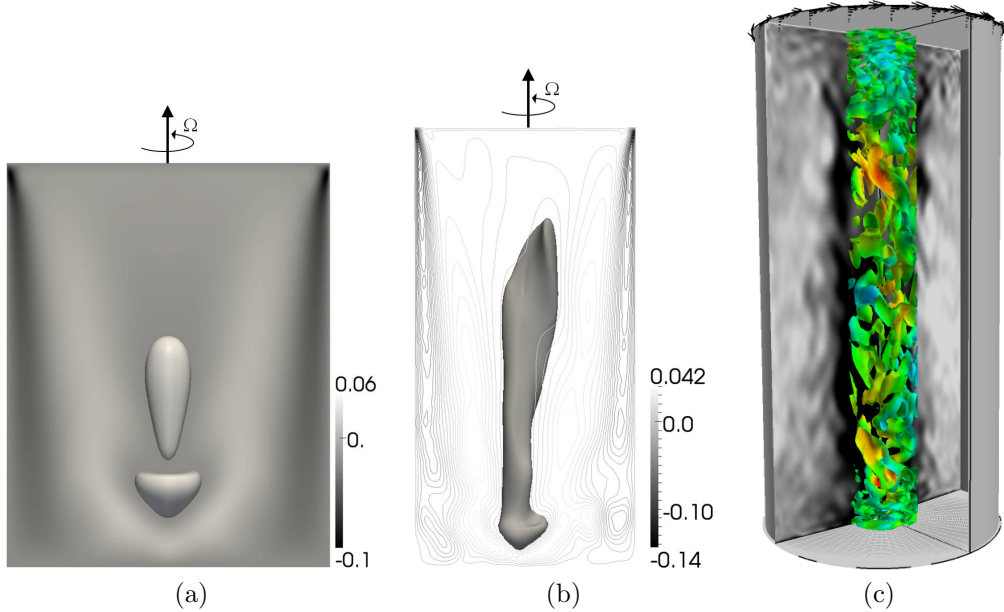


Figure 3.3: (a) Oscillating axisymmetric vortex breakdown of period $36.2\Omega^{-1}$ for ($G = 0.4$, $Re = 2750$); (b) Unsteady and three-dimensional S-shaped vortex breakdown for $G = 0.25$ and $Re = 6500$; (c) LES of a turbulent flow in a rotor-stator cavity heated from below at $Re = 10^5$, $G = 0.4$ and $Ra = 10^6$ (see in [242]).

The present method developed by Peres [241] to take into account the $r = 0$ -singularity has been validated against reliable experimental data in rotor-stator cavities of aspect ratio larger than 1, for which the vortex breakdown phenomenon may appear. Figure 3.3 presents the different regimes: time-dependent vortex breakdown at $Re = 2750$, then an unsteady 3D S-shaped vortex at $Re = 6500$.

Some calculations at a transitional Reynolds number $Re = 10^5$ with the SVV method described below have also been performed under non-isothermal conditions. The validation against analytical solutions as well as other simulations are available in [242].

3.6 Multidomain decomposition: the influence matrix technique

During his PhD thesis, that I co-supervised with Éric Serre, Guillaume Fontaine [97] improves the existing pseudospectral divergence free algorithm, in order to extend its properties to a multidomain patching of a rotating cavity. He worked on the multidomain extension of the existing divergence-free Navier-Stokes solver with a Schur approach. It has the particularity not to require any subdomain superposition: the value of a variable on the boundary between two adjacent subdomains is treated as a boundary condition of a local Helmholtz solver. This value is computed on a direct way via a so-called continuity influence matrix and the derivative jump of an homogeneous solution computed independently on each subdomain. Such a method is known to have both good scalability and accuracy. This technique is a direct Schur multidomain technique used by Raspo [268] for rotating flows using the vorticity-stream function formulation.

3.6.1 Multidomain geometry

One will limit the discussion to a radial multidomain decomposition (Fig.3.4), because the curvature terms vary only along this direction. The generalization of this technique to an axial decomposition is quite immediate. Local geometrical parameters $(L^{(m)}, R_m^{(m)})_{m \in [1;M]}$ (M the number of subdomains) satisfy :

$$\sum_{m=1}^M L^{(m)} = L \quad (3.56)$$

$$R_m^{(m)} - 1 = R_m^{(m+1)} + 1 \quad (3.57)$$

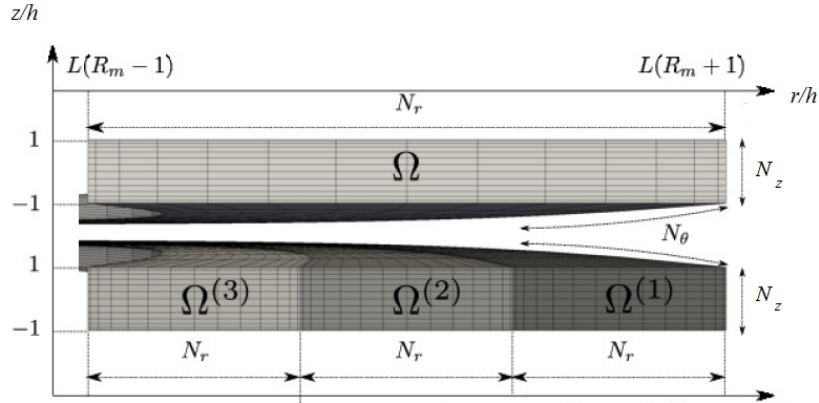


Figure 3.4: Example of a multidomain decomposition in the radial direction with 3 subdomains.

Local derivation matrixes are deduced from these local parameters, in order to have a good approximation for the curvature terms from one subdomain to another and to adapt the local mapping to the one which would be used in a monodomain approach.

3.6.2 Multidomain decomposition of the solutions

Let Ψ be either (u, v, w, p, ϕ) , $\Omega^{(m)}$ and $\Omega^{(n)}$ two adjacent subdomains, ξ the border between these two subdomains and λ the value of Ψ on ξ . For both subdomains, the local problems to be solved

may be written as :

$$\begin{cases} \Delta^{(m)}\Psi^{(m)} - \sigma^{(m)}\Psi^{(m)} = S^{(m)} & \text{in } \Omega^{(m)} \\ A^{(m)}\Psi^{(m)} = b^{(m)} & \text{on } \Gamma^{(m)} \end{cases} \quad (3.58)$$

$$\begin{cases} \Delta^{(n)}\Psi^{(n)} - \sigma^{(n)}\Psi^{(n)} = S^{(n)} & \text{in } \Omega^{(n)} \\ A^{(n)}\Psi^{(n)} = b^{(n)} & \text{on } \Gamma^{(n)} \end{cases} \quad (3.59)$$

The resulting problem is that the boundary conditions to be imposed on the parts of $\Gamma^{(m)}$ and $\Gamma^{(n)}$ corresponding to ξ are unknown. To find λ , one chooses to ensure both \mathcal{C}^0 and \mathcal{C}^1 continuities through ξ . Ψ is written as the combination of an homogeneous solution $\widetilde{\Psi}$ and a boundary solution $\overline{\Psi}$: $\Psi = \widetilde{\Psi} + \overline{\Psi}$.

On $\Omega^{(m)}$:

$$\begin{cases} \Delta^{(m)}\widetilde{\Psi}^{(m)} - \sigma^{(m)}\widetilde{\Psi}^{(m)} = S^{(m)} & \text{in } \Omega^{(m)} \\ A^{(m)}\widetilde{\Psi}^{(m)} = b^{(m)} & \text{on } \Gamma^{(m)} \\ \widetilde{\Psi}^{(m)} = 0 & \text{on } \xi^{(m)} \end{cases} \quad (3.60)$$

$$\begin{cases} \Delta^{(m)}\overline{\Psi}^{(m)} - \sigma^{(m)}\overline{\Psi}^{(m)} = 0 & \text{in } \Omega^{(m)} \\ A^{(m)}\overline{\Psi}^{(m)} = 0 & \text{on } \Gamma^{(m)} \\ \overline{\Psi}^{(m)} = \lambda^{(m)} & \text{on } \xi^{(m)} \end{cases} \quad (3.61)$$

On $\Omega^{(n)}$:

$$\begin{cases} \Delta^{(m+1)}\widetilde{\Psi}^{(n)} - \sigma^{(n)}\widetilde{\Psi}^{(n)} = S^{(n)} & \text{in } \Omega^{(n)} \\ A^{(m)}\widetilde{\Psi}^{(n)} = b^{(n)} & \text{on } \Gamma^{(m)} \\ \widetilde{\Psi}^{(n)} = 0 & \text{on } \xi^{(n)} \end{cases} \quad (3.62)$$

$$\begin{cases} \Delta^{(n)}\overline{\Psi}^{(n)} - \sigma^{(n)}\overline{\Psi}^{(n)} = 0 & \text{in } \Omega^{(n)} \\ A^{(n)}\overline{\Psi}^{(n)} = 0 & \text{on } \Gamma^{(n)} \\ \overline{\Psi}^{(n)} = \lambda^{(n)} & \text{on } \xi^{(n)} \end{cases} \quad (3.63)$$

If λ is assumed to be known, one can verify easily that (Eq. 3.58)=(Eq. 3.60)+(Eq. 3.61) and (Eq. 3.59)=(Eq. 3.62)+(Eq. 3.63).

3.6.3 The influence matrix technique

Let's consider the boundary solution $\overline{\Psi}$. It can be written as the linear combination of Green's elementary solutions $\mathbf{G}_{k\xi}^{(m)}$, defined for each subdomain $\Omega^{(m)}$ by :

$$\begin{cases} \Delta^{(m)}\overline{\mathcal{G}}_{k\xi}^{(m)} - \sigma^{(m)}\overline{\mathcal{G}}_{k\xi}^{(m)} = 0 & \text{in } \Omega^{(m)} \\ A^{(m)}\overline{\mathcal{G}}_{k\xi}^{(m)} = 0 & \text{on } \Gamma^{(m)} \\ \overline{\mathcal{G}}_{k\xi}^{(m)}(\eta_l \in \xi^{(m)}) = \delta_{kl} \quad \forall l \in \llbracket 1; N_\xi \rrbracket \end{cases} \quad (3.64)$$

Assuming that ξ is the only boundary (i.e. there are only 2 subdomains $\Omega^{(m)}$ and $\Omega^{(n)}$), the boundary solution should be written as:

$$\begin{cases} \Psi^{(m)} = \widetilde{\Psi}^{(m)} + \sum_{k=1}^{N_\xi} \lambda_k \mathcal{G}_{kE}^{(m)} & \text{in } \Omega^{(m)} \\ \Psi^{(n)} = \widetilde{\Psi}^{(n)} + \sum_{k=1}^{N_\xi} \lambda_k \mathcal{G}_{kS}^{(n)} & \text{in } \Omega^{(n)} \end{cases} \quad (3.65)$$

$\widetilde{\Psi}^{(m)} \cup \widetilde{\Psi}^{(n)}$ is obviously continuous through ξ , but not $\frac{\partial \widetilde{\Psi}^{(m)}}{\partial r} \cup \frac{\partial \widetilde{\Psi}^{(n)}}{\partial r}$. As the boundary solution is continuous too, $\Psi^{(m)} \cup \Psi^{(n)}$ should be continuous for any value of λ . The influence matrix technique aims to find λ in order to make it \mathcal{C}^0 and \mathcal{C}^1 through ξ . One denotes $\partial_r = \frac{\partial}{\partial r}$. This \mathcal{C}^1 -continuity problem on ξ writes:

$$\widetilde{\partial_r \Psi^{(1)}}(\xi) - \widetilde{\partial_r \Psi^{(2)}}(\xi) = \sum_{l=1}^{N_\xi} \lambda_l [\partial_r \mathcal{G}_{lS}^{(2)}(\xi) - \partial_r \mathcal{G}_{lE}^{(1)}(\xi)] \quad (3.66)$$

This can be written in a matrix form:

$$\mathcal{D} = \lambda \mathcal{M} \quad (3.67)$$

where \mathcal{D} is the derivative (time-dependent) jump vector and \mathcal{M} the continuity influence matrix of the problem. Note that it depends only on the time-independent Green solutions, so it just has to be computed in pre-processing. This matrix is diagonal-dominant. If there are more than 2 frontiers in the domain, the influence matrix is built by blocks. The block dimension is then N_{front} , the number of frontiers. Each diagonal block is a Green derivative jump vector along each frontier. Some non-diagonal blocks appear, resulting locally of the influence of 2 frontiers on one another through a single subdomain, as shown on Figure 3.5.

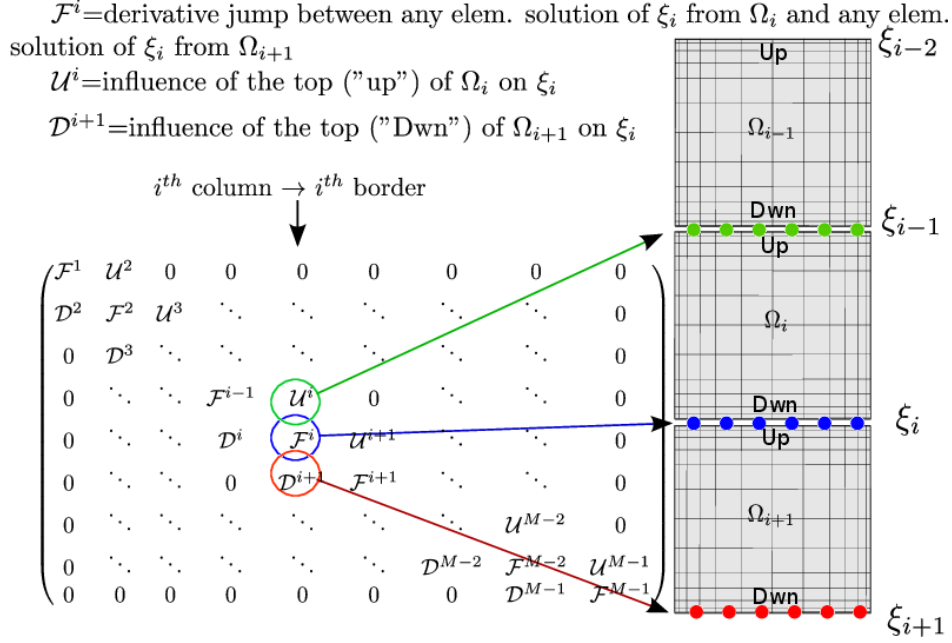


Figure 3.5: Block definition of the influence matrix for an 1-D multidomain decomposition.

If \mathcal{M} is inversible, one can find λ as:

$$\lambda = \mathcal{D} \mathcal{M}^{-1} \quad (3.68)$$

This vector is then used as a boundary condition on ξ in the local Helmholtz solvers to get a \mathcal{C}^0 and $\mathcal{C}^1 \Psi^{(m)} \cup \Psi^{(n)}$ solution.

3.6.4 Singularity of the Poisson-problem

The Neumann-Poisson problem has an infinity of solutions defined up to an additive constant. As Dirichlet boundary conditions are implemented on the frontiers, this problem no longer exists locally. Nevertheless, it is transposed to the influence matrix of the Poisson-problem of the $k = 0$ Fourier mode, which has a null-eigenvalue. It is treated by a diagonalisation technique of this modal matrix. The derivative jump is expressed in the diagonalisation basis and its i_0 -th component is set to zero, if i_0 is the null eigenvalue index, as proposed by Abide [2].

3.6.5 Validation of the multidomain approach

The multidomain approach developed by Fontaine [97] within the pseudospectral code has been validated in two fundamental configurations: a Taylor-Couette system ($\eta = 0.85$, $\Gamma = 40$) and an interdisk rotor-stator system ($G = 6.26$, $R_m = 1.8$). For Taylor-Couette flows, the two first instabilities, Taylor

vortices and wavy Taylor vortices (see Fig.3.6a) are recovered with the expected characteristics. In the rotor-stator cavity, the two first bifurcations, circular and then spiral patterns, are also recovered in good agreement with the former studies by Poncet *et al.* [261] and Peres [241] using the monodomain version of the code. Again the validation against analytical solutions as well as other simulations are available in [97, 98].

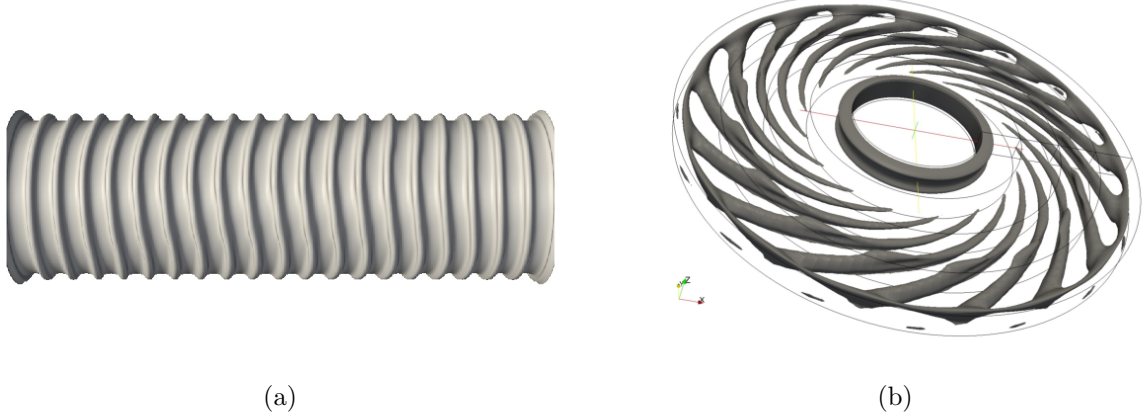


Figure 3.6: (a) Wavy Vortex Flow at $Ta/Ta_c = 1.36$ ($\eta = 0.85$, $\Gamma = 40$, Ta_c being the critical Taylor number for the appearance of Taylor vortices); (b) 17 spiral arms obtained for a 3D rotor-stator flow at $Re = 25000$ ($G = 6.26$, $R_m = 1.8$). See in Ref.[98].

3.7 Subgrid scale modeling

In Large Eddy Simulation (LES), each flow variable f is split into a large anisotropic scale component \bar{f} , which is computed and a small subgrid scale component f' , which has to be modeled. This separation is obtained by applying a spatial filter to the momentum and continuity equations in order to reduce the amount of spatial scales to be solved:

$$\frac{\partial \bar{u}_i}{\partial t} + \frac{\partial}{\partial x_j} (\bar{u}_i \bar{u}_j) = -\frac{\partial \bar{p}}{\partial x_i} - \frac{\partial T_{ij}}{\partial x_j} + \frac{1}{Re} \frac{\partial^2 \bar{u}_i}{\partial x_j \partial x_j} \quad (3.69)$$

$$\frac{\partial \bar{u}_i}{\partial x_i} = 0 \quad (3.70)$$

Due to the divergence free constraint, pressure is modified according to $\bar{p} = \overline{p/\rho} + T_{kk}/3$. Scales smaller than the grid size are modeled through the subgrid scale tensor T_{ij} given by the Leonard decomposition:

$$T_{ij} = \overline{u_i u_j} - \bar{u}_i \bar{u}_j \quad (3.71)$$

where the overbar denotes an appropriate low-pass filter and incompressibility is assumed. The complex interactions between the resolved and unresolved scales are modeled using a turbulent eddy-viscosity assumption. The anisotropic part of the subgrid scale stress T_{ij} is linked to the eddy viscosity ν_t through the following expression:

$$T_{ij} - \frac{1}{3} T_{kk} \delta_{ij} = 2\nu_t \bar{S}_{ij} \quad (3.72)$$

where the deformation tensor of the resolved field \bar{S}_{ij} writes:

$$\bar{S}_{ij} = \frac{1}{2} \left(\frac{\partial \bar{u}_i}{\partial x_j} + \frac{\partial \bar{u}_j}{\partial x_i} \right) \quad (3.73)$$

3.7.1 The Spectral vanishing viscosity (SVV) technique

High Reynolds number flows are difficult to simulate when using spectral accurate numerical methods, since the spectral approximations are less diffusive than the low-order ones leading to the accumulation of energy on the highest spatial frequencies and consequent divergence of computations [244]. Several stabilization techniques are available in the literature but generally these techniques degrade the spectral convergence [116]. In this work, a Spectral Vanishing Viscosity (SVV) formulation is used here as an efficient stabilizer for the high-accurate spectral method described previously. This technique seeks to define a spectral viscosity that reaches a maximum at high wave numbers vanishing gradually until reaches a given threshold at low wave numbers. The stabilization is therefore achieved through damping at small length scales without degrading the accuracy properties of the discretization. It has the property to preserve the spectral accuracy of the approximation developed in DNS [316] and keeps the fast time integration of the DNS because it is condensed in pre-processing jobs.

The SVV concept was initially developed by Tadmor [334], who applied it to solve hyperbolic equations, more precisely the inviscid Burger's equation. He demonstrated that this method prevents oscillations while keeping spectral accuracy. Maday *et al.* [196] were the first to consider the non-periodic Legendre pseudospectral viscosity method for an initial-boundary value problem introducing a smooth viscosity kernel. Ma [195] developed the non-periodic Chebyshev-Legendre approximation, based on the ideas of hyper Spectral Viscosity. A formulation of the method for Galerkin spectral/hp element has been proposed by Karamanos and Karniadakis [146] to solve the incompressible Navier-Stokes equations and employed for turbulent channel flows. A formulation of the SVV method for spectral element approximations has also been adapted by Xu and Pasquetti [358] and validated in the computation of the two-dimensional turbulent wake of a cylinder. Due to the conceptual simplicity and inherent spectral accuracy, the SVV technique has been seen as a real tool for LES.

The SVV technique used here is based on the work of Séverac and Serre [316], who extended it to 3D cylindrical flow problems. Later, Séverac *et al.* [315] used this technique to study turbulent flows in an enclosed rotor-stator configuration with a rotating hub and a stationary shroud for Reynolds numbers up to 10^6 . Its implementation into the Navier-Stokes equations is made by defining a new diffusion operator Δ_{SVV} . This operator is simply implemented by combining the classical diffusion and the new SVV terms to obtain in 1D:

$$\nu \Delta_{SVV} \equiv \nu \Delta + \nabla \cdot (\varepsilon_N Q_N \nabla) = \nu \nabla \cdot S_N \nabla \quad (3.74)$$

where ν is the diffusive coefficient and where:

$$S_N = 1 + \frac{\varepsilon_N}{\nu} Q_N \quad (3.75)$$

with ε_N the maximum of viscosity and Q_N a 1D viscosity kernel defined in the spectral space by:

$$\widehat{Q}_N(\omega_n) = 0, \quad 0 \leq \omega_n \leq \omega_T \quad (3.76)$$

$$\widehat{Q}_N(\omega_n) = \exp \left[- \left(\frac{\omega_n - \omega_N}{\omega_n - \omega_T} \right)^2 \right], \quad \omega_T < \omega_n \leq \omega_N \quad (3.77)$$

where ω_T is the threshold after which the viscosity is applied, ω_N the highest mode calculated and $\varepsilon_N Q_N \equiv \text{diag}(\varepsilon_{N_i}^i Q_{N_i}^i)$ ($i = r, \theta, z$). The SVV operator is then parametrized in each direction by $(\omega_T, \varepsilon_N)$. According to the theoretical results obtained by Tadmor [334], good values of such parameters are $\omega_T \approx O(\sqrt{N})$ and $\varepsilon_N \approx O(1/N)$, where N is the degree of approximation in each direction. These values have also provided a good compromise between stability and accuracy in former numerical studies [146, 234].

Figure 3.7 shows the viscosity kernel normalized by its maximum value at $\omega_n = \omega_N$ for different values of the cutoff wave number ω_T showing that the SVV operator affects at most two-third of the spectrum at the highest frequencies for $\omega_T = 0$. Consequently, DNS results are easily recovered for laminar flows, contrarily to some classical LES techniques as for example with the spectral eddy viscosity model of Kraichnan [160].

The main drawback of this approach is that the viscosity operator does not depend neither on space and so nor on the flow dynamics. That is why Koal *et al.* [157] have recently developed three modified kernels with enhanced stabilization in the axis region that could be of great interest in some applications.

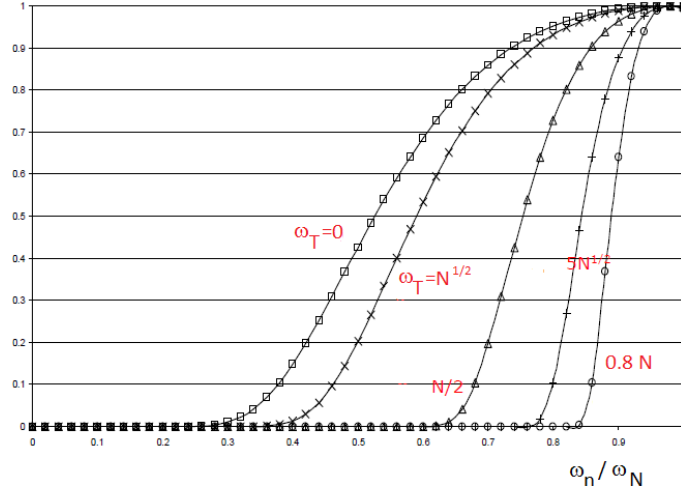


Figure 3.7: Influence of the threshold frequency on the shape of the spectrum of the spectral viscosity operator with $N = 50$.

3.7.2 Subgrid scale models based on an eddy-viscosity assumption

The direct numerical simulation code based on fourth-order compact schemes for the inhomogeneous directions (Section 3.4.2) has been extended to large eddy simulation, denoted LES-FD in the following, using three subgrid scale models used to model the turbulent eddy-viscosity ν_t (Eq.(3.72)):

- the Smagorinsky-Lilly model [323],
- the Germano dynamic model [106, 183],
- the WALE (Wall-Adapting Local Eddy-viscosity) model developed by Nicoud and Ducros [222].

In the Smagorinsky model, the eddy-viscosity is assumed to be proportional to the subgrid characteristic length scale $\bar{\Delta}$ and to a characteristic turbulent velocity taken as the local strain rate $|\bar{S}|$:

$$\nu_t = (C_s \bar{\Delta})^2 |\bar{S}| \quad (3.78)$$

$$|\bar{S}| = \sqrt{2\bar{S}_{ij}\bar{S}_{ij}} \quad (3.79)$$

where $\bar{\Delta} = (r\Delta r\Delta\theta\Delta z)^{1/3}$ is the grid filter width. The constant C_s is obtained assuming that the cut-off wave number $k_c = \pi/\bar{\Delta}$ lies within a $k^{-5/3}$ Kolmogorov cascade for the energy spectrum $E(k) = C_K \varepsilon^{2/3} k^{-5/3}$ and requiring that the ensemble-averaged subgrid dissipation is identical to ε . An approximate value for the constant is then:

$$C_s = \frac{1}{\pi} \left(\frac{3C_K}{2} \right)^{-3/4} \quad (3.80)$$

The value of the Smagorinsky constant strongly depends on the particular flow geometry. This method assumes that the energy production and dissipation of the small scales are in equilibrium. The classical Smagorinsky model was tested as a first approach in the case of turbulent rotor-stator interdisk flows (discussed in Chapter 8) with $C_s = 0.2$. As in the case of the turbulent flow due to a plane impinging jet [19], this model was found to be too dissipative and predicts incorrect behaviour near the walls and in the laminar regions.

The dynamic Smagorinsky model developed by Germano *et al.* [106] overcomes some of the drawbacks of the classical Smagorinsky model: it corrects its excessive dissipation, exhibits the correct behaviour close to the walls and in laminar regions and does not formally prohibit energy backscatter from the small to the large scales. The constant C_s^2 is replaced by a coefficient C_d , which is dynamically computed. C_d is evaluated with a least-squares approach as a part of the solution at each time step using a test filter denoted by a hat:

$$C_d = -\frac{1}{2} \frac{[(L_{ij} - \frac{1}{3}L_{kk}\delta_{ij}) M_{ij}]}{M_{ij}M_{ij}} \quad (3.81)$$

$$L_{ij} = \widehat{u_i u_j} - \widehat{u_i} \widehat{u_j} \quad (3.82)$$

$$M_{ij} = \widehat{\Delta}^2 \left| \widehat{S} \right| \widehat{S}_{ij} - \overline{\Delta}^2 \left| \overline{S} \right| \overline{S}_{ij} \quad (3.83)$$

The coefficient C_d is a local and instantaneous quantity: $C_d(r, \theta, z, t)$. Negative values of C_d may lead to numerical instabilities. To overcome this problem, C_d is averaged in the homogeneous tangential direction. The required stabilizing averaging could be done also over the fluid particle pathlines as proposed by Méneveau *et al.* [204]. Furthermore, negative values of ν_t are set to zero if the total viscosity $\nu + \nu_t$ is negative. Thus, no backscatter is taken into account here as for the LES-SVV model.

It is a common practice in the literature to choose the test filter width $\widehat{\Delta}$ as twice the grid-filter width $\overline{\Delta}$ [183]. In the homogeneous direction, a cutoff filter was applied with the Fourier approximation. The test filter used sequentially in each non-homogeneous direction is a symmetric discrete filter based on the trapezoidal rule:

$$\widehat{f}_i = \frac{1}{4} (f_{i-1} + 2f_i + f_{i+1}) \quad (3.84)$$

In order to improve time stability, the eddy viscosity is split into an averaged value in the azimuthal direction treated semi-implicitly by the way of internal iterations during the resolution of the predictor step and a fluctuation part treated fully explicitly. In practice, five iterations are required to obtain a convergence criterion of 10^{-6} . Finally, as expected from the dynamic procedure, the eddy viscosity acts more significantly where the turbulence intensity is higher and vanishes in the laminar regions.

The Smagorinsky model is based on the second invariant of the symmetric part \overline{S}_{ij} of this tensor. The main drawbacks are that this invariant is of order $O(1)$ close to a wall and it is not related to the rotation rate of the turbulent structure. To avoid that, Nicoud and Ducros [222] developed the WALE model based on the gradient velocity tensor \overline{g}_{ij} , which is a good candidate to represent the velocity fluctuations at the length scale $\overline{\Delta}$. The turbulent eddy-viscosity is then modeled by:

$$\nu_t = (C_m \overline{\Delta})^2 \frac{(S_{ij}^d S_{ij}^d)^{3/2}}{(\overline{S}_{ij} \overline{S}_{ij})^{5/2} + (S_{ij}^d S_{ij}^d)^{5/4}} \quad (3.85)$$

$$S_{ij}^d = \frac{1}{2} (\overline{g}_{ij}^2 + \overline{g}_{ji}^2) - \frac{1}{3} \delta_{ij} \overline{g}_{kk}^2, \quad \overline{g}_{ij} = \frac{\partial \overline{u_i}}{\partial x_j} \quad (3.86)$$

The operator S_{ij}^d is based on the traceless symmetric part of the square of the gradient velocity tensor \overline{g}_{ij} . The constant C_m is fixed to $C_m^2 \simeq 10.6 C_s^2$ as suggested by Nicoud and Ducros [222]. The WALE model has a proper behavior near the wall and is defined to handle with transitional problem in parietal flow. The WALE model provided very fair results in various complex turbulent flows in the context of turbomachinery, that is the reason why it is now available in many CFD softwares such as the AVBP code developed by CERFACS [80].

Reynolds Stress Model

Despite the relative simple geometry of the rotating flows considered here, such flows contain a complex physics, which makes their modeling a very challenging task for numerical methods. These flows present indeed several complexities such as the high rotation rates, confinement effects, transitional zones, very thin boundary layers, recirculation zones, curvature of the streamlines, which are severe conditions for turbulence modeling methods. An impinging jet may yield the flows even more complex because of the interaction between the jet and the base rotor-stator flow.

During my PhD thesis under the supervision of Dr R. Schiestel (IRPHE), I widely used and validated the Reynolds Stress Model (RSM), formerly developed by Elena and Schiestel [84, 85, 298], in various rotating disk flow configurations [83, 85, 119, 249, 253, 258] and for a wide range of the flow parameters (aspect ratio of the cavity, imposed throughflow, rotation rate, heat transfer). This level of closure appeared to be adequate in many flow configurations, while the usual $k - \epsilon$ model, which is blind to any rotation effect, presented serious deficiencies.

In some of the following Chapters, this well established turbulence model will be used to extend its application to new flow conditions and to get a better insight into the dynamics of highly turbulent rotating confined flows between disks or cylinders with or without heat transfer.

4.1 The differential Reynolds Stress Model (RSM)

4.1.1 The transport equations for the Reynolds stress tensor

To get the transport equations for the Reynolds stress tensor, one needs first to decompose each instantaneous variable (velocity and pressure) into a statistical average part (capital letters) and a fluctuating component (lowercase letters): $\tilde{V}_i = V_i + v_i$ and $\tilde{P} = P + p$. They are introduced in the Navier-Stokes equations. The Reynolds equations are then obtained by taking the statistical average of these equations. The equations for the fluctuating velocities write by difference:

$$\frac{\partial v_i}{\partial t} + V_j v_{i,j} = -v_j V_{i,j} - v_j v_{i,j} - \left(\frac{p}{\rho}\right)_{,i} + (\nu v_{i,j} + \overline{v_i v_j})_{,j} \quad (4.1)$$

The equation for v_i is multiplied by v_j and is added to the equation for v_j multiplied by v_i . By statistically averaging, one finally gets the transport equations for the Reynolds stress tensor $R_{ij} = \overline{v_i v_j}$. The different terms can be gathered in the following way to highlight the different turbulent interaction processes:

$$\frac{\partial R_{ij}}{\partial t} + A_{ij} = P_{ij} + \Phi_{ij} - \varepsilon_{ij} + D_{ij} \quad (4.2)$$

with:

$$A_{ij} = V_l R_{ij,l} \quad (4.3)$$

$$P_{ij} = -R_{il} V_{j,l} - R_{jl} V_{i,l} \quad (4.4)$$

$$\Phi_{ij} = \frac{p}{\rho} \overline{(v_{i,j} + v_{j,i})} \quad (4.5)$$

$$\varepsilon_{ij} = 2\nu \overline{v_i v_{j,l}} \quad (4.6)$$

$$D_{ij} = \left[-\overline{v_i v_j v_l} - \frac{p}{\rho} \overline{(v_i \delta_{jl} + v_j \delta_{il})} + \nu R_{ij,l} \right]_{,l} \quad (4.7)$$

where A_{ij} is the advection term. P_{ij} is the work of the Reynolds stress tensor submitted to the mean velocity gradient. As it does not introduced any new correlation, it does not need to be modeled. Φ_{ij} is the pressure-strain correlation term, which represents a distribution of energy along the components of the Reynolds stress tensor due to the pressure fluctuations. ϵ_{ij} is the viscous dissipation term and D_{ij} contains the turbulent and molecular diffusion contributions.

The main problem is to determine 10 unknown variables (6 Reynolds stress tensor components, 3 velocity components and the pressure) by solving only 4 equations (3 equations for v_i and the continuity equation). It is then absolutely necessary to model some terms to solve the system. One solution would be to form new equations but it will introduce new high-order correlations. One need to fix the closure order for the equations. Second-order models seem nowadays to offer the best compromise between the calculation cost and the description level of turbulence.

The approach chosen here is based on one-point statistical modeling using a low Reynolds number second-order full stress transport closure derived from the Launder and Tselepidakis [173] model and sensitized to rotation effects [85]. It corresponds to the RSM3 model fully described in [85]. This approach allows for a detailed description of near-wall turbulence and is free from any eddy viscosity hypothesis. In order to obtain confident heat transfer prediction, it is necessary to reach already a good description of the velocity and turbulence fields. The general equation for the Reynolds stress tensor R_{ij} can be written:

$$\frac{dR_{ij}}{dt} = P_{ij} + D_{ij} + \Phi_{ij} - \epsilon_{ij} + S_{ij} \quad (4.8)$$

where P_{ij} , D_{ij} , Φ_{ij} and ϵ_{ij} respectively denote the production, diffusion, pressure-strain correlation and dissipation terms. The term S_{ij} takes into account the implicit effects of rotation on turbulence.

The production term can be expressed as $P_{ij} = -R_{ij}V_{j,l} - R_{jl}V_{i,l}$ and does not need to be modeled.

4.1.2 Modeling of the diffusion terms

The diffusion term $D_{ij} = [-\overline{v_i v_j v_m} - \overline{p/\rho(v_i \delta_{jm} + v_j \delta_{im})} + \nu R_{ij,m}]_{,m}$ is split into two parts:

$$D_{ij} = D_{ij}^T + D_{ij}^\nu \quad (4.9)$$

The turbulent diffusion D_{ij}^T is the sum of two contributions: the triple correlations of the fluctuating velocities $\overline{v_i v_j v_m}$ and the diffusion due to pressure fluctuations $\overline{p/\rho(v_i \delta_{jm} + v_j \delta_{im})}$. This last term is besides often neglected due to the lack of experimental data. The turbulent diffusion term includes then only the contribution of $\overline{v_i v_j v_m}$, which is modeled according to the form proposed by Daly and Harlow [69]:

$$D_{ij}^T = (c_s \frac{k}{\epsilon} R_{ml} R_{ij,l})_{,m} \quad (4.10)$$

The c_s constant is fixed to 0.22 to enable the term D_{ij}^T to be compatible with the diffusion term found in the equation of the turbulence kinetic energy.

The viscous diffusion D_{ij}^ν has not to be modeled. It can be neglected at high Reynolds numbers but not in the low Reynolds number regions and especially close to the walls. It writes:

$$D_{ij}^\nu = -\nu R_{ij,ll} \quad (4.11)$$

4.1.3 Modeling of the pressure-strain correlation term

$\Phi_{ij} = \overline{p/\rho(v_{i,j} + v_{j,i})}$ is the pressure-strain correlation term, which can be decomposed into three contributions: the first one contains only the turbulent interactions, the second term is due to the interactions between turbulence and the mean velocity gradient and the last term acts only close to the walls. Applying the divergence to the fluctuating velocity equation, one gets a Poisson equation for the fluctuating pressure:

$$\frac{1}{\rho} p_{,ii} = -2v_{i,j} V_{j,i} - (v_i v_j - R_{ij})_{,ij} \quad (4.12)$$

By integrating this equation over the flow domain v , one gets a relation for p including two volume integrals over the domain v and one surface integral along the frontier σ of the domain. The term Φ_{ij} at a given location point A can be expressed as:

$$\overline{(v_{i,j} + v_{j,i})^A} = \frac{1}{4\pi} \iiint_{\mathcal{V}} \overline{(v_l^B v_m^B)_{,lm} (v_{i,j}^A v_{j,i}^A)} \frac{dv}{r} \quad (4.13)$$

$$+ \frac{1}{2\pi} \iiint_{\mathcal{V}} \overline{V_{l,m}^B v_{m,l}^B (v_{i,j}^A v_{j,i}^A)} \frac{dv}{r} \quad (4.14)$$

$$+ \frac{1}{2\pi\rho} \iint_{\sigma} \left(\frac{1}{r} \frac{\partial p^B}{\partial n} - p^B \frac{\partial}{\partial n} \left(\frac{1}{r} \right) \right) \overline{(v_{i,j}^A v_{j,i}^A)} d\sigma \quad (4.15)$$

The point B is the current point in the integrals.

In a classical way, the pressure-strain correlation term Φ_{ij} can be decomposed into three contributions as below:

$$\Phi_{ij} = \Phi_{ij}^{(1)} + \Phi_{ij}^{(2)} + \Phi_{ij}^{(w)} \quad (4.16)$$

$\Phi_{ij}^{(1)}$ is interpreted as a slow nonlinear return to isotropy and is modeled as a quadratic development in the stress anisotropy tensor a_{ij} , with coefficients sensitized to the invariants of anisotropy. This term, which contains the turbulent interactions, is damped near the wall:

$$\Phi_{ij}^{(1)} = -(\tilde{c}_1 a_{ij} + c'_1 (a_{il} a_{lj} - \frac{1}{3} A_2 \delta_{ij})) \varepsilon \quad (4.17)$$

where a_{ij} denotes the stress anisotropy tensor and \tilde{c}_1 and c'_1 are two functions adapted for confined flows, which vanish at the walls:

$$a_{ij} = \frac{R_{ij}}{k} - \frac{2}{3} \delta_{ij} \quad (4.18)$$

$$\tilde{c}_1 = (3.1 \sqrt{AA_2} + 1) (1 - e^{-\frac{Re_t^2}{40}}) \quad (4.19)$$

$$c'_1 = 3.72 \sqrt{AA_2} (1 - e^{-\frac{Re_t^2}{40}}) \quad (4.20)$$

Here $A = 1 - 9/8(A_2 - A_3)$ is the Lumley flatness parameter with A_2 and A_3 the second and third invariants of the anisotropy tensor. $Re_t = k^2/(\nu\varepsilon)$ is the turbulence Reynolds number.

The second contribution $\Phi_{ij}^{(2)}$ represents the linear rapid part. It is induced by the interactions between turbulence and the mean velocity gradient and includes cubic terms. It can be written as:

$$\begin{aligned} \Phi_{ij}^{(2)} = & -c_2 (P_{ij} - \frac{1}{3} P_{oo} \delta_{ij}) + 0.3 \varepsilon a_{ij} \frac{P_{oo}}{\varepsilon} - 0.2 \left[\frac{R_{oj} R_{li}}{k} (V_{o,l} + V_{l,o}) - \frac{R_{lo}}{k} (R_{io} (V_{j,l} + \varepsilon_{jml} \Omega_m) \right. \\ & \left. + R_{jo} (V_{i,l} + \varepsilon_{iml} \Omega_m)) \right] - \min(0.6, A) (A_2 (P_{ij} - \mathcal{D}_{ij}) + 3a_{mi} a_{nj} (P_{mn} - \mathcal{D}_{mn})) \end{aligned} \quad (4.21)$$

with $\mathcal{D}_{ij} = -R_{io} V_{o,j} - R_{jo} V_{o,i}$ and the constant c_2 is fixed to 0.6, value used in isotropic turbulence. Since the slow part of the pressure-strain correlation is already damped near the wall, a wall correction $\Phi_{ij}^{(w)}$ is only applied to the rapid part. It is modeled using the Gibson and Launder hypothesis [108] with a strongly reduced numerical coefficient. The classical length scale $k^{3/2} \varepsilon^{-1}$ is replaced by $k/\varepsilon (R_{ij} n_i n_j)^{1/2}$ which is the length scale of the fluctuations normal to the wall:

$$\Phi_{ij}^{(w)} = 0.2 \left[(\Phi_{lm}^{(2)} + \Phi_{lm}^{(R)}) n_l n_m \delta_{ij} - \frac{3}{2} (\Phi_{il}^{(2)} + \Phi_{il}^{(R)}) n_l n_j - \frac{3}{2} (\Phi_{lj}^{(2)} + \Phi_{lj}^{(R)}) n_i n_l \right] \frac{k \sqrt{R_{pq} n_p n_q}}{\varepsilon y} \quad (4.22)$$

where y is evaluated by the minimal distance of the current point from the four walls, n_i the unit normal vector along the i component and $c'_2 = 0.2$. The term $\Phi_{ij}^{(w)}$ redistributes the energy along the orthogonal components of the Reynolds stress tensor. Its effect is noticeable at a distance from the wall equal approximately to the integral scale.

4.1.4 Modeling of the viscous dissipation term

The term $\varepsilon_{ij} = 2\nu\overline{v_{i,m}v_{j,m}}$ represents the dissipation rate of the Reynolds stress tensor. At the wall, this term is strongly inhomogeneous. Far from the walls, ε_{ij} varies between $2\varepsilon\delta_{ij}/3$ for high Reynolds numbers and $\varepsilon R_{ij}/k$ for low Reynolds numbers. The viscous dissipation tensor ε_{ij} has been modeled in order to conform with the wall limits obtained from Taylor series expansions of the fluctuating velocities [171]:

$$\varepsilon_{ij} = f_A \varepsilon_{ij}^* + (1 - f_A) \left[f_s \frac{\varepsilon R_{ij}}{k} + \frac{2}{3} (1 - f_s) \varepsilon \delta_{ij} \right] \quad (4.23)$$

The $\varepsilon R_{ij}/k$ term supposes that the dissipating vortices have the same structure as the vortices with a high energy and the $2/3\varepsilon\delta_{ij}$ term represents the local isotropy of micro-turbulence. The dissipation rate of the Reynolds stress tensor ε_{ij} is modeled by ponderating these two effects using the functions f_A and f_s . These functions and ε_{ij}^* for the near-wall regions are defined as:

$$f_A = e^{-20A^2} e^{-\frac{Re_t^2}{20}} \quad (4.24)$$

$$f_s = e^{-\frac{Re_t^2}{40}} \quad (4.25)$$

$$\varepsilon_{ij}^* = \frac{(R_{ij} + R_{im}n_jn_m + R_{jm}n_in_m + R_{ml}n_mn_l n_in_j)}{\frac{k}{\varepsilon} \left(1 + \frac{3}{2} \frac{R_{pq}}{k} n_p n_q \right)} \quad (4.26)$$

This form of ε_{ij}^* ensures that outside the near wall region and very low Reynolds number regions, dissipation is an isotropic phenomenon. The functions f_A and f_s enable the model to respect some realizability constraints.

4.1.5 Modeling of the extra terms sensitized to rotation effects

The extra term S_{ij} accounts for implicit effects of rotation on turbulence. Indeed, high speed rotation produces indirect effects on the turbulence field that are not modeled in usual closures, even in second-order closures. These effects modify the structure of the turbulence eddies in a complex manner that can be evidenced in two-point statistics [44]. The term S_{ij} is decomposed into four terms:

$$S_{ij} = \Phi_{ij}^{(R)} + D_{ij}^R + B_{ij} + J_{ij} \quad (4.27)$$

$\Phi_{ij}^{(R)}$ is a part of the pressure-strain correlation term. It is obtained by supposing that Φ_{ij} is also function of the dimensionality tensor C_{ij} and so that Φ_{ij} is modified in presence of rotation, which acts on the turbulence structure. It is a linear effect, modeled as:

$$\Phi_{ij}^{(R)} = -0.6 \left[(\mathcal{D}_{cij} + \frac{1}{2} \mathcal{D}_{c\Omega ij}) - \frac{2}{3} P_c \delta_{ij} \right] - \frac{2}{5} k (V_{i,j} + V_{j,i}) \quad (4.28)$$

where \mathcal{D}_{cij} , $\mathcal{D}_{c\Omega ij}$ and P_c are defined as:

$$\mathcal{D}_{cij} = -C_{ip} V_{p,j} - C_{jp} V_{p,i} \quad (4.29)$$

$$\mathcal{D}_{c\Omega ij} = -2(\epsilon_{ipl} \Omega_p C_{lj} - \epsilon_{jpl} \Omega_p C_{li}) \quad (4.30)$$

$$P_c = -C_{ip} V_{i,p} \quad (4.31)$$

One proposes a simple behavior law for C_{ij} :

$$C_{ij} = \frac{2}{3} \left(1 + \frac{f_c}{2} \right) k \delta_{ij} - f_c k \frac{\Omega_i^* \Omega_j^*}{\Omega^{*2}} \quad (4.32)$$

$$f_c = \frac{Ro_t^{-1}}{5 + Ro_t^{-1}} \quad (4.33)$$

This law takes into account bidimensionalisation effects and contains somewhat the non-linear effects of rotation. $Ro_t = \varepsilon/(k\Omega^*)$ is the turbulence Rossby number and $\Omega^* = \|\Omega_i^*\|$ the intrinsic rotation.

C_{ij} is the dimensionality tensor, which represents the spatial properties of the turbulent structures such as the stretching of the vortices. It is defined in case of homogeneous turbulence by:

$$C_{ij} = \int \frac{\kappa_i \kappa_j}{\kappa^2} E(\vec{\kappa}) d\vec{\kappa} \quad (4.34)$$

where $E(\vec{\kappa})$ is the energy spectrum. The reader can refer to the work of Reynolds [276] for the extension to the inhomogeneous case.

The second term D_{ij}^R is an inhomogeneous diffusion term, which slows down the bidimensionalisation of turbulence close to the walls:

$$D_{ij}^R = (c_s \frac{k^2}{\varepsilon} f_{Ro} Y_{lm} R_{ij,l}),_m \quad (4.35)$$

where f_{Ro} and Y_{lm} are defined as:

$$f_{Ro} = \frac{2Ro_t^{-1/2}}{1 + 15Ro_t^{-1/2}} \quad (4.36)$$

$$Y_{lm} = \frac{\Omega_l^* \Omega_m^*}{\Omega^{*2}} \quad (4.37)$$

$c_s = 0.22$ is an empirical constant and $\Omega_i^* = \Omega_i - 0.5\epsilon_{ijl}V_{j,l}$ the intrinsic rotation vector. The second term $0.5\epsilon_{ijl}V_{j,l}$ corresponds the rotation of the fluid particles on themselves. This term subsists even without any rotation ($Re = 0$) but its effect is negligible. Ω^* acts only in case of strong rotation and/or if $\Omega^* \gg \partial V_z / \partial r$.

B_{ij} is a homogeneous source term, which rectifies the pressure-strain correlation and which acts only in case of strong rotation. It produces spectral phase scrambling (angular dispersion). It writes:

$$B_{ij} = -\alpha_B (R_{ij} - k\delta_{ij} + \frac{1}{2}C_{ij}) \quad (4.38)$$

with α_B defined by:

$$\alpha_B = \frac{1}{2}\Omega^* \frac{C_{pq} \Omega_p^* \Omega_q^*}{2k \Omega^{*2}} \quad (4.39)$$

The rapid distortion theory shows indeed that the Coriolis forces produce, in the spectral space, a rotation of the Fourier modes \hat{u}_i around their wave vector κ_i at a given frequency, which depends on the angle between κ_i and Ω_i , which induces a decorrelation of the modes rotating at different velocities. Under these conditions, R_{ij} tends to $-1/2C_{ij} + k\delta_{ij}$.

The rotation also reduces the energy transfer from large to small turbulent scales. Elena [83] proposed to model it through an inverse flux J considered as isotropic for high Reynolds numbers and introduced only in the transport equation for the turbulence kinetic energy. The inverse flux is defined by:

$$J = \frac{f_J}{1 + f_J} \tilde{\varepsilon} \quad (4.40)$$

As there is no information about the blocking of the energy cascade for low Reynolds number flows, Elena [83] introduced the function f_J defined by:

$$f_J = \frac{0.12Ro_t^{-2} + 0.015Ro_t^{-1} - 0.3 e^{-Re_t^2} (0.4Ro_t^{-2} + 0.05Ro_t^{-1})}{0.254Ro_t^{-2} + 0.1567Ro_t^{-1} + 1} \quad (4.41)$$

This function does not modify the dissipation in the viscous sublayer. The inverse flux for the Reynolds stress tensor components J_{ij} is modeled by:

$$J_{ij} = \frac{2}{3} [(1 - f_T)\delta_{ij} + f_T \frac{3R_{ij}}{2k}] J \quad (4.42)$$

with f_T defined by:

$$f_T = \frac{1}{1 + Re_t/10} \quad (4.43)$$

The effect of J_{ij} , which is a corrective term of ε_{ij} , is to increase the turbulence levels in the central part of the flow.

These four terms allowed some improvements of results in an enclosed rotor-stator cavity [85]. They are fully described in [85, 298].

4.1.6 Transport equations for the turbulence kinetic energy k and its dissipation rate ε

Below is the proposal of Launder and Tselepidakis [173] for the dissipation rate equation ε :

$$\frac{d\varepsilon}{dt} = -c_{\varepsilon_1} \frac{\varepsilon}{k} R_{ij} V_{i,j} - c_{\varepsilon_2} f_\varepsilon \frac{\tilde{\varepsilon}}{k} + (c_\varepsilon \frac{k}{\varepsilon} R_{ij} \varepsilon_{,j} + \nu \varepsilon_{,i})_{,i} + c_{\varepsilon_3} \nu \frac{k}{\varepsilon} R_{jp} V_{i,jl} V_{i,pl} + (c_{\varepsilon_4} \nu \frac{\tilde{\varepsilon}}{k} k_{,i})_{,i} \quad (4.44)$$

$\tilde{\varepsilon}$ is the isotropic part of the dissipation rate $\tilde{\varepsilon} = \varepsilon - 2\nu k_{,i}^{1/2} k_{,i}^{1/2}$. $c_{\varepsilon_1} = 1$, $c_{\varepsilon_2} = 1.92$, $c_\varepsilon = 0.15$, $c_{\varepsilon_3} = 2$, $c_{\varepsilon_4} = 0.92$ are five empirical constants and f_ε is defined by: $f_\varepsilon = 1/(1 + 0.63\sqrt{AA_2})$. This equation is sensitive to the anisotropy of the Reynolds stress tensor through the destructive term of ε .

The source term with a diffusive form $(c_{\varepsilon_4} \nu \frac{\tilde{\varepsilon}}{k} k_{,i})_{,i}$ has been proposed by Launder and Tselepidakis [173] to take into account the diffusion effects due to pressure fluctuations. It is negligible outside the boundary layers. Inside the boundary layers, it is positive and has the tendency to increase ε .

The turbulence kinetic energy equation is redundant in a RSM model but it is however still solved numerically in order to get faster convergence:

$$\frac{dk}{dt} = -R_{ij} V_{i,j} + J - \varepsilon + 0.22 \left(\frac{k}{\varepsilon} R_{ij} k_{,j} + \nu k_{,i} \right)_{,i} + 0.22 \left(\frac{k^2}{\varepsilon} \frac{2Ro_t^{-1/2}}{1 + 15Ro_t^{-1/2}} \frac{\Omega_i^* \Omega_j^*}{\Omega^{*2}} k_{,i} \right)_{,j} \quad (4.45)$$

It is verified after convergence that k is exactly $0.5R_{jj}$ within 0.05% at each grid point.

4.1.7 Energy equation

For the thermal field, as a first approach, one considered only relatively small differences between the temperature of the inlet fluid T_0 and the wall temperature T_w . As a consequence, density is not significantly affected by temperature differences, which allows to dissociate the dynamical effects from the heat transfer process. Poncet and Schiestel [258] obtained indeed very satisfactory results using this approach for temperature differences up to 75 K in similar geometries. Then, the temperature equation writes:

$$\frac{\partial T}{\partial t} + V_j T_{,j} = \alpha T_{,jj} - F_{j,j}^t \quad (4.46)$$

where $\alpha = \nu/Pr$ (Pr the molecular Prandtl number) and F_i^t is the turbulent flux approximated by a gradient hypothesis with tensorial diffusive coefficient:

$$F_i^t = -c_t \frac{k}{\varepsilon} R_{ij} T_{,j} \quad (4.47)$$

where $c_t = c_\mu/Pr_t = 0.1$ with $c_\mu = \nu_t \varepsilon/k^2 = 0.09$ a coefficient used to define the turbulent viscosity ν_t and Pr_t the turbulent Prandtl number assumed to be constant at 0.9. It is indeed a common feature for two-dimensional computations in rotating flows and more generally for near-wall turbulent flows to fix the value of the turbulent Prandtl number Pr_t to 0.9 (see the monographs of Launder et al. [169] and Schiestel [297]). The numerical work of Ong [229] and Iacovides and Chew [134] can also be cited.

The effects of the anisotropy of the turbulence field and the effects of rotation are already included in the term kR_{ij}/ε of Equation (4.47) for most of them.

4.2 Numerical method

The computational procedure is based on a finite volume method using staggered grids for the mean velocity components with axisymmetry hypothesis in the mean. The computer code is elliptic and the numerical solution proceeds iteratively. The power PLDS scheme has been chosen as the convection-diffusion scheme for its stability and its weak computational cost. It implies the linearization of the source terms using the decomposition proposed by Patankar [235]. The new linear system is solved by the tridiagonal algorithm of Thomas [235], which is a recursive algorithm of scanning line by line and column by column. The velocity-pressure coupling is solved using the SIMPLER algorithm.

In order to overcome stability problems, several stabilizing techniques have been introduced in the numerical procedure: diffusive formulation for the Reynolds stress tensor components deduced from the discretized stress equations and reported into the momentum equations, implicit treatment of Coriolis type terms and regular and inertial relaxations. Also, the stress component equations are solved using matrix block tridiagonal solution to enhance stability using non staggered grids.

4.3 Boundary conditions

The boundary conditions are as follows:

- Along the symmetry axis:

$$\frac{\partial \phi}{\partial r} = 0, \quad \phi = V_r, V_\theta, V_z, k, \varepsilon, R_{rr}, R_{\theta\theta}, R_{zz} \quad (4.48)$$

$$R_{r\theta} = R_{rz} = R_{\theta z} = 0 \quad (4.49)$$

- At the walls: $V_r = V_z = k = R_{ij} = 0$ for $(i, j) = (r, \theta, z)$ and $\epsilon = \nu k_{,j} k_{,j} / (2k)$. $V_\theta = 0$ on a stationary wall and $V_\theta = \Omega r$ on a rotating wall.
- At the inlet: V_θ is supposed to vary linearly from zero on the stationary wall up to Ωr on the rotating wall. When a throughflow is enforced, a laminar or turbulent Poiseuille profile is then imposed for the axial velocity V_z with or without preswirl depending on the flow configuration. A given level of turbulence intensity is also imposed corresponding to a turbulence kinetic energy at the inlet equal to $0.01(\Omega r)^2$ and a turbulence Reynolds number equal to $Re_t = 1500$.
- At the outlet: the pressure is permanently fixed, whereas the derivatives for all the other independent quantities are set to zero if reversed flow occurs, and fixed external values are imposed if the fluid re-enters the cavity. A special treatment for this type of mixed boundary conditions has been developed. During the calculation, if reversed flow occurs, an advection equation for all quantity is solved in a region located just outside the physical domain (see Poncet [249]). It enables to moderate the evolution of these quantities and so to stabilize the calculations.

The flow in the similarity area is practically not sensitive to the shape of velocity profiles or to the intensity level imposed at the inlet [249]. The turbulence levels calculated inside the cavity are indeed always larger than those imposed at the inlet. Moreover, these choices are justified by the wish to have a model as universal as possible. The calculation is initialized using realistic data fields, which satisfy the boundary conditions.

The reader can refer to the previous works of Elena and Schiestel [84, 85, 298] and Poncet *et al.* [119, 249, 253, 258] for more details about the statistical modeling and the numerical method.

Part III

Rotating disk flows

Part III: Rotating disk flows

Summary: This part is devoted to rotating flows in interdisk cavities. It is divided into five chapters corresponding to five different flow configurations in terms of geometry or/and flow regimes. It is organized by increasing progressively both the relative complexity of the geometry and the global flow parameters. Thus, Chapter 5 presents some numerical results about the laminar flow of a non-Newtonian fluid over a stationary infinite disk (known as the Bödewadt flow). Chapter 6 is devoted to the combined experimental and numerical study of a shear-layer instability over a finite rotating disk with a free surface. The route to turbulence is then investigated still experimentally and numerically in Chapter 7 in the case of rotor-stator flows with unmerged boundary layers. Chapter 8 presents the turbulent regime in the same configuration, with comparisons of three turbulence modelings and velocity measurements. To finish with, some RANS predictions are shown and compared to velocity measurements for the Von Kármán flow between counter-rotating disks equipped or not with straight blades in Chapter 9.

Bödewadt flow of a non-Newtonian fluid

This Chapter is the result of a close collaboration with Dr Bikash Sahoo (National Institute of Technology, Rourkela, India) initiated in 2010. The goal is to provide numerical solution of academic flow problems by reducing the system of highly nonlinear equations using appropriate variable transformations. It has been done by Von Kármán [348] in the context of rotating disk flows. This kind of flow still receives a constant attention with about 8000 references published in Science Direct for the last five years. Of course, more complex effects are considered now such as a magnetic field, heat transfer, partial slip, non-Newtonian fluid, porous walls

The steady flow arising due to the rotation of a fluid at a larger distance from a stationary disk is extended to the case where the disk surface admits partial slip for both Newtonian and non Newtonian fluids. The constitutive equation of the non-Newtonian fluid is modeled by that for a Reiner-Rivlin fluid. The momentum equation gives rise to a highly nonlinear boundary value problem. Numerical solutions of the governing nonlinear equations are obtained over the entire range of the physical parameters. The effects of slip and non-Newtonian fluid characteristics on the momentum boundary layer are discussed in details. It is observed that slip has prominent effect on the velocity field, whereas a predominant influence of the non-Newtonian parameter is observed on the moment coefficient. The results have been published in *Commun. Nonlinear Sci. Numer. Simulat.* in 2012 (Ref.[286]) and compared also to those obtained by Dr. Abbasbandy (Islamic Azad Univ. in Tehran) using the Keller-box method in the Newtonian case.

5.1 Introduction

The flow of non-Newtonian fluids over an infinite disk has received much attention during the last decades [10, 13, 329] due to its immense industrial applications such as for designing gaseous core nuclear reactor or power generators, increasing storage density in hard-disk drives and in rheology. Sahoo and Sharma [288] then Sahoo [283] have discussed the steady Von Kármán flow and heat transfer of an electrically conducting Reiner-Rivlin fluid with partial slip boundary conditions. The twin problem arising when the fluid rotates with an uniform angular velocity at a larger distance from a stationary disk is one of the classical problems of fluid mechanics, which has both theoretical and practical value. In this case, the particles rotate at a large distance from the wall. They are in equilibrium under the influence of the centrifugal force which is balanced by the radial pressure gradient. Those particles close to the disk whose circumferential velocity is retarded under the same pressure gradient directed inwards. However, the centrifugal force they are subjected to is greatly decreased. This set of circumstances causes the particle near the disk to flow radially inwards, and for reasons of continuity that motion must be compensated by an axial flow upwards, as shown in Figure 5.1. A flow which arises in the boundary layer in this manner such that its direction deviates from that of the outer flow is generally called a secondary flow. Such type of flow can be clearly observed in a teacup: after the rotation has been generated by vigorous stirring and again after the flow has been left to itself for a short while. The radial inward flow field near the bottom will be formed. Its existence can be inferred from the fact that tea leaves settle in a little heap near the center at the bottom.

This problem was studied by Bödewadt [26] by making boundary layer approximations. That is why the flow problem is widely known as the Bödewadt flow. For this problem, the Ackroyd's method [5] of expansion is not so suitable. Bödewadt approached the solution through a very laborious method similar to that used by Cochran [55] for the Von Kármán equations. The method consists of a power series expansion at $z = 0$ and an asymptotic expansion for $z \rightarrow \infty$. Bödewadt's solution shows that the boundary layer effects extend out to about $\zeta = 8$, where ζ is the non-dimensional

distance measured along the rotation axis. A correction to this problem was worked out by Browning (unpublished, see in [301]). He noticed a much thicker boundary layer than in the case of a disk rotating in a fluid at rest. Batchelor [16] generalized these analysis to include one parameter family of solutions having a mathematical structure very similar to that of Von Kármán. It corresponds to the flow above an infinite disk rotating with certain angular velocity, with the fluid in the far off region in solid body rotation. The general problem of an infinite rotating fluid of which the above two problems are particular cases has been later investigated by Hannah [122]. Subsequently, this case has been treated by Stewartson [330]. Fetti [95] had been concerned largely with the problem of Bödeadt. Rogers and Lance [278] studied numerically a similar problem when the disk rotates with an angular velocity ω in a fluid rotating with a different speed Ω . When $\Omega = 0$, the system reduces to the free-disk problem of Von Kármán; when $\omega = \Omega$, there is a solid-body rotation; and when $\omega = 0$, the problem is the same as that discussed by Bödeadt. It was pointed out by Schwiderski and Lugt [305] that the non-existence of a proper solution to the boundary value problems for rotating flows of Von Kármán and Bödeadt types is an indication that, in reality, the flow is separated from the surface of the disk. The simple ‘*Tea cup experiment*’ described above, displays very clearly a separation of the fluid from the bottom of the cup. Application of the suction is an effective device to reduce the chances of separation. Later, the local boundary layer approximations of first-order derived in [305] have been generalized by Schwiderski and Lugt [306] to axisymmetric motions, which rotate over a rotating disk of infinite dimensions. Numerical results are computed and discussed for a variety of Reynolds numbers and for cases for which the disk is rotating in the same sense and in the opposite sense as the fluid far away from the disk. The critical Reynolds numbers for steady laminar motions which are attached to the surface of the disk are computed and displayed. Nanda [216] studied the effects of uniform suction on the revolving flow of a viscous liquid over a stationary disk. It was found that the presence of suction introduces an axial inflow at infinity. Nydahl [228] has extended the Bödeadt flow problem by incorporating the heat transfer phenomena. The results obtained by Nydahl effectively confirm those of Bödeadt. Those of Rogers and Lance [279] gave a significantly larger value of H_∞ . The momentum and the displacement thicknesses decrease as the suction velocity increases. The spin-up process in the Bödeadt flow of a viscous fluid has been studied by Chawla and Purushothaman [47]. A comprehensive review of earlier works on flow and heat transfer due to a single and two parallel rotating disks up to 1989 has been included in a monograph by Owen and Rogers [233]. Recently, Chawla and Srivastava [48] have considered the physical situation in which the disk is performing torsional oscillations in contact with a fluid in a state of rigid-body rotation in the far field. Kitchens and Chang [156] have considered the Bödeadt flow for a non-Newtonian second-order fluid.

A literature survey indicates that there has been an extensive literature available regarding the boundary layer flow over a rotating disk (Kármán flow) in various situations. Such studies include different fluid models, magnetohydrodynamic and hydrodynamic cases, with and without heat transfer analysis. But there has been relatively little information regarding the Bödeadt type flow. The present study is an endeavor to fill this gap. An important application of such flow arises from modelling atmospheric flows. Besides the above reason, few other curious findings have motivated the present investigation.

First of all, the steady Bödeadt flow of a viscous, incompressible fluid is one of the few problems in fluid dynamics for which the Navier-Stokes equations admit an exact solution. Again as reported by Owen and Rogers [233], there is a discrepancy in the numerical value of H_∞ (axial flow velocity at a sufficiently large distance from the surface of the disk), which was found to be 1.3494 using the method of Rogers and Lance [278] on a **VAX 8530** computer with a typical precision of 16 significant figures. This depicts that the accuracy achieved by Rogers and Lance [278] was not sufficient to give an accurate value of H_∞ . Moreover, it has been pointed out by many authors that Bödeadt’s solution implies that there is a flow out of the boundary layer everywhere and no mechanism for supplying fluid to it! For an infinite disk, the problem may be overcome by assuming an infinite reservoir of fluid from which the boundary layer can draw in an unspecified way. For the more practical case of a finite disk, it must be supposed that a similarity solution does not hold near the edge of the disk. However, it is consistent with experience in other fields that a similarity solution becomes valid as the boundary layer flow develops. It may then be assumed that fluid enters the boundary layer near the edge of the disk and that this fluid is available for continuity in the similarity solution.

Most of the studies mentioned above admit no-slip condition on the walls, which is more a hypothesis rather than a condition deduced from any principle, and thus its validity is questionable and

has been continuously debated in the scientific community in various configurations. Evidences of slip of a fluid on a solid surface have been reported by Matthews and Hill [200]. For example, if one considers a zero-thickness disk admitting stress-free on its surface and rotating around its own axis, it does not modify the motion of the surrounding fluid, which would remain at rest. It confirms an intuitive result that the boundary condition on the disk surface plays a key role on the fluid motion. Slip condition may have also some industrial relevance when the fluid is composed of emulsions, suspensions, foams or polymer solutions. In other situations where the wall surface is rough, the no-slip boundary condition becomes also impractical to apply exactly. In all these cases, the proper boundary condition is well described by the general Navier's condition [218], where the amount of relative slip is proportional to the local shear stress through the slip length(es). Up to now, no particular attention has been given to the effects of partial slip on rotating disk flows. If the characteristic scale of roughness is small compared to the boundary layer thickness on the disk, the no-slip condition may be well approximated by a partial slip condition [218]. Miklavčič and Wang [210] have considered the von Kármán swirling flow of a viscous fluid with slip boundary condition. In a recent paper, Sherwood [318] solved, among others, the flow due to a zero-thickness disk rotating around its own axis by the use of Hankel transforms. The combined effects of slip and non-Newtonian cross-viscous parameter on the rotating flows past free rotating disks have been thoroughly studied by Sahoo [283].

Literature survey however shows that hardly any attention has been given to the effects of slip on the Bödewadt flow of a viscous fluid. The present work is devoted to study the effects of slip on the steady Bödewadt flow of a viscous fluid. A second-order finite-difference method and the Keller-box method are used to solve the resulting fully coupled and highly nonlinear differential equations for a Newtonian fluid. The results are matched with the benchmark results corresponding to the no-slip case [233] and are found to be in excellent agreement. The results are then extended for a Reiner-Rivlin fluid using the finite-difference schemes.

5.2 Flow analysis

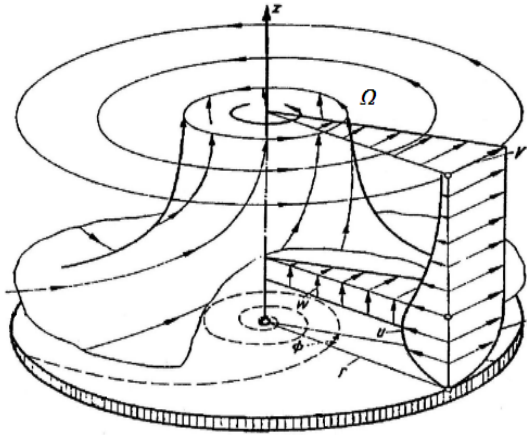


Figure 5.1: Schematic representation of the Bödewadt flow after Schlichting [301].

In this case, the non-Newtonian Reiner-Rivlin fluid model where the stress tensor τ_{ij} is related to the rate of strain tensor e_{ij} [13] has been considered:

$$\tau_{ij} = -p\delta_{ij} + 2\mu e_{ij} + 2\mu_c e_{ik}e_{kj} \quad (5.1)$$

$$e_{jj} = 0 \quad (5.2)$$

where p is the pressure, μ is the coefficient of viscosity and μ_c is the coefficient of cross-viscosity.

The fluid occupies the space $z > 0$ over an infinite stationary disk (Fig. 5.1), which coincides with $z = 0$. The motion is due to the rotation of the fluid like a rigid body with constant angular velocity Ω at a large distance from the disk.

The flow is described in the cylindrical polar coordinates (r, ϕ, z) . In view of the rotational symmetry $\frac{\partial}{\partial \phi} \equiv 0$. The no-slip boundary conditions for the velocity field are given as:

$$\begin{aligned} z = 0, \quad u = 0, \quad v = 0, \quad w = 0, \\ z \rightarrow \infty, \quad u \rightarrow 0, \quad v \rightarrow r\Omega, \quad p \rightarrow p_\infty \end{aligned} \quad (5.3)$$

The Von Kármán transformations [348]

$$u = r\Omega F(\zeta), \quad v = r\Omega G(\zeta), \quad w = \sqrt{\Omega\nu}H(\zeta), \quad z = \sqrt{\frac{\nu}{\Omega}}\zeta, \quad p - p_\infty = -\rho\nu\Omega P \quad (5.4)$$

reduce the Navier-Stokes equations for a Newtonian fluid to a set of ordinary differential equations. The same is also true for a non-Newtonian Reiner-Rivlin fluid. One defines the non-Newtonian cross-viscous parameter $L = \frac{\mu_c\Omega}{\mu}$. With these definitions and by considering the usual boundary layer approximations, the equations of continuity and motion take the form:

$$\frac{dH}{d\zeta} + 2F = 0, \quad (5.5)$$

$$\frac{d^2F}{d\zeta^2} - H\frac{dF}{d\zeta} - F^2 + G^2 - \frac{1}{2}L\left[\left(\frac{dF}{d\zeta}\right)^2 - 3\left(\frac{dG}{d\zeta}\right)^2 - 2F\frac{d^2F}{d\zeta^2}\right] = 1, \quad (5.6)$$

$$\frac{d^2G}{d\zeta^2} - H\frac{dG}{d\zeta} - 2FG + L\left(\frac{dF}{d\zeta}\frac{dG}{d\zeta} + F\frac{d^2G}{d\zeta^2}\right) = 0, \quad (5.7)$$

$$\frac{d^2H}{d\zeta^2} - H\frac{dH}{d\zeta} - \frac{7}{2}L\frac{dH}{d\zeta}\frac{d^2H}{d\zeta^2} + \frac{dP}{d\zeta} = 0 \quad (5.8)$$

and the boundary conditions (5.3) become:

$$\begin{aligned} \zeta = 0: \quad F = 0, \quad G = 0, \quad H = 0, \\ \zeta \rightarrow \infty: \quad F \rightarrow 0, \quad G \rightarrow 1 \end{aligned} \quad (5.9)$$

The fluid adheres to the surface partially and the motion of the fluid exhibits partial slip conditions. A generalization of Navier's partial slip condition gives, in the radial direction:

$$u|_{z=0} = \lambda_1 T_{rz}|_{z=0}, \quad (5.10)$$

and in the azimuthal direction:

$$v|_{z=0} = \lambda_2 T_{\phi z}|_{z=0}, \quad (5.11)$$

where λ_1, λ_2 are respectively the slip coefficients, and $T_{rz}, T_{\phi z}$ are the physical components of the stress tensor. One defines the dimensionless slip coefficients:

$$\lambda = \lambda_1 \sqrt{\frac{\Omega}{\nu}}\mu, \quad \eta = \lambda_2 \sqrt{\frac{\Omega}{\nu}}\mu \quad (5.12)$$

With the help of the transformations (5.4) the corresponding partial slip boundary conditions (5.10)-(5.11) become:

$$\begin{aligned} F(0) = \lambda[F'(0) - LF(0)F'(0)], \quad G(0) = \eta[G'(0) - 2LF(0)G'(0)], \quad H(0) = 0, \\ F(\infty) \rightarrow 0, \quad G(\infty) \rightarrow 1 \end{aligned} \quad (5.13)$$

The governing equations are still equations (5.5)-(5.7). The boundary conditions (5.9) are replaced by the partial slip boundary conditions (5.13). It is clear that the boundary conditions at infinity remain unaltered.

5.3 Numerical solutions of the problem

5.3.1 Finite-difference solution

The system of nonlinear differential equations (5.5) to (5.7) is solved under the boundary conditions (5.13) by adopting the same second-order numerical scheme described in our previous works

[283, 284, 288]. The semi-infinite integration domain $\zeta \in [0, \infty)$ is replaced by a finite domain $\zeta \in [0, \zeta_\infty)$. In practice, ζ_∞ should be chosen sufficiently large so that the numerical solution closely approximates the terminal boundary conditions.

Now, the following mesh distribution is introduced:

$$\zeta_i = ih \quad (i = 0, 1, \dots, n), \quad (5.14)$$

$h = 0.05$ being the mesh size. Equations (5.5) to (5.7) are then discretized using the central difference approximations for the derivatives:

$$\begin{aligned} \frac{F_{i+1} - 2F_i + F_{i-1}}{h^2} - H_i \left(\frac{F_{i+1} - F_{i-1}}{2h} \right) - F_i^2 + G_i^2 - F_i - \frac{1}{2}L \left[\left(\frac{F_{i+1} - F_{i-1}}{2h} \right)^2 \right. \\ \left. - 3 \left(\frac{G_{i+1} - G_{i-1}}{2h} \right)^2 - 2F_i \left(\frac{F_{i+1} - 2F_i + F_{i-1}}{h^2} \right) \right] - 1 = 0, \end{aligned} \quad (5.15)$$

$$\begin{aligned} \frac{G_{i+1} - 2G_i + G_{i-1}}{h^2} - H_i \left(\frac{G_{i+1} - G_{i-1}}{2h} \right) - 2F_i G_i - G_i \\ + L \left[\left(\frac{F_{i+1} - F_{i-1}}{2h} \right) \left(\frac{G_{i+1} - G_{i-1}}{2h} \right) + F_i \left(\frac{G_{i+1} - 2G_i + G_{i-1}}{h^2} \right) \right] = 0, \end{aligned} \quad (5.16)$$

$$H_{i+1} = H_i - h(F_i + F_{i+1}). \quad (5.17)$$

Note that in Equations (5.15) and (5.16), which are written at the i^{th} mesh point, the first and second derivatives are approximated by the central differences centered at the i^{th} mesh point, while in Equation (5.17), which is written at the $(i+1/2)^{\text{th}}$ mesh point, the first derivative is approximated by the difference quotient at the i^{th} and $(i+1)^{\text{th}}$ mesh points and the right hand sides are approximated by the respective averages at the same two mesh points. This scheme ensures to preserve the second-order accuracy of the spatial discretization.

Equations (5.15) and (5.16) are three term recurrence relations in F and G respectively. Hence, in order to start the recursion, besides the values of F_0 and G_0 the values of F_1 and G_1 are also required. These values can be obtained by Taylor series expansion near $\zeta = 0$ for F and G :

$$F'(0) = s_1, \quad G'(0) = s_2, \quad (5.18)$$

$$F_1 = F(0) + hF'(0) + \frac{h^2}{2}F''(0) + O(h^2), \quad (5.19)$$

$$G_1 = G(0) + hG'(0) + \frac{h^2}{2}G''(0) + O(h^2) \quad (5.20)$$

The values $H(0)$ and $G(0)$ are given as boundary conditions in Equation (5.13). The values $F''(0)$ and $G''(0)$ can be obtained directly from Equations (5.6) and (5.7). After obtaining the values of F_1 and G_1 , the integration can now be performed as follows. H_1 can be obtained from Equation (5.17). Using the values of H_1 in Equations (5.15) and (5.16), the values of F_2 and G_2 are obtained. At the next cycle, H_2 is computed from Equation (5.17) and is used in Equations (5.15) and (5.16) to obtain F_3 and G_3 respectively. The order indicated above is followed for the subsequent cycles. The integration is carried out until the values of F , G and H are obtained at all the mesh points. Note that one needs to satisfy the two asymptotic boundary conditions (Eq.(5.13)). In fact, s_1 and s_2 are found by shooting method along with a fourth-order Runge-Kutta method so as to fulfil the free boundary conditions at $\zeta = \zeta_\infty$ in Equation (5.9).

A noteworthy fact is that for the same values of the flow parameters, the value of the numerical infinity should be chosen larger ($\zeta_\infty = 28$) as compared to the von Kármán flow problem ($\zeta_\infty = 10$) [283], so that the numerical solution closely approximates the terminal boundary conditions at ζ_∞ .

The above algebraic system of equations are solved by a generalized Gauss-Seidel method [289] instead of successive over relaxation method and thus the involvement of more parameters is avoided. The convergence of the generalized Gauss-Seidel method for the above diagonally dominant system of equations is quite fast.

5.3.2 The Keller-box method

The Keller-box method (KBM) originally developed by Keller [153] to solve parabolic partial differential equations describing boundary layer flow problems can be decomposed into four basic steps:

1. Reduce the governing equations to a first-order system,
2. Write difference equations using central schemes,
3. Linearize the resulting equations,
4. Write the equations under a matrix-vector form and solve the linear system by block tridiagonal elimination method.

The Keller-box method is only used here in the Newtonian case for which $L = 0$. The nonlinear Eqs. (5.6)-(5.7), by considering (5.5), are reduced to:

$$\frac{d^3 H}{d\zeta^3} - H \frac{d^2 H}{d\zeta^2} + \frac{1}{2} \left(\frac{dH}{d\zeta} \right)^2 - 2G^2 + 2 = 0, \quad (5.21)$$

$$\frac{d^2 G}{d\zeta^2} - H \frac{dG}{d\zeta} + G \frac{dH}{d\zeta} = 0 \quad (5.22)$$

and boundary conditions (5.13) are converted to:

$$H'(0) = \lambda H''(0), \quad G(0) = \eta G'(0), \quad H(0) = 0, \quad H'(\infty) \rightarrow 0, \quad G(\infty) \rightarrow 1 \quad (5.23)$$

Obviously, after solving the system (5.21)-(5.23), one can solve Eq.(5.6) very easily. In this method, Eqs. (5.21)-(5.22) first converted into a system of five first-order equations are then expressed using central differences. For this purpose, one introduces new dependent variables $S(\zeta)$, $Q(\zeta)$ and $T(\zeta)$ so that Eqs. (5.21)-(5.22) can be written as:

$$\frac{dH}{d\zeta} = S(\zeta), \quad (5.24)$$

$$\frac{dS}{d\zeta} = Q(\zeta), \quad (5.25)$$

$$\frac{dG}{d\zeta} = T(\zeta), \quad (5.26)$$

$$\frac{dQ}{d\zeta} - HQ + \frac{1}{2} S^2 - 2G^2 + 2 = 0, \quad (5.27)$$

$$\frac{dT}{d\zeta} - HT + SG = 0 \quad (5.28)$$

In terms of the new dependent variables, the boundary conditions (5.23) are given by:

$$S(0) = \lambda Q(0), \quad G(0) = \eta T(0), \quad H(0) = 0, \quad S(\infty) \rightarrow 0, \quad G(\infty) \rightarrow 1 \quad (5.29)$$

One now considers the segment $[\zeta_{j-1}, \zeta_j]$, with $\zeta_{j-1/2}$ as the midpoint, which is defined as below:

$$\zeta_0 = 0, \quad \zeta_j = \zeta_{j-1} + h, \quad \zeta_J = \zeta_\infty, \quad (5.30)$$

where $h = 0.01$ is the $\Delta\zeta$ -spacing and $j = 1, \dots, J$ is a sequence number that indicates the coordinate location. The finite-difference approximations of Eqs.(5.24)-(5.28) are written for the midpoint $\zeta_{j-1/2}$:

$$H_j - H_{j-1} - \frac{h}{2}(S_j + S_{j+1}) = 0, \quad (5.31)$$

$$S_j - S_{j-1} - \frac{h}{2}(Q_j + Q_{j+1}) = 0, \quad (5.32)$$

$$G_j - G_{j-1} - \frac{h}{2}(T_j + T_{j+1}) = 0, \quad (5.33)$$

$$Q_j - Q_{j-1} - \frac{h}{4}(H_j + H_{j-1})(Q_j + Q_{j-1}) + \frac{h}{8}(S_j + S_{j-1})^2 - \frac{h}{2}(G_j + G_{j-1})^2 + 2h = 0, \quad (5.34)$$

$$T_j - T_{j-1} - \frac{h}{4}(H_j + H_{j-1})(T_j + T_{j-1}) + \frac{h}{4}(S_j + S_{j-1})(G_j + G_{j-1}) = 0 \quad (5.35)$$

Equations (5.31)-(5.35) are imposed for $j = 1, 2, \dots, J$ for sufficiently large ζ_∞ , the boundary layer thickness. The boundary conditions (5.29) are converted to:

$$S_0 = \lambda Q_0, \quad G_0 = \eta T_0, \quad H_0 = 0, \quad S_J = 0, \quad G_J = 1 \quad (5.36)$$

One can linearize the nonlinear system (5.31)-(5.35) by the Newton's method, and the linearized difference system can be solved by the block elimination method as outlined by Cebeci and Bradshaw [45], since the obtained linear system has block-tridiagonal structure.

5.3.3 Performances of the two methods

To compare the efficiency of the aforementioned two numerical schemes, Table 5.1 shows the CPU time (in seconds) for $L = 0$, different values of the slip parameter and a given mesh distribution ($\zeta_\infty = 14$ and $h = 0.01$). Converged results are obtained after 15 iterations. Though the finite difference method (FDM) is more effective than the KBM in some sense, the CPU time for the FDM is significantly much higher as compared to the Keller-box method. It should be taken with certain caution as the methods have been runned using different machines with different configurations. However, the calculations remain quite fast and for both schemes, the CPU time increases with an increase in λ .

$\lambda(= \eta)$	FDM	Keller-box method
0	820.2	21.5
1	852.6	21.7
2	906.6	25.6
3	931.8	25.7

Table 5.1: Values of the CPU time (in seconds) for $L = 0$ and different values of $\lambda(= \eta)$.

5.4 Results and discussion

The value of $\zeta_\infty = 28$ has been taken larger as compared to the previous problem [283] ($\zeta_\infty = 10$) and kept constant. Although, the results are shown only from the disk surface $\zeta = 0$ to $\zeta = 14$, the numerical integrations were performed over a substantially larger domain in order to assure that the asymptotic boundary conditions are satisfied.

5.4.1 Viscous fluid ($L = 0$)

To validate our approach, the values of F , G and H for the no-slip condition ($\lambda = 0$) are compared with those reported by Owen and Rogers [233] for a viscous fluid ($L = 0$) and reported in Table 5.2. The present numerical results presented herein both for the finite-difference method and the Keller-box method confirm the calculations of Owen and Rogers [233] for the velocity components.

ζ	F			G			H		
	FDM	Keller-box	Owen & Rogers [233]	FDM	Keller-box	Owen & Rogers [233]	FDM	Keller-box	Owen & Rogers [233]
	0.0	0.000000	0.000000	0.0000	0.000000	0.000000	0.0000	0.000000	0.000000
0.5	-0.348651	-0.348651	-0.3487	0.383430	0.383427	0.3834	0.194374	0.194365	0.1944
1.0	-0.478766	-0.478769	-0.4788	0.735429	0.735425	0.7354	0.624103	0.624090	0.6241
1.5	-0.449634	-0.449639	-0.4496	1.013401	1.013399	1.0134	1.098743	1.098730	1.0987
2.0	-0.328745	-0.328751	-0.3287	1.192367	1.192368	1.1924	1.492876	1.492870	1.4929
2.5	-0.176207	-0.176210	-0.1762	1.272136	1.272140	1.2721	1.745870	1.745870	1.7459
3.0	-0.036086	-0.036088	-0.0361	1.271405	1.271411	1.2714	1.849641	1.849640	1.8496
3.5	0.066311	0.066310	0.0663	1.218219	1.218225	1.2182	1.830807	1.830810	1.8308
9.5	-0.010216	-0.010217	-0.0102	1.011849	1.011850	1.0118	1.361698	1.361690	1.3617
10.0	-0.003282	-0.003283	-0.0033	1.012120	1.012121	1.0121	1.368330	1.368320	1.3683
10.5	0.001820	0.001819	0.0018	1.009906	1.009907	1.0099	1.368882	1.368880	1.3689
11.0	0.004738	0.004738	0.0047	1.006537	1.006537	1.0065	1.365423	1.365420	1.3654
11.5	0.005681	0.005681	0.0057	1.003090	1.003090	1.0031	1.360067	1.360060	1.3601
12.0	0.005170	0.005171	0.0052	1.000271	1.000272	1.0003	1.354546	1.354540	1.3545
12.5	0.003827	0.003827	0.0038	0.998411	0.998411	0.9984	1.350003	1.350000	1.3500
20.0	0.000102	0.000102	-	0.999893	0.999893	-	1.349325	1.349320	-
25.0	0.000009	0.000009	-	1.000014	1.000013	-	1.349457	1.349450	-
25.5	0.000011	0.000011	-	1.000007	1.000007	-	1.349447	1.349440	-
26.0	0.000010	0.000010	-	1.000001	1.000001	-	1.349437	1.349430	-
26.5	0.000008	0.000008	-	0.999997	0.999997	-	1.349428	1.349420	-
28.0	0.000000	0.000000	0.0000	1.000000	1.000000	1.0000	1.349421	1.349410	1.3494

Table 5.2: Variations of F , G and H for $L = \lambda(= \eta) = 0$.

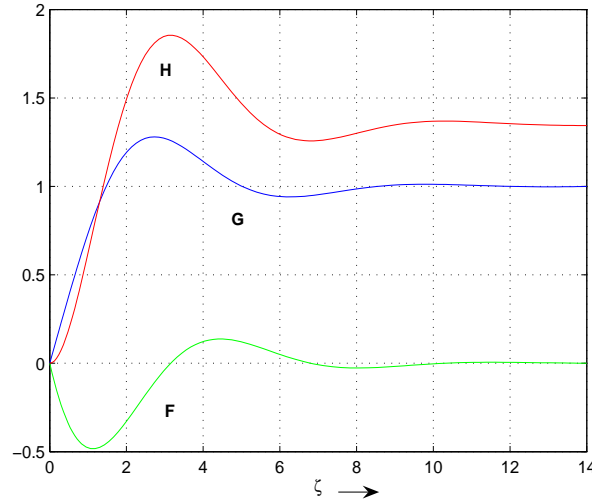


Figure 5.2: Velocity profiles for the Newtonian case ($L = 0$) and $\lambda(= \eta) = 0$ obtained by the FDM.

Figure 5.2 depicts that near the disk, the radial velocity component F is radially inwards. It may be of interest to note that this radially inward flow is the cause of the accumulation of the tea leaves at the center of a stirred cup. The behaviors of the three velocity components confirm the sketch shown in Figure 5.1. From the profile of G , one can deduce the value of the boundary layer thickness ζ_{99} , which is defined as the axial coordinate for which the tangential velocity of the fluid is equal to the tangential fluid velocity at infinity within 1%. For $L = 0$ and $\lambda = 0$, the classical value $\zeta_{99} = 8$ is recovered by the present approach [233].

In order to have an insight into the effects of the slip, results are shown for the uniform roughness ($\lambda = \eta$) using the FDM only. More comparisons between the two approaches are provided at the end of this section. It is noteworthy that, for other combinations of λ and η , a similar behavior has been obtained but is not shown here.

Figure 5.3 shows the effects of slip on the velocity field. Figure 5.3a shows the variation of the radial velocity component F with the slip parameter λ . The effect of slip on F is prominent near the disk. Clearly, the maximum value of the radial inflow decreases with an increase in slip and its location moves towards the disk. The velocity profiles reverse the direction away from the disk and approach the asymptotic value at a shorter distance from the disk for larger λ . Multiple cross-overs are observed for the radial velocity profiles. Figure 5.3b shows the azimuthal velocity represented by $G(\zeta)$. Its value increases with ζ , attains its maximum, then decreases and attains its asymptotic value 1. One can observe that G increases with an increase in slip, near the disk and decreases away from the disk, as was expected. The oscillations occurring in the boundary layer when the fluid rotates near a stationary disk can be explained in the following manner. The radial inflow, induced by the retardation of the tangential velocity in the vicinity of the stationary disk, tends to conserve the angular momentum of the flow and thus to increase the tangential velocity with decreasing radius. For an overshoot, radial advection of the angular momentum near the disk must be strong enough to more than balance the dissipation of angular momentum caused by the wall shear. This inward radial advection of surplus angular momentum is possible as long as the distribution of circulation in the outer flow increases with increasing radius. A local overshoot in the tangential velocity increases the centrifugal force locally which then tends to induce a radial outflow. This radial outflow advects an angular momentum defect to force an undershoot in the tangential velocity, and the above process is repeated to yield oscillatory approach to infinity. The variation of the axial velocity component H with λ can be seen in Figure 5.3c. It is observed that H decreases significantly with an increase in slip. The axial profiles become flatter with an increase in λ . The axial velocity at infinity H_∞ is strongly reduced compared to the basic no-slip case $\lambda = 0$, for which $H_\infty = 1.349421$. It is interesting to find that slip dominates the oscillations in the velocity profiles.

Another important parameter of this flow problem is the effect of slip on the pressure distribution. The prominent effect can be observed in Figure 5.3d. It is evident that in absence of slip ($\lambda(= \eta) = 0$), the dimensionless pressure P has a dominating effect near the surface of the stationary disk. This causes the radial inward flow near the disk surface. Pressure decreases with an increase in slip near

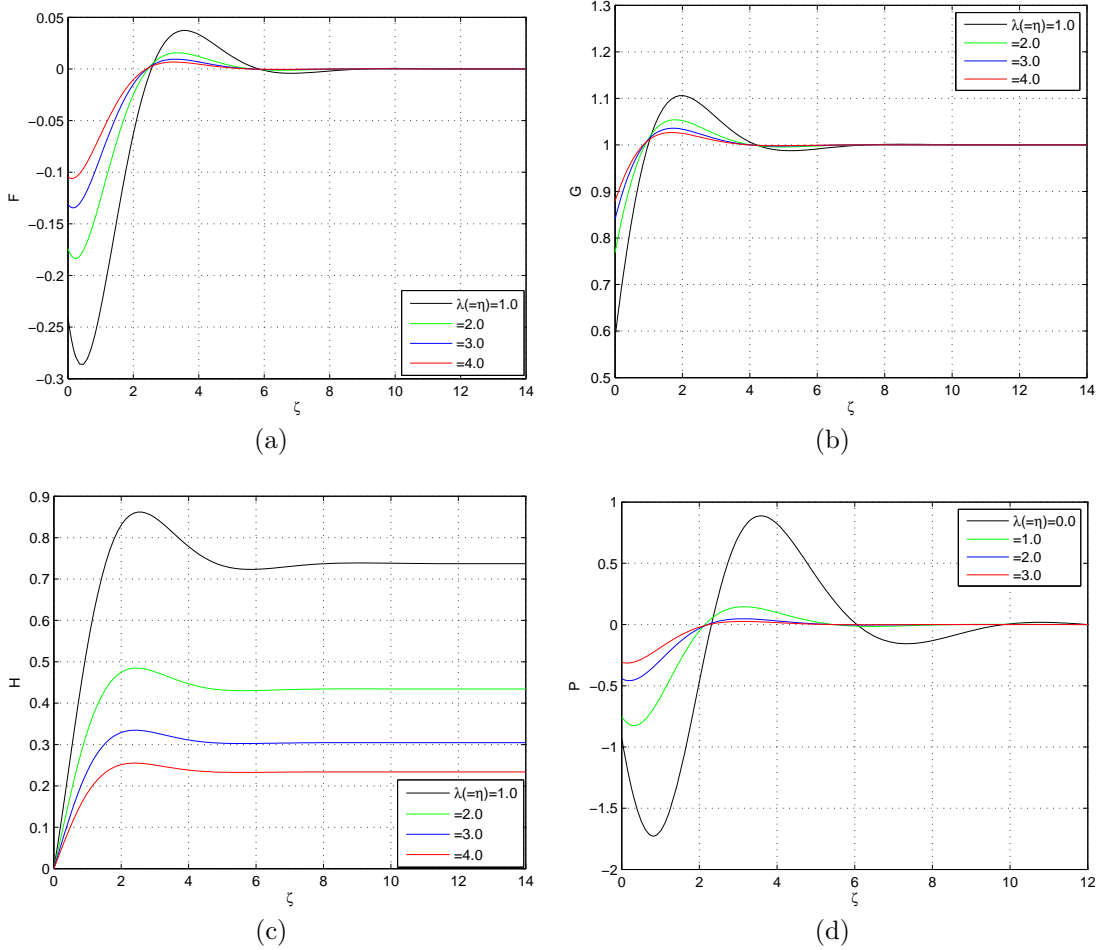


Figure 5.3: Variations of F , G , H and P with $\lambda (= \eta)$ for $L = 0$ obtained by the FDM.

the surface and consequently the strength of the radial inflow decreases, as shown on Figure 5.3b. In presence of slip, the pressure profiles attain their asymptotic value $P = 0$ closer to the disk surface.

The expressions of the tangential shear stress $\bar{\tau}_\phi$, radial shear stress $\bar{\tau}_r$ and the dimensionless moment coefficient C_M are:

$$\tau_\phi = \frac{\bar{\tau}_\phi}{\rho r \sqrt{\nu} \Omega^3} = \frac{dG(0)}{d\zeta}, \quad \tau_r = \frac{\bar{\tau}_r}{\rho r \sqrt{\nu} \Omega^3} = \frac{dF(0)}{d\zeta}, \quad C_M = \frac{-\pi G'(0)}{\sqrt{Re}} \quad (5.37)$$

where $Re = \frac{R^2 \Omega}{\nu}$ is the Reynolds number based on the radius R and the tip velocity ΩR . Throughout the computations, the value of Re has been fixed to $Re = 1$. This definition of C_M is an extension of the finite disk problem, which supposes that the disk radius is large enough. Note that the present value of $G'(0)$ for a Newtonian fluid and no slip condition ($L = \lambda = 0$) is in excellent agreement with the value $G'(0) = 0.77289$ obtained by Owen and Rogers [233]. Thus, one got the classical value $C_M = -4.86$ in that basic case.

Figure 5.4a depicts the effects of slip on the surface shear stress in the radial direction τ_r , and compares the finite-difference and Keller-box methods. It shows that the magnitude of τ_r decreases with an increase in λ and remains negative throughout the range of the slip parameter. Figure 5.4b shows that the tangential shear stress τ_ϕ also decreases with an increase in slip, but its value remains positive for the entire range of the slip parameter.

Figure 5.5 presents the variation of the dimensionless moment coefficient C_M with slip. For the whole range of slip parameter, C_M exhibits negative values. It may be attributed to the flow problem: the flow due to an infinite rotating disk [283]. The Von Kármán flow considered by Sahoo [283] is precisely the inverse problem, which explains the different signs in C_M . Moreover, it is important to note that the linear nature of the τ_r , τ_ϕ and C_M profiles for the current viscous flow is contrary to

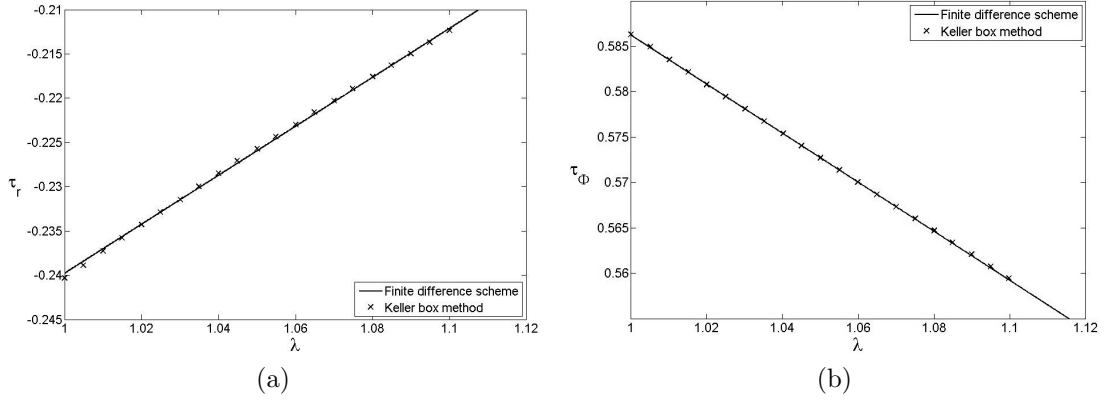


Figure 5.4: Variations of (a) τ_r and (b) τ_ϕ with $\lambda(= \eta)$ for $L = 0$; Comparison between the finite-difference and the Keller-box methods.

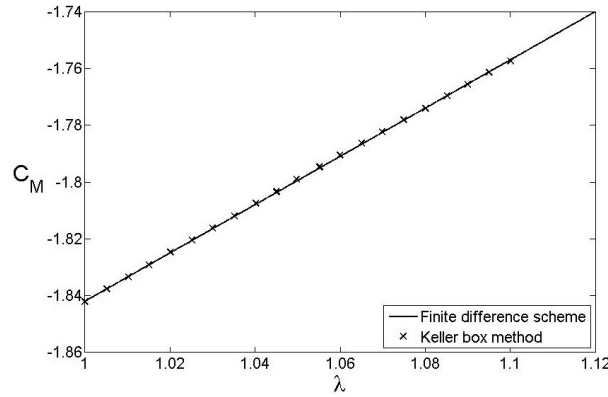


Figure 5.5: Variation of C_m with $\lambda(= \eta)$ for $L = 0$; Comparison between the finite-difference and the Keller-box methods.

the corresponding profiles for non-Newtonian fluids [283, 286]. This may be due to the presence of extra nonlinear terms in the expressions for τ_r , τ_ϕ and C_M , associated with the non-Newtonian cross-viscous parameter in [283, 286]. For these three quantities, there is an excellent agreement between the finite-difference schemes and the Keller-box method.

5.4.2 Non-Newtonian fluid ($L \neq 0$)

In order to have an insight of the flow characteristics in the non-Newtonian case, results are plotted for the uniform roughness ($\lambda = \eta$), and different values of the flow parameters only using the finite-difference method (FDM). The variations of the radial velocity component F with the non-Newtonian cross-viscous parameter L and the slip parameter $\lambda(= \eta)$ are shown in Figures 5.6 and 5.7 respectively, when the other flow parameters are kept constant. Figure 5.6 reveals that L has a prominent effect on F , near the disk. The magnitude of the radial inflow, near the disk, decreases with an increase in L . The radial velocity component near the disk remains negative for all values of the non-Newtonian parameter L , reverses the direction away from the disk, and finally approaches its asymptotic value. Thus, cross-overs are found in the velocity profile. Figure 5.7 shows the variation of F with the slip parameter $\lambda(= \eta)$, when other flow parameters are kept constant. It is clear that the effect of slip on F is also prominent near the disk. The velocity profiles reverse the direction away from the disk and approach the asymptotic value at a shorter distance from the disk as compared to the former case.

Figures 5.8 and 5.9 depict the variations of the azimuthal velocity component with L and $\lambda(= \eta)$ respectively. The non-Newtonian parameter L has a spectacular effect on G , away from the disk (near $\zeta = 2$). An increase in L decreases the velocity profile G near the disk. The velocity component increases (see Figure 5.9) near the disk with an increase in $\lambda(= \eta)$. Thus, it is interesting to find that

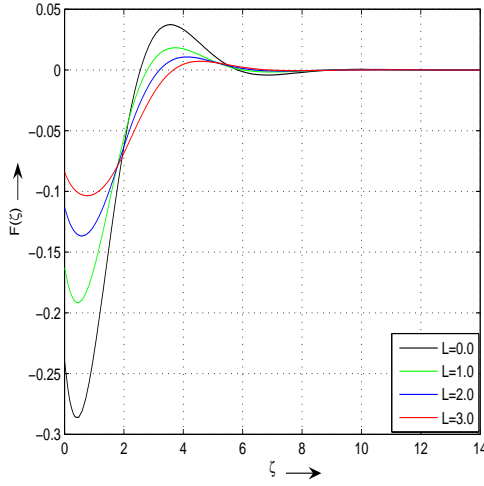


Figure 5.6: Variations of F with L for $\lambda(= \eta) = 1$.

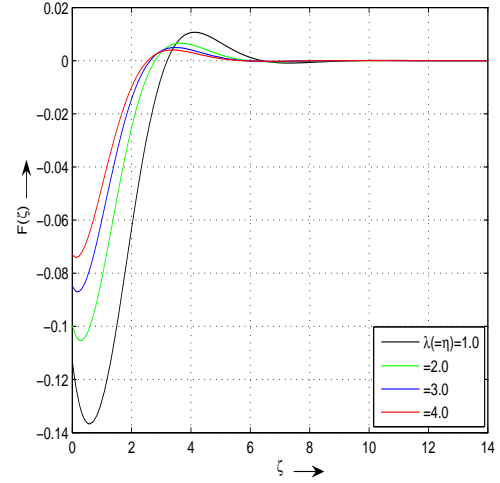


Figure 5.7: Variations of F with $\lambda(= \eta)$ for $L = 2$.

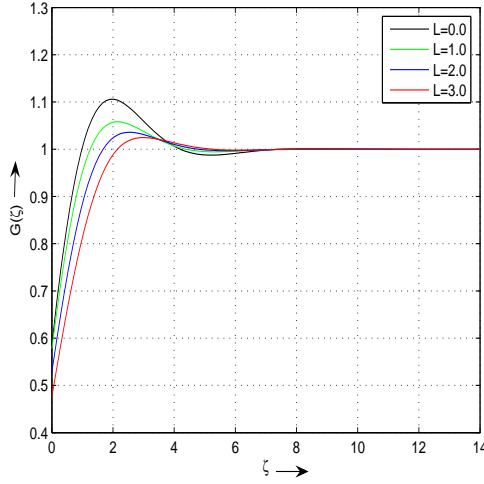


Figure 5.8: Variations of G with L for $\lambda(= \eta) = 1$ (FDM).

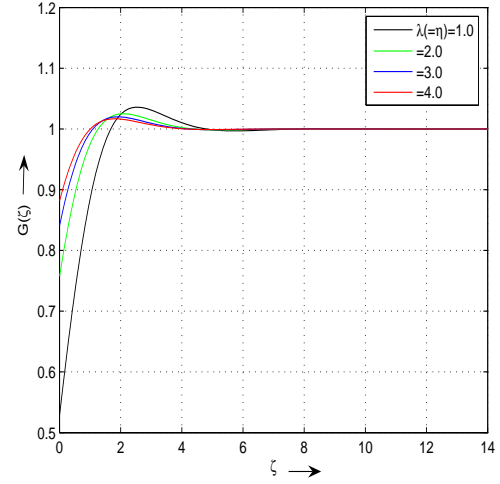


Figure 5.9: Variations of G with $\lambda(= \eta)$ for $L = 2$ (FDM).

the slip has an opposite effect to that of the cross-viscous parameter on G . From these profiles, the boundary layer thickness ζ_{99} can be calculated for all flow parameters. The variations of ζ_{99} with the slip parameter λ and the non-Newtonian parameter L are shown in Figures 5.10 and 5.11 respectively and compared with the classical value $\zeta_{99} = 8$ obtained for a Newtonian fluid $L = 0$ and no slip condition $\lambda = 0$. For $L = 2$, ζ_{99} slightly increases with increasing values of the slip parameter λ , following the quadratical fitting law:

$$\zeta_{99} = 0.098\lambda^2 - 0.061\lambda + 2.8 \quad (5.38)$$

For a given value of the slip parameter $\lambda = 1$, ζ_{99} slightly increases also with increasing values of the non-Newtonian parameter L , following also a quadratical law:

$$\zeta_{99} = 0.055L^2 - 0.027L + 3.9 \quad (5.39)$$

It is noteworthy that the values of ζ_{99} are much weaker than the ones obtained for no-slip condition ($\lambda = 0$) in the case of a Newtonian fluid ($L = 0$): $\zeta_{99} = 8$ [233].

Another interesting quantity, which can be deduced from the profiles of F and G , is the turning moment for the disk with fluid on both sides. The expression of the dimensionless moment coefficient C_M is given by:

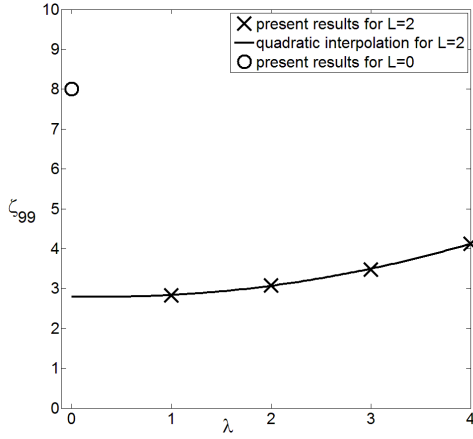


Figure 5.10: Variation of the boundary layer thickness ζ_{99} with λ for $L = 2$ (FDM).

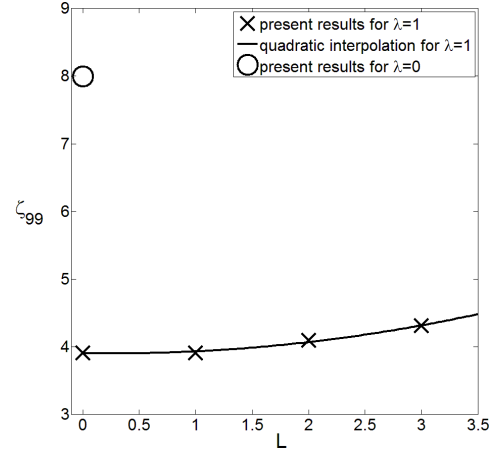


Figure 5.11: Variation of the boundary layer thickness ζ_{99} with L for $\lambda = 1$ (FDM).

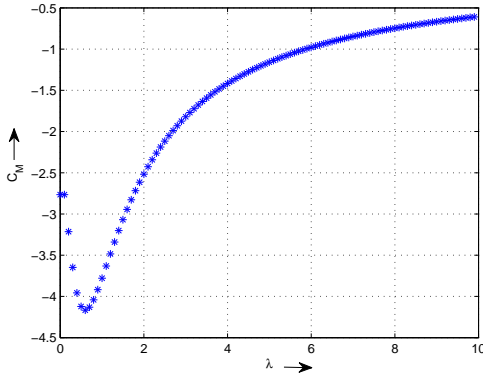


Figure 5.12: Variation of the moment coefficient C_M with λ for $L = 1$ and $Re = 1$ (FDM).

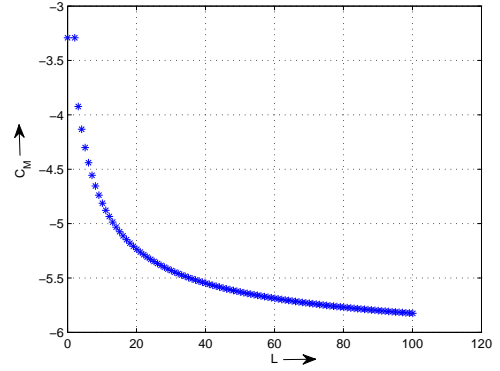


Figure 5.13: Variation of the moment coefficient C_M with L for $\lambda = 1$ and $Re = 1$ (FDM).

$$C_M = \frac{-2\pi G'(0)[1 - 2LF(0)]}{\sqrt{Re}} \quad (5.40)$$

The variations of C_M with the slip λ and non-Newtonian L parameters are shown in Figures 5.12 and 5.13 respectively. Whatever the flow parameters, C_M exhibits negative values. It may be attributed to the flow problem: a rotating fluid at infinity over a stationary disk. Thus, the axial gradient of the tangential velocity G' is still positive and C_M is then always negative. The Von Kármán flow considered by Sahoo [283] is precisely the inverse problem, which explains the different signs. For $L = 1$ and $Re = 1$ (see Fig.5.12), the moment coefficient C_M in absolute values strongly increases (resp. decreases) with increasing values of the slip parameter λ for $\lambda < 0.6$ (resp. $\lambda > 0.6$). It tends rapidly to zero for high values of λ , which means that the torque required to maintain the disk at its original speed is almost zero when the slip parameter is high. Omitting the different boundary conditions between the two problems, the present results confirm the previous ones of Sahoo [283] for Von Kármán flows and comparable values are obtained.

The slip parameter λ is now fixed to unity and the non-Newtonian parameter L varies between 0 and 100 for $Re = 1$ (Fig.5.13). C_M increases in magnitude with the parameter L . In that case, the torque required to maintain the disk at rest is much higher than those necessary to maintain the disk at Ω for the Von Kármán flow considered by Sahoo [283].

The variations of the axial velocity component H with L and $\lambda (= \eta)$ have been plotted in Figures 5.14 and 5.15 respectively. The figures show that both parameters have a similar effect on H . It

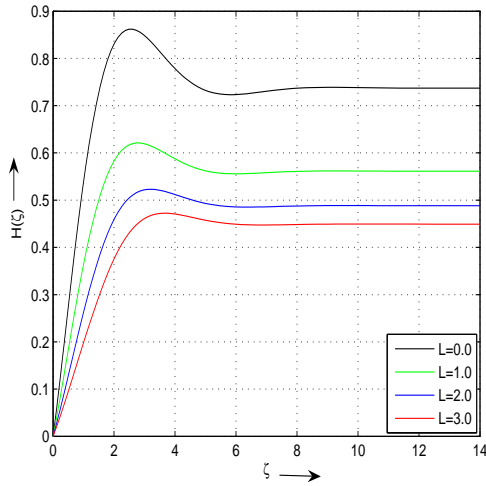


Figure 5.14: Variations of H with L for $\lambda(= \eta) = 1$ (FDM).

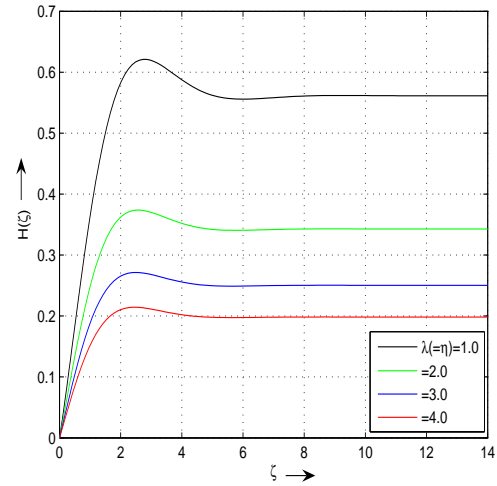


Figure 5.15: Variations of H with $\lambda(= \eta)$ for $L = 2$ (FDM).

is clear that the axial velocity becomes flatter with an increase in L and $\lambda(= \eta)$. The axial velocity at infinity H_∞ in both cases is strongly reduced compared to the basic case $L = 0$ and $\lambda = 0$, for which $H_\infty \simeq 1.3494$.

5.5 Conclusion

In this work, the slip flow due to the rotation of a both a Newtonian viscous fluid and of a non-Newtonian Reiner-Rivlin fluid near a stationary disk have been examined precisely for the first time.

In the Newtonian case, the resulting highly nonlinear differential equations are solved by two methods: a second-order numerical scheme based on the finite-difference method and the Keller-box method. It is found that slip decreases the radial inflow near the disk. With an increase in slip, the azimuthal velocity G increases near the disk and decreases away from the disk. It is also observed that slip dominates the oscillations in the velocity profiles. One of the significant findings of the present study is that the moment coefficient C_m , which is a measure of the torque required to maintain the disk at rest, decreases with an increase in slip.

Then, the Bödewadt flow problem is extended to the non-Newtonian case using the Reiner-Rivlin fluid model. The combined effects of the slip ($\lambda = \eta$) and the non-Newtonian parameter (L) on the velocity field are studied in details using the finite-difference schemes. It is interesting to find that $\lambda(= \eta)$ and L have similar effects on the radial and axial velocity components. For increasing values of λ or L , a slight thickening of the boundary layer on the stationary disk is observed. On the other hand, both parameters have opposite effects on the azimuthal velocity component and the moment coefficient. Thus, the torque required to maintain the disk at rest tends to zero for increasing values of λ and increases (in absolute values) with L showing a predominant influence of the non-Newtonian parameter.

The present work is a step forward in the computation of the rotor- stator flow with partial slip effects and/or using non-Newtonian fluids to establish reference solutions for future numerical benchmarks. A more faraway outlook is the inclusion of finite cavity and confinement effects.

The same analysis can be done in many other flow configurations: plane stagnation-point flow (Hiemenz flow), flow past a stretching sheet, flow past an infinite plate (Blasius flow) ... One has performed the same kind of analysis in the two latter cases, whose results have been published in references [285] and [287] respectively.

Shear-layer instability over a rotating disk

In this Chapter, a spectacular shear-layer instability generic of rotating flow arrangements is studied in details mainly by flow visualizations and image processing but also by recent DNS calculations. This work was initiated when I was assistant lecturer at IRPHE. With Marie-Pierre Chauve, one has discovered this instability a little bit by chance, simply by coming apart the rotor-stator experiment. The experimental results have been published in *J. Flow Visualization & Image Processing* (Ref. [250]). In the framework of a collaboration with Laurent Martin-Witkowski (LIMSI), the present results have been compared to the stability analysis of Kahouadji et al. [144].

The shear-layer instability in the flow over a rotating disk with a free surface is thus investigated mainly experimentally by flow visualizations and by DNS using the pseudospectral code described in Chapter 3 for a large range of the flow parameters: the aspect ratio G of the cavity, the rotational Reynolds number Re and the radius ratio η between the inner and outer radii of the disk. This instability develops along the cylindrical shroud as sharp-cornered polygonal patterns characterized by their number of vortices m . This number m can be scaled by considering an Ekman number based on the water depth, which confirms that the shroud boundary layer is of Stewartson type. The appearance threshold of the first polygonal mode is constant by considering the mixed Reynolds number introduced by Niino and Misawa [223]. For large values of η , the instability patterns appear along the hub as small stationary cells.

6.1 Introduction

The stability of rotating disk flows has been addressed for a long time, mostly in the case of a single infinite rotating disk [91] and more recently in the rotor-stator configuration [61, 252]. The present work considers an experimental system where a shear-layer instability is obtained over a finite rotating disk with a free surface. Shear layers in rapidly rotating systems (called Stewartson layers) are of primary importance from a geophysical point of view, as they can be observed in oceans or in planetary atmospheres. For examples, the Great Red Spot on Jupiter (Fig.6.1a) and the Blue spot on Neptune result from differential rotation with sharply sheared zonal flows. Figure 6.1b presents another spectacular example: the hexagonal vortex formed at the North pole of Saturn. Rotating shear layer instabilities have been seen also in flows enclosed in computer hard drives. The instability that affects a circular shear-zone has then been widely studied in various configurations.

Stewartson [331] considered the stationary linear problem in the case of a split rotating cylinder. He showed, using an asymptotical method, that the flow generated by a slight differential rotation of one part of the shell is composed by two cylindrical shear layers aligned with the axis of rotation and located at the split radius. The largest one is geostrophic and its width scales like $E_b^{1/4}$ (where $E_b = \nu/(\Omega b^2) = 1/Re$ is the Ekman number based on the cylinder radius b , ν the kinematic viscosity of the fluid, Ω the rate of rotation of the cylinder and Re the rotational Reynolds number), whereas the width of the thinner ones scales like $E_b^{1/3}$.

Hide and Titman [127] investigated experimentally the linear stability of the Stewartson layers, which develop on a differentially rotating disk suspended in a rotating tank. The instability appears as non-axisymmetric patterns of m waves in planes perpendicular to the rotation axis above a well-defined threshold. The number m is maximum at the threshold and decreases with the amplitude of the differential rotation. In their experiments, the Coriolis force plays an important role in the development of the vortices proving that this is not just a Kelvin-Helmholtz instability. Rabaud and Couder [265] performed experiments on the destabilization of a thin layer of air between two plates. The instability is of Kelvin-Helmholtz type and induces regular, steady patterns of m vortices. Neither

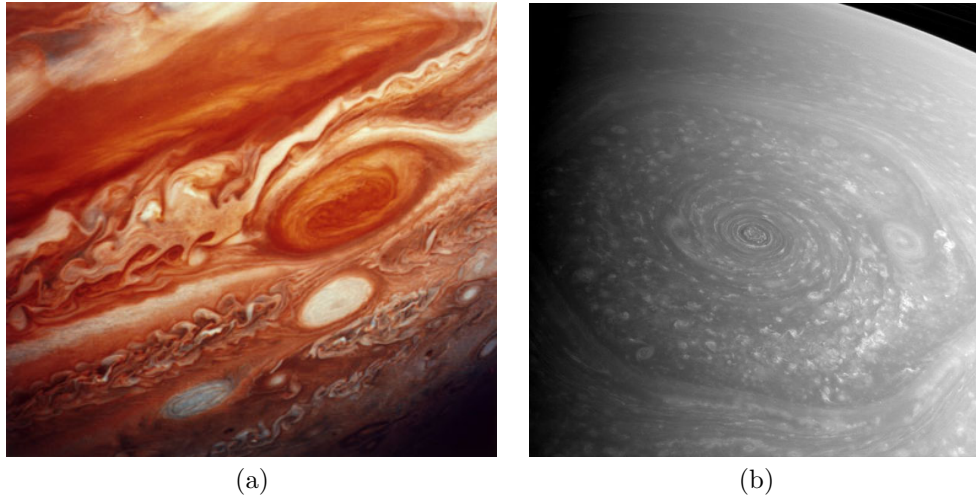


Figure 6.1: (a) The Great Red Spot on Jupiter as discovered by Giovanni Cassini; (b) Image of the Saturn North polar hexagonal vortex taken by the Cassini Solstice Mission (Source: NASA / JPL-Caltech / Space Science Institute, November 27, 2012).

the centrifugal nor the Coriolis forces are involved in the motion. The same configuration has been considered later by Chomaz *et al.* [53], who compared the results presented in Rabaud and Couder [265] with new experiments and numerical simulations. They showed in particular the dependence on the aspect ratio of the cell on the dynamical behavior of the flow. In large cells, transitions from a mode with m vortices to a mode with $(m - 1)$ vortices occur through localized processes. On the contrary, in small cells, transitions occur after a series of bifurcations corresponding to successive breakings of all the symmetries of the flow. The same configuration has been studied numerically by Bergeron *et al.* [22]. They compared the results of their numerical code with the experimental data and the linear stability analysis of Rabaud and Couder [265] and Chomaz *et al.* [53] with a reasonable agreement between the different approaches, although Bergeron *et al.* [22] found a clear dependence of the critical Reynolds number on the aspect ratio of the shell.

Niino and Misawa [223] considered a flow driven by a thin disk at the bottom of a tank to study the barotropic instability of horizontal shear flows. They compared their experimental results with a linear stability analysis applied to an initially circular shear-layer, including viscous diffusion and Ekman pumping. They found that the number of vortices should decrease with increasing Reynolds number. In a laboratory experiment, Früh and Read [100] studied also the barotropic shear layer in a rotating fluid. Above a critical shear, the shear layer breaks up through a barotropic instability, which appears as a string of vortices along the shear zone. They showed that the transition from the axisymmetric mode to regular vortices occurs through a Hopf bifurcation. They obtained between $m = 2$ and 8 modes. Van de Konijnenberg *et al.* [341] investigated experimentally and numerically the instability of a forced, circular shear layer in a rotating fluid. They applied a radial pumping to a shallow layer of water in a parabolic tank to model a geophysical β -effect. The instability appears as a sequence of vortices, the number of which decreases with increasing the shear strength. The radial pumping of fluid from the periphery to the center of the cavity induces an azimuthal flow, which stabilizes the shear flow if it is opposite to the rotation or destabilizes it otherwise. A β -effect may prevent the formation of a steady vortex chain.

Dolzanskii *et al.* [76] considered a MHD device for the generation of both a circular shear flow and a Kolmogorov flow. They compared their experimental results to the stability theory of quasi-two-dimensional flows with a close agreement between the different approaches. In the circular geometry, the modes $m = 3, 5$ and 6 of the shear layer instability have been observed.

The flow between an enclosed corotating disk pair (ECDP) offers a well-known configuration to observe polygonal patterns. Abrahamson *et al.* [4] studied experimentally this type of flow for a radius ratio $\eta = a/b = 0.5$, $1.5 \times 10^5 \leq Re \leq 1.5 \times 10^6$ and $0.013 \leq G = h/b \leq 0.1$ (a and b are respectively the inner and outer radii of the cavity and h is the interdisk spacing). They observed three distinct regions: a solid body inner region near the hub, an outer region dominated by large counter-rotating

vortices and a boundary layer along the shroud, the last one being three-dimensional (3D) contrary to the two others. They considered two flow parameters: the Ekman number E_b and the aspect ratio of the cavity G . When E_b decreases or G increases, the number of vortices m decreases but they become larger. Herrero *et al.* [126] established numerically the bifurcation diagram in the ECDP case in the plane (Re, G) for $\eta = 0.537$, $Re \leq 82380$ and $0.05 \leq G \leq 0.2$. They distinguished three regions corresponding respectively to axisymmetric steady flow with interdisk midplane symmetry, to 3D unsteady flow with shift-and-reflect symmetry and to 3D unsteady flow with symmetry breaking with respect to the midplane. In the last case, they obtained the mode $m = 4$ for $Re = 13710$ and $G = 0.18$ and the mode $m = 5$ for $Re = 82380$ and $G = 0.091$ in agreement with the observations of Abrahamson *et al.* [4]. Randriamampianina *et al.* [267] presented a numerical investigation of the flow in the ECDP case for $\eta = 0.5$, $0.01 \leq G \leq 0.6$ and $Re = 1.06 \times 10^4$. For $G \geq 0.26$, they showed that the transition to unsteady 3D flow occurs after the pitchfork bifurcation. The flow structure is then characterized by a shift-and-reflect symmetry, which is consistent with the experiments of Abrahamson *et al.* [4]. For smaller values of the aspect ratio, the 3D flow shows a symmetry breaking. For $G = 0.6$ and increasing values of the rotation rate, they obtained successively the mode $m = 8$ for $Re = 3750$, the mode $m = 6$ for $Re = 4250$ and the mode $m = 5$ for $Re = 10^4$.

The shear layer instability in the flow between two counter-rotating disks enclosed by a cylinder has been investigated experimentally and numerically by Moisy *et al.* [212] for $\eta = 0$ and $0.048 \leq G \leq 0.5$. It develops as a sharp-cornered polygonal pattern with m sides, already observed by Lopez *et al.* [187], surrounded by a set of $2m$ spiral arms. The lower modes $m = 3 - 5$ (Fig.6.2) are observed essentially for large aspect ratios and the number of sides increases for decreasing values of the aspect ratio. No hysteresis is reported for the instability threshold but a noticeable one is present for the onset mode. The authors believe that the bifurcation remains supercritical for the whole range of the flow control parameters. The reader is referred to the work of Moisy *et al.* [212] for a more extensive literature survey on such a flow configuration.

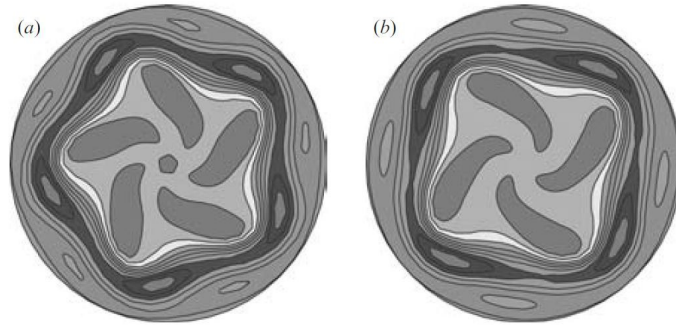


Figure 6.2: Results after Moisy *et al.* [212] in the counter-rotating disk cavity for $G = 1/3$, $Re_{top} = 2520$ and $Re_{bottom} = 720$: (a) Mode $m = 5$ after a sudden increase of Ω ; (b) Mode $m = 4$ after a progressive increase of Ω .

The reader is referred also to the review paper of Dolzhanskii *et al.* [75] and to the work of Bergeron *et al.* [21] for discussion about the analysis of the shear layer with weakly nonlinear theory, which accounts for phenomena such as hysteresis and saturation of the amplitude of the unstable wave mode.

6.2 Experimental set-up and flow parameters

6.2.1 The apparatus

A sketch of the experimental cell is presented in Figure 6.3. It consists of a smooth rotating stainless-steel disk of radius $b = 140$ mm enclosed by a fixed cylindrical shroud of radius $b + j$ ($j = 0.85 \pm 0.05$ mm). A central hub of radius a equal to either 40, 75 or 105 mm can be attached or not to the rotating disk. The disk drive shaft is going through the bottom of the tank and is connected to an electric engine by means of a belt, so that the disk can rotate with an angular velocity Ω varying from 0 to 200 rpm. A servo-control system for the rotation rate permits to maintain Ω constant with an accuracy of 0.2%. Note that both the disk and the hub rotate clockwise. The heights of the cylinder and the

hub are fixed to $e = 20$ mm. The cavity is filled up by water at a constant working temperature 20°C (kinematic viscosity of water $\nu = 10^{-6} \text{ m}^2/\text{s}$). The water depth at rest is denoted h and can vary between 0 and 15 mm.

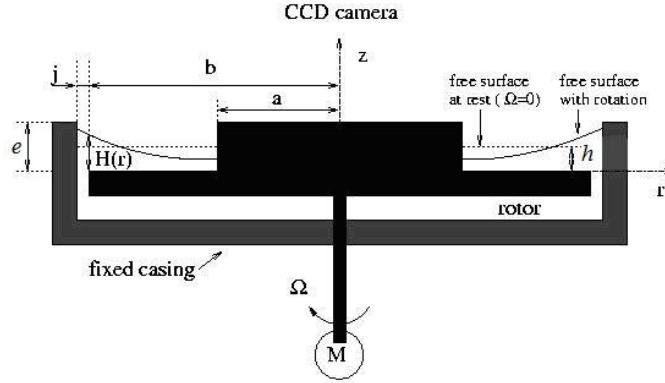


Figure 6.3: Schematic representation of the cavity with relevant notation.

In order to visualize the hydrodynamic structures, which develop in the flow, the water is seeded with reflective anisotropic particles of “kalliroscope” (size $30 \times 6 \times 0.07 \mu\text{m}$) in suspension, whose orientation depends upon the shear stress of the flow. The flow is illuminated with an annular neon and the surface of the stainless steel rotor is painted black to improve flow visualizations. Images (768×576 pixels) are taken at a video frequency of 25 images per second using a CCD video camera situated one meter above the cavity.

6.2.2 The flow global parameters

The flow is mainly controlled by three global parameters: the rotational Reynolds number Re based on the outer radius b of the rotating disk, the aspect ratio G of the cavity and the radius ratio η defined as:

$$Re = \frac{\Omega b^2}{\nu} \leq 1.2 \times 10^5 \quad G = \frac{h}{b} \leq 0.107 \quad \eta = \frac{a}{b} = 0, 0.286, 0.536, 0.75$$

Note that $\eta = 0$ corresponds to the case where no hub is attached to the rotating disk. These dimensionless numbers appeared to be the more common ones as they contain only one varying parameter. The axial z^* and r^* radial dimensionless coordinate are defined as followed: $z^* = z/H$ and $r^* = r/b$, where $H(r)$ is the local water depth (see next section). $z^* = 0$ corresponds to the rotating disk surface and $z^* = 1$ to the free surface. For future discussions, the Ekman number based on the water depth h at rest is introduced: $E_h = \nu/(\Omega h^2)$. It measures the viscous dissipation compared to the Coriolis term. Numerous authors introduced also a Rossby number Ro based on the differential rotation of their system. In the present work, the shear layer is produced by the differential rotation between the rotating fluid (Ω_f) and the fixed shroud ($\Omega_s = 0$). The Rossby number Ro based on the differential rotation $(\Omega_f - \Omega_s)/\Omega_f$ is then equal to $Ro = 1$ and does not appear to be a relevant parameter to study the stability of this flow.

6.2.3 The experimental procedure

One has observed that the stability of the basic flow is very sensitive to the initial conditions (in particular to the initial shear stress), but also to the time history of the rotation rate as it is the only varying flow parameter during a sequence of observations. Thus, the thresholds and the sequence of the instabilities depend strongly on the experimental procedure, which must be always the same. In order to impose a continuous shear between the rotating fluid and the shroud, the rotation rate Ω is increased by step of one rpm between two observations. According to the linear Ekman dynamics [114], the time evolution in rotating flow systems is characterized by the Ekman time: $\tau_E = b/\sqrt{\nu\Omega} = 137$ s for $\Omega = 10$ rpm. As long as the symmetry (the number of vortices) is constant, the adjustment of the flow to changes in Re is almost instantaneous [22] but the time scale related to the transition between

two modes is much longer and close to τ_E . As soon as the last pattern is obtained for large values of the rotation rate, the same procedure is applied for decreasing values of Ω until the last mode disappears. The shear is supposed to be constant along the axial direction as the water depth h remains small. All results reported in the next section were found to be repeatable. For future discussions, as already introduced by Bergeron *et al.* [22], spin up (resp. spin down) refers to a sequence of observations where the values of the Reynolds number Re are increased (resp. decreased).

6.2.4 Shape of the free surface for $\eta = 0$

The experiments were performed in a shallow layer of water over a rotating disk. It has been checked that the flow parameters are such that a wet central zone is guaranteed close to the rotation axis in all cases (see in [8]). The local water depth $H(r)$ (see Fig.6.3) may be determined in the unperturbed equilibrium state by balancing the gravitational acceleration and the centrifugal one. For $\eta = 0$ and a rotating endwall, it may be expressed as:

$$H(r) = h + \frac{\Omega_f^2}{2g} \left(r^2 - \frac{b^2}{2} \right) \quad (6.1)$$

where $\Omega_f = F\Omega$ is the fluid rotation rate and $g = 9.81 \text{ m/s}^2$ is the acceleration of gravity. One has experimentally verified this relation for different values of Ω with a good agreement in the inner region. This relation being established for a rotating endwall, it overestimates the value of the local water depth close to the outer stationary cylinder. To our knowledge, the only detailed work on the shape of the free surface is the one by Bouffanais and Lo Jacono [32], who developed a 3D code, which takes into account the deformation of the free surface in all directions. But they considered very large aspect ratios ($G \simeq 1$) and larger Froude numbers $Fr = \Omega^2 b/g = 0.1$ and the shape of the free surface is then quite far from those given by Equation (6.1). Some calculations of the free surface deformation may also be found in the PhD thesis of Kahouadji [143].

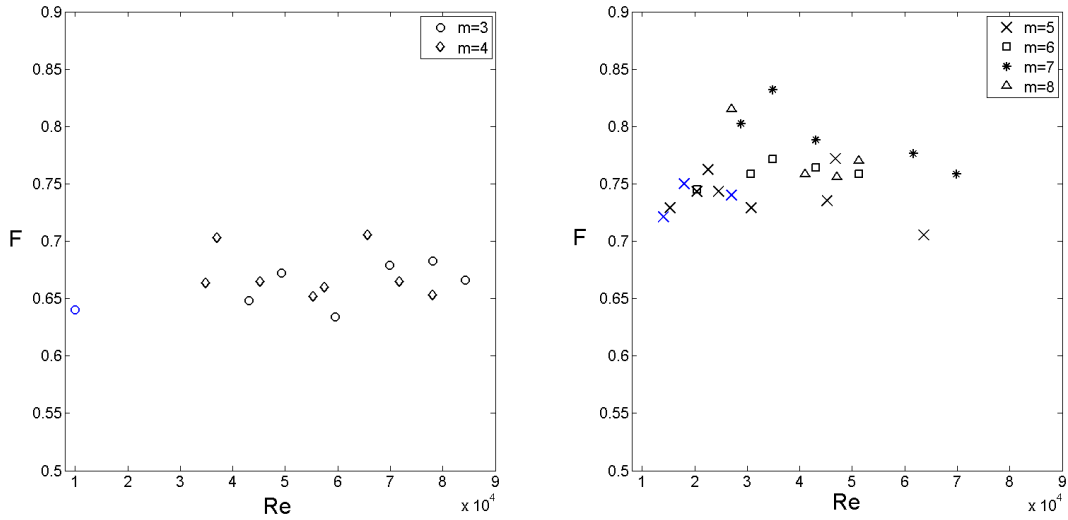


Figure 6.4: Influence of the Reynolds number on the dimensionless azimuthal velocity F of the polygon patterns deduced from the flow visualizations (black symbols) and the DNS (blue symbols) for $0.0143 \leq G \leq 0.143$ and modes between $m = 3$ and 8.

The fluid rotation rate Ω_f has been measured mainly from the flow visualizations but also by laser Doppler anemometry (LDA). It rotates almost as a solid body with a tangential velocity directly proportional to the rotating disk speed: $\Omega_f = F\Omega$, with F the entrainment coefficient of the fluid. As shown on Figure 6.4 for all values of G within the range $[0.0143 - 0.143]$, the experimental values of F depend slightly on Re and G , which confirms the experimental results of Huang and Hsieh [132] in the ECDP case (for $0.1 \leq G \leq 0.22$). One can note a decrease of F when one decreases the modes: $F \simeq 0.8$ for $m = 7$ and 8 and decreases to $F \simeq 0.65$ for $m = 3$. Huang and Hsieh [132] found that $F = 0.8 \pm 0.01$ for $m = 5$ and decreases to $F = 0.6 \pm 0.02$ for $m = 2$. The four DNS results are within the range of the experimental values.

6.3 Results and discussion

Extensive flow visualizations have been performed for a wide range of the flow parameters G , η and Re and compared in some specific cases to new DNS results obtained using the pseudospectral code described in Chapter 3 and to the linear stability analysis (LSA) of Kahouadji *et al.* [144]. As the Froude number $Fr = \Omega^2 b/g$ remains small (here $\max(Fr) = 0.027 \ll 1$), the free surface may be supposed to be undeformable and planar in the simulations. The LSA [144] also assumes a flat free surface.

6.3.1 Structure of the flow for $\eta = 0$

Figure 6.5 illustrates an example of the flow structure (mode $m = 5$) observed for $\eta = 0$, $Re = 45155$ and $G = 0.0429$. This illustration is quite comparable to the vorticity maps obtained using DNS by Randriamampianina *et al.* [267] in the ECDP case. The vortical structure occupies all the water depth as the shear is supposed to be constant along the axial direction (small values of G). One can distinguished three distinct radial regions, the inner and outer regions, separated by a polygonal boundary.

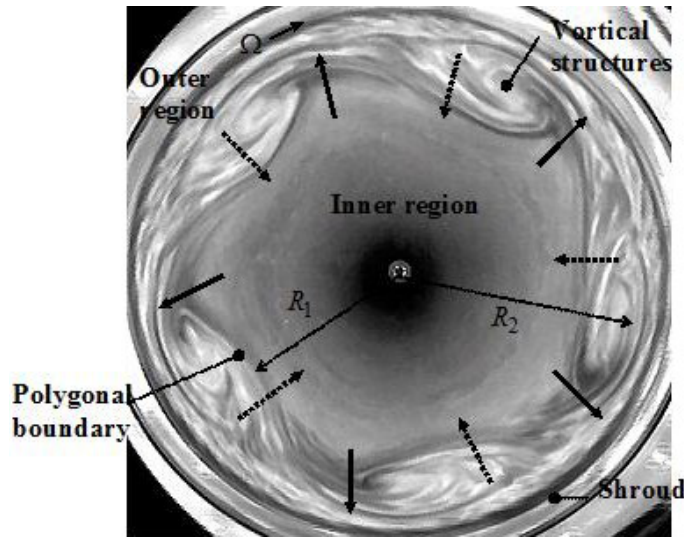


Figure 6.5: Experimental flow visualization showing the flow structure (mode $m = 5$) for $\eta = 0$, $G = 0.0429$ and $Re = 45155$.

The inner region is observed for $0 \leq r^* = r/b \leq 0.64$, in which the flow is two-dimensional, laminar and rotates roughly as a solid body. The shape of the inner region is polygonal with $m = 5$ sides. During flow visualization in the rotating frame of reference, one observed that the polygon rotates slightly relative to the rotating disk, which is induced by the passage of the vortical structures in the outer region.

The outer region, confined between the inner region and the shroud, is actively turbulent. It contains $m = 5$ counterclockwise vortical structures. These structures are almost distributed along a circle of radius $r_c^* = (R_1 + R_2)/(2b)$, where R_1 and R_2 are the location of the polygonal boundary and the maximum radial location of the vortical structures as being defined in Figure 6.5. This critical radial location for the appearance of the polygonal patterns is equal to $r_c^* \simeq 0.73$ and rather constant whatever the values of the parameters.

The five vortices, which span the radial extent of the outer region, rotate relatively to the rotating disk with a speed, estimated from the flow visualization, of about 73.5% of the disk speed relative to the laboratory (see Fig.6.4). This value is in good agreement with the 75% obtained by Abrahamson *et al.* [4] for $m = 5$, $G = 0.05$ and $Re = 4.924 \times 10^5$.

The vortical structures are responsible for the deformation of the inner region, which produces the polygonal boundary. As showed by the straight arrows in Figure 6.5, the portion of the vortex that flows outward induces the lobes of the polygon by pulling the inner region fluid away from the center

of the rotating disk. In the same way, the portion of the vortex that flows inward (dashed arrows) flattens the boundary by forcing it radially inward. Thus, the shape of the boundary moves with the vortices. The inner region moves with the vortices too. In response to the passing train of vortices, it moves slightly along a cyclic orbital.

At the periphery of the disk, a boundary layer develops along the fixed cylindrical shroud. This shroud boundary layer is three-dimensional according to the observations of Abrahamson *et al.* [4].

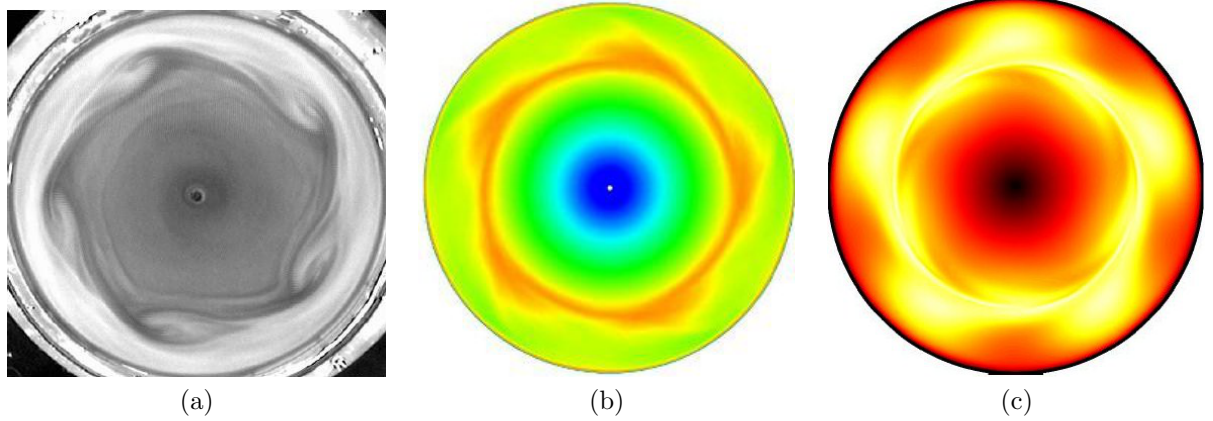


Figure 6.6: Mode $m = 5$ for $\eta = 0$ and $G = 0.0714$: (a) flow visualizations at $Re = 16425$; (b) DNS results at $Re = 18000$ and $z^* = 0.32$ (iso- V_θ ; $130 \times 128 \times 65$ mesh points in the (r, θ, z) directions with $\delta t = 10^{-4}\Omega^{-1}$); (c) stability analysis [144] at $Re = 16974$. The disk rotates clockwise.

Figure 6.6 compares the flow structure of the mode $m = 5$ obtained by flow visualizations, DNS and the stability analysis of Kahouadji *et al.* [144] for $\eta = 0$, $G = 0.0714$ close to the threshold ($Re \simeq 16425 - 18000$). The pentagonal form is well defined but the vortices in the outer region have a weak intensity. A very good agreement between the three approaches is then observed in terms of the flow structure, which validates the assumption of a flat free surface.

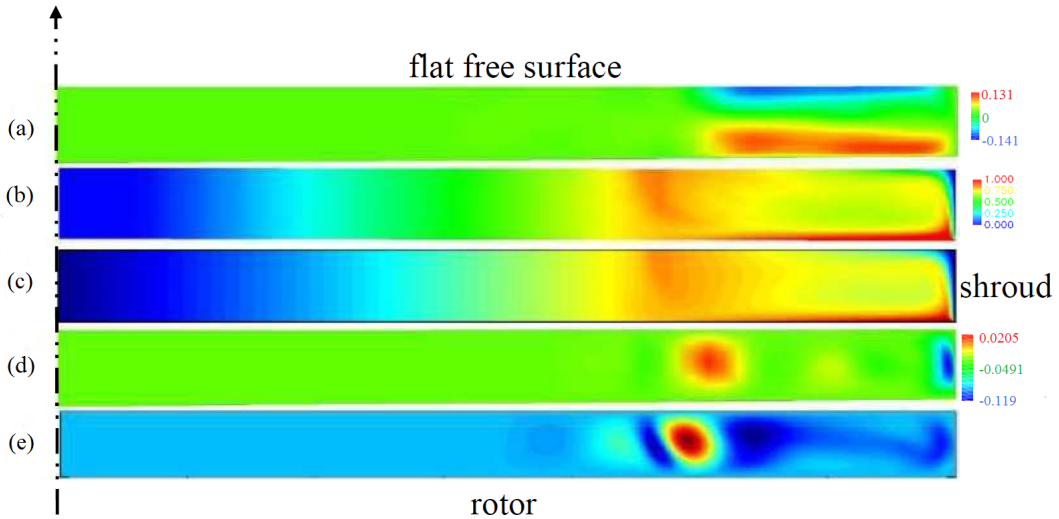


Figure 6.7: Flow structure of the mode $m = 5$ in a (r, z) plane for $\eta = 0$ and $G = 0.0714$: (a) $V_r/(\Omega b)$ (DNS), (b) $V_\theta/(\Omega b)$ (DNS), (c) V_θ (stability analysis [144]), (d) $V_z/(\Omega b)$ (DNS), (e) V_z (stability analysis [144]); DNS results for $Re = 18000$ ($130 \times 128 \times 65$ mesh points in the (r, θ, z) directions with $\delta t = 10^{-4}\Omega^{-1}$) and the stability analysis for $Re = 16974$.

To go in more details, some maps of the mean velocity components are shown in Figure 6.7. For the tangential and axial velocity components, the same flow structures are obtained by DNS and the stability analysis of Kahouadji *et al.* [144]. For r^* up to 0.6, the fluid rotates as a solid body

with a constant and weak value of the normalized tangential velocity and quasi zero radial and axial velocities. For $0.6 \leq r^* \leq 0.75$, V_θ remains independent of the axial position but gets stronger. For larger radii $r^* \geq 0.75$, the flow structure gets closer to the one observed in rotor-stator configurations. The appearance of the polygonal mode leads in that region to the creation of a secondary flow. The radial velocity is positive at the periphery of the rotor due to centrifugal effects and by conservation of mass gets negative along the free surface.

6.3.2 Transition diagram for $\eta = 0$

The main results concern a cavity where no hub is attached to the rotating disk ($\eta = 0$). The two only flow parameters are the water depth h ($G = h/b$) and the rotation rate Ω ($Re = \Omega b^2/\nu$). The purpose to the two next subsections is to provide flow visualizations of the shear instability and transition diagrams for various geometries. The reader is referred to the numerical studies of Chomaz *et al.* [53] and Bergeron *et al.* [22] for a detailed description of the transition processes during spin-up and spin-down, which is quite difficult to report from experimental observations.

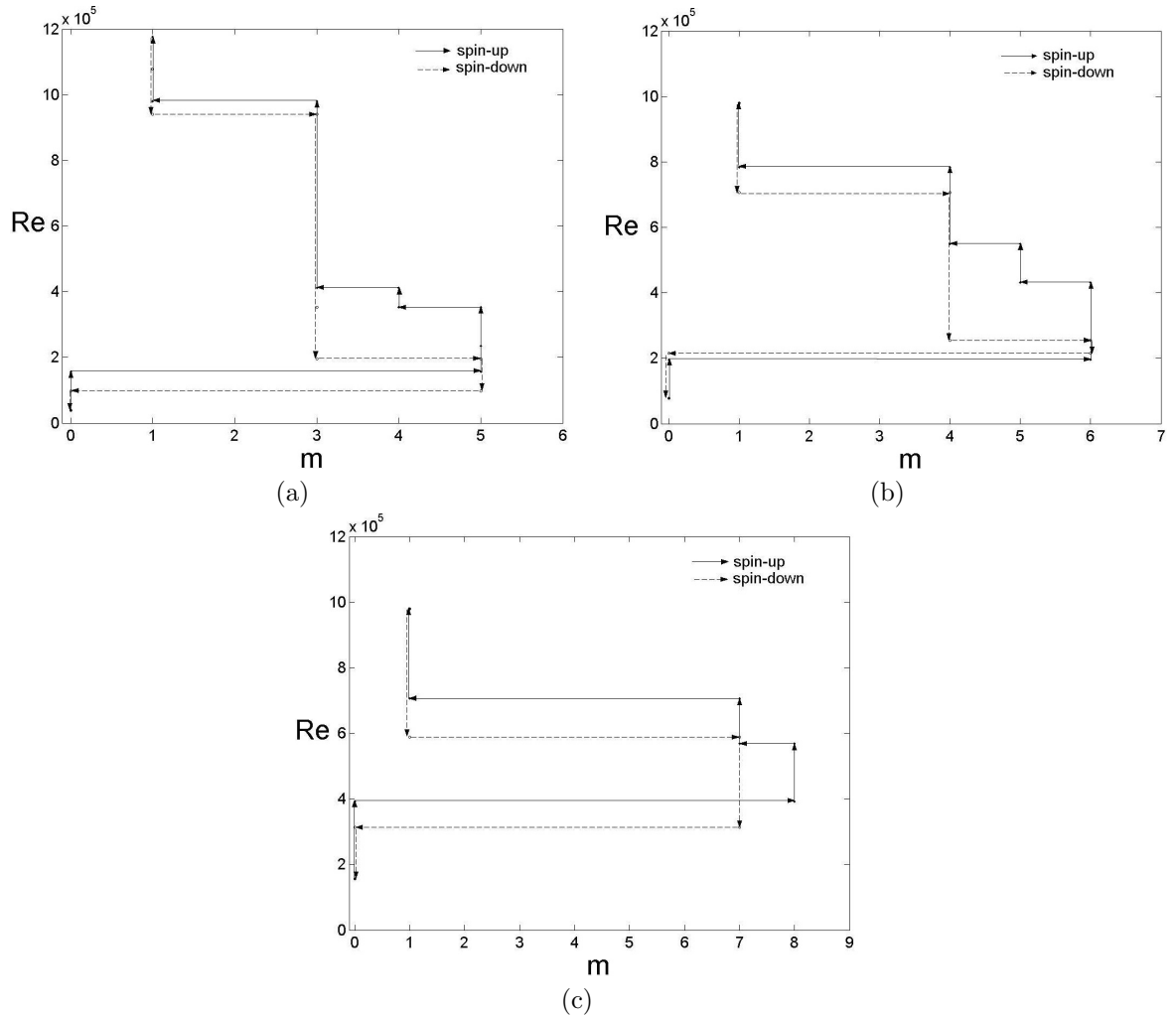


Figure 6.8: Stability diagram for $\eta = 0$ and: (a) $G = 0.0714$, (b) $G = 0.0429$, (c) $G = 0.0179$. Results obtained by experimental flow visualizations.

Figure 6.8 represents the stability diagram of the basic flow in the plane (m, Re) for three characteristic aspect ratios. One can recall that m is the number of vortices. For $G = 0.0714$ (Fig.6.8a), the flow becomes unstable above a first threshold $Re = 4105$ and the axisymmetric mode denoted $m = 0$ appears as a first circle C1 (Fig.6.9a) moving slightly towards the center of the rotating disk for increasing values of the Reynolds number. A second circle C2 appears along the shroud and moves

also towards the center of the disk. The flow is then almost entirely laminar. When both circles interact for $Re = 16420$ (it corresponds to Re_{NM} introduced below), a second pattern develops as a sharp cornered polygon with five vortices (Fig.6.9e). When the Reynolds number is further increased above this critical value, a series of two symmetry-breaking bifurcations occur. Each one of these is characterized by a reduction of the number of vortices in the system. The transition from the mode $m = 5$ to the mode $m = 4$ (Fig.6.9f) occurs above a third threshold $Re = 36945$. The existence domain of the mode $m = 4$ is quite narrow, contrary to the mode $m = 3$ (Fig.6.9g), which subsists in the range $4310 \leq Re \leq 102625$. For larger Reynolds numbers, an axisymmetric state (Fig.6.9h) is restored but the flow at the periphery of the cavity is turbulent and the mode denoted $m = 1$ appears. During spin-down (dashed arrows in Figure 6.8a), only the modes $m = 1, 3, 5$ and 0 are successively obtained. The sequence has then changed and the thresholds are slightly shifted to smaller values of Re than in the case of spin-up. Finally the flow becomes again stable for $Re = 4105$. During spin-down, the number of vortices in the flow has increased by more than one when the transition from mode $m = 3$ to mode $m = 5$ occurred. It could be assigned to a too fast spin-down or to an external noise, which postpones the transition as suggested by Bergeron *et al.* [22].

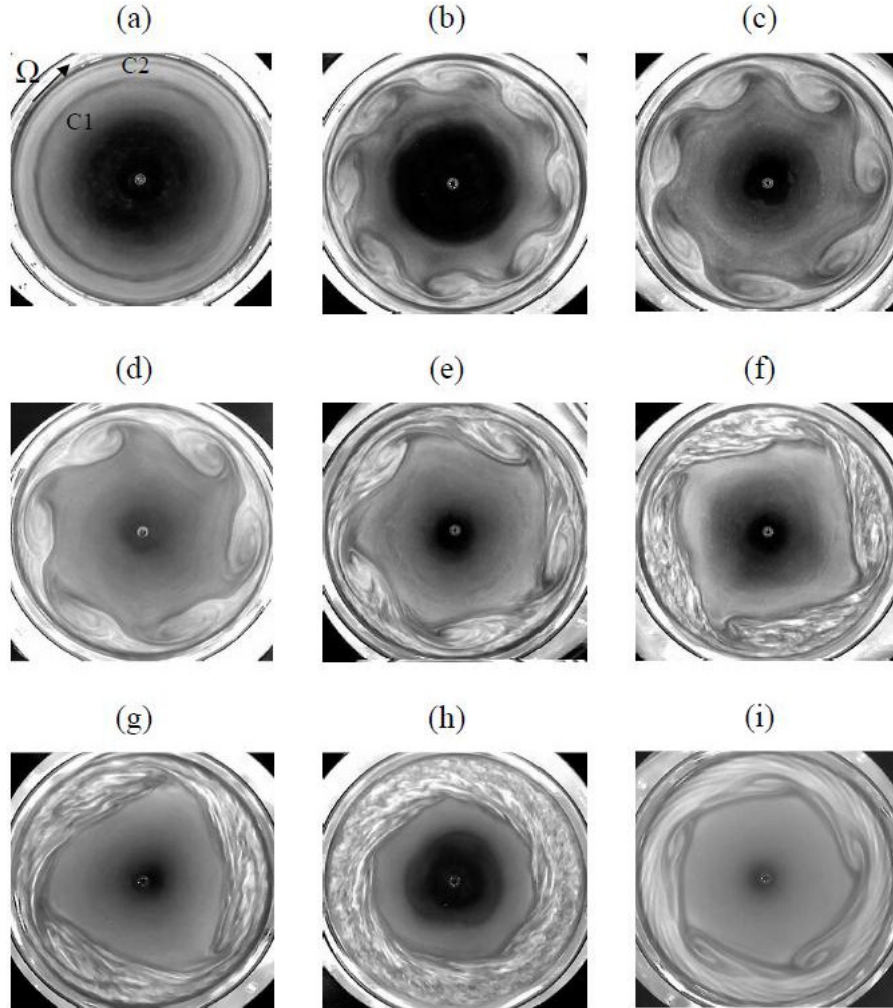


Figure 6.9: Experimental flow visualizations highlighting the shear-layer instabilities for $\eta = 0$: (a) $m = 0$, $G = 0.0179$, $Re = 38998$; (b) $m = 8$, $G = 0.0179$, $Re = 51313$, (c) $m = 7$, $G = 0.0286$, $Re = 43101$; (d) $m = 6$, $G = 0.0429$, $Re = 34893$; (e) $m = 5$, $G = 0.0429$, $Re = 45155$; (f) $m = 4$, $G = 0.0429$, $Re = 61575$; (g) $m = 3$, $G = 0.0714$, $Re = 49260$; (h) $m = 1$, $G = 0.0714$, $Re = 102625$; (i) $m = 5$, $G = 0.0714$, $Re = 24630$.

Note that the mode $m = 2$ has never been observed for $\eta = 0$ and that the modes $m = 0$ and 1 are always obtained whatever the geometry of the cavity (all values of G and η). All the observations

reported here are in good agreement with other experiments [53, 212], where strong hysteresis is observed for the modes, although no or a weak hysteresis is present for the threshold values. This problem is generic for systems where the geometrical confinement leads to azimuthal wavenumber quantization [265]. The weak hysteresis obtained for $G = 0.0714$ has been confirmed by present DNS calculations. The $m = 5$ instability threshold is $Re = 18000$ during the spin-up process, while this mode remains stable up to $Re = 15000$ during spin-down showing the subcritical nature of this instability. From the experiments, the hysteresis is stronger with a threshold equal to $Re = 15700$ (resp. $Re = 9800$) during spin-up (resp. spin-down).

When the aspect ratio G decreases (Fig.6.8), the number of vortices of the first polygonal pattern increases: $m = 5$ for $G = 0.0714$ (Fig.6.8a), $m = 6$ for $G = 0.0429$ (Fig.6.8b) and $m = 8$ for $G = 0.0179$ (Fig.6.8c). The sequence is almost the same whatever the aspect ratio. N polygonal patterns are observed during the spin-up and $(N - 1)$ patterns during the spin-down. The number of observed polygonal structures N decreases from $N = 3$ for $G = 0.0719$ and $G = 0.0429$ to $N = 2$ for $G = 0.0179$. The instability thresholds are also slightly shifted to smaller values of the Reynolds number when G decreases. Note that the hysteresis on these thresholds is more important for the smallest value of $G = 0.0179$ (Fig.6.8c). Moreover for this aspect ratio, the transition process during the spin-down does not continue until the same number of vortices obtained at the threshold is reached. This result is in contrast with the numerical simulations of Bergeron *et al.* [22], which is probably due to both the configuration and especially to the experimental procedure.

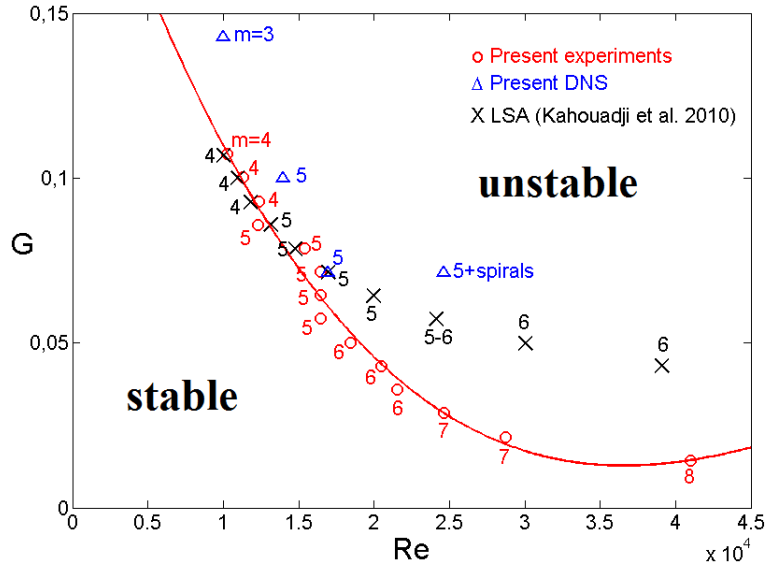


Figure 6.10: Marginal stability diagram of the first observed polygonal mode in the plane (Re, G) for $\eta = 0$ and increasing values of Re . Experimental results (red circles) compared to the stability analysis of Kahouadji *et al.* [144] (black crosses) and DNS results (blue triangles).

Figure 6.10 presents the marginal stability diagram of the primary bifurcation in the plane (Re, G) for $\eta = 0$ and increasing values of the Reynolds number Re . The present experimental and numerical results compare quite well with the stability analysis of Kahouadji *et al.* [144] for $G \geq 0.07$ in terms of the instability threshold but also in terms of the number of vortices for the first bifurcation. For large aspect ratios G , the first polygonal pattern appears for small values of Re and the number of vortices m is then small. When G decreases, Re and m increase. For $\eta = 0$, modes in the range $m = 4 - 8$ have been obtained for $G \leq 0.12$. The discrepancies between the flow visualizations and the stability analysis are more noticeable for small aspect ratios $G \leq 0.07$, which is due to the flat free surface hypothesis. The first mode appears indeed for larger Reynolds numbers, which induces a larger deformation of the free surface not taken into account in the stability analysis presented here. Kahouadji [143] developed a method with a curvilinear formulation during his PhD thesis to take into account a deformation of the free surface. It does not modify significantly the previous results obtained with a flat free surface in terms of the first instability threshold. More surprisingly, for $G \leq 0.06$, he observed a decrease of the number of vortices from 5 to 4 for increasing values of the

Reynolds number.

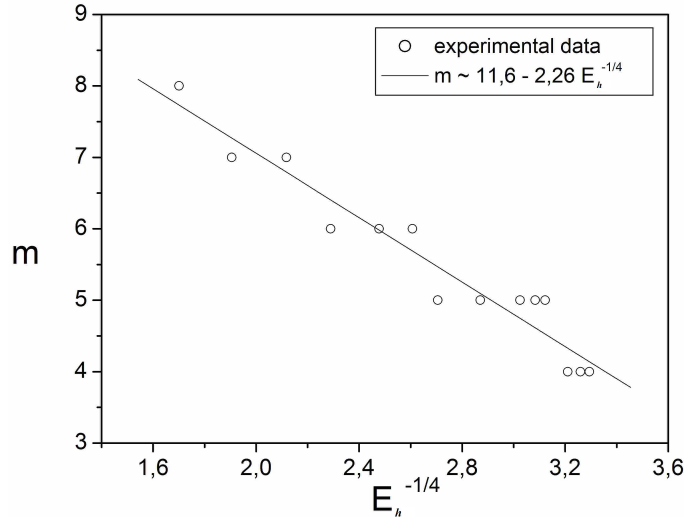


Figure 6.11: Evolution of the number of vortices with the Ekman number based on the water depth at rest for $\eta = 0$ and increasing values of Re . Results obtained by flow visualizations.

The first observed polygonal mode m (during spin-up) can be scaled by: $m \sim E_h^{-1/4}$ as already mentioned by Schaeffer and Cardin [295] in their study of the instabilities of the Stewartson layer in flat and depth-varying containers or by Moisy *et al.* [212] in the flow between counter-rotating disks, where $E_h = \nu/(\Omega h^2)$ is the Ekman number based on the water depth h at rest. The reader is referred also to the brief review of Manin [198] for similar behaviors and to the pioneering work of Stewartson [331]. Figure 6.11 shows indeed that, in the present case, $m \sim -2.26 \times E_h^{-1/4}$. It confirms that the boundary layer along the shroud is a Stewartson boundary layer, whose thickness is given by $E_h^{-1/4}b$.

From figures 6.9b to 6.9g, one can deduce the critical radius location for the appearance of the polygonal patterns: $r_c^* = r_c/b$, with $r_c = (R_1 + R_2)/2$ (see Fig.6.5). It appears from all the observations that this critical radius is almost constant whatever the number of vortices m : $r_c^* \simeq 0.73$. Note that it is not the case for the minimum radial location of the polygonal boundary R_1 and for the maximum radial location of the vortical structures R_2 .

Niino and Misawa [223] proposed a Reynolds number, denoted here $Re_{NM} = VL/\nu$, as the only parameter which governs the stability of the base flow, where V and L are the characteristic velocity and length of the base flow. They found a critical Reynolds number $Re_{NM} \simeq 11.7 \pm 0.5$, to be compared to $Re_{NM} \simeq 110 \pm 20$ obtained by Moisy *et al.* [212] for counter-rotating disk flows or to $Re_{NM} = 85 \pm 10$ obtained by Rabaud and Couder [265] for a circular shear-layer system. Note that Manin [198] mentioned that the value of Re_{NM} depends on the axial profile of the radial velocity. In the present case, V is defined by $V = \Omega b$ as the shear is produced at the periphery of the rotating disk, and the thickness L of the shear layer is given by $L = (E_h/4)^{1/4} \times h$ [223]. Thus, Re_{NM} can be expressed as: $Re_{NM} = bh^{1/2}(\Omega/\nu)^{3/4}/\sqrt{2}$. One has verified, in Figure 6.12, that the critical Reynolds number Re_{NM} is almost constant: $Re_{NM} \simeq 248$. This value is an estimate since the instability takes place for radii lower than the cell radius b . It confirms that, as the Rossby number is close to 1, the Reynolds number Re_{NM} is the only preponderant parameter to study the stability of the base flow. It means also that the ratio m/δ between the number of vortices and the Ekman layer thickness is constant.

Spiral patterns have also been observed both experimentally and numerically. They can coexist with the polygonal structures as they are located at the periphery of the rotating disk as shown in Figure 6.13 for the mode $m = 5$. For $G = 0.0714$, a close agreement is obtained on the flow structure especially on the spiral characteristics as one will see below. Nevertheless, the $m = 5$ mode appears to be weaker in the DNS. Figures 6.13c-e show that the spirals are characterized by a relatively high turbulence kinetic energy, and that they flow from the rotor to the free surface ($V_z > 0$) and radially inwards ($V_r < 0$). The pentagonal pattern corresponds to the boundary between two regions with

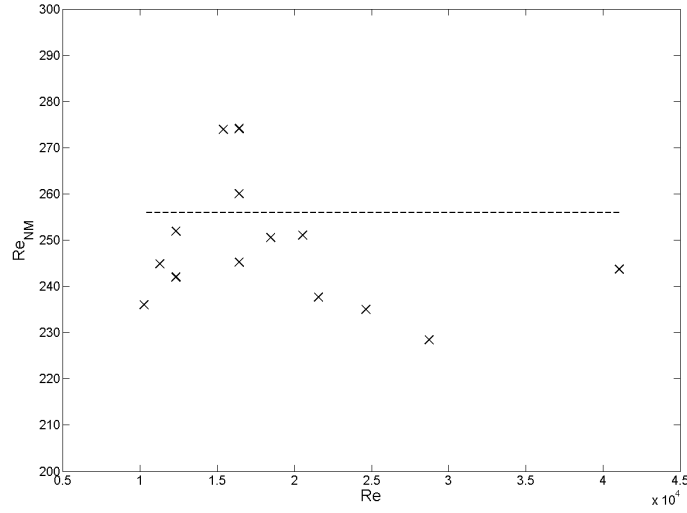


Figure 6.12: Evolution of the critical Reynolds number Re_{NM} with the rotational Reynolds number Re for $\eta = 0$. Results obtained by flow visualizations.

high (outer region) and low (inner region) turbulence kinetic energy levels. It is characterized by: $V_r > 0$ and $V_z > 0$.

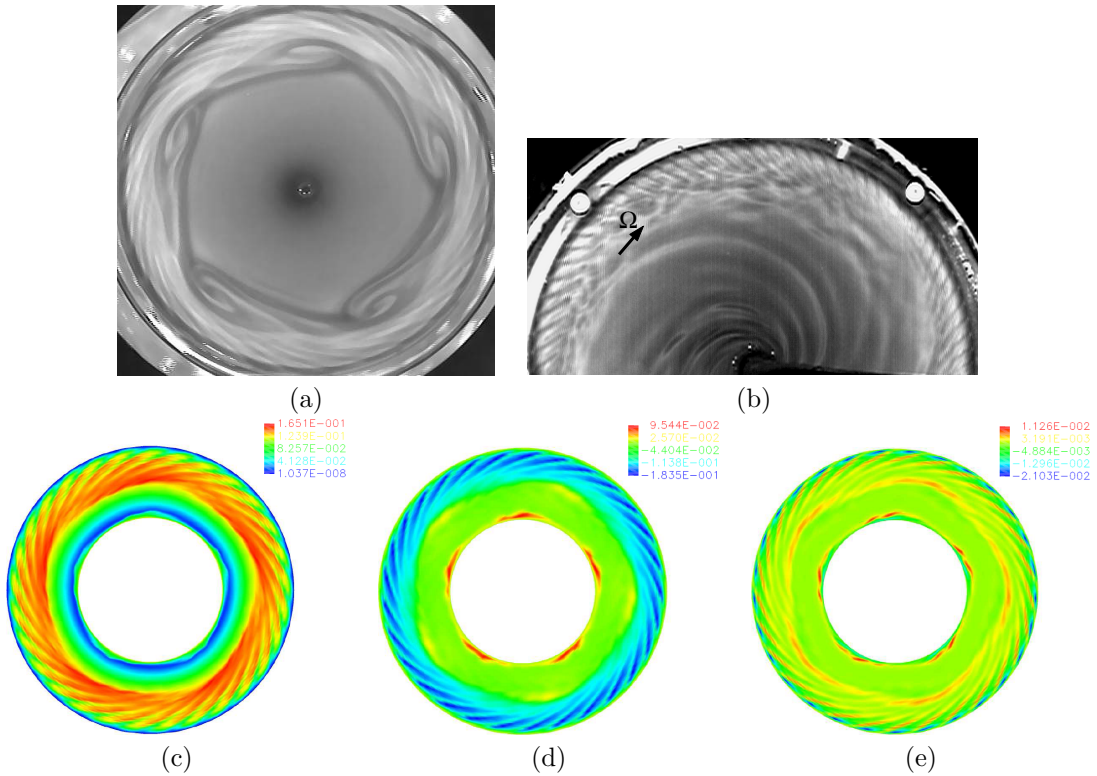


Figure 6.13: SRJ2 spiral rolls: (a) experimental results for $\eta = 0$, $Re = 24630$ (spin-up) and $G = 0.0714$ coexisting with the mode $m = 5$ in the case of a free surface; (b) rotor-stator flow with inward throughflow as observed by Poncet and Chauve [252] for $\eta = 0$, $Re = 20500$, $G = 0.0429$ and $C_w = 39.52$. DNS results ($73 \times 192 \times 65$ mesh points in the (r, θ, z) directions with $\delta t = 5 \times 10^{-5} \Omega^{-1}$) for $\eta = 0.5$, $Re = 27000$ and $G = 0.0714$ at $z^* = 0.97$ coexisting with a weak $m = 5$ mode in the case of a flat free surface: (c) turbulence kinetic energy $k/(\Omega b)^2$, (d) instantaneous radial velocity $V_r/(\Omega b)$, (e) instantaneous axial velocity $V_z/(\Omega b)$. Note that the disk rotates clockwise in the experiments and counterclockwise in the simulations.

Figure 6.14 represents two space-time diagrams respectively in terms of an angle $\theta^* = \theta/(2\pi)$ (at $r^* = 0.95$) and in terms of a radius r^* of the flow for $\eta = 0$, $Re = 24630$ (spin-up) and $G = 0.0714$. They correspond to the flow visualization in Figure 6.13a in the frame of reference of the polygonal pattern. One defines the dimensionless time as $t^* = 2\pi t/\Omega$. The diagonal lines in Figure 6.14a correspond to the spiral passing. The negative slope indicates that they move slower than the vortices (16.6% of the passing velocity of the polygonal structures ie $0.125\Omega r$). The space-time diagram according to a radius (Figure 6.14b) shows the radial extent of the spiral rolls, their inclination angle ε and their azimuthal wavenumber n , which is also the number of structures by rotation. One can notice also the passing of the vortical structures.

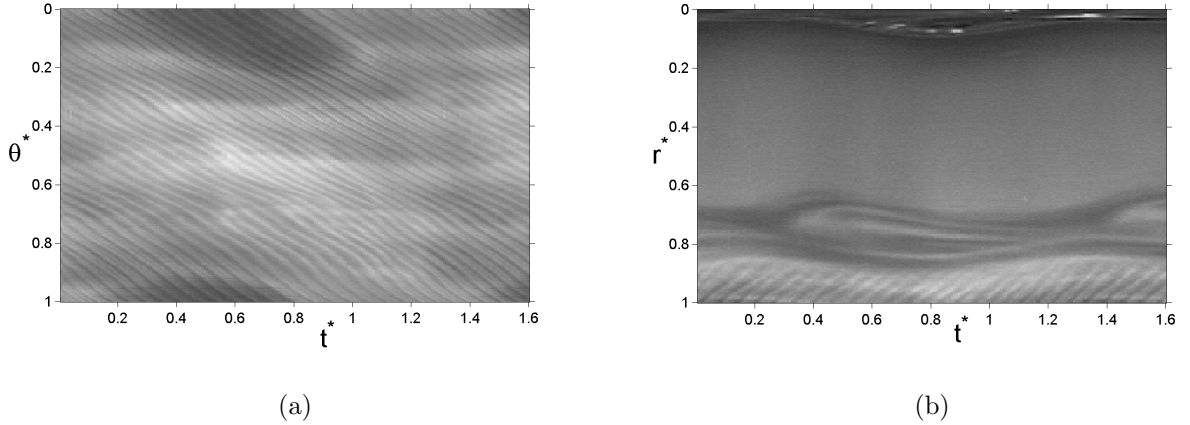


Figure 6.14: Space-time diagrams for $\eta = 0$, $Re = 24630$ (spin-up) and $G = 0.0714$ in terms of: (a) a fixed circle (θ^*) at $r^* = 0.95$; (b) a radius r^* for $\theta = \pi/2$. Results obtained by experimental flow visualizations.

The characteristics of the spirals obtained experimentally are summed up in Table 6.1. Note that they have not been observed for $G = 0.0179$. These are positive spiral patterns as they are rolled up towards the disk axis in the rotation sense of the rotor. The inclination angle remains small $14 \leq \varepsilon \leq 25^\circ$ compared to the values obtained by Poncet and Chauve [252] in a rotor-stator cavity with throughflow ($\varepsilon \rightarrow 70^\circ$). The number of spiral arms $28 \leq n \leq 40$ is also much lower compared to $n \rightarrow 90$. $n = 29$ spiral arms with a positive angle $\varepsilon \simeq 25^\circ$ have been observed numerically for $\eta = 0.5$, $Re = 27000$ and $G = 0.0714$ (Fig.6.13c-e), in excellent agreement with the present flow visualizations. It can be noticed that the characteristics of the spirals slightly depend on the aspect ratio of the cavity G . In fact, the value of G (and the one of Re) settles the number of vortices, which settles itself the characteristics of the SRJ2 rolls. As for the polygonal patterns, a weak hysteresis is observed on the thresholds of the spiral instability.

G	Re (spin-up)	Re (spin-down)	n	ε ($^\circ$)	r^*
0.0714	24630 – 43102	16420 – 36945	28 – 30	23 – 25	0.85 – 0.89
0.0429	30788 – 57470	24630 – 45155	38 – 40	14 – 19	0.88 – 0.92
0.0179	–	–	–	–	–

Table 6.1: Characteristics of the SRJ2 spirals obtained experimentally.

As already mentioned, the spirals are located at the periphery of the cavity for $r^* \geq 0.85$. They are very similar to the SRJ2 spirals studied by Poncet and Chauve [252] in the case of weak inward throughflow (Fig.6.13b). These authors showed that it is a crossflow instability due to the inflexion point in the axial profile of the mean radial velocity. Figure 6.15 shows some axial profiles of the radial velocity component obtained by DNS at different radial locations for $\eta = 0.5$, $Re = 27000$ and $G = 0.0714$. Very close to the outer cylinder, at $r^* = 0.96$, an inflexion point may be also observed here. It confirms that these spirals are also due to a crossflow instability (type I inviscid instability).

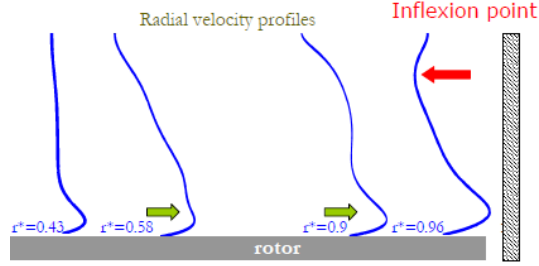


Figure 6.15: Axial distributions of the radial velocity component obtained by DNS at different radial locations $r^* = (r - a)/(b - a)$ for $\eta = 0.5$, $Re = 27000$ and $G = 0.0714$.

6.3.3 Influence of the radius ratio η

Four values of the radius ratio η have been considered: $\eta = 0, 0.286, 0.536$ and 0.75 . Figures 6.8b and 6.16 present the stability diagrams of the flow for $G = 0.0429$ and three values of the radius ratio in the plane (m, Re) .

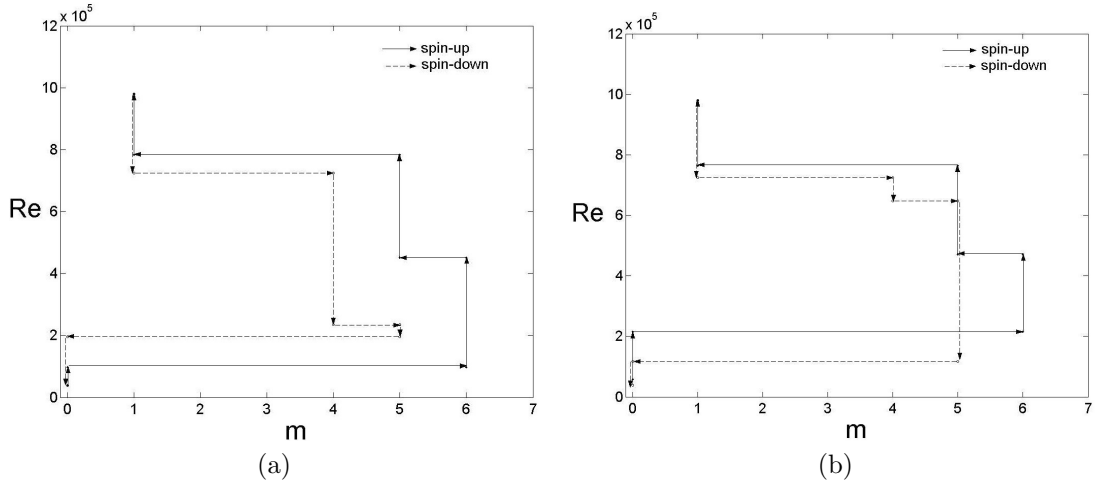


Figure 6.16: Stability diagrams for $G = 0.0429$ and: (a) $\eta = 0.286$; (b) $\eta = 0.536$. Results obtained by experimental flow visualizations.

Whatever the value of $\eta \leq 0.536$, modes in the range $m = 4 - 6$ have been obtained but the thresholds and the sequences are different. When the size of the hub increases, the radial extent of the inner region decreases strongly and the fluid rotates slightly faster, which settles the values of the thresholds. Note that for $\eta = 0.536$ and $G = 0.0714$, the mode $m = 2$ (Fig. 6.17) has been observed in the range $32840 \leq Re \leq 41050$ only during spin-down.

Figures 6.18a to 6.18d represent the influence of the radius ratio η on the flow pattern for $G = 0.0429$, $Re = 36945$ (spin-up). Apart from the largest value of the radius ratio $\eta = 0.75$, the mode $m = 6$ is observed. The critical radius r_c^* is almost constant whatever the value of η : $r_c^* = r_c/b \simeq 0.73$ for $\eta = 0, 0.286$ and 0.536 . When the radius ratio η is larger than the value of the critical radius, the radial extent between the hub and the shroud is too small for the development of the vortical structures. Thus, for $\eta = 0.75$ (Fig.6.18d), the critical size of the system has been reached and no patterns are observed.

For $\eta = 0.75$, no vortical structures are obtained but new stationary patterns develop along the hub as small cells (Fig.6.19a to Fig.6.19f) only for $G \geq 0.0714$. 10 cells appear above a first threshold $Re = 10263$. From $Re = 10263$ (Fig.6.19a) to $Re = 16420$ (Fig.6.19b), the number of cells decreases from 10 to 9 but they grow both in the radial and tangential directions. They break up into 11 cells for $Re = 20525$ (Fig.6.19c), then into 12 larger cells for $Re = 24630$ (Fig.6.19d). From $Re = 24630$ (Fig.6.19d) to $Re = 28735$ (Fig.6.19e), some cells merge and only 8 structures can be observed. When the Reynolds number is further increased, the number and the size of the patterns do not change but

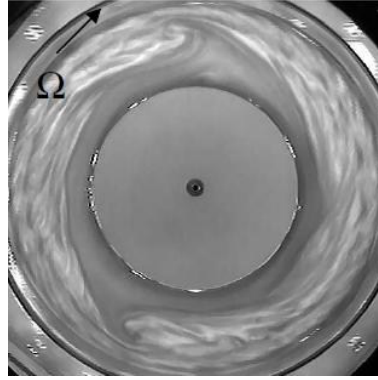


Figure 6.17: Mode $m = 2$ of the shear-layer instability for $\eta = 0.536$, $G = 0.0714$ and $Re = 41050$ (spin-down). Result obtained by experimental flow visualizations.

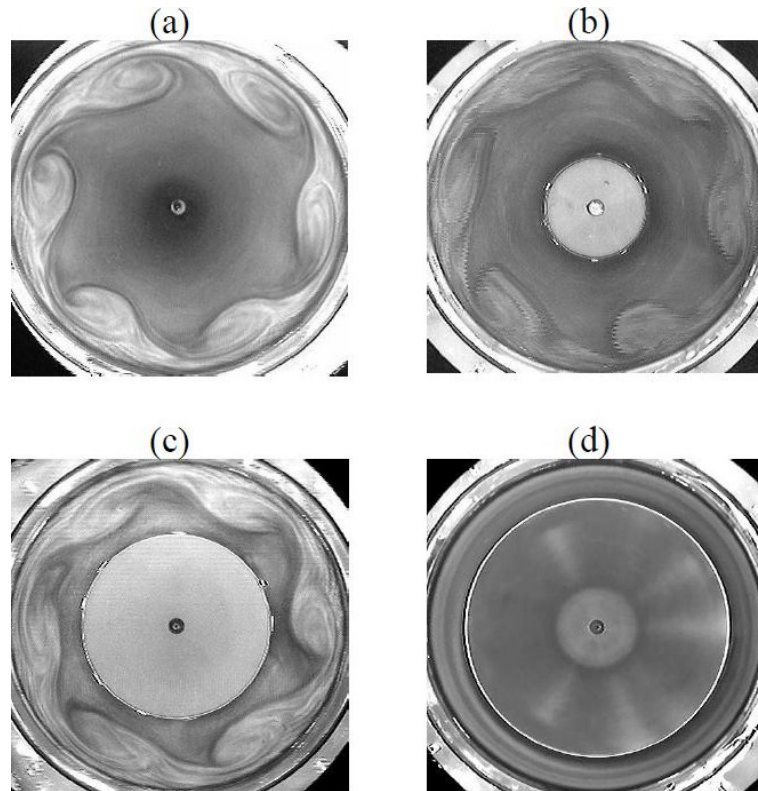


Figure 6.18: Influence of the radius ratio η on the flow pattern for $G = 0.0429$ and $Re = 36945$ (spin-up): (a) $\eta = 0$, (b) $\eta = 0.286$, (c) $\eta = 0.536$, (d) $\eta = 0.75$. Results obtained by experimental flow visualizations.

the flow confined between the cells and the shroud becomes turbulent (Fig.6.19f) and is fully turbulent for $Re = 36945$.

6.4 Conclusion

One has presented flow visualizations of a shear layer instability developed on a rotating disk with a free surface. Despite the different flow medias (gas, water, plasma) and the different forcing mechanisms producing the shear layer, the qualitative behavior of the flow is remarkably similar. For low Reynolds numbers, the flow is axisymmetric and becomes unstable above a first threshold Re_{NM} with a well

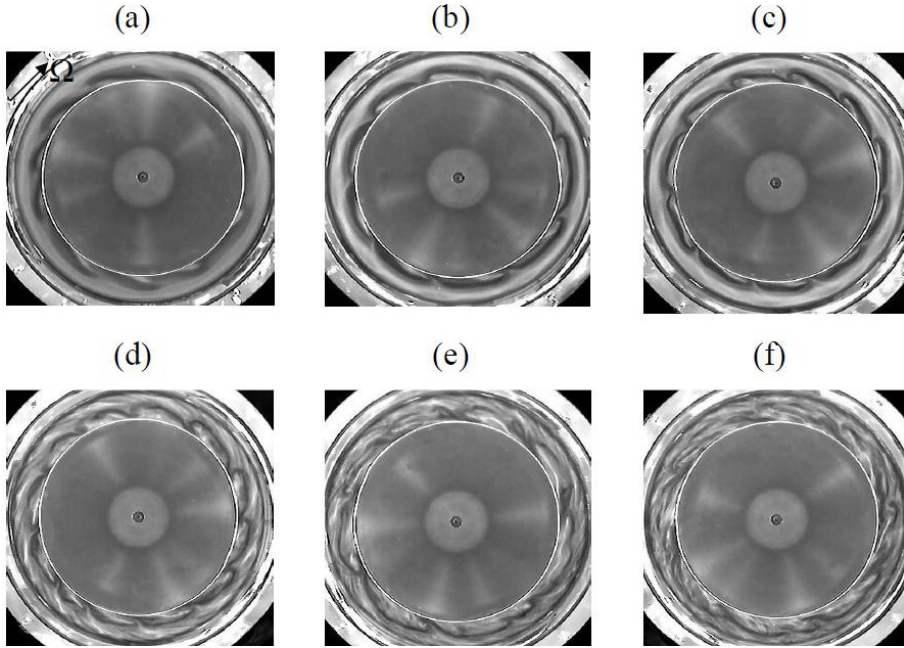


Figure 6.19: Shear-layer instabilities on the hub for $\eta = 0.75$ and $G = 0.0714$ (spin-up): (a) $Re = 10263$, (b) $Re = 16420$, (c) $Re = 20525$, (d) $Re = 24630$, (e) $Re = 28735$, (f) $Re = 34893$. Results obtained by experimental flow visualizations.

defined azimuthal wave number m . The instability appears as a sharp-cornered polygonal pattern with m vortices. In some specific cases, the experimental results are supported by DNS calculations under the assumption of a flat free surface with a very good agreement between the two methods in terms of the instability threshold and characteristics.

The number of vortices of the first polygonal mode can be scaled by the Ekman number based on the water depth at rest to the power $-1/4$, showing that the shroud boundary layer is of Stewartson type [295]. The instability sets in at a well defined value of the Reynolds number based on the thickness of the shear layer: $Re_{NM} = 248$. This supports the validity of the quasi-geostrophic approximation used in the theoretical work of Niino and Misawa [223]. The critical radial location for the appearance of the polygonal patterns is also constant and equal to $r_c^* \simeq 0.73$. At a given aspect ratio, when the Reynolds number Re is increased (spin-up), these m vortices transform into new arrangements with a decreasing number of vortices (until $(m - 2)$ in particular cases). For decreasing values of Re (spin-down), the flow demonstrates a noticeable hysteresis for the modes and a slight hysteresis for the thresholds, as already mentioned by Rabaud and Couder [265]. At a given rotation rate, the number of vortices increases for decreasing values of the water depth. Note that modes up to $m = 8$ have been obtained.

Finally, the influence of the radius ratio has been investigated. The development of the shear layer instability is constrained by the geometry of the system. When the size of the hub increases, the fluid rotates slightly faster, which shifts the values of the thresholds. Above the critical value of the radius ratio, new patterns are observed and develop along the hub as small stationary cells.

Transition to turbulence of a Batchelor flow in a rotor-stator system

The stability of the flow enclosed between a stationary and a rotating disk is here revisited by flow visualizations and direct numerical simulations in the Batchelor regime with unmerged boundary layers. It is now well known [303] that the first instability in such flow appears above a first threshold as circular rolls (denoted CR, type 2 instability), which propagate along the stator before vanishing in the vicinity of the hub. Above a second threshold, spiral rolls (denoted SR1, type 1 instability), appear at the periphery of the cavity and can coexist with the circular rolls. Nevertheless, some important matters remain to be dealt with:

- the confirmation or not of the convective nature of the circular rolls, which appear in the IRPHE's experiment under permanent conditions and in a transient state after a given perturbation in the experiment of Gauthier et al. [105];
- the nature and the origin of the spiral patterns;
- the transition scenario in the rotor boundary layer, which is still the subject of an intense debate.

These results have been published in *Phys. Fluids* (Ref.[261]) for the stability of the stator boundary layer and in *J. Comp. Phys.* (Ref.[242]) for the stability of the rotor boundary layer. This was done in collaboration with Dr P. Le Gal (IRPHE) for the stability of the stator boundary layer and in the framework of the PhD thesis of N. Peres (M2P2) for the transition scenario on the rotating disk.

7.1 Introduction

The stability of the flow confined between a rotating (rotor) and a stationary (stator) disk is mainly governed by two global parameters [303]: the aspect ratio $G = h/b$ of the cavity and the rotational Reynolds number $Re = \Omega b^2/\nu$ (see Fig.3.1). In such rotating disk cavity, two types of instability have been identified: type 1 instability results from an inviscid mechanism due to unstable inflection points in the boundary layer velocity profiles, whereas type 2 instability is viscous and associated with the Coriolis terms. Itoh et al. [138] observed experimentally that the first instabilities occur in the stator boundary layer, which is confirmed by the linear stability analysis (LSA) of San'kov and Smirnov [290] and Serre et al. [314] and also by the DNS of Serre et al. [311]. The transition to turbulence in a cylindrical rotor-stator cavity has been considered later by Schouveiler et al. [302, 303, 304], who established the transition diagram in a (Re, G) plane (see Fig.7.1).

Schouveiler et al. [302, 303, 304] reported that, for $G > 0.071$, the two first stages of the transition are due to the developments of instabilities in the stator boundary layer. Above a first threshold, they observed the formation of circular rolls (CR) centered on the rotation axis, which propagate towards the center of the cavity. The CR instability, which is a type 2 instability has been formerly observed by Savas [293, 294] during the spin-down of a rotating disk and later by Schouveiler et al. [302, 303, 304] under permanent conditions. Above a second threshold, Schouveiler et al. [302, 303, 304] observed spiral rolls (SR1), which appear at the periphery of the cavity and coexist with the CR instability. The SR1 patterns are a type 1 instability with a band of stable modes limited by the Eckhaus secondary instability. Their radial wavelength strongly varies between DNS results (between 4.4 and 14.7 for $G = 0.2$) and the a LSA (between 21.2 and 24.35) [314]. When the Reynolds number is further increased, a transition to a kind of wave turbulence occurs [61]. Gauthier et al. [105] showed, by

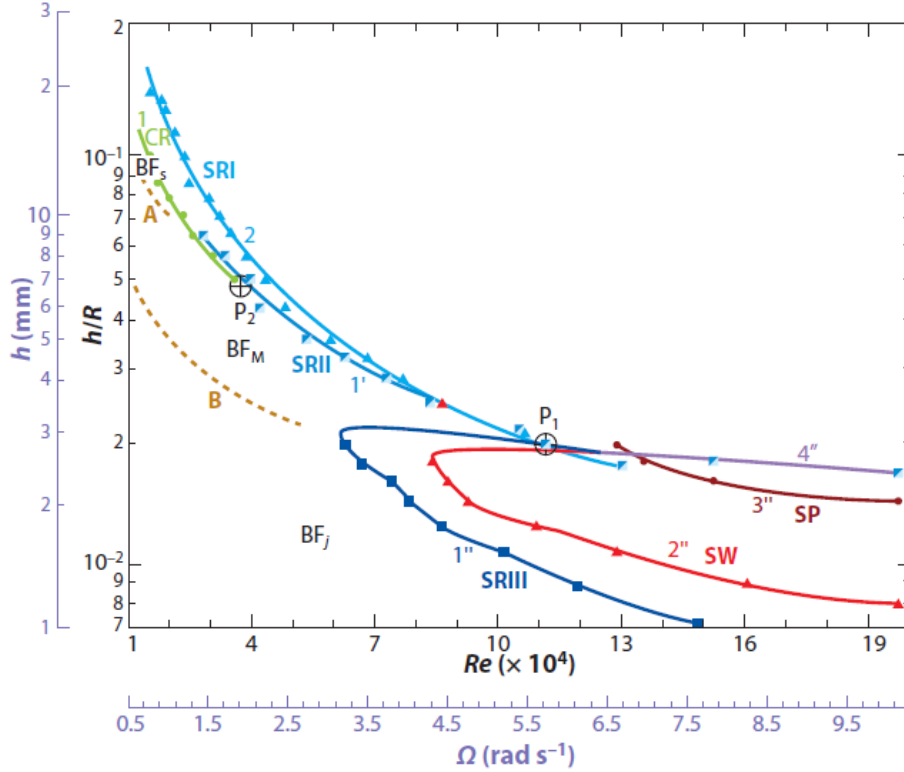


Figure 7.1: Transition diagram by Schouveiler *et al.* [303]. Curves A and B (dashed gold lines) separate the mixed-base flow (BFM) from the basic flows with separate boundary layers (BFS) and with joined boundary layers (BFJ), respectively. Curves labeled 1 indicate the thresholds for circular rolls (CR). Curves labeled 2, 1', and 1'' (blue colored lines) indicate the thresholds for spiral rolls (SRI, SRII, and SRIII, respectively). Curves labeled 2'' and 3'' (red colored lines) indicate the thresholds for solitary waves (SW) and turbulent spots (SP), respectively. Curve 4'' is the threshold for the simultaneous disappearance of the spiral rolls (SRIII) and the solitary waves (SW).

flow visualizations, that the CR are very sensitive to an external (un)controlled forcing and then highlighted the convective nature of this instability.

Numerous experimental [105, 138, 302, 303, 304], theoretical [290] or numerical [311, 314] works have already been dedicated to the stability of the flow with unmerged boundary layers corresponding to $G > 0.071$. Nevertheless, the nature of both the circular and spiral rolls remains unclear. The scenario first proposed by Schouveiler *et al.* [303] for the transition to turbulence in the enclosed rotor-stator cavity is revisited in the first part of the present Chapter essentially by numerical experiments using Direct Numerical Simulation (DNS) but also by flow visualizations in an annular cavity with a central hub. The second part is dedicated to the scenario of transition to turbulence in the rotor boundary layer using DNS. There is indeed still a persisting debate about the existence or not of a direct route to turbulence in this boundary layer.

7.2 Geometrical configuration

The experimental part of this work has been performed on the set-up developed at IRPHE [61, 62, 252, 302, 303, 304]. It consists of two smooth parallel disks enclosed by an inner rotating cylinder (hub) of radius a and an outer stationary casing (shroud) of radius $b + j = 140.85$ mm (Fig.3.1). In the experiments, various hubs have been tested: $a = [6, 5; 40; 55; 75; 110]$ mm. The lower disk of outer radius $b = 140 \pm 0.05$ mm is rotating (rotor), while the upper disk is stationary (stator). The interdisk spacing h is equal to 16 ± 0.02 mm. Thus, the value of the aspect ratio $G = h/b$ is here fixed to $G = 0.114$, whereas the curvature parameter $R_m = (b + a)/(b - a) = (1 + \eta)/(1 - \eta)$ varies

between 1 for a cylindrical cavity and 3.308 for the narrowest annular cavity ($\eta = a/b$ the radius ratio). The rotor and the hub rotate clockwise at the same uniform rotation rate Ω with an accuracy of 0.2%. The shroud is fixed. The cavity is filled up with water maintained at a working temperature of $20 \pm 0.1^\circ\text{C}$ and seeded with reflective particles of kalliroscope ($30 \times 6 \times 0.07 \mu\text{m}$) in order to visualize the hydrodynamic structures. This implies an accuracy better than 0.7% on the rotational Reynolds number $Re = \Omega b^2/\nu$. Images (768×576 pixels) are taken at a video frequency of 25 images per second using a CCD video camera. More details about the experimental set-up can be found in [61, 252].

7.3 Two first bifurcations of Batchelor flows on the stator side

In this section, numerical results obtained using the pseudo-spectral code described previously in Chapter 3 are compared to flow visualizations performed at IRPHE. In the following, a grid resolution composed of $73 \times 49 \times 100$ mesh points respectively in the radial, axial and azimuthal directions is sufficient to get grid independent solutions. The dimensionless time step has been set to $\delta t/\Omega^{-1} = 10^{-3}$.

7.3.1 Influence of the curvature parameter on the stability of rotor-stator flows

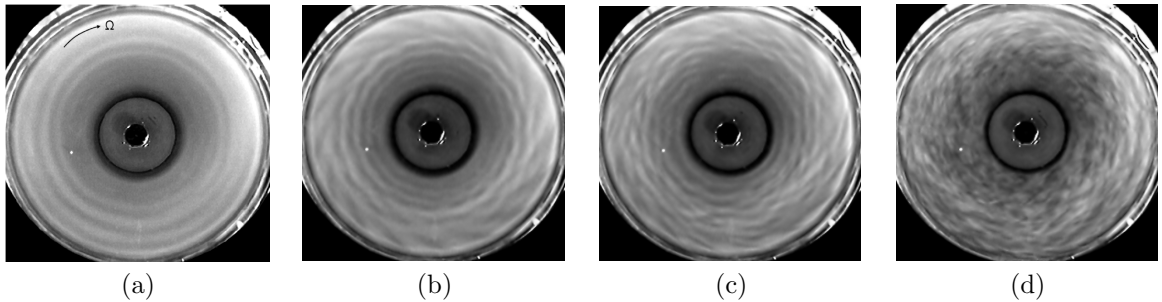


Figure 7.2: Experimental flow visualizations for $G = 0.114$, $R_m = 1.8$ and: (a) $Re = 16400$, (b) $Re = 24600$, (c) $Re = 32500$, (d) $Re = 61600$.

Figure 7.2 shows some experimental visualizations of the flow from above the stator for $G = 0.114$, $R_m = 1.8$ and various Reynolds numbers in the range $16400 \leq Re \leq 61600$. Note that, for the range of parameters investigated, the flow along the rotating disk remains stable. These new visualizations above the stator confirm the scenario proposed by Schouveiler *et al.* [302, 303, 304] for the transition to turbulence in a cylindrical rotor-stator cavity (without central hub) in the case of unmerged boundary layers. For this aspect ratio, the flow remains stable until the appearance of circular rolls CR (Fig.7.2a) above a first threshold $Re_{c1} = 12300$ ($Re_{h1} = ReG^2 = 160$, $Re_{\delta1} = (\Omega r_c^2/\nu)^{1/2} = 63$, with r_c the critical radial location for the appearance of the patterns), which is in excellent agreement with the value $Re_{c1} = 12000$ obtained by these authors [302, 303, 304] for $G = 0.114$, $R_m = 1$ and $j = 0$. Note that Serre *et al.* [314] obtained lower values by DNS ($25.8 \leq Re_{\delta1} \leq 62$ for $G = 0.2$ and $R_m = 1$ without any perturbation) and with their LSA for type II instability in the stator boundary layer: $34.7 \leq Re_{\delta1} \leq 62$. Above a second threshold $Re_{c2} = 20500$ ($Re_{h2} = 267$, $Re_{\delta2} = 100$), the SR1 instability (Fig.7.2b,c) appears along the stator at the periphery of the cavity and coexists with the CR instability. This value matches with the experimental one of Cros *et al.* [61] for $G = 0.114$, $R_m = 1$ and $j = 0.46$ mm. Buisine *et al.* [39] obtained similar spiral waves by numerical simulation with additional perturbations for $Re_{h2} > 228$ and without any perturbation for $Re_{h2} > 400$ ($G = 0.114$ and $R_m = 1.857$). The value $Re_{\delta2} = 100$ obtained in the experiment remains in the range $47.5 \leq Re_{\delta2} \leq 200$ obtained by LSA for type I instability in the stator boundary layer. In the experiment, when one increases further the Reynolds number, a transition to a kind of wave turbulence (Fig.7.2d) appears for $Re \geq 41000$ (see [61] for more details).

The influence of the parameter R_m on the stability diagram, in a (R_m, Re) plane, of the flow with unmerged boundary layers is presented in Figure 7.3 for $G = 0.114$. The appearance thresholds of the CR and SR1 patterns, which are both permanently observed, are very weakly shifted to lower values

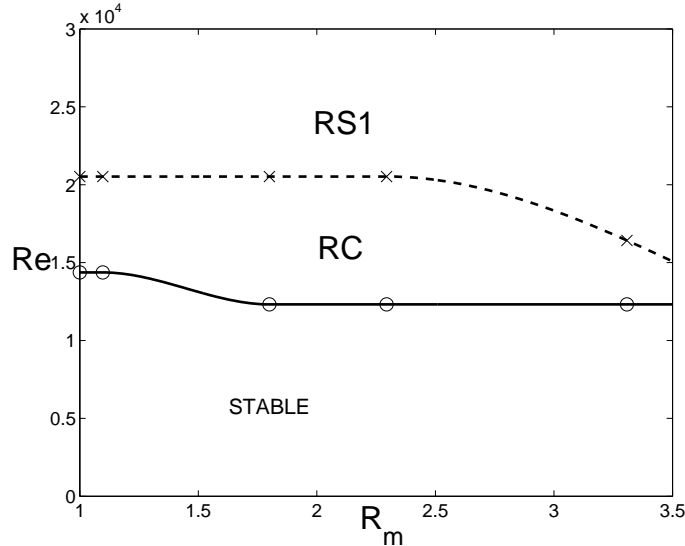


Figure 7.3: Stability diagram of the flow with unmerged boundary layers in the plane (R_m, Re) deduced from the experiments in a rotor-stator cavity with a central hub for $G = 0.114$.

of Re compared to the base case with no inner cylinder ($R_m = 1$), when R_m is increased. There are two possible reasons for that. Firstly, the rotating hub connects the rotating and the stationary disks, which creates a stronger shear for the flow along the stator coming from the outer radii, than if the hub was stationary. Secondly, the main effect of the inner rotating cylinder, which increases with R_m , is to speed up the local fluid rotation rate Ω_f in the core region and so, for a same value of Ω or Re , it slightly accelerates the transition to the SR1 regime. It can be seen as a “Rossby effect”, the Rossby number Ro being defined as $Ro = \Omega_f/\Omega$. Note that the effect of the curvature parameter R_m remains weak compared to the effect of a forced inward throughflow [252] for instance.

The main characteristics of these two instabilities deduced from the experiments are given below for $G = 0.114$, $R_m = 1.8$ and $j = 0.85$ mm. The CR frequency f_{CR}/Ω , which increases with the radial location because of successive pairings [302], remains in the range $[0.32 - 0.35]$ at $r^* = r/b = 0.53$ whatever Re for $R_m = 1.8$, in agreement with the value 0.32 of Cros *et al.* [61] for $G = 0.114$, $R_m = 1$ and $j = 0.46$ mm. The mean critical radial location r_{CR}^* for the disappearance of the CR, in the range $Re = [1.5 \times 10^4 - 4 \times 10^4]$, is around 0.4. Thus, $Re_{\delta 1}$ varies between 52 and 109. The number of circular rolls, denoted k_{CR} , varies strongly with Re from 3 at the threshold to 6 just before the appearance of the spiral waves. It confirms the value $k_{CR} = 6$ obtained by Cros *et al.* [61] for $Re = 18500$. Then, k_{CR} remains equal to 4 for a wide range of Re values and decreases for $Re \geq 3.5 \times 10^4$ until their disappearance. The critical radius r_{SR1}^* of appearance of the SR1 patterns slightly increases from 0.71 at $Re = 20500$ to 0.81 at $Re = 41000$.

For the same set of parameters ($G = 0.114$, $R_m = 1.8$ and $j = 0.85$ mm), the frequency of the spirals f_{SR1}/Ω remains almost constant in the range $[0.32 - 0.36]$ at $r^* = 0.867$ for $Re = [20500 - 41000]$. As the magnitude of the mean tangential flow increases with the disk rotation rate, the angle ε_{SR1} of the spirals with the tangential direction decreases with increasing values of Re from 31° at threshold to 28° for $Re = 24600$ and finally to 24° for $Re = 41000$. The number of spiral arms k_{SR1} increases with rotation. $k_{SR1} = 17$ up to $Re \simeq 2.95 \times 10^4$ and increases to 18 for Re up to 3.8×10^4 then to 19 for larger Re values. Finally, the phase velocity V_ϕ of the spirals is positive: $V_\phi/(\Omega b) = 0.101$ for $Re = 24600$ at $r^* = 0.867$. The results concerning the spirals are in good agreement with the previous results of Cros *et al.* [61] for $G = 0.114$, $R_m = 1$ and $j = 0.46$ mm: $f_{SR1}/\Omega = 0.334$ and $\varepsilon_{SR1} \simeq 25^\circ$ for $Re = 24600$.

7.3.2 Nature of the circular and spiral patterns

These new experiments using a central hub have shown that the scenario proposed by Schouveiler *et al.* [303] for the transition to turbulence in a cylindrical rotor-stator cavity ($R_m = 1$) as well as the

main characteristics of the two instabilities remain almost the same in the case of an annular cavity ($R_m = 1.8$). The nature of these circular and spiral waves is now investigated in more details using DNS for an annular cavity defined by $G = 0.114$ and $R_m = 1.8$ already considered experimentally. In the following, t^* denotes the dimensionless time defined as $t^* = t \times \Omega$.

7.3.2.1 Circular rolls (CR)

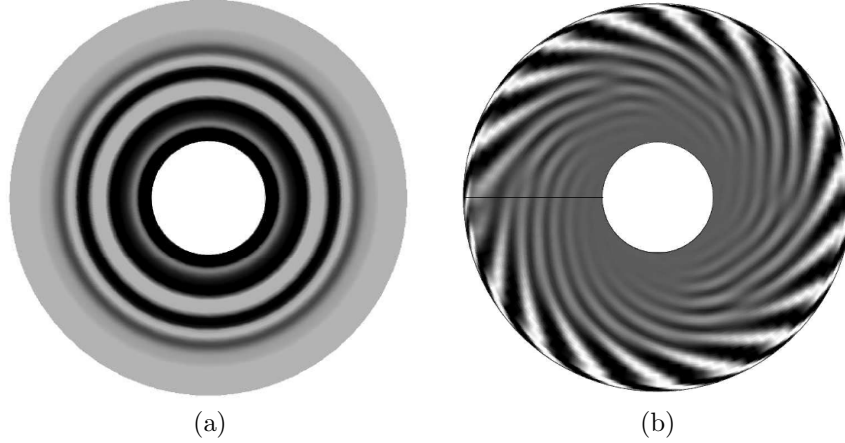


Figure 7.4: Iso-values of the instantaneous axial component V_z of the velocity vector obtained by DNS for $G = 0.114$ and $R_m = 1.8$ at $z^* = 0.86$ showing (a) the circular waves for $Re = 15000$ at $t^* = 3.83$ and (b) the spiral waves for $Re = 24630$ at $t^* = 175.9$ ($A = 0.2$, $N = 5$).

The DNS is initialized using conditions corresponding to a fluid at rest. Then the Reynolds number is increased regularly until the appearance threshold Re_{c1} of the CR instability. Whatever the spin-up to reach this threshold and without any spatial perturbation, Re_{c1} remains in the range $[10000 - 10500]$ by DNS ($28.6 \leq Re_{\delta 1} \leq 29.3$), while they are visible from $Re_{c1} = 12300$ in the experiment. The numerical values are in close agreement with previous DNS ($Re_{\delta 1} = 27$) of Serre et al. [311] for $G = 0.2$ and $R_m = 1$. The LSA of Serre et al. [314] showed that the stator boundary layer is convectively unstable for $Re_{\delta} \geq 34.7$, which corresponds also to the appearance threshold for the type II instability. This weak discrepancy between the LSA of Serre et al. [314] and the present DNS results may be attributed to a ‘‘Rossby effect’’. The LSA has been indeed performed for $Ro = 0.313$ corresponding to Batchelor flows between infinite disks, whereas the Rossby number varies in the present calculations between 0.34 and 0.53 far from the cylinders. The stator boundary layer is then more stable when the Rossby number is increased in agreement with [314]. The stability of such boundary layers depends thus more on local parameters such as the Rossby number than on global ones like Re . Figures 7.4a and 7.5a present respectively, the iso-values of the instantaneous axial velocity V_z in the stator boundary layer and some iso-contours of V_z in a ($r^* = r/b$, $z^* = z/h$) plane for $Re = 15000$ at $t^* = 3.83$. It reveals that the circular rolls appear in the Stewartson layer attached to the external fixed cylinder (Fig.7.5a) and moves along the stator towards the rotation axis with a negative phase velocity $V_{\phi}/(\Omega b) = -0.143$ at ($r^* = 0.604$, $z^* = z/h = 0.611$). Previous measurements of Schouveiler et al. [304] using an Ultrasonic Doppler Anemometer (UDA) showed that the CR occupy the half upper part of the cavity and that, for $Re = 17200$, $G = 0.114$, $R_m = 1$ and $j = 0$, they propagate with a negative phase velocity equal to -0.032 at $r^* = 0.57$. This difference for V_{ϕ} may be attributed to the presence of the hub that accelerates the poloidal circulation of the flow, the circular rolls being advected by the secondary inward throughflow passing along the stator. Note that the axial extent of the CR increases when approaching the hub. For $r^* = 0.693$, they are confined between $z^* = 0.4$ and $z^* = 0.933$, whereas, very close to the hub, the CR occupies about 90% of the interdisk spacing. The number of circular rolls $k_{CR} = 4$ remains the same in the experiment and in the DNS for $Re = 15000$ and the CR frequency obtained numerically $f_{CR}/\Omega = 0.318$ is in excellent agreement with the experimental value ($f_{CR}/\Omega = 0.32$).

Nevertheless, there is one main difference between the two approaches. Figure 7.7a shows the space-time diagram of the dimensionless mean axial velocity $V_z^* = V_z/(\Omega r)$ along a given circle

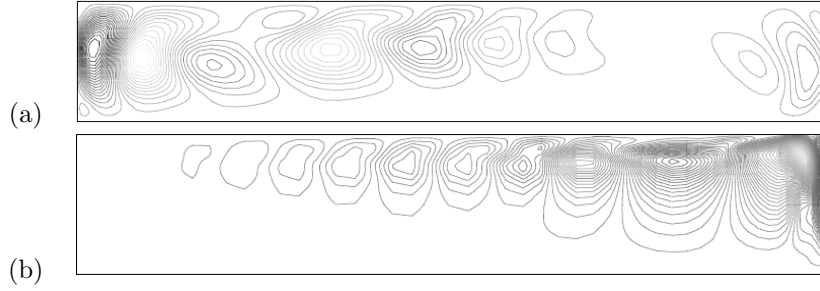


Figure 7.5: Iso-values of the instantaneous axial component V_z of the velocity vector obtained by DNS for $G = 0.114$ and $R_m = 1.8$ in a (r^*, z^*) plane: (a) the CR patterns for $Re = 15000$ at $t^* = 3.83$ and (b) the SR1 spirals for $Re = 24630$ at $t^* = 175.9$ ($A = 0.2$, $N = 5$). $r^* \in [0.286, 1]$ and $z^* \in [0, 1]$.

($0 \leq \theta^* = \theta/(2\pi) \leq 1$) at $r^* = 0.604$ and $z^* = 0.812$ for $Re = 24630$. It reveals that, for this value of Re , the circular rolls, which appear on this figure as vertical black and white stripes, disappear after 20 disk turns. For $Re = 15000$, they disappear after only 10 disk turns. These 10 disk turns correspond in fact to the spin-up time $\tau = O(E^{-1/2}\Omega^{-1})$ introduced by Weidman [350], with $E = \nu/(\Omega h^2)$ the Ekman number: $t^* = 10 \simeq 4.05 \times E^{-1/2}\Omega^{-1}$. It supports also the observations of Savas [294] during the spin-down of a single rotating disk enclosed by an outer fixed cylinder. Moreover, it confirms the conclusions of Gauthier *et al.* [105] on the convective nature of this instability. Thus, the CR seem to be maintained in the present experimental set-up by an experimental noise probably due to the driving-belt of the electrical motor. One recalls that Schouveiler *et al.* [302, 303, 304] and then Cros and Le Gal [61, 62] used the same device.

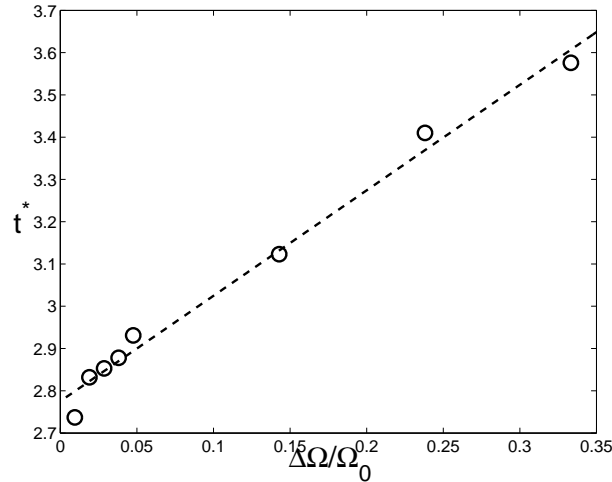


Figure 7.6: Duration time t^* of the CR patterns versus a relative variation of rotation rate $\Delta\Omega = \Omega_1 - \Omega_0$ during the spin-up of the rotor. Plot obtained by DNS (circles) for $G = 0.114$, $R_m = 1.8$ and $\Omega_0 = 0.536 \text{ rad/s}$ ($Re = 10500$) interpolated by $t^* = 2.5\Delta\Omega/\Omega_0 + 2.8$ (dashed line).

Some numerical calculations have been performed to show the sensibility of the circular rolls to the amplitude of a spin-up $\Delta\Omega = \Omega_1 - \Omega_0$ starting from the stable flow at $Re = 10500$ ($\Omega_0 = 0.536 \text{ rad/s}$). Figure 7.6 shows the duration time t^* (equivalent to the number of disk turns) of the CR patterns against $\Delta\Omega/\Omega_0$. The spin-up of the rotor can be seen as an axisymmetric perturbation of the base flow. When the amplitude of the spin-up increases, the disappearance of the circular rolls is delayed according to the interpolation law: $t^* = 2.5\Delta\Omega/\Omega_0 + 2.8$. These results are very similar to the numerical ones of Lopez and Weidman [190] during the spin-down of a rotating disk in a stationary cylinder. They showed, in particular, that during the first radians of rotation, the endwall boundary layer has a structure very similar to Bödewadt and stator boundary layers. They obtained axisymmetric waves travelling radially inwards in this boundary layer. They conjectured that these

are eigenmodes of the Bödewadt layer.

7.3.2.2 Spiral rolls (SR1)

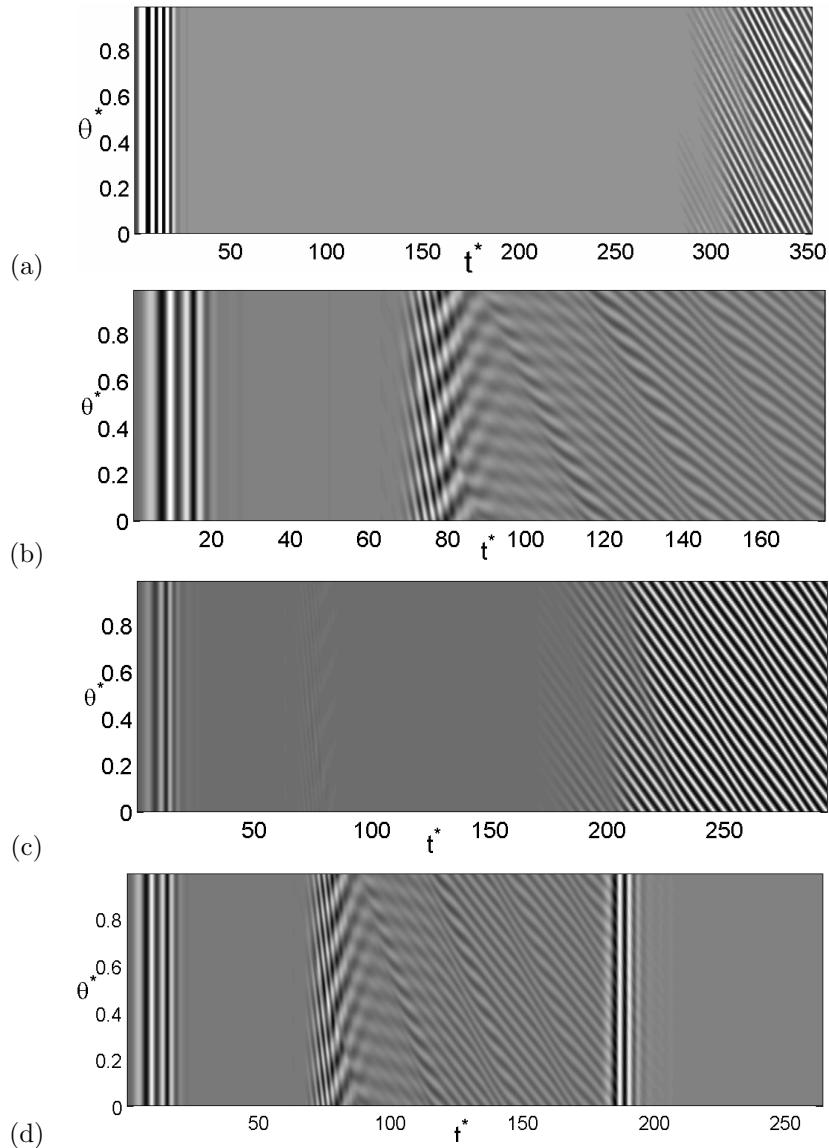


Figure 7.7: Space-time diagrams of the axial velocity $V_z^* = V_z/(\Omega r)$ deduced from the DNS for $Re = 24630$, $G = 0.114$ and $R_m = 1.8$. $\theta^* = \theta/(2\pi)$ is the azimuthal angle on a fixed circle at $r^* = 0.604$ and $z^* = 0.812$. (a) Case 1, (b) Case 2, (c) Case 3, (d) Case 4.

To highlight the nature of the SR1 instability, calculations have been performed for $Re = 24630 > Re_{c2} = 20525$ starting from the converged solution obtained at $Re = 18473$ for which the flow remains stable. The values of G and R_m are still fixed to 0.114 and 1.8 respectively. Note that the critical Reynolds number for the appearance of the SR1 patterns obtained by DNS is about $Re_{c2} = 19781$ (see Fig.7.9) in agreement with the experimental value $Re_{c2} = 20500$. It corresponds to $Re_{\delta 2} = 68$ close to the DNS results $Re_{\delta 2} = 63.2$ of Serre et al. [311] for $G = 0.5$ and $R_m = 1$. Two types of boundary condition for the tangential velocity imposed on the external cylinder have been considered: the first one (BC1) is a stationary cylinder with a small regularization at the corner between the rotor and the shroud ($V_\theta^* = \alpha e^{-z^*/\mu}$ with $\alpha = 0.16$ and $\mu = 0.003$). The second condition (BC2) corresponds to a linear profile for V_θ^* ($V_\theta^* = 1 - z^*$). Note that, for Cases 2, 3 and 4 defined below, a sinusoidal perturbation is applied to the axial velocity component in the whole domain such as:

$V_z = V_z \times (1 + A \sin(2\pi i/N_\theta))$. Thus, the following scenarios have been considered (see Fig.7.7):

- Case 1: BC1. One does not introduce any imposed sinusoidal perturbation.
- Case 2: BC1. A sinusoidal perturbation ($A = 0.2$, $N = 5$) is introduced at $t^* = 62.8$.
- Case 3: BC2. The sinusoidal perturbation ($A = 0.2$, $N = 5$) is introduced at $t^* = 62.8$.
- Case 4: Case 2 but at $t^* = 175.9$, one switches to BC2.

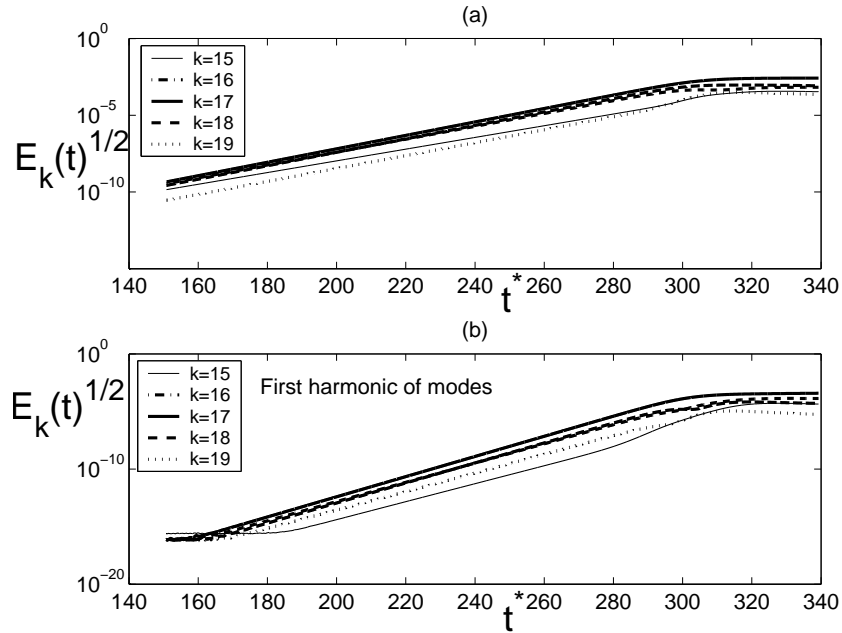


Figure 7.8: Amplitude of the spectral energy E_k after the saturation contained in the Fourier mode 17 versus the Reynolds number, obtained by DNS in Case 1 for $Re = 24630$, $G = 0.114$ and $R_m = 1.8$.

For all cases, the jump in Reynolds number between $Re = 18473$ and $Re = 24630$, corresponding to the spin-up in the experiments of Savas [294], first generates the circular rolls (see Fig.7.7a-d) already observed at lower Reynolds numbers. For Case 1, they disappear after about 20 disk turns and then, the flow becomes stationary. The SR1 patterns appear, without any imposed perturbation, after 290 disk turns. Figures 7.8a and 7.8b show the exponential growth of $E_k(t)^{1/2}$ contained in each Fourier modes k of the velocity in the range [15 – 19] and their first harmonic respectively. The saturation of $E_k(t)$ is reached after around $t^* = 310$. Mode 17 appears to be the most unstable mode in this configuration, close to the experimental value 18 obtained by Schouveiler et al. [302] for $G = 0.114$ and $R_m = 1$. This saturation is a classical non-linear saturation as the slopes (in logarithmic scale) of the first harmonics (Fig.7.8b) are twice steeper as the ones of the modes themselves (Fig.7.8a). It shows that this SR1 instability appear through a Hopf bifurcation. Figure 7.9 confirms the supercritical nature of the bifurcation observed by Schouveiler et al. [302] and Cros et al. [61] as the spectral energy varies linearly with the Reynolds number. It provides also the value for the critical Reynolds number ($Re_{c2} = 19781$) already invoked. One has measured the frequency of the spirals during their growth in order to obtain a non-linear shift of this frequency. Amazingly, this frequency remains constant whatever the amplitude of the spirals is. It implies that the Landau constant associated with the Hopf bifurcation is equal to zero. Due to the periodicity of the flow in the azimuthal direction that implies a quantification of the azimuthal wavenumber k , it appears that k remains constant during the growth of the spirals (or at least during some lapse of time of this growth, see Fig.7.7). As the frequency also remains constant (no non-linear frequency shift), it means that the phase velocity of the SR1 patterns in the azimuthal direction is also constant. This can indeed be checked on the space-time diagrams of Figure 7.7, where the spiral traces appear as rigorously straight lines. It suggests

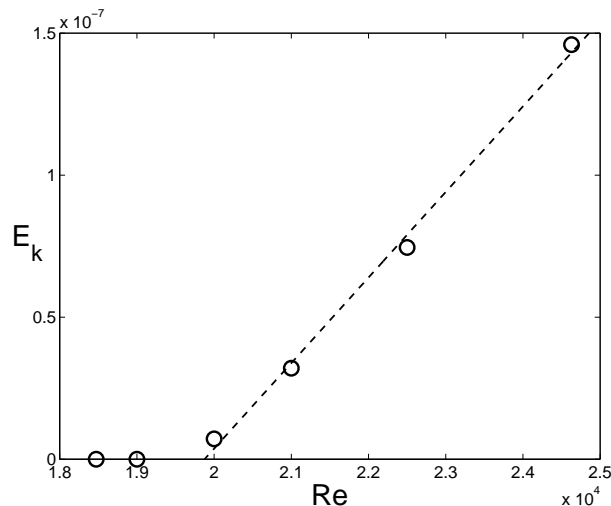


Figure 7.9: Amplitude of the spectral energy $E_k(t)$ after the saturation contained in the Fourier mode 17 versus the Reynolds number, obtained by DNS in Case 1 for $Re = 24630$, $G = 0.114$ and $R_m = 1.8$.

that the phase velocity of the waves may be locked to some hydrodynamical velocity independent of the wave amplitude.

Schouveiler *et al.* [302] have shown experimentally that the SR1 patterns are the subject to a secondary Eckhaus instability and thus, the wavenumber selection is very sensitive to the experimental procedure. To investigate its sensitivity and also to accelerate the transition to the SR1 spiral regime, the same calculation as the one described above is performed for the same parameters but a sinusoidal perturbation is introduced at $t^* = 62.8$. The space-time diagram corresponding to ($A = 0.2$, $N = 5$) is shown in Figure 7.7b. After a short transient state, 18 positive spiral arms (Fig.7.4b) appear along the stator (Fig.7.5b). The amplitude of the perturbation is strong enough to speed up and control the transition process to the SR1 regime. From the 128 iso-contours of the instantaneous axial velocity V_z in a (r, z) plane (Fig.7.5b), a decrease of the spiral size in the axial direction can be seen when approaching the rotation axis. The frequency of the SR1 spirals $f_{SR1}/\Omega = 0.352$ and their angle with the tangential direction $\varepsilon = 26^\circ$ are in excellent agreement with the present experiments $f_{SR1}/\Omega = 0.34$ and $\varepsilon = 28^\circ$ also for $G = 0.114$ and $R_m = 1.8$.

In Case 3 (Fig.7.7c), the boundary condition 2 (BC2) corresponding to a linear profile for V_θ^* on the external cylinder is applied at $t^* = 0$. It means that the shear between the wall and the fluid in solid body rotation is reduced to approximately zero, as both rotate at approximately half the disk speed at mid-height of the cavity. The increase in Reynolds number from 18473 to 24630 generates the CR patterns, which disappear after about 20 disk turns. The sinusoidal perturbation is applied at $t^* = 62.8$ and after a short transient state (5 negative spiral arms with $\varepsilon = -7^\circ$ attached to the stator), the flow becomes stable again until $t^* \simeq 175$. The SR1 appear progressively with time. Thus, this BC2 on the external cylinder has a strong stabilizing effect on the flow but do not annihilate totally their growth.

The results obtained in Case 2 are used as initial conditions for Case 4 (Fig.7.7d). At $t^* = 175.9$, one switches to BC2 on the external cylinder. This change of boundary condition acts as a spin-up at the periphery of the cavity and as a consequence, during a short transient state, circular rolls appear and move towards the center of the cavity. At $t^* = 201.1$, two CR coexist with 16 positive spiral arms ($\varepsilon = 25^\circ$). At $t^* = 226.2$, the flow becomes stable again. This sudden change has a more effective stabilizing effect on the flow compared to Case 3. The modulations observed in the space-time diagrams in Figures 7.7b,d are due to the growth of modes $k = 17$ and $k = 19$ together, which are not negligible compared to the dominant mode $k = 18$ (Fig.7.4b).

These two last numerical experiments (Cases 3 and 4) show that by diminishing the shear between the mean flow in the core region and the endwall, the appearance of the spirals has been delayed. Moreover, it confirms that even if these spirals are due to the destabilization of the stator boundary layer, the perturbation at the origin of the SR1 is produced in the Stewartson layer attached to the shroud (see also Figure 7.5b).

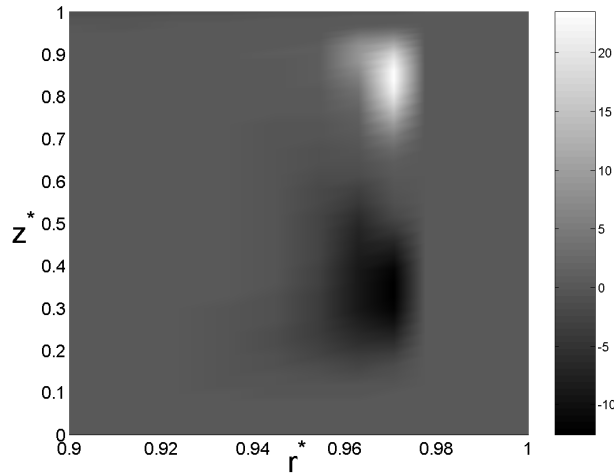


Figure 7.10: Iso-values of \mathfrak{Ra} at $t^* = 276.46$ in Case 1 for $r^* \in [0.9, 1]$ and $z^* \in [0, 1]$ and for $Re = 24630$, $G = 0.114$ and $R_m = 1.8$.

Buisine et al. [39] presumed that the spiral patterns, that they obtained for two values of $G = [0.114; 0.3]$ and $R_m = 1.857$, were generated at the corner between the stator and the shroud and were due to the change of direction of the secondary flow. In the present cases, whatever the boundary condition applied to the endwall, the boundary layer attached to it is centrifugally unstable regarding the modified Rayleigh criterion of Leibovich and Stewartson [176] for an inviscid axisymmetric instability: $\mathfrak{Ra} = V_\theta \partial_r \Omega [\partial_r \Omega \partial_r \Gamma + \partial_r V_z] < 0$, with $\Gamma = rV_\theta$ the circulation, $\Omega = V_\theta/r$ the angular velocity and ∂_r the radial derivative. Figure 7.10 shows an example of iso-values of \mathfrak{Ra} for Case 1 at $t^* = 276.46$. This map matches with the numerical results of Lopez and Weidman [190] for the impulsive spin-down problem of a rotating disk in a stationary cylinder. There are two main regions surrounded by zero \mathfrak{Ra} values: one region characterized by $\mathfrak{Ra} > 0$ is situated at the corner between the stator and the cylinder and the other is just below with $\mathfrak{Ra} < 0$. The SR1 spirals appear to be analog to the corner vortices obtained by Lopez and Weidman [190] at the junction between the endwall and the stator. These authors showed that they are formed by the kinematics of the flow and that their formation is not controlled by a noise level in their calculation.

Several values for the selected Fourier mode and A the amplitude of the sinusoidal perturbation have been computed. The main result is obtained for $A = 0.01$. The 17 spiral waves are recovered, which shows that the flow is linearly unstable to such sinusoidal perturbation.

Finally, Figure 7.11 presents the dispersion relation for the spiral waves. The present DNS results obtained for $Re = 24630$, $G = 0.114$, $R_m = 1.8$ and $j = 0.85$ mm are compared to the experimental data of Schouveiler et al. [302] for $Re = 25000$, $G = 0.114$, $R_m = 1$ and $j = 0$. One calculates the normalized frequency $f^* = f/\Omega$ and the azimuthal wavenumber k of each mode from the transients observed in Figure 7.7. As it can be observed, all the data collapse on the same dispersion relation curve, although modes computed by DNS have been only observed during transient states ($k = 5, 11, 16$). All the data can be fitted by the following second-order polynomial giving the azimuthal wavenumber k as a function of the spiral frequency f^* : $k = -8.7f^{*2} + 27f^* + 10$. The relation possesses a notable curvature and does not go through $(0, 0)$, showing that the spiral propagation is dispersive. An isolated mode $k = 5$ ($f^* = 0.62$), which may belong to another branch of the dispersion relation, is also observed. This illustrates the possibility of multiple solutions in the rotor-stator problem [219].

7.4 Transitional flow regime on both rotor and stator sides

The rotor-stator cavity of aspect ratio $G = 0.195$ ($R_m = 1$) presented in Czarny et al. [63] is now considered for some simulations up to $Re = 4 \times 10^5$. The main difference lies in the absence here of the central rotating cylinder attached to the rotor, which strongly modifies both the main flow and the stability of the Ekman layer along the rotor. For a cylindrical cavity, as in the present case, the fluid is pumped radially outwards along the rotor by the centrifugal effects, flows axially along the

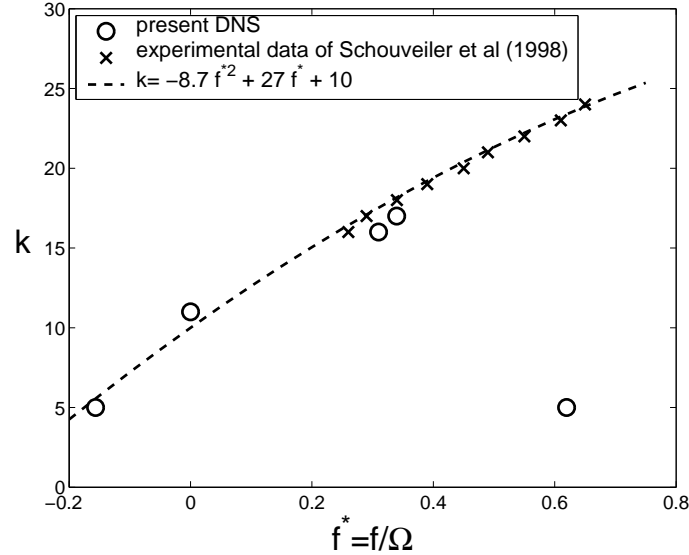


Figure 7.11: Dispersion relation obtained by DNS for $Re = 24630$, $G = 0.114$, $R_m = 1.8$ and $j = 0.85$ mm and by experimental visualizations performed by Schouveiler *et al.* [302] for $Re = 25000$, $G = 0.114$, $R_m = 1$ and $j = 0$.

external cylinder before coming back along the stator. As there is no inner cylinder, the Ekman and Bödewadt layers are no more connected and all instabilities developed along the stator side can not be advected along the rotor to disturb the rotor boundary layer.

The study of transition to turbulence was performed using the Spectral Vanishing Viscosity (SVV) technique described in Section 3.7.1. The final grid in the radial, azimuthal and axial directions is $196 \times 288 \times 71$ ($\sim 4 \times 10^6$ nodes) and is associated with the time step $\delta t = 5 \times 10^{-4} \Omega^{-1}$, corresponding to a memory size of 3.6 GB and an average time by iteration of 10 seconds. The SVV is active for Reynolds numbers above 10^5 with parameterized amplitudes and cutoff wavenumbers equal to $\varepsilon_N = (1/N, 1/N, 1/N)$ and $\omega_T = (\sqrt{N}, \sqrt{N}, \sqrt{N})$ in the (r, θ, z) directions, respectively (N the number of mesh points in the corresponding direction).

7.4.1 Boundary layers instabilities and turbulence in the Bödewadt layer

Solutions have been analyzed by increasing step by step the Reynolds number. As illustrated on Figure 7.12, the boundary layer on the stator side globally behaves like those described in the previous section. The response to spin-up still gives rise to circular patterns related to the convective instability. At a sufficiently high Reynolds number, spiral arms related to the absolute instability are found: 10 spirals are obtained at $Re = 2 \times 10^4$, while 16 spirals appear at the periphery of the cavity at $Re = 3 \times 10^4$. In this last case, some pairings may be observed at intermediate radii. A kind of waveless turbulence appears on the stator side at about $Re = 4 \times 10^4$, in agreement with the experimental observations of Cros *et al.* [61]. It is characterized by more circular and thinner structures that extend to the vicinity of the axis as shown on Figure 7.12 and at a higher Reynolds number on Figure 7.13a.

7.4.2 Boundary layers instabilities and turbulence in the Ekman layer

On the rotor side, the flow remains stable up to very high Reynolds numbers. In contrast to annular cavity, any perturbation produced within the stator boundary layer is able to reach the rotor boundary layer due to the stable flow region around the axis whatever the rotation rate. The first organized structure related to boundary layer instability appears here at about $Re = 4 \times 10^5$. It is characterized by a high-wavenumber multi-armed spiral pattern ($k = 68$) immediately followed by a disorganized flow, characteristic of incipient turbulence as shown on Figure 7.13b.

Incipient turbulence appears at the periphery of the disk at about $Re = 2.5 \times 10^5$. When turbulence occurs in the rotor layer, it reaches an extremum. The maximum of turbulence kinetic energy that

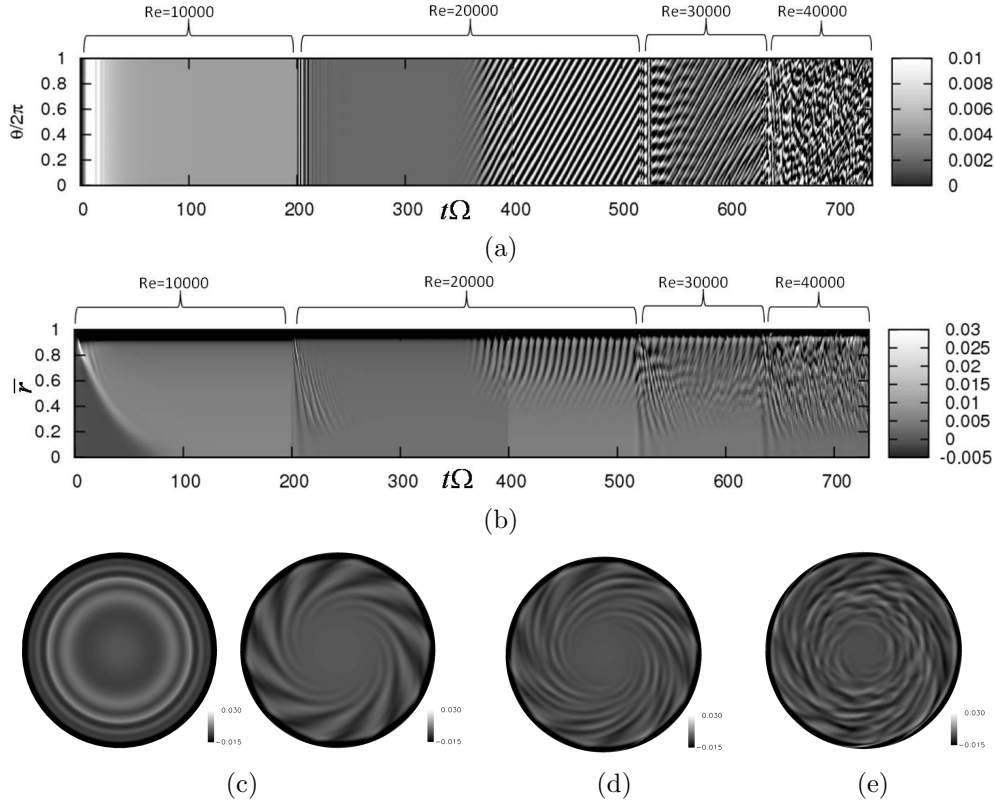


Figure 7.12: Transition to a turbulent stator boundary layer flow in a cylindrical cavity of aspect ratio $G = 0.195$. Spatio-temporal diagrams showing the dynamics of the instability structures when increasing rotation: (a) V_z ($r^* = 0.809$, $z^* = 0.89$, θ , t); (b) V_z (r^* , $z^* = 0.89$, 0 , t^*). (c, d, e) isolines of V_z showing the instability patterns: (c left) transient circular rolls alone at $Re = 2 \times 10^4$ ($t^* = 207 \Omega^{-1}$), (c right, d) $m = 10$ spiral arms at $Re = 2 \times 10^4$ and $Re = 3 \times 10^4$, respectively, (e) turbulent patterns at $Re = 4 \times 10^4$. The disk rotates counterclockwise.

was located on the stator at the impact of the swirling jet flowing along the cylinder wall, moves to the periphery of the rotor when one increases the rotation rate.

The rotor layer being very stable, the investigation of the transition scenario is easier because instability modes can grow successively over a wide range of Reynolds number, in contrast to the stator boundary layer. The aim was to confirm the scenario of Viaud *et al.* [344].

As shown in Figure 7.13b, the spiral arms occur at a radial location $r^* \approx 0.69$, where the turbulence kinetic energy suddenly increases forming a step front (Fig. 7.14). At this position, the local Rossby and Reynolds numbers are equal to $Ro = -0.72$ and $Re_\delta = 314$, respectively. The results compare well with the theoretical study of Lingwood [184]. In this work, Lingwood [184] presents a study of the laminar Ekman layer and the family of related rotating problems that includes the Bödewadt, Ekman and von Kármán boundary layer flows, usually referred as BEK system. Figure 7.15 presents the critical Reynolds and radii for the onset of absolute instability for the BEK system obtained by Lingwood [184]. This diagram shows that, for a Rossby number equal to $Ro = -0.72$, the local Reynolds number and dimensionless radius are equal to $Re \approx 300$ and $r^*/\sqrt{Re} \approx 400$, respectively.

From Figure 7.15 and $Ro = -0.72$, a theoretical value of the radial position, $R_{CA}(= r^*/\sqrt{Re}) = 6.76$ is obtained. The radius R_{CA} may be interpreted as the position, where the convective-absolute instability transition occurs.

Figure 7.14 represents the theoretical position, R_{CA} together with the turbulence kinetic energy in the rotor boundary layer as a function of the radial position obtained for $Re = 4 \times 10^5$, allowing the visualization of the convective and absolute regions (noted by C and A respectively) and the value of the absolute spatial growth rate, $k_{0,i} \approx 3.635$ indicated by the slope. The linear theory of Lingwood [184] also predicts an unstable mode $k = 67$ for $Ro = -0.72$. This value was obtained by an interpolation of the theoretical values and allows us to obtain a theoretical prediction of the unstable

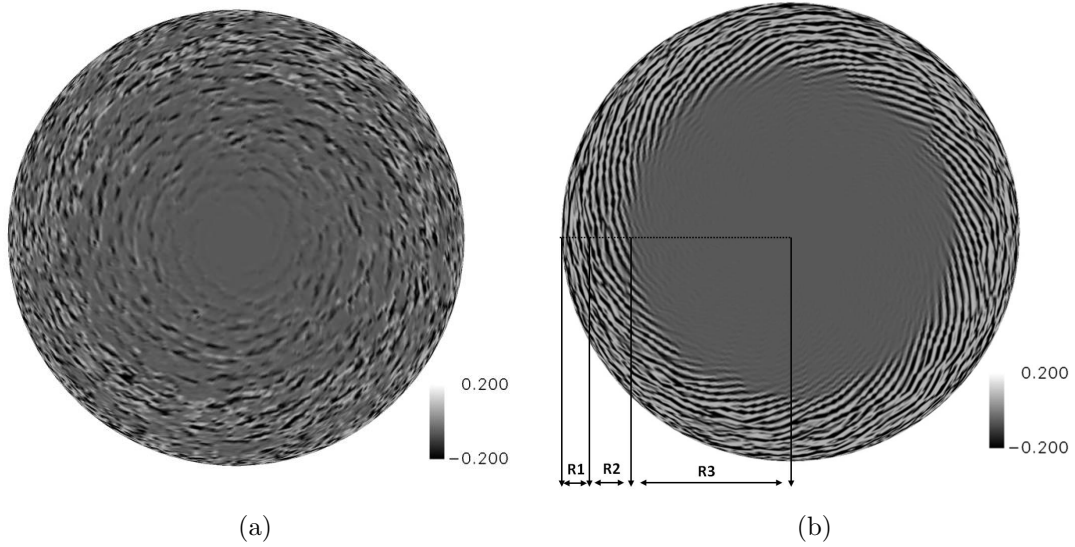


Figure 7.13: Isolines of the Q-criterion for $G = 0.195$ and $Re = 4 \times 10^5$: (a) stator boundary layer with quasi-circular patterns; (b) rotor boundary layer with a stable flow region (R_1) and a multi-armed spiral front ($k = 68$) of the absolute mode of the crossflow instability (R_2) immediately followed by incipient turbulence (R_3).

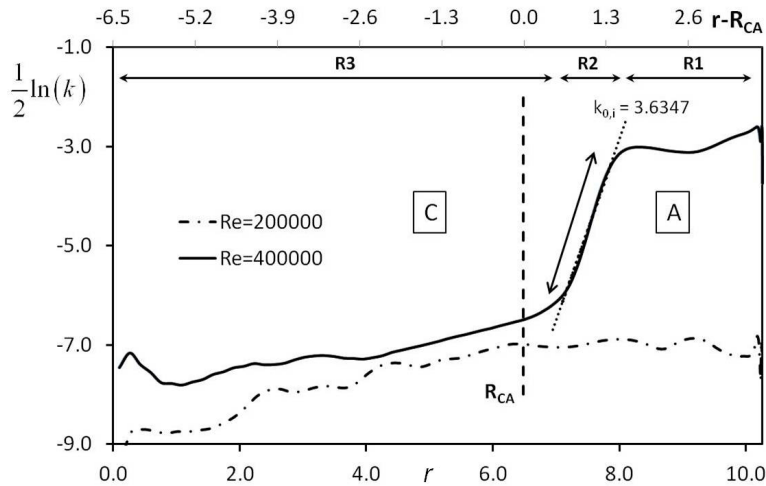


Figure 7.14: Turbulence kinetic energy k in the rotor boundary layer for $G = 0.195$ and $Re = 4 \times 10^5$ showing the structure of a steep front immediately followed by incipient turbulence. R_{CA} is the local radius for convective/absolute transition and $k_{0,i}$ is the linear absolute spatial growth rate.

mode. This estimate is close to the present LES results. The energy spectrum of the turbulence kinetic energy is shown on Figure 7.16 for three different regions in the rotor boundary layer (referred in Figure 7.13b as R_1 , R_2 and R_3). The wide spectrum in the R_1 -region is characteristic of incipient turbulence while in the R_3 -region the energy is one order smaller indicating that the flow is still stable. The spectrum corresponding to the R_2 -region, where are located the spiral arms, shows that the mode 68 is the most unstable. However, about ten neighboring modes are also unstable showing the strong non-linearity of the solution. All these modes could play a role in the slight vacillation of the spiral front in the tangential direction. This vacillation may correspond to a small coupling between the perturbations and the mean flow that changes the local properties and feedback on the

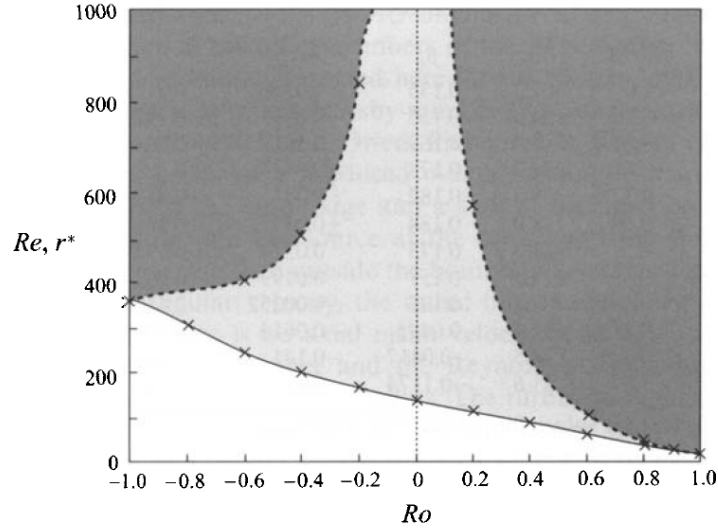


Figure 7.15: Critical local Reynolds numbers(-) and radii (—) for the onset of absolute instability for the BEK system by Lingwood [184]. The bounding lines are fitted to the calculated data points (X) and the shaded areas correspond to the absolutely unstable regions.

radius of transition of the mean flow.

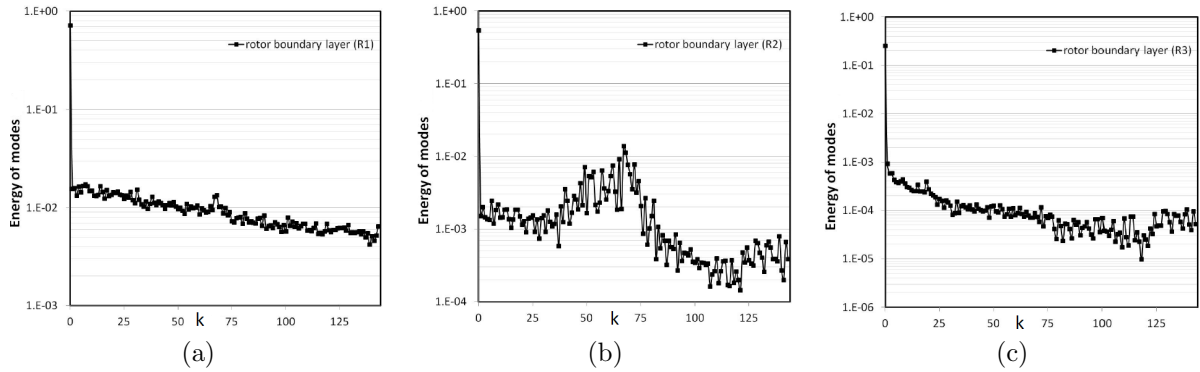


Figure 7.16: Energy spectrum of the turbulence kinetic energy in the rotor boundary layer: (a) region R_1 , (b) region R_2 and (c) region R_3 .

To conclude, these results show that the scenario of a direct transition to turbulence suggested in the theoretical study of Pier [245] and obtained in the recent numerical studies of Viaud *et al.* [344] can be naturally selected in a rotor-stator flow. The $k = 68$ spiral wave would correspond to a non-linear global mode characterized by a steep front (Fig. 7.14) located on the upstream limit of the absolutely unstable domain, followed downstream by a disordered state (Fig. 7.13b) related to incipient turbulence and preceded upstream by a low level perturbation region.

7.5 Conclusion

A combined experimental and numerical study of the transition to turbulence of the flow in an annular rotor-stator cavity has been first performed. One focused on the two instabilities, which occur in the case of unmerged boundary layer flow. The influence of the hub on the stability diagram has been investigated. It slightly increases the ratio between the fluid and the disk velocities (and so the Rossby number) but this effect remains weak. Then, flow visualizations and DNS results have been compared for $R_m = 1.8$ and an excellent agreement has been obtained for the main characteristics of the circular and spiral rolls.

These two instabilities have been revisited using accurate DNS and the convective nature of the first instability, which appears as circular rolls attached to the stator, has been highlighted in agreement with previous results [105]. Above a second threshold, a second instability appears as positive spiral patterns (SR1) also propagating along the stationary disk. Numerically and without any perturbation, mode $k = 17$ appears to be the most unstable mode, in agreement with the results of Schouveiler *et al.* [302]. This mode saturates through the production of higher harmonics following the classical supercritical Hopf bifurcation picture. Whatever the boundary conditions on the end-wall, the flow remains unstable according to the criterion of Leibovich and Stewartson [176]. This endwall condition introduces a permanent perturbation, which destabilizes the stator boundary layer and induces the formation of the SR1 patterns, that propagates dispersively in the stator boundary layer. The convective nature of the circular rolls and the crossflow instability appearing as multiarmed spiral waves via a supercritical Hopf bifurcation have been confirmed a little bit later by the linear stability analysis of Lopez *et al.* [189] in a similar rotor-stator system ($R_m = 1$, $G = 0.2$).

Along the rotor side, present results are consistent with the scenario of transition to turbulence obtained in recent theoretical and numerical studies of Pier [245] and Viaud *et al.* [344] with a $k = 68$ spiral non-linear global mode. In this sense, they should interfere in the debate around the existence of a direct route to turbulence in the rotating disk boundary layer.

Turbulent enclosed rotor-stator disk flows

This topic is the main thread of my research activities up to 2012. When I moved to the M2P2 laboratory, I switched to numerics and performed LES calculations using the approach based on the spectral vanishing viscosity (SVV) technique developed by Séverac & Serre [316] (see Chapter 3). It has been applied to enclosed rotor-stator flows under both isothermal and non-isothermal conditions. One of the main goal was to reproduce and understand the 3D unsteady large-scale structures highlighted experimentally by the team of Prof. B.E. Launder [60, 63].

In this Chapter, quantitative comparisons of two high-order LES are reported to predict a turbulent rotor-stator flow at a rotational Reynolds number $Re = \Omega b^2/\nu = 10^6$. A classical dynamic Smagorinsky model for the subgrid-scale stress (LES-FD) is here compared to the spectral vanishing viscosity technique (LES-SVV). Numerical results include both instantaneous data and post-processed statistics. Results show that both LES are able to accurately describe the unsteady flow structures and to predict satisfactorily mean velocities as well as the Reynolds stress tensor components. A slight advantage is given to the spectral SVV approach in terms of accuracy and CPU cost. The strong improvements obtained in the present results with respect to RANS results confirm that LES is the right level of modeling for such flows. The results are then extended using the SVV code to investigate the influence of the Reynolds number, finite cavity effects and the three-dimensional nature of the two boundary layers.

The effects of thermal convection have been examined then for a turbulent flow and Rayleigh numbers up to $Ra = 10^8$ still using the LES-SVV. The averaged results show small effects of density variation on the mean and turbulent fields. The turbulent Prandtl number is a decreasing function of the distance to the wall with 1.4 close to the disks and about 0.3 in the outer layers. The local Nusselt number is found to be proportional to the local Reynolds number to the power 0.7. The evolution of the averaged Bolgiano length scale with the Rayleigh number indicates that temperature fluctuations may have a large influence on the dynamics at the largest scales of the system for $Ra \geq 10^7$.

To conclude, some flow visualizations performed using the MACE facility in Manchester are provided and confirm the former results [60, 63] obtained in a cylindrical cavity. Large scale precessing vortices may appear within the central core of the flow in the turbulent regime. When the cavity is annular with a central hub, there is no evidence of these structures confirming the present LES results.

8.1 Introduction

8.1.1 Why studying rotor-stator flows?

Rotating disk flows have been the subject of a constant interest over the last decades because of their relevance to applications in rotating machinery systems as computer storage, axial thrust bearings and turbine disk cooling. For example, most of the works on rotor-stator flows shown in this manuscript as well as the ones developed during my PhD thesis [249], have been motivated by the predictions of the base rotor-stator flows found in the Liquid Hydrogen Turbopump of the Vulcain engine shown in Figure 8.1. In such cavities, the centrifugal and the Coriolis forces have a strong influence on the turbulence by producing a secondary flow in the meridian plane composed of two thin boundary layers along the disks separated by a non-viscous geostrophic core. Thus, a good prediction of the mean tangential velocity in the core enables to evaluate the axial thrusts on the rotating disk, which is one key point for manufacturers [249, 251].

Under non-isothermal conditions, these flows are important in a large number of industrial applications such as in the ventilation of electrical air cycle machines, in semi-conductor manufacturing processes with rotating wafers and in a lot of other rotating machineries. For example, in high-speed

rotating gas turbines, the cooling air flow is used to both cool the disk and prevent the ingestion of hot turbine passage gases into the cavity. A good knowledge of heat transfers and fluid flows in such systems is crucial: an excessive amount of coolant is often supplied to the cavity that imposes an unnecessary penalty on the engine cycle and leads to a loss of efficiency.

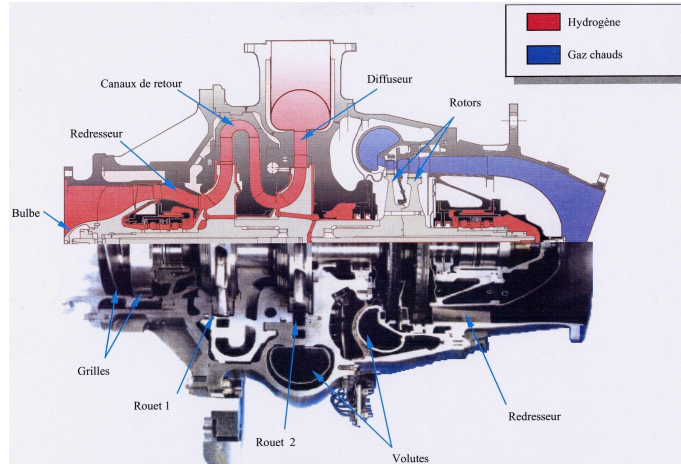


Figure 8.1: Exploded view of the Liquid Hydrogen Turbopump (TPH) of the Vulcain engine of Ariane V developed by the group Snecma Moteurs.

The rotor-stator problem has also proved to be a fruitful means of studying turbulence properties with wall confinement and rotation as this specific configuration is a relatively simple case where rotation brings significant modifications to the turbulent field. Finally, rotating disk flows are also among the simplest flows where the boundary layers are three-dimensional from their inception and they are therefore well suited for studying the effects of mean-flow three-dimensionality on the turbulence and its structure [145, 185, 193].

8.1.2 Regime IV of Daily and Nece [67]

Rotor-stator flow structure is largely dependent on the combination of the rotation speed Ω and the interdisk spacing h . Daily and Nece [67] carried out an exhaustive theoretical and experimental study of sealed rotor-stator flows and pointed out the existence of four flow regimes. These correspond respectively to two laminar regimes (I and II) and two turbulent regimes (III and IV), each characterized by either merged (I and III) or separated (II and IV) boundary layers. In the latter case, the two boundary layers are separated by a central rotating core. The limits of the four regimes are shown in Figure 8.2.

These authors provided also an estimated value for the local Reynolds number at which turbulence originates with separated boundary layers, $Re_r = \Omega r^2 / \nu = 1.5 \times 10^5$ (r is the radial location) for aspect ratios $G \geq 0.04$. However, experiments have revealed that transition to turbulence can appear at a lower value of Re_r within the Bödewadt layer on the stator, even though the flow remains laminar in the Ekman layer along the rotor.

Major experiments concerning this flow regime have been performed by Itoh et al. [136, 137] in a closed cavity. They measured the mean flow and all the Reynolds stress tensor components, and brought out the existence of a relaminarized region towards the axis even at high rotation rates. From detailed measurements, Itoh et al. [137] reported a turbulent regime occurring earlier along the stator side at $Re_r \simeq 8. \times 10^3$, while along the rotor side, turbulent flow develops later for $3.6 \times 10^5 < Re_r < 6.4 \times 10^5$ for $G = 0.08$. This is in agreement with the experiment of Cheah et al. [49] performed for rotational Reynolds numbers ranging $3 \times 10^5 < Re_r < 1.6 \times 10^6$ inside a rotor-stator system of aspect ratio $G = 0.127$. The rotor side becomes turbulent for $Re_r = 4. \times 10^5$ while the stator is shown to be turbulent at all Reynolds numbers considered. Cheah et al. [49] found differences in turbulence characteristics between the rotor and the stator and that the turbulent flow field is also affected by the radial location. These authors concluded to an influence of the radial convective transport of turbulence on the flow field. Czarny et al. [63] displayed by flow visualizations the appearance

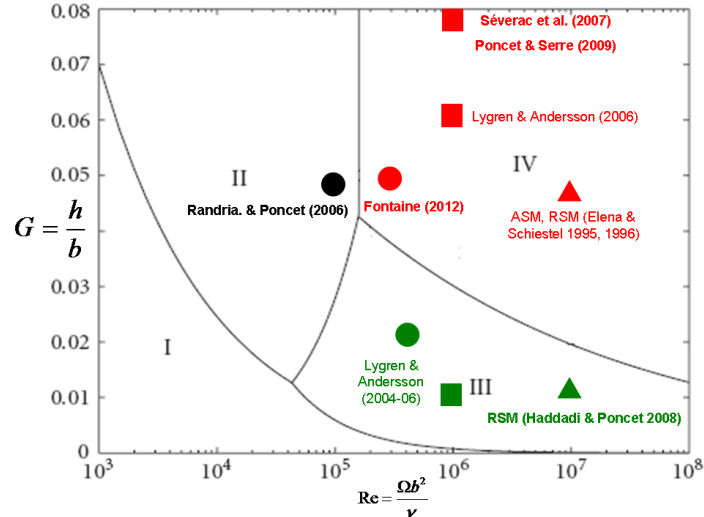


Figure 8.2: Base flow regimes in enclosed rotor-stator cavities after Daily and Nece [67] with the main numerical contributions (triangles=RANS modeling, circles=DNS, squares=LES).

of organized precessing vortex structures in a rotor-stator cavity of aspect ratio $G = 0.126$. These three-dimensional patterns subsist at high Reynolds numbers $Re \rightarrow 1.78 \times 10^6$ and might explain the failure to predict heat and mass transfers accurately when only axisymmetric and steady approaches are used. In the case of an outward throughflow, Poncet *et al.* [253] characterized, using the RSM of Elena and Schiestel [85], the transition between the Batchelor and Stewartson flow structures as a function of a modified Rossby number.

Relatively few experimental data are available in the literature for heat transfer in rotating disk flows mainly because of the complexity and the cost of making accurate heat transfer measurements. A large review of the fundamental investigations relevant to heat and mass transfers in rotor-stator cavities carried out until 1989 has been performed by Owen and Rogers [233]. In the flow regime with unmerged boundary layers, the dynamics of thermal convection with a rotating top wall can be characterized essentially by three global physical parameters in a closed cavity, which are the rotational Reynolds number Re , the Rayleigh number Ra and the Prandtl number Pr defined by:

$$Re = \Omega b^2 / \nu \quad Ra = \frac{\Omega^2 b \Delta T h^3}{\nu \kappa T_r} \quad Pr = \frac{\nu}{\kappa}$$

where ν and κ are the kinematic viscosity and the thermal diffusivity of the fluid, respectively. ΔT is the temperature difference between the disks and T_r is the reference temperature equal to the average of the wall temperatures. The total heat flux through the disks is usually expressed in terms of the local Nusselt number $Nu = hr/\lambda$ (h the convective heat transfer coefficient and λ the conductivity of the fluid) or of the averaged Nusselt number Nu_{av} . Both depend in a complicated manner on (Ra, Re, Pr) but also on the flow rate coefficient for open cavities. The influence of the aspect ratio G of the cavity on the distribution of the local Nusselt number along the disks is weak compared to the ones of rotation for example [233].

In the regime IV (turbulent with unmerged boundary layers), Dorfman [78] proposes, from experiments, a correlation for the local Nusselt number:

$$Nu = 0.0197 Pr^{0.6} Re_r^{0.8} \quad (8.1)$$

Note that the aspect ratio and the Rayleigh number do not appear in this correlation. Dorfman [78] proposes other correlations depending on the temperature distributions imposed on the disks. This author showed also that heat transfer on the rotating disk was not affected by the presence of the stator for $G \geq 1.05 Re^{-0.2}$. That implies that the correlation laws obtained in the single disk case [78, 233] can also be applicable here. Daily and Nece [67] proposed a correlation for the mean Nusselt number on the rotor:

$$Nu_{av} = 0.0173\left(\frac{G}{2}\right)^{0.1} Re^{0.8} \quad (8.2)$$

Djaoui et al. [73, 74] examined the turbulent flow in a rotor-stator cavity of large aspect ratio subjected to a superimposed radial inflow and heat transfer effects. Detailed velocity and Reynolds stress tensor measurements as well as temperature and temperature-velocity correlations have been carried out using a hot and cold wire anemometry technique. They studied in particular the external peripheral geometry effects and the critical importance of the inlet conditions on the mean tangential fluid velocity. They focused also on the dependence of the flow structure and heat transfer effects on the Rossby and Reynolds numbers. Comparisons with an asymptotical formulation based on the assumption of inviscid fluid were displayed and were shown to be in good agreement with the experimental data. Harmand et al. [124] investigated both the flow structure by Particule Image Velocimetry (PIV) and the heat transfers using a thermally rotor heated by infrared radiation in the case of turbulent rotor-stator flows. The local heat flux distribution from the rotor was identified by solving the Laplace equation by finite-difference schemes. The local Nusselt number Nu on the rotor was found to be an increasing function of the Reynolds number and remains almost constant along the radius contrary to the free disk case, where Nu increases from the axis to the periphery of the cavity. Pellé and Harmand [237] studied experimentally the influence of the dimensionless interdisk spacing G on the local Nusselt number. It remained almost constant whatever the Reynolds number for $G = 0.08$. They identified four heat transfer regimes corresponding to the four flow regimes of Daily and Nece [67] and gave correlations for the local and averaged Nusselt numbers depending on the aspect ratio and the Reynolds number. For turbulent flows with separated boundary layers, the general laws for Nu and Nu_{av} are:

$$Nu = 0.035(1 - e^{-40 \times G})(1 - e^{-4.2 \times 10^5 Re})Re_r^{0.746} \quad (8.3)$$

$$Nu_{av} = 0.0325(1 - e^{-40 \times G})(1 - e^{-4.2 \times 10^5 Re})Re^{0.746} \quad (8.4)$$

The last step towards the real machinery has been done experimentally by Verhille et al. [343], who studied the resonances of a rotor-stator cavity filled with sulfur hexafluoride. They showed in particular that such fluid near its critical point enables to reach the similarity parameters of the real turbopump and that the resonances can be well predicted by considering a Helmholtz resonator model.

8.1.3 Turbulent rotor-stator flows: a challenge for numerical methods

Until now, numerical studies have been dedicated to simpler flows: single disk flows [357], axisymmetric flows using statistical approaches (Reynolds Averaged Navier-Stokes) [253], idealized rotor-stator cavities [193], or enclosed rotor-stator cavities but at much lower rotation rates using Direct Numerical Simulation (DNS) [266, 311]. So far very few investigations have been done using Large Eddy Simulation (LES).

These flows are indeed very challenging for numerical modeling particularly in turbulent regimes relevant to industrial conditions. A characteristic feature of such flows is indeed the coexistence of adjacent coupled flow regions involving laminar, transitional and turbulent regions completely different in terms of the flow properties. Moreover, the turbulence is strongly inhomogeneous and anisotropic because of finite cavity effects, flow curvature and rotational effects.

At the present time, computer performances only permit DNS of transitionally turbulent cavity flows ($Re \approx 10^5$) [253, 266, 311] as shown in Figure 8.2. In a simpler flow model, where the flow is restricted to an angular section of the cavity and assumed homogeneous also in the radial direction, Lygren and Andersson [193] performed DNS at a higher Reynolds number ($Re = 4 \times 10^5$) using a second-order finite-difference scheme. They provided a detailed set of data to analyze the coherent structures near the two disks. In the non-isothermal case, Serre et al. [310] performed DNS of non-isothermal transitional flows under the Boussinesq approximation at $Re = 1.1 \times 10^5$ and showed in particular that the effects of density variation remain small for Rayleigh numbers up to $Ra = 2 \times 10^6$.

Attempts to compute turbulent rotor-stator flows using statistical approaches had only partial success. Indeed, the turbulence model must be able to solve the low-Reynolds number regions not only near the disks but also in the core of the flow. Moreover, the model has to predict precisely

the location of the transition from the laminar to the turbulent regime, even though it is bounded by instabilities, and so cannot be completely represented by a steady flow model. The second-order closures could be a more appropriate level of closure to predict such complex flows [85, 173, 253] but even if they provide a correct distribution of laminar and turbulent regions, the Reynolds stress behavior is not fully satisfactory, particularly near the rotating disk and in the core region.

Consequently, Large Eddy Simulation (LES) constitutes a valuable way to compute such flows. Wu and Squires [357] have been the first to develop LES to predict the statistically three-dimensional turbulent boundary layer (3DTBL) over a single rotating disk. They compared three dynamical subgrid models to the experimental data of Littell and Eaton [185] for $Re = 6.5 \times 10^5$. Their results have offered new evidence to support the observations of Littell and Eaton [185] that streamwise vortices with the same sign as the mean streamwise vorticity are mostly responsible for strong sweep events, while streamwise vortices having opposite sign to the mean streamwise vorticity promote strong ejections. Lygren and Andersson [194] compared the results obtained from three LES models with their DNS calculation and suggested that improved subgrid models have to be implemented to get closer agreement. In their latter work, Andersson and Lygren [11] performed “wide-gap” and “narrow-gap” simulations to investigate the degree of three-dimensionality in both Ekman and Bödewadt layers for $Re \leq 1.6 \times 10^6$. Their results support the same conclusions as Littell and Eaton [185] that the mean flow three-dimensionality affects the near wall vortices and their ability to generate shear-stresses.

The fact that only few experimental works have been done under non-isothermal conditions has slowed down the development of specific advanced heat transfer models. Abe et al. [1] developed a two-equation heat transfer model, which incorporates essential features of second-order modeling. They introduced the Kolmogorov velocity scale to take into account the low Reynolds number effects in the near-wall region and also complex heat transfer fields with flow separation and reattachment. But this model has not been yet implemented for rotating disk flows. A major numerical work is the one of Iacovides and Chew [134]. They have used four different turbulence models to study the convective heat transfer in three axisymmetric rotating disk cavities with throughflow. Three models were based on a zonal modeling approach and one was based on a mixing-length hypothesis. Their numerical predictions were compared to experimental data available in the literature but none of the four models was entirely successful. Nevertheless, considering overall performance, the $k - \epsilon$ model with the one-equation near-wall treatment was preferred. Schiestel et al. [299] have examined the turbulent flow in a rotating cavity with a radial outward throughflow and heat transfer effects. They compared a standard $k - \epsilon$ low-Reynolds number model and a zonal approach using second-order Algebraic Stress Model (ASM) in the core of the flow. They showed that second-order modeling is necessary to obtain a detailed near-wall treatment. Recently, Poncet and Schiestel [258] compared the RSM of Elena and Schiestel [85] to data available in the literature. They considered the temperature as a passive scalar ($Ra = 0$) and found a close agreement in the case of an open cavity even for large temperature differences $\Delta T = 75$ K. Most turbulence modelings do not take into account three-dimensional effects due to highly structured large-scale vortices, which have a large influence on the resultant heat transfer coefficients at the disk surface as shown in [27, 63]. Thus, all workers concluded that further numerical research is required before a mathematical model can be recommended with any confidence.

Figure 8.2 sums up the main numerical contributions to rotor-stator disk flows in enclosed cavities and under isothermal conditions. RANS models are able to predict the flow field until $Re = 10^7$ [84, 119], which remains quite far from the value $Re = 2.8 \times 10^8$ reached in the real turbopump ($G \simeq 0.45$) sketched in Figure 8.1. At this Reynolds number, it is clearly unthinkable to perform a 3D well resolved DNS as more than 4×10^{18} grid points will be required to resolve up to the Kolmogorov length scale.

8.2 The experimental set-up

The cavity considered here and sketched in Figure 3.1 was developed at IRPHE. It is composed of a smooth stationary disk (the stator) and a smooth rotating disk (the rotor) delimited by an inner rotating cylinder (the hub) and an outer stationary casing (the shroud). The rotor and the central hub attached to it rotate at the same uniform angular velocity Ω . The mean flow is governed by three main parameters: the aspect ratio of the cavity G , the curvature parameter R_m and the rotational Reynolds number Re based on the outer radius b of the rotating disk defined as follows:

$$G = \frac{h}{b} = \frac{1}{7} \quad R_m = \frac{b+a}{b-a} = 1.8 \quad 10^5 \leq Re = \frac{\Omega b^2}{\nu} \leq 10^6$$

where ν is the kinematic viscosity of water, $a = 40$ mm and $b = 140$ mm the inner and outer radii of the rotating disk, $h = 20$ mm the interdisk spacing and Ω the rotation rate of the rotating disk. The values of the geometrical parameters have been chosen in order to be relevant with industrial devices such as real stage of turbopump, and to satisfy technical constraints of the experimental device as well as computational effort to reach statistically converged states. A variable speed numerical controller drives the angular velocity Ω with an accuracy better than 1%. In the experimental set-up, two small clearances exist: the first one $\delta_1 = 0.85$ mm between the rotor and the shroud ($\delta_1/b = 0.0061$) and the second one $\delta_2 = 0.1$ mm between the hub and the stator ($\delta_2/h = 0.005$) because of mechanical constraints. During one experiment, the temperature is almost constant: $20 \pm 0.5^\circ C$. One defines the dimensionless radial r^* and axial z^* coordinates as: $r^* = (r - a)/(b - a)$ and $z^* = z/h$.

The measurements are performed using a two component laser Doppler velocimeter (LDV). The LDV technique is used to measure from above the stator the mean radial $V_r^* = V_r/(\Omega r)$ and tangential $V_\theta^* = V_\theta/(\Omega r)$ velocity components and the associated Reynolds stress tensor components $R_{rr}^* = \overline{v_r'^2}/(\Omega r)^2$, $R_{r\theta}^* = \overline{v_r'v_\theta'}/(\Omega r)^2$, $R_{\theta\theta}^* = \overline{v_\theta'^2}/(\Omega r)^2$ in a vertical plane (r, z) . This method is based on the accurate measurement (error margin of $\pm 5\%$ on the second order momentums) of the Doppler shift of laser light scattered by small particles (Optimage PIV Seeding Powder, 30 μm) carried along with the fluid. Its main qualities are its non intrusive nature and its robustness. The measurement is found to be more difficult close to the rotating disk, because of strong reflections of the laser beams and seeding problems. Note that the size of the probe volume in the axial direction (0.8 mm) is not small compared to the interdisk spacing and to the boundary layer thicknesses. It has been experimentally verified [249] that about 5000 validated data are necessary to obtain the statistical convergence of the velocity fluctuations.

8.3 Numerical approaches

Two LES codes described in Chapter 3 have been used in the following to investigate turbulent isothermal rotor-stator disk flows:

1. The first one is based on a pseudospectral method associated with the SVV technique (Section 3.7.1) developed by Séverac and Serre [316]. It will be denoted LES-SVV in the following. The values of the SVV parameters w_T and ϵ_N are given in Table 8.1.
2. The second code, denoted LES-FD in the following, is associated with fourth-order compact schemes for the spatial discretization in the non homogeneous directions and a dynamic Smagorinsky model as subgrid scale model (Section 3.7.2).

Re	$w_T(r, \theta, z)$	ϵ_N	grid	$\Omega \delta t$
10^5	$3N/4, N/2, \sqrt{N}$	$1/(2N), 1/(2N), 1/(2N)$	81, 150, 49	10^{-4}
4×10^5	$0.8\sqrt{N}, \sqrt{N}, \sqrt{N}$	$1/(2N), 1/(2N), 1/(2N)$	121, 181, 65	10^{-4}
10^6	$2\sqrt{N}, 5\sqrt{N}, 4\sqrt{N}$	$1/N, 1/N, 1/N$	151, 241, 81	5×10^{-5}

Table 8.1: Computational parameters for the LES-SVV.

The same computational grid with $121 \times 65 \times 180$ mesh points in the (r, z, θ) directions has been sized for the two methods at $Re = 10^6$. For the LES-SVV, a time step equal to $\delta t = 5 \times 10^{-5} \Omega^{-1}$ has been used to be compared to the one used for the LES-FD $\delta t = 3 \times 10^{-4} \Omega^{-1}$. The calculations have been performed in a half-cavity $[0, \pi]$ in order to save CPU time. An a priori verification of the resolution has been performed by calculating an estimation of the ratio of the resolved to modeled scales, i.e. Δ_{max}/η where Δ_{max} is the maximum cut-off wavelength given by the grid and η the Kolmogorov length scale estimated from the homogeneous isotropic turbulence theory using measurements of the size and velocity of the primary rolls given by the linear stability analysis of Serre et al. [314]. In LES-SVV and LES-FD calculations, the ratio Δ_{max}/η is around 2.5 and 3.3 respectively.

This permits to resolve near-wall structures. The numerical resolution has been checked a posteriori by calculating the friction velocity in both boundary layers and in the core. Both LES-SVV and LES-FD grids correspond to an axial wall-coordinate z^+ around unity slightly varying with r as the total friction velocity increases towards the periphery of the cavity whereas r^+ and θ^+ are around 10 at mid-cavity. The LES-SVV has been used for 2 other values of the Reynolds number and also in the non-isothermal case.

After the time-dependent flow is settled at a statistically steady state, turbulence statistics are averaged both in the homogeneous tangential direction and in time during around 10 global time units (in term of Ω^{-1}). The state is considered statistically steady when the fluctuations of the averaged values in time are less than 1%.

The solution in the isothermal case is used as an initial solution for the non-isothermal calculations using the LES-SVV code. The data in the non-isothermal cases are averaged on 77 disk revolutions, which is sufficient as the averaging for the Nusselt number converges quite rapidly, about 20 dimensionless time units in the similar system of Kunnen *et al.* [162].

8.4 Turbulent isothermal rotor-stator disk flows

8.4.1 Benchmark of two Large Eddy Simulations

The benchmark has been performed at a rotational Reynolds number equal to 10^6 guaranteeing that both boundary layers are turbulent. The results have been published in *Flow, Turbulence & Combustion* (see Ref.[345]). The LES are compared also to the predictions of the RSM model described in Chapter 4 (grid composed of 140×80 mesh points in the radial and axial directions). Both LES-FD and LES-SVV provide the same axisymmetric base flow. It is characterized by a secondary flow in the meridian plane induced by the centrifugal force. As a consequence of the Coriolis force (Taylor-Proudman theorem), the flow is composed of two thin boundary layers along the disks separated by a geostrophic core at zero axial pressure gradient as shown on Figure 8.3 from the velocity profiles. The fluid is pumped centrifugally outwards along the rotor ($V_r^* > 0$) and is deflected in the axial direction after impingement on the external cylinder. After a second impingement on the stator, it flows radially inwards along the stator ($V_r^* < 0$), due to conservation of mass, before turning along the hub and being centrifuged again by the rotating disk. Note that due to a smaller radial velocity, the Bödewadt layer along the stator is almost twice as thick as the Ekman layer on the rotor. By analogy with the single disk problem, the boundary layer close to the rotor is known as the Ekman layer (although Ekman layer solutions are linear, one retains this terminology in the non-linear case), whereas the boundary layer close to the stator is called the Bödewadt layer. The thicknesses of both boundary layers are scaled by the characteristic viscous length $\delta = (\nu/\Omega)^{1/2}$. These two boundary layers are separated by a nearly homogeneous core region, characterized by a quasi zero radial velocity ($V_r^* \simeq 0$) and by a constant tangential velocity $V_\theta^* = K$, where K is called the entrainment coefficient (denoted sometimes β). As the laminar regime [311], there exists on average, a main flow in the tangential direction coupled with a secondary flow in the meridional plane.

The radial confinement by both cylinders makes the solutions inconsistent with self-similarity solutions, although they can be close far from the endwalls. In particular, both boundary layers are not parallel. Thus, comparisons between LES results and available linear stability results can be local only. In consequence, quantitative comparisons between LES-SVV and LES-FD have been made at three radial locations of the cavity $r^* = 0.3, 0.5$ and 0.7 , that correspond to a local Reynolds number $Re_r = (r/\delta)$ varying in the range $90.4 \leq Re_r \leq 10^3$. Figure 8.3 shows the axial profiles of the mean radial V_r^* and tangential V_θ^* velocity components normalized by the rotor velocity at these radial locations. The mean axial velocity component is not shown here because it is nearly zero in this range of radii far from the endwalls. The agreement between experimental measurements and both LES predictions is satisfactory. Nevertheless, LES-SVV provides better overall results than the LES-FD and the RSM. The boundary layer thicknesses are globally well predicted. Both LES methods slightly underestimate thicknesses, especially at large radii for LES-FD. The velocity maxima within the boundary layers are well predicted by both LES over the stator but strongly overestimated over the rotor. The core swirl ratio or entrainment coefficient K is crucial for engineering applications because it is directly linked to the radial pressure gradient in the cavity and consequently to the axial thrusts applied on the rotor [251]. The LES-FD slightly underestimates K , predicting $K = 0.345$ at

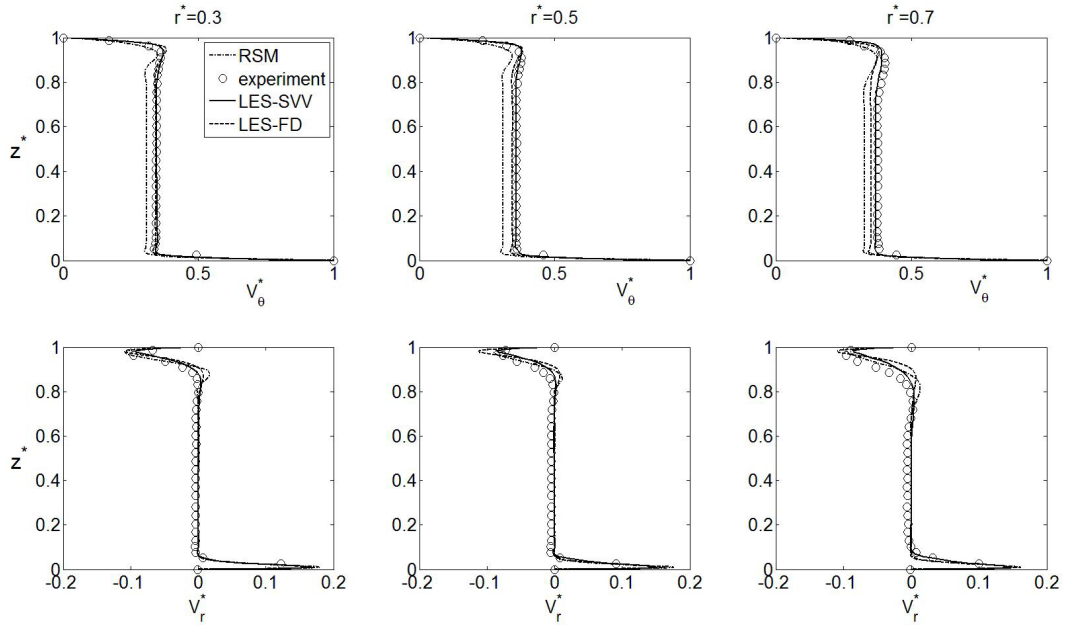


Figure 8.3: Axial profiles of the mean tangential and radial velocity components normalized by the local speed of the disk at three radial locations for $G = 1/7$, $R_m = 1.8$ and $Re = 10^6$. Comparisons between the LES-SVV (full lines), the LES-FD (dashed lines), the velocity measurements (circles) and the RSM model (dash-dotted lines).

$r^* = 0.5$ with respect to $K = 0.36$ given by LES-SVV as well as experimental measurements. This underestimation is more pronounced by the RSM, which predicts $K = 0.315$ close to the value for laminar similarity solutions ($K = 0.313$) [236].

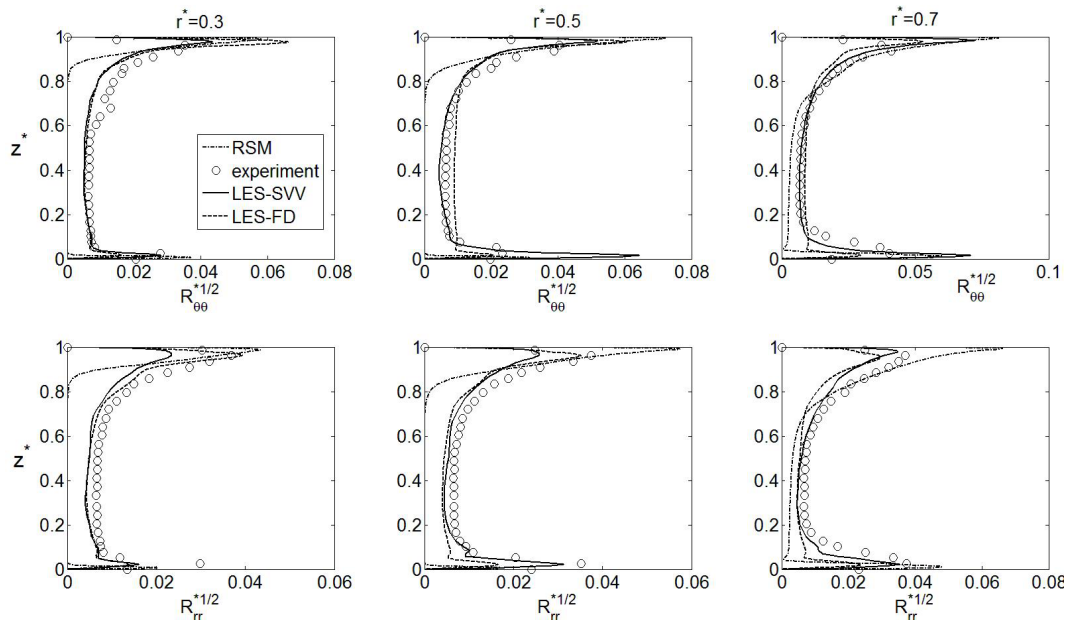


Figure 8.4: Axial profiles of the two main Reynolds stress tensor components R_{rr}^* and $R_{\theta\theta}^*$ at three radial locations for $G = 1/7$, $R_m = 1.8$ and $Re = 10^6$. Comparisons between the LES-SVV (full lines), the LES-FD (dashed lines), the velocity measurements (circles) and the RSM model (dash-dotted lines).

Second-order statistics available from experimental measurements in the radial $R_{rr}^* = \overline{v_r'^2}/(\Omega r)^2$ and tangential directions $R_{\theta\theta}^* = \overline{v_\theta'^2}/(\Omega r)^2$ have been computed in Figure 8.4 at the same radial locations. LES results provide an overall agreement with the experimental data both in boundary layers and in the core with a slightly better estimation of the turbulence intensity by LES-SVV than LES-FD. Surprisingly, RSM seems to strongly overestimate the maxima of the normal components of the Reynolds stress tensor within the stator boundary layer at all locations while it underpredicts the turbulence intensity in the core and completely misses the transition in the rotor layer. The peaks of the normal Reynolds stress tensor components are relatively well predicted by both LES within the stator layer at a wall distance of $0.05h$ and $0.025h$ for the radial and tangential components, respectively. Both LES models overpredict $R_{\theta\theta}$ in both boundary layers, the maximum being reached by the LES-SVV within the rotor layer at mid-radius. That leads to a much stronger anisotropy of the Reynolds stress tensor than in experiments. Such behavior could be related to the anisotropy of the grid computation, which is globally much coarser in the tangential direction, especially at large radii. This hypothesis is supported by the LES of Wu and Squires [357], who observed a strong sensitivity of this component depending on the resolution.

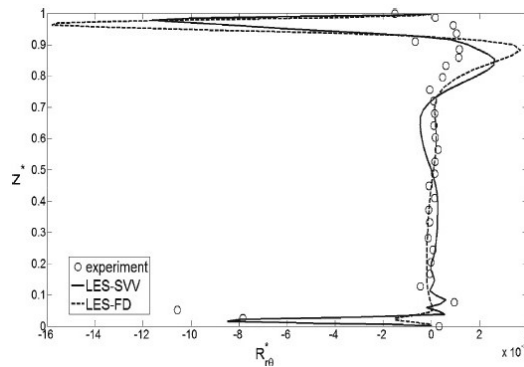


Figure 8.5: Axial profiles of the shear Reynolds stress tensor component $R_{r\theta}^*$ at mid-radius for $G = 1/7$, $R_m = 1.8$ and $Re = 10^6$. Comparisons between the LES-SVV (full lines), the LES-FD (dashed lines) and the velocity measurements (circles).

Figure 8.5 illustrates the $R_{r\theta}^*$ shear stress at mid-radius. The other components are not illustrated because the two other cross components were not available using the LDV technique. Both LES methods show a global agreement in terms of sign and intensity within the stator boundary layer. On the rotor side, however, LES-FD underpredicts its intensity due to a lower turbulence level. As expected from the literature, the shear stress magnitude is much smaller than the normal components (see DNS results in [193]). This is a feature of rotating disk boundary layers that indicates an important structural change in the turbulence compared to the more classical plane boundary layer.

Instantaneous results also show a good agreement between both LES methods that provide almost similar coherent structures. Vortical structures are identified using positive isosurfaces of the Q -criterion. The Q -criterion defines a vortex as a spatial region where the Euclidean norm of the vorticity tensor $\mathbf{\Omega} = \frac{1}{2}[\nabla\mathbf{v} - (\nabla\mathbf{v})^T]$ dominates that of the rate strain $\mathbf{S} = \frac{1}{2}[\nabla\mathbf{v} + (\nabla\mathbf{v})^T]$: $Q = \frac{1}{2}[|\mathbf{\Omega}|^2 - |\mathbf{S}|^2] > 0$. As already observed in the turbulence statistics, the rotating disk layer is only weakly turbulent. This is featured in the flow structure by coherent negative spiral arms (as they roll up in the opposite rotation sense of the disk) at intermediate radii (Fig.8.6a & 8.20e) forming an angle of about -15° with the tangential direction. This feature is characteristic of the viscous linear instability referred to in the literature as Type II and is known to play an important role in the transition process to turbulence (see in [314]). Around the hub, where the flow coming from the stator impinges the rotor, both simulations predict a highly turbulent region with smaller disorganized structures. The LES-SVV gives the transition to turbulence at the right threshold expected from theory and experiments at large radii, that is at a local Reynolds $Re_r = 386$. These spiral arms break into much smaller and more concentric structures similar to the ones observed along the stator. Along the stator, both LES exhibit very thin coherent vortical structures aligned with the tangential direction (Fig.8.6b & 8.20f). This is typical of a turbulent rotating boundary layer since the anisotropy invariant map shows that turbulence tends to the axisymmetric limit in this flow region [315]. The thinner structures predicted

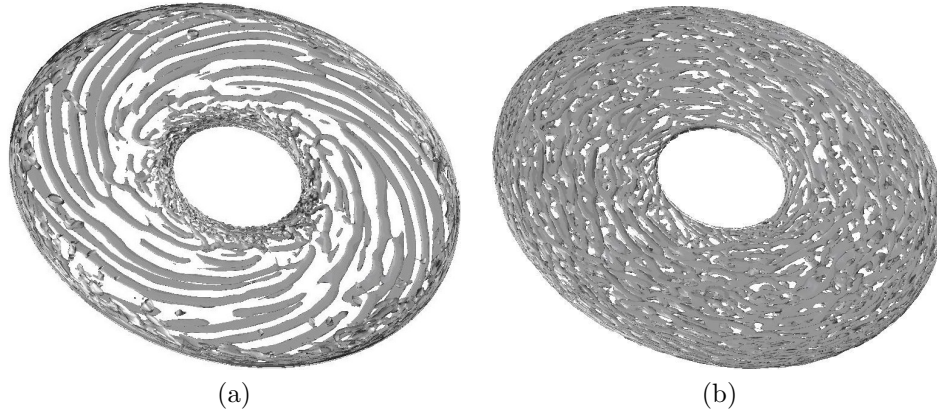


Figure 8.6: Isosurfaces (top view) of the Q-criterion in the (a) rotor boundary layer and in the (b) stator boundary layer for $G = 1/7$, $R_m = 1.8$ and $Re = 10^6$ obtained using the LES-FD. Note that the disk rotates counterclockwise.

by the LES-SVV confirm nevertheless a globally higher level of turbulence.

8.4.2 Influence of the rotational Reynolds number

The better overall agreement has been obtained in the previous section by the LES-SVV approach. It has been used to investigate other flow regimes in the following. The mean and turbulent quantities obtained with the LES-SVV approach are presented in this subsection for three values of the Reynolds number Re in the range $[10^5 - 10^6]$ for the same geometry. All the following results have been published in *Phys. Fluids* (see Ref.[315]).

The axial profiles of the mean radial V_r^* and tangential V_θ^* velocity components at mid-radius ($r^* = 0.5$) are shown for three Reynolds numbers in Figure 8.7. As the axial mean velocity component is everywhere very small compared to the two other components, it will not be discussed here. Whatever the Reynolds number considered in this study, the mean flow (Fig.8.7) still corresponds to the regime IV [67], turbulent with unmerged boundary layers. It is noteworthy that the entrainment coefficient K is consistently below 0.5 midway between the disk, which is the value obtained for the plane Couette flow. Its value at mid-radius $r^* = 0.5$ (Table 8.2) increases with the Reynolds number from 0.35 for $Re = 10^5$ to 0.38 for $Re = 10^6$ in the calculations and from 0.35 to 0.41 in the experiments. These values can be compared to the value $K \simeq 0.35$ measured by Cheah *et al.* [49] for Re_r up to 2.6×10^5 and to the one $K = 0.4$ obtained by Andersson and Lygren [11] at $Re = 6.4 \times 10^5$ ($G = 0.1$). Nevertheless, they remain substantially smaller than the semi-empirical value $K = 0.43$ of Poncet *et al.* [251] for highly turbulent enclosed rotor-stator flows at $Re \geq 10^6$.

Reynolds number	K	δ_E/h	δ_B/h	δ/h
10^5	0.35	0.104	0.222	0.022
4×10^5	0.36	0.071	0.147	0.011
10^6	0.38	0.055	0.084	0.007

Table 8.2: Influence of the Reynolds number on the entrainment coefficient K and on the thicknesses of the boundary layers for $r^* = 0.5$. Results obtained by the LES-SVV for $G = 1/7$ and $R_m = 1.8$.

By comparing the V_r -profiles (Fig.8.7), the thickness of the Ekman boundary layer δ_E , which is known to behave as $\sqrt{\nu/\Omega}$, decreases with Re by about a factor two between $Re = 10^5$ and $Re = 10^6$ (Table 8.2). This is characteristic of a rotating boundary layer, which becomes turbulent. By conservation of mass, as there is no radial flow in the core, the Bödewadt boundary layer thickness δ_B behaves like the Ekman one. All the main results are summed up in Table 8.2. The Bödewadt layer is almost two times thicker than the Ekman layer, which is itself about 10 times thicker than the thickness of the boundary layer over a free rotating disk $\delta/h = \sqrt{\nu/\Omega h^2}$.

It is encouraging to observe from Figure 8.7 that the agreement between the numerical results and

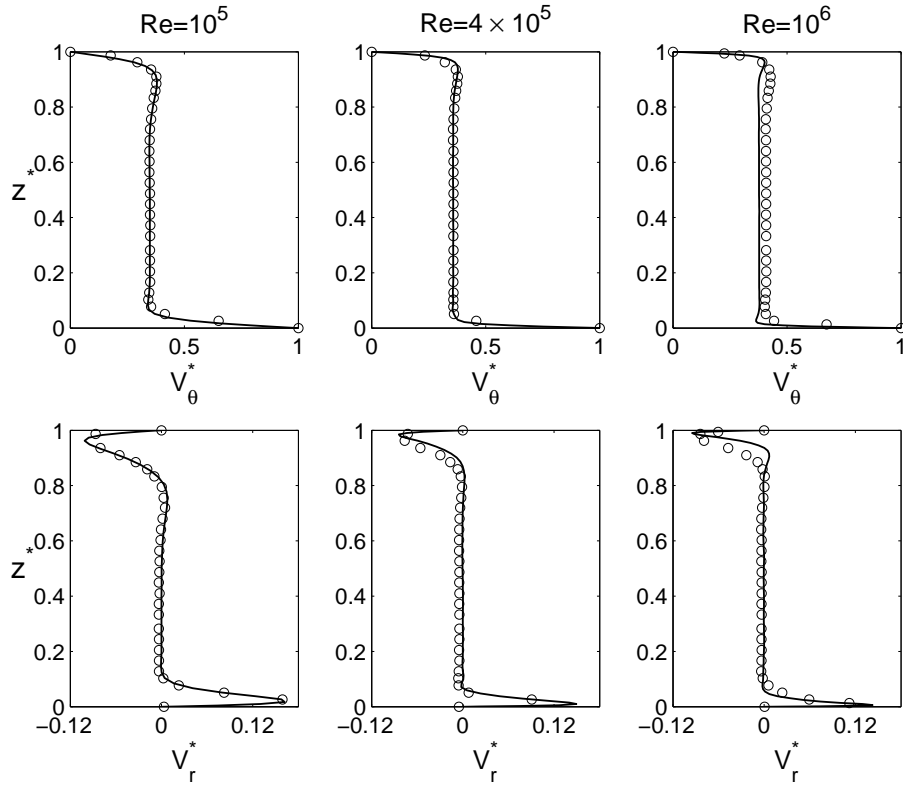


Figure 8.7: Axial profiles of the mean radial V_r^* and tangential V_θ^* velocity components at $r^* = 0.5$ for $G = 1/7$, $R_m = 1.8$ and three Reynolds numbers. Comparison between (—) the LES-SVV results and (o) the LDV data.

the velocity measurements is very satisfactory for the mean field. Both boundary layers along the rotor and the stator are well described by the LES, which captures the main features of rotor-stator flows. The largest differences with the LDV measurements are observed for $Re = 10^6$. The calculations underestimate the measures of the K coefficient of about 7%, as previously observed by Andersson and Lygren [11] in a “wide-gap” cavity. The radial velocity component maximum on the rotor side is overestimated of about 14% at mid-radius. It appears from these remarks that LES calculations at $Re = 10^6$ are certainly too dissipative at this location. A better agreement has been obtained at other radial locations as will be shown in the next Section. Some discrepancies on the velocity maxima can be also attributed to the size (in the axial direction) of the LDV probe volume, which becomes not negligible compared to the boundary layer thicknesses when the Reynolds number increases. This leads indeed to averaged values in space only.

Additional characteristics of the mean flow are provided by polar plots of the tangential and radial velocity components in the whole gap between the disks at $r^* = 0.5$ (Figure 8.8). Whatever the Reynolds number considered, the polar profile is located between the similarity solution of Von Kármán [348] and the DNS calculations of Lygren and Andersson [193] performed at $Re = 4 \times 10^5$. By increasing the Reynolds number, the LES polar plot goes away from the laminar solution. Whatever the value of Re , the polar plot corresponding to the stator boundary layer ($V_r < 0$) largely differs from the laminar flow, that confirms the turbulence feature of this boundary layer. Let’s notice that at $Re = 4 \times 10^5$ the LES profile almost matches the DNS profile. On the contrary, on the rotor side ($V_r > 0$), the polar plot is globally closer to the Von Kármán profile even if it goes away when Re increases. Such behavior suggests a transition to a turbulent regime from about $Re = 4 \times 10^5$ that corresponds to a local Reynolds number at mid-radius of about $Re_r^{1/2} = 407$. This is in agreement with the experimental and theoretical results of Lingwood [184]. The large difference observed with the profile of Lygren and Andersson [193] is then surprising and cannot be only explained by finite cavity effects.

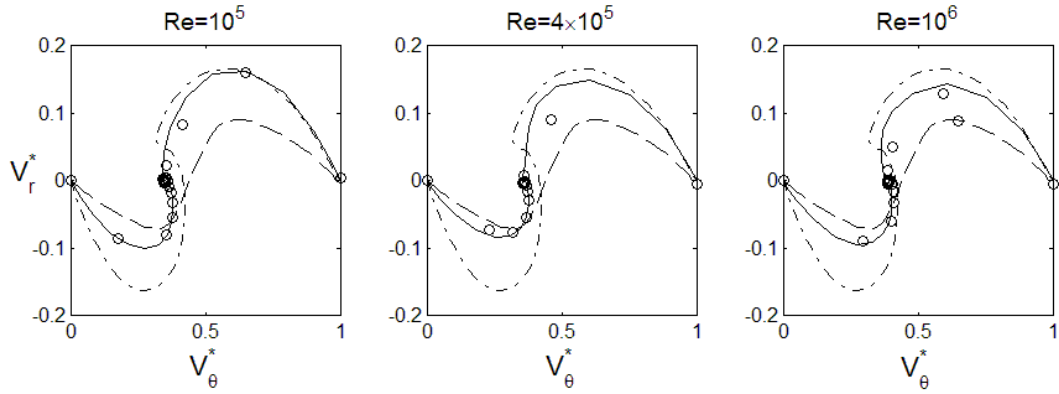


Figure 8.8: Polar plots of the velocity distribution in the whole gap between the disks at $r^* = 0.5$ for $G = 1/7$, $R_m = 1.8$ and three Reynolds numbers. Comparison between (—) the LES-SVV results, (o) the LDV data, (---) the laminar Von Kármán solution [348] and (- - -) the DNS results of Lygren and Andersson [193].

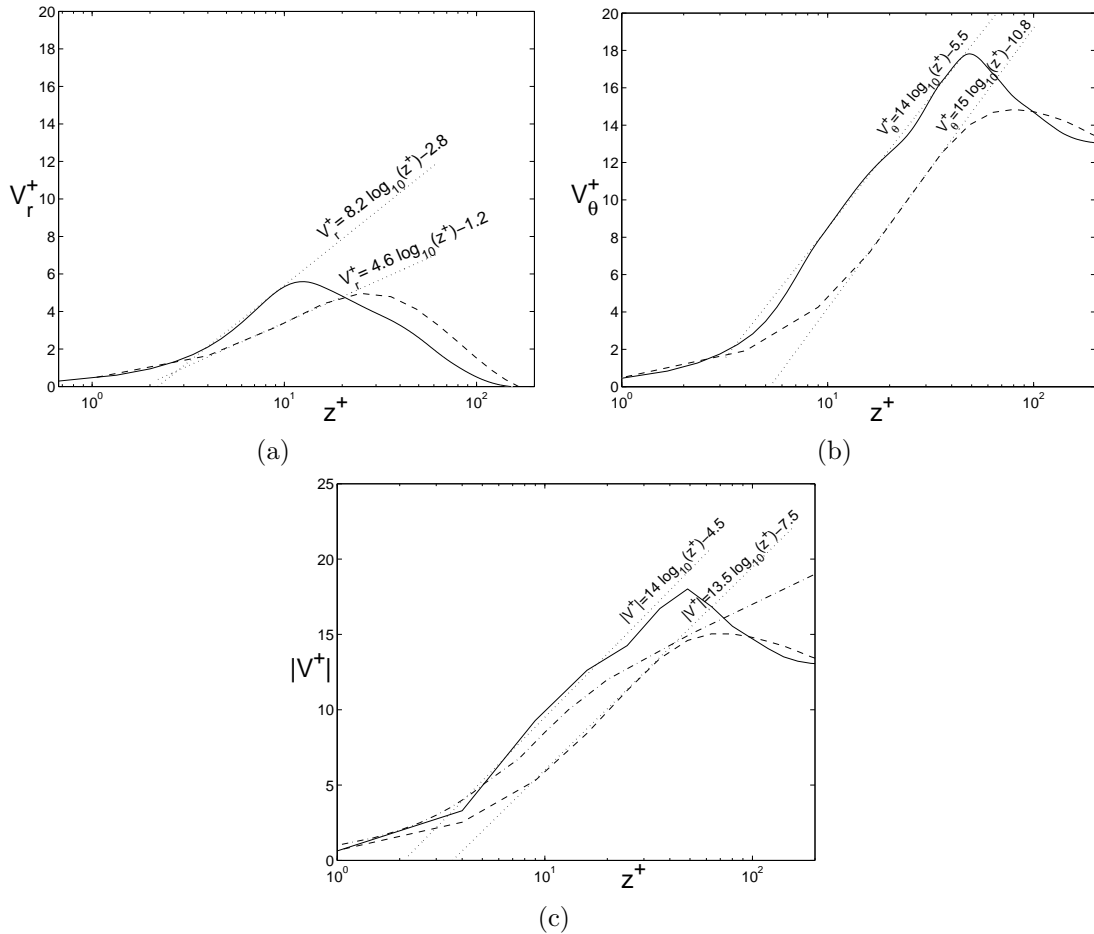


Figure 8.9: Mean (a) radial V_r^+ and (b) tangential V_θ^+ velocity components in wall units near the rotor (solid lines) and the stator (dashed lines) normalized by the tangential friction velocity for $Re = 10^6$ at $r^* = 0.5$. (c) Magnitude of the corresponding velocity vector $|V^+|$ near the rotor (solid lines) and the stator (dashed lines) compared to the turbulent boundary layer over a flat plate (dash-dotted lines) by Rotta [280]. Results obtained by the LES-SVV for $G = 1/7$ and $R_m = 1.8$.

Figures 8.9a to 8.9c show respectively the axial variations of V_r^+ , V_θ^+ and $|V^+| = (V_r^{+2} + V_\theta^{+2})^{1/2}$ in wall coordinate z^+ (z^+ is the relative distance to the nearest disk) for $Re = 10^6$ and $r^* = 0.5$. These are respectively the two streamwise mean velocity components relative to the disk speed and the magnitude of the corresponding velocity vector. One has numerically verified that the axial velocity component V_z^+ is fairly close to zero along the disks. The velocities have been normalized by the tangential friction velocity $v_{\tau_\theta} = (\nu \partial V_\theta / \partial z)^{1/2}$ to enable direct comparisons with the work of Lygren and Andersson [193]. The magnitude of the velocity vector (Fig.8.9c) follows rather closely the law of the wall as obtained by Lygren and Andersson [193] in an open rotor-stator cavity. The profiles along both disks are compared to the profile of a turbulent boundary layer on a flat plate obtained by Rotta [280]. The linear region $|V^+| = z^+$ of the velocity profile, called the viscous sublayer, expands to $z^+ = 10$ near the rotor, whereas it is more reduced along the stator (about to $z^+ = 5$). Lygren and Andersson [193] obtained a linear profile up to $z^+ \simeq 7$ on both disks. Further from the walls, the “log-region” $V^+ = a + b \times \log_{10}(z^+)$ is recovered with two coefficients a and b , which differ from the values ($a = 5$, $b = 5.62$) obtained by Lygren and Andersson [193] along the rotor. Note that for Couette-Poiseuille turbulent flows, the law of the wall is very close to: $V^+ = 1.0857 \log_{10}(z^+) + 5.5$ as shown by Nakabayshi *et al.* [215]. The fundamental study of Bradshaw [37] has revealed that rotation substantially affects turbulence by introducing an extra linear term, depending on the Monin-Obukhov coefficient, in the logarithmic law of the wall. By comparison with the turbulent boundary layer on a flat plate [280], Figure 8.9c clearly shows that no buffer region, which is usually the region enclosed between the sublayer and the log-region, is obtained in the present case because of rotation. Another effect of rotation is the reduction of the log-region extent. To enable direct comparisons with the results of Lygren and Andersson [193] in their open cavity, the profiles of V_r^+ and V_θ^+ are also presented in Figures 8.9a and 8.9b respectively. The same remarks arise from the variations of V_θ^+ compared to the ones of $|V^+|$. By considering the profiles of V_r^+ (Fig.8.9a), the locations of the maximum crossflow are in close agreement with the values obtained by Lygren and Andersson [193] at $Re = 4 \times 10^5$ although as expected, the location of the peaks here is further out from the wall as the Reynolds number is larger. Near the rotor, the maximum crossflow is reached at $z^+ = 16$ ($z^+ = 15$ in [193]) while near the stator the maximum is located further from the disk at $z^+ = 25$ ($z^+ = 22$ in [193]). Thus, for this radial location $r^* = 0.5$, the location of the peak in the crossflow is not modified by finite cavity effects.

All six Reynolds stress tensor components have been calculated. The axial distributions of the two main normal components are shown together with available experimental measurements at mid-radius on Figure 8.10. The normal component R_{zz}^* as well as the three shear components being found more than one order smaller than the previous ones are presented all together in Figure 8.11 at $Re = 10^6$ only.

For the three considered Reynolds numbers, turbulence is mainly concentrated in the boundary layers. Apart from the R_{zz}^* component, the other five components reach indeed their maxima in the boundary layers and decrease to a value one order below ($6 \times 10^{-3} \Omega r$) in the core (Fig.8.11). On the contrary, in their open cavity, Lygren and Andersson [193] reported that, except from the tangential components of the Reynolds stress tensor, the other components reach a maximum at the edge of the boundary layers. On Figure 8.10, the turbulence statistics confirm that whatever the Reynolds number the Bödewadt layer is turbulent at mid-radius while the Ekman layer gets turbulent at about $Re = 4 \times 10^5$ but with a turbulence intensity larger than on the stator. The turbulence intensities (scaled on the local speed of the rotor) remain almost constant in the turbulent boundary layers when increasing the Reynolds number. That means that the turbulence intensity is intrinsic to the geometrical characteristics of the cavity and not to the energy injected into the system. Whatever the Reynolds number, LES results and experimental measurements fit quite well even in the core region, where the turbulence intensity is weak. Let’s notice that it is generally not the case with RANS modeling for which the predictions in this low-Reynolds number flow region far from the disks are not satisfactory [253]. The locations of the peaks near the walls are also well predicted by the LES. When increasing the Reynolds number, these maxima go closer to the disks. At $Re = 10^6$, the tangential and radial turbulence intensities have maxima at the same location $z^* = 0.9904$ near the stationary disk and at different locations near the rotating disk: $z^* = 0.0138$ for the R_{rr}^* component and $z^* = 0.0096$ for the $R_{\theta\theta}^*$ component.

The maximum error occurs in the prediction of the peak values. The singular behavior observed at $Re = 10^5$ on the rotor side can be explained by the inherent difficulties of the LDV system previously mentioned. At $Re = 10^6$, the turbulence intensities are rather the same in both boundary layers

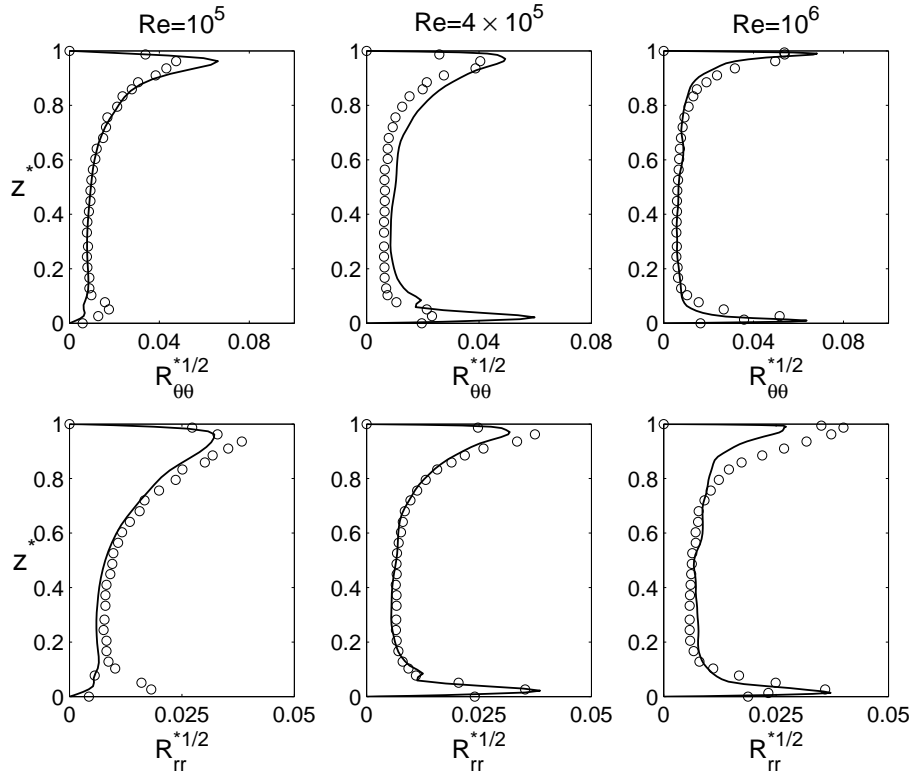


Figure 8.10: Axial profiles of the radial R_{rr}^* and tangential $R_{\theta\theta}^*$ Reynolds stress tensor components at $r^* = 0.5$ for $G = 1/7$, $R_m = 1.8$ and three Reynolds numbers. Comparison between (—) the LES-SVV results and (○) the LDV data.

by considering the experimental data, whereas the LES leads to a regime where the Ekman layer is slightly more turbulent than the Bödewadt layer by looking at the R_{rr}^* -profile. This feature has been formerly reported by Lygren and Andersson [193] when they compared their DNS results with the experiments of Itoh [135]. They attributed this discrepancy to the increased mixing between the boundary layers due to the presence of the shroud in the experiments of Itoh [135]. The present results show that the presence of the shroud cannot explain this discrepancy, as LES and experiments used the same cavity model.

The general trend is that LES results overestimate the turbulence intensity in the tangential direction $R_{\theta\theta}^*$ while they underestimate it in the crossflow direction R_{rr}^* , particularly in the stator boundary layer. On Figure 8.10 and at $Re = 10^6$, the numerical results predict a $R_{\theta\theta}^*$ component almost twice larger than the R_{rr}^* component, whereas the experimental measurements give components of about the same order. That suggests that the turbulence anisotropy is stronger in LES than in experiments. There is no clear reason that explains such behavior if not the anisotropy of the grid computation, which is globally coarser in the radial direction than in two other ones. This reason was previously advocated by Scotti *et al.* [308] to explain some discrepancies between LES and experiments in wall-bounded flows. The grid is indeed non homogeneous and tighter close to the walls. For example, at mid-radius, the grid spacing is $0.052h$, $0.033h$ and $0.019h$ in the radial, tangential and axial directions respectively. This phenomenon could certainly be reduced with grid refinement in the radial and tangential directions. As a consequence, the predicted Reynolds stress tensor is more anisotropic than the measured one.

If one considers the shear components of the Reynolds stress tensor at $Re = 10^6$ (Fig.8.11), one can clearly see that the peaks of $R_{r\theta}^*$ are the largest in both boundary layers compared to the two other shear components. It is a major difference with two-dimensional boundary layer flows where this component is usually neglected. One major difference between the idealized flow considered by Lygren and Andersson [193] and the present study is that the R_{rz}^* and $R_{\theta z}^*$ components are negligible in the present LES, whereas these authors obtained magnitudes of these two components quite comparable

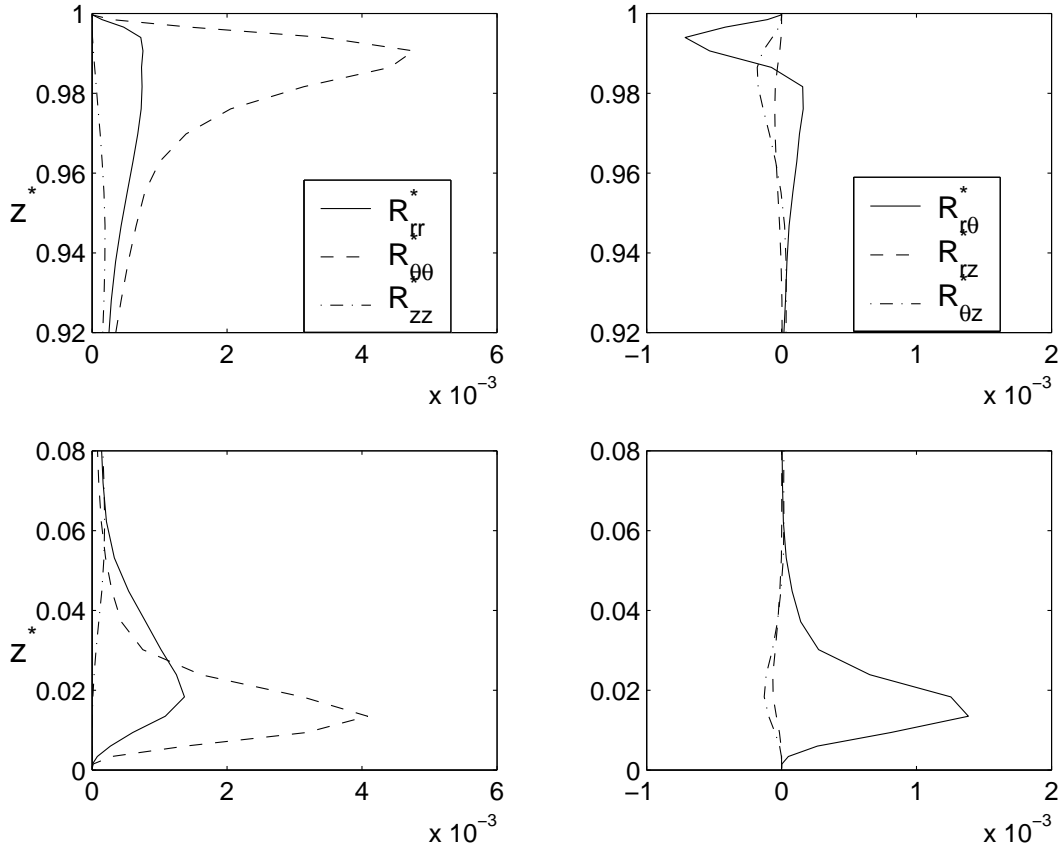


Figure 8.11: Axial variations of the Reynolds stress tensor components in the stator (top graphs) and rotor (bottom graphs) boundary layers for $r^* = 0.5$, $G = 1/7$, $R_m = 1.8$ and $Re = 10^6$ using the LES-SVV.

to the $R_{r\theta}^*$ component. Moreover, the $R_{r\theta}^*$ shear component is negative on both disks in the open cavity of [193], whereas the shear is found here to be positive on the rotor with a magnitude higher than on the stator side.

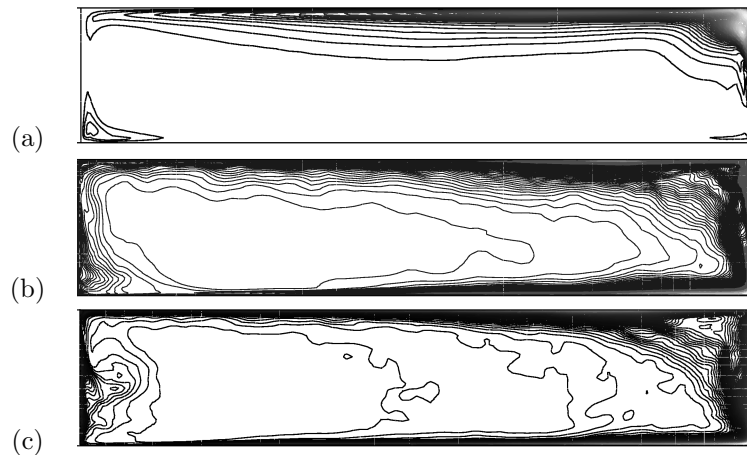


Figure 8.12: Isolines of the turbulence kinetic energy $k^* = k/(\Omega b)^2$ at: (a) $Re = 10^5$, $k^* \leq 4.6 \times 10^{-3}$, (b) $Re = 4 \times 10^5$, $k^* \leq 7 \times 10^{-3}$, (c) $Re = 10^6$, $k^* \leq 6 \times 10^{-3}$. Results obtained by the LES-SVV for $G = 1/7$ and $R_m = 1.8$.

In order to show the turbulent flow regions in the meridional plane, the isolines of the turbulence

kinetic energy $k^* = k/(\Omega b)^2$ are presented in Figure 8.12 at three Reynolds numbers. The maximum value of the turbulence kinetic energy evolves from $k_{max}^* = 4.7 \times 10^{-3}$ to $k_{max}^* = 9 \times 10^{-3}$ for increasing values of the Reynolds number, and its location moves from the stator boundary layer to the edge of the rotor layer. At $Re = 10^5$, turbulence is mainly confined in the boundary layers along the stator and the shroud. A small turbulent region is also observed at the impingement on the rotor of the flow coming from the stator and accelerated along the rotating hub. The maximum of k^* is obtained at the junction between the stator and the shroud where the flow coming from the rotor impinges the stator. By increasing the Reynolds number up to $Re = 4 \times 10^5$, the Ekman layer gets turbulent from about mid-radius to $r^* = 1$ corresponding to the largest values of the local Reynolds number. The maximum of k^* has moved to the bottom of the shroud and the hub is also turbulent. At $Re = 10^6$, the map is relatively similar to the previous one at $Re = 4 \times 10^5$. The maximum is nevertheless two times larger and has slightly moved on the left hand side along the rotor boundary layer.

8.4.3 Finite cavity effects

Due to the presence of the inner and outer cylinders at $r^* = 0$ and $r^* = 1$ respectively, the flow is radially confined. Then, finite cavity effects on the mean field and turbulence statistics have been explored at $Re = 10^6$ using the LES-SVV.

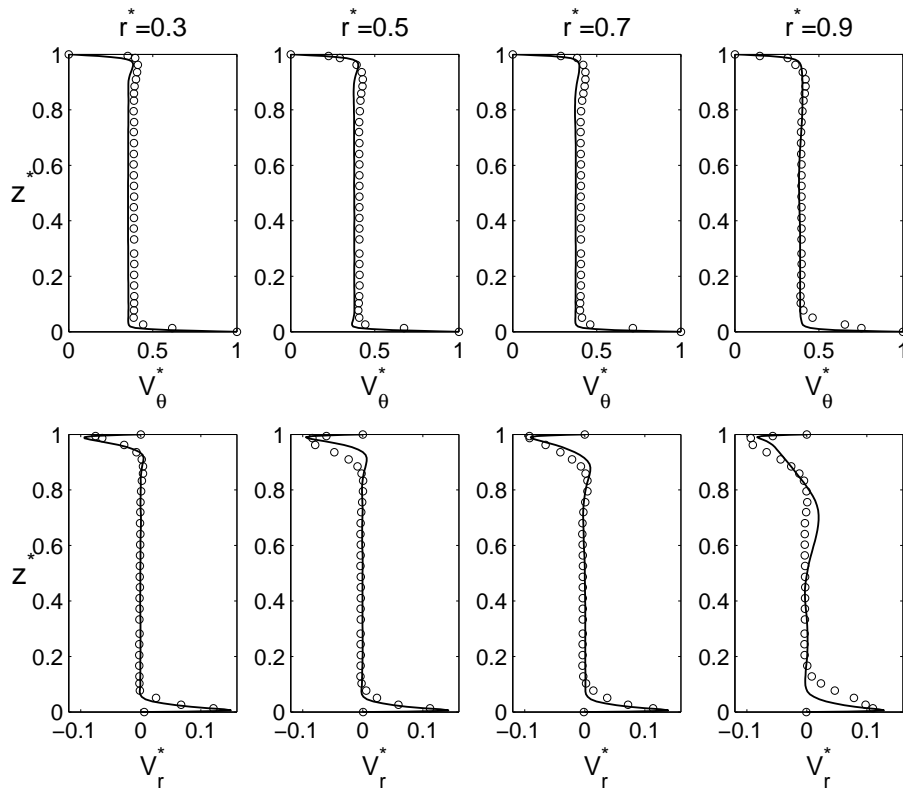


Figure 8.13: Axial profiles of the mean radial V_r^* and tangential V_θ^* velocity components for $G = 1/7$, $R_m = 1.8$ and $Re = 10^6$ at four radial locations. Comparison between (-) the LES-SVV results and (o) the LDV data.

Axial profiles of the mean radial V_r^* and tangential V_θ^* velocity components at four radial locations are shown on Figure 8.13. The same agreement observed at mid-radius (Fig.8.7) between the experimental measurements and the LES results is observed for the three other radial locations. In a flow region of radial extension $0.3 \leq r^* \leq 0.7$, a self-similar behavior is observed and the boundary layers remain separated. Close to the outer shroud ($r^* = 0.9$), the Bödewadt layer thickens and the flow in the core is clearly influenced by the boundary conditions. This effect on the core region is besides larger on the LES results than on the experimental data. According to the mass flow conservation, the

entrainment coefficient K increases with the radius from 0.35 at $r^* = 0.3$ to 0.38 at $r^* = 0.9$ whereas the maxima of $|V_r^*|$ decrease in both layers.

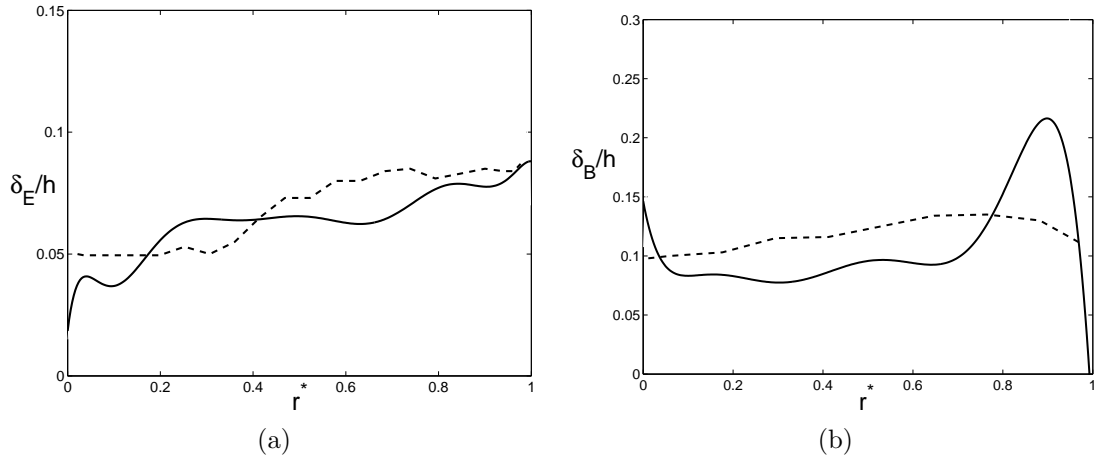


Figure 8.14: Radial distributions of the boundary layer thicknesses: (a) Ekman boundary layer thickness δ_E/h , (b) Bödewadt boundary layer thickness δ_B/h . Comparisons between (—) the present LES-SVV ($Re = 10^6$, $G = 1/7$, $R_m = 1.8$) and (---) the predictions of the Reynolds Stress Model of Poncet [249] ($Re = 1.04 \times 10^6$, $G = 0.036$, $R_m = 1.36$).

As the consequence, the flow along the disks is no longer parallel contrary to the flows in infinite cavities [193]. The radial evolutions of the thicknesses of both boundary layers are shown on Figure 8.14, together with the predictions of the RSM of Poncet [249] for the same Reynolds number $Re \simeq 10^6$ but in a cavity of aspect ratio about five times larger ($G = 0.036$, $R_m = 1.36$). Except in the endwall regions, both numerical results give qualitatively a good agreement. On the rotor side, the boundary layer thickness increases with the radius whereas on the stator side the flow remains almost parallel outside the endwall regions ($0.1 \leq r^* \leq 0.7$). In that zone, the averaged value of δ_B/h is 1.5 larger than the averaged value of the Ekman layer thickness: $\delta_B/h \simeq 1.5\delta_E/h = 0.061$. This result is close to the one obtained by Daily and Nece [67] for turbulent flows with separated boundary layers: $\delta_B \simeq 1.7\delta_E$. Let's notice that this behavior seems different of the one observed in the laminar regime. Indeed, Gauthier *et al.* [105] reported a decreasing of δ_B for increasing radial locations, as $\delta_B = \delta(6.9 - 5.3r^*)$, and an almost constant Ekman layer thickness $\delta_E = 2.2\delta$ far from the endwalls. The discrepancies between the LES and the RSM close to the cylinders is firstly attributed to the much larger value of G considered by Poncet [249] that considerably diminishes the effects of the endwall layers. The difficulty of the RSM to take into account large recirculation zones as well as the two-dimensional hypothesis can be also evoked.

In the shroud boundary-layer, an intense shear is produced by the differential rotation between the core region in solid body rotation ($K \simeq 0.4$) and the outer stationary cylinder. By analogy with the classical Taylor-Couette problem between differentially rotating cylinders or spheres, this internal shear layer is called the Stewartson layer [331]. The present cavity can be indeed considered as a rotor-stator Taylor-Couette system of very low aspect ratio with the flow confined between an inner rotating cylinder and an outer stationary cylinder. For $Re = 10^6$, the LES-SVV results can be scaled by a linear fit $\delta_s/b = 17 \times z^* - 0.076$ showing that the Stewartson layer is non homogeneous in the axial direction contrary to the classical Taylor-Couette problem. After the impingement of the outward radial flow along the rotor, the axial flow slows down along the shroud and as a consequence δ_s increases. At the edge of the rotor, the Ekman layer turns into the axial flow of the Stewartson layer in a region of which both the radial and axial dimensions are $O(Re^{-1/2})$ [342]. In the present case, the connection between the two boundary layers occurs when both dimensions are $1.62 \times Re^{-1/2}$, which corresponds to $\delta_s/b = 0.0115$ and to $\delta_E/h = 0.081$ (Fig.8.14). Along the stator, the thickening of the Stewartson layer is also closely linked to the thickening of the Bödewadt layer at the periphery of the cavity.

Finite cavity effects also influence the turbulence statistics as shown on Figure 8.15. Whatever the radial location, turbulence remains mainly confined in the boundary layers, whereas the inviscid core

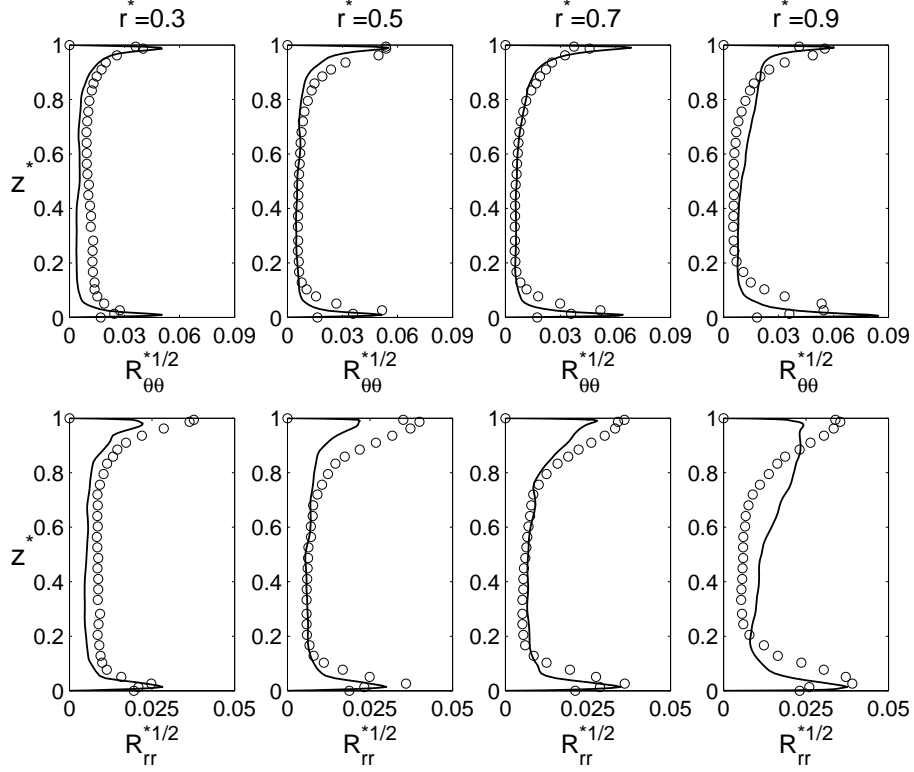


Figure 8.15: Axial profiles of the radial R_{rr}^* and tangential $R_{\theta\theta}^*$ Reynolds stress tensor components for $G = 1/7$, $R_m = 1.8$ and $Re = 10^6$ at four radial locations. Comparison between (—) the LES-SVV results and (o) the LDV data.

remains laminar. The turbulence intensities slightly increase towards the periphery of the cavity as expected by the increase of the local Reynolds number. At $r^* = 0.3$ ($Re_r = 2 \times 10^5$), the boundary layers are already turbulent with comparable turbulence intensities. At the periphery of the cavity $r^* = 0.9$ ($Re_r = 8.62 \times 10^5$), the Ekman layer becomes more turbulent than the Bödewadt layer. Note that, whatever the radial location, the $R_{\theta\theta}^*$ component remains almost twice larger than the R_{rr}^* component along the disks. The agreement between the LES and the velocity measurements remains still satisfactory over the radius. Nevertheless, as already observed when varying the Reynolds number, the general trend of the LES is to underestimate the turbulence level in the crossflow direction and to overestimate it in the tangential direction in the whole cavity.

To investigate the effects on the flow structures arising from the three-dimensionality of the mean flow, anisotropy invariant maps are shown at four different radial locations and $Re = 10^6$ (Fig.8.16). The second A_2 and third A_3 invariants of the anisotropy tensor a_{ij} of the second moments of the fluctuations are defined as $A_2 = a_{ij}a_{ji}$ and $A_3 = a_{ij}a_{jk}a_{ki}$, where $a_{ij} = R_{ij}/k - \frac{2}{3}\delta_{ij}$ [192] and δ_{ij} the Kronecker symbol. Thus, the anisotropy invariant maps do not provide spatial informations on the flow structures but crucial informations on the structure properties and especially on their velocity fluctuations. Let's notice that, whatever the radial location, the LES results respect the realizability diagram of Lumley [192] as they remain within the region delimited by the three solid lines. Very close to the disks, turbulence tends to follow the two-component behavior ($A_3 = A_2 - 8/9$) as the wall normal fluctuations are damped more effectively than fluctuations parallel to the disks. Whatever the radial location, turbulence is fairly close to the isotropic case ($A_2 = A_3 = 0$) in the core region. The domination of the $R_{\theta\theta}^*$ component (Fig.8.11) as well as the positive sign of the third invariant A_3 of the anisotropy tensor in the Bödewadt layer suggest a “cigar-shaped” structuring of turbulence in the tangential direction. This kind of structuring is well known in dominantly rotating turbulence [43]. At the edge of the Ekman layer ($z^* \simeq 0.05$), for $0.3 \leq r^* \leq 0.7$, the third invariant gets negative and close to the two-dimensional isotropic turbulence limit ($-2/9, 2/3$). In that region, the levels of the two normal components $R_{\theta\theta}^*$ and R_{rr}^* are quite comparable as it can be seen on Figure 8.11. This

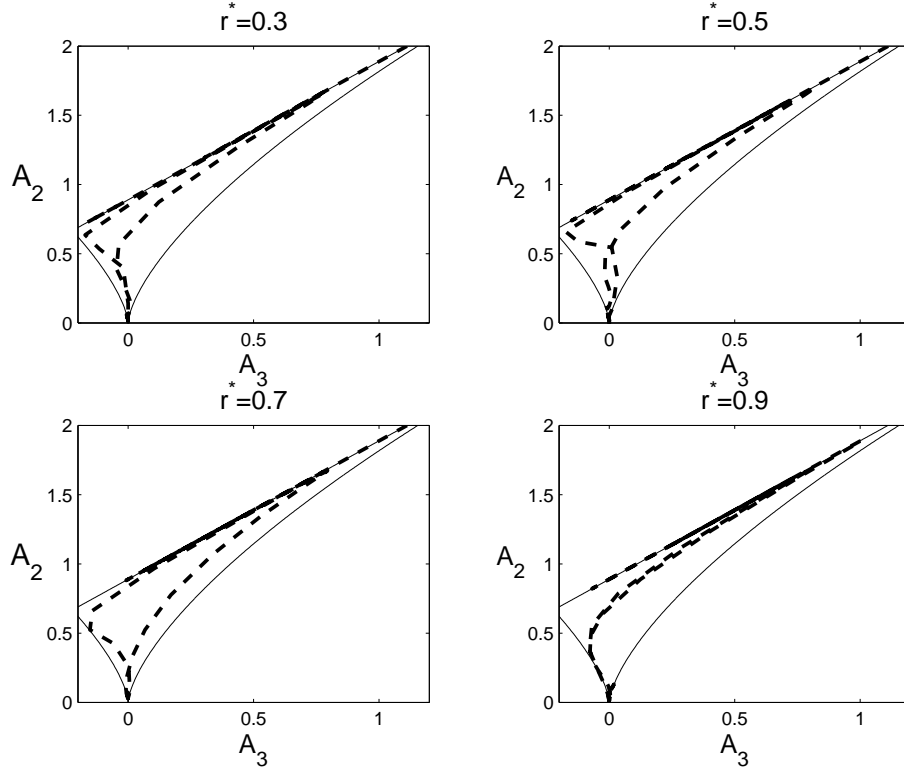


Figure 8.16: Anisotropy invariant map for $G = 1/7$, $R_m = 1.8$ and $Re = 10^6$ at four radial locations. Dashed lines: LES-SVV, solid lines: realizability diagram of Lumley [192].

is an indicator of “pancake” structuring contained in planes perpendicular to the rotation axis. One interesting feature is that closer to the shroud ($r^* = 0.9$) where high turbulence level prevails, these vortex disappear, which is certainly due to the confinement.

8.4.4 Three-dimensional boundary layers

The flow between rotating disks is one of the simplest case where the boundary layers are three-dimensional from their inception. In a classical way, a three-dimensional turbulent boundary layer (3DTBL) is a boundary layer where:

- the direction of the mean velocity vector is non-constant with respect to the distance from the wall,
- the direction of the Reynolds shear stress vector in planes parallel with the wall is not aligned with the mean velocity gradient vector,
- the value of the Townsend structural parameter $a_1 = \tau/2k$, defined as the ratio of the shear stress vector magnitude $\tau = (\overline{v'_\theta v'_z}^2 + \overline{v'_r v'_z}^2)^{1/2}$ to twice the turbulence kinetic energy k is lower than the typical limit for two-dimensional turbulent boundary layers (2DTBL): $a_1 = 0.15$.

The 3DTBL behaviors of the rotor and stator boundary layers are here investigated at $Re = 10^6$. Figure 8.17 shows the axial variations of the mean velocity angle $\gamma_m = \arctan(V_r/V_\theta)$ in the two boundary layers at $r^* = 0.3$. On the rotor side, the angle increases from 0 at the rotating disk to 16.5° at $z^+ = 25$, then slightly decreases to about -0.5° outside the Ekman layer. On the stator side, the angle monotonically decreases from 0 to -34° . Let’s notice that the same behaviors have been obtained for $0.3 \leq r^* \leq 0.9$.

The misalignment between the direction of the Reynolds shear stress vector in planes parallel with the wall and the mean velocity gradient vector is observed in the present LES on both disks. In Figure 8.17, the axial variations of two characteristic angles, the mean gradient velocity angle

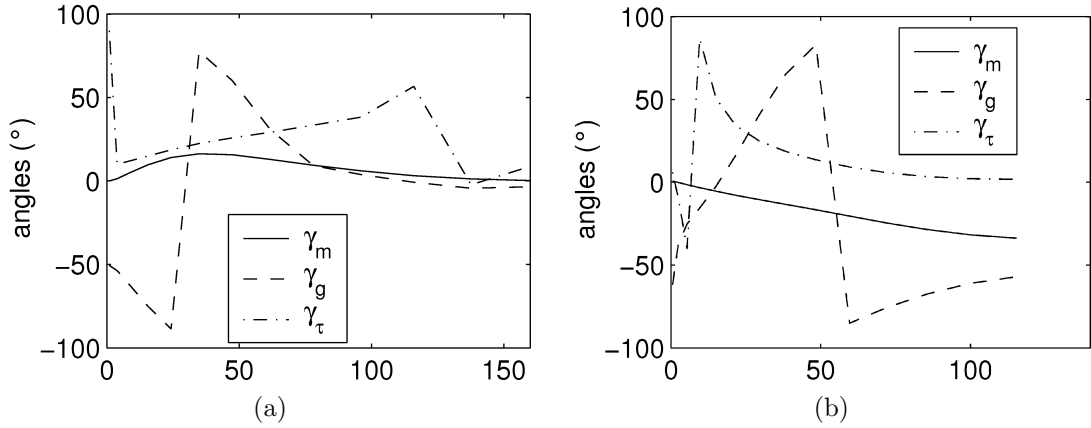


Figure 8.17: Axial evolutions of the mean velocity angle γ_m , the mean gradient angle γ_g and the shear stress angle γ_τ for $G = 1/7$, $R_m = 1.8$ and $Re = 10^6$ at $r^* = 0.3$ (LES-SVV): (a) along the rotor side, (b) along the stator side.

$\gamma_g = \arctan\left(\frac{\partial V_r/\partial z}{\partial V_\theta/\partial z}\right)$ and the turbulent shear stress angle $\gamma_\tau = \arctan(\overline{v'_r v'_z}/\overline{v'_\theta v'_z})$ are shown. The lag between γ_τ and γ_g is large towards the boundary layers γ with a maximum value equal to 94° on the rotor at $r^* = 0.3$ to be compared with the value 18° reported by Lygren and Andersson [193] in an infinite disk system. Note that this lag increases up to 151° at $r^* = 0.9$ (not presented here). In their numerical study of non-stationary 3DTBL, Coleman *et al.* [56] obtained large values of the lag especially near the wall and inferred it from the slow growth of the spanwise component of the shear stress. These authors observed also the change of the sign of the gradient angle γ_g . Such large values of this lag make the assumption of eddy-viscosity isotropy to fail for the prediction of such flows.

Compared to a 2DTBL as the one found in a Couette flow, one characteristic of a 3DTBL is the relative reduction of the magnitude of the shear-stress vector in planes parallel with the disks with the turbulence kinetic energy k . This measure is done using the Townsend structural parameter $a_1 = \tau/2k$. Typically $a_1 = 0.15$ for a wide range of 2DTBLs. The variations of a_1 have been reported in Figure 8.18 at four radial locations in both the Ekman and Bödewadt layers, whose thicknesses depend on the local radius. Whatever the considered locations, the maximum and minimum peak values of a_1 are 0.062 and 0.038, respectively. They are reached on the stator side and are significantly lower than the limiting value 0.15 for a 2DTBL. This behavior is similar to this reported by Itoh *et al.* [137] and Littell and Eaton [185] from their measurements and suggests the three-dimensional turbulent nature of the flow along the rotor and stator walls. This reduction of a_1 indicates also that the shear stress in this type of flow is less efficient in extracting turbulence energy from the mean field. Note that $a_1 > 0.15$ is obtained only very locally on the inner and outer cylinders. These values are much smaller than those found by Andersson and Lygren [11] in the open cavity, suggesting that finite cavity effects increase the three-dimensionality of the mean flow.

As a conclusion, the very large lag between γ_τ and γ_g as well as the strong reduction of the a_1 parameter under the 2DTBL limit indicates a strong three-dimensionality of both disk boundary layers compared to the idealized configuration of Lygren and Andersson [11, 193]. In their open cavity [11], the degree of three-dimensionality is gradually reduced with the distance from the axis of rotation, which has not been obtained in the present LES. It may be attributed to both a lower value of the Reynolds number and most of all to confinement effects in the present calculation.

8.4.5 Flow structures

The flow structures in the boundary layers evolve from spiral arms to annuli when one increases the rotation rate of the disk. The transition to turbulence for separated boundary layer flows has been widely addressed experimentally [249, 303] and numerically [311]. During the transition process in the laminar regime, the flow structures evolve from circular to spiral rolls.

Some flow visualizations have been firstly performed from above the stator for two Reynolds numbers $Re = 4.1 \times 10^4$ and $Re = 10^5$ using a CCD video camera. The cavity has been filled up

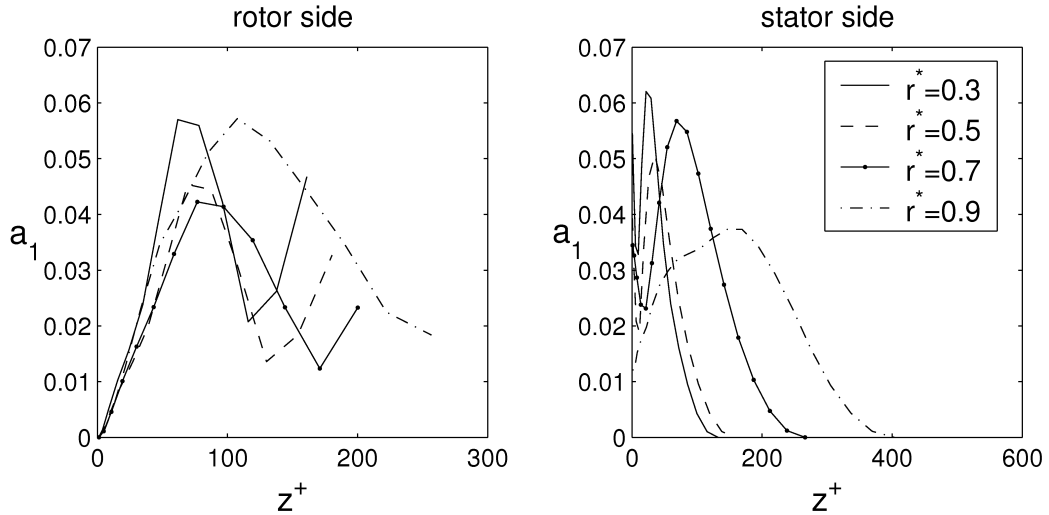


Figure 8.18: Townsend structural parameter $a_1 = \tau/(2k)$ on both disks for $G = 1/7$, $R_m = 1.8$ and $Re = 10^6$ (LES-SVV).

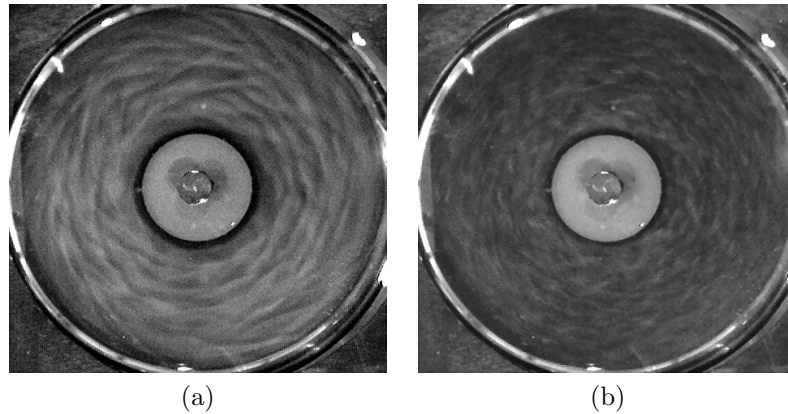


Figure 8.19: Flow visualizations from above the stator for $G = 1/7$, $R_m = 1.8$ and (a) $Re = 4.1 \times 10^4$, (b) $Re = 10^5$.

with water and seeded with reflective particles of kalliroscope ($30 \times 6 \times 0.07 \mu\text{m}$). For $Re = 4.1 \times 10^4$ (Fig.8.19a), the flow structure is already complex but it is still organized by large structures showing spiral patterns with defects. For $Re = 10^5$, the Bödewadt layer is now clearly turbulent (Fig.8.19b). The flow structures are much thinner and more aligned on the tangential direction.

Figure 8.20 presents the isosurfaces of the Q-criterion in both boundary layers and for the three Reynolds numbers under consideration. At $Re = 10^5$, only the stator boundary layer (Fig.8.20b) is turbulent with increasing intensities towards the periphery. On the rotor side, turbulent flow regions are only confined close to the junctions with the hub and the shroud where the flow strongly impacts the wall. The inner rotating hub is found to have a strong destabilizing effect, accelerating the flow and strengthening the vortices coming from the Bödewadt layer to the Ekman layer. It is contrary to the configuration where the hub is stationary [309]. For $Re = 4 \times 10^5$, the flow along the stator is fully turbulent as expected, while the rotor layer is now transitional turbulent. About 19 spiral arms forming a positive angle $\epsilon \simeq 16^\circ$ with the tangential direction (as they roll up in the rotation sense) appear in the Ekman layer for $0.14 \leq r^* \leq 0.61$ (Fig.8.20c) where the flow is laminar unstable ($89 \leq Re_r^{1/2} \leq 386 < 500$). These structures are characteristic of the Type I instability (crossflow instability), which plays an important role in the transition process to turbulence. These results are consistent with previous results (see the review of Saric *et al.* [292]). Close to the outer radius, the

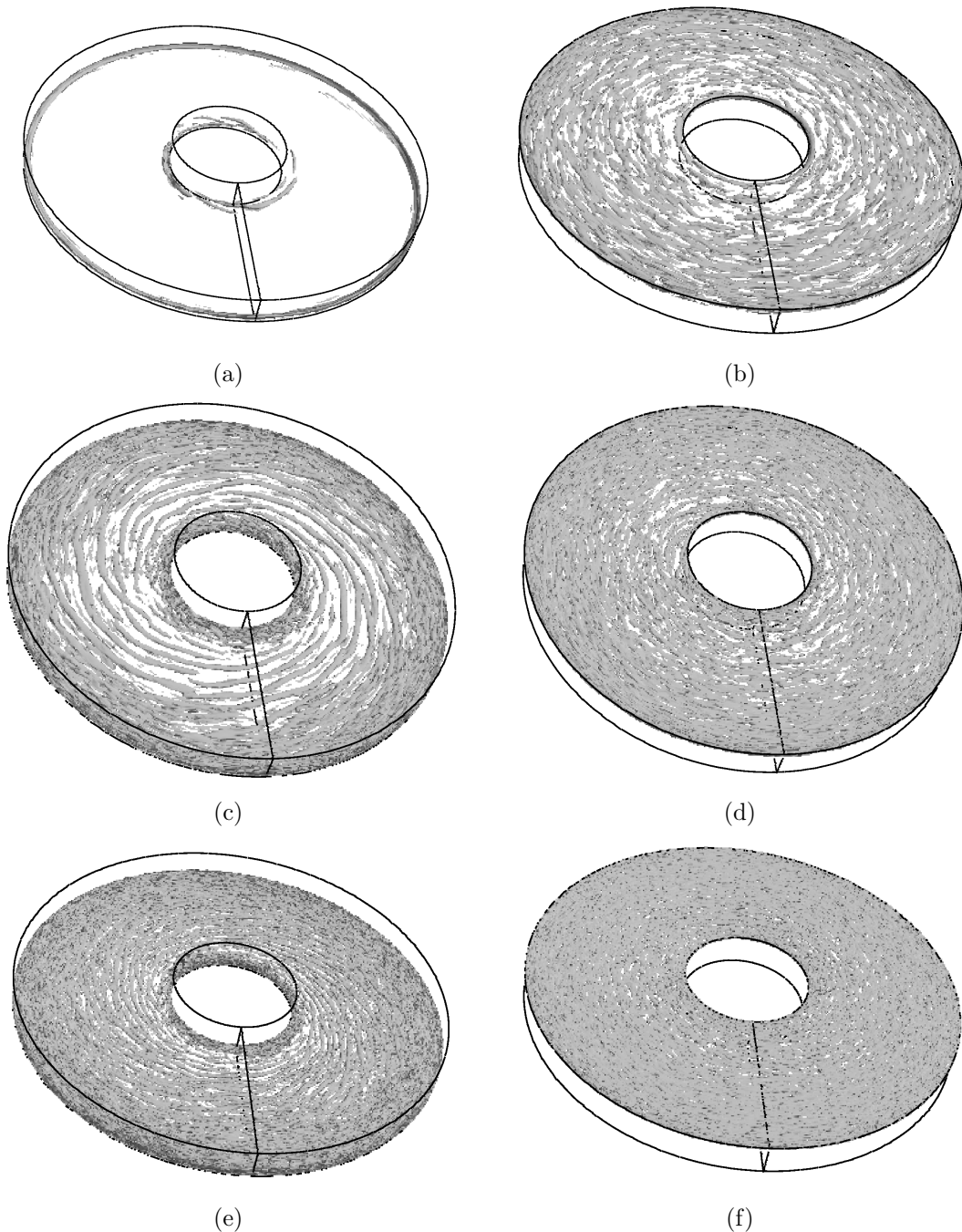


Figure 8.20: Isosurfaces (top view) of the Q-criterion in the rotor boundary layer (a,c,e) and in the stator boundary layer (b,d,f) for $G = 1/7$, $R_m = 1.8$ and (a,b) $Re = 10^5$, (c,d) $Re = 4 \times 10^5$ and (e,f) $Re = 10^6$. Note that the disk rotates counterclockwise and that the results have been obtained by the LES-SVV.

structures are thinner and more axisymmetric, which is characteristic of a turbulent flow. At $Re = 10^6$ (Fig.8.20e,f), the flow gets fully turbulent in both boundary layers. Along the stator, as expected, turbulence intensities increase for increasing values of the local Reynolds number and the coherent vortical structures, which are aligned with the tangential direction, get thinner. Let's notice that, for all considered Reynolds numbers, any three-dimensional vortical structures were observed in the core region, contrary to the experimental observations of Czarny *et al.* [63].

8.5 Heat transfer in turbulent rotor-stator flows

The previous LES-SVV results obtained under isothermal conditions have been here extended to the non-isothermal case for the same rotor-stator cavity ($G = 1/7$, $R_m = 1.8$). The effects of convective heat transfers on the turbulent air flow ($Re = 10^6$) in an enclosed rotor-stator cavity are here investigated using the Boussinesq approximation. The cavity is heated from below along the stator side, while the upper disk is rotating and cooled. Thus, it is an unstable configuration, where the density gradient is opposed to gravity acceleration. All the numerical parameters are summed up in Table 8.1. All the results have been published in *Int. J. Heat Fluid Flow* (see Ref.[260]).

8.5.1 Heat transfer parameters

Conducting and insulating thermal boundary conditions have been considered on the disks and the cylinders, respectively. The temperature is normalized by the temperature difference applied between the stator and the rotor: $T^* = 2(T - T_r)/\Delta T$ with $\Delta T = T_{hot} - T_{cold}$ and $T_r = (T_{hot} + T_{cold})/2$. The stator is thus maintained at the constant dimensionless temperature $T^* = 1$, while the rotor is maintained at $T^* = -1$. The hub and the shroud are thermally insulated with zero heat flux. The Prandtl number Pr and the Rayleigh number Ra based on the maximum radial acceleration have also to be taken into account to study the flow dynamics. They are defined as follows:

$$Pr = \frac{\nu}{\kappa} = 0.7 \quad 0 \leq Ra = \frac{\Omega^2 b \Delta T h^3}{\nu \kappa T_r} \leq 10^8$$

where κ is the thermal diffusivity of the fluid. Note that the value of Pr chosen here corresponds to the typical value for air at 293 K. For this value of Prandtl number, the thermal diffusivity is slightly dominant. In a classical Rayleigh-Bénard system without rotation, there is no motion for $Pr = 0.7$ until the appearance of steady rolls at $Ra = 5 \times 10^3$ [107]. All the parameters are then fixed except for the Rayleigh number Ra , whose influence on the flow dynamics is here investigated. To have an idea of the physical temperature difference between the disks, if the temperature of the rotor is fixed to the initial temperature of air (293 K), the maximum value of the Rayleigh number $Ra = 10^8$ corresponds to a temperature difference of 15.82 K, which is 50% larger than the temperature difference considered by Elkins and Eaton [86]. Thus, some thermal effects may be expected in the present case while the Boussinesq approximation considered here remains valid.

8.5.2 Influence of the heat transfer on the flow structures

The flow is here analysed at $Ra = 10^7$ in the case of a turbulent flow ($Re = 10^6$) of air ($Pr = 0.7$). Instantaneous fields are first presented before quantifying the effect of Ra on the statistical data in the following section.

Figure 8.21 shows the iso-values of the instantaneous tangential velocity component $V_\theta/(\Omega b)$ in both boundary layers and the corresponding instantaneous normal temperature gradient $\partial T^*/\partial z^*$ at the disk surfaces, which is proportional to the local heat transfer rate through the surface. Although the grey scales do not correspond perfectly, it is clear that these heat-fluxes pictures reveal the same structures. Along the cooled rotor (Fig.8.21a), the structure of the iso-values of $\partial T^*/\partial z^*$ resembles the one of the iso-values of $V_\theta/(\Omega b)$ (Fig.8.21c) with large positive spiral arms appearing at intermediate radial positions. They are enclosed by two turbulent flow regions. The first one is located at the junction between the rotor and the hub. The hot fluid coming from the stator side flows along the hub and impinges the rotor. It is then cooled by this disk. That is the reason why this turbulent flow region is characterized by a temperature equal to zero (see Fig.8.22a). The second region of high turbulence intensities appears at the periphery of the cavity where the highest values of the local Reynolds number prevail. The spiral arms disappeared and more thin structures are created. They are also characterized by a dimensionless temperature close to zero (see Fig.8.22a). The cooled fluid coming from the rotor after impingement on the shroud and then on the stator is heated by this lower disk. It creates a crown of fluid with a zero dimensionless temperature at the periphery of the cavity (see Fig.8.22a). Afterwards, this fluid flows along the stator from the periphery to the axis of the cavity. The fluid is progressively heated until the axis and so higher temperature levels are obtained (Fig.8.22a). The heat-fluxes picture is more chaotic in this boundary layer. It resembles to the one

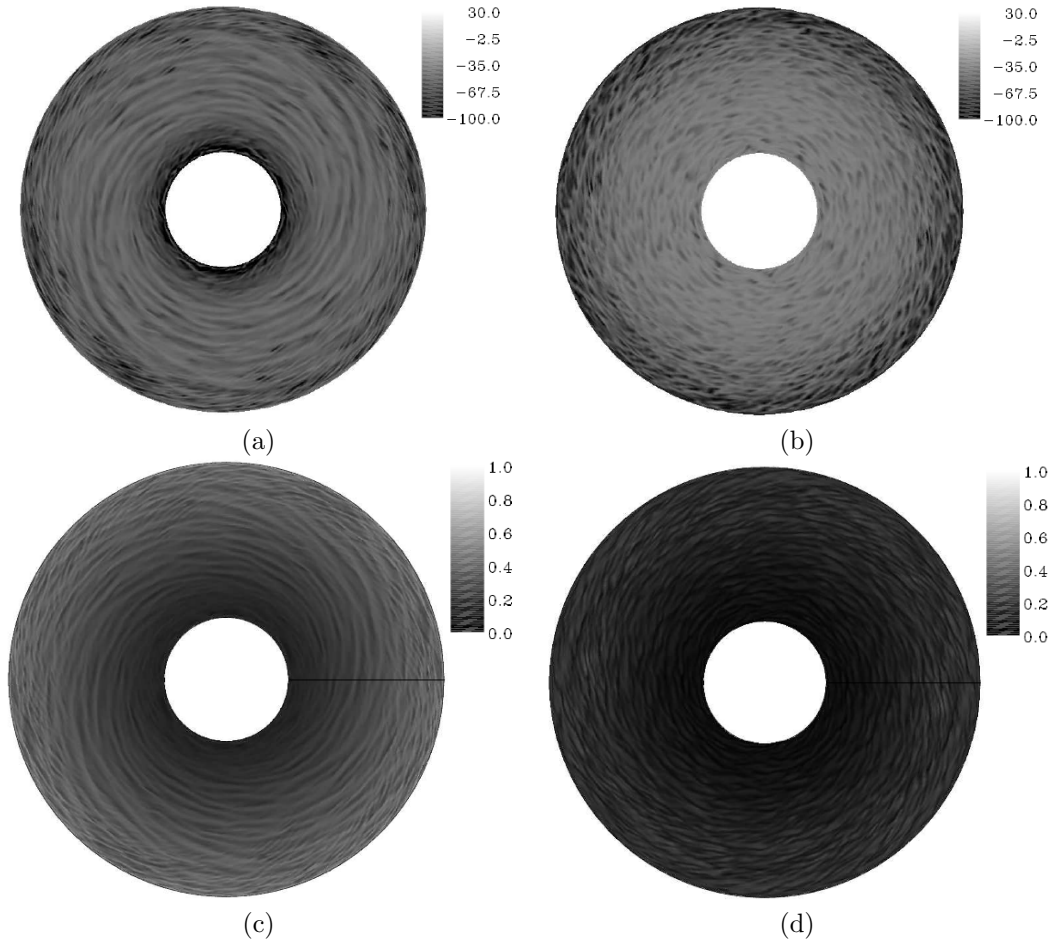


Figure 8.21: Iso-values of the instantaneous normal temperature gradient $\partial T^*/\partial z^*$ at the (a) rotor surface and at the (b) stator surface and of the instantaneous tangential velocity V_θ normalized by the maximum disk speed Ωb in (c) the rotor boundary layer ($z^* = 0.97$) and in (d) the stator boundary layer ($z^* = 0.03$). Results obtained using the LES-SVV for $G = 1/7$, $R_m = 1.8$, $Re = 10^6$ and $Ra = 10^7$.

of the iso-values of $V_\theta/(\Omega b)$ with very thin structures (Fig.8.21d). To conclude, the pattern of heat transfer rate is strongly affected by any organized structure in the flow field.

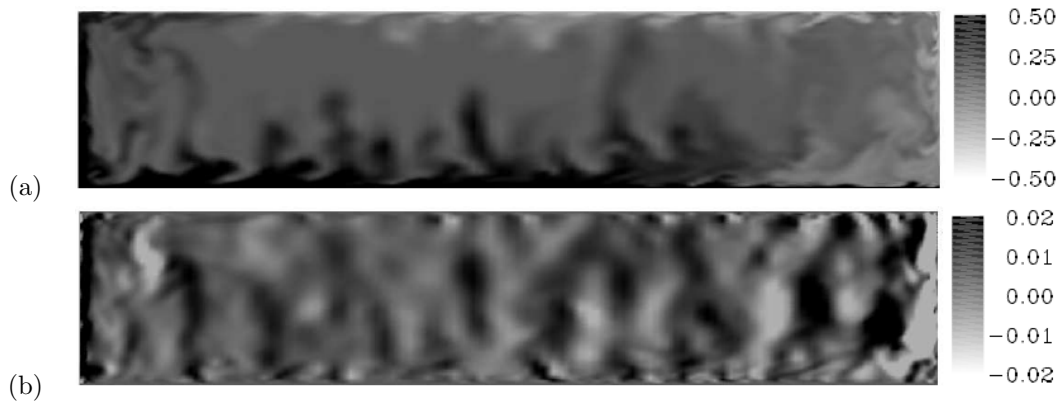


Figure 8.22: Iso-values of (a) the instantaneous temperature T^* and (b) the instantaneous axial velocity V_z normalized by Ωb in a (r, z) plane. Results obtained using the LES-SVV for $G = 1/7$, $R_m = 1.8$, $Re = 10^6$ and $Ra = 10^7$.

Figure 8.22a presents the isotherms at $Ra = 10^7$ in a (r, z) plane. This map confirms that the fluid heated along the stator is carried along the hub (dark areas on Fig.8.22a) with a positive axial velocity ($V_z/(\Omega b) > 0$ corresponds to dark areas on Fig.8.22b) and then cooled by the fluid flowing along the rotor (bright areas on Fig.8.22a). In the same way, the flow cooled by the rotor impinges the shroud and then the stator to be heating along this wall. The axial velocity of the fluid in the Stewartson layer along the external cylinder is then negative (bright areas on Fig.8.22b). As a consequence, there are two regions along the walls of quasi zero temperature: at the junction between the hub and the rotor and at the junction between the shroud and the stator. The temperature in the core is also quasi equal to zero in the whole cavity, which means that the secondary flow in the wall layers is responsible for most of the heat transfer in the cavity. Nevertheless, it can be seen in Figure 8.22a that vertical thermal plumes appear along the stator, essentially for inner radii. They are characterized by a dimensionless temperature close to unity. The well defined vertical structure of these plumes corresponds to regions of relatively high positive axial velocities (Fig.8.22b). At the periphery of the cavity, where the highest turbulence intensities are obtained, there are no thermal plumes due to the intense mixing between hot and cold fluids. Along the rotating disk, some cooled fluid is moving down with a smaller vertical extension (Fig.8.22a). Thus, the effect of the heated disk seems to dominate the heat transfer in the cavity.

8.5.3 Mean flow and turbulence statistics

The aim of this section is to quantify the effect of the Rayleigh number Ra on the mean and turbulent flow fields, on the temperature field and then, on the heat fluxes along the disks for a turbulent air flow ($Pr = 0.7$, $Re = 10^6$). All the data have been averaged both in time and in the tangential direction. One recalls that the mean velocity components and the components of the Reynolds stress tensor are respectively normalized as follows: $V_i^* = \bar{V}_i/(\Omega r)$ and $R_{ij}^* = \overline{v'_i v'_j}/(\Omega r)^2$ for $i, j = (r, \theta, z)$.

8.5.3.1 Flow field

To quantify the buoyancy effects on the flow field, one firstly defines a convective Rossby number $Ro_c = \sqrt{Ra/(PrTa)}$, where $Ta = (2\Omega h^2/\nu)^2$ is the Taylor number equal to 1.67×10^9 in the present case. It compares the buoyancy and the Coriolis forces. For $Ro_c > 1$, buoyancy forces are larger than Coriolis forces.

Figure 8.23 shows axial profiles of the mean velocity components at four radial locations in the range $0.3 \leq r^* \leq 0.9$. Four values of the Rayleigh number have been considered and the results are compared to the isothermal case. Whatever the value of Ra considered, the Batchelor flow model best describes the flow structure with fluid pumped radially outwards in the rotor boundary layer ($V_r^* > 0$ close to $z^* = 1$), called the Ekman layer, moving axially across the stator in the Stewartson boundary layer over the cylindrical outer shroud. Then, the fluid flows radially inwards along the stator side ($V_r^* < 0$ close to $z^* = 0$), in the Bödewadt layer, and impinges the rotating inner hub before going along the rotor again. The rotor and stator boundary layers are separated by an inviscid rotating core of fluid that rotates at around 38% of the rotating disk velocity, value which slightly depends on the radial location. The value of this swirl ratio $K = 0.382$ at $r^* = 0.9$ in the isothermal case is in good agreement with the one provided by the correlation $K = 0.49 - 0.57h/b = 0.409$ given by Daily et al. [68] for fully turbulent flows. So, for this set of parameters, the mean flow structure remains thus unchanged, i.e. with unmerged boundary layers.

The influence of Ra remains weak as the maximum value of the convective Rossby number reached for $Ra = 10^8$ is equal to 0.293. It confirms the previous results of Serre et al. [310] at lower Reynolds ($Re = 110000$) and Rayleigh ($Ra = 2 \times 10^6$) numbers. For example, the value of the swirl ratio $K = 0.382$ at $r^* = 0.9$ obtained in the isothermal case remains the same within less than 1% at this radius even for the largest value of Ra . The maximum difference on K reaches 1.5% at $r^* = 0.5$. The influence of Ra is more noticeable by looking at the profiles of the mean radial and axial velocity components. Even though there is no significant change on the maximum of V_r^* in the Ekman layer, there is a strong modification of the inflow in the Bödewadt layer. At $r^* = 0.9$, there is a decrease of 14% on the minimum of V_r^* between $Ra = 10^6$ and $Ra = 10^8$. This decrease reaches 26% at mid-radius. For all radial locations, the axial flow remains very weak compared to the main tangential flow, whatever the value of Ra . The reason is that for these parameters, the convective Rossby number is small, whereas the Taylor number is large. Thus, the bulk flow is in the thermal wind balance and so

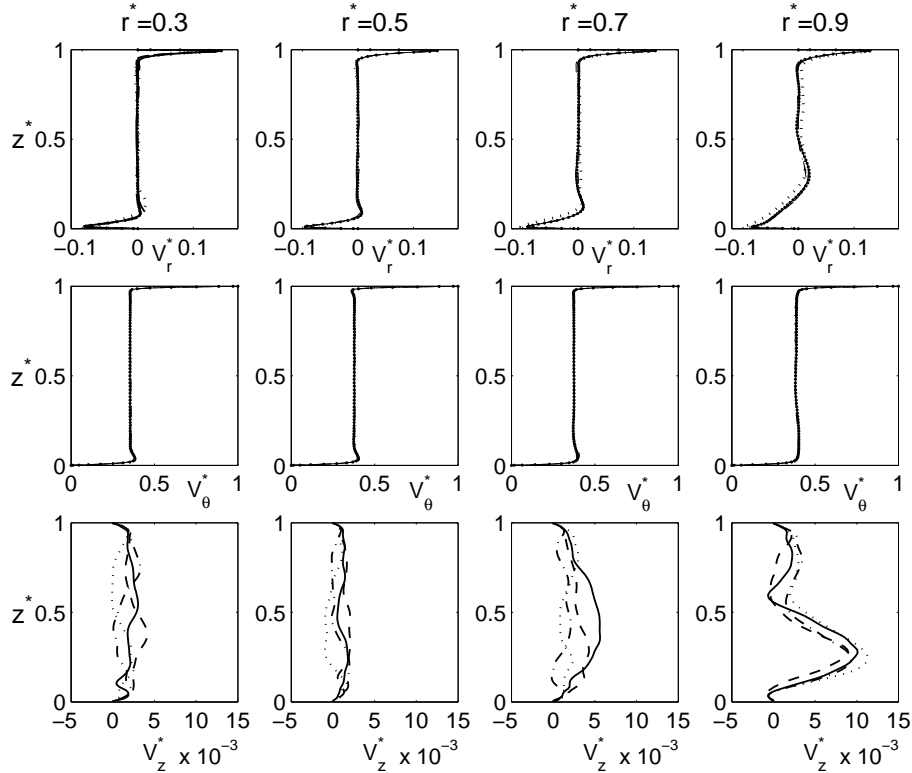


Figure 8.23: Axial profiles of the three mean velocity components at four radial locations in the range $0.3 \leq r^* \leq 0.9$ and for four values of the Rayleigh number: (solid lines) $Ra = 0$, (dashed lines) $Ra = 10^3$, (dash-dotted lines) $Ra = 10^6$, (dotted lines) $Ra = 10^8$. Comparison with the isothermal case (points). Results obtained using the LES-SVV for $G = 1/7$, $R_m = 1.8$ and $Re = 10^6$.

vertical motion is independent of the vertical coordinate. As no-slip boundary conditions are imposed on the boundaries, the vertical motion is very weak.

Turbulence is mainly confined in the boundary layers where the peak values of the normal components of the Reynolds stress tensor are obtained (Fig.8.24). On the other side, the central core remains almost laminar. The turbulence intensities are rather the same in both boundary layers with values of R_{rr}^* and $R_{\theta\theta}^*$ much larger than the ones of R_{zz}^* . Note that the values of the cross-components, not shown here, are rather weak in the whole cavity. The influence of the Rayleigh number Ra on the turbulent field is quite weak for Ra up to 10^6 . Turbulence intensities slightly increase with Ra in the boundary layers for $0 \leq Ra \leq 10^6$. The maximum values of the normal stresses increase indeed at least of 7% compared to the isothermal case. There are two exceptions: the maxima of R_{rr}^* and R_{zz}^* in the Bödewadt layer at $r^* = 0.9$, where peripheral effects may appear, are almost constant whatever the Rayleigh number. For the highest value of the Rayleigh number $Ra = 10^8$ considered here, there is a strong increase of R_{zz}^* especially for $0.3 \leq r^* \leq 0.7$. For these radial locations, some plumes similar to the ones shown in Figures 8.22 & 8.27 appear and enhance turbulence in the axial direction. For $r^* = 0.9$ where they are not obtained, the component R_{zz}^* remains rather the same whatever the Rayleigh number.

8.5.3.2 Temperature field

Figure 8.25 exhibits the temperature profiles along the axial direction for four Rayleigh numbers at four radial locations. Whatever the radial location r^* and the value of Ra , the temperature is almost constant and equal to zero in the core region. Nevertheless, two cases have to be distinguished: $Ra = 0$ for which temperature can be considered as a passive scalar and $Ra \neq 0$, for which temperature may have an influence on the hydrodynamic field. Thus, for $Ra = 0$, the thermal boundary layers coincide with the Ekman and Bödewadt layers from the hydrodynamic field. The structure of the thermal

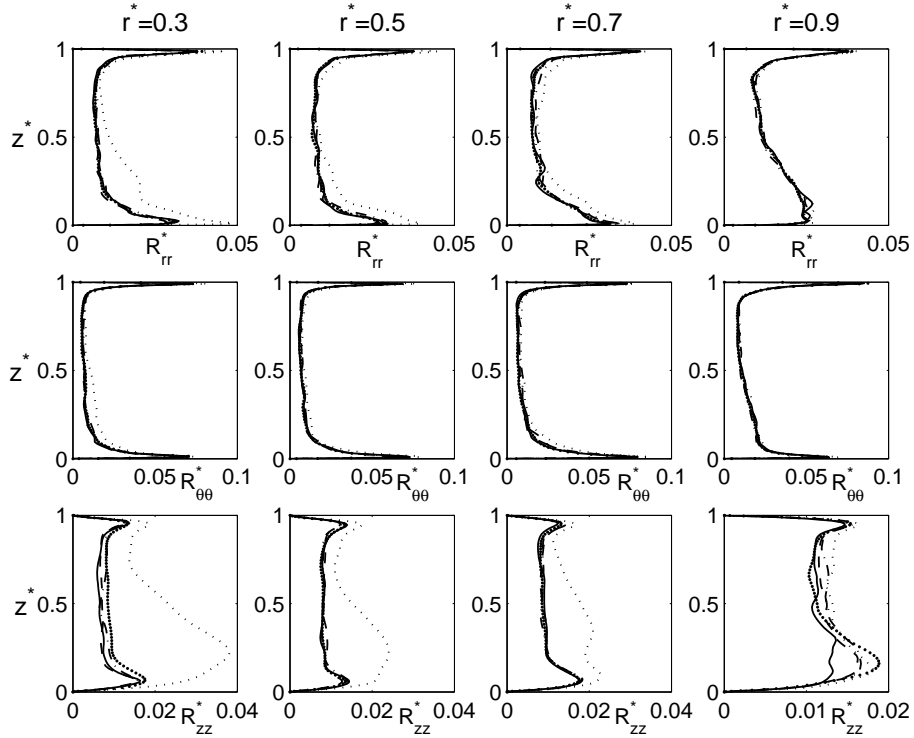


Figure 8.24: Axial profiles of the three normal Reynolds stress components at four radial locations in the range $0.3 \leq r^* \leq 0.9$ and for four values of the Rayleigh number: (solid lines) $Ra = 0$, (dashed lines) $Ra = 10^3$, (dash-dotted lines) $Ra = 10^6$, (dotted lines) $Ra = 10^8$. Comparison with the isothermal case (points). Results obtained using the LES-SVV for $G = 1/7$, $R_m = 1.8$ and $Re = 10^6$.

field is so a Batchelor-like structure. For $Ra \neq 0$, the thermal boundary layers are thicker than the velocity boundary layers as the Prandtl number Pr , which is the ratio of the velocity boundary layer thicknesses to the thermal boundary layer thicknesses is lower than unity ($Pr = 0.7$).

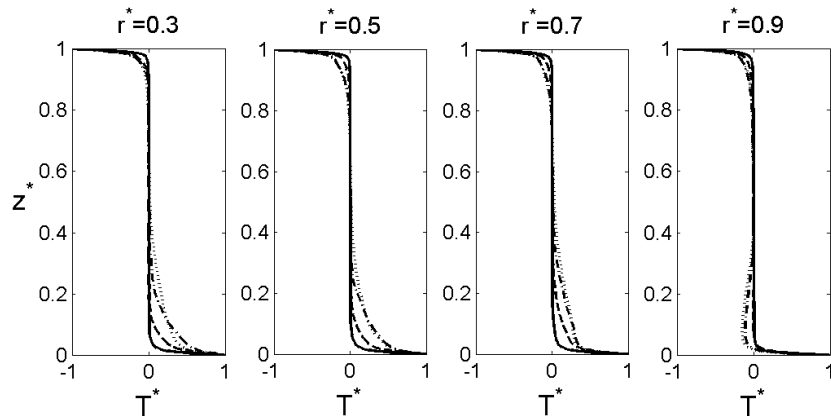


Figure 8.25: Axial profiles of the mean temperature at four radial locations and for four values of the Rayleigh number: (solid lines) $Ra = 0$, (dashed lines) $Ra = 10^3$, (dash-dotted lines) $Ra = 10^6$, (dotted lines) $Ra = 10^8$. Results obtained using the LES-SVV for $G = 1/7$, $R_m = 1.8$ and $Re = 10^6$.

From the axial profiles of T^* (Fig.8.25), one can deduce the values of the thermal boundary layer thicknesses, denoted δ_{R_T} for the rotor side and δ_{S_T} for the stator one. δ_{R_T} (respectively δ_{S_T}) is the height at which the mean temperature reaches -0.01 (resp. 0.01). δ_{S_T} is found to be larger than δ_{R_T} , which confirms the preponderant influence of the heated disk on thermal convection. For a given

Rayleigh number, $Ra = 10^3$ for example, both thermal boundary layers strongly vary with the radial location. δ_{R_T}/h increases from 0.08 at $r^* = 0.3$ to 0.15 at $r^* = 0.9$. In the same time, δ_{S_T}/h decreases from 0.17 to 0.06.

At a given radius, when Ra is increased, the axial extension of the core decreases as the thermal boundary layers thicken. At $r^* = 0.3$, δ_{R_T}/h (resp. δ_{S_T}/h) increases from 0.08 (resp. 0.17) for $Ra = 10^3$ to 0.19 (resp. 0.53) for $Ra = 10^8$. In the similarity area $0.3 \leq r^* \leq 0.7$, the temperature of the fluid at the edge of the stator boundary layer is increased with Ra due to the main influence of the heated disk. On the other hand, at $r^* = 0.9$ where the cold fluid coming from the shroud is mixed with the hot fluid flowing along the stator, a small decrease appears in the axial temperature profiles.

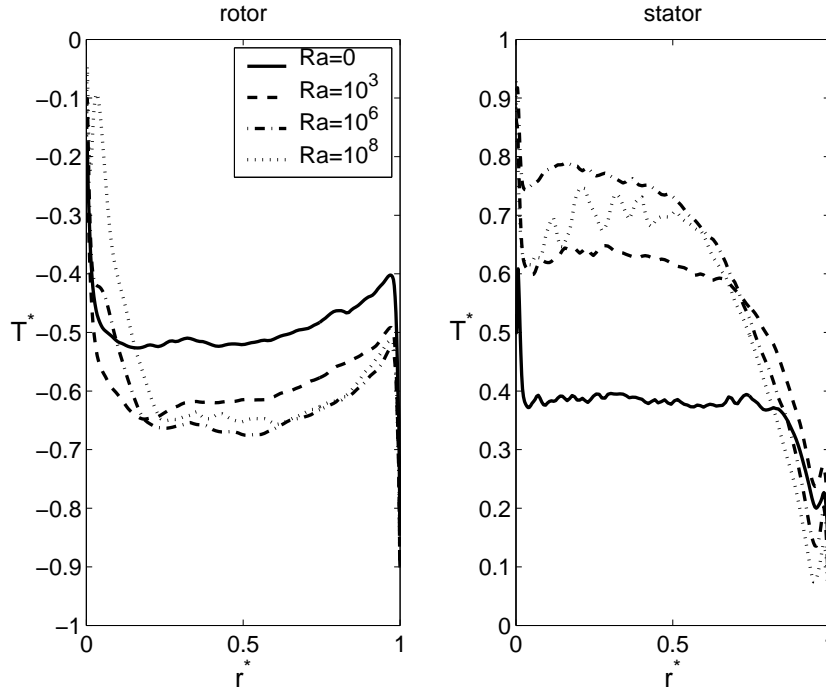


Figure 8.26: Radial distributions of the mean temperature along the rotor at $z^* = 0.99$ and along the stator at $z^* = 0.01$ for four values of the Rayleigh number. Results obtained using the LES-SVV for $G = 1/7$, $R_m = 1.8$ and $Re = 10^6$.

The results of Figure 8.25 are confirmed by the radial distributions of T^* shown in Figure 8.26 for both boundary layers and the same values of Ra . T^* slightly increases with the radius along the rotor apart from some peripheral effects. On the stator side, T^* is almost constant close to the axis and strongly decreases towards the periphery. The radial extent of the region of constant temperature decreases rapidly with the Rayleigh number. The magnitude of T^* is almost constant whatever $Ra \neq 0$ and then diminishes for $Ra = 0$. One can recall that, in that case, the temperature can be considered as a passive scalar. Note that T^* tends to 0 at the corner between the insulating hub ($r^* = 0$) and the rotor, where an intense mixing is obtained and tends to 1 at the corner between the insulating shroud ($r^* = 1$) and the rotor. In the same way, T^* tends to the stator temperature at the junction hub-stator ($r^* = 0$) and to 0 at the junction stator-shroud ($r^* = 1$).

8.5.3.3 Heat fluxes along the disks

Figure 8.27 shows the iso-values of the turbulent heat fluxes as well as the ones of the turbulent temperature fluctuations in a (r, z) plane for $Ra = 10^7$. All these quantities are close to zero around mid-plane and increase in magnitude towards the disks with a magnitude of order 10^{-3} , which confirms the experimental results of Djaoui and Debuchy [73] for the closed cavity. The highest values of these correlations are observed along the hub and along the heated stationary disk. $\overline{v_z' t'}$ is found to be different from zero along the disks and in particular along the stator, which is a characteristic of three-dimensional turbulent boundary layers [86]. Areas with positive values of $\overline{v_r' t'}$ and especially of

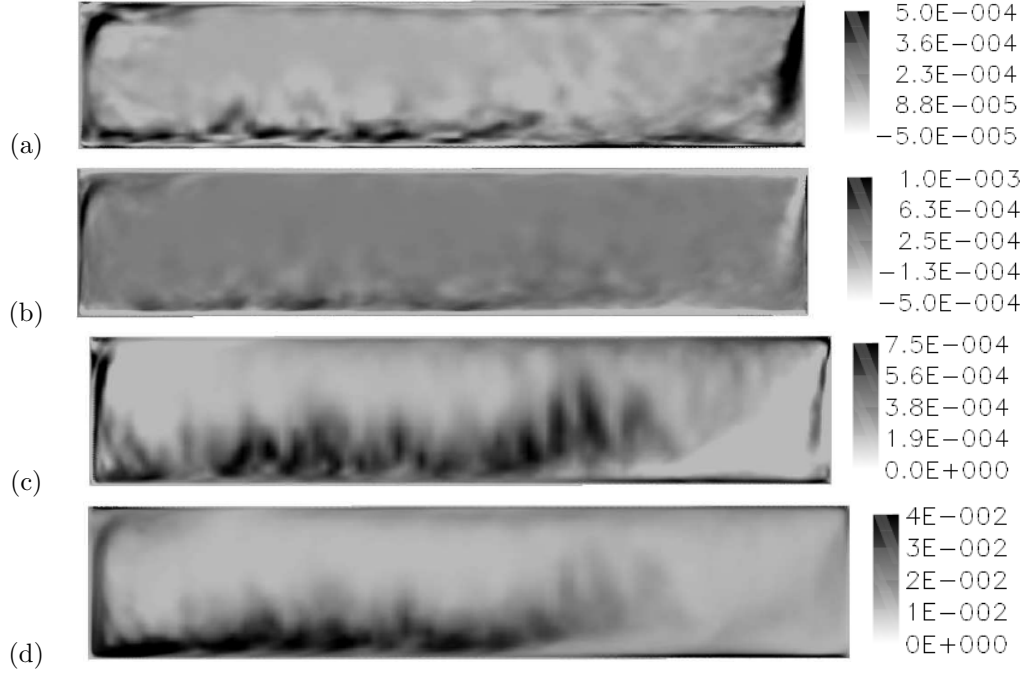


Figure 8.27: Iso-values of the turbulent heat fluxes (a) $\overline{v'_r t'}$, (b) $\overline{v'_\theta t'}$ and (c) $\overline{v'_z t'}$ normalized by $\Omega b \Delta T$ and of (d) the turbulent temperature fluctuations $\overline{t'^2}/(\Delta T)^2$ in a (r, z) plane. Results obtained using the LES-SVV for $G = 1/7$, $R_m = 1.8$, $Re = 10^6$ and $Ra = 10^7$.

$\overline{v'_z t'}$ and $\overline{t'^2}$ along the stator correspond to the thermal plumes already observed from the isotherms in Figure 8.22a. The axial extension of these plumes increases towards the periphery of the cavity. There is a close relationship between the axial heat flux and the temperature fluctuations, contrary to the single disk case, where Elkins and Eaton [86] obtained a stronger relationship between $\overline{v'_r t'}$ and $\overline{t'^2}$. This difference may be attributed to the radial confinement in the present study, which induces strong axial flows along the inner and outer cylinders. It is noteworthy that $\overline{v'_\theta t'}$ is almost equal to zero in the whole cavity, which confirms the vertical structure of the plumes.

One interesting parameter for numerical modeling is the turbulent Prandtl number Pr_t , defined here as the ratio of the eddy diffusivity for momentum to the eddy diffusivity for heat:

$$Pr_t = \frac{-\overline{v'_\theta v'_z} \frac{\partial \overline{T}}{\partial z}}{\overline{v'_z t'} \frac{\partial \overline{V_\theta}}{\partial z}} \quad (8.5)$$

Even though it is not a rigorous definition of Pr_t for a three-dimensional turbulent boundary layer, where Pr_t should be a second-order tensor, this definition is the one used Elkins and Eaton [86] and appears simpler to enable direct comparisons with the results of these authors. Moreover, this definition deals with the vertical direction along which the thermal plumes are aligned. Typical values of the turbulent Prandtl number are around unity. Pr_t is strictly equal to 1 in accordance with the Reynolds analogy and equal to 0.9 in classical RANS models.

The distributions of the turbulent Prandtl number in the disk boundary layers are shown in Figure 8.28 for $Ra = 10^7$ and four radial locations. z/δ_R and z/δ_S represent the distances from the rotor and the stator respectively, with δ_R and δ_S the boundary layer thicknesses along the rotor and the stator deduced from the velocity profiles (Fig.8.23). The same evolution is obtained along both disks. The influence of the radial location remains weak apart at $r^* = 0.9$, where Pr_t is lower close to the disks than at the other radii. The averaged value of Pr_t for $0.3 \leq r^* \leq 0.9$ decreases from 1.4 very close to the disk to about 0.3 at the edge of the boundary layer. The assumption of $Pr_t \simeq 0.9$ is consistent for z/δ_R or z/δ_S up to 0.25 but this level is too high over most of the outer layers. These results are consistent with the measurements of Elkins and Eaton [86] for the turbulent flow over a rotating disk. They obtained $Pr_t \simeq 1.2$ (uncertainty of about 17%) at the disk surface and Pr_t decreases monotonically to 0.5 in the outer layer. These values are slightly lower than the ones obtained

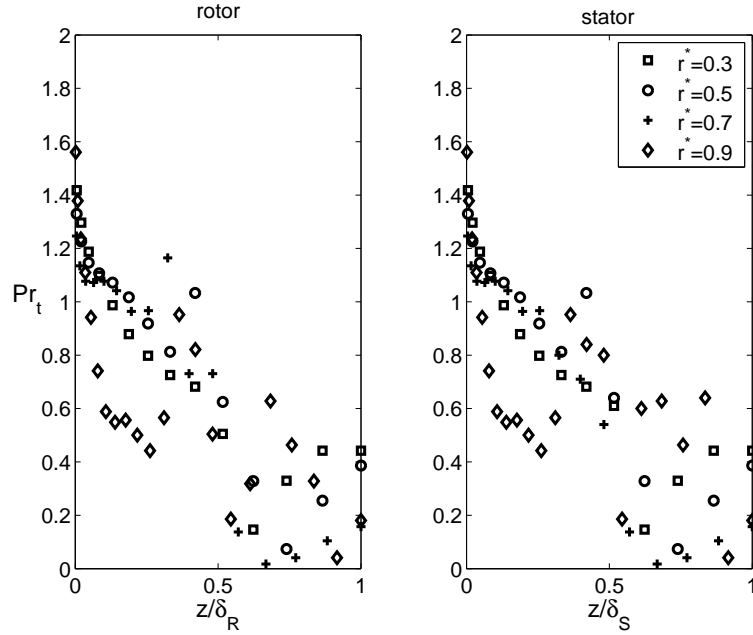


Figure 8.28: Axial variations of the turbulent Prandtl number in the rotor and stator boundary layers at four radial locations. Results obtained using the LES-SVV for $G = 1/7$, $R_m = 1.8$, $Re = 10^6$ and $Ra = 10^7$.

by Wroblewski [356] in a two-dimensional turbulent boundary layer, where Pr_t decreases to 0.8 at the edge of the boundary layer. The present results and the ones of Elkins and Eaton [86] indicate so that the diffusivity for momentum is reduced more than the diffusivity for heat. Nevertheless, according to Kays [151], the concepts of eddy viscosity and eddy diffusivity are not valid in three-dimensional turbulence and consequently, the turbulent Prandtl number has no meaning. Since the Ekman and Bödewadt boundary layers are three-dimensional turbulent boundary layers, the conclusions on the distributions of Pr_t must be considered tentative.

The effect of the Rayleigh number Ra on the local Nusselt number Nu along the two disks is investigated in Figure 8.29 for given Reynolds $Re = 10^6$ and Prandtl $Pr = 0.7$ numbers. Apart from some peripheral effects for r^* very close to 0 and 1, Nu is an increasing function of the radial location. It can be explained for the rotor side by looking at the radial distribution of the relative velocity $V_{rel}^* = [(1 - V_\theta^*)^2 + V_r^{*2}]^{1/2}$ (Fig.8.30). In the region $0.2 \leq r^* \leq 0.95$, when moving towards the periphery of the cavity, higher velocities are obtained, which enhances the heat transfer coefficient. Moreover the relative velocity is almost constant whatever the Rayleigh number, which may explain the weak influence of Ra on the local Nusselt number distribution. A second explanation has been provided by Dorfman [78], which showed that the local Nusselt number varies proportionally to the square root of the local Reynolds number $Re_r = \Omega r^2 / \nu$ and so varies linearly with the radial location. Along the rotor side, this linear dependence is obtained (Fig.8.29) at $Ra = 0$ for $0.145 \leq r^* \leq 0.68$: $Nu = 470r^* + 160$. The radial extension of this zone decreases when the Rayleigh number increases. On the stator, the linear dependence is obtained at $Ra = 0$ for a much larger radial domain $0.02 \leq r^* \leq 0.85$: $Nu = 440r^* + 140$. Two cases have to be distinguished: $Ra = 0$ and $Ra \neq 0$. As soon as $Ra \neq 0$, there is a strong decrease of Nu in the main part of the cavity. For $10^3 \leq Ra \leq 10^8$, there is no significant effect of the Rayleigh number on the radial distribution of Nu apart from at the junction between the rotor and the hub and at the junction between the stator and the shroud where an intense turbulent mixing between cold and hot fluids appears (see also Fig.8.22a). In these zones, Nu increases with the Rayleigh number in agreement with previous results described in Owen and Rogers [233].

In the present case, the numerical results can be correlated by:

$$Nu \propto Re_r^{0.7} \quad (8.6)$$

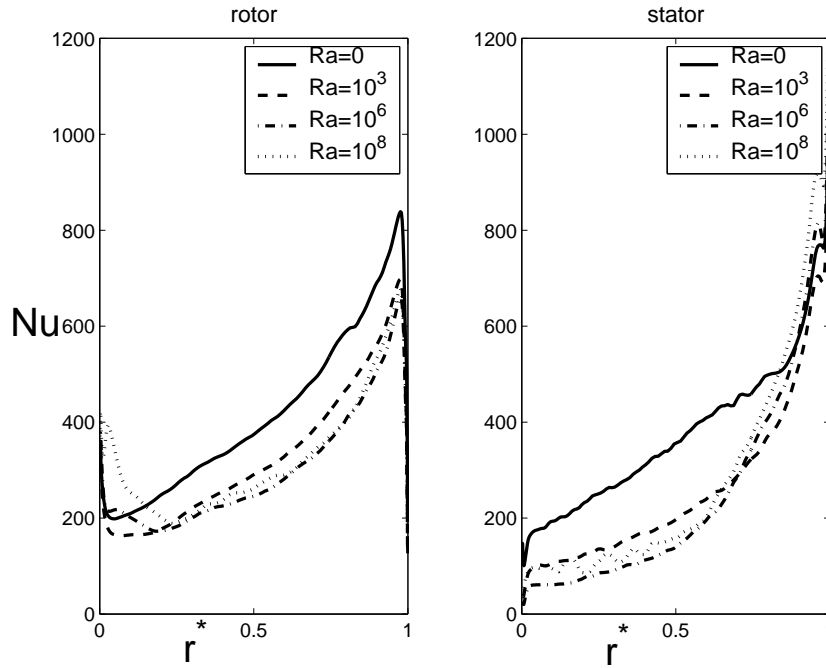


Figure 8.29: Radial distributions of the local Nusselt number Nu along the rotor and the stator for four values of the Rayleigh number. Results obtained using the LES-SVV for $G = 1/7$, $R_m = 1.8$ and $Re = 10^6$.

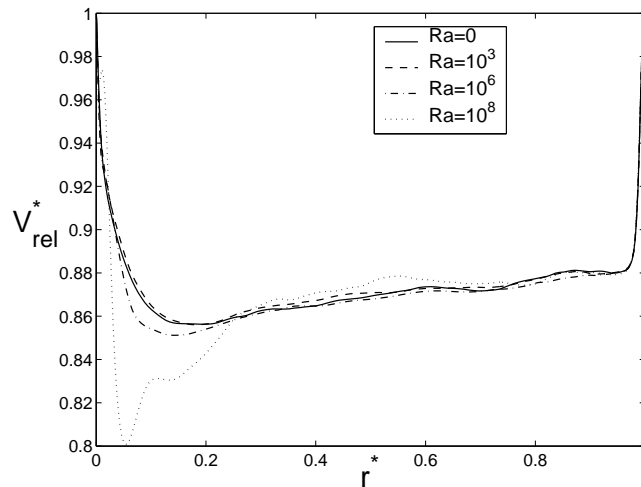


Figure 8.30: Radial distributions of the relative velocity V_{rel}^* along the rotor ($z^* = 0.99$) for four values of the Rayleigh number. Results obtained using the LES-SVV for $G = 1/7$, $R_m = 1.8$ and $Re = 10^6$.

Thus, the local Nusselt number depends on the local Reynolds number to the power $\gamma = 0.7$. This exponent is close to the one $\gamma = 0.746$ given by Pellé and Harmand [237] (Eq.8.3) for turbulent flows in an open rotor-stator cavity. It confirms that the Nusselt number is generally lower in an enclosed domain than in an unbounded one [107]. The value of γ falls between the classical values given by Owen and Rogers [233] in the single disk case for the laminar regime $\gamma = 0.5$ and for the turbulent regime $\gamma = 0.8$, confirming the turbulent nature of the flow here. The present calculations are also in good agreement with the empirical correlation of Yu *et al.* [363] in the same configuration (turbulent flow enclosed between a lower heated stationary disk and an upper cooled rotating disk for $Re > 1.5 \times 10^5$) with the terms corresponding to the superimposed mass flow rate set to zero.

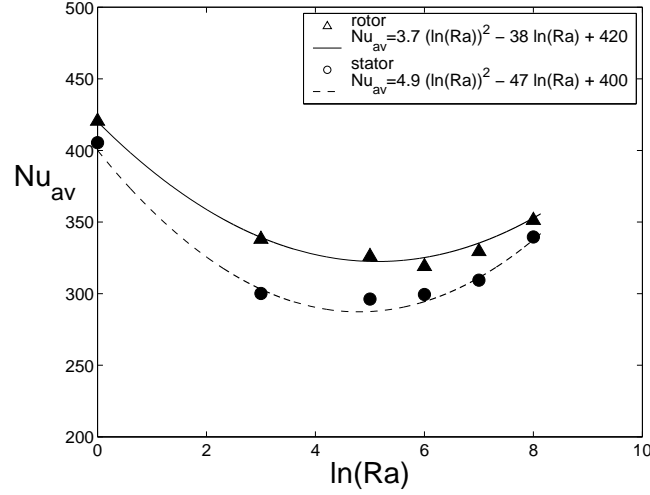


Figure 8.31: Influence of the Rayleigh number Ra on the averaged Nusselt number Nu_{av} on both disks. Results obtained using the LES-SVV for $G = 1/7$, $R_m = 1.8$ and $Re = 10^6$.

Figure 8.31 presents the dependence of the averaged Nusselt number Nu_{av} on the Rayleigh number for both disks. The inner and outer cylinders being insulated, the overall energy balance implies that the averaged Nusselt numbers are the same along both disks. Here, Nu_{av} is the average value of Nu over the range $0.05 \leq r^* \leq 0.95$. Thus, one removes the strong peripheral effects, which appear in the values of the local Nusselt number close to the inner and outer cylinders (Fig.8.29). That is why Nu_{av} appears slightly higher on the rotating disk. Nevertheless, for both disks, the evolution remains the same: Nu_{av} decreases with Ra up to $Ra = 10^5$ and then increases. Thus, the results for the averaged Nusselt number on the rotor and stator can respectively be scaled by:

$$Nu_{av} = 3.7(\ln(Ra))^2 - 38\ln(Ra) + 420 \quad (8.7)$$

$$Nu_{av} = 4.9(\ln(Ra))^2 - 47\ln(Ra) + 400 \quad (8.8)$$

The present value obtained for $Ra = 0$ along the stator is close to the one $Nu_{av} = 496.6$ provided by the correlation given by Poncet and Schiestel [258]. The weak difference may be attributed to the confinement effects and to the insulating conditions imposed on the cylinders in the present case.

From these results, one can deduce the values of the Bolgiano length L_B , which is the typical length characterizing the forcing mechanism in a convective system defined as:

$$L_B = \left(\frac{\varepsilon^5}{(g\alpha)^6 N^3} \right)^{1/4} \quad (8.9)$$

where ε is the turbulence kinetic energy dissipation rate, N the temperature variance dissipation rate and α the thermal expansion coefficient of the fluid. Even though this length scale is a local quantity, Chillá et al. [52] proposed an estimate of the averaged value valid for $Nu \gg 1$:

$$\langle L_B \rangle / h = \left(\frac{Nu_{av}^2}{RaPr} \right)^{1/4} \quad (8.10)$$

The turbulent dynamics below the Bolgiano length L_B is unaffected by buoyancy effects, while above it, it may be strongly influenced by the temperature fluctuations, because of their active feedback on the velocity field. From Equation 8.10, one can estimate the mean value of $\langle L_B \rangle / h$ in the two boundary layers as a function of the Rayleigh number (Fig.8.32a).

As the mean values of the Nusselt number Nu_{av} are rather the same in the two boundary layers, the evolution with the Rayleigh number of $\langle L_B \rangle / h$ is rather the same too along both disks.

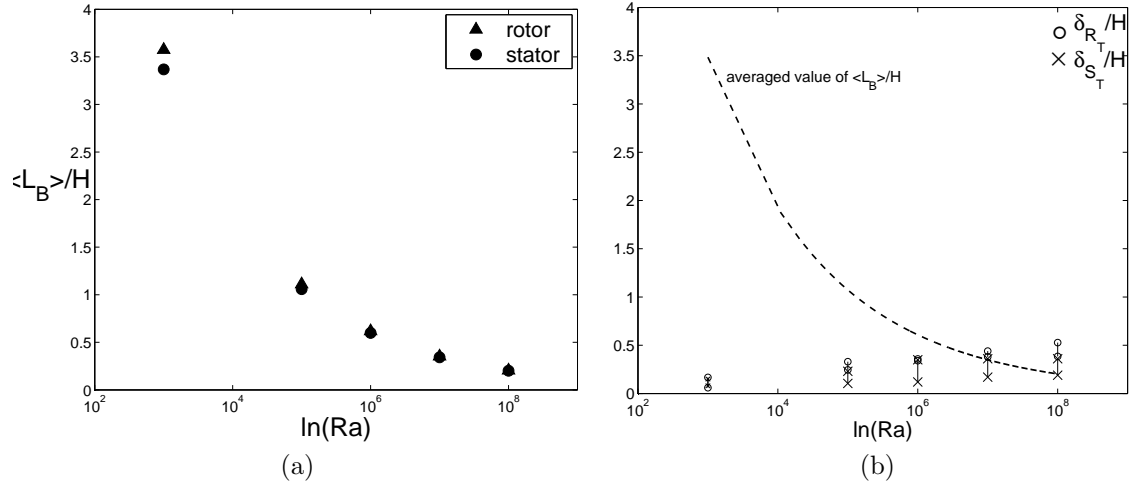


Figure 8.32: (a) Influence of the Rayleigh number on the mean Bolgiano scale $\langle L_B \rangle / h$ for both boundary layers; (b) Comparison with the thermal boundary layer thicknesses. Results obtained using the LES-SVV for $G = 1/7$, $R_m = 1.8$ and $Re = 10^6$.

$\langle L_B \rangle / h$ is almost equal to 3.5 for $Ra = 10^3$. It means that temperature fluctuations can not have any influence in the system. The same remark can be done at $Ra = 10^5$, where $\langle L_B \rangle$ is still larger than the interdisk spacing h . To conclude if the temperature fluctuations may have an influence in the system, it is required to compare $\langle L_B \rangle$ with the boundary layer thicknesses. The distributions of $\langle L_B \rangle / h$ in both boundary layers have been first averaged using the laws (8.7) to get only one trend curve as these distributions are quite similar. This curve is plotted on Figure 8.32b. It is compared to the extrema values of δ_{R_T} and δ_{S_T} obtained in the similarity area $0.3 \leq r^* \leq 0.9$. From Figure 8.32b, it can be seen that δ_{R_T} is lower than $\langle L_B \rangle$ whatever the radial location for $Ra \leq 10^7$ and gets larger for $Ra = 10^8$ for the whole radial extent. For this value of Ra , temperature fluctuations may have a large influence on the dynamics only at the largest scales of the system. In the same time, $\delta_{S_T} \geq \langle L_B \rangle$ for $Ra \geq 10^6$ whatever r^* . It confirms that heat transfers are enhanced along the stator and that the thermal plumes appear to be larger on this disk than on the rotor as shown in Figure 8.22a.

8.6 3D unsteady large scale vortices in turbulent flows

Three-dimensional unsteady large scale vortices have been highlighted experimentally in a cylindrical rotor-stator cavity of aspect ratio $G = [0.126; 0.195]$. Experimental flow visualizations by dye injection have been performed for a wide range of rotation rate $\Omega = [30; 250]$ rpm using the MACE facility in Manchester to confirm or not the former work of Czarny et al. [63] on the same set-up. Such large scale vortices may explain why some RANS models assuming the axisymmetry of the flow fail to predict the good heat transfer distribution [231]. It is important to note firstly that the same experiments have been also performed at IRPHE in Marseilles also by dye injection or using other colourings. They did not reveal the existence of these large scale vortices for the same values of G , R_m , Ω , Re and Re_r . Secondly, the LES-SVV results did not highlight the presence of such structures in the case of an annular cavity. It was then interesting to check the repeatability of the experiments previously performed by Czarny et al. [63] and to extend them to a wider range of operating conditions. These new experimental results have been then compared to calculations performed by a 3D unsteady $k - \epsilon$ modeling with analytical wall functions [60]. Both approaches reveal the existence of such vortical structures for the set of parameters considered.

8.6.1 A general feature in rotating flows

Computations for turbulent flow in rotating disk cavities assume most of the time the base flow to be axisymmetric and steady. Though the geometry is strictly axisymmetric, some numerical simulations

[60, 139, 340] and experimental flow visualizations [63] have revealed the presence of precessing large scale vortical structures even in the turbulent regime. Tucker [340] computed the temporal flow behaviors in a heated rotating cavity with an axial throughflow and in a sealed annulus. For both systems, three-dimensional unsteady patterns have been obtained: a three-lobe instability for $\Omega = 9.6$ rpm in the annular cavity (Fig.8.33) and a two-lobe structure for $\Omega = 162.3$ rpm in the cavity with throughflow. Jakoby *et al.* [139] reported the findings from an investigation with unsteady cavity pressure measurements and the requirements to produce sufficiently accurate CFD predictions in an axial bladed turbine. A large scale low frequency pulsating rotating structure was identified inside the rotor-stator cavity comprising three low pressure bubbles rotating at 80% of the rotor speed (9000 rpm). Owen [231] has drawn attention to difficulties in predicting the flow in rotating disk arrangements using bidimensional steady calculations and speculated that the cause might be related to the formation of these large scale unsteady vortices. Now, it appears to be crucial to take into account these three-dimensional unsteady effects to determinate accurately fluid flow and heat transfer in such cavities as 5% of error in the prediction of heat transfer are responsible for 60% of unscheduled stops.

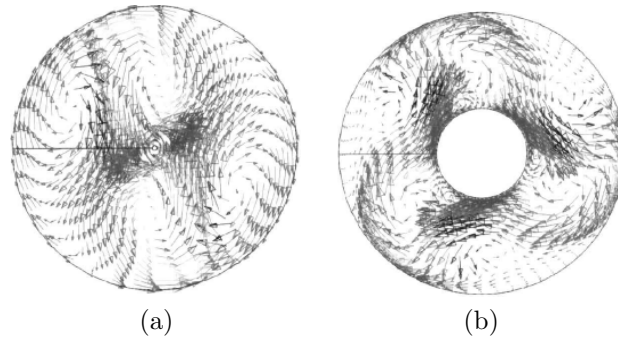


Figure 8.33: Velocity vector plots obtained by Tucker [340] highlighting (a) two-lobe and (b) three-lobe structures in a rotating cavity with throughflow.

Besides their practical importance in the turbomachinery industry, such large scale vortices embedded in a turbulent rotating flow are also relevant in geophysical and astrophysical applications. Sommeria [327] has indeed reproduced experimentally the formation of well structured vortices similar to the well-known Red Spot of Jupiter. It is certainly the most spectacular and romantic example of an organized three-dimensional structure persisting in a highly turbulent flow. In the experiment, this pattern was obtained using a rotating water tank, one meter in diameter and for a rotation rate Ω equal to 180 rpm, corresponding to a rotational Reynolds number of 7.54×10^7 .

8.6.2 The MACE rotor-stator facility

New experimental flow visualizations have been performed using the MACE facility under isothermal condition for various rotor-stator cavities and in a wide range of rotation rate. The overall apparatus consists of a motor-driven turntable mounted in an open cylindrical tank, 1.22 m in diameter. The turntable can be driven over a continuous range of rotation rates from $\Omega = 30$ to 250 rpm. On this, is mounted a smooth rotating disk, $b = 307$ mm in radius (Fig.3.1) and 25 mm thick. An upper stationary disk is facing the rotor at an axial distance h , which is fixed in the present study either to 38.7 mm or to 60 mm. The stator is in transparent plexiglas to allow flow visualizations. The rotor-stator cavity is enclosed by an outer stationary cylinder (the shroud), $b + j = 309$ mm in radius. An inner rotating cylinder (the hub), $a = 87.7$ mm in radius can be fixed or not to the rotor to consider either a cylindrical or an annular cavity. The rotor and the hub rotate counter-clockwise at the same uniform rotation rate Ω . The global flow parameters vary as follows: $G = [0.126; 0.195]$ and $2.57 \times 10^5 \leq Re \leq 2.15 \times 10^6$, whereas $R_m = 1$ for a cylindrical cavity.

The cavity is filled up with water maintained at a working temperature of $15^\circ C$ (kinematic viscosity $\nu = 1.15 \times 10^{-6} m^2/s$). Ink is used to visualize the hydrodynamic structures. It is introduced to the cavity, usually at mid-radius, via a hypodermic tube inserted through a small hole in the stator. Dye is released continuously during about 30 seconds typically. Gradually the dye disperses and the injection is renewed to verify that the flow structure previously observed remains the same. After Daily and

Nece [67], the flow in such a cavity exhibits a Batchelor-like flow structure with two very thin boundary layers developed on each disk separated by a central core in near solid body rotation characterized by a quasi zero radial velocity component $V_r \simeq 0$ and a constant tangential velocity component $V_\theta \simeq 0.4\Omega r$. Different radial and axial positions have been investigated for ink injection and the same results have been obtained for $r^* = r/b$ in the range $[0.404; 0.603]$ and $z^* = z/h = [0.1; 0.9]$ ever since ink is injected in the geostrophic core region far from the inner and outer cylinders where confinement effects may appear. Images (768×576 pixels) are taken at a video frequency of 25 images per second using a CCD camera situated above the stator.

8.6.3 Flow visualizations of 3D unsteady vortices in turbulent Batchelor rotor-stator flows

New experimental flow visualizations have been performed from above the stationary disk for various cavities in a wide range of rotation rate Ω . The existence domains of the precessing vortex structures in terms of Ω have been established for two different aspect ratios, $G = 0.126$ (Fig.8.34a) and $G = 0.195$ (Fig.8.34b). The present experiments are compared to the previous ones of Czarny *et al.* [63] performed using the same device and for the same flow parameters and with previous DNS results of Serre *et al.* [309, 312].

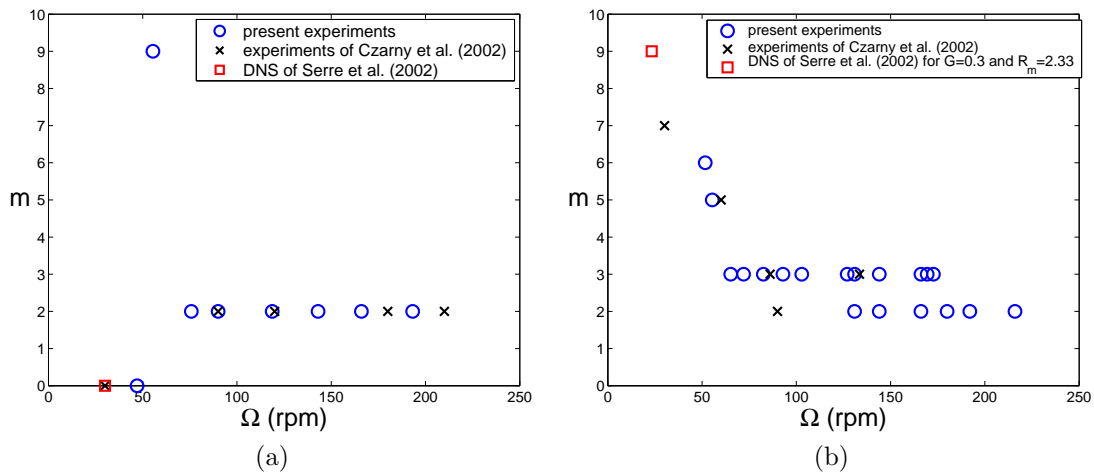


Figure 8.34: Evolutions of the number of vortices m against the rotation rate Ω (rpm) in the cylindrical case for two values of the aspect ratio: (a) $G = 0.126$, (b) $G = 0.195$. Comparisons between the present experiments (circles), the experiments of Czarny *et al.* [63] (cross symbols) and the DNS results of Serre *et al.* [309, 312] (squares).

For the lowest aspect ratio $G = 0.126$ (Fig.8.34a), the flow exhibits a Batchelor like flow structure with two boundary layers developed on each disk separated by a central geostrophic core. The transition to turbulence for $G \geq 0.042$ occurs for $Re \simeq 1.5 \times 10^5$ [67]. It corresponds to a critical rotation rate equal to $\Omega \simeq 17.5$ rpm. For Ω up to 50 rpm, there is no evidence of large scale precessing vortices (Fig.8.35a) even if the flow is not purely axisymmetric. It is referred in the following as the mode $m = 0$. If one slightly increases further Ω to 55.4 rpm, the mode $m = 0$ destabilizes and an 9-sided polygon (Fig.8.35b) is observed. It is consistent with the DNS of Serre *et al.* [312] for $G = 0.3$ (see Figures 8.34b & 8.36b). One recalls that the disk rotates counter-clockwise but Czarny *et al.* [63] have shown that clockwise rotation provides no discernibly different patterns. The number of lobes strongly decreases to $m = 2$ for $\Omega = 75.6$ rpm (Fig.8.35c). For $\Omega \geq 96$ rpm, a reversed S -shaped two-lobe pattern subsists in the flow (Fig.8.35d). Note that these two different patterns are both referred as two-lobe structures but they are not distinguished in Figures 8.34a,b. Comparisons between the experiments of Czarny *et al.* [63] and the present ones show a certain repeatability of the observations.

For $G = 0.126$, the two-vortex structure forming a reversed S -shape has also been found in the computations. Figure 8.36a presents the iso-values of the turbulence kinetic energy, which match the dye trace in appearance even if the rotation rate is much higher: $\Omega = 1287$ rpm. This S -shaped pattern rotates at about 50% of the disk speed. In fact, all the large scale vortical structures presented

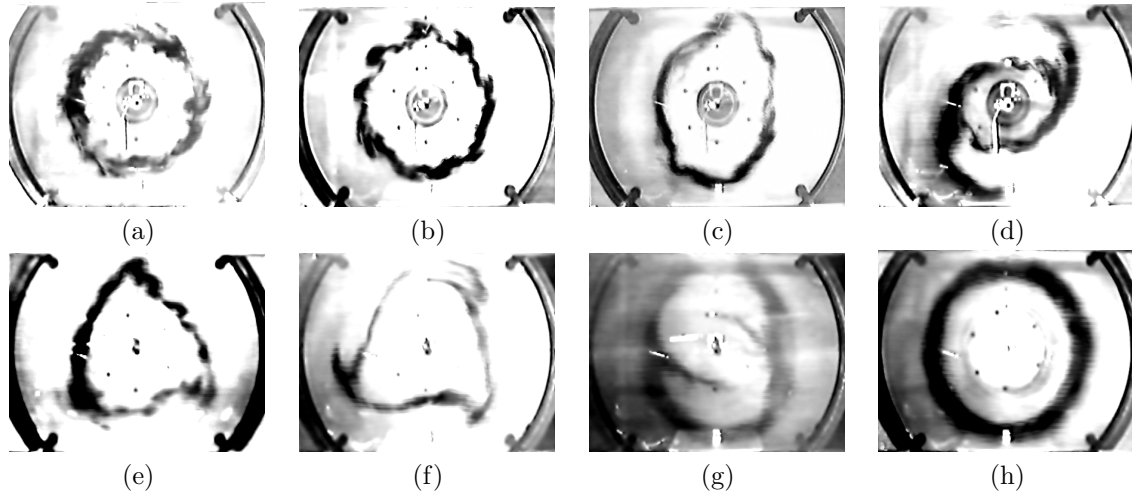


Figure 8.35: Experimental flow visualizations for different flow conditions $(\Omega(\text{rpm}), G, R_m)$: (a) axisymmetric mode $m = 0$ for $(47, 0.126, 1)$; (b) mode $m = 9$ for $(55.4, 0.126, 1)$; (c) mode $m = 2$ for $(75.8, 0.126, 1)$; (d) S-shaped mode $m = 2$ for $(96, 0.126, 1)$; (e) mode $m = 3$ for $(72, 0.195, 1)$; (f) mode $m = 3$ for $(103, 0.195, 1)$; (g) S-shaped mode $m = 2$ for $(180, 0.195, 1)$; (h) axisymmetric mode $m = 0$ for $(192, 0.195, 1.8)$. The disk rotates counter-clockwise.

here rotate at approximately half the rate of the rotor Ω underlining that these are vortices located in the central geostrophic core of the cavity, where the tangential velocity is nearly invariant with the axial distance and also with the radius.

If one slightly increases the axial gap between the disks, so that $G = 0.195$, similar patterns are obtained. There are no three-dimensional unsteady vortices for Ω up to 30 rpm [63]. For $\Omega = 30.1$ rpm, the mode $m = 7$ is observed. Then, the number of lobes m decreases for increasing values of the rotation rate and the modes $m = [6; 5; 3]$ are thus obtained for $\Omega = [51.7; 55.4; 65.2]$ rpm, respectively. The increasing importance of conventional small-scale mixing as Ω is raised means that the contribution of these large scale vortices to the overall transport of heat and momentum gradually diminishes with increase in Ω . The mode $m = 3$ subsists for a wide range of $\Omega = [65.2 - 172.7]$ rpm but different forms of three-lobe modes are observed as shown in Figures 8.35e-f. For $\Omega \geq 180$ rpm, the S-shaped two-lobe mode is recovered (Fig.8.35g) but its form is quite different from the one observed for $G = 0.126$ (Fig.8.35d). As shown in Figure 8.34b, within certain bands of operation $\Omega = [130.9 - 166.1]$ rpm, the vortex structure appears to be highly sensitive to the time history of the flow and depending on the experimental procedure, the modes $m = 2$ or $m = 3$ can be indifferently obtained, which confirms the former study of Czarny *et al.* [63]. These patterns are very similar to those observed by Poncet and Chauve [250] for the flow over a rotating disk enclosed by an outer stationary cylinder or to the ones of Abrahamson *et al.* [4] in the flow between shrouded co-rotating disks. It shows that they are basic structures common to many rotating flow devices. Poncet and Chauve [250] reported also the same sensitivity of these patterns to the time history of the flow and more generally to the experimental procedure.

Similar patterns have also been obtained by Craft *et al.* [60] near the stator for $G = 0.195$ using a three-dimensional unsteady $k - \varepsilon$ modeling within the STREAM code. The computations performed for $\Omega = 724$ rpm reveal a successive change of structure with time (Fig.8.37a-c). After 7 disk revolutions, a three-lobe vortex (Fig.8.37a) develops and is maintained until more than 20 revolutions. It reorganizes to a two-lobe pattern by 40 revolutions (Fig.8.37b), which still continues to evolve until 70 revolutions (Fig.8.37c). This corresponds to the maximum number of revolutions that resources and time permitted. Zacharos [364] have performed more computations using a second-moment transport closure but the result was that the flow developed rapidly to a steady form with none of the three-dimensional vortices reported above.

The effect of a central hub on the existence of these patterns has also been investigated. The flow visualizations performed for $R_m = 1.8$ and $G = [0.126; 0.195]$ do not reveal the existence of any large scale organized structure in the geostrophic core over the entire range of rotation rate $\Omega = [30; 250]$

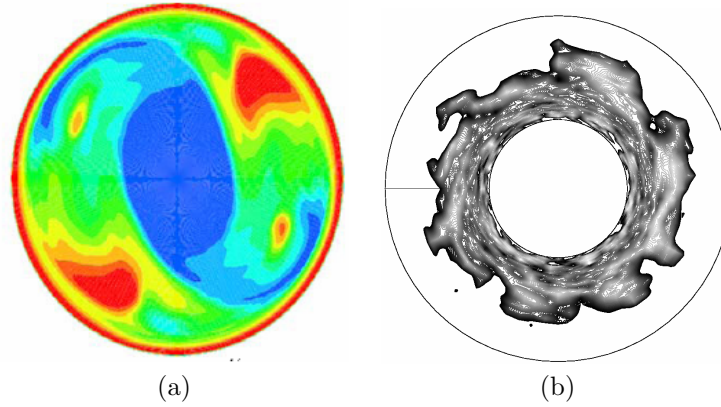


Figure 8.36: Unsteady vortical structures obtained numerically: (a) iso-values of the turbulence kinetic energy revealing a reversed S -shaped pattern for $\Omega = 1287$ rpm, $G = 0.126$ and $R_m = 1$ (three-dimensional $k - \varepsilon$ modeling of [60]); (b) Iso-values of a passive scalar obtained by DNS for $\Omega = 23.3$ rpm, $G = 0.3$ and $R_m = 2.33$ [312].

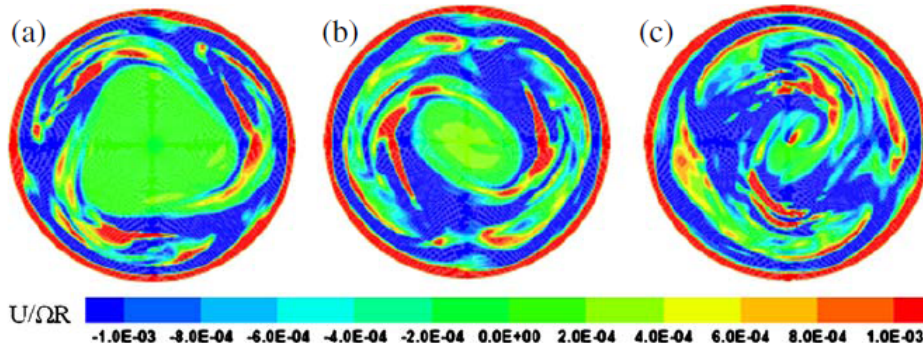


Figure 8.37: Unsteady vortical structures obtained by the three-dimensional $k - \varepsilon$ modeling of Craft et al. [60] for $\Omega = 724$ rpm and $G = 0.195$ near the stator. Contours of axial velocity after: (a) 20 disk revolutions, (b) 40 revolutions, (c) 70 revolutions.

rpm considered. Figure 8.35h presents an example of axisymmetric mode ($m = 0$) obtained in the case of an annular cavity ($\Omega = 192$ rpm, $G = 0.195$). It confirms both the DNS results of Serre et al. [312] for $G = 0.12$ and $R_m = 2.33$ and the recent LES results of Séverac et al. [315] for $G = 0.143$ and $R_m = 1.8$. One can not draw final conclusions about the existence or not of these patterns in an annular cavity as Serre et al. [312] reported using DNS the existence of a 9-lobed pattern for $G = 0.3$ and $R_m = 2.33$ (Fig.8.34b).

One recalls that the same experiments have been recently performed at IRPHE in Marseilles also by colouring injection. They did not reveal the existence of these large-scale vortices for the same values of G , R_m , Ω , Re and Re_r . It may be attributed to size effects as the rotor in the IRPHE's cavity is only 140 mm in radius. It is more probably due to the smallest gap between the rotor and the shroud ($j = 0.85$ mm) in the IRPHE's experiment compared to the present one $j = 2$ mm. It prevents the ingestion of fluid coming from below the rotor. In the MACE's facility, this gap may be large enough for the fluid coming from the region confined between the shroud and the rim to enter the cavity as in the simulation of Jakoby et al. [139].

8.7 Conclusion

Turbulent flows in an enclosed rotor-stator cavity have been investigated up to $Re = 10^6$ both numerically using two high-order LES and experimentally using LDV measurements. As far as the authors are aware, efficient LES of fully turbulent flow in an enclosed rotor-stator cavity have not been per-

formed before. The disks are enclosed by an inner hub attached to the rotor and an outer shroud attached to the stator involving finite cavity effects that were not taken into account in the former LES results of Lygren and Andersson [11, 193, 194].

The LES have been performed first using a spectral vanishing viscosity method (LES-SVV) preserving the spectral accuracy of smooth solutions. Such flows are difficult to compute when using spectrally accurate numerical schemes, that results directly from the fact that spectral approximations are much less diffusive than low-order ones. Their results have been compared to a second code (LES-FD) using fourth-order compact schemes in the non-homogeneous directions and a dynamic Smagorinsky subgrid-scale model.

Numerical results using the LES-SVV and experimental measurements have been presented for three Reynolds numbers, $Re = 10^5, 4 \times 10^5$ and 10^6 in order to show the increasing complexity in modeling these flows when rotation is increased. The boundary layers are separated with a turbulent Ekman layer on the rotor from $Re = 4 \times 10^5$ and a Bödewadt layer on the stator already turbulent at $Re = 10^5$. On both layers, finite cavity effects have been shown at $Re = 10^6$ with a radial dependence of the main features of the turbulent flow. The turbulence intensities slightly increase going towards the periphery. In the flow regions where the turbulence level is the weakest, the Q-criterion reveals spiral arm patterns related to the crossflow instability. In the fully turbulent flow regions, the structures become much thinner and aligned on the tangential direction. At $Re = 10^6$, the anisotropy invariant map reveals some features related to “cigar-shaped vortex” aligned on the tangential direction on the rotor side and related to “pancake-shaped vortex” on the stator side. The reduction of the Townsend structural parameter a_1 under the typical limit 0.15, as well as the strong misalignment between the shear stress vector and the mean velocity gradient vector, highlight the three-dimensional nature of both boundary layers with a degree of three-dimensionality much higher than in the idealized system studied by Lygren and Andersson [11, 193].

The LES-SVV results compare very favorably with the LDV measurements that is very encouraging for this numerical approach to deal with complex flows with a slightly better overall agreement compared to the LES-FD approach. Improvements in the future should come from a coupling of the SVV procedure to the flow dynamics in order to optimize the dissipation of the model.

The results using the LES-SVV have been also extended to the non-isothermal case. Buoyancy effects have been investigated under the Boussinesq approximation for Rayleigh numbers up to $Ra = 10^8$ and a given Prandtl number $Pr = 0.7$. Some instantaneous views of the velocity and temperature fields have been provided and reveal that the temperature field is strongly affected by the hydrodynamic structures even at large Ra values. The averaged results show small effects of density variation on the mean and turbulent hydrodynamic fields. The main features of non-isothermal turbulent rotor-stator flows have been caught by the LES-SVV and compared to previous results. The turbulent Prandtl number decreases from 1.4 at the walls to 0.3 at the edge of the boundary layers. The local Nusselt number is found to be proportional to the local Reynolds number to the power $\gamma = 0.7$. This exponent is close to the one $\gamma = 0.746$ given by Pellé and Harmand [237] for turbulent flows in an open rotor-stator cavity, which confirms that the Nusselt number is generally lower in an enclosed domain than in an unbounded one. Correlations for the averaged Nusselt number on both disks as a function of the Rayleigh number are also provided. The evolution of the averaged Bolgiano length scale $\langle L_B \rangle$ with the Rayleigh number indicates that temperature fluctuations may have a large influence on the dynamics only at the largest scales of the system for $Ra \geq 10^7$.

The LES calculations did not reveal the existence of the 3D unsteady vortices observed experimentally using the MACE facility. One has reported indeed flow visualizations of three-dimensional unsteady vortices embedded in a turbulent rotor-stator flow with separated boundary layers. These large scale organized structures appear in the geostrophic core, where the tangential velocity is invariant with the axial position. Two values of the aspect ratio G have been investigated revealing that a wider range of different vortex patterns is obtained for the highest value of G . Moreover, a clearly established tendency for the number of vortices to decrease as the rotation rate is increased is observed in both cases. Similar structures have also been found in the computations using a three-dimensional unsteady $k - \varepsilon$ modeling with analytical wall functions but for much higher rotation rates [60]. In an annular cavity with a central hub, there is no experimental evidence of such structures, which confirms our numerical investigations using LES. LES calculations are now required in the cylindrical case to confirm the existence of these large scale vortices and to perform a more detailed investigation.

Turbulent Von Kármán flow between counter-rotating disks

In this Chapter, the turbulent Von Kármán flow generated by two counter-rotating smooth flat (viscous stirring) or bladed (inertial stirring) disks is considered. Numerical predictions based the RSM model previously described in Chapter 4 are compared to velocity measurements performed at CEA (Commissariat à l'Énergie Atomique, France) by Romain Monchaux, who was PhD student there at that time. The main and significant novelty is the use of a drag force in the momentum equations to reproduce the effects of inertial stirring instead of modeling the blades themselves. The influences of the rotational Reynolds number, the aspect ratio of the cavity, the rotating disk speed ratio and of the presence or not of impellers are investigated and discussed in details. In particular, the transitions between the merged and separated boundary layer regimes and the one between the Batchelor [16] and the Stewartson [330] flow structures have been highlighted in the smooth disk case. The transition between the one cell and the two cell regimes has also been determined for both viscous and inertial stirrings. The results have been published in *Int. J. Heat Fluid Flow* in 2008 (Ref.[259]).

9.1 Introduction

The flow between two finite counter-rotating disks enclosed by a cylinder, known as the Von Kármán [348] geometry, is of practical importance in many industrial devices. Counter-rotating turbines may indeed be used to drive the counter-rotating fans in gas-turbine aeroengines. Moreover, this configuration is often used for studying fundamental aspects of developed turbulence and especially of magneto-hydrodynamic turbulence.

From an academic point of view, the laminar flow between two infinite disks has justified many works since the beginning of the controversy between Batchelor [16] and Stewartson [330] on the flow structure. Batchelor [16] solved the system of differential equations relative to the steady rotationally-symmetric viscous flow between two infinite disks. In the exactly counter-rotating regime, the distribution of tangential velocity is symmetric around the mid-plane and exhibits five distinct zones: two boundary layers developed on each disk, a transition shear layer at mid-plane, where the axial and tangential velocities change sign and two rotating cores on either side of the transition layer. The central cores rotate with a tangential velocity proportional to the disk velocities. The proportionality coefficient is always inferior to 1. This solution can be regarded as the connection of two Batchelor flows in the rotor-stator configuration. As stated by Batchelor [16] himself, “this singular solution may not be realizable experimentally, of course”, which supposes that another solution may exist. In 1953, Stewartson [330] found that the flow is divided into only three zones for large values of the Reynolds number $Re_h = \Omega h^2/\nu > 100$ based on the interdisk spacing h : one boundary layer on each disk separated by a zone of zero tangential velocity and uniform radial inflow. Lance and Rogers [167] found numerically in the exactly counter-rotating regime a Stewartson solution for $Re_h = 1023$. The existence at large Reynolds numbers of the Stewartson solution has been confirmed by the analysis of McLeod and Parter [202] in an infinite counter-rotating disk system. The Stewartson solution has also been obtained numerically by Pesch and Rentrop [243] at $Re_h = 2000$. Kreiss and Parter [161] have proved the existence and non-uniqueness of solutions at sufficiently large Reynolds numbers for the two-disk configuration. Thus, both Batchelor and Stewartson solutions are possible depending on the initial and boundary conditions but the Batchelor prediction has not been mentioned in the literature for the exact counter-rotating disk case. Pearson [236] obtained numerically a base inviscid solution of the Von Kármán flow, which differs from both the Batchelor and Stewartson solutions: at high Reynolds number ($Re_h = 10^3$), the solution is asymmetric and the main body of the fluid rotates faster than that of either disk. In the counter-rotating regime, Dijkstra and Van Heijst [72] showed

numerically that the transition from the one cell to the two cell structure occurs for a given Reynolds number and corresponds to the appearance of a detached shear layer on the slower disk. The reader is referred to the work of Holodniok *et al.* [131] and to the review of Zandbergen and Dijkstra [367] for a more extensive survey until 1987. More recently, Nore *et al.* [225] studied experimentally by flow visualizations and particle image velocimetry the bifurcations and the nonlinear dynamics of the von Kármán flow between exactly counter-rotating disks for a low aspect ratio cavity ($G = h/R = 2$ with R the disk radius). It has been extended in [224] both experimentally and by a stability analysis for $2 \leq G \leq 20$. Yang and Liao [359] solved the Von Kármán swirling viscous flow using the homotopy analysis method.

In the turbulent case, the Von Kármán flow is a model flow to study the turbulence characteristics on small scales. The main flow is axisymmetric and so offers an interesting intermediate situation between two-dimensional and three-dimensional flows. Fauve *et al.* [93] reported measurements of pressure fluctuations in the turbulent Von Kármán flow. They showed that the pressure probability function is strongly non-Gaussian and displays an exponential tail toward low pressures. Maurer *et al.* [201] used low-temperature helium gas to obtain high Reynolds numbers and well-defined scaling properties. They established the turbulence characteristics such as structure functions or the probability density function of the velocity differences and confirmed that turbulence on small scales has universal properties independent of the forcing. Mordant *et al.* [214] investigated the dynamical behavior of the Von Kármán flow at moderate to high Reynolds numbers using spatially averaged measurements. Data of the power input and of pressure fluctuations at the walls are sufficient to calculate the main turbulence characteristics such as the velocity fluctuations or the typical length scales. Cadot *et al.* [41] measured the mean rates of energy injection and energy dissipation in steady regimes of turbulence in the flow between counter-rotating stirrers. The smooth stirrers are found to be less efficient in setting the fluid into motion than in the case of bladed disks. Pinton *et al.* [247] measured the power consumption of the turbulent Von Kármán flow at constant Reynolds number and showed that power fluctuations occur and involve coherent fluid motions in the whole cell. Marié and Daviaud [199] performed full velocity measurements linking velocity fluctuations with the turbulent drag in this geometry. They showed especially that the turbulent drag is dominantly generated by coherent structures at the largest scales of the flow. Cadot and Le Maître [42] considered the turbulent between two co- and counter-rotating stirrers. They measured the instantaneous torques driving the flow and compared them to similarity laws having no dependence on the Reynolds number with a good agreement.

Ravelet *et al.* [270, 272] reported experimental evidence of a global bifurcation for a highly turbulent flow between two counter-rotating impellers. The transition between the symmetric and the asymmetric solutions is subcritical and the system keeps a memory of its history. Monchaux *et al.* [213] investigated the properties of the mean and most likely velocity fields in the same configuration. They showed that these two fields are described by two families of functions [181] depending on both the viscosity and the forcing. For large values of the Reynolds number, in some regions, the flow behaves like a Beltrami flow in which vorticity is locally aligned with velocity. Boroński [28] simulated the laminar Von Kármán flow between two counter-rotating disks equipped or not by straight blades. For a rotational Reynolds number $Re = \Omega R^2/\nu$ equal to 500, the poloidal-to-toroidal ratio is increased from 13% in the smooth disk case to 51% in the bladed disk case.

A renewal of interest for the Von Kármán flow is born from the dynamo experiments. The flow between counter-rotating impellers is considered as a possible candidate for the observation of a homogeneous fluid dynamo less constrained than the Riga and Karlsruhe devices. The flow needs to be highly turbulent in order for nonlinearities to develop in the magnetic induction. Numerous experimental [34, 347] or numerical [35, 271] studies have then been dedicated to magneto-hydrodynamics turbulence in the Von Kármán geometry (see for example the VKS experiment developed in Cadarache on Fig. 9.1a). In the latter work, the flow has been optimized using a water model experiment, varying the driving impeller configuration, well described in [270]. An example of the magnetic field produced by a kinematic dynamo outside a Von Kármán container is displayed in Figure 9.1b. One can cite also the review paper of Léorat and Nore [178], who took stock of the numerical developments, which have accompanied the VKS experiment until 2006.

To our knowledge, only very few numerical works have been devoted to the characterization of the mean and turbulent flow properties in the Von Kármán geometry. Kilic *et al.* [154] performed a combined numerical and experimental study of the transitional flow between smooth counter-rotating disks with a central hub for $-1 \leq s \leq 0$, $Re = 10^5$ and $G = 0.12$, where $s = \Omega_2/\Omega_1$ is the ratio

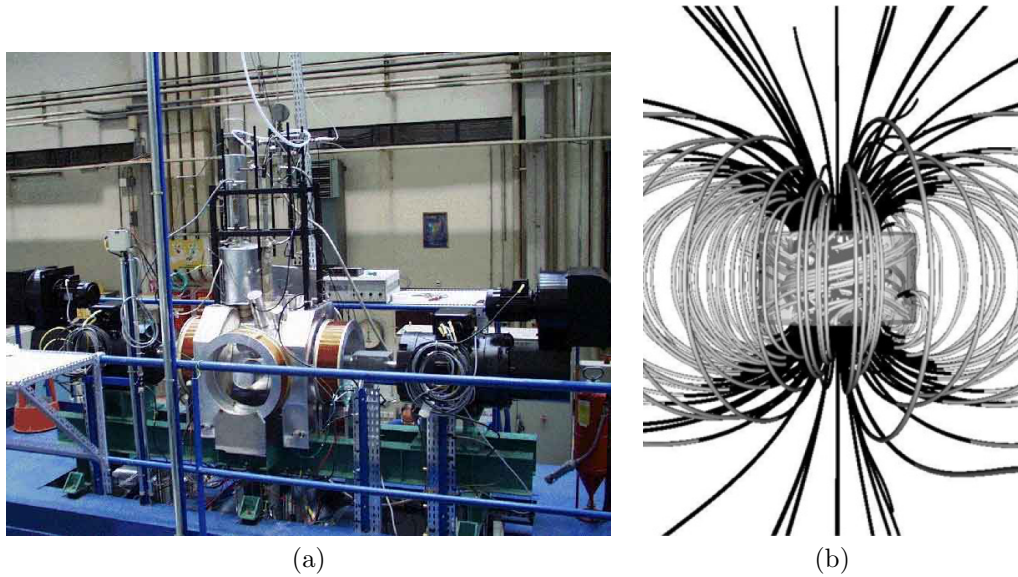


Figure 9.1: (a) Photography of the experimental Von Kármán Sodium (VKS) setup developed at CEA Cadarache; (b) Magnetic field produced by a kinematic dynamo outside a Von Kármán container, after Léorat and Nore [178].

between the rotating speeds of the two disks. They compared mean radial and tangential velocity measurements using a single-component laser Doppler anemometer with computed results using either the low Reynolds number $k - \epsilon$ turbulence model of Launder and Sharma [172] or a laminar elliptic code. For $s = -1$, the weakly turbulent flow is of Stewartson type, whereas the laminar computations and measurements produce a Batchelor type of flow. The transitions from laminar to turbulent regime and from Batchelor to Stewartson flow structure occur for $s = -0.4$. A good agreement is obtained in the rotor-stator configuration ($s = 0$) and in the exactly counter-rotating regime ($s = -1$) but at intermediate values of s , the agreement is less satisfactory. The same authors [102] performed the same comparisons when a radial outflow of air is superimposed.

In this Chapter, the numerical predictions using the Reynolds Stress Model described in Chapter 4 are compared to velocity measurements performed at CEA for the turbulent flow between two counter-rotating disks. The main objective is to acquire a precise knowledge of both the flow structure and the turbulence properties of the highly turbulent Von Kármán flow between smooth disks for a large range of the flow parameters. A second objective is to propose an easy and efficient way to model impellers and to quantify their effect on the Von Kármán flow at high Reynolds number.

9.2 Geometrical configuration and flow parameters

Velocity measurements using a laser Doppler velocimeter have been performed at CEA in the Von Kármán geometry during the PhD thesis of Ravelet [270] and then by Romain Monchaux [213] in two cases: viscous and inertial stirrings.

9.2.1 Geometrical configuration

The Von Kármán flow generated by two counter-rotating disks fitted or not by straight blades in a cylindrical vessel is illustrated in Figure 9.2. The geometrical parameters are fixed by the values studied experimentally by Ravelet [270]. The cylinder and disk radii are respectively $R_c = 100$ mm and $R = 92.5$ mm. The radius ratio R/R_c is then fixed to 0.925. The distance between the inner faces of the disks h can vary between 1 and 180 mm. Disks 1 and 2 rotate respectively clockwise and counterclockwise with two rotation rates denoted Ω_1 and Ω_2 . The motor rotation rates can be varied independently in the range $0 - 900$ rpm, with $|\Omega_1| \geq |\Omega_2|$. One uses bladed disks (n blades of height h_b equal to 10 or 20 mm) to ensure inertial stirring or flat disks for viscous stirring. The impellers are driven by two independent brushless 1.8 kW motors.

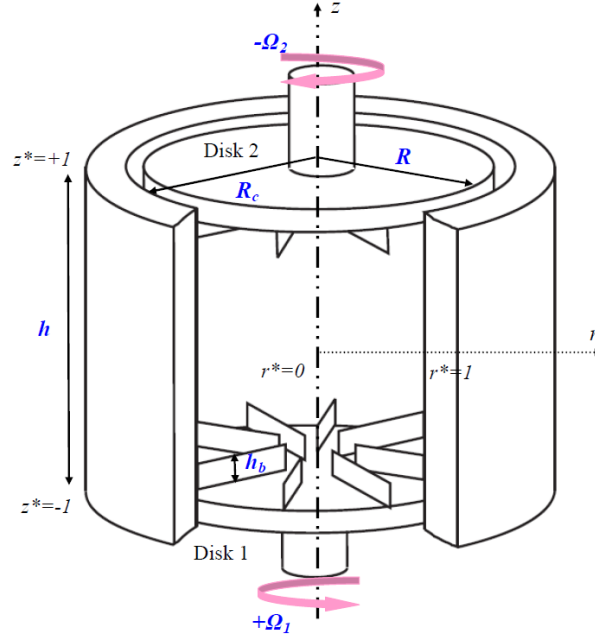


Figure 9.2: Sketches of the Von Kármán flow configuration with relevant notation.

9.2.2 Measurement technique

Velocity measurements are performed using a laser doppler velocimetry (LDV). A basic acquisition of 190.000 randomly sampled values of one velocity component at one point of the flow lasts about two minutes. Due to geometry constraints, one can measure only the axial V_z and tangential V_θ mean velocity components. From this raw data, one may compute the time-averaged flow at every point on a 11×15 grid.

9.2.3 Flow parameters

In the smooth case, the mean flow is mainly governed by three global parameters: the aspect ratio of the cavity G , the rotational Reynolds number Re based on the disk radius and the ratio s between the two rotation rates, defined as follows:

$$0.01 \leq G = \frac{h}{R_c} \leq 1.8 \quad 2 \times 10^5 \leq Re = \frac{\Omega_1 R^2}{\nu} \leq 4 \times 10^6 \quad -1 \leq s = -\frac{\Omega_2}{\Omega_1} \leq 0$$

where ν is the kinematic viscosity of water. In the exact counter-rotating regime and in the rotor-stator configuration, the ratio s is equal to -1 and 0 respectively. One defines also the radial $r^* = r/R_c$ and axial $z^* = 2z/h$ coordinates. Thus, $r^* = 0$ is obtained at the center of the disks and $r^* = 1$ on the outer cylinder for $r = R_c$. In the same way, $z^* = -1$ on the lower disk 1 and $z^* = 1$ on the upper disk 2. In the case of inertial stirring, the number of straight blades n and their dimensionless height $h^* = h_b/R_c$ have also to be considered (h_b the blade height).

9.3 Numerical approach and blade modeling

The predictions of the Reynolds Stress Model (RSM) fully described in Chapter 4 have already been validated in the rotor-stator configuration ($s = 0$) [83, 85, 249, 253] for a wide range of the aspect ratio G and the Reynolds number Re .

It has been verified here that a 120×120 mesh in the (r, z) frame is sufficient in the smooth rotating disk cases to get grid-independent solutions. A refined mesh 160×160 is necessary to model flows with straight blades. About 20000 iterations (almost 20 hours on a bi-Opteron 18 nodes cluster) are necessary to obtain the numerical convergence of the calculation.

At the wall, all the variables are set to zero except for the tangential velocity V_θ , which is set to $\Omega_1 r$ on disk 1, $-\Omega_2 r$ on disk 2 and zero on the stationary cylinder. The usual value $\varepsilon = \nu k_{,j} k_{,j} / (2k)$ is imposed at the wall for the dissipation rate ε of the turbulence kinetic energy. At the periphery of the disks, for $R \leq r \leq R_c$, V_θ is supposed to vary linearly from zero on the stationary cylinder up to $\Omega_1 R$ on disk 1 and $-\Omega_2 R$ on disk 2 and the radial V_r and axial V_z velocity components are fixed to zero.

One can not implement real straight blades in this two-dimensional code. As the most important effect to be modeled is to increase the efficiency of the disks in forcing the flow, a volumic drag force f has been added in the equation of the tangential velocity component V_θ . For n straight blades, the volumic drag force f can be written as:

$$f = \frac{n}{2\pi r} F = \frac{n}{4\pi r} \rho C_D |V_{rel}| V_{rel} \quad (9.1)$$

where F is the drag force of one blade, ρ the fluid density, C_D the dimensionless drag coefficient and $V_{rel} = \Omega_i r - V_\theta$ the relative tangential velocity on disk $i = 1, 2$. The force is designed to make the fluid velocity closer to the local disk velocity near the disks. This form is close to the one proposed by Boroński [28] for spectral code. For curved blades, the same approach could be used: a volumic lift force could be indeed added in the equation of the radial velocity component V_r . Another way to take into account the presence of blades has been proposed by Laguerre *et al.* [166], who introduced a tangential component of the electromotive force in the induction equation only in the two fluid cylinder region occupied by the blades.

The height of the blades ($h^* = 0.1$ or 0.2) is considered to be much larger than the boundary layer thickness $\delta/R_c \simeq Re^{-1/2} \leq 2 \times 10^{-3}$ (for $Re = 2 \times 10^5$). In this case, Blevins [25] proposed some values for the drag coefficient (expected errors of $\pm 20\%$) in an uniform flow. For a thin rectangular plate perpendicular to the mean flow, the value of C_D is in the range $[1.05 - 1.9]$, depending on the size of the plate. As the flow is here not uniform along the blades and as the drag coefficient is supposed to decrease for increasing values of the Reynolds number, C_D is expected to be lower than 2 depending on the flow and blade parameters. Some calculations have been performed for $s = -1$, $G = 1.8$, $Re = 2 \times 10^5$ and straight blades ($h^* = 0.2$, $n = 8$) to study the influence of the trailing coefficient C_D . The differences on the extrema of the tangential velocity component are inferior to 0.5% for C_D in the range $[0.1 - 2]$. Thus, the value of C_D has been fixed to 0.5.

9.4 Smooth disk case: viscous stirring

In this section, the turbulent flow between two counter-rotating smooth disks is considered. Thus, a viscous stirring is ensured: the actuation is done by the setting in rotation of the smooth walls and the movement is communicated to the fluid by diffusion of the momentum through the boundary layers. The influence of the Reynolds number Re , the aspect ratio of the system G , and the ratio s between the two rotation rates on the mean and turbulent fields is investigated in details.

9.4.1 Flow structure in the exact counter-rotating regime

The structure of the mean flow in the exact counter-rotating regime is henceforth globally well known: it can be decomposed into two toroidal cells in the tangential direction θ (not modeled here because of the axisymmetry hypothesis) and into two poloidal recirculations in the (r, z) plane [271].

Regarding the poloidal cells (Fig.9.6a), the fluid at the top and the bottom of the cavity is forced into two opposite rotation speeds, and is then entrained by the disks. Consequently, a shear layer develops in the equatorial plane. This is perceptible in Figure 9.3, which presents axial variations of the tangential velocity component for $s = -1$, $Re = 6.28 \times 10^5$, $G = 1.8$ at five radial locations in the range $r^* = [0.346 - 0.865]$. The radial and axial velocity components are not presented here because they are almost zero in the whole cavity both in the experiments and in the calculations. The tangential component is quite weak too except in the two very thin boundary layers, which develop on each disk and whose size is shown in Figure 9.4 and close to the periphery, where the shear layer is observed. For $r^* \leq 0.476$ (Fig.9.3a,b), the profile exhibits a Stewartson [330] flow structure: a quasi zero tangential velocity zone enclosed by two boundary layers on each disk. The flow in the boundary layers is characterized by a strong tangential velocity component (positive on disk 1 and negative on disk 2) and by a radial outward component not shown here. Towards the periphery (Fig.9.3c-e), the

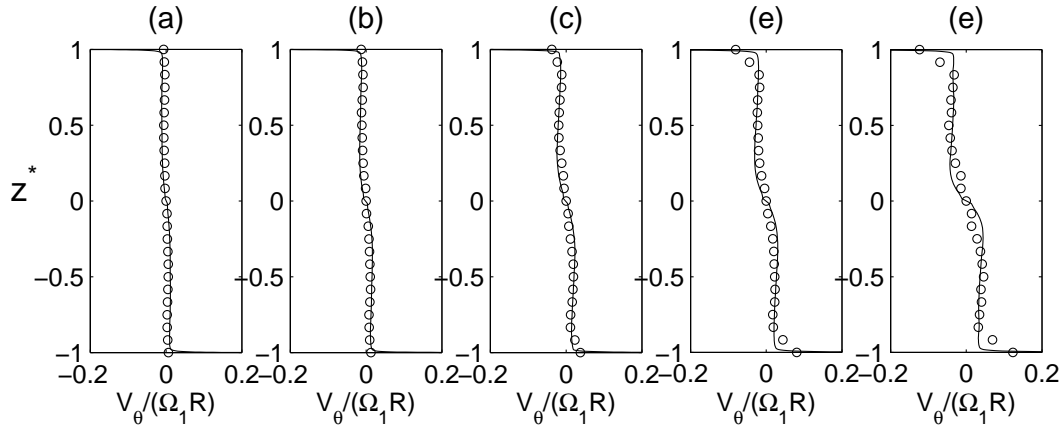


Figure 9.3: Axial profiles of the tangential velocity component for $s = -1$, $Re = 6.28 \times 10^5$ and $G = 1.8$ at five radial locations: (a) $r^* = 0.346$, (b) $r^* = 0.476$, (c) $r^* = 0.605$, (d) $r^* = 0.735$, (e) $r^* = 0.865$. Comparisons between the RSM (—) and the experimental data (\circ) in the smooth disk case.

flow gets of Batchelor type with five distinct zones: two boundary layers on the disks, a shear layer at mid-plane and two zones enclosed between the two. These last two zones are characterized by a weak but non zero tangential velocity component. The shear layer thickens when the local radius r^* increases. Contrary to the laminar case reported by Kilic *et al.* [154], there is practically no radial inflow around $z^* = 0$.

A good agreement between the numerical results and the experimental data is obtained even if the values are quite weak. The RSM model catches the appearance and the thickening of the shear layer. On the other hand, the size of the LDV probe volume in the axial direction (1 mm) is not negligible compared to the boundary layer thickness. It is the main reason why the agreement between the numerical predictions and the measurements is less satisfactory in the boundary layers as it can be seen in Figure 9.3.

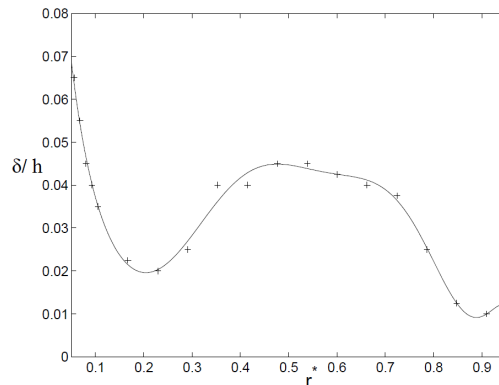


Figure 9.4: Radial evolution of the boundary layer thickness δ/h in the smooth disk case for $s = -1$, $Re = 6.28 \times 10^5$ and $G = 1.8$ (symbols: RSM, line: polynomial interpolation).

The transition between the Stewartson and Batchelor flow structures can also be seen in Figure 9.4 from the radial evolution of the boundary layer thickness δ for the same set of parameters. Very close to the rotation axis, the axial flow impinges the disks and creates very large boundary layers on both disks, whose size decreases with the local radius as expected [104]. The flow is then of Stewartson type. During the transition, δ increases as already observed by Poncet [249] for rotor-stator flows ($s = 0$). For $r^* \simeq 0.47$, the flow is clearly of Batchelor type and then, δ decreases towards the periphery of the cavity. It confirms the visualizations of the laminar flow between co- and counter-rotating disks ($-0.2 \leq s \leq 0.87$) performed by Gauthier *et al.* [104]. They found indeed that the boundary layer

thickness of the slower disk decreases for increasing values of the radial location r^* .

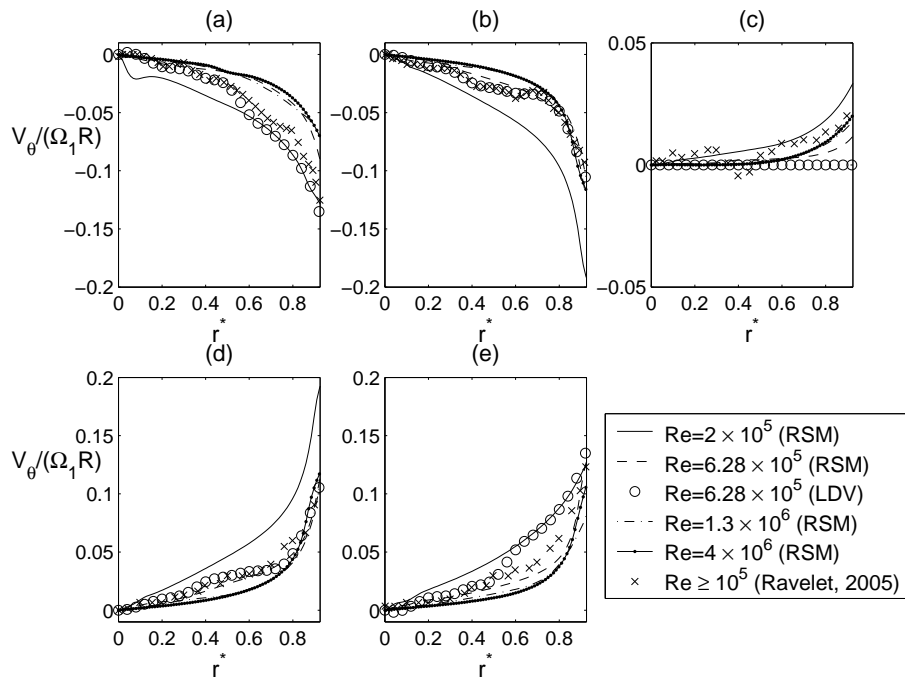


Figure 9.5: Radial profiles of the tangential velocity component in the smooth disk case for $s = -1$, $G = 1.8$ and four Reynolds numbers at different axial locations: (a) $z^* = 0.91$, (b) $z^* = 0.59$, (c) $z^* = 0.02$, (d) $z^* = -0.59$, (e) $z^* = -0.92$.

The influence of the Reynolds number on the mean flow is now investigated. Figure 9.5 presents radial profiles of the tangential velocity component for $s = -1$, $G = 1.8$ and four Reynolds numbers at different axial locations. The numerical predictions of the RSM model are compared to present LDV measurements and to the velocity measurements of Ravelet [270] for $Re \geq 10^5$. The numerical data for $Re \geq 6.28 \times 10^5$ merge almost into a single fitting curve. It means that there is practically no effect of the Reynolds number on the mean field ever since the flow is turbulent. For $Re = 2 \times 10^5$, a significant increase of the magnitude of V_θ is observed whatever the axial position, which is characteristic of the laminar regime. The critical Reynolds number for the transition from the laminar to the turbulent state is thus overestimated compared to the one obtained by Ravelet [270]: $Re = 10^5$. Nevertheless, the present velocity measurements performed on the same experimental set-up as [270] confirm the numerical results. Compared to the previous measurements, an effect of Re is observed on the radial profiles of V_θ at the periphery of the cavity. In fact, the critical Reynolds number for the laminar to turbulent state transition depends strongly on the boundary conditions and especially on the conditions imposed in the radial gap $0.925 \leq r^* \leq 1$. One recalls that a linear profile is imposed in the numerical code for V_θ , that does not take into account any recirculation zone and that could explain this difference. This tendency for relaminarization of the RSM model has already been noticed by Poncet *et al.* [249, 253] in the rotor-stator configuration. As a conclusion, there is no significant effect of the Reynolds number on the mean flow for $Re \geq 10^5$, which confirms the results of Cadot *et al.* [41] and Ravelet [270].

Figure 9.6 presents the corresponding streamline patterns. The mean flow is divided into two symmetric poloidal cells, whose size is equal here to $0.5h$ along the axial direction and independent of the Reynolds number. In the radial direction, the diameter of the largest eddies observed is of the order of the disk radius R , showing that this scale is the order of the energy scale injection. Experimentally, Ravelet [271] observed a weak asymmetry of the flow in the (r, z) plane, which disappears for increasing values of the Reynolds number.

The influence of the aspect ratio of the cavity G on the mean field has also been investigated for $0.01 \leq G \leq 1.8$ (Fig.9.7) and a given Reynolds number $Re = 1.3 \times 10^6$. Note that the radial and most of all the axial velocity components are quite weak compared to the tangential one and to the

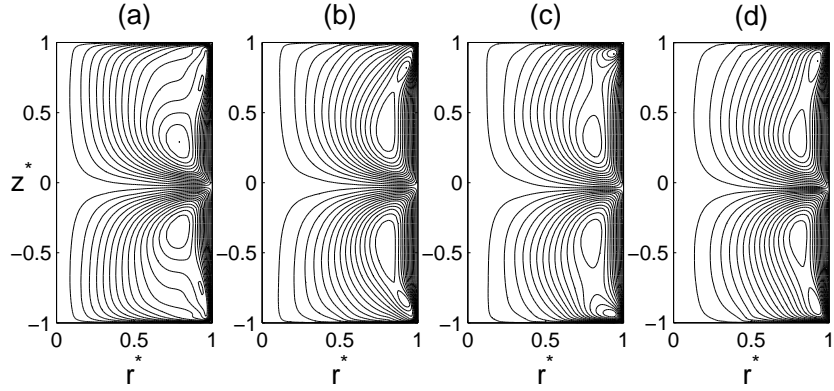


Figure 9.6: Computed streamlines between smooth disks for $s = -1$ and $G = 1.8$ (RSM): (a) $Re = 2 \times 10^5$; (b) $Re = 7.8 \times 10^5$; (c) $Re = 1.3 \times 10^6$; (d) $Re = 4 \times 10^6$.

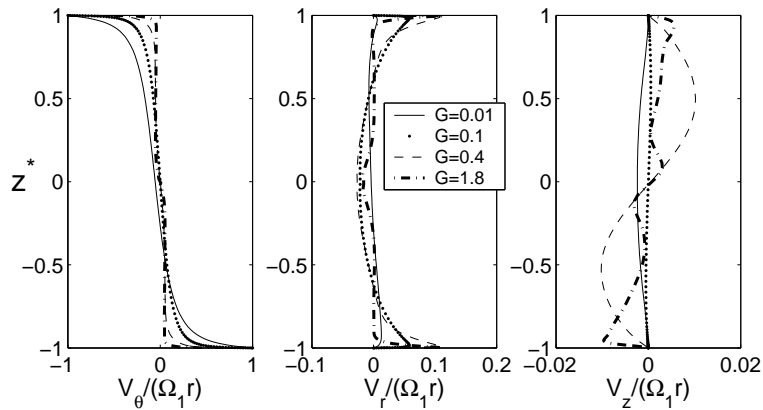


Figure 9.7: Axial profiles of the mean velocity components at $r^* = 0.81$ for $s = -1$, $Re = 1.3 \times 10^6$ and four values of G in the smooth disk case (RSM).

disk velocity. For $G = 1.8$, the boundary layers are separated as already mentioned and the mean tangential velocity component is constant in the core of the flow. For $G = 0.01$, the flow is of torsional Couette type with merged boundary layers as V_θ (Fig.9.7a) varies linearly in the median region of the flow. This is to be compared to the value $G = 0.012$ obtained in the rotor-stator configuration [249]. For intermediate values $G \simeq 0.4$, both boundary layers interact. The transition between the two main regimes is continuous and not clear from the V_θ -profile. Nevertheless, if one considers the V_z -profile (Fig.9.7c), one can clearly see that the axial velocity component is almost zero whatever the value of G , except for $G = 0.4$, where the fluid moves towards the upper and lower disks. The transition can also be characterized by considering the V_r -profiles (Fig.9.7b), which exhibit the thinning of the boundary layers for increasing values of the aspect ratio.

9.4.2 Flow structure for $-1 \leq s \leq 0$

Another interesting feature in counter-rotating disk flows is the influence of the ratio s between the two rotating disk speeds (Fig.9.8). The Reynolds number and the aspect ratio of the cavity are respectively fixed to $Re = 1.3 \times 10^6$ and $G = 1.8$. One focuses on the counter-rotating disk case for which $-1 \leq s \leq 0$.

In the exact counter-rotating regime (Fig.9.8a), the flow is symmetric and two cells with the same size $0.5h$ coexist. For small rotating speed differences, the structure of the mean flow is strongly dominated by the faster disk (Fig.9.8b). Varying the ratio s displaces the shear layer towards the slower disk. The cell close to the lower disk invades almost the whole interdisk spacing for $s = -0.7$ (Fig.9.8d). For $s = -0.2$ (Fig.9.8e), the flow structure resembles the one observed in the rotor-stator

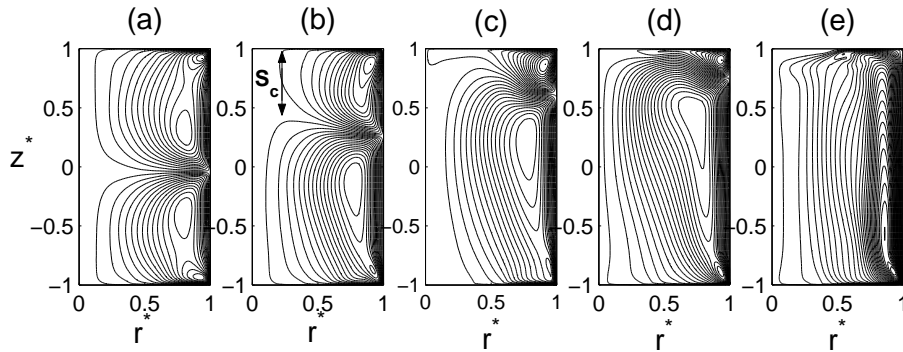


Figure 9.8: Computed streamlines between smooth disks for $Re = 1.3 \times 10^6$ and $G = 1.8$ (RSM): (a) $s = -1$; (b) $s = -0.9$; (c) $s = -0.8$; (d) $s = -0.7$; (e) $s = -0.2$.

configuration [249] with streamline patterns parallel to the rotating axis. This transition between the two cell and the one cell regimes can be seen also from Figure 9.9. It presents the evolution with s of the dimensionless size S_c/h of the smallest cell (along the upper disk) in the axial direction defined in Figure 9.8b. In the smooth disk case, one can notice that S_c decreases rapidly for decreasing values of $|s|$ in the range $-1 \leq s \leq -0.8$ (see also Fig.9.8a-c) following $S_c/h \propto -2.2s$. For smallest values of $|s|$, the cell is reduced to a very thin region attached to the upper disk (Fig.9.8d), which disappears progressively along the external cylinder and so S_c tends to zero.

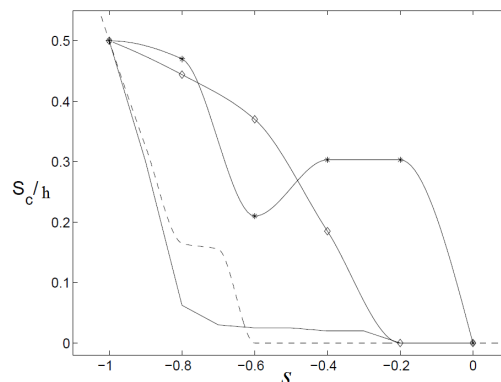


Figure 9.9: Size S_c/h of the smallest cell against s for $G = 1.8$ (RSM). Comparison between (—) the smooth disk case ($Re = 1.3 \times 10^6$), (---) the bladed disk case ($Re = 2 \times 10^5$) and previous numerical results of (*) Kilic et al. [154] and (◇) Gan et al. [102] in the smooth disk case.

In Figure 9.9, the present results are compared to the ones obtained by Kilic et al. [154] and Gan et al. [102], who performed calculations for $-1 \leq s \leq 0$ and $G = 0.12$ using a classical $k - \varepsilon$ turbulence model. Considering that the $k - \varepsilon$ prediction of these authors is in relatively good agreement with the smooth disk case, the comparison given in Figure 9.9 may be meaningful to get an idea of the effect of the aspect ratio. For $Re = 10^5$, Kilic et al. [154] found that the evolution of S_c against s is non monotonous. It decreases more slowly from $s = -1$ to $s = -0.2$ than in our case. It is a combined effect of both the Reynolds number and the aspect ratio of the cavity. For $s = -0.4$, they observed a double transition: from laminar to turbulent flow and from Batchelor to Stewartson type of flow. The decrease of S_c is much faster with s in the laminar case [154]. For $Re = 1.25 \times 10^6$, Gan et al. [102] obtained streamline patterns different from the ones shown in Figure 9.8 for $s = [-0.8; -0.2]$ essentially because of the small value of G . A large cell along the slower disk is still observed for $s = -0.4$. This cell is trapped by the main flow due to the faster disk in the zone $0.3 \leq r^* \leq 0.45$.

9.4.3 Turbulence field in the exact counter-rotating regime

As already mentioned above, the influences of both the Reynolds number and the aspect ratio are relatively weak (compared to the effect of the ratio s between the rotation rates). In the following, one focuses on the exact counter-rotating regime $s = -1$ and Re and G are fixed respectively to $Re = 6.28 \times 10^5$ and $G = 1.8$.

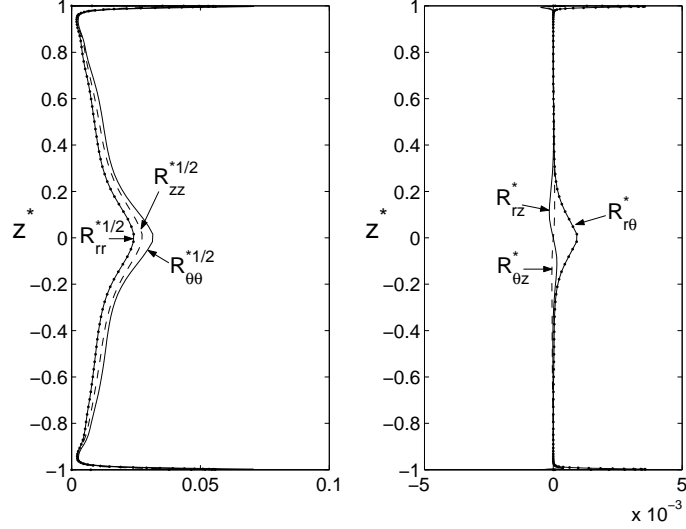


Figure 9.10: Axial profiles of the six Reynolds stress tensor components at $r^* = 0.81$ for $s = -1$, $G = 1.8$ and $Re = 6.28 \times 10^5$ in the smooth disk case (RSM).

Figure 9.10 presents the axial profiles of the six components of the Reynolds stress tensor. These components are normalized by the local disk 1 velocity $\Omega_1 r$. For example, R_{rr}^* is defined as: $R_{rr}^* = \overline{v_r^2} / (\Omega_1 r)^2$. As in all rotating disk problems [253], turbulence is mainly concentrated in the boundary layers with the same turbulence levels in the upper and lower disk boundary layers. The main difference with the rotor-stator configuration is that turbulence is also generated in the median region of the interdisk spacing and is due to the shear, stretched by the recirculations. The Von Kármán arrangement is indeed known to produce an intense turbulence in a compact region of space [201]. The magnitudes of the three normal components are almost the same in the equatorial plane. It means that turbulence is quasi isotropic in that region. The cross components are quite weak except for the $R_{r\theta}^*$ component, which behaves like the normal components with a bump at mid-plane.

As expected, the maximum of the turbulence Reynolds number $Re_t = k^2 / (\nu \varepsilon) = 5836$ is located in the shear layer close to the periphery of the cavity, where the highest values of the local Reynolds number $Re_r = \Omega_1 r^2 / \nu$ are obtained (Fig.9.11a). This maximum is to be compared to the maximum value $Re_t \simeq 500$ obtained by Poncet [249] for $s = 0$ and $Re \simeq 10^6$, which indicates the high turbulence level in that region.

Figure 9.11b shows the anisotropy invariant map for the Reynolds stress tensor in the whole interdisk spacing at $r^* = 0.51$. The second A_2 and third A_3 invariants of the anisotropy tensor a_{ij} of the second moments of the fluctuations are defined as: $A_2 = a_{ij} a_{ji}$ and $A_3 = a_{ij} a_{jk} a_{ki}$ [192], where $a_{ij} = R_{ij} / k - \frac{2}{3} \delta_{ij}$ (δ_{ij} the Kronecker symbol). The results of the RSM model satisfy the realizability diagram of Lumley [192]. Very close to the disks, the turbulence tends to follow the two-component behavior as the wall normal fluctuations are damped more effectively than fluctuations parallel to the disk. Outside the boundary layers and especially in the shear layer, turbulence is fairly close to the isotropic case ($A_2 = A_3 = 0$), which confirms the results observed from Figure 9.10. Note that very close to the mid-plane, the flow tends to the axisymmetric limit.

9.5 Bladed disk case: inertial stirring

To increase the efficiency of the disks in forcing the flow, n blades of height h^* are mounted on both disks. The stirring is called inertial because the fluid is set into motion thanks to areas of forcing

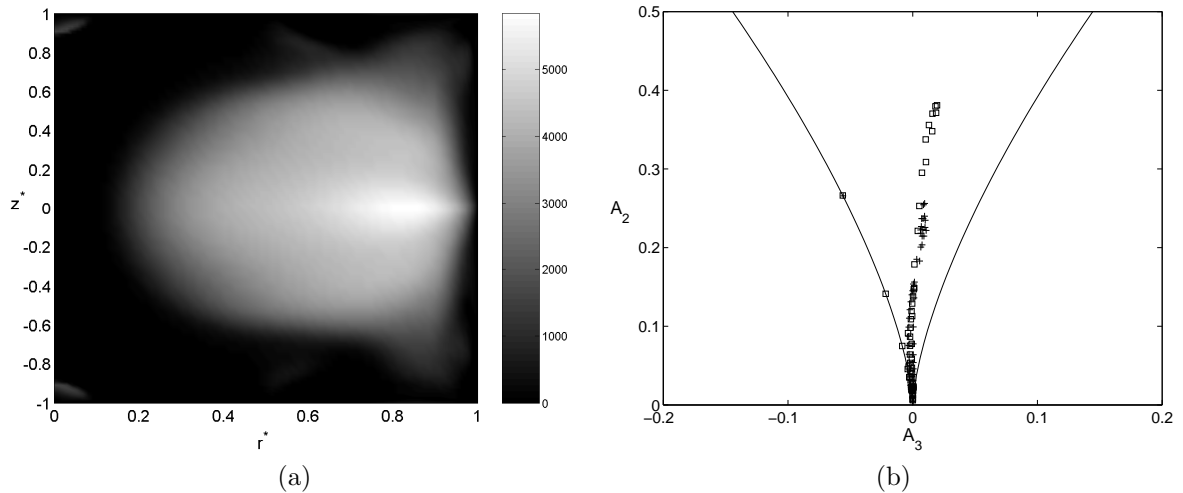


Figure 9.11: $s = -1$, $G = 1.8$ and $Re = 6.28 \times 10^5$ in the smooth disk case (RSM): (a) Iso-turbulence Reynolds number $Re_t = k^2/(\nu\varepsilon)$ - (b) Anisotropy invariant map at $r^* = 0.51$: (\times) $-1 \leq z^* \leq 0$, (\square) $0 \leq z^* \leq 1$.

perpendicular to the motion itself. In that case, Ravelet [270] showed that all mean and turbulent quantities are independent of the Reynolds number in the range $Re = [10^5, 2 \times 10^6]$. Thus, the parameters are fixed to $Re \simeq 2 \times 10^5$ and $G = 1.8$. In that case, the boundary layers are separated and the flow is found to be highly turbulent. Moreover, direct comparisons with the experiments of Ravelet [270] can be performed. The purpose of this section is to propose an efficient way to model the effect of straight blades on both the mean and turbulent fields.

9.5.1 Flow structure in the exact counter-rotating regime

In the bladed disk case, the flow structure is completely different from the smooth disk case, where the velocity gradient are located in the boundary layers along the disks and decrease when the Reynolds number increases. For an inertially driven flow, the mean flow does not present any appreciable velocity gradient in the vicinity of the blades (Fig.9.12) and the gradients are distributed in the median region of the flow. The mean flow is divided into three main regions: a shear layer at mid-plane and two fluid regions close to each bladed disk. The intensity of the shear at mid-plane is increased compared to the viscous stirring case. This shear is due to the two recirculation cells. It induces a strong radial inflow ($V_r < 0$) around $z^* = 0$ and two opposite axial flows towards the disks. The magnitude of the mean axial and radial velocity components increase from the periphery (Fig.9.12c) to the rotation axis (Fig.9.12a). From the disk to the top of the blades, the tangential fluid velocity is fairly close to the local disk velocity. Moreover, a strong radial outflow is created along the bladed disks and goes with the impellers. At the top of the blades, there is a strong decrease of $|V_\theta|$ interpreted as the wake of the blades. There is a very good agreement between the numerical predictions and the velocity measurements concerning the V_θ -profiles. A small difference is observed in the shear layer, where the RSM model predicts a thinner layer than the one measured by Ravelet [270]. This last author observed, for the same set of parameters, high energy levels for frequencies inferior to the injection frequency. This contribution is attributed to the appearance of strong coherent structures in the shear layer not observed in the smooth disk case and which may explain the weak discrepancies obtained.

9.5.2 Flow structure for $-1 \leq s \leq 0$

The same analysis as in the smooth disk case is performed by varying the ratio s between the two rotating disk speeds. Figure 9.9 presents comparisons between the smooth and bladed disk cases concerning the size S_c of the cell along the slowest disk for $-1 \leq s \leq 0$. The same behavior is obtained but the transition between the two cell and the one cell structures ($S_c \rightarrow 0$) is slightly delayed. It occurs in the inertial stirring case for $s \simeq -0.65$, which is close to the experimental value obtained by Cadot and Le Maître [42] in the same configuration $s = -0.69$ and the analytical one

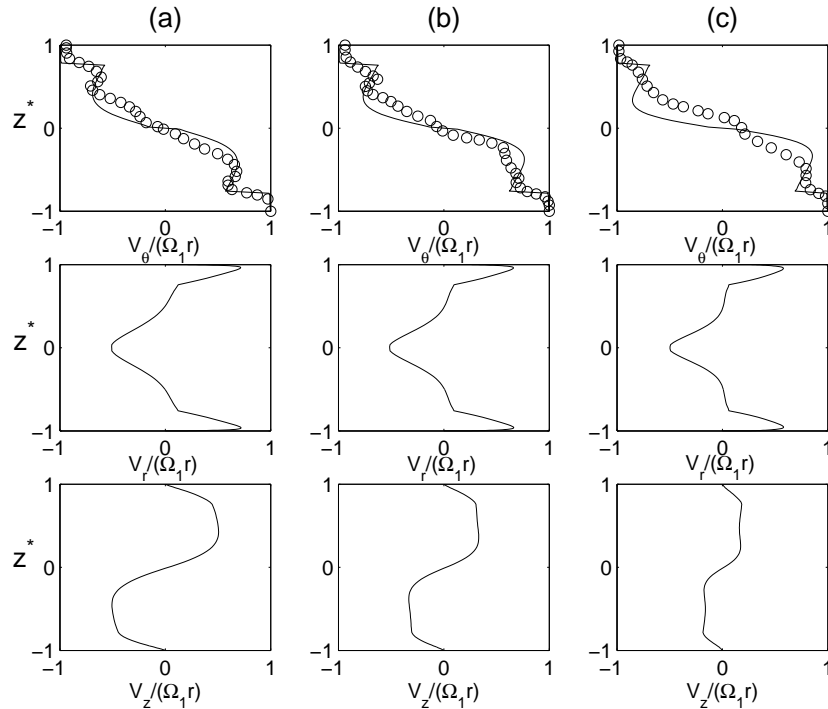


Figure 9.12: Axial profiles of the mean velocity components for $s = -1$, $Re = 2 \times 10^5$, $G = 1.8$ and straight blades ($n = 8$, $h^* = 0.2$) at three radial locations: (a) $r^* = 0.4$, (b) $r^* = 0.5$, (c) $r^* = 0.6$. Comparisons between the RSM model (lines) and the LDV measurements of Ravelet [270] (o).

obtained by Dijkstra and Van Heijst [72] for $Re \rightarrow 0$ and $s = -2/3$ in the smooth disk case. The measurements of Ravelet [270] reveal a transition for $s = -0.78$. It confirms the similitude observed by Cadot and Le Maître [42] between the smooth disk flow with a large viscosity and the mean flow in the inertial stirring case.

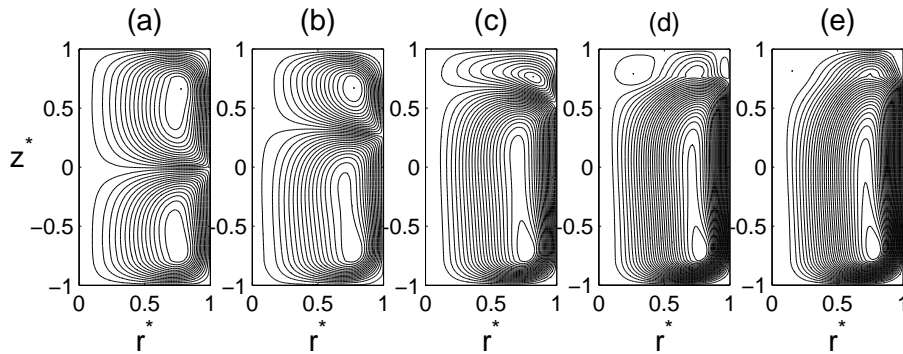


Figure 9.13: Computed streamlines obtained by the RSM for $Re = 2 \times 10^5$, $G = 1.8$ and straight blades ($n = 8$, $h^* = 0.2$): (a) $s = -1$; (b) $s = -0.9$; (c) $s = -0.8$; (d) $s = -0.7$; (e) $s = -0.6$.

The transition from the two cell to the one cell structures can be seen also from Figure 9.13. Compared to the smooth disk case, the cell along the slowest disk is larger for $s = -0.8$ (Fig.9.13b). For $s = -0.7$, only a small recirculation subsists along the upper disk and completely disappears for $s = -0.6$. For $s \geq -0.6$, the same pattern is observed with streamlines parallel to the rotation axis.

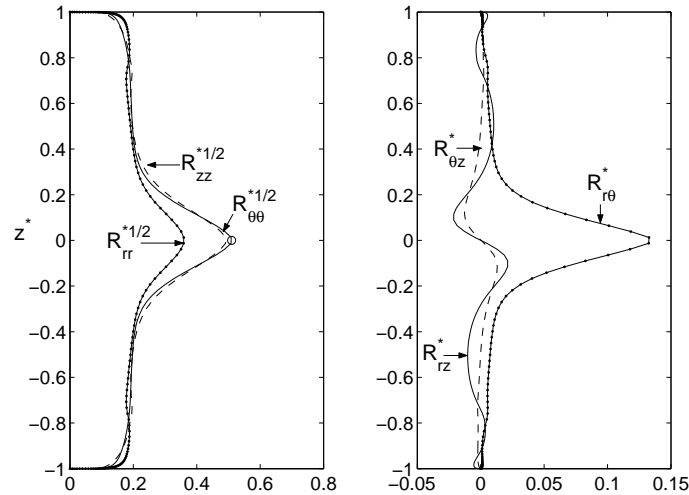


Figure 9.14: Axial profiles of the six Reynolds stress tensor components at $r^* = 0.81$ for $s = -1$, $G = 1.8$, $Re = 2 \times 10^5$ and straight blades ($n = 8$, $h^* = 0.2$)(RSM). (o) LDV data of Ravelet [270] for $R_{\theta\theta}^{*1/2}$.

9.5.3 Turbulence field in the exact counter-rotating regime

To enable direct comparisons with the viscous stirring case, Figure 9.14 presents the axial profiles of the six components of the Reynolds stress tensor at the same radius $r^* = 0.81$ and for the same values of G and s . The main difference between the smooth and the bladed disk configurations is that, in the latter case, the turbulence intensities vanish towards the disks. Apart from that, turbulence is also mostly generated at mid-plane because of the shear stretched by the recirculations. The blades induce a much stronger shear zone in the equatorial plane compared to the smooth disk case as already seen from the mean velocity profiles (Fig.9.12). Thus, the turbulence levels, regarding the normal Reynolds stress components (Fig.9.14a), are almost 20 times larger than for viscous stirring and quite comparable to the mean fluid velocity. It confirms the previous measurements of Cadot *et al.* [41] in steady regimes of turbulence in the Von Kármán geometry. They found that the fluid velocity fluctuations are close to the fluid mean velocity and 6 times larger in the bladed disk case than in the smooth disk case. In the present study, the R_{rr}^* component is much weaker than the two other normal components, which indicates the turbulence anisotropy in the core of the flow. The cross components are also stronger than in the smooth disk case. The level of the $R_{r\theta}^*$ component (Fig.9.14b) is of the order of R_{rr}^* . Note that the maximum of the $R_{\theta\theta}^{*1/2}$ component obtained at mid-plane ($z^* = 0$) using the RSM model is in excellent agreement with the asymptotic value measured by Ravelet [270] for $Re \geq 10^4$ (relative error inferior to 0.1%). Nevertheless, one must remark that only a single measurement point is available, and consequently it is hard to derive definite conclusions. Another point is that the periodic unsteadiness introduced by the blades is not exactly accounted for in the calculation and may explain small discrepancies in the mean velocity profiles.

To study the influence of the number n of blades and their height h^* on the turbulent field, Figure 9.15 shows radial profiles of the turbulence kinetic energy k^* normalized by $(\Omega_1 R)^2$ for various impeller configurations. These profiles are plotted at mid-plane where the maximum of k^* prevails. As expected, k^* increases towards the periphery of the cavity, it means for increasing local Reynolds number. Then, k^* decreases for radial locations in the gap between the disks and the external cylinder. One can first notice the very weak level of turbulence kinetic energy in the smooth disk case compared to the other bladed disk cases. Secondly, the influence of the blade number n is quite weak for $n = 4$, 8 or 16. Only very close to the rotation axis, one can remark a different behavior in the configuration with 16 blades. Nevertheless, in the whole flow, four blades seem to be sufficient to force the flow. On the other hand, the blade height plays a more important role. The k^* level is twice higher when the blades are twice higher too.

It is now established that all mean and turbulent quantities are independent of the Reynolds number in the range $Re = [10^5, 2 \times 10^6]$. The turbulent dissipation is indeed much stronger than the

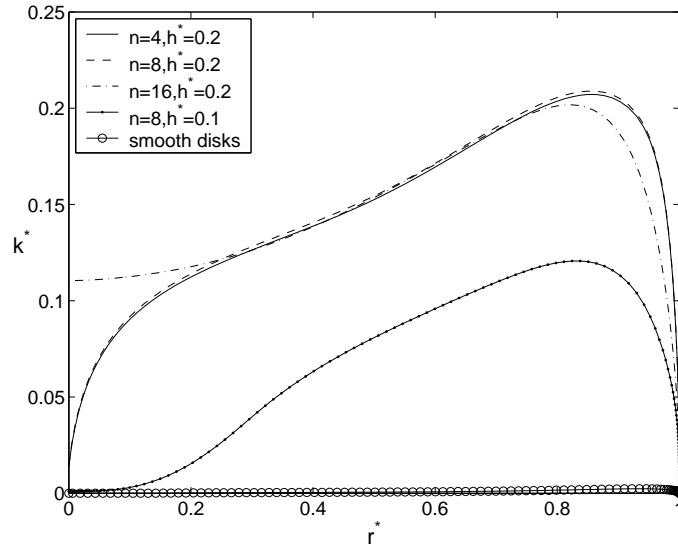


Figure 9.15: Radial profiles of the turbulence kinetic energy $k^* = k/(\Omega_1 R)^2$ at $z^* = 0$ for $s = -1$, $G = 1.8$, $Re = 2 \times 10^5$ and different bladed disk configurations - comparison with the smooth disk case ($Re = 6.28 \times 10^5$) (RSM).

dissipation due to the boundary layers and hides the dependence on Re . All these results can thus be extended to higher Reynolds numbers.

9.6 Conclusion

Some comparisons between numerical predictions using a RSM model and velocity measurements have been performed for the turbulent flow between two flat or bladed counter-rotating disks. This configuration known as the Von Kármán geometry is used to produce an intense turbulence in a compact region of space.

For viscous stirring, the flow is of Stewartson type close to the rotation axis and so exhibits three distinct regions: two boundary layers and one shear layer at mid-plane. When one approaches the periphery of the cavity, for $r^* \simeq 0.476$, the flow gets of Batchelor type. Turbulence is mainly concentrated in the boundary layers and in the transitional shear layer, where turbulence is almost isotropic. Turbulence intensities increase towards the outer cylinder. When one decreases the aspect ratio of the cavity until $G \leq 0.4$, the boundary layers mixed and the flow is then of torsional Couette type for lower values of G . In the case of inertial stirring, the impellers are more efficient to force the flow. Thus, the transitional shear layer intensifies. Turbulence is so mainly concentrated around $z^* = 0$ and vanish towards the disks. The turbulence intensities are almost 20 times larger than in the flat disk case. The height of the blades is found to be the preponderant parameter to increase the turbulence intensities more than the number of blades. In the flat and bladed disk cases, it has been numerically verified the statement of Cadot *et al.* [41]: “smooth or rough, the efficiency of a given type of stirrer to set the bulk of the fluid in motion is independent of the Reynolds number”. Moreover, one has characterized the transition between the two cell and the one cell regimes. For inertial stirring, it occurs for $s \simeq -0.65$ close to the values obtained by Dijkstra and Van Heijst [72] and Cadot and Le Maître [42].

The agreement between the numerical predictions and the LDV measurements is very satisfactory in both cases. For the first time, an easy and efficient way to model the main effect of straight blades has then been proposed.

Part IV

Taylor-Couette flows between concentric cylinders

Part III: Taylor-Couette flows between concentric cylinders

Summary: In this part, we switch to flows confined between two concentric cylinders with the inner one being rotating and the outer one being stationary. It has been totally inspired by the industrial contract with the Liebherr Aerospace company on the effective cooling of rotating walls in electrical motors, which will be considered in Chapter 12. The two first chapters are only pleas to validate the numerical code based on the fourth-order compact schemes. Thus, in Chapter 10, the stability of Taylor-Couette flows with radial temperature gradient is investigated by DNS to validate both the heat transfer approach and the multidomain decomposition technique. Chapter 11 is a numerical benchmark of turbulence models considering the original geometrical configuration of Burin *et al.* [40] with endcap rings to validate the multidomain decomposition technique in the turbulent regime.

Influence of a radial temperature gradient on the flow stability

In 2008, one initiated a collaboration with a new industrial partner, Liebherr Aerospace Toulouse, on the cooling of electrical motors. These flows can be simply modeled by a Taylor-Couette system with a superimposed axial Poiseuille flow and a radial temperature gradient. It will be the subject of Chapter 12. To simulate these flows with the in-house DNS code based on compact schemes, it was necessary to make some numerical developments to take into account heat transfer effects and most of all, the large aspect ratio of the cavity in the axial direction. The experimental data on the stability of Taylor-Couette flow with a radial thermal gradient obtained by Guillerm [117], who was at that time postdoc on that project, was then a valuable database to validate both the implementation of the energy equation and the multidomain approach. The goal was thus mainly to validate the numerics and so the stability diagram established by Guillerm [117] has been explored by extensive computations without going into too much details. As a consequence, this Chapter is without any doubt the less accomplished one of this habilitation thesis also because some calculations are still in progress. The results presented during the Euromech Conference held in Roma in 2012 are currently under review.

10.1 Introduction

Taylor-Couette flows confined between two concentric cylinders have been widely considered since the pioneering work of Couette [59] in 1890, which has led up to now to an abundant literature. Nowadays it still receives a constant attention from the scientific community because of its relevance to numerous engineering applications: the cooling of electronic motors [256], thermal energy storage systems or electrical transmission cables. In rheology, the Taylor-Couette flow confined between a permeable rotating inner cylinder and an impermeable concentric outer cylinder is a prototype flow for dynamic rotating filtration [338]. When an axial flow is superimposed, it is used as a novel reactor type offering a wide range of mixing regimes [332]. In the presence of axial stratification, it finds also direct applications in geophysics to model atmospheric or oceanic flows and in astrophysics for accretion disks [174].

For an enclosed annulus with independently rotating cylinders, a wide variety of flow states, both laminar and turbulent, as well as states with the co-existence of laminar and turbulent regions, can occur after the first transition to the regular Taylor vortex flow. The critical Taylor numbers for the appearances of these various patterns are dependent on a large number of factors, including the rotation ratio and cavity dimensions. Di Prima and Swinney [71] proposed a large review of the different studies up to 1981 with, in particular, the values of the critical Taylor numbers as a function of the radius ratio and the angular velocity ratio. Andereck *et al.* [9] established the transition diagram according to the Reynolds numbers based on the tangential velocity of the inner and outer cylinders respectively. It became a very useful guide for the experimental [112], numerical [65] or theoretical investigations, which followed. When the inner cylinder is stationary and the outer one is rotating, Taylor-Couette flows as well as other shear flows like Hagen-Poiseuille flows, plane Couette flows ... are linearly stable. Thus, the transition to turbulence can occur via the appearance of edge states. Compared to these other configurations, the Taylor-Couette problem has the main advantage to be 2π -periodic, which does not require very long cavities as in pipe flows for example. Very recently, Borrero-Echeverry *et al.* [29] observed that, at sufficiently high Reynolds numbers, laminar and turbulent patches can coexist with the same decay characteristics than in the other configurations. The reader can refer to Lueptow [191] for fundamentals on Taylor-Couette flows and to F enot *et al.* [94] for a recent exhaustive review.

In the non-isothermal case, the strong competition between two mechanisms, an azimuthal flow due to rotation and an axial flow due to convection effects, leads indeed to a wide variety of spectacular instability patterns with some noticeable differences compared to the isothermal case. Snyder and Karlsson [325] have performed extensive measurements in a tall narrow-gap annulus (aspect ratio $\Gamma = h/\Delta R = 337$, radius ratio $\eta = a/b = 0.958$) to understand the influence of a weak radial temperature gradient on the stability of water flows (a and b the radii of the inner and outer cylinders respectively, $\Delta R = b - a$ and h the cylinder height). They have observed that small positive or negative radial temperature gradient stabilizes the base flow. For larger temperature gradients, they successively obtained spirals, wavy vortices and then a transition to Taylor vortices at high Taylor numbers. Sorour and Coney [328] have found experimentally that an imposed radial temperature gradient leads first to the appearance of stationary axisymmetric toroidal vortices for oils with large Prandtl numbers ($Pr \in [300 - 860]$). Ball *et al.* [14] classified the different flow regimes obtained by flow visualizations using the Richardson number $Ri = Gr/Re^2$ (Gr and Re the Grashof and Reynolds numbers), which is the ratio between the buoyancy and inertia forces. For $Ri < 0.01$, rotation is dominant over the buoyancy, whereas for $Ri \in [0.01; 10]$, both effects play an important role in the transition process. For $Ri > 10$, the flow is destabilized by the buoyancy only. Ali and Weidman [7] performed a linear stability analysis for non-axisymmetric perturbations for a wide range of the global flow parameters. Liu *et al.* [186] investigated the stability of Taylor-Couette flows with a radial temperature gradient by digital PIV for four different outer cylinders, smooth or with different number of slits ($\eta = 0.825$, $\Gamma = 48$). Lepiller *et al.* [180] studied the influence of a radial temperature gradient on the stability of circular Couette flows in the non-rotating case. It is found to destabilize the flow leading to a pattern of traveling helicoidal vortices occurring only near the bottom of the system. They invade progressively the whole cavity by increasing the Taylor number Ta . It has been extended later by Guillerm [117] for small rotation rates of the inner cylinder. He provided the most exhaustive experimental study in this configuration, which will serve as reference data in the present work. Using flow visualizations and thermochromic liquid crystals, he established the stability diagram in a (Gr, Ta) plane and the main instability characteristics. Recently, Yoshikawa *et al.* [360] performed a linear stability analysis (LSA) for given values of Pr and η . A small stabilization zone is obtained near the isothermal situation. Otherwise, the radial temperature gradient destabilizes the flow and leads to spiral vortices traveling in the azimuth with large wavelengths compared to the stationary Taylor modes. By studying the perturbation kinetic energy, they proposed different values of the Richardson number compared to Ball *et al.* [14] to distinguish the three flow regimes: $Ri < 0.002$ (rotation dominates), $Ri \in [0.01; 10]$ (both effects coexist) and $Ri > 3.75$ (buoyancy dominates).

At the present time, there is clearly a lack of numerical investigations in this configuration to obtain more quantitative data, especially for large aspect ratio cavity as pointed out by Yoshikawa *et al.* [360]. To our knowledge, Kuo and Ball [163] and Kedia *et al.* [152] are the only ones to consider this problem numerically. Kuo and Ball [163] performed six simulations using a pseudo-spectral method with Chebychev polynomials in the radial and axial directions in a small aspect ratio cavity ($\Gamma = 10$, $\eta = 0.5$). Kedia *et al.* [152] investigated the effects of the gravitational and centrifugal potentials on the stability of Taylor-Couette flows assuming the problem as being periodic in both tangential and axial directions. They calculated the heat transfer coefficients for an air flow at fixed Taylor number ($Ta = 200$) and radius ratio ($\eta = 0.5, 0.7$) considering a large range of Grashof numbers. The present work is then an attempt to fill this gap in the case of an enclosed cavity of large aspect ratio ($\Gamma = 80$) avoiding the appearance of edge effects as observed by Kuo and Ball [163] for $\Gamma = 10$. Very elongated Taylor-Couette systems are very challenging for numerical methods. The present work represents the first DNS for such a high-aspect ratio cavity. The goals are firstly to confirm or not the stability diagram established experimentally by Guillerm [117], secondly to describe all instability regimes in terms of the flow and thermal fields and thirdly to characterize the heat transfer process.

The Chapter is organized as follows: the global flow parameters and the numerical method are first briefly described in Sections 10.2 and 10.3 respectively. The numerical method is first validated in Section 10.4 against analytical solutions, enabling also to describe the base flow. The large variety of instability patterns and their main characteristics are then shown and discussed in Section 10.5. The distributions of the moment and heat transfer coefficients are presented in Section 10.6. Some concluding remarks are finally provided in Section 10.7.

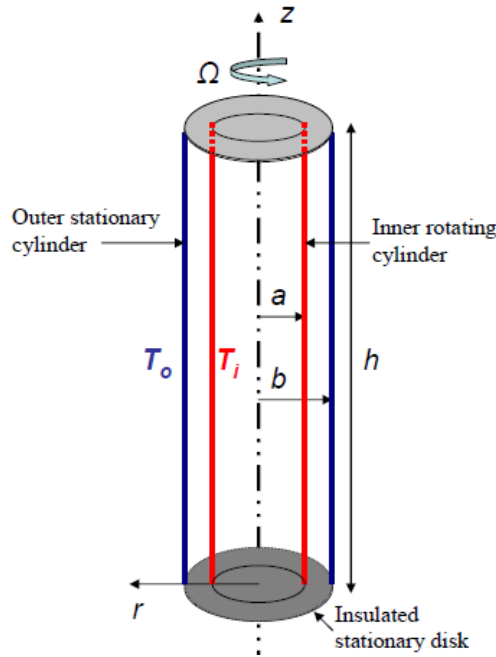


Figure 10.1: Schematic representation of the Taylor-Couette system submitted to a radial temperature gradient with relevant notations ($T_i > T_o$).

10.2 Global flow parameters

The cavity sketched in Figure 12.2 consists of two smooth concentric and vertical cylinders of height $h = 400$ mm. The radii of the inner and outer cylinders are fixed to $a = 20$ and $b = 25$ mm respectively, so that the gap width is set to $\Delta R = b - a = 5$ mm. The cylinders are enclosed by two insulated stationary disks attached to the outer cylinder. The inner rotating cylinder rotates at a constant rotation rate Ω . A temperature gradient $\Delta T = T_i - T_o$ is applied between the inner (at T_i) and outer (at $T_o < T_i$) cylinders. The results will be discussed later in terms of four global parameters defined as follows to enable direct comparisons with Guillerm [117]:

- the radius ratio of the cavity $\eta = a/b = 0.8$ (narrow-gap system);
- the aspect ratio $\Gamma = h/\Delta R = 80$ of the cavity. This value is slightly reduced compared to the experimental one $\Gamma = 111.8$ of Guillerm [117] to save computation time;
- the Taylor number $Ta = \tau_\nu/\tau_e = \Omega a \Delta R (\Delta R/a)^{1/2}/\nu$ defined as the ratio between the viscous diffusion time $\tau_\nu = (\Delta R)^2/\nu$ (ν the kinematic viscosity) and the Ekman time related to the centrifugal force $\tau_e = (\Delta R/a)^{1/2}\Omega^{-1}$;
- the Grashof number $Gr = (\tau_\nu/\tau_a)^2 = g\alpha\Delta T(\Delta R)^3/\nu^2$, which compares the viscous diffusion time and the characteristic time related to buoyancy $\tau_a = (\Delta R/(g\alpha\Delta T))^{1/2}$. The Prandtl number $Pr = \tau_\kappa/\tau_\nu = \nu/\kappa$, which is the ratio between the thermal ($\tau_\kappa = (\Delta R)^2/\kappa$) and viscous diffusion times, is here fixed to $Pr = 5.5$ (κ the thermal diffusivity). These two parameters can be gathered in only one parameter: the Rayleigh number $Ra = Gr \times Pr$.

Some authors [14] use also the Richardson number $Ri = Gr/Re^2$ ($Re = (a/\Delta R)^{1/2}Ta$) to investigate the stability of Taylor-Couette flows with a thermal gradient. All the computed cases are summed up in Figure 10.2.

10.3 Numerical details

The DNS code used here is the one based on the fourth-order compact schemes for the inhomogeneous directions fully described in Chapter 3. The thermal effects are considered using the Boussinesq

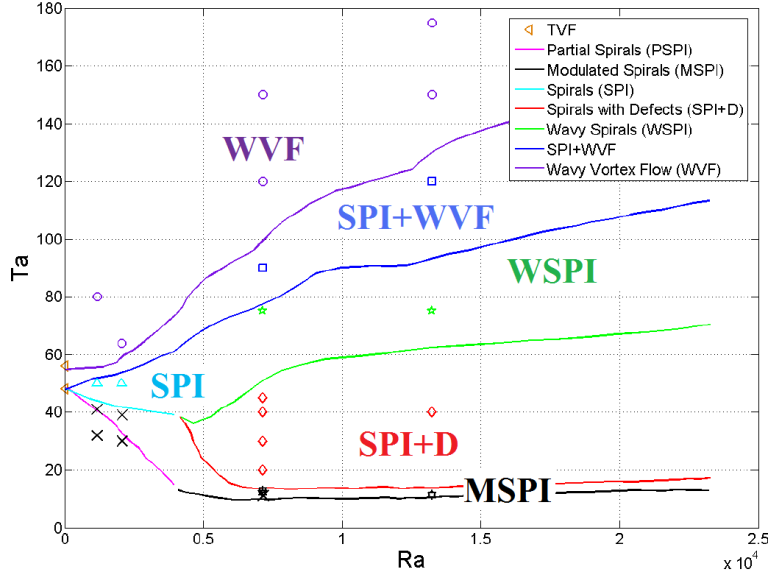


Figure 10.2: Stability diagram in the plane ($Ra > 0, Ta$) obtained experimentally by Guillerm [117] with the present calculations (symbols). Crosses indicate that the flow remains stable.

approximation [113] as temperature differences remain small. Density variations are taken into account only in the gravitational buoyancy term. The maximum value for the Froude number $Fr = \Omega^2 a/g$, which controls the importance of the centrifugal effects, is here $Fr \simeq 0.03$ ($Ta = 175$) well below the common value $Fr = 0.1$ [188] such that the effect of thermal dilatation on the centrifugal body force may be neglected.

Due to the very large aspect ratio of the cavity $\Gamma = 80$, the domain is axially decomposed into 8 subdomains in all the computations. Each subdomain contains $N_\theta = 64$ Fourier modes over 2π and $N_r \times N_z = 61 \times 61$ grid points in the radial and axial directions. This mesh arrangement has proved to be sufficient to get grid independent solutions. In the radial and axial directions, the grid is refined near the interfaces and the physical boundaries using a coordinate transform mapping [3]. The time step δt varies in the range $[2 \times 10^{-3} - 4 \times 10^{-3}]$ s. All calculations performed using the M2P2 cluster have been keeping on until, at least, 20 times the thermal diffusion time. One recalls that the inner and outer cylinders are maintained at constant temperatures T_i and T_o respectively, while the lower and upper stationary disks are insulated. No-slip boundary conditions for the velocity field are applied at all walls.

It is noticeable that some calculations for the same flow parameters have also been performed using Star-CCM+ but this software appears to be not able to capture the present instabilities. For all sets of parameters considered, Taylor vortices have been observed. It proves the importance to use high-order spatial and temporal schemes.

10.4 Base flow

In the case ($\Delta T = 0, \Omega \neq 0$), the base flow is a laminar circular Couette flow far from the endcap disks. The axial and radial velocity components are then null and the azimuthal velocity component U_θ depends only on the radial position r under the form: $U_\theta = Ar + B/r$, where A and B are constants deduced from the boundary conditions on the inner and outer cylinders. On the contrary, for (weak $\Delta T \neq 0, \Omega = 0$), a radial stratification of the density induces a baroclinic flow characterized by a large convection cell within the gap. Far from the disks, an axial upward flow is induced along the inner hot wall and by conservation of mass, fluid moves downwards close to the outer cold wall. The axial velocity component depends only on the radial position r . The radial velocity becomes not negligible in the vicinity of the endcap stationary disks. When both effects coexist ($\Delta T \neq \Omega \neq 0$), the two base flows are superimposed. Maps of these two velocity components, the temperature and the azimuthal vorticity ($\omega_\theta = \partial U_r / \partial z - \partial U_z / \partial r$) are displayed in Figure 10.3 and confirm the superposition of these

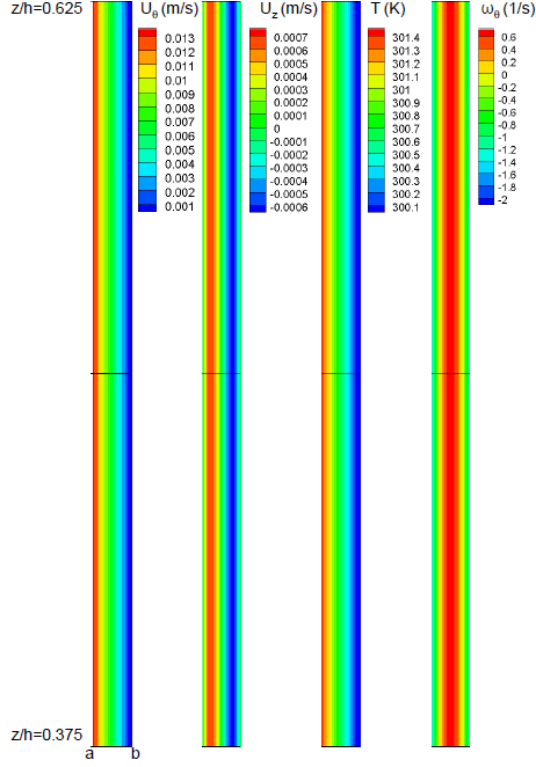


Figure 10.3: Maps of the tangential and axial velocity components, the temperature and the azimuthal vorticity for $Ta = 30$ and $Ra = 2063$ in a $(r \in [a, b], z/h \in [0.375, 0.625])$ plane.

two base flows. The azimuthal vorticity is maximum around mid-gap and this flow region delimitates the upward flow of hot fluid along the rotor and the downward flow of cold fluid along the stator.

For infinite Taylor-Couette systems, analytical solutions for the dimensionless temperature T^* , the axial U_z^* and azimuthal U_θ^* velocity components may be found from the energy and Navier-Stokes equations with the corresponding boundary conditions. They are briefly recalled below (see [117, 360] for more details):

$$T^*(r) = \frac{T(r) - T_o}{\Delta T} = \frac{\ln[(1 - \eta)r/\Delta R]}{\ln \eta} \quad (10.1)$$

$$U_z^*(r) = \frac{U_z(r)}{\alpha \Delta T g (\Delta R)^2 / \nu} = AB \left[(1 - \eta^2) \left(\left(\frac{r}{\Delta R} \right)^2 + T^*(r) \right) - 1 \right] - 4A \left[(1 - \eta)^2 \left(\frac{r}{\Delta R} \right)^2 - \eta^2 \right] T^*(r) \quad (10.2)$$

$$A = \frac{1}{16(1 - \eta)^2} \quad B = \frac{(1 - \eta^2)(1 - 3\eta^2) - 4\eta^4 \ln \eta}{(1 - \eta^2)^2 + (1 - \eta^4) \ln \eta}$$

$$U_\theta^*(r) = \frac{U_\theta(r)}{\Omega a} = \frac{\eta}{1 + \eta} \left[-\frac{r}{\Delta R} + \frac{1}{(1 - \eta)^2} \frac{\Delta R}{r} \right] \quad (10.3)$$

The present DNS is compared to the analytical solution for $Ta = 30$ and $Ra = 2063$ in Figure 10.4. There is a perfect agreement between the two approaches, which validates the numerical approach. The temperature and azimuthal velocity profiles exhibit a weak curvature due to the high value of the radius ratio $\eta = 0.8$. A weak asymmetry is observed for the axial velocity component induced by the curvature of the system and inflexion points may be observed. This profile may become unstable to infinitesimal perturbations after the Rayleigh criterion, leading to different modes of instability. The radial profile of the azimuthal vorticity is also asymmetric and confirms that ω_θ^* is maximum at $r^* = 0.5$.

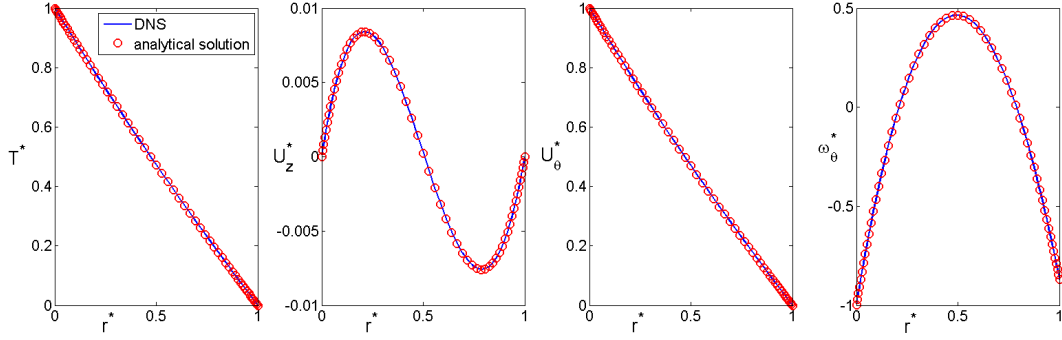


Figure 10.4: Radial distributions of the temperature T^* , the axial V_z^* and tangential V_θ^* velocity components and the azimuthal vorticity ω_θ^* for $Ta = 30$ and $Ra = 2063$ at mid-height. Comparisons with the analytical solution (Eqs.10.1 - 10.3).

10.5 Instability regimes

28 DNS calculations have been performed here and compared to the experimental data of Guillerm [117]. This author showed that the sign of the temperature gradient does not affect significantly the stability of such flows confirming the former work of Snyder and Karlsson [325]. The slight departure from a symmetric behavior is attributed, according to these last authors, to the Rayleigh instability in the centrifugal field, which makes the flow slightly more stable for $\Delta T < 0$ than for the corresponding positive values. In the following, one will focus only on the case $Ra > 0$.

10.5.1 Stability diagram

At a given Rayleigh number, the flow becomes unstable with the appearance of vortices when the Taylor number is increased without any numerical perturbation. The stability diagram obtained experimentally by Guillerm [117] is plotted here in a (Ra, Ta) plane (Fig.10.2) together with the present simulations. The Taylor Vortex Flow regime (TVF) is recovered under isothermal conditions ($Ra = 0$) at a critical Taylor number equal to $Ta = 48$, in close agreement with the theoretical value $Ta = 47.4$ obtained by Taylor [337]. Above a second threshold $Ta = 56$, DNS results report the classical Wavy Vortex Flow regime (WVF). These two thresholds perfectly match with the measurements of Guillerm [117].

In the non-isothermal case, the stability diagram shows a large variety of instability patterns appearing as spirals, wavy vortices or the coexistence of both shown in Figure 10.5 in terms of temperature maps. The Partial SPIral regime (PSPI) observed by Lepiller *et al.* [180] and Guillerm [117] using the same device appears as regular helicoidal vortices located at the bottom of the cavity. The PSPI regime has not been obtained here confirming the numerical study of Kedia *et al.* [152], who reported a direct transition from the axisymmetric TVF to a regular spiral flow for $Ta = 50$ ($\eta = 0.5$ and 0.7) around $Ra \simeq 910$. It is probably due to experimental imperfections in the thermal heating not included in the numerics. Moreover, it has been carefully checked that the flow and thermal fields are similar to the base state even in the vicinity of the endcap disks, which supposes also a direct transition to the regular spiral regime (SPI). The six other instability regimes have been recovered by DNS for different combinations of (Ra, Ta) values. The temperature maps in Figure 10.5 clearly show that endcap effects are relatively weak and confined in the vicinity of the disks.

At low Rayleigh numbers, for example $Ra = 2063$, the first transition leads to the appearance of the SPIral regime (SPI, Fig.10.5a). Even for a slight departure from the critical Taylor number, the spirals invade the whole system. These helicoidal vortices are very regular along the axial direction with only weak endwall effects close to the top and bottom stationary disks. Above a second threshold, these spirals may coexist with a Wavy Vortex Flow, regime denoted SPI+WVF (Fig.10.5e) in the following. Increasing further the Taylor number leads to a progressive encroachment of the wavy vortices in the whole system. Finally, above a third threshold, the WVF regime (Fig.10.5f) is obtained because of the progressive decreasing influence of the thermal effects compared to the inertial ones. By numerical simulations, Kuo and Ball [163] observed successively the SPI regime and Taylor vortices but the

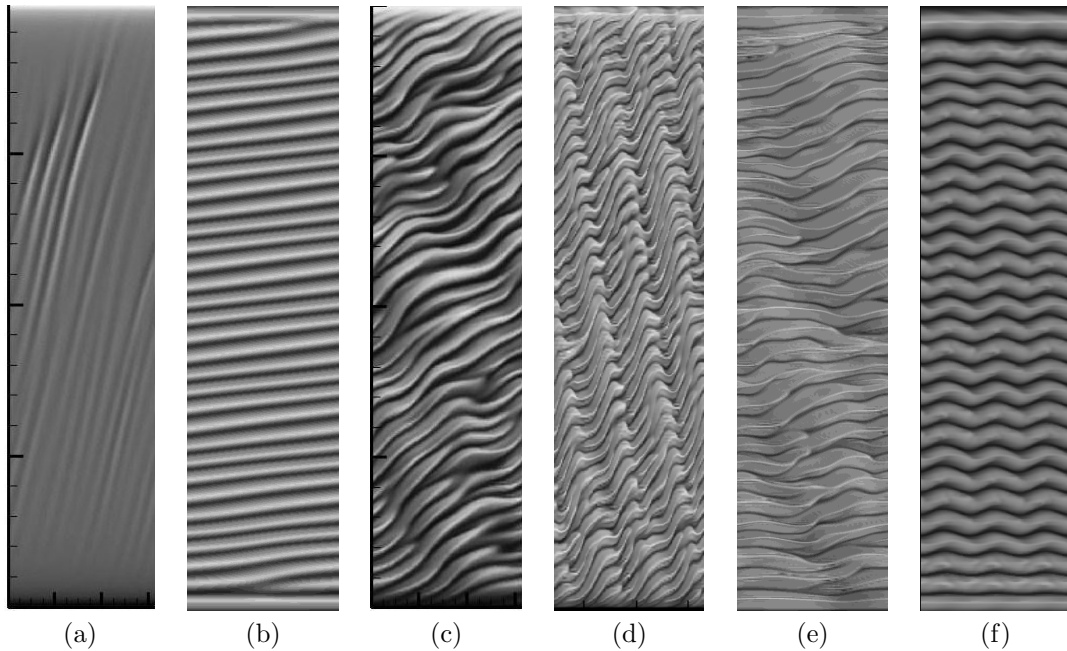


Figure 10.5: Temperature maps obtained by DNS in a $(\theta = [0, 2\pi], z = [0, h])$ plane at mid-radius highlighting 6 different instabilities: (a) MSPI ($Ra = 7150, Ta = 11$), (b) SPI ($Ra = 1166, Ta = 50$), (c) SPI+D ($Ra = 7150, Ta = 40$), (d) WSPI ($Ra = 7150, Ta = 75$), (e) SPI+WVF ($Ra = 7150, Ta = 90$), (f) WVF ($Ra = 7150, Ta = 150$). The aspect ratio has been modified for readability.

authors did not report the existence of the WVF regime. They combined the Taylor and Grashof numbers to form the mixed convection parameter $\sigma = \frac{Gr}{Ta^2} \frac{\Delta R}{a}$ and showed that, for a fixed Prandtl number, the onset of the spiral patterns is governed only by σ .

At larger Rayleigh numbers, for example $Ra = 13228$, the base flow destabilizes at $Ta = 11.3$ in agreement with Guillemin [117] with the appearance of the Modulated SPIral regime (MSPI, Fig.10.5a). These modulated spirals are characterized by the alternation of spirals with laminar flow regions. They are matched by groups and are observed in the whole cavity but for a very narrow range of Taylor numbers. Above a second threshold, the flow switches to the regime denoted SPI+D, for SPIrals with Dislocations (Fig.10.5c). This pattern is very irregular as the spirals are affected by numerous defects and dislocations. Thus, their inclination angle strongly varies depending on their spatial location. Increasing further the Taylor number induces the third instability regime: the Wavy SPIral regime (WSPI, Fig.10.5d). The spirals get wavy with a temporal and spatial variation of their inclination angle. The two following regimes are successively the SPI+WVF and the WVF regimes already evoked for low Rayleigh numbers. The present DNS confirm the diagram of Guillemin [117].

10.5.2 Primary bifurcations at low Taylor numbers

The regular spiral regime (SPI) pattern has been observed for $Ta = 50$ and two Rayleigh numbers $Ra = 1166$ and 2063 . At $Ra = 1166$, a slight increase in Taylor number from $Ta = 41$ to 50 destabilizes the base flow and these regular spirals invade the whole system. In this case, $Ri = 0.12$, indicating a competition between rotation and temperature gradient effects. It is noticeable that the PSPI is not obtained here even in a transient state at ($Ra = 1166, Ta = 41$).

The flow structure for this regime is depicted in details in Figure 10.6. The spirals are very regular as it can be seen from the temperature map in Figure 10.2. Thus, iso-values of the Q-criterion and maps of the velocity components (U_r, U_θ, U_z), the temperature T and the azimuthal vorticity ω_θ are shown only for $z/h \in [0.375, 0.625]$. The spirals are composed of co-rotating vortices located in the middle of the gap. The axial velocity is zero in the vortex core and as for the convective cell, the fluid moves upwards along the rotor and downwards close to the stator. The radial velocity has an opposite behavior. It is equal to zero close the walls. A vortex corresponds to the alternation of positive (top of the vortex) and negative (bottom) radial velocities in the axial direction. The tangential

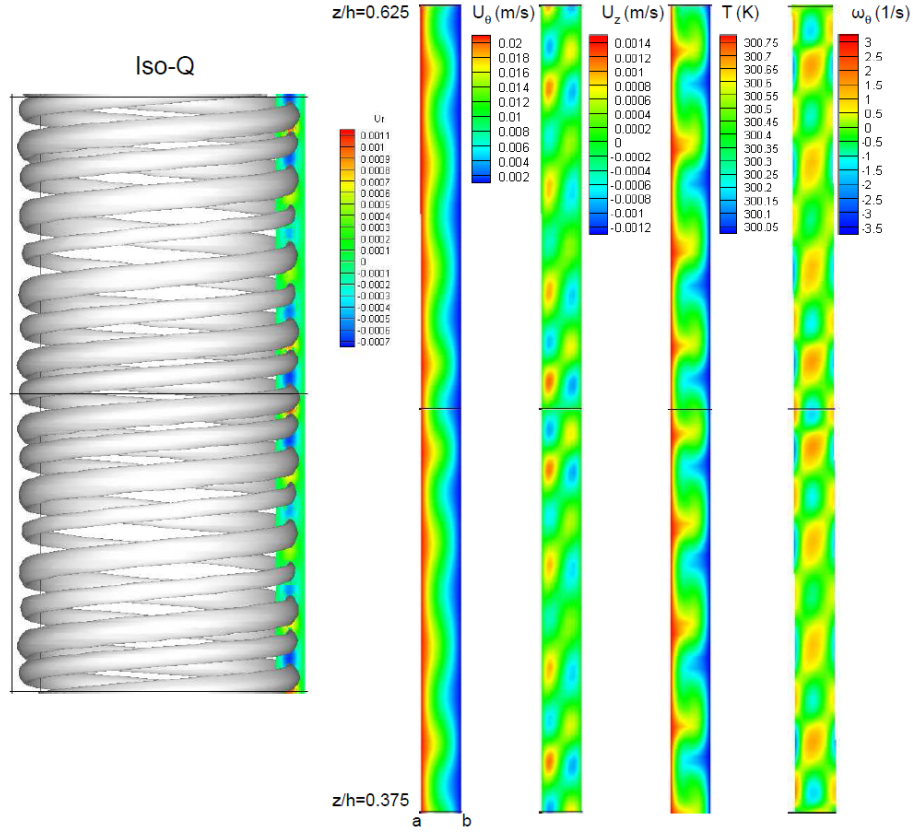


Figure 10.6: SPI regime ($Ta = 50$, $Ra = 1166$). From left to right: iso-values of the Q criterion and maps of the three velocity components, the temperature and the azimuthal vorticity in a $(r \in [a, b], z/h \in [0.375, 0.625])$ plane.

velocity component U_θ presents a modulation in the axial direction, weakly shifted compared to the temperature modulation. The radial profile of U_r exhibits an inflexion point at mid-gap. The temperature field is indeed perturbed compared to the base convection cell. Large temperature perturbations are localized in the middle of the gap with an alternation of hot and cold fluid regions. In the vortex core, the thermal field is not modified compared to the base convection cell. These spirals, whose absolute nature has been shown by Lepiller *et al.* [180], are somewhat similar from those one observed in isothermal Taylor-Couette flows with an axial throughflow by Snyder and Karlsson [325].

The modulated spiral regime (MSPI) pattern appears for larger Rayleigh numbers. Guillermin [117] showed that the critical Rayleigh number is $Ra = 4675$ for a large range of Taylor numbers. The MSPI is recovered here for $Ta = 12$ and 13 at $Ra = 7150$ and at the experimental threshold $Ta = 11.3$ for $Ra = 13228$. The last case corresponds to the maximum value of the Richardson number $Ri = 4.71$ reached in the present work. According to the classification of Ball *et al.* [14], both thermal gradient and rotation affect the flow stability. Recently, Yoshikawa *et al.* [360] showed that for $Ri > 3.75$, rotation has no more effect on the stability. An alternation of spirals with laminar regions are observed in the entire system. In laminar regions, the flow and temperature fields are similar to the stable base flow. Two maps of U_z in a (r, θ) plane are shown on the left of Figure 10.7 at two axial positions $z/h = 0.438$ and 0.563 . It clearly highlights the 3D nature of the MSPI instability. Figure 10.7 presents maps of the flow and thermal fields in a region $z/h \in [0.375 - 0.625]$ where the modulated spirals appear. The radial velocity component is almost zero there. The tangential velocity and temperature fields are deformed compared to those obtained for the stable base flow. This modulation induces the appearance of hot and cold fluid regions. The axial velocity field exhibits the same modulation. High positive (resp. negative) axial velocities are observed in the hot (resp. cold) regions. The perturbed temperature field is localized at mid-gap. Between two zones characterized by an intense axial flow (alternately upwards and downwards), the azimuthal vorticity exhibits an

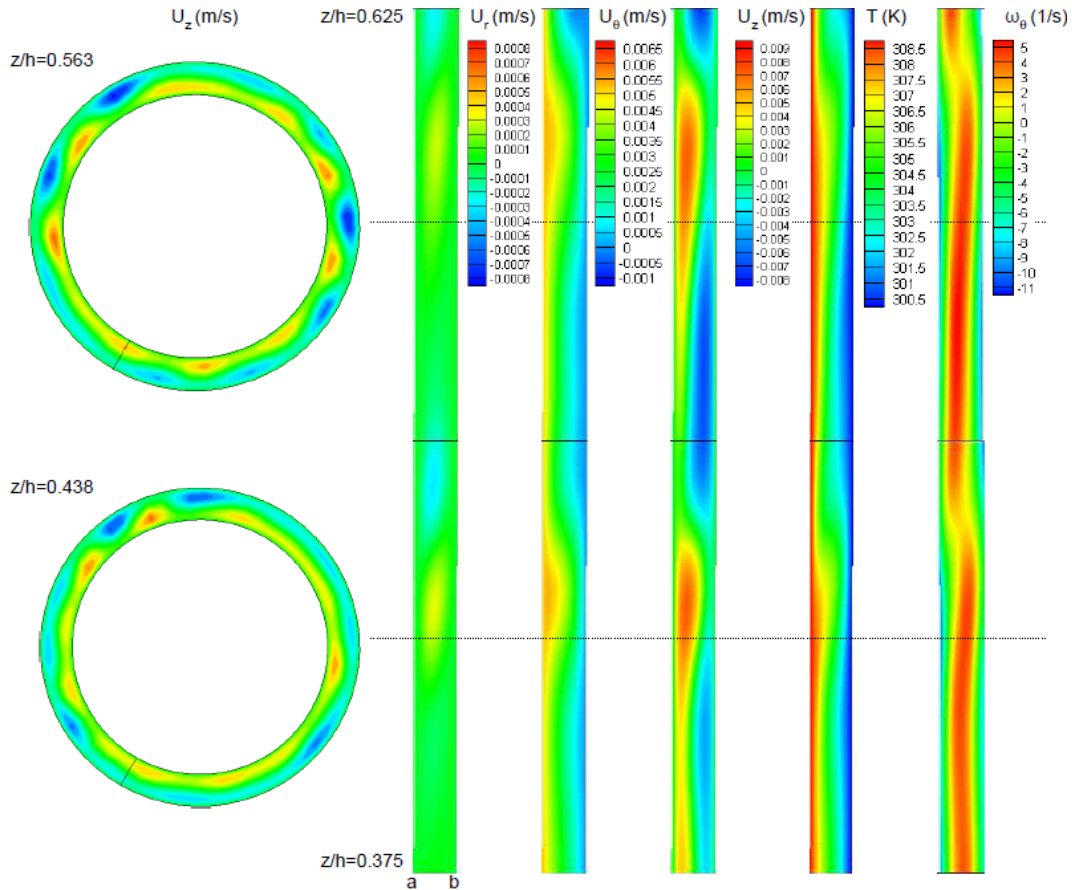


Figure 10.7: MSPI regime ($Ta = 11.3$, $Ra = 13228$). From left to right: maps of the axial velocity U_z in a (r, θ) plane at two axial positions $z/h = 0.438$ and 0.563 , maps of the three velocity components, the temperature and the azimuthal vorticity in a $(r \in [a, b], z/h \in [0.375, 0.625])$ plane.

undulatory behavior corresponding to a perturbation of the temperature and velocity fields. This modulation delimits the ascending flow of hot fluid along the rotor and the descending flow of cold fluid along the stator. The different maps indicate that rotation may have a limiting role in the transition process. This pattern presents a certain analogy with a Kelvin-Helmholtz wave as suggested first by Guillerm [117].

To go into more details, the characteristics of the spiral networks have been deduced from space-time diagrams. The experimental values of Guillerm [117] were obtained at the threshold of the primary instability. It is not strictly the case in the simulations due to the computational cost but all results concern the primary instability at a given Rayleigh number.

Figure 10.8a presents the evolution of the inclination angle θ against the Rayleigh number. The spiral networks form a positive angle with the azimuthal direction as they roll up in the rotation sense of the inner cylinder. It confirms that the sign of θ is fixed by the product $Ra \times Ta > 0$. θ is an increasing function of Ra . A good agreement is particularly obtained at low Ra values, where the behavior is quasi-linear. At higher Ra , θ tends to an asymptotical value, ranging between 60 and 70° in the experiments. By LSA, Yoshikawa et al. [360] showed that it saturates to about 80° for the same flow parameters. If the present simulations slightly overestimate the asymptotical experimental value [117], they seem to be in good agreement with the LSA of [360].

The evolution of the axial wavenumber q as a function of the Rayleigh number is given in Figure 10.8b with a close agreement between the DNS and the experimental results. It decreases exponentially with Ra and reaches a limit value of 0.5 for large Rayleigh numbers. Thus, the axial size of the spiral rolls increases for increasing temperature gradients.

From the inclination angle θ and the axial wavenumber q , the azimuthal wavenumber m can be evaluated through: $m = (1 + \eta)q \tan \theta / [4(1 - \eta)]$ [117]. The azimuthal wavenumber, which can take

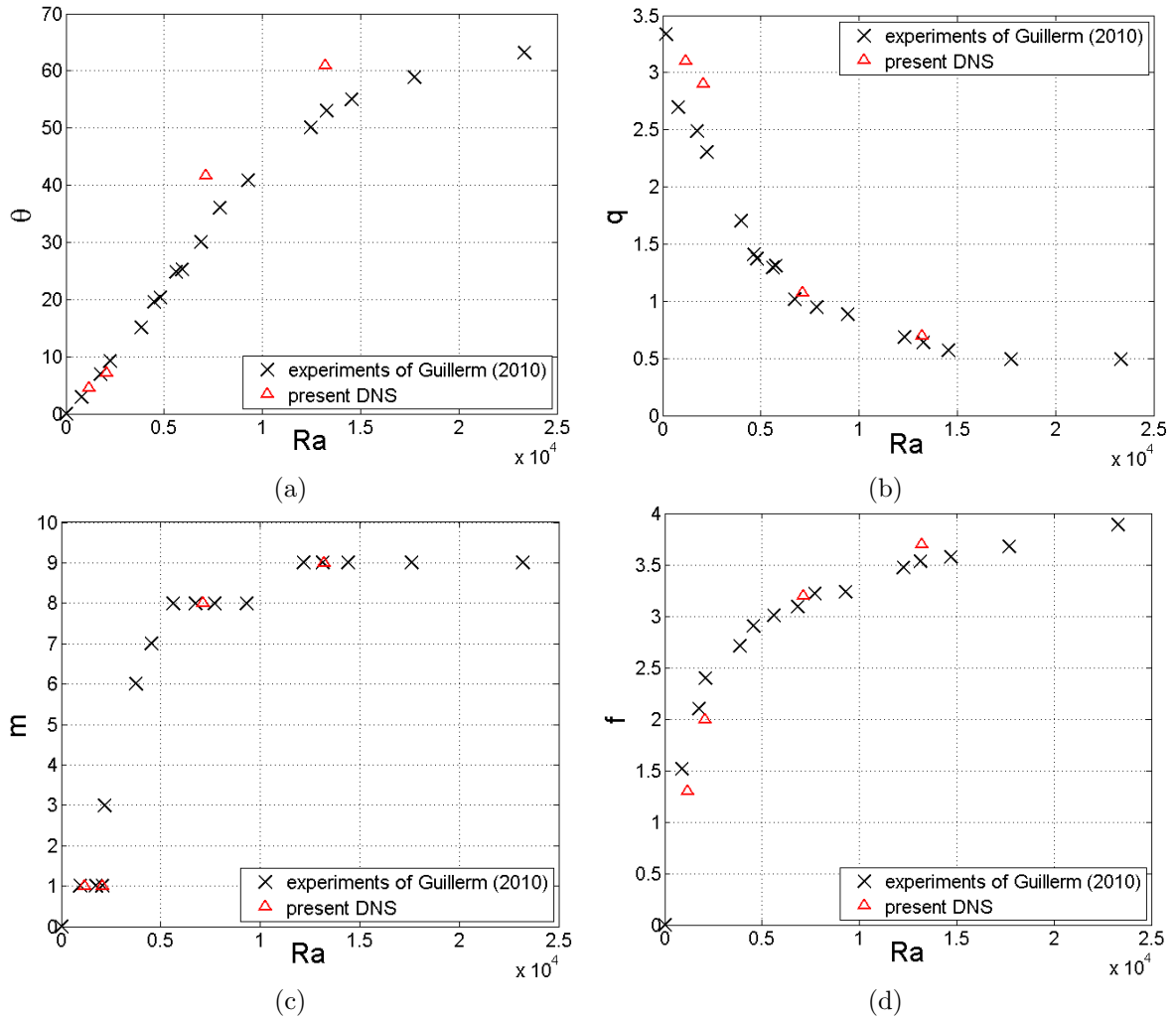


Figure 10.8: Influence of the Rayleigh number on some characteristics of the spirals close to the threshold of the primary instability: (a) inclination angle θ , (b) axial wavenumber q , (c) azimuthal wavenumber m , (d) frequency f .

only integer values, increases with the Rayleigh number (Fig.10.8c). It increases quite rapidly up to $m = 8$ for Ra up to 5000. It increases more slowly by plateau to reach a limit value equal to $m = 9$. One can consider also the total wavenumber $k = \sqrt{q^2 + m^2}$, which saturates to about 9 in the experiments and in the numerics, whereas the LSA of Yoshikawa *et al.* [360] predicts a value around $k = 2.2$ at the threshold of the primary instability.

As reported by Guillerm [117], for small Ra values, there is only one characteristic frequency, which is the one of the spiral itself. For larger temperature gradients, a modulation frequency appears. The frequency of the spiral is reported in Figure 10.8d. It increases first quite rapidly with Ra and more slowly at large Ra values with a good agreement between the two approaches.

The spiral regime reported here is somewhat different to the one obtained by Snyder and Karlsson [325] for small Ra . The authors observed indeed an alternation of small and large cells (in the axial direction) with a constant wavenumber and a weak inclination angle for $-5 \leq \Delta T \leq 5^\circ C$. It may be attributed to a larger radius ratio $\eta = 0.958$ inducing a more intense shearing in their experiments.

10.5.3 Secondary instabilities at higher Taylor numbers

Secondary instabilities have not been considered so far in the literature [117]. At $Ra = 7150$ for example, after a second critical Taylor number, a transition from the MSPI regime to the SPI+D regime (spirals with dislocations) is observed. Maps of the three velocity components, the temperature

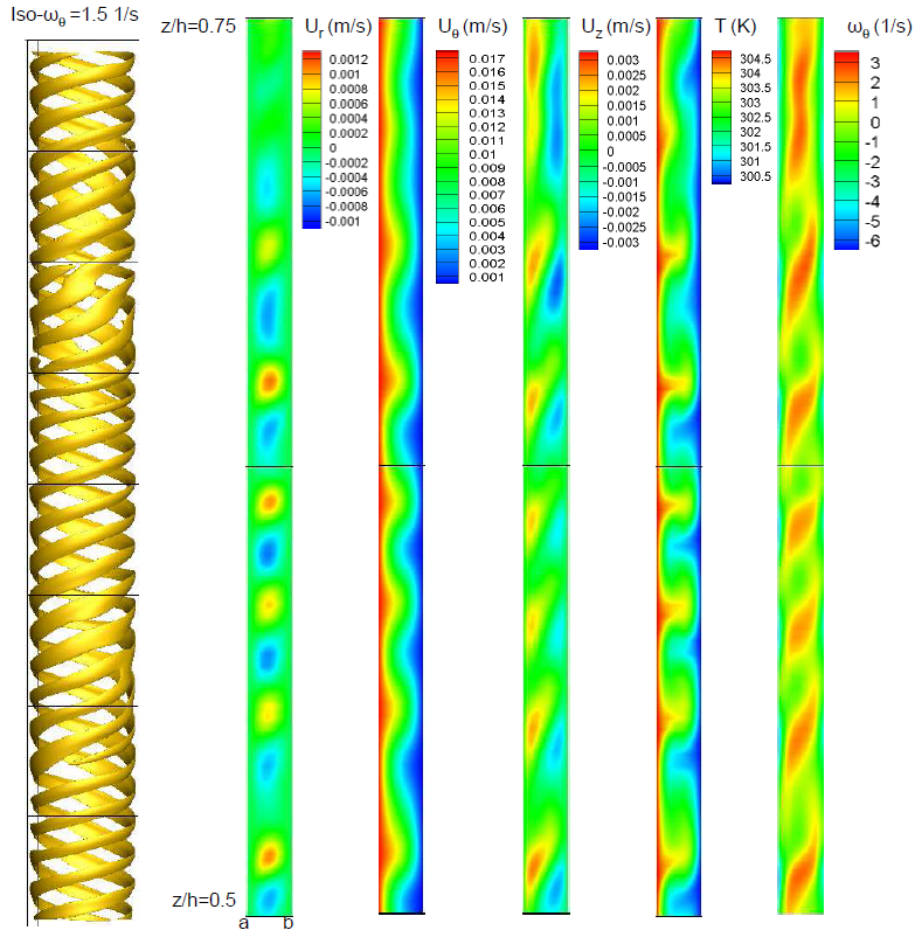


Figure 10.9: SPI+D regime ($Ta = 40$, $Ra = 7150$). From left to right: iso-values of the azimuthal vorticity ω_θ and maps of the three velocity components, the temperature and the azimuthal vorticity in a ($r \in [a, b]$, $z/h \in [0.5, 0.75]$) plane.

and the azimuthal vorticity in a (r, z) plane are shown in Figure 10.9 for $Ta = 40$ and $Ra = 7150$. Some defects may be clearly observed in the spiral network (see also Fig.10.5c), which goes with strong variations of their inclination angle. Compared to the MSPI regime, the axial wave number is significantly increased, which induces a decrease in size for the spirals. The radial velocity is almost zero in the whole cavity. The tangential velocity and the temperature are in phase and quite similar to those obtained for the SPI regime (Fig.10.6). The axial velocity and the azimuthal vorticity have an intermediate behavior between the MSPI and the SPI regimes. The azimuthal vorticity ω_θ is mainly localized at mid-gap as for the MSPI regime and delimits the two regions close to the cylinders where hot fluid moves upwards along the rotor and cold fluid moves downwards close to the stator. It can be seen also like a wave of Kelvin-Helmholtz type with also some defects in the ω_θ -map.

At $Ra = 7150$, when one increases further the Taylor number, the flow switches to the wavy spiral regime (WSPI). The radial velocity remains quite weak also for this instability regime (Fig.10.10). An axial undulation of the tangential velocity and temperature fields may be observed with hot fluid coming more closer to the outer cold cylinder. More noticeable are the behaviors of the axial velocity and azimuthal vorticity. There is an alternation of negative and positive axial velocities around mid-gap corresponding to the same alternation of positive and negative values of ω_θ . It indicates that the WSPI does not correspond to a progressive wave as the SPI+D instability but corresponds to counter-rotating vortices, confirming the observations of Guillerm [117]. The azimuthal vorticity in the core of the vortex varies with the axial position within the cavity between 40% and 83% of the maximum vorticity.

Increasing further the Taylor number at $Ra = 7150$ leads to the appearance of spirals coexisting

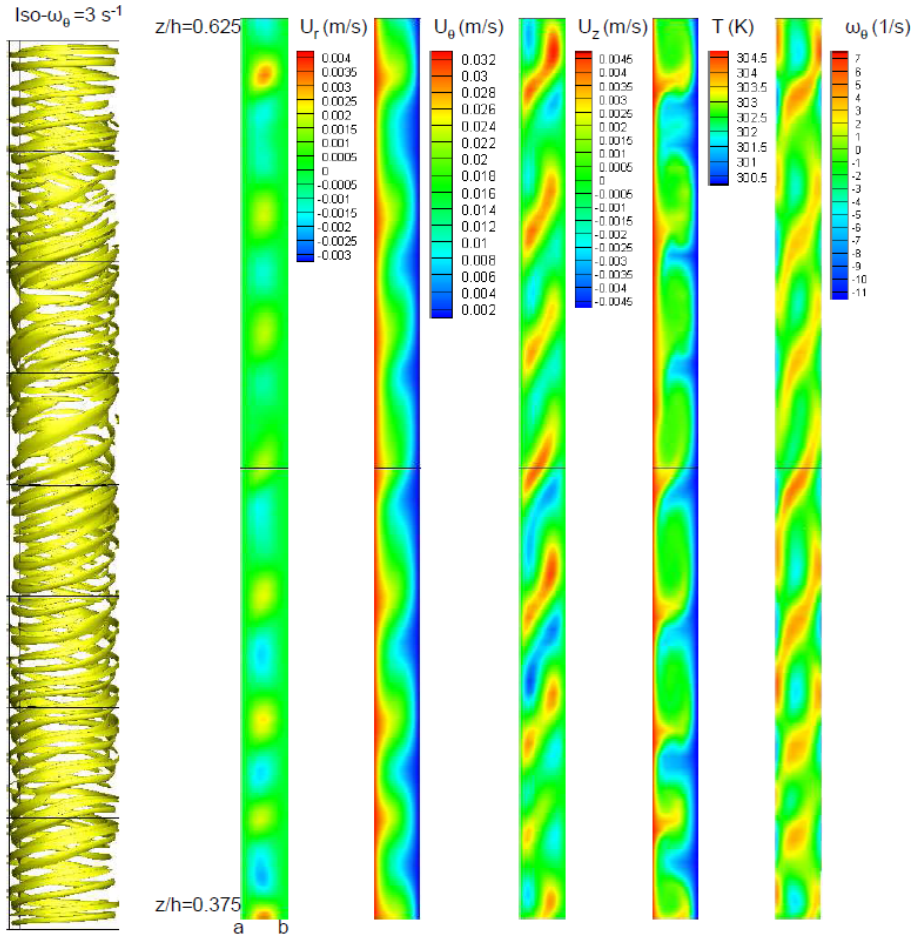


Figure 10.10: WSPI regime ($Ta = 75$, $Ra = 7150$). From left to right: iso-values of the azimuthal vorticity ω_θ and maps of the three velocity components, the temperature and the azimuthal vorticity in a ($r \in [a, b]$, $z/h \in [0.375, 0.625]$) plane.

with a wavy vortex flow (SPI+WVF), whose velocity and temperature fields are depicted in Figure 10.11. The Richardson number is equal to 0.023 close to the limit value $Ri = 0.01$, where thermal effects still play a role in the transition process. The maps of the radial and axial velocities indicate that they correspond also to counter-rotating vortices.

The wavy vortices invade progressively the whole system (Wavy vortex flow regime, WVF) by increasing the rotation rate. Some edge effects occur in regions close to the endcap disks (Fig.10.5f). As for the other instability regimes, the critical Taylor number depends on the Rayleigh number. In fact, Lepiller [179] showed that this regime appears for a constant value of the Richardson number $Ri \simeq 0.034 \pm 0.003$, which remains far from the one $Ri = 0.12$ obtained by Kuo and Ball [163] for $\Gamma = 10$ and $\eta = 0.5$. Here $Ri = 0.014$, which corresponds to a weak influence of the thermal effects compared to the inertial ones. This regime is characterized by a pattern of traveling waves, which are periodic in the tangential direction. The transition to the WVF regime is not unique and is subject to strong hysteresis, which has not been investigated here. At the onset of this instability, only one fundamental frequency corresponding to the traveling tangential waves is observed. A second fundamental frequency corresponding to a modulation of the waves may appear for $Ta > 19.3Ta_c$, which is far above the range of Taylor numbers considered here.

The azimuthal waviness of the vortices may be seen from the isotherm map in Figure 10.2. For $Ta = 150$ and $Ra = 7150$, three waves travel around the annulus as shown from the maps of the axial velocity in Figure 10.12. The number of azimuthal waves strongly depends on the flow parameters and the experimental conditions but still remains less than 6 after Coles [58]. They travel here at a speed corresponding to 35% of the inner cylinder rotation speed, value which remains in the classical

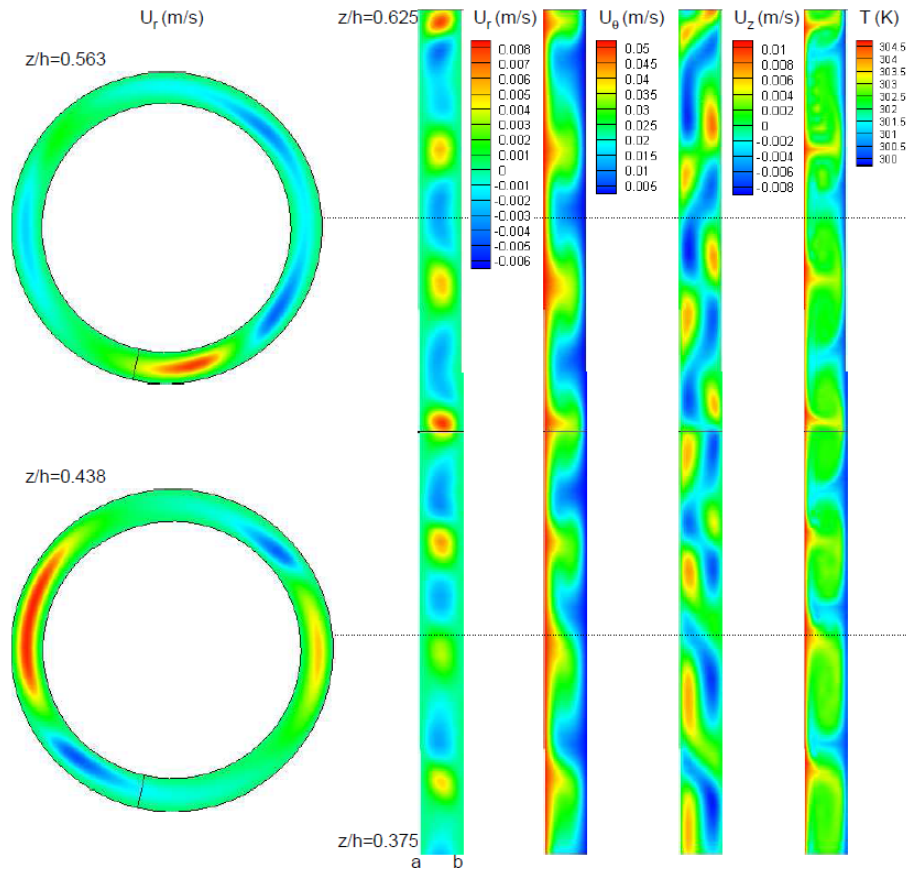


Figure 10.11: SPI+WVF regime ($Ta = 120$, $Ra = 7150$). From left to right: maps of the radial velocity component in two (r, θ) planes at $z/h = 0.438$ and 0.563 and maps of the three velocity components and the temperature in a $(r \in [a, b], z/h \in [0.375, 0.625])$ plane.

range [30 – 50%] depending on the Taylor number among other things [155].

The structure of the hydrodynamic and thermal fields are displayed in Figure 10.12 for the WVF regime. The map of the azimuthal vorticity clearly shows that these are counter-rotating vortices. For $z/h \in [0.375 - 0.625]$, 14 vortices are observed in the axial direction, which perfectly matches with the observations of Guillerm [117]. The number of vortices in this direction does not depend so much on the values of Ra and Ta . The isotherms reveal that temperature gradients are located very close to the walls, while temperature remains almost constant within the gap. Periodically in the axial direction, hot fluid penetrates more deeply the gap to form some mushroom patterns. The same phenomenon is observed along the cold outer cylinder with a small axial shift. The same behavior is obtained for the tangential velocity, showing that increasing the inertial effects leads to a redistribution of the temperature field. The wavy vortices are located on either side of these hot and cold fluid regions. Outside the thin thermal boundary layers (about 10% of the gap width), the temperature increases from cold to hot fluid regions, with a value close to $(T_i + T_o)/2$ in the vortex core region.

10.6 Moment coefficient and heat transfer distributions

It may be useful for engineering applications to determine the power P required to overcome the frictional drag of the inner rotating cylinder. It can be directly linked to the torque T exerted by the fluid on the inner cylindrical surface or to the moment coefficient C_m through: $P = 0.5\pi\rho\Omega^3 a^4 h C_m$. C_m represents the normalized torque acting on the inner cylinder ($r = a$) and may be defined as:

$$C_m(r) = \frac{T}{0.5\pi\rho r^2 h (\Omega a)^2} \quad (10.4)$$

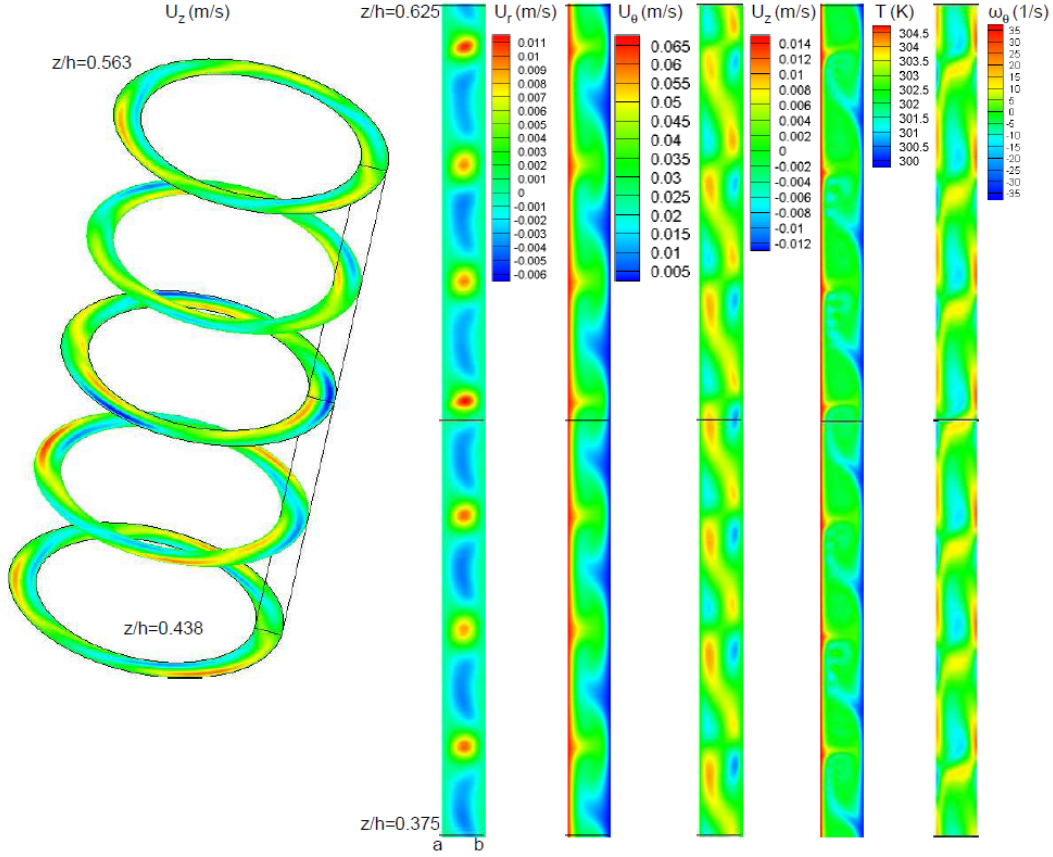


Figure 10.12: WVF regime ($Ta = 150$, $Ra = 7150$). From left to right: maps of the axial velocity component in five (r, θ) planes at different axial positions z/h and maps of the three velocity components, the temperature and the azimuthal vorticity in a $(r \in [a, b], z/h \in [0.375, 0.625])$ plane.

$$\begin{aligned} \text{with } T(r) &= 2\pi r h \tau_{r\theta}(r) \\ \text{and } \tau_{r\theta}(r) &= -\mu \left[r \frac{\partial}{\partial r} \left(\frac{U_\theta}{r} \right) + \frac{1}{r} \frac{\partial U_r}{\partial \theta} \right] \end{aligned}$$

Bilgen and Boulos [24] provided the following equation for the moment coefficient in the case of an annulus with inner cylinder rotation and no axial pressure gradient in the laminar regime:

$$C_m = f(\eta) Re^\alpha \quad (10.5)$$

where $Re = 2Ta$ in the present case. $f(\eta) = 174.375$ and $\alpha = -1$ for $Ta < 32$ and $\alpha = -0.6$ for $32 < Ta < 250$. They reported that the maximum mean deviation from their experimental data was $\pm 5.8\%$. The present DNS results are compared to Equation (10.5) on Figure 10.13 taking into account the confidence interval of $\pm 5.8\%$.

First, there is an excellent agreement with the experimental data of Bilgen and Boulos [24] up to $Ta \simeq 55$. Then, the computed moment coefficient is slightly higher than the experimental one. The second important point is that the evolution of the moment coefficient with the Taylor number is continuous and not sensitive to the Rayleigh number proving that it is not affected by the various instability patterns.

The second quantity for engineering applications is the heat transfer coefficient, which can be evaluated along both walls. The heat transfers are discussed here in terms of the averaged Nusselt numbers (conductive Nusselt numbers) calculated along both walls as: $Nu = \frac{-\Delta R}{\Delta T} \frac{\partial T}{\partial r} |_{w}$. They have been averaged both in time but also in the azimuthal and axial directions. Figure 10.14 clearly shows that the Nusselt numbers along the rotor and the stator increase for increasing values of the Taylor

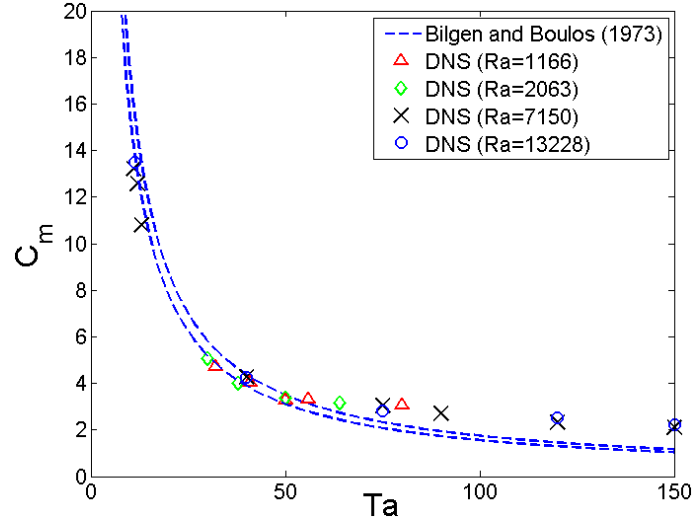


Figure 10.13: Moment coefficient C_m against the Taylor number Ta for four Rayleigh numbers. Comparisons with the experimental data of Bilgen and Boulos [24] for $f(\eta) = 174.375$ and $\alpha = -1$.

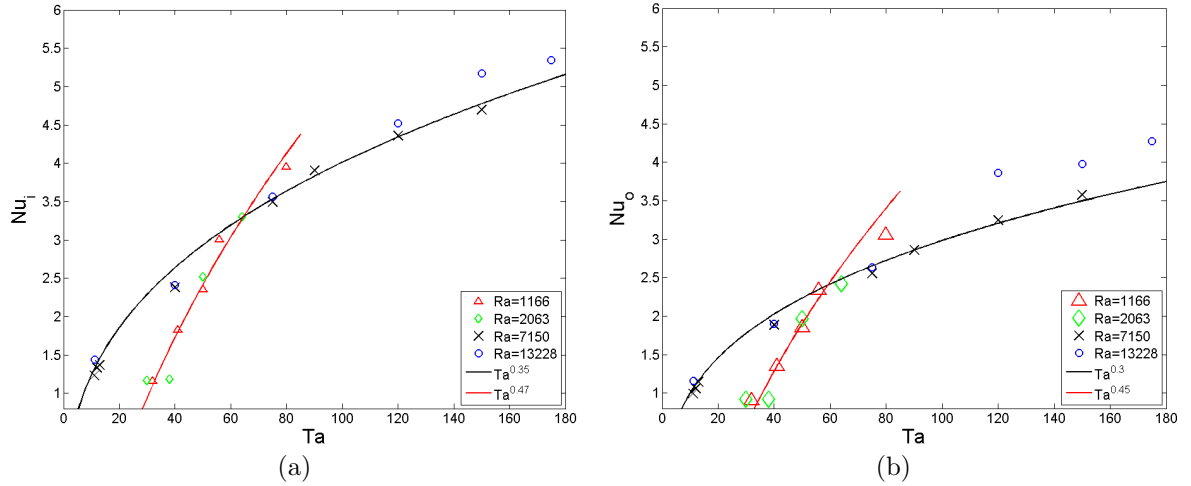


Figure 10.14: Distributions of the averaged Nusselt numbers Nu against the Taylor number Ta for four Rayleigh numbers along (a) the rotor Nu_i and (b) the stator Nu_o .

number. The averaged Nusselt number along the rotor Nu_i is besides slightly higher than Nu_o along the stationary outer wall. For all values of the Rayleigh number Ra , Nu remains close to unity at very low Taylor numbers $Ta < 40$ on both sides, which confirms the experiments of Aoki *et al.* [12] for various fluids including air, water and a spindle oil flow (Pr up to 160). Becker and Kaye [20] observed also a constant Nusselt number equal to 1 for $\Gamma = 172$ and $\eta = 0.81$ up to $Ta \simeq 570$. For larger Ta values, two different behaviors are observed in the present simulations. It is convenient to search for scalings under the form: $Nu \propto Ta^n$. For large Rayleigh numbers $Ra \geq 7150$, the DNS results are well fitted using $n = 0.35$ and 0.3 on the inner and outer cylinders respectively and the Rayleigh number has only a weak effect on the Nusselt number distribution. It perfectly falls between the values predicted by the boundary layer theory: $n = 0.5$ in the laminar regime [12] and $n = 2/7$ in the turbulent regime (using the present definition of Ta).

For $Ra \leq 2063$, a similar behavior is observed with $n = 0.47$ and 0.45 along the rotor and stator respectively. The instabilities do not affect significantly the heat transfer process, as the exponent on the rotating cylinder is fairly close to the one predicted by the boundary layer theory in the laminar regime. Once again, Ra has only a weak influence on the heat transfer coefficients. Around $Ta \simeq 75$, the WVF regime seems to enhance the heat transfer compared to the WSPI regime. Finally, it is

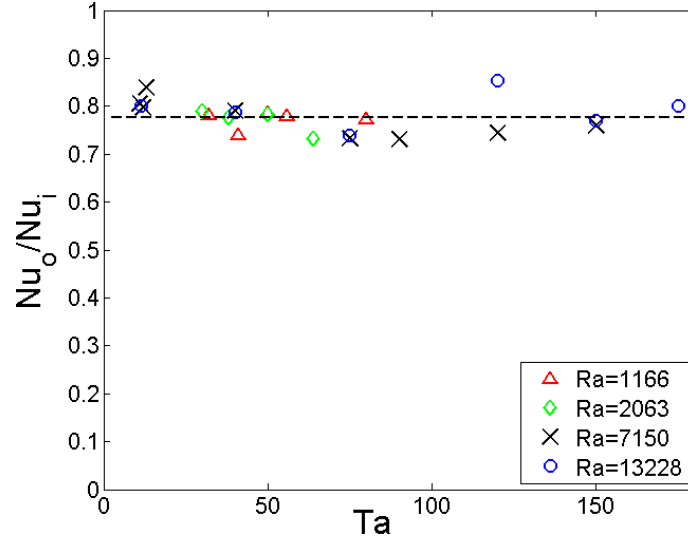


Figure 10.15: Distributions of the ratio Nu_o/Nu_i against the Taylor number Ta for four Rayleigh numbers.

noteworthy to mention that apart from very low Taylor numbers, the evolution of the Nusselt numbers is continuous whatever the instability regime.

The ratio between the averaged Nusselt numbers Nu_o/Nu_i is found to be rather constant $Nu_o/Nu_i = 0.78$ whatever the global parameters Ra and Ta as shown in Figure 10.15. It is to be compared with the value 0.83 obtained by Guillerm [117] for $Ra = 13228$ and $Ta = 42.2$. By a simple energy balance, one can easily show that this ratio is fixed by the value of the radius ratio $\eta = 0.8$, which confirms the validity of the present approach. For the base flow as well as the primary instabilities, the Nusselt numbers are close to unity, which means that the heat transfer is purely conductive. For secondary instabilities and further, the appearance of the different spirals or wavy vortices enhances the heat transfer along both walls in a proportional way.

10.7 Conclusion

The first high-order direct numerical simulations of Taylor-Couette flows subjected to a radial temperature gradient have been compared to the experimental data of Guillerm [117] in a tall system characterized by $\Gamma = 80$ and $\eta = 0.8$ for a wide range of Taylor and Rayleigh numbers. Seven over the eight instability regimes appearing as spiral rolls (MSPI, SPI, SPI+D, WSPI), regular (TVF) or wavy vortices (WVF) or a combination of both (SPI+WVF) observed experimentally have been recovered by DNS. The spatio-temporal properties of the flow patterns have been investigated in details with a particular good agreement for the main characteristics of the spiral regimes close to the threshold of the primary instability. Finally, correlations for the moment coefficient and the averaged Nusselt numbers along both walls have been provided against the Taylor number. These thermo-convective structures enhance the heat transfer process along both walls in a proportional way as the ratio between the averaged inner and outer Nusselt numbers remains constant ($= 0.78$).

The discrepancy observed between the numerics and the experiments concerns the partial spiral regime observed by Lepiller *et al.* [180] and Guillerm [117] in the non-rotating and rotating cases respectively, using the same device. It may be attributed either to heating asymmetries in the experiments or to some differences in the variations of Ta and Ra before reaching the instability threshold. Further calculations are then required to clarify this point but also to go into more details on the secondary instability mechanisms. The goal of this chapter to validate the numerical code (the multidomain approach and the implementation of the hydrodynamic/thermal coupling through the Boussineq approximation) has been reached. It is a first step on the road to the simulation of fluid flow and heat transfer in the rotor-stator gap of electrical motors discussed in Chapter 12.

Turbulent flows with endwall effects

The aim of this Chapter, as for the previous one, was at the early beginning to validate the multidomain approach developed for the finite-difference DNS code. It was also the opportunity to perform a numerical benchmark of the different CFD approaches available in the laboratory. The accurate prediction of fluid flow within rotating systems has indeed a primary role for the reliability and performance of rotating machineries and the selection of a suitable model to account for the effects of turbulence on such complex flows remains an open issue in the literature. Riccardo Da Soghe and Cosimo Bianchini from the Energy Engineering Department “S. Stecco” at the University of Florence are involved in this project and bring their skills in RANS and LES modelings using CFX and OpenFOAM respectively.

The CFD calculations are compared to the experimental data of Burin *et al.* [40], who developed an atypical Taylor-Couette apparatus with endcap rings. The results are discussed in details for both the mean and turbulent fields. A particular attention has been turned to the scaling of the turbulent angular momentum G with the Reynolds number Re . By DNS, G is found to be proportional to Re^α , the exponent $\alpha = 1.9$ being constant in our case for the whole range of Reynolds numbers. Most of the approaches predict quite well the good trends apart from the $k-\omega$ SST model, which provides relatively poor agreement with the experiments even for the mean tangential velocity profile. Among the RANS models, even though no approach appears to be fully satisfactory, the RSM closure offers the best overall agreement. The results have been recently published in *Int. J. Heat Fluid Flow* (see Ref.[254]).

11.1 Introduction

The present investigation is concerned with the numerical modeling of fluid flow in an enclosed Taylor-Couette system. The turbulent flow is confined between two coaxial cylinders, with an inner rotating cylinder and an outer stationary one. This kind of Taylor-Couette flows is of great importance, since they found many applications in process engineering (dynamic membrane filtration, rheology, UV disinfection), in astrophysics (accretion disks) and most of all in turbomachineries for bearings, asynchronous motor with axial ventilation, rotating heat exchangers or gas turbine engines among others. In rotating machineries, a better knowledge of the fluid flow is required to better predict the heat transfer distribution and thus to optimize the performances of the device.

For many years, the turbulent flow regime has then been treated, in computations but also in experiments, as though the flow patterns were steady and axisymmetric. Treating the turbulent flow as statistically stationary implicitly assumed that the coherent structures present in the transitional modes disappeared or that their effect when averaged out was accounted for in the model without explicit treatment. Owen [231] first suggested that the flow within such cavity might not be steady. In the case of rotating disk systems with throughflow, the RANS model he used failed to converge for a certain range of parameters and he speculated that some form of organized large-scale structure may have been present in the flow. These three-dimensional patterns might be responsible for some discrepancies between experiments and axisymmetric computations. Even if three-dimensional calculations may be required in some specific configurations, their highly expensive computational cost makes the selection of a suitable turbulence model for the study of rotating cavity flows still pertinent. One can cite, among the 3D simulations, the work of Bazilevs and Akkerman [17], who presented an application of the residual-based variational multiscale turbulence modeling methodology to the computation of turbulent Taylor-Couette flow at high Reynolds numbers. Its formulation globally conserves angular momentum, a feature that is felt to be important for flows dominated by rotation, and that is not shared by standard stabilized formulations. One can cite also the DNS results of Dong [77] for turbulent Taylor-Couette flows between counter-rotating cylinders.

The aim of the present work is then to perform a numerical benchmarking of turbulence models and Large Eddy Simulations (LES) against three-dimensional direct numerical simulation (DNS) results and experimental data. The geometrical configuration corresponds to the Taylor-Couette apparatus developed by Burin *et al.* [40], who offered reliable velocity measurements in a rather complex geometry. Enclosed Taylor-Couette systems have been widely considered since the work of Wendt [354] because they offer an academic and relatively simple geometry to investigate the influence of rotation on turbulence for fundamental purposes or applications in astrophysics. When the inner cylinder is rotating while the outer one is at rest, the base flow depends mainly on three global parameters: the rotational Reynolds number of the inner cylinder based on the gap width $Re = \Omega a \Delta R / \nu$ ($\Delta R = b - a$), the aspect ratio of the cavity $\Gamma = h / \Delta R$ and its radius ratio $\eta = a / b$, where a and b are the radii of the inner and outer cylinders respectively and h is the cavity height. Biage and Campos [23] proposed a classification of the systems depending on the value of their radius ratio η as follows: narrow-gap cavities for $\eta > 0.67$, middle-gap cavities for $0.33 < \eta < 0.67$ and wide-gap cavities for $\eta < 0.33$. Most of the experiments up to now including the seminal one of Taylor [337] have considered narrow-gap cavities with an aspect ratio larger than 100. Experiments with small aspect $\Gamma < 20$ and radius $\eta < 0.5$ ratios are less common. Kageyama *et al.* [142] considered both experimentally and numerically the flow in a small aspect ratio Taylor-Couette apparatus for $\eta = 0.256$ and $\Gamma = 0.9$. For such parameters, the vertical boundaries have a dynamical role on the secondary flow, that is why these authors proposed a novel approach to increase control over the velocity profile by increasing the number of endcap boundary conditions. Thus, they designed a new system with multiple independent endcap rings (up to 5) rotating at different speeds. Such apparatus with endcap rings was formerly considered by Coles [58] to investigate the transition scenarios in circular Couette flows. Compared to classical Taylor-Couette systems, these rings allow for a reduction of the Ekman circulation in order to create a Couette-like velocity profile: $V_\theta \propto 1/r^2$. Ji *et al.* [140] developed a similar Taylor-Couette apparatus characterized by a low aspect ratio $\Gamma = 2.12$ and a low radius ratio $\eta = 0.35$ with two independent end-rings between the inner and outer cylinders. By playing with the rotation rates of the 6 walls (Fig.11.1b), they can obtain various flow structures (centrifugally unstable flow or quasi-Keplerian flow) even if the visualizations displayed in Figure 11.1a do not highlight different flow structures along the outer cylinder. Burin *et al.* [40] reported velocity fluctuations and the fluctuation-driven radial transport of angular momentum in the same apparatus. Fluctuation levels and the mean specific angular momentum were found to be roughly constant over a radius, in accordance with previous studies featuring narrower gaps. At lower Taylor numbers, Sobolik *et al.* [326] investigated the effect of a confining ring on the onset of Ekman vortices for $\Gamma = 4.93$ and $\eta = 0.91$ and showed that they appear below the critical rotation rate for the onset of Taylor vortices in an infinite system. Czarny *et al.* [64] studied by direct numerical simulations the case $\Gamma = 3$ and $\eta = 0.75$, for different endcap boundary conditions (no-slip stationary or rotating endwalls, stress-free). They investigated the interaction between the endwall Ekman layers and the Taylor vortices near the transition to the vortical flow regime.

Taylor-Couette flows as well as Rayleigh-Bénard convection are used also as canonical flows to analyse the transport properties in closed turbulent systems with a strong analogy between them [79]. Besides their primary concern with astrophysical flows, the main goal is to understand the interplay between the boundary layers and the bulk flow. By torque measurements, Wendt [354] proposed some correlations for the dimensionless torque per unit length G for $\eta = 0.68, 0.85, 0.935$:

$$G = 1.45 \frac{\eta^{3/2}}{(1-\eta)^{7/4}} Re^{1.5}, \quad 400 < Re < 10^4 \quad (11.1)$$

$$G = 0.23 \frac{\eta^{3/2}}{(1-\eta)^{7/4}} Re^{1.7}, \quad 10^4 < Re < 10^5 \quad (11.2)$$

Other experiments indicated the existence of two scaling regimes, one for small Re , where the exponent, denoted α in the following, is 1.5 and one for larger Re , where α remains in the range $[1.7 - 1.8]$ [337, 354]. From their torque measurements, Tong *et al.* [339] found indeed that $G \propto Re^{1.8}$ for $4 \times 10^4 < Re < 4 \times 10^5$ and $\eta = 0.448$. The experimental data of Burin *et al.* [40] for the turbulent angular momentum scale with the Reynolds number to the power $\alpha = 1.7$, whatever the flow being laminar or turbulent. Dubrulle and Hersant [79] identified three logarithmic regimes using an analogy with turbulent Rayleigh-Bénard convection:

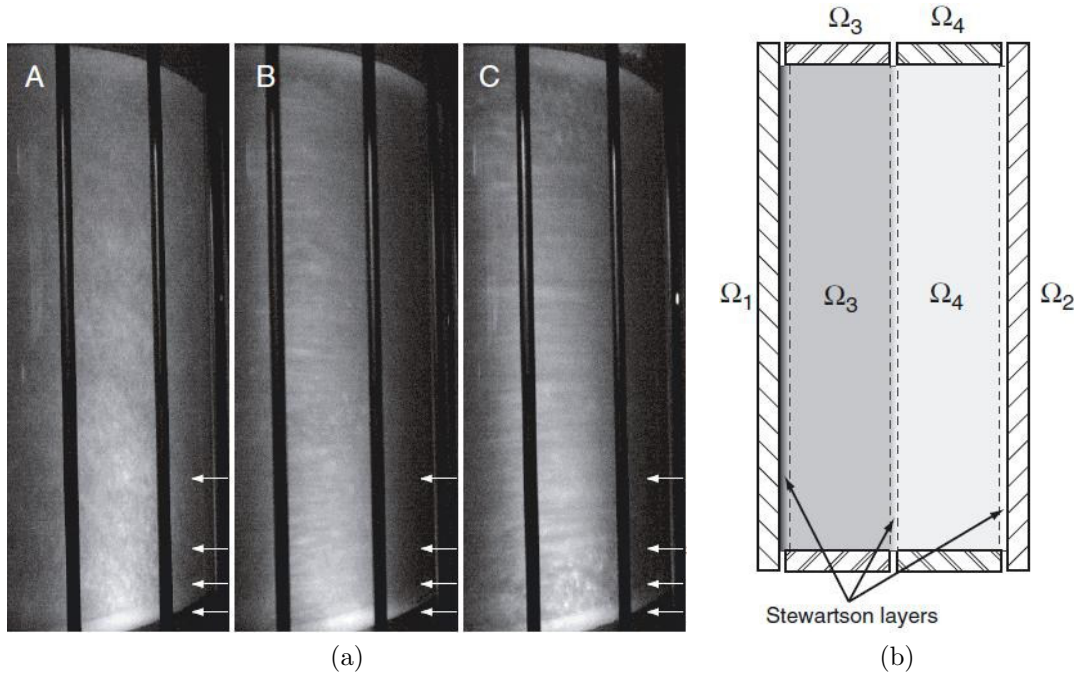


Figure 11.1: (a) Kalliroscope image of three flows at $Re \simeq 5 \times 10^5$: (A) centrifugally unstable flow with $[\Omega_1, \Omega_2, \Omega_3, \Omega_4] = [41.8, 0, 0, 0]$ rad/s, (B) a quasi-Keplerian flow using the Ekman configuration with $[\Omega_1, \Omega_2, \Omega_3, \Omega_4] = [41.8, 5.6, 5.6, 5.6]$ rad/s, (C) a quasi-Keplerian profile with endring speeds optimized to produce the best approximation to the ideal Couette flow with $[\Omega_1, \Omega_2, \Omega_3, \Omega_4] = [41.8, 15.3, 4.2, 5.6]$ rad/s; (b) Boundary conditions for the experiment of Ji's group after [296].

- Regime 1 or “mean flow dominated” regime for $400 < Re < 10^4$:

$$G = 1.46 \frac{\eta^{3/2}}{(1-\eta)^{7/4}} Re^{3/2} \quad (11.3)$$

- Regime 2 is not always observed in Taylor-Couette systems:

$$G = 2.12 \frac{\eta^{2/3}}{(1-\eta)^{5/3}} \frac{Re^{5/3}}{\ln[\eta^2(1-\eta)Re^2/20]^{2/3}} \quad (11.4)$$

- Regime 3 or “fluctuation dominated” regime for $4 \times 10^3 < Re < 10^6$:

$$G = 0.5 \frac{\eta^2}{(1-\eta)^{3/2}} \frac{Re^2}{\ln[\eta^2(1-\eta)Re^2/10^4]^{3/2}} \quad (11.5)$$

On the other hand, the experiments of Lathrop *et al.* [168] and Lewis and Swinney [182] yielded no region of constant exponent. For $800 < Re < 1.23 \times 10^6$, these authors found indeed that α can vary between 1.6 and 1.86 in the turbulent regime. Eckhardt *et al.* [82] argued that there is not a single scaling but a superposition of different scalings: from $\alpha = 1.5$ for small Re to $\alpha = 2$ for larger ones. The exact value of α is then still debated since the pioneering work of Wendt [354].

11.2 Details of the geometrical configuration and flow parameters

The fluid is confined between two concentric cylinders of radii $a = 0.071$ m and $b = 0.203$ m and height $h = 0.28$ m (Fig.11.2). The inner cylinder is rotating at a constant angular rate Ω , while the outer cylinder is stationary. The originality of the apparatus developed by Burin *et al.* [40] is that each

endcap is divided into two independently driven rings of equal radial extension. The inner cylinder and the inner ring rotate at Ω , while the other walls are stationary. In the following, the radial and axial coordinates are normalized as: $r^* = (r - a)/\Delta R$ and $z^* = z/h$. The junction between the rings is then at $r^* = 0.5$.

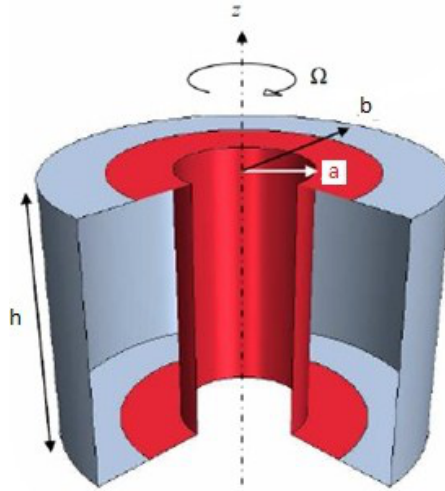


Figure 11.2: Geometrical configuration corresponding to the system considered by Burin et al. [40]. Red walls are rotating and grey ones are stationary.

Under isothermal conditions, the main flow is governed by three flow parameters: the rotational Reynolds number Re based on the gap width $\Delta R = b - a$, the aspect ratio of the cavity Γ and the radius ratio η defined as:

$$Re = \frac{\Omega a \Delta R}{\nu} = 5 \times 10^4, 10^5, 2 \times 10^5, 4 \times 10^5 \quad \Gamma = \frac{h}{\Delta R} = 2.12 \quad \eta = \frac{a}{b} = 0.35$$

The radius ratio remains in the range $0.33 < \eta < 0.67$, so that the cavity is considered as a middle gap cavity [23]. For enclosed systems characterized by a low aspect ratio Γ , such as in the experiment of Burin et al. [40], the choice of the boundary conditions on the endcap disks is primordial and can favour the development of large Ekman recirculations in the meridian plane (r, z) . Depending on the rotation rates of the rings, the flow can be either in solid body rotation (constant angular velocity V_θ/r of the fluid) or present some characteristics of quasi-keplerian flows ($V_\theta/r \propto r^{-3/2}$) or of pure Couette flows ($V_\theta/r \propto r^{-2}$).

11.3 Numerical modeling

The present flow configuration presents several complexities (high rotation rate, confinement effect and singularities in the boundary conditions among other things), which are very challenging for numerical methods. Different numerical approaches including DNS, RANS and LES models either developed at the M2P2 laboratory or at the University of Florence or available within commercial CFD codes have been compared against the velocity measurements of Burin et al. [40]. A brief description of the various numerical methods used is given in the following.

The DNS code based on the fourth-order compact finite-difference schemes already used in the Chapters 8 & 10 has been here considered in its multidomain version as the reference tool. It has been compared to the predictions of the Reynolds Stress Model of Elena & Schiestel [85] described in Chapter 4. All computations have been runned on the M2P2 cluster. The numerical details are provided in Table 11.1.

The turbulence model considered within CFX is the innovative $k - \omega$ SST SAS (scale-adaptative simulation) originally proposed by Menter and Egorov [206] and available within CFX 12.0. The Scale-Adaptive Simulation (SAS) is an improved URANS formulation, which allows the resolution of

the turbulent spectrum in unstable flow conditions. The SAS concept is based on the introduction of the von Kármán length scale into the turbulence scale equation. The information provided by the von Kármán length scale allows SAS models to dynamically adjust to resolved structures in a URANS simulation, which results in a LES-like behavior in unsteady regions of the flow field. At the same time, the model provides standard RANS capabilities in stable flow regions. The governing equations of the $k - \omega$ SST SAS model differ from those of the SST RANS model by an additional source term in the transport equation for the turbulence eddy frequency. Further details regarding the $k - \omega$ SST SAS model are available in the literature [206, 207]. The time step have been selected assuring, for each operating velocity, a RMS Courant number lower than 1. The convective fluxes were solved using a second-order upwinded scheme. Automatic wall treatment (i.e. automatic blending from low to high Reynolds treatment as a function of the local first node wall distance) have been considered. A multi-block hexahedral grid has been used. Computations have been performed on 4 cores of an Intel Xeon 3430 at 2.4 GHz. Please refer to Table 11.1 for the computational details concerning the SAS approach. Note that calculations have been performed on a 5° sector.

OpenFOAM is an open-source CFD code composed of a set of libraries implemented to resolve continuum mechanics problems in 3D on unstructured grids [352]. A pressure based segregated solver implementing the PISO loop to solve the pressure-velocity coupling is used in a transient formulation. Both the convective and diffusive flux schemes employed are based on a purely linear interpolation. The time advancement is achieved by means of the implicit backward Euler scheme, guaranteeing a second-order accuracy both in space and in time. The time step was generally chosen to achieve a maximum Courant number inside the domain close to 1 to guarantee stability and improve the convergence rate. The LES subgrid effects are evaluated by means of a one-equation model chosen among the available SGS treatments as the most suited to reproduce near-wall behavior. Such model exploits a transport equation for the subgrid-scale turbulence kinetic energy for which low-Reynolds boundary conditions on the wall were imposed [205, 362]:

$$\frac{\partial k}{\partial t} + \frac{\partial(U_i k)}{\partial x_i} - \frac{\partial}{\partial x_i} \left(\left(\nu + \frac{\nu_{SGS}}{\sigma_k} \right) \frac{\partial k}{\partial x_i} \right) = \nu_{SGS} \|S\|^2 - \frac{c_e k^{3/2}}{\Delta}, \quad \nu_{SGS} = c_k \sqrt{k} \Delta \quad (11.6)$$

The LES filter width is a simple cube root of the cell volume. A multi-block hexahedral grid mesh has been used and calculations have been performed on 6 cores of an Intel Xeon 3430 at 2.4 GHz for the case $Re = 10^5$ (see the numerical details in Table 11.1).

Classical RANS models ($k-\varepsilon$, $k-\omega$ SST, RSM, $\overline{v^2} - f$) including both high and low-Reynolds number approaches, but also a Detached Eddy Simulation based on the Spalart-Allmaras model available within Star CCM+ 5.04 have been compared for the present test case in Guillerm *et al.* [118]. The LES model considered here uses a standard Smagorinsky model as subgrid scale model with a model constant C_s equal to 0.1 offering a good compromise between the value 0.165 for homogeneous isotropic decaying turbulence and 0.07 for channel flows. The synthetic eddy method has been used to provide an initial perturbed flow field. A polyhedral unstructured mesh grid has been generated. To take into account the thin boundary layers developed along the cylinders and the rings, 12 prismatic layers are imposed on each wall on just 2% of the gap width to guarantee acceptable values for the wall coordinates (see Table 11.1). Computations have been conducted on a HP Z400 workstation with a quadcore Intel Xeon CPU W3520 processor at 2.67 GHz.

All the numerical approaches together with the corresponding computational details are summed up in Table 11.1. Note that N_r , N_θ and N_z represent the number of mesh points in the radial, tangential and axial directions respectively. The values of N_r , N_θ and N_z for each approach have been optimized to guarantee grid independent solutions while saving computation time. Some computations have been performed considering a half cavity or only a 90° sector, which is justified by the absence of large scale vortical structures as highlighted by the DNS of Fukushima *et al.* [101] for Re up to 12000. The parameters for the DNS have been chosen to guarantee a CFL number lower than 0.3.

From Table 11.1, though calculations have been done on different types of machines, one can deduce for each model the CPU time required to perform 1 s of physical time advance. Not surprisingly, the in-house RSM is ranked first using this criterion with 1.6×10^3 s. Then, 1.34×10^5 s, 1.75×10^5 s and 5.73×10^5 s of calculation time are required for the LES-StarCCM+, the LES-OpenFOAM and

modeling	time step (s)	$N_r \times N_\theta \times N_z$	geometry	wall coordinates	time per iteration (s)
DNS	3×10^{-5}	$152 \times 64 \times 242$	3D (half cavity)	$r^+ < 4$ $z^+ < 6$	17.2
LES (OpenFOAM)	4×10^{-4}	$200 \times 70 \times 300$	3D (90° sector)	$r^+ < 0.9$ $z^+ < 1.3$	70
LES (Star CCM+)	10^{-3}	$74 \times 104 \times 115$	3D	$r^+ < 0.7$ $z^+ < 0.95$	13.4
RSM [85]	10^{-2}	$140 \times 1 \times 280$	2D axisymmetric	$r^+ < 0.02$ $z^+ < 0.06$	16
k- ω SST SAS	5×10^{-5}	$140 \times 5 \times 280$	2D axisymmetric	$r^+ < 5$ $z^+ < 5$	30

Table 11.1: Computational details for $Re = 10^5$.

the DNS respectively to get 1 s of physical time advance. Finally, the SAS model require 6×10^5 s for 1 s of physical time though the calculations are 2D axisymmetric, which is more than for the 3D DNS. It can be explained by the fact that the SAS model consists in an adaptative model. Thus, the run time adaptation of the model source terms increases the number of iterations needed to reach the calculation convergence.

11.4 Results

The numerical results are compared to the velocity measurements of Burin *et al.* [40] in terms of the mean tangential velocity and angular momentum and of the cross-correlation coefficient and the turbulent angular momentum. The DNS results provide also useful data to investigate the three-dimensional structure of the flow field. All the computed data have been averaged both in time and in the tangential direction.

11.4.1 Flow structures

The critical Reynolds number Re for the transition to turbulence in such a flow depends upon a large number of factors, including the aspect ratio of the cavity, the curvature and the flow history. Nevertheless, one commonly admitted value deduced from the Reynolds number dependence of the mean torque at the inner cylinder is around 10^4 [168]. In the present case, the transition to a state of featureless turbulence appears for lower values of Re . At very low Re values, the flow is laminar unstable with some circular rolls of different sizes propagating towards the gap ($Re = 5 \times 10^3$, Fig.11.3a). They are somewhat different from classical Taylor vortices, which would have occupied the whole cavity with a corresponding axial wave number of 2. At $Re = 10^4$ (Fig.11.3b), some spiral patterns aligned with the tangential direction appear along the inner rings and around the midplane ($z^* = 0.5$). They coexist with the circular rolls on the top and bottom stationary rings. Some evidence of a disorganized flow structure can be seen from this Q-criterion map. When one increases further the Reynolds number, the flow gets clearly turbulent at $Re = 5 \times 10^4$ (Fig.11.3c) with fine scale eddies elongated in the tangential direction. Some circular rolls (not shown here) persist along the inner cylinder, with a structure similar to the toroidal vortices observed by Biage and Campos [23] for $Re = 2.04 \times 10^5$, $\eta = 0.38$ and $\Gamma = 10$. At $Re = 10^5$, the iso-values of the Q-criterion obtained by DNS (Fig.11.3d) show that the flow is clearly turbulent with even thinner turbulent structures. There is absolutely no evidence of large scale vortical structures embedded in the flow apart from large circular patterns, which appear along the inner cylinder. Turbulence is mainly concentrated at midplane ($z^* = 0.5$) because of the shear produced by the intense recirculation bubbles (Fig.11.5). Thus, the critical Reynolds number for the transition to turbulence is not significantly modified by the presence of the endcap rings compared to classical Taylor-Couette flows.

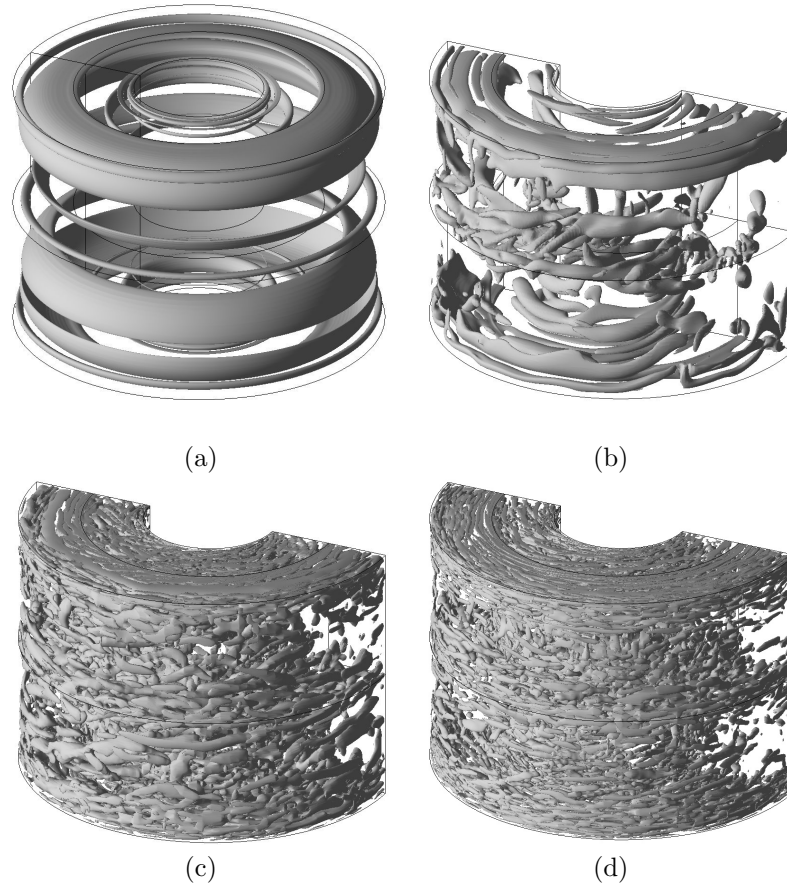


Figure 11.3: Iso-values of the Q-criterion obtained by DNS for $\Gamma = 2.12$, $\eta = 0.35$ and (a) $Re = 5 \times 10^3$, (b) $Re = 10^4$, (c) $Re = 5 \times 10^4$ and (d) $Re = 10^5$.

11.4.2 Mean hydrodynamic field

In such configuration, the main flow is directed tangentially due to the high rotation rate of the inner cylinder and rings. Due to centrifugal and confinement effects, a secondary flow develops in the meridional plane (r, z) . The results for the mean field are first qualitatively analysed considering bidimensional streamlines averaged in time for unsteady approaches.

Figure 11.4 presents the streamline patterns obtained by DNS and the RSM for $Re = 5 \times 10^4$. In the bulk flow, the pressure balances the centrifugal force. The pressure being approximately uniform axially, the difference in the centrifugal force between the bulk flow and the endcap rings generates a radial secondary flow in the (r, z) plane. The fluid is pumped along the rotating disks and being not blocked by the fixed rings, continues to flow radially outward. After that, it moves axially to the center of the cavity. Then the two axial flows create an intense shear layer at midplane, where the flow is mainly radially inwards. By conservation of mass, the fluid goes back axially along the inner cylinder to the rotating rings. Thus, the two approaches predict a meridional circulation with a 2-lobe flow structure, known as Ekman cells. Some small bubbles can be observed at the junction between the outer rings and the outer cylinder. The DNS predicts also 2 small recirculations along the inner cylinder.

When one increases the Reynolds number up to $Re = 10^5$, very different patterns arise from the different computations (Fig.11.5). The DNS (Fig.11.5a), LES (Fig.11.5d&e) and RSM (Fig.11.5b) predict a main big vortex for each of the two sides with some differences between these approaches. Looking at the streamline patterns obtained by DNS, the $k-\omega$ SST SAS (Fig.11.5c) and the LES of StarCCM+, asymmetry can develop at this Reynolds number. The secondary flow structure in the meridional plane gets more complex with the presence of small vortices arising along the inner cylinder or in the corners between the rings and the cylinders.

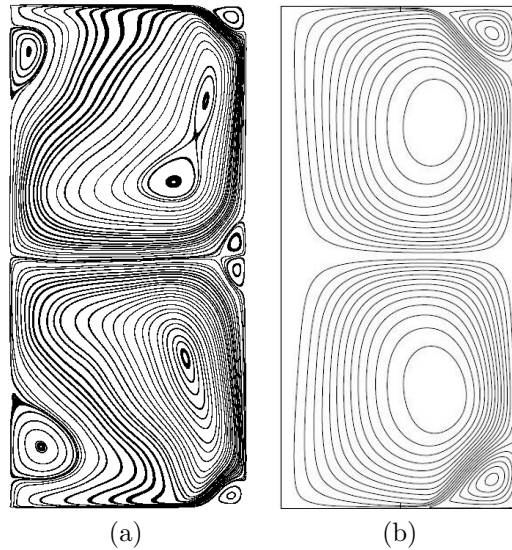


Figure 11.4: Mean streamline patterns obtained for $\Gamma = 2.12$, $\eta = 0.35$ and $Re = 5 \times 10^4$ by (a) DNS and (b) RSM. The rotation axis is located on the left of each subfigure.

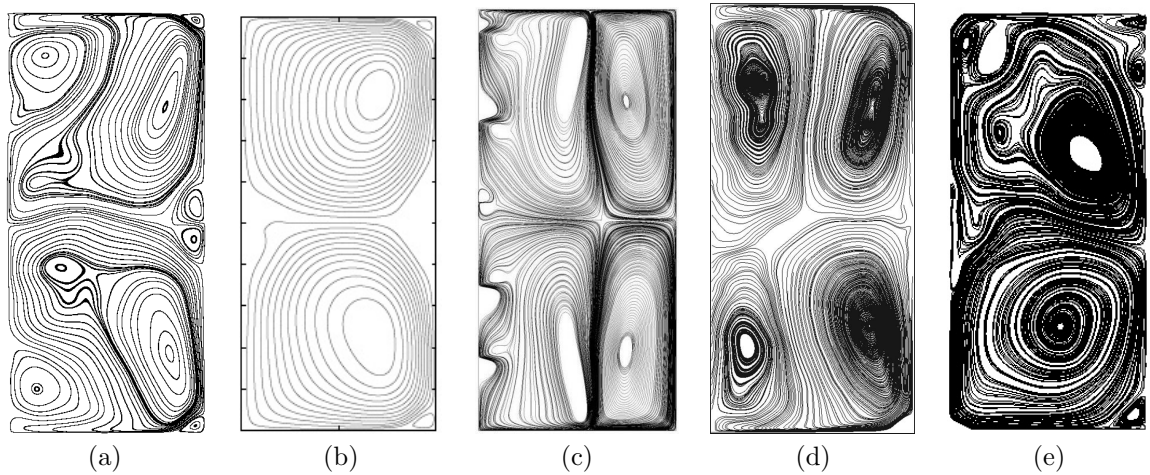


Figure 11.5: Mean streamline patterns obtained for $\Gamma = 2.12$, $\eta = 0.35$ and $Re = 10^5$ by (a) DNS, (b) RSM, (c) $k-\omega$ SST SAS, (d) LES (OpenFOAM) & (e) LES (Star CCM+). The rotation axis is located on the left of each subfigure.

The $k-\omega$ SST SAS model predicts a mean velocity pattern characterized by four rotating structures in the meridional plane, which is confirmed by computations performed by other $k-\omega$ models, indifferently in their unsteady or steady-state formulations and whatever the flow solver: CFX, OpenFOAM or STAR CCM+ (some results can be found in [118]). The fluid pumped along the rotating disks is deviated away from the wall almost as soon as it reattaches on the fixed rings creating a high tangential velocity zone around mid-radius (Fig.11.6). Such movement towards the center of the cylinder creates two counter-rotating bubbles in the inner and outer zones. While the outer bubble is almost symmetric in the axial direction, the inner one is centered quite close to the rotating disk showing a quite stretched shape. Smaller recirculations attached to the inner cylinder can also be observed. These smaller vortical structures are formed close to mid-height of the cylinder and are convected towards the rings.

Figure 11.6 presents the radial profiles of the mean tangential velocity component $V_\theta^* = V_\theta/(\Omega R_1)$ at the axial position $z^* = 1/4$ for four Reynolds numbers from $Re = 5 \times 10^4$ to $Re = 4 \times 10^5$.

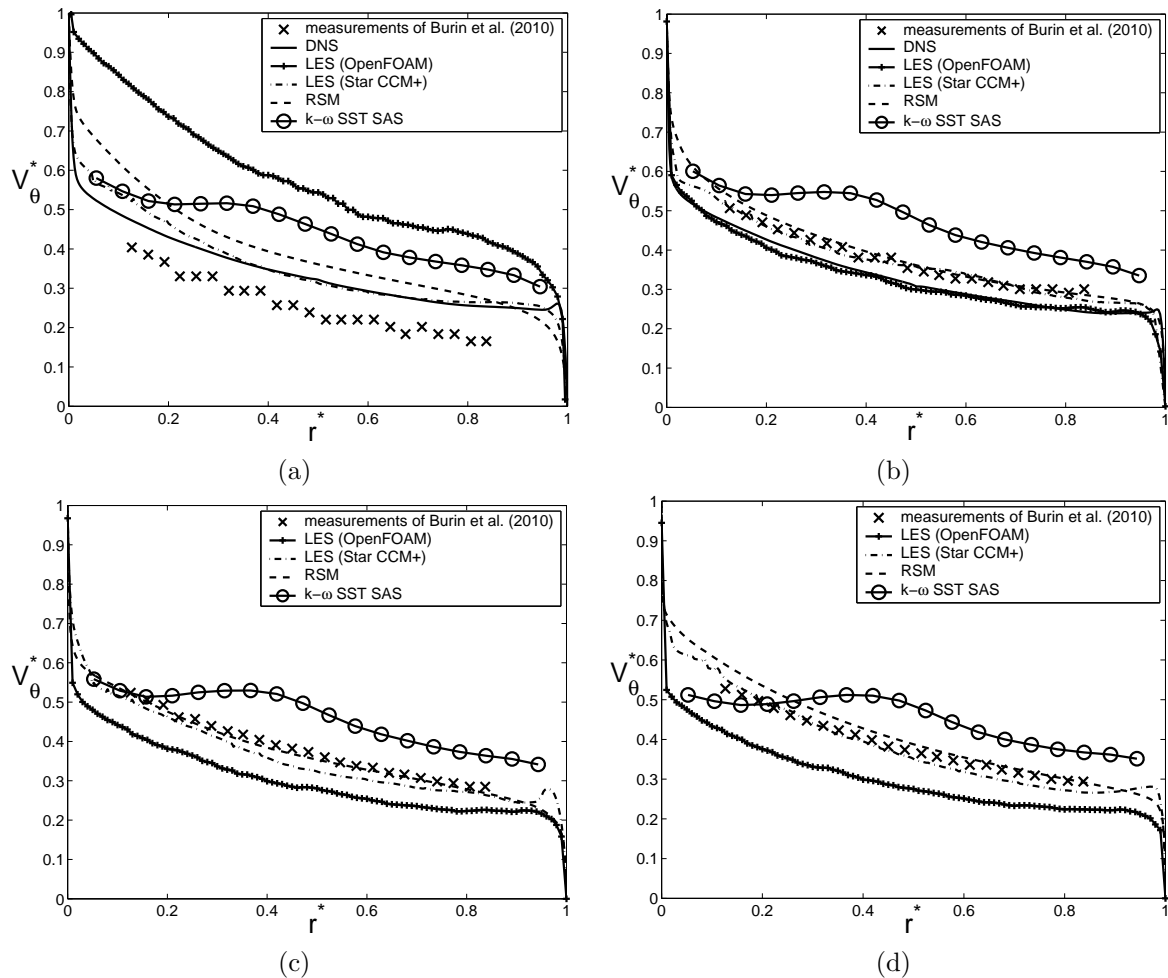


Figure 11.6: Radial profiles of the mean tangential velocity at $z^* = 1/4$ for $\Gamma = 2.12$, $\eta = 0.35$ and (a) $Re = 5 \times 10^4$, (b) $Re = 10^5$, (c) $Re = 2 \times 10^5$ and (d) $Re = 4 \times 10^5$.

At $Re = 10^5$ for example (Fig.11.6b), all the numerical approaches apart from the $k-\omega$ SST SAS model predict a radial profile of the mean tangential velocity divided into three areas. Two very thin boundary layers develop along the cylinders with a thickness of the order of 1% of the gap width. They are separated by a central region where the tangential velocity component is a quadratic function of the radius. From the DNS, $V_\theta^*(r) = 0.43 \times r^{*2} - 0.78 \times r^* + 0.59$ for example. Hollerbach and Fournier [130] pointed out that, at this Reynolds number, the shear layers developed close to the discontinuity should penetrate into the cavity and create a small discontinuity in the velocity profile. Burin *et al.* [40] attributed the absence of this discontinuity to an inadequate resolution of their measurements. The present data do not indicate any discontinuity in the velocity profile confirming the results of Burin *et al.* [40].

The $k-\omega$ SST SAS model as well as all the other $k-\omega$ SST models considered in [118] fail to predict the expected profile with a large overestimation of the mean tangential velocity within the gap (Fig.11.6b). While most of the models predict $V_\theta^*(r^* = 0.5)$ between 0.3 (LES OpenFOAM) and 0.36 (RSM), the SAS model predicts $V_\theta^*(0.5) \simeq 0.48$. A local maximum is also observed around $r^* \simeq 0.36$ from the SAS results, which is not the case in the experiments. The unsatisfying agreement between the $k-\omega$ SST and the experimental data in terms of the tangential velocity is probably related to the presence of the four rotating structures in the meridian plane. The velocity peak close to the radius $r^* = 0.36$ on Figure 11.6 can be indeed justified by the tangential momentum transport operated by these inner vortices. This behavior is similar to what obtained both experimentally and numerically by Kageyama *et al.* [142] for $Re \simeq 10^6$, $\eta = 0.256$ and $\Gamma = 0.45$. The tangential velocity profile is nearly constant over a radius in their case and the authors attribute it to the reduction of the Ekman cells due to endcap ring effects. It is noteworthy that the DNS predicts a local maximum close to the

outer cylinder but due to the lack of experimental data very close to the wall, no definitive conclusion can be drawn.

By comparing Figures 11.6a to 11.6d, a noticeable influence of the Reynolds number on the mean velocity profiles can be observed. For $Re \geq 10^5$, the mean tangential velocity slightly increases for increasing values of Re but this effect remains weak. It is besides not observed from the LES (OpenFOAM) results, which underpredict the tangential fluid velocity in that cases. The SAS model still overestimates V_θ^* in the main part of the gap. For $Re = 5 \times 10^4$ (Fig. 11.6a), the experimental profile is much lower, which is characteristic of much weaker turbulence levels. All the numerical approaches fail to reproduce the good profile. The DNS seems to offer the best agreement with the experiment at this Reynolds number. The overestimation of the tangential velocity of the fluid may be attributed to higher turbulence intensities and to an earlier transition to the fully turbulent regime in the numerics. Surprisingly, the LES of OpenFOAM strongly overestimates the mean velocity profile in that case, with a profile quite similar to the laminar circular Couette profile ($V_\theta^* = R_1(R_2^2/r - r)/(R_2^2 - R_1^2)$), indicating much lower turbulence levels than in the experiments or in the DNS for examples.

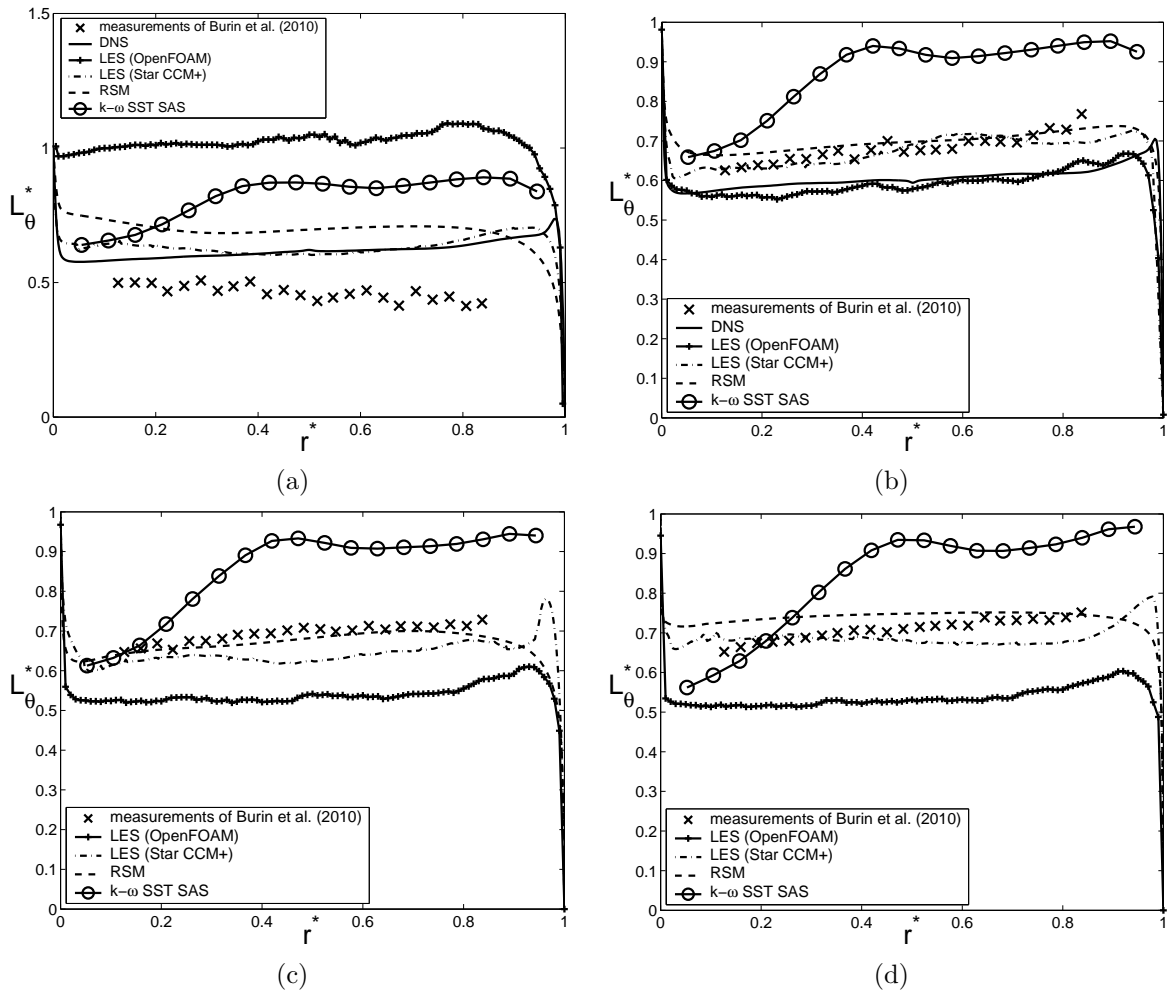


Figure 11.7: Radial profiles of the normalized angular momentum at $z^* = 1/4$ for $\Gamma = 2.12$, $\eta = 0.35$ and (a) $Re = 5 \times 10^4$, (b) $Re = 10^5$, (c) $Re = 2 \times 10^5$ and (d) $Re = 4 \times 10^5$.

The same data can also be plotted in terms of the angular momentum $L_\theta = rV_\theta$ of the mean flow. Thus, Figure 11.7 presents the radial profiles of L_θ at the same axial location $z^* = 1/4$. It has been made dimensionless using the value of L_θ at the inner cylinder $L_\theta(R_1) = \Omega R_1^2$. For $Re = 5 \times 10^4$, the angular momentum is rather constant over the radius with a measured value around 0.5, whereas a slight increase may be observed from the numerical profiles with $L_\theta^*(r^* = 0.5) \simeq 0.62$ for the DNS.

Surprisingly, the LES of OpenFOAM predicts an angular momentum, which can be slightly higher than one. For $Re \geq 10^5$, the influence of Re on L_θ^* remains weak. Apart very close to the walls, the numerical approaches predict an angular momentum almost constant over the radius, while a slight increase with r^* may be noticed from the measurements. The value at mid-gap is around 0.65, which is much larger than the usual value 0.5 obtained in classical Taylor-Couette flows [324]. It can be explained by considering the additional torque from the inner rotating rings, which rotate at the same rate as the inner cylinder but at a larger radius. Even if most of the models predict quite well the mean tangential velocity, the variations of the angular momentum with the radius highlight larger discrepancies mainly because of the normalization. The DNS slightly underestimates the slope of the profile in the central region, where the RSM of Elena and Schiestel [85] offers the best agreement with the experimental data of Burin *et al.* [40]. The $k-\omega$ SST SAS model strongly overestimates the mean angular momentum in the whole gap.

11.4.3 Turbulent statistics

11.4.3.1 Cross-correlation coefficient

Burin *et al.* [40] provided also the variations with the Reynolds number of the cross-correlation coefficient $C_{r\theta}$ defined as:

$$C_{r\theta} = \frac{\overline{v'_\theta v'_r}}{\sqrt{\overline{v'^2_\theta}} \sqrt{\overline{v'^2_r}}} \quad (11.7)$$

The variation of $C_{r\theta}$ with the Reynolds number Re are provided on Figure 11.8 at a given position ($r^* = 3/4$, $z^* = 1/4$). Burin *et al.* [40] observed that $C_{r\theta}$ slightly decreases with Re as the flow becomes increasingly random. As it can be seen from Figure 11.8, the time averaged value obtained by the different models at the monitoring point is close to 20% and does not vary so much with Re in the range $[500, 4 \times 10^5]$, in quite good agreement with [40]. For $Re = 5 \times 10^4$, Burin *et al.* [40] have inferred from the data of Smith and Townsend [324] that $C_{r\theta} = 30 - 40\%$. This value has been found using the RSM of Star CCM+ (not shown here), in the same geometry as [40], whereas all the other approaches predict $C_{r\theta} = 0.24$ or less. The high value obtained by Smith and Townsend [324] is due, according to [40], to the presence of large scale vortical structures embedded in the flow. This conclusion is not supported by none of the present calculations, which, even if some of them are performed assuming a periodicity in the tangential direction, do not highlight such type of vortices.

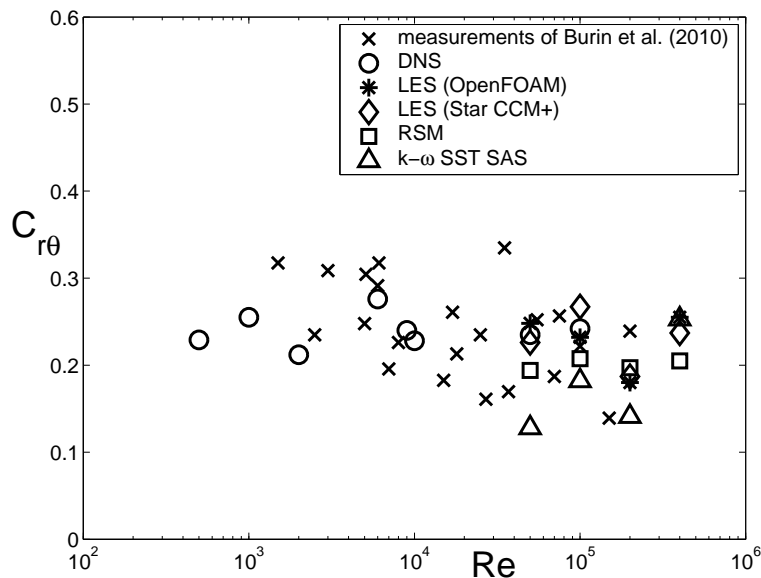


Figure 11.8: Variations of the cross correlation coefficient $C_{r\theta}$ with the Reynolds number Re at $r^* = 3/4$ and $z^* = 1/4$ for $\Gamma = 2.12$ and $\eta = 0.35$.

In fact, the LES results (OpenFOAM) show that the cross-correlation coefficient strongly varies between -0.4 and 0.4 depending on the computed position in a meridian plane, as it can be seen from the $C_{r\theta}$ -map in Figure 11.9. Thus, those punctual values have to be considered carefully and might be not so representative of the time averaged cross correlation in that region.

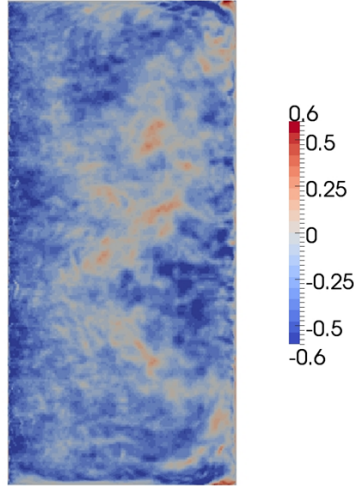


Figure 11.9: Map of the cross-correlation coefficient $C_{r\theta}$ in a meridian plane obtained by the LES of OpenFOAM for $\Gamma = 2.12$, $\eta = 0.35$ and $Re = 10^5$.

11.4.3.2 Transport of turbulent angular momentum

The measured velocity correlation is discussed also in terms of a dimensionless torque per unit length G , in which the viscous term has been neglected as in [40]:

$$G = \frac{2\pi r^2 \overline{v'_\theta v'_r}}{\nu^2} \quad (11.8)$$

Its variation with the Reynolds number is shown in Figure 11.10 for all the approaches and compared to the measurements of Burin *et al.* [40]. It is also compared to the scalings proposed by Dubrulle and Hersant [79] (Eqs.11.3-11.5). For this range of Reynolds numbers, the DNS, LES (OpenFOAM) and RSM results confirm that G depends on Re following a unique power law: $G \propto Re^\alpha$ with $\alpha = 1.9$, which suggests that the transport of angular momentum may be seen as a diffusive process. This value remains slightly larger than the one $\alpha = 1.7$ deduced from the measurements of Burin *et al.* [40] or Wendt [354]. Tong *et al.* [339] obtained $\alpha = 1.8$ for $\eta = 0.448$ and $4 \times 10^4 < Re < 4 \times 10^5$. It shows that only one regime is obtained here corresponding to the regime 3 of Dubrulle and Hersant [79]. Equation (11.5) would fit indeed quite well our numerical results with a lower radius ratio η .

Most of the models underestimate the values of G compared to the predictions of Equation (11.5) or to the measurements of [354]. Two main reasons can be advocated in the present case. Firstly, the aspect ratio of the Burin *et al.*'s [40] apparatus is low compared to classical Taylor-Couette systems, which increases the influence of the endcap disks on the flow. The fact that only the inner rings are rotating with the inner cylinder may partly explain the reduced values of the turbulent angular momentum. Secondly, looking at Figure 11.11, one may also argue whether comparing a punctual value is an efficient strategy to verify turbulence levels when, as this is the case here, the local variability of the resolved part of G is high. Figure 11.11 shows also how the modeled contributions are important only very close to the outer walls and are of the same order of magnitude as the resolved part in that regions.

A preliminary calculation on a 5 degree sector using the LES within OpenFOAM has been performed providing much lower values of both $C_{r\theta}$ and G with at least one order of magnitude. This finding confirms the importance of large tangential vortical structures on the behavior of the flow.

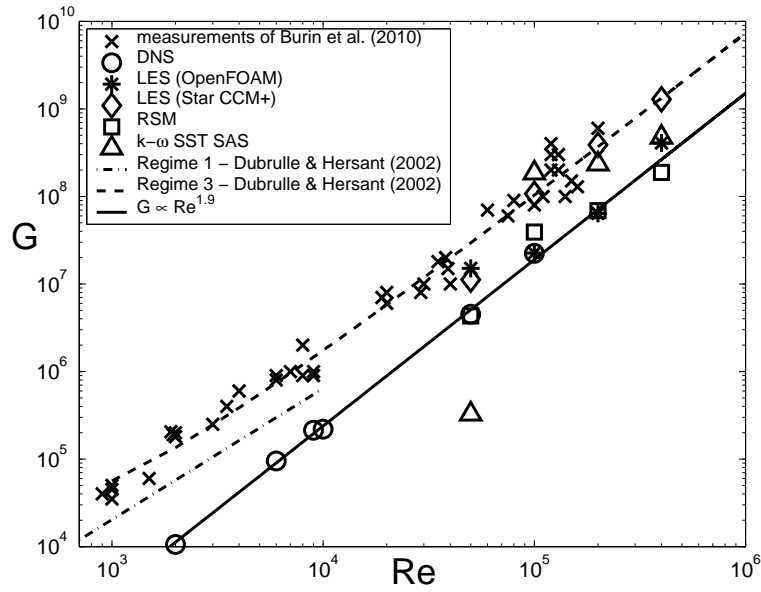


Figure 11.10: Variations of the turbulent angular momentum transport G with the Reynolds number Re at $r^* = 3/4$ and $z^* = 1/4$ for $\Gamma = 2.12$ and $\eta = 0.35$.

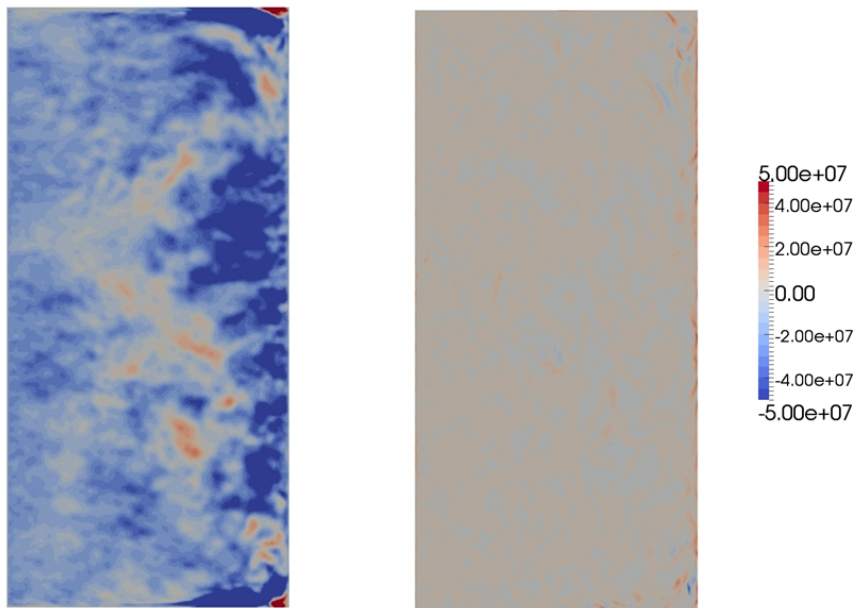


Figure 11.11: Maps of the turbulent angular momentum G in a meridional plane obtained by the LES of OpenFOAM for $\Gamma = 2.12$, $\eta = 0.35$ and $Re = 10^5$. The resolved and modeled parts are shown on the left and right figures respectively.

It could be also pertinent to average the turbulent angular momentum transport G along the inner cylinder as done in Figure 11.12. The values obtained by the in-house DNS code are globally lower than those expected by the different laws provided by Dubrulle and Hersant [79]. G depends here on the Reynolds number to the power $\alpha = 2.2$ for the whole range of Re -values. The exponent α is slightly higher than the value $\alpha = 2$ proposed by Eckhard *et al.* [82].

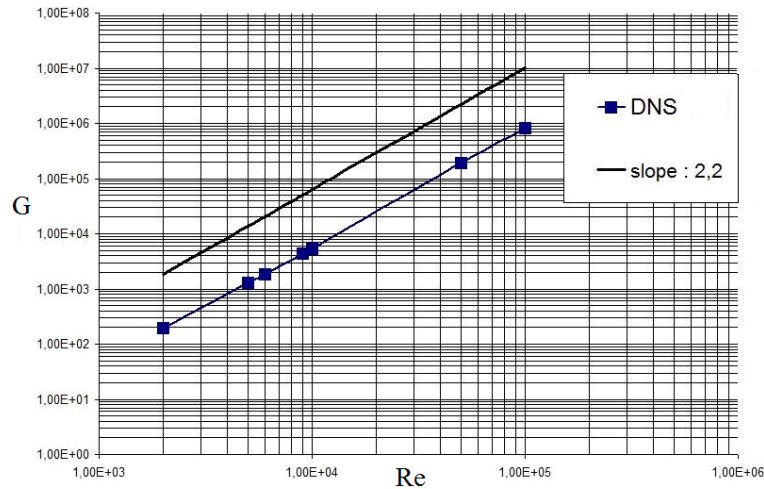


Figure 11.12: Influence of the Reynolds number Re on the turbulent angular momentum transport G averaged along the inner cylinder. DNS results for $\Gamma = 2.12$ and $\eta = 0.35$.

11.5 Conclusion

Numerical predictions have been performed using a DNS code, the RSM closure of Elena and Schiestel [85] and some LES and RANS models available within OpenFOAM, StarCCM+ or CFX. The computed results have been compared to experimental data available in the literature for an original Taylor-Couette arrangement initially developed by Burin *et al.* [40] characterized by endcap rings enclosing the cavity.

In the present cavity, the difficulty arises from the presence of two endcap rings attached to both cylinders. It appeared then crucial to take into account accurately the brutal variations in the boundary conditions on the upper and lower walls. A multidomain DNS code has then been developed providing very valuable data for comparisons with the experimental data and other numerical results. DNS showed that there is no evidence of Taylor vortices embedded in the turbulent flow apart very close to the inner cylinder where circular vortices have been observed. It explains why the 2D unsteady RSM [85], which has been sensitized to the implicit effects of rotation on turbulence, provides the best overall agreement in that case, where the rotation rate is quite high. On the contrary, all the $k-\omega$ SST models including the innovative SAS model fail to predict the mean tangential velocity profiles with large discrepancies even in the core of the flow. It can be attributed to the existence of four large recirculations in a meridian plane, whereas all the other models predict only two bubbles. All the models predict the good tendency for the turbulent angular momentum transport G , which is found to vary as $Re^{1.9}$ in agreement with previous approaches [79]. Nevertheless, most of the models including the RSM [85], the LES (OpenFOAM) but also the DNS underpredict the shear stress tensor component. The cross correlation coefficient $C_{r\theta}$ is well predicted by all the approaches with almost a constant value around 0.2 (at a given location) for a wide range of Reynolds numbers. The LES provides very useful data showing the high variability of these two parameters.

For industrial applications, the DNS remains computationally expensive compared to the other approaches. The LES within Star-CCM+ and the RSM model [85] showed a good behavior in this challenging test case providing fair results for the mean and turbulent fields. It offers then a good compromise between accuracy and calculation cost. More comparisons at higher Reynolds numbers are now required to confirm these tendencies.

Turbulent Taylor-Couette-Poiseuille flows

As already evoked in the two previous Chapters, this topic on the turbulent flow and heat transfer in the rotor-stator gap of an electrical motor has been inspired by the need of Liebherr Aerospace Toulouse to know more accurately what are the heat transfers in such rotating machineries depending on the operating conditions. It started in 2008 with the Master 2 internship of S. Haddadi. This project called “Entrefer” is financially supported by Liebherr Aerospace Toulouse for the period 2010-2013. It is a close collaboration with the IRPHE lab and the team “Geophysical and rotating flows” in particular, which is in charge of the experimental part. The problem can be simply modeled by a Taylor-Couette-Poiseuille flow with thermal gradients. The first results obtained using the RSM during the internship of S. Haddadi have been published in 2011 in *Int. J. Heat Fluid Flow* (Ref.[256]). LES calculations have been then performed to investigate prospective 3D effects, which could explain the discrepancies in the Nusselt number distributions between the experiments and the numerics. They have been compared to the velocity and temperature measurements performed using a new experimental set-up developed at IRPHE on that occasion. This work will partly fill the need of a wide database of velocity profiles and heat transfer distributions for a wide range of global parameters as pointed out in the recent review of Fénot et al. [94].

12.1 Introduction

The present investigation is concerned with the numerical modeling of fluid flow and heat transfer in a Taylor-Couette-Poiseuille system. The turbulent flow is confined between two differentially heated coaxial cylinders, with an inner rotating cylinder and an outer stationary one. An axial throughflow of fresh fluid is also superimposed. This kind of Taylor-Couette flows with a superimposed Poiseuille flow is of great importance, since these flows have many applications in process engineering (dynamic membrane filtration, rheology, UV disinfection, pasteurization), geophysics (mantle convection) and also in the turbomachinery industry for bearings, asynchronous motor with axial ventilation [110], rotating heat exchangers and the drilling of oil wells among other things. In the present work, the Taylor-Couette-Poiseuille system is a simple representation of the gap between the rotating and the stationary parts of an electrical motor (Fig.12.1) contained in an air conditioning pack. A better knowledge of the convective heat transfer in the annular gap is required to optimize the performances of such a rotating machinery. Usually, the radial gap between the cylinders is quite weak (of the order of 1 mm) and the rotation rate of the inner cylinder can reach more than 2×10^5 rpm. The difficulty to perform accurate measurements in such closed clearances and especially in the very thin boundary layers along the cylinders has slowed down the development of specific turbulence models. It explains why relatively few works have been dedicated to such complex flows up to now.

The effect of an axial throughflow in a Taylor-Couette system, where only the inner cylinder is rotating, has been considered experimentally by Kaye and Elgar [150] in the isothermal case. Their results showed in particular the existence of four flow regimes depending on the Reynolds number (based on the incoming flow velocity \overline{V}_z and the radial gap between the cylinders $\Delta R = e = b - a$, a and b being the radii of the inner and outer cylinders respectively) and on the Taylor number: laminar and turbulent flows, with or without Taylor vortices. Becker and Kaye [20] performed temperature measurements for a large range of rotation rate and superimposed flowrate. They studied the heat transfer in the gap between a heated inner rotating cylinder and a cooled outer stationary one. Compared to the isothermal case, they did not highlight the existence of Taylor vortices in the turbulent regime.

Most of the experimental works so far have been performed in Taylor-Couette systems characterized

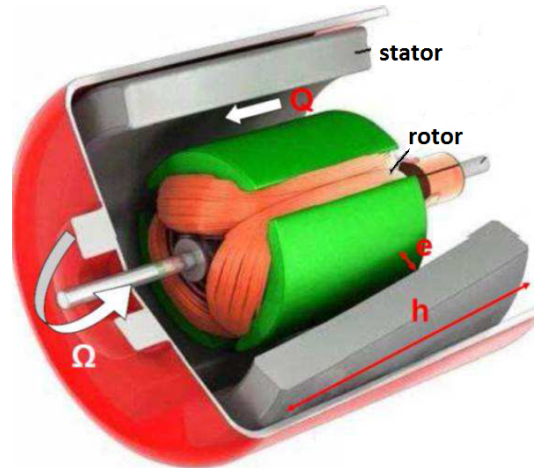


Figure 12.1: Exploded view of an electrical motor and its rotor-stator gap.

by a large aspect ratio $\Gamma = h/\Delta R$ and a large radius ratio $\eta = a/b$, with h the length of the cylinders. Aoki *et al.* [12] performed a combined theoretical and experimental investigation of turbulent Taylor-Couette flows without any Poiseuille flow. The most noticeable result is that the gap ratio $\Delta R/a$ in the range $[0.055 - 0.132]$ has only a small effect on the heat transfer for three different fluids: air, iso-butyl alcohol and spindle oil. They provided also numerous correlations for the Nusselt number according to the Taylor and Prandtl numbers. Kuzay and Scott [165] studied experimentally the turbulent heat transfer in the gap between an inner rotating or non rotating insulated cylinder and an outer stationary and heated cylinder combined with an axial air flow. They established correlations for the Nusselt numbers against a new physical parameter, called the rotation parameter $N = \Omega a/\bar{V}_z$, which combines both the rotation and axial flow effects. This parameter is defined as the ratio between the rotating speed of the inner cylinder Ωa and the mean axial velocity of the incoming fluid \bar{V}_z . Lee and Minkowycz [175] highlighted experimentally the effects of the gap ratio $\Delta R/a$ in the range $[0.0083 - 0.051]$ and of grooved cylinders on the heat transfer. They showed in particular that the heat transfer process is enhanced for increasing values of the gap ratio. Escudier and Gouldson [89] performed velocity measurements by Laser Doppler Anemometry (LDA) in a cavity characterized by $\Gamma = 244$ and $\eta = 0.506$ for various flow conditions (rotation rate Ω and flowrate Q) and different fluids including Newtonian and shear-thinning fluids. For the Newtonian fluid in the turbulent regime, the radial distribution of the axial velocity and the pressure drop are similar to the ones observed in pipe flows. The radial distribution of the tangential velocity reveals a flow structure divided into three regions: two very thin boundary layers, one on each cylinder, separated by a central core in near solid body rotation. The main effect of the superimposed axial throughflow is to reduce the tangential velocity in the core region. Nouri and Whitelaw [226] measured the three mean velocity components and the associated Reynolds stress tensor for the flow subjected to an axial superimposed throughflow in a concentric annulus ($\Gamma = 98$, $\eta = 0.496$) with or without rotation of the inner cylinder. Compared to the non rotating case (for $C_w = Q/(\nu b) = 42306$), the rotation of the inner cylinder at $\Omega = 300$ rpm ($Re_i = \Omega a \Delta R/\nu = 1616.6$) does not affect the drag coefficient and the radial distribution of the mean axial velocity in the turbulent regime. It slightly enhances turbulence intensities especially close to the walls. For $C_w = 125039$, there is absolutely no effect of the rotation of the inner shaft on both the mean axial flow and turbulence intensities. In a further paper, Nouri and Whitelaw [227] extended their work to the case of eccentric cylinder arrangements and proposed a review of previous works on Taylor-Couette flows including Newtonian and non-Newtonian fluids and rotating and non rotating flows. Bouafia *et al.* [30] performed extensive temperature measurements in the gap between a heated rotating inner cylinder and a cooled stationary outer one. An axial Poiseuille flow of air can be superimposed or not. The heat transfer is increased in the case of grooved cylinders compared to the basic case with smooth walls for an enclosed cavity. When an axial flow is imposed, the heat transfer along the rotating wall is increased in the smooth case. Numerous correlations for the Nusselt numbers along both surfaces are provided against a modified Taylor number and an effective Reynolds number for various flow conditions.

Naser [217] compared the predictions of a $k - \varepsilon$ model with the experimental data of Escudier and Gouldson [89] for the same flow conditions. For a turbulent Newtonian flow, the model showed large discrepancies for the mean velocity components. The profiles depend strongly on the axial position, which is not observed in the experiments [89]. The author attributed these deviations to the fact that the eddy viscosity concept, on which the model is developed, is incompatible with the simulated flow conditions. It can be attributed also to the fact that the $k - \varepsilon$ model is not sensitized to the implicit effects of rotation on turbulence. Char and Hsu [46] conducted numerical predictions using a modified version of the Launder-Sharma $k - \varepsilon$ model for turbulent mixed convection of air in a concentric horizontal rotating annulus. This model includes both the Yap correction and the Kato-Launder modification, which slightly improves the predictions compared to the classical Launder and Sharma model. The authors performed a parametric study of the fluid flow and heat transfer for various radius ratios $0.1 \leq \eta \leq 0.385$, Reynolds numbers $0 \leq Re_i \leq 10^5$ and Rayleigh numbers $10^7 \leq Ra \leq 10^{10}$. For this range of Ra , they highlighted the three-dimensional structure of the flow with a two-cell structure in a (r, θ) plane for Re up to 10^4 . Kuosa et al. [164] considered the cooling of high-speed electrical machines, where only the inner cylinder is rotating. They compared the predictions of three different models: an algebraic model, a low-Reynolds number $k - \varepsilon$ model and a $k - \omega$ SST model. The hydrodynamic and thermal fields are established for various rotation rates and mass flowrates. The three turbulence models underestimated the heat transfer coefficients along both cylinders. Moreover, the entrainment coefficient of the fluid is far from the theoretical value for a fully turbulent flow. These discrepancies were attributed by the authors to the boundary conditions imposed at the inlet and outlet sections and to the turbulence models used. More recently, Giret [110] performed a combined experimental and numerical investigation of the convective heat transfers in the air gap of an alternator. Heat transfer measurements were compared to two-equation models available within the commercial code ANSYS CFX for various flow conditions and different geometries for the inner rotating cylinder. The convective heat transfers were underestimated by the models on the rotor and overestimated on the stator. The experimental results were found to be almost the same when the inner cylinder is smooth or with four inter-polar gaps.

To our knowledge, Chung and Sung [54] were the first to perform Large Eddy Simulation (LES) in such complex configurations. They compared their numerical data to the experimental ones of Nouri and Whitelaw [226] for $\eta = 0.5$, $C_w = 20970$ and $Re_i = [954.5; 1909.1; 3818.1]$. They obtained a relatively close agreement for the mean velocity and the Reynolds stress tensor components. The mean tangential velocity was slightly overestimated in the main part of the radial gap between the cylinders. They focused their numerical investigation on the appearance of turbulent structures attributed to the destabilization of the flow along the inner rotating cylinder and giving rise to strong events (sweeps and ejections).

Recently, Fénot et al. [94] performed a review on the heat transfer between concentric rotating cylinders with or without axial flow. They concluded their paper by: *notwithstanding the sizable quantity of studies focused on the subject of flows in rotating annular space, the similarly large number of influence and impact factors still leaves many question marks pertaining to the dynamics and, more specifically, to the heat transfer in the flow ... the published results hinge to a great extent on the configurations that have been studied, and do not yet offer an adequate basis for large-scale extrapolation.*

The purpose of this Chapter is to predict the turbulent flow and heat transfer in the gap of an electrical machine schematized here by a very narrow Taylor-Couette-Poiseuille system for a wide range of operating conditions (see Table 12.1). The Reynolds Stress Model (RSM) of Elena and Schiestel [84, 85, 298], which has shown to offer the best trade-off between accuracy and calculation cost in various rotating flow arrangements [119, 249, 253, 258, 259], has thus been chosen for a preliminary study. Then, some LES results are compared to velocity and temperature measurements performed at IRPHE using a new experimental set-up. The two codes have been first validated under isothermal conditions on well established data available in the literature before being applied to the real flow conditions operating in the electrical motor developed by Liebherr Aerospace Toulouse. It is also to get a better insight into the dynamics and the heat transfer process of the turbulent Taylor-Couette-Poiseuille flow in a very narrow cavity.

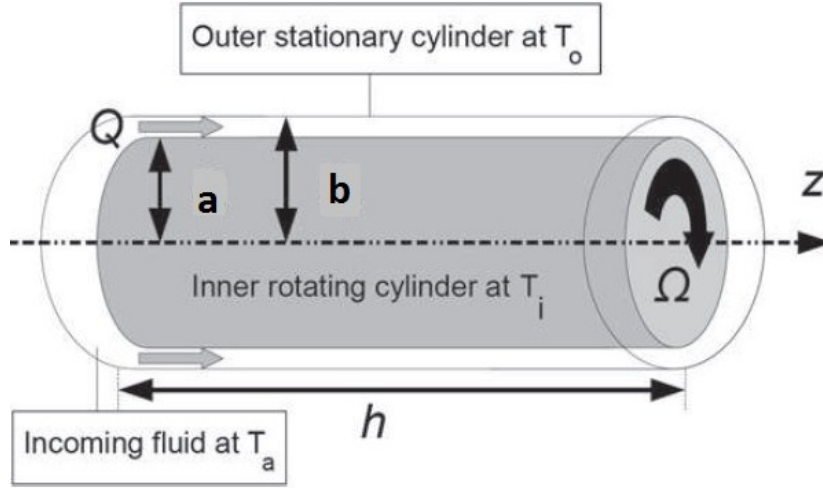


Figure 12.2: Schematic representation of the Taylor-Couette-Poiseuille configuration with relevant notations.

12.2 Geometrical configuration and flow global parameters

The cavity sketched in Figure 12.2 is composed of two smooth concentric cylinders. The inner cylinder of radius a is rotating at a given rotation rate Ω , while the outer cylinder of radius b is stationary. The height of the cavity is denoted h in the following. An axial voluminal flowrate Q can be superimposed at the cavity inlet.

The mean flow is mainly governed by four global parameters: the aspect ratio of the cavity Γ , its radius ratio η , the rotational Reynolds number Re_i based on the rotating speed of the inner cylinder Ωa and half the hydraulic diameter $\Delta R = b - a$ and the flowrate coefficient C_w defined as follows:

$$\Gamma = \frac{h}{\Delta R} \quad \eta = \frac{a}{b}$$

$$Re_i = \frac{\Omega a \Delta R}{\nu} \quad \text{or} \quad Ta = \frac{\Omega^2 a (\Delta R)^3}{\nu^2} = \frac{\Delta R}{a} Re_i^2$$

$$C_w = \frac{Q}{\nu b} \quad \text{or} \quad Re_Q = \frac{2 \bar{V}_z \Delta R}{\nu} = \frac{2}{\pi \Delta R (1 + \eta) C_w}$$

where ν is the fluid kinematic viscosity. In the last section, the results will be discussed in terms of an axial Reynolds number Re_Q and the Taylor number Ta for easier comparisons with published data, where $\bar{V}_z = Q/[\pi(b^2 - a^2)]$ is the axial velocity imposed at the inlet. These two parameters can be gathered to form the rotation parameter $N = \Omega a / \bar{V}_z$.

For the thermal field, one important parameter is the Prandtl number Pr defined as:

$$Pr = \frac{\nu}{\alpha} \quad (12.1)$$

where α is the fluid thermal diffusivity. The thermal field will depend also on other parameters under the form of dimensionless thermal gradients, which will be introduced later in the corresponding sections.

Four different geometries will be considered in the following, two under isothermal conditions and the two others under non-isothermal conditions correspond to real operating conditions in the rotating machineries developed by Liebherr Aerospace Toulouse. The values of all parameters for these four configurations are summarized in Table 12.1. The values of Re_i considered here are much higher than the critical value $Re_i = 210$ for the transition to turbulence found experimentally by Aoki *et al.* [12], which ensures that the flow is highly turbulent without Taylor vortices in all cases.

Test case	Γ	η	Re_i Ta	C_w Re_Q	N	Pr
Escudier and Gouldson [89]	244	0.506	961.1 9.02×10^5	2839; 5914; 17742 1202; 2497; 7501	1.6; 0.77; 0.26	–
Liebherr 1	77	0.961	$[3744 - 37443]$ $[5.69 \times 10^5 - 5.69 \times 10^7]$	$[0 - 30000]$ $[0 - 46805]$	$[1.6; \infty[$	$[0.01 - 12]$
Nouri and Whitelaw [226]	9	0.5	954.5; 1909.1; 3818.1 $9.11; 36.4; 146 \times 10^5$	20970 8900	0.2145; 0.429; 0.858	–
“Entrefer project”	50	8/9	8391; 16733; 25140 $0.88; 3.5; 7.9 \times 10^7$	222.2; 332.3 7490; 11200	$[149.8 - 671.4]$	0.7; 7

Table 12.1: Values of the flow parameters for the four configurations considered in this Chapter.

12.3 Preliminary results using the RSM model

The flow is studied here using the RSM model described in Chapter 4. The grid independence of the solution has been checked for the two configurations considered here: the first one corresponds to the experiment of Escudier and Gouldson [89] and the second one to a real machinery developed by Liebherr Aerospace Toulouse. A $(N_r = 180) \times (N_z = 400)$ mesh in the (r, z) frame provides the best arrangement between accuracy and CPU time compared to the other meshes considered. Table 12.2 summarizes the computational details used in this section. For this grid, the sizes of the thinner mesh $\Delta_1 r$ and $\Delta_1 z$ in the radial and axial directions respectively remain quite low. It is also verified that the grid is sufficiently refined close the cylinders to describe accurately the viscous sublayers. For example, the wall coordinate $r^+ = \Delta_1 r u^* / \nu$ (u^* the friction velocity at the wall) remains below 0.05 along both cylinders for configuration 2, which is quite below the classical value $r^+ = 1$. About 30000 iterations (20 hours) on the M2P2 cluster are necessary to obtain the numerical convergence of the calculations.

configuration	test case	$N_r \times N_z$	$\Delta_1 r/h$	$\Delta_1 z/h$	$max(r^+)$
1	Escudier and Gouldson [89]	180×400	5.65×10^{-5}	6.38×10^{-3}	0.21
2	Liebherr 1	180×400	9×10^{-8}	3.89×10^{-6}	0.05

Table 12.2: Computational details for the two test cases of Escudier and Gouldson [89] and Liebherr 1. $\Delta_1 r$ and $\Delta_1 z$ are the size of the first cell in the radial and axial directions and $max(r^+)$ is the maximum value of the wall coordinate along both cylinders.

12.3.1 Benchmark of RANS models in the configuration of Escudier and Gouldson [89]

The predictions of the RSM [85] and other models available within OpenFOAM, Fluent and Star-CCM+ are compared to the LDA measurements of Escudier and Gouldson [89] and to the previous $k - \varepsilon$ computations of Naser [217] in a very elongated Taylor-Couette system defined by $\Gamma = 244$ and $\eta = 0.506$ (middle-gap cavity [23]). The rotational Reynolds number is fixed here to $Re_i = 961.07$ and the comparisons are performed at a given axial position $z^* = z/h = 0.1$ for three values of the flowrate coefficient: $C_w = 2839, 5914$ and 17742 . Thus, three values of the rotation parameter are considered: $N = 0.968, 0.465$ and 0.148 . It corresponds to the values 1200, 2500 and 7500 for the Reynolds number based on the bulk velocity in [89]. All the comparisons and the numerical details are presented in details in two proceeding papers (Ref.[118, 255]). It was done in close collaboration with R. Da Soghe and C. Bianchini from the University of Florence. It is noticeable that all computations performed with StarCCM+ are 3D unsteady and use unstructured grids with 2.8 millions of mesh points and time step lower than 0.01 s. Calculations with the LES of OpenFOAM are also 3D unsteady (periodicity of $\pi/2$) and use unstructured grids with 3.8 millions of mesh points and a time step equal to 0.0015 s. The computations using the in-house RSM are 2D steady and use structured grids with 72000 mesh points (see Table 12.2).

In order to offer an idea of the turbulent structures arising in the flow, maps of the instantaneous tangential and axial velocities are reported in Figures 12.3b & c respectively together with the isovalues of the Q-criterion in Figure 12.3a obtained by LES (OpenFOAM) for $Re_i = 961.07$ and $C_w = 17742$. Note that the isocontours of Q are reported from the point where turbulent flow behavior first arises,

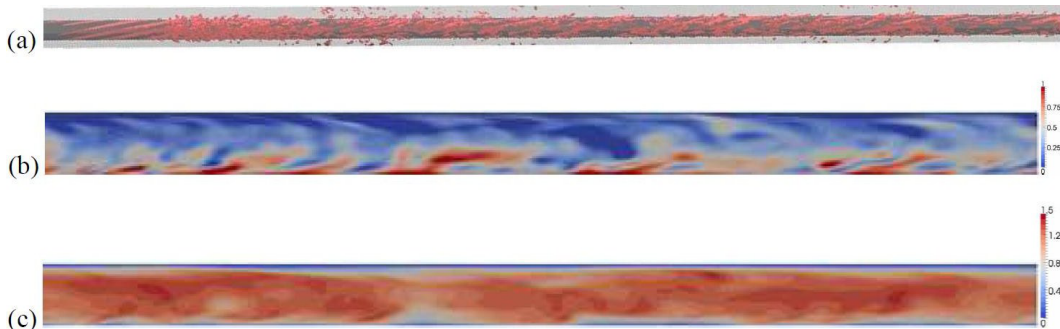


Figure 12.3: (a) Iso-values of the Q-criterion ($Q = -2000$) and maps of the instantaneous (b) tangential and (c) axial velocity components in a meridian plane (the rotation axis is at the bottom of each figure and it flows from the left to the right). Results obtained by LES using OpenFOAM for $\Gamma = 244$, $\eta = 0.506$, $Re_i = 961.07$ and $C_w = 17742$.

at approximately one-fourth of the entire axial extension (due to the laminar behavior imposed by the inflow boundary conditions). The radial velocity component (not reported here) is almost zero in the whole cavity for this set of parameters. Thus, the flow is a combination of an intense Taylor-Couette flow close to the inner rotating cylinder due to rotation and of an axial Poiseuille flow within the gap. It explains the presence of helical vertical patterns, which roll up along the inner wall. Otherwise there is no evidence of 3D large scale structures embedded in the flow. The main flow is dominated by the axial Poiseuille flow, which can be explained by the low value of the rotation parameter $N = \Omega a / \bar{V}_z = 0.148$.

As a preliminary, one defines the following dimensionless quantities: the dimensionless radial $r^* = (r - a) / \Delta R$ and axial $z^* = z / h$ positions. Thus, $r^* = 0$ on the inner cylinder and $r^* = 1$ on the outer cylinder. In the same way, $z^* = 0$ corresponds to the cavity inlet and $z^* = 1$ to the outlet. The mean tangential velocity component is normalized using the rotational speed of the inner cylinder Ωa , whereas the mean axial velocity component is normalized using the mean axial velocity \bar{V}_z imposed at the inlet: $V_\theta^* = V_\theta / (\Omega a)$ and $V_z^* = V_z / \bar{V}_z$. To enable direct comparisons with the measurements of Escudier and Gouldson [89], the tangential v'_θ and axial v'_z normal stresses are normalized by \bar{V}_z : $v'_\theta^* = \sqrt{v'^2_\theta} / \bar{V}_z$ and $v'_z^* = \sqrt{v'^2_z} / \bar{V}_z$. Note that the measurements of Escudier and Gouldson [89] for V_θ^* and v'_θ^* have been obtained for values of C_w slightly different than for V_z^* and v'_z^* : $C_w = 2839, 6387, 17505$. It corresponds to the values $Re_Q = 1200, 2700, 7400$ for the Reynolds number based on the bulk velocity [89].

As it can be seen from Figure 12.4, the tangential velocity varies with $1/r$ within the gap apart close to the walls where two boundary layers develop. The tangential velocity profile is quite far from the laminar circular Couette profile: $V_\theta(r) \propto 1/r^2$ highlighting the turbulent nature of the flow. The boundary layer thicknesses are here quite thick (15% of the gap width each), because of a low value of the rotation rate Ω . Most of the computed results are found in good agreement with the experimental data for the mean tangential velocity. The DES and most of all the RSM of Elena & Schiestel [85] and the $k-\omega$ SST of OpenFOAM provide the best results. On the contrary, the LES and RSM of StarCCM+ predict a centerbody rotation within the gap with an overestimation of the mean tangential velocity whatever the radial position is, leading to around 17% of error at $r^* = 0.5$. This behavior is characteristic to higher values of the rotation parameter N . The radial variations of the mean axial velocity component displayed in Figure 12.4 confirm the turbulent nature of the flow by comparison with the laminar Poiseuille profile. The results of the LES, the $k-\omega$ SST (OpenFOAM) and the in-house RSM predict the same symmetric profile as in the experiments of Escudier and Gouldson [89]. All the other approaches found in StarCCM+ overestimate the axial velocity in the bulk of the flow and by conservation of mass, they overestimate also the boundary layer thicknesses. It is noteworthy that fully developed conditions are reached at $z^* = 0.1$ using the RSM in agreement with the observations of Escudier and Gouldson [89].

Another calculation on a 1° sector using the LES within OpenFOAM has also been performed (but not shown here) providing, among other things, a profile for the axial velocity fairly close to the classical laminar Poiseuille profile with a much higher maximum velocity at mid-gap.

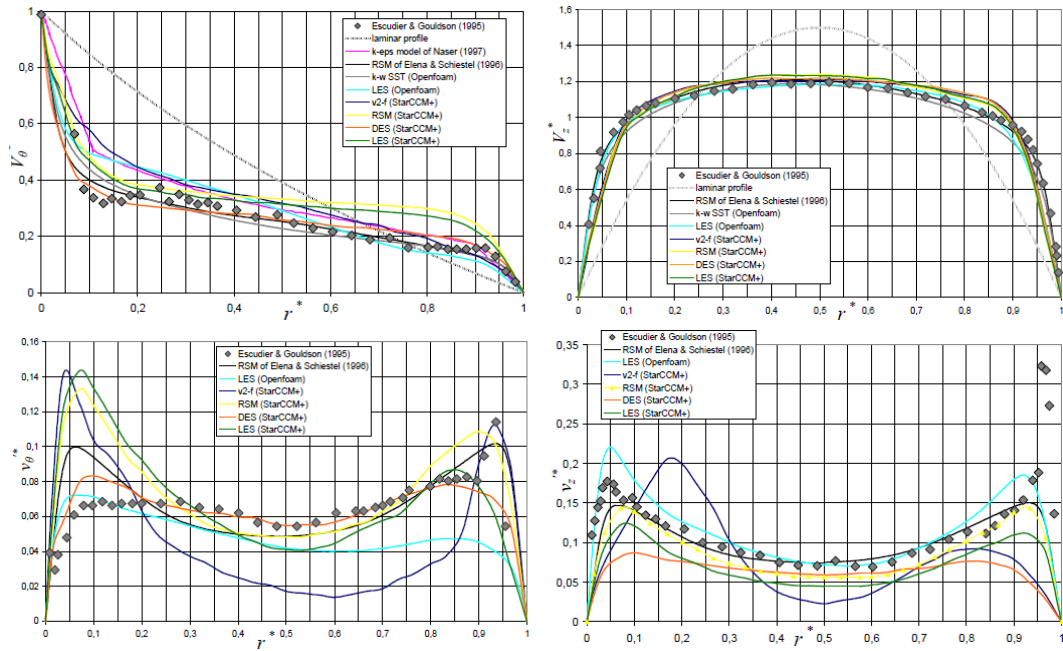


Figure 12.4: Radial profiles of the mean (a) tangential and (b) axial velocity components and of the corresponding fluctuating (c) tangential and (d) axial velocity components at $z^* = 0.1$ for $\Gamma = 244$, $\eta = 0.506$, $Re_i = 961.07$ and $C_w = 17742$. Comparisons between various turbulence models (lines) and the velocity measurements (symbols) of Escudier and Gouldson [89].

Figure 12.4 presents also the radial distributions of the tangential and axial normal Reynolds stress tensor components for the same set of parameters. Turbulence is mainly concentrated in the core region with peak values at the edge of each boundary layer. Then, it vanishes towards the walls. Turbulence intensities are much higher close the outer cylinder as it can be seen from the experiments of Escudier and Gouldson [89], which is not captured by any of the numerical approaches. This behavior observed in the experiments looks surprising. The same authors report indeed similar measurements in Reference [90] for another value of $C_w = 16672$ very close to the present one. In that case, the profile of the fluctuating axial velocity is almost symmetric, with values remaining lower than 0.2. The values around 0.35 may be attributed in the experiments to the difficulty to perform accurate measurements very close to the walls. The RSM of Elena & Schiestel [85] provides the best overall agreement with good intensity levels in the gap and close to the inner cylinder. The LES of OpenFOAM offers also quite good results excepted for the $v_\theta'^*$ intensity at large radial locations.

For industrial applications, the $v^2 - f$ model showed a good behavior providing especially good results for the mean field. It offers then a good compromise between accuracy and calculation cost. For more specific applications where turbulence intensities have to be computed accurately, the RSM, which has been sensitized to the main rotation effects, has shown to predict quite accurately both the mean and turbulent fields.

Figure 12.5 shows the distributions of the dimensionless mean tangential and axial velocity components at $z^* = 0.1$ for the same value of Re_i but for three values of the flowrate coefficient. For the two lowest values of C_w , the tangential velocity profiles (Fig.12.5a) exhibit a structure divided into three regions: two thin boundary layers developed on each cylinder separated by a core rotating at a constant velocity. The central region rotates at 32% (resp. 34%) of the cylinder speed for $C_w = 2839$, $N = 0.968$ (resp. $C_w = 5914$, $N = 0.465$) well below the value 0.53 given by Taylor [336] in the absence of throughflow. The flow is here mainly governed by rotation for these values of N . A decrease of the rotation parameter to $N = 0.148$ (corresponding to an increase of the flowrate coefficient to $C_w = 17742$) implies a decrease of the rotating speed of the core region. Moreover, the tangential velocity is no more constant in the gap but is inversely proportional to the radius. Thus, the mean angular momentum is almost constant in that region.

There is only a weak effect of the flowrate coefficient on the radial distributions of the axial veloc-

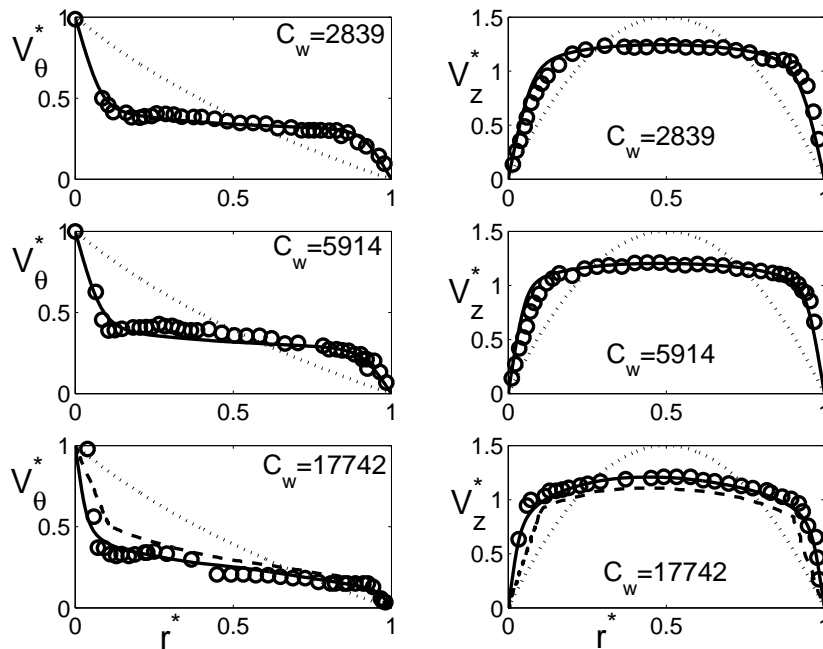


Figure 12.5: Radial distributions of the mean tangential and axial velocity components for $\Gamma = 244$, $\eta = 0.506$ and $Re_i = 961.1$ at $z^* = 0.1$; Comparisons between the present RSM (straight lines) and the LDA measurements of Escudier and Gouldson [89] (symbols) for three values of C_w : $C_w = 2839$, $C_w = 5914$ and $C_w = 17742$. The laminar profiles (dotted lines) and the predictions of the $k - \varepsilon$ model of Naser [217] (dashed lines) for $C_w = 17742$ are also shown.

ity (Fig.12.5b). The profiles are close to the turbulent Poiseuille flow profiles in pipes with a nearly constant axial velocity in the gap and thin boundary layers on the cylinders. For this value of radius ratio $\eta = 0.506$, the profiles are almost symmetric. The profiles become flatter with increasing N as already noted by Nouri and Whitelaw [226]. It is noteworthy that, whatever the value of C_w , the mean velocity profiles are far from the laminar profiles highlighting the turbulent nature of the flow.

For the mean field, the predictions of the RSM model are in very good agreement with the experimental data. The RSM predicts quite well the mean tangential velocity in the core region. Moreover, it offers a good description of the boundary layer thicknesses along the cylinders as it can be seen from the mean axial velocity profiles. For $C_w = 17742$, the RSM improves significantly the results of the $k - \varepsilon$ of Naser [217], which fails to predict the right profiles with large discrepancies for both the axial and tangential velocity components. The axial velocity is largely underestimated in the core and the tangential velocity is slightly overestimated. It is besides surprising that, by integration of the mean axial velocity profile, mass is not conserved. Fully developed conditions are reached at $z^* = 0.1$ using the RSM in agreement with the observations of Escudier and Gouldson [89], whereas the predictions of the $k - \varepsilon$ model of Naser [217] showed a large dependence of the tangential velocity profiles on the axial position. This last author attributed the discrepancies obtained by the $k - \varepsilon$ model to the fact that its model is blind to any rotation effects, and that the eddy viscosity concept, on which this model is based, is unsuitable with the present flow situation. On the contrary, the present RSM model is both sensitized to rotation effects and free from any eddy viscosity hypothesis, which may explain the better overall agreement with the experimental data.

Figure 12.6 presents the radial distributions of the tangential and axial normal Reynolds stress tensor components for the same sets of parameters. Turbulence is mainly concentrated in the core region and vanishes towards the walls. The tangential and axial velocity fluctuations show a progressive decrease with increasing flowrate coefficient (or decreasing rotation parameter) in agreement with the experimental data of Escudier and Gouldson [89] and the LES results of Chung and Sung [54]. It is attributed by Escudier and Gouldson [89] to the vortical structures observed for low values of C_w induced by the centerbody rotation. For high values of C_w , the radial penetration of the rotational influence is reduced and turbulent fluctuations are suppressed as if there was no solid body rotation.

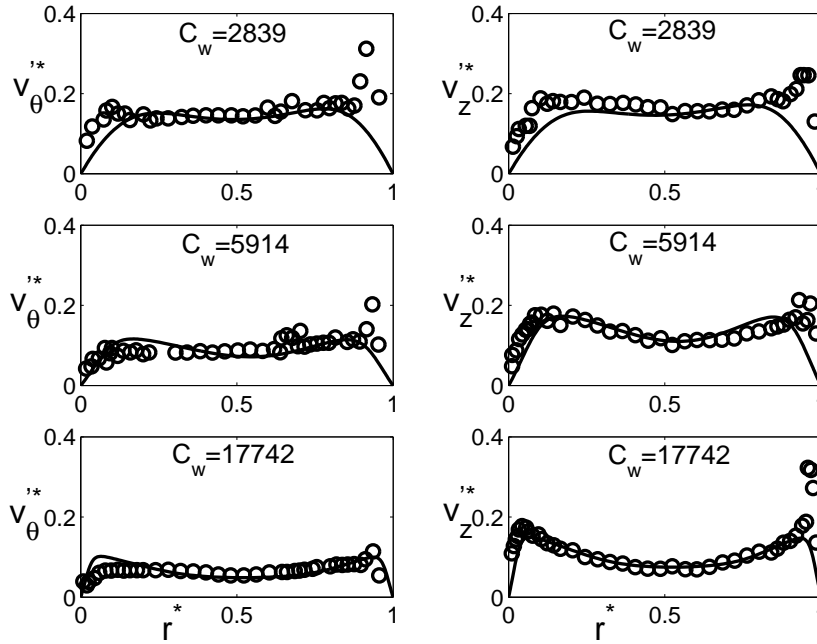


Figure 12.6: Radial distributions of the tangential $v_{\theta}^{\prime*}$ and axial $v_z^{\prime*}$ normal Reynolds stress tensor components. See legend of Figure 12.5.

The profiles of $v_{\theta}^{\prime*}$ and $v_z^{\prime*}$ are asymmetric for the highest value of the rotation parameter $N = 0.968$ ($C_w = 2839$) in agreement with Chung and Sung [54], which can be attributed to the destabilizing effect of the centrifugal forces. All these phenomena are well reproduced by the RSM, which predicts also quite good the turbulent intensities in the core of the flow. Some discrepancies are obtained in the boundary layers, especially for the peak values very close to the walls. The variations in the radial direction of the turbulent levels along each cylinder are also smoother than the experimental ones, which was also the case for the LES results of Chung and Sung [54] against the measurements of Nouri and Whitelaw [226].

12.3.2 Are second order RANS models suitable for modeling heat transfer in electrical motors?

The RSM is now used to carry a parametric study of turbulent Taylor-Couette-Poiseuille flows with heat transfers in a narrow-gap cavity characterized by a large aspect ratio $\Gamma = 77$ and a large radius ratio $\eta = 0.961$ and for a wide range of the flow parameters (see Table 12.1). It corresponds to a real rotating machinery developed by Liebherr Aerospace Toulouse. All the results obtained using the in-house RSM of Elena and Schiestel [85] and, in particular, the parametric study (variations of Re_i , C_w and Pr) can be found in Reference [256].

12.3.2.1 Mean and turbulent flow field in the Configuration ‘‘Liebherr 1’’

The mean and turbulent flow fields are very similar to those obtained in the previous configuration of Escudier & Goulson [89]. The mean radial velocity component is quasi zero in the whole cavity. The mean flow is then helical with a tangential main flow due to the rotation of the inner cylinder (Taylor-Couette flow) and an axially secondary flow due to the superimposed throughflow (Poiseuille flow) as shown in Figure 12.7. One interesting feature is that, from $z^* \simeq 0.2 \simeq 15.6/\Gamma$ to 0.8, the mean flow is well established and the profiles do not depend anymore neither on the axial position z^* nor on the boundary conditions imposed at the inlet (see in Reference [256]). The mean profiles of V_{θ}^* and V_z^* are characteristic of the turbulent regime with two very thin boundary layers developed on each cylinder. The central region between the two boundary layers is characterized by a quasi constant mean axial velocity equal to approximately 1.07, close to a turbulent Poiseuille-like profile in pipes.

The mean tangential velocity component increases linearly when moving from the outer to the inner cylinders in that region in agreement with the LES results of Chung and Sung [54]. This behavior is analogous to the turbulent torsional Couette flow found in very flat rotor-stator disk cavities [119]. V_θ^* is exactly equal to 0.5 at mid-radius, which is to be compared to the theoretical value 0.48 of Polkowski [248], whereas Kuosa *et al.* [164] obtained 0.083 with the $k-\omega$ SST model. Note that this swirl level is much higher than the measured or computed one obtained in the case of the Escudier and Gouldson's [89] experiment, which is a direct effect of both the narrow gap between the walls and to the high value of the rotation parameter $N = 4.24$ considered here. From the radial profiles in Figure 12.7, one can deduce the thicknesses of the boundary layers δ_{V_i} and δ_{V_o} on the inner and outer cylinders respectively. δ_{V_i} (resp. δ_{V_o}) is the height at which the mean tangential velocity component reaches 99% (resp. 1%) of Ωa . For $0.2 \leq z^* \leq 0.8$, these thicknesses are almost constant and equal to $\delta_{V_i}/(\Delta R) = 0.03$ and $\delta_{V_o}/(\Delta R) = 0.04$.

In the outlet section ($z^* = 1$) where a given pressure is imposed, absolutely no reversed flow has been observed in the present case. At the outlet, V_θ^* varies non monotonously with r^* . Close to the inner rotating cylinder, it varies very quickly from 0.1 for $r^* = 0.1$ to 1 on the rotor. The axial velocity profile tends to the laminar profile at the outlet with a strong axial velocity in the center of the gap.

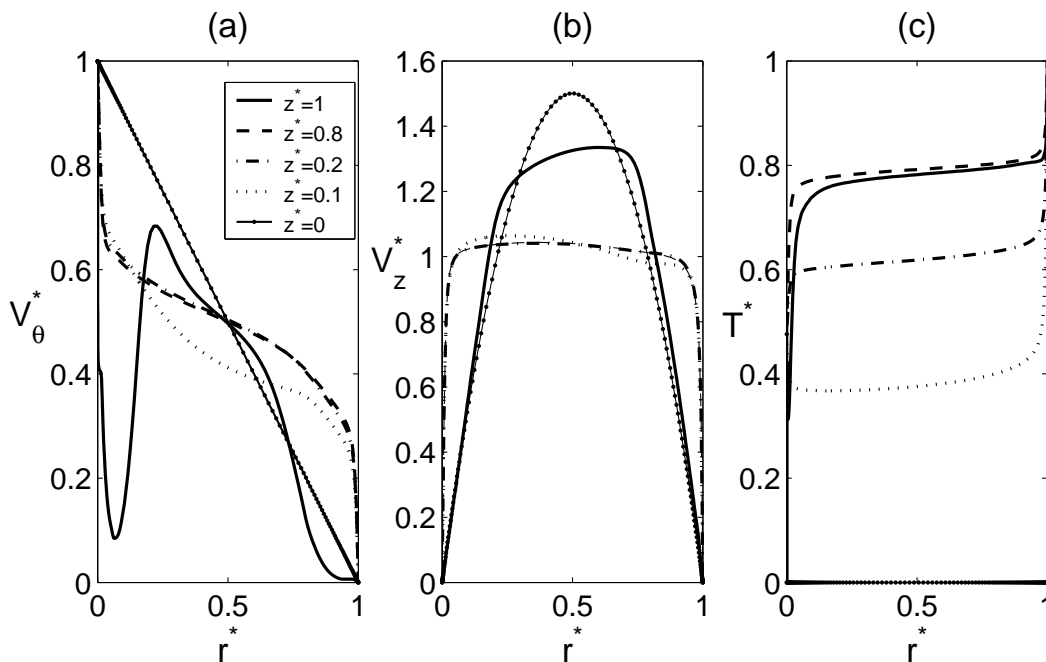


Figure 12.7: Radial profiles of the mean (a) tangential V_θ^* , (b) axial V_z^* velocity components and (c) dimensionless temperature T^* for different axial positions z^* and $\Gamma = 77$, $\eta = 0.961$, $Re_i = 10216$, $C_w = 14858$ and $Pr = 0.7$. Results obtained by the in-house RSM.

Concerning the thermal field, the fluid at the inlet enters the cavity at a constant temperature denoted T_a . The inner and outer cylinders are maintained at constant temperatures T_i and T_o respectively. Thus, the heat transfer is driven by three main parameters, two heating factors κ_i and κ_o for the inner and outer cylinders respectively and the Prandtl number Pr defined as follows:

$$\kappa_i = \frac{T_i - T_a}{T_a} = 0.117 \quad \kappa_o = \frac{T_o - T_a}{T_a} = 0.245 \quad 0.01 \leq Pr \leq 12$$

The two heating factors $\kappa_i = 0.117$ and $\kappa_o = 0.245$, which are proportional to Gr/Re_i^2 , where Gr is the Grashof number based on the temperature T_a , are small enough to make the hypothesis of no density variation. The gravitational effects are indeed small compared to the inertial effects ($Gr \ll Re_i^2$).

As for the hydrodynamic mean flow, the temperature field T^* does not depend on the axial position for $z^* \geq 0.4$ (Fig.12.7c). Note that the temperature T is normalized as follows: $T^* = (T - T_a)/(T_o - T_a)$. Thus, $T^* = 0$ in the inlet section ($z^* = 0$) and $T^* = 1$ along the outer cylinder ($r^* = 1$), where the

highest temperature is reached. The mean temperature profiles can also be divided into three areas: two thermal boundary layers separated by a region, where the temperature is quasi constant. For $z^* \geq 0.4$, the temperature reached in the core region tends to $T^* = 0.768$. It is slightly higher than the value $T^* = 0.738$ corresponding to the averaged value between the cylinder temperatures T_i and T_o . It shows in particular the dominating influence of the (warmest) outer cylinder. For this set of parameters, rotation effects on the mean flow are dominant compared to the superimposed throughflow as the value of the rotation parameter $N = 4.24$ is high. Thus, the residence time of the incoming fluid (at $T^* = 0$) inside the cavity is large enough for the walls to warm significantly the fresh incoming fluid. It explains why the mean temperature remains in the range $0.7 \leq T^* \leq 0.9$. From the temperature profiles in Figure 12.7c, one can evaluate the thicknesses of the thermal boundary layers denoted δ_{T_i} and δ_{T_o} on the inner and outer cylinders respectively. δ_{T_i} (resp. δ_{T_o}) is the height at which the mean temperature reaches 99% (resp. 1%) of the averaged temperature in the core. Thus, $\delta_{T_i}/\Delta R = 0.023$ and $\delta_{T_o}/\Delta R = 0.06$ for $0.4 \leq z^* \leq 0.8$. As expected, the thermal boundary layer is thicker than the hydrodynamic one along the stator. The Prandtl number, which compares the hydrodynamic and thermal boundary layer thicknesses, is indeed equal to $Pr = 0.7 \leq 1$ in the present case.

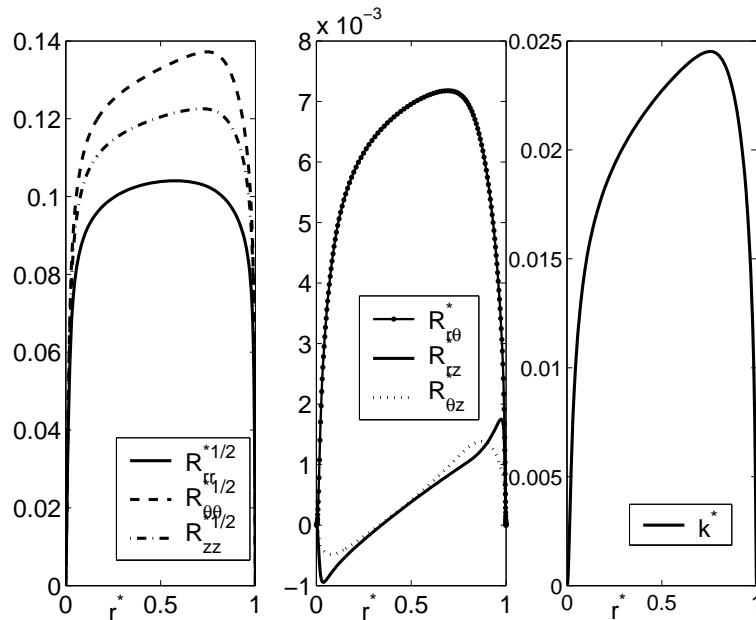


Figure 12.8: Radial profiles of the six Reynolds stress tensor components and of the turbulence kinetic energy for $\Gamma = 77$, $\eta = 0.961$, $Re_i = 10216$, $C_w = 14858$ and $Pr = 0.7$ at $z^* = 0.5$. Results obtained by the in-house RSM.

Figure 12.8 shows the radial profiles of the six Reynolds stress tensor components R_{ij}^* and of the turbulence kinetic energy k^* at mid-height $z^* = 0.5$ for the same set of parameters. Note that the Reynolds stress tensor components as well as k^* are normalized by $(\Omega a)^2$. It is not shown here but as for the mean field, there is no axial dependence of these turbulent quantities for $0.2 \leq z^* \leq 0.8$. Turbulence is then fully developed in that region and not influenced by the inlet and outlet areas. The highest levels of the normal Reynolds stress tensor components are reached in the core of the flow with maxima closest to the outer cylinder. As for the highest value of the rotation parameter $N = 0.968$ considered in Configuration 1, it can be attributed to the destabilizing effect of the centrifugal forces. Turbulence intensities vanish at the walls. The magnitudes of the three normal Reynolds stress tensor components are quite comparable indicating that the turbulence is only weakly anisotropic. The $R_{r\theta}^*$ behaves like the normal components, with a maximum along the external cylinder. The two other cross components, which are one order of magnitude below, indicate a strong shear along the cylinders in agreement with the LES results of Chung and Sung [54].

12.3.2.2 Budgets for the turbulence kinetic energy transport equation

To highlight the influence of the additional terms taking into account the implicit effects of rotation on turbulence in the present RSM, budgets for the turbulence kinetic energy transport equation are here performed. The equation for the turbulence kinetic energy k is given in Elena and Schiestel [85] as:

$$\frac{dk}{dt} = P + D^T + D^\nu - \epsilon + D^R + J \quad (12.2)$$

The terms D^R and J model two implicit effects of rotation on turbulence. D^R is an inhomogeneous diffusion term, which slows down the tendency of bidimensionalization close to the walls. Its empirical term takes also into account the significant increase of the turbulent diffusion due to the triple fluctuating velocity correlation and to the fluctuating pressure in the case of strong rotation. Another characteristic phenomenon due to rotation is a reduction of the energy transfer from large to small turbulent scales. This last phenomenon is modeled here through an inverse flux J . All details about these terms can be found in Elena and Schiestel [85] or in Chapter 4.

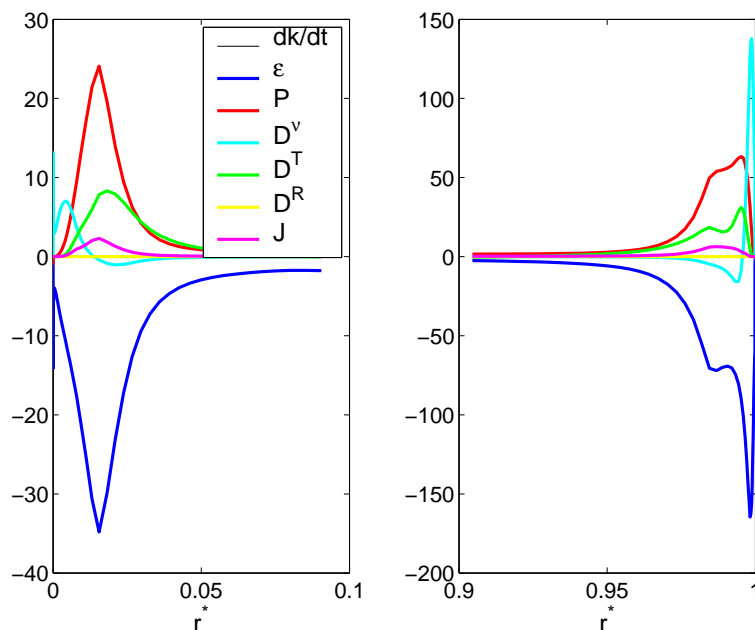


Figure 12.9: Turbulence kinetic energy budgets at $z^* = 0.5$ along both cylinders for $\Gamma = 77$, $\eta = 0.961$, $Re_i = 10216$ and $C_w = 14858$. Results obtained by the in-house RSM.

Budgets for the turbulence kinetic energy k (normalized here by $(\Omega h)^2$) are presented in Figure 12.9 at mid-height of the cavity in both boundary layers. The transport of k is mainly governed by the production P and the dissipation ϵ terms, which compensate almost each other. The molecular D^ν and turbulent D^T diffusion terms can not be neglected close to the walls. In the viscous sublayers, where low Reynolds numbers are reached, D^ν compensates exactly the dissipation ϵ , whereas the term D^T is almost zero. The inhomogeneous diffusion term D^R , which usually flattens the turbulence kinetic energy by diffusion along the rotation axis [249], does not contribute here to the k budgets. The inverse flux J , which increases the turbulence level in the core of the flow, has only a weak contribution to the k budgets in both boundary layers, which does not mean that it does not affect the mean and turbulent fields. It can be noticed that the values reached along the stationary outer cylinder are much higher (in absolute value) than those obtained along the inner one. It confirms in particular the RSM predictions of Poncet [249] in the case of rotor-stator disk flows with throughflow.

The influence of the additional terms contained in T_{ij} has been already addressed by Elena and Schiestel [85] for rotor-stator disk flows. They compared the predictions of three low-Reynolds number RSM models from the base model of Hanjalic and Launder [121] to the final version described here with experimental data available in the literature. The introduction of the new terms did not produce

important changes. Nevertheless, the final model was found to improve the predictions of the former ones. The turbulence levels close to the rotor and the location of the relaminarized and turbulent regions were better predicted. Here, the term J , which is not a redistributive term, slightly increases the energy levels at the edge of the boundary layers and also in the core.

12.3.2.3 Distributions of the Nusselt numbers

18 calculations have been performed to investigate the influence of the flow parameters: the rotational Reynolds number Re_i , the flowrate coefficient C_w and the Prandtl number Pr . These 18 sets of parameters cover a wide range of the rotation parameter N : from 2.1 up to infinity, when no throughflow is superimposed. Thus, for all cases, the parameter N is higher than 0.8, which ensures that the Nusselt numbers depend on both the rotation Ω and the axial throughflow Q (see in [165]). Only the results on the thermal field are shown below but the influence of these parameters on the flow field may be found in Reference [256].

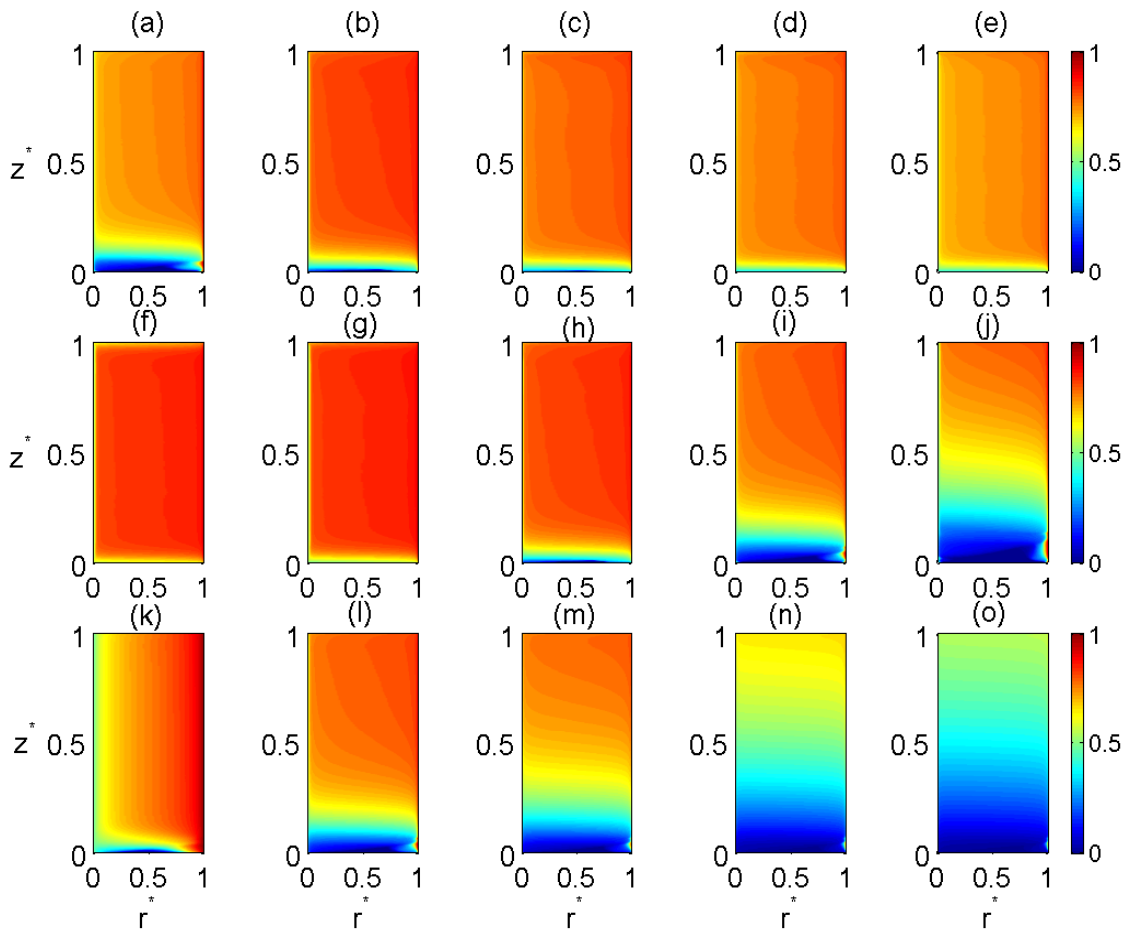


Figure 12.10: Isovalues of the mean temperature T^* obtained by the in-house RSM for $\Gamma = 77$ and $\eta = 0.961$. Influence of the Reynolds number for $C_w = 5000$, $Pr = 0.7$: (a) $Re_i = 3744$, (b) $Re_i = 10216$, (c) $Re_i = 14959$, (d) $Re_i = 26189$, (e) $Re_i = 37443$. Influence of the flowrate coefficient for $Re_i = 10216$, $Pr = 0.7$: (f) $C_w = 0$, (g) $C_w = 10^3$, (h) $C_w = 5 \times 10^3$, (i) $C_w = 14858$, (j) $C_w = 3 \times 10^4$. Influence of the Prandtl number Pr for $Re_i = 10216$, $C_w = 14858$: (k) $Pr = 0.01$, (l) $Pr = 0.7$, (m) $Pr = 2$, (n) $Pr = 7$, (o) $Pr = 12$.

Figure 12.10 presents the isotherm maps in a (r, z) plane for all the cases considered here highlighting the influence of the flow parameters on the thermal field. The effect of the rotational Reynolds number is illustrated by comparing Figures 12.10a to 12.10e for $C_w = 5000$ and $Pr = 0.7$. For a given superimposed throughflow, when the rotation rate of the inner cylinder is increased, the centrifugal

effect increases. The main flow is still helical but the thread of the screw gets even smaller. As a consequence, the time of residence increases with increasing values of Re_i , which implies a more efficient mixing and a better homogenization of the mean temperature in the whole cavity. So, the mean temperature in the center of the cavity $T_{mid}^* = T^*(r^* = 0.5, z^* = 0.5)$ is a decreasing function of Re_i following the quadratic law: $T_{mid}^* = 7.5 \times 10^{-11} Re_i^2 - 6.4 \times 10^{-6} Re_i + 0.88$. For very high rotational Reynolds numbers, T_{mid}^* tends to the value 0.738 corresponding to the averaged between the wall temperatures. For all cases, the isotherms are parallel to the rotation axis. The size of the cold fluid region around the inlet increases with the rotation rate of the inner cylinder.

The effect of the flowrate coefficient on the temperature field (Fig.12.10f-12.10j) is more noticeable than the one of the rotational Reynolds number. Without any superimposed throughflow (Fig.12.10f), the isotherms are parallel to the rotation axis and T_{mid}^* is equal to 0.841, which is much warmer than the averaged temperature 0.738 between the two walls, showing the preponderant effect of the outer cylinder. When the flowrate coefficient increases, the isotherms get progressively inclined. For the highest value $C_w = 30000$ (Fig.12.10j), the effect of C_w is preponderant compared to the effect of the rotation rate ($N = 2.1$). T_{mid}^* appears to be a decreasing function of C_w following the quadratic law: $T_{mid}^* = -1.3 \times 10^{-10} C_w^2 - 2.6 \times 10^{-6} C_w + 0.84$. It is simply due to the fact that the fresh incoming fluid spends a shorter time in the cavity when C_w is high.

The influence of the Prandtl number Pr on the thermal field is now investigated for $Re_i = 10216$, $C_w = 14858$ and $0.01 \leq Pr \leq 12$. $Pr = 0.01$ is a typical value for liquid metals, $Pr = 0.7 - 1$ for gases ($Pr = 0.71$ for air at $20^\circ C$) and $Pr = 2 - 12$ for water. For $Pr = 0.01$ (Fig.12.10k), the heat transfer process is dominated by conduction from the outer to the inner cylinders. For this Prandtl number, the fluid behaves thermally like a solid. The isotherms are then parallel to the rotation axis except very close to the inlet region. The mean temperature increases linearly from the hub to the shroud. When the Prandtl number $Pr = \nu/\sigma$ increases (Fig.12.10l - 12.10o), the thermal diffusivity of the fluid σ decreases. Thus, the characteristic time for the heat transfer between the cylinders and the fluid increases. As the residence time of the fluid in the cavity remains the same (Re_i and C_w being constant), the fluid requires more time to exchange heat with the walls. The thermal effects diminish then with increasing values of Pr and the flow behavior is essentially hydrodynamic. That is the reason why the mean temperature in the center of the cavity T_{mid}^* decreases for increasing values of Pr following the quadratic law: $T_{mid}^* = 0.0014 Pr^2 - 0.052 Pr + 0.79$.

From the isotherm maps, one can deduce the axial distributions of the local Nusselt numbers Nu_i and Nu_o along the inner and outer cylinders respectively defined by:

$$Nu_i(z) = \frac{\Delta R}{T_i - T_a} \frac{\partial T}{\partial r} \Big|_i(z) \quad (12.3)$$

$$Nu_o(z) = \frac{\Delta R}{T_o - T_a} \frac{\partial T}{\partial r} \Big|_o(z) \quad (12.4)$$

The axial distributions of the local Nusselt numbers along the inner cylinder Nu_i and the outer one Nu_o are presented in Figure 12.11a for $C_w = 5000$, $Pr = 0.7$ and different Reynolds numbers. For this flowrate, Nu_i tends to zero for $z^* \simeq 0.1$ and $Re_i = 3744$ as the incoming fluid warms and reaches the same temperature than the inner cylinder at this axial location. For the other Reynolds numbers, Nu_i increases with z^* in the region close to the inlet and then, for $z^* \leq 0.2$, Nu_i remains almost constant as the mean flow and thermal fields are established. Giret [110] did not measure the heat transfer coefficients close to the inlet where the strong variations are expected. Nevertheless, he observed also a strong decrease of Nu_i from $z^* \simeq 0.15$ to $z^* \simeq 0.8$. Along the outer cylinder, Nu_o decreases with z^* at the cavity inlet and then remains constant. Except very close to the inlet, Nu_i and Nu_o increase for increasing values of the Reynolds number Re_i , which is expected in such rotating flows [233]. Figure 12.11b sums up the results presented in Figure 12.11a at a given axial position $z^* = 0.5$, and confirms the dependence of Nu_i and Nu_o on the rotational Reynolds number Re_i .

The influence of the axial Poiseuille flow on the local Nusselt numbers is depicted in Figure 12.12a for $Re_i = 10216$, $Pr = 0.7$ and different values of the flowrate coefficient. Along the hub and for $C_w \leq 5000$, the local Nusselt number Nu_i does not depend on the axial location for $0.05 \leq z^* \leq 0.95$. Nu_i depends weakly on C_w for $C_w < 5000$ then increases strongly for higher flowrates. For $C_w \geq 10^4$, when C_w increases, the axial location for which Nu_i tends to 0 moves towards the cavity outlet: $Nu_i \simeq 0$ at $z^* \simeq 0.095$ for $C_w = 10^4$, at $z^* \simeq 0.14$ for $C_w = 14858$ and at $z^* \simeq 0.27$ for $C_w = 30000$. In the same time, the region where Nu_i is quasi constant gets always smaller for increasing values of

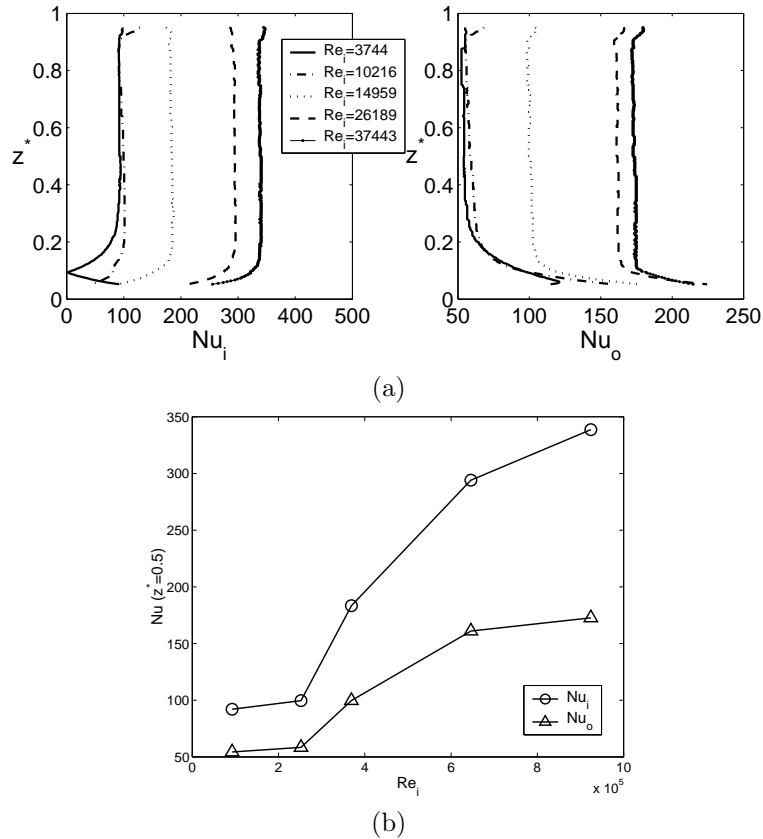


Figure 12.11: Local Nusselt numbers along both cylinders for $C_w = 5000$, $Pr = 0.7$ and different Reynolds numbers Re_i : (a) Axial profiles; (b) Variations against Re_i at mid-height $z^* = 0.5$. Results obtained by the in-house RSM for $\Gamma = 77$ and $\eta = 0.961$.

C_w . Along the stationary cylinder, the same behavior is observed. For $C_w < 5000$, Nu_o depends very weakly on both z^* and C_w . When increasing C_w up to 30000, Nu_o reaches a maximum close to the cavity inlet. This maximum is shifted to larger z^* values, when C_w increases. Thus, Nu_o is maximum at $z^* \simeq 0.06$ for $C_w = 10^4$, at $z^* \simeq 0.1$ for $C_w = 14858$ and at $z^* \simeq 0.17$ for $C_w = 30000$. Note that the axial positions for the maxima of Nu_o do not coincide with the locations of the minima reached by Nu_i because of the helicity of the main flow. Figure 12.12b confirms these previous results at a given location $z^* = 0.5$. Nu_i and Nu_o both increase for increasing values of C_w . The local decrease of Nu_i or Nu_o corresponds to the fact that the fluid gets close the wall temperatures at this given location. Except for $C_w = 30000$, the heat transfer coefficient along the rotating cylinder is higher than the one along the stationary cylinder at $z^* = 0.5$.

Figure 12.13a shows the axial distributions of the local Nusselt numbers for $Re_i = 10216$, $C_w = 14858$ and different Prandtl numbers. For liquid metals ($Pr = 0.01$), both Nu_i and Nu_o are quite low and remain independent of z^* , which reflects the dominating influence of the molecular diffusivity on the heat transfer process. For higher Prandtl numbers $Pr \geq 0.7$, Nu_i decreases for increasing values of z^* , reaches a minimum value at a given axial location and then increases weakly when moving towards the cavity outlet. The minimum value is obtained when the fluid is at approximately the same temperature than the wall. The axial location for which Nu_i reaches this minimum value is shifted towards the outlet for increasing Prandtl numbers. Along the outer cylinder, Nu_o increases for increasing Pr values. For gases ($Pr = 0.7$) and liquids ($Pr = [2, 7, 12]$), Nu_o reaches a maximum close to the cavity inlet and diminishes for larger axial locations. These results are confirmed by Figure 12.13b, highlighting the influence of Pr on the local Nusselt number at mid-height. It clearly shows that Nu_o strongly increases for increasing Pr values and also that, for a given Prandtl number, Nu_o is larger than Nu_i . Nu_i does not vary monotonously with Pr , because at mid-height and for $Pr = 7$, the fluid reaches the wall temperature and so Nu_i tends to zero. Apart from $Pr = 7$, Nu_i slightly

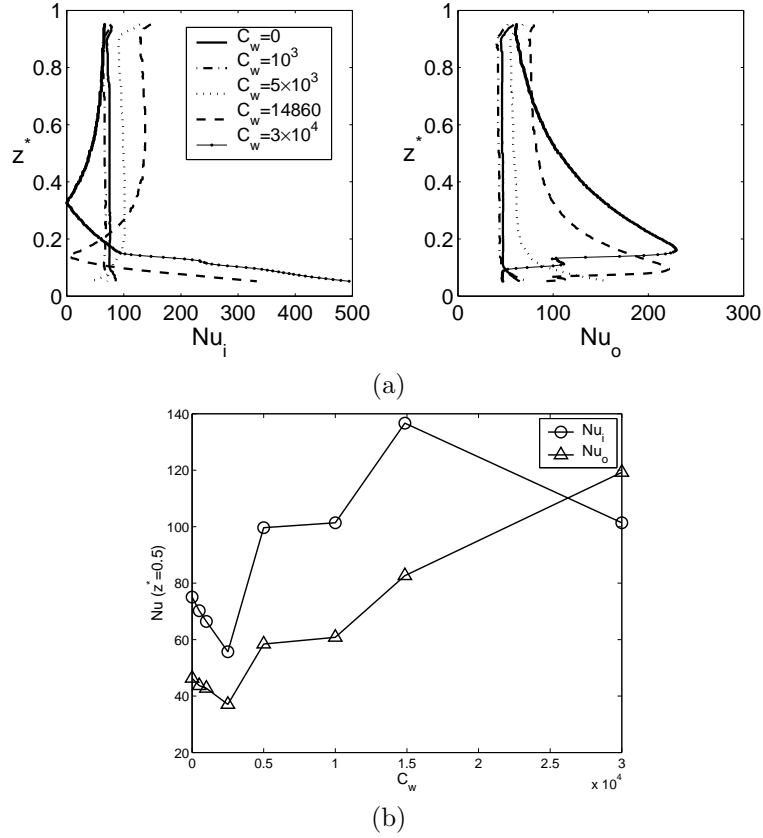


Figure 12.12: Local Nusselt numbers along both cylinders for $Re_i = 10216$, $Pr = 0.7$ and different values of the flowrate coefficient C_w : (a) Axial profiles; (b) Variations at mid-height $z^* = 0.5$ against C_w . Results obtained by the in-house RSM for $\Gamma = 77$ and $\eta = 0.961$.

increases with Pr .

From an engineering point of view, the most interesting quantities are the averaged Nusselt numbers \overline{Nu}_i and \overline{Nu}_o for the inner and outer cylinders respectively. They are the averaged values of the local Nusselt numbers along the heated surfaces, defined as follows:

$$\overline{Nu}_i = \frac{\Delta R}{h} \frac{1}{T_i - T_a} \int_0^h \frac{\partial T}{\partial r} \Big|_i(z) dz \quad (12.5)$$

$$\overline{Nu}_o = \frac{\Delta R}{h} \frac{1}{T_o - T_a} \int_0^h \frac{\partial T}{\partial r} \Big|_o(z) dz \quad (12.6)$$

The goal is to provide correlations for \overline{Nu}_i and \overline{Nu}_o according to the flow parameters (Re_i , C_w and Pr). Figure 12.14 shows that the averaged Nusselt numbers on both cylinders can be correlated according to the three flow parameters as follows:

$$\overline{Nu}_i = 0.0291 \times Re_i^{0.82} \times Pr^{0.3} \times C_w^{0.09} \quad (12.7)$$

$$\overline{Nu}_o = 0.0454 \times Re_i^{0.75} \times Pr^{0.8} \times C_w^{0.08} \quad (12.8)$$

These two correlations are valid for $3744 \leq Re_i \leq 37443$, $0 \leq C_w \leq 30000$ and $0.01 \leq Pr \leq 12$ for a cavity characterized by a large aspect ratio $\Gamma = 77$ and a large radius ratio $\eta = 0.961$ and for two given heating factors $\kappa_i = 0.117$ and $\kappa_o = 0.245$.

These results are in agreement with previous results in various rotating flow arrangements. For turbulent rotating flows, the mean Nusselt number is usually proportional to $Re^{0.8}$ [233], which is the case in rotor-stator disk cavities [258] and also in Taylor-Couette systems [164]. In rotor-stator disk

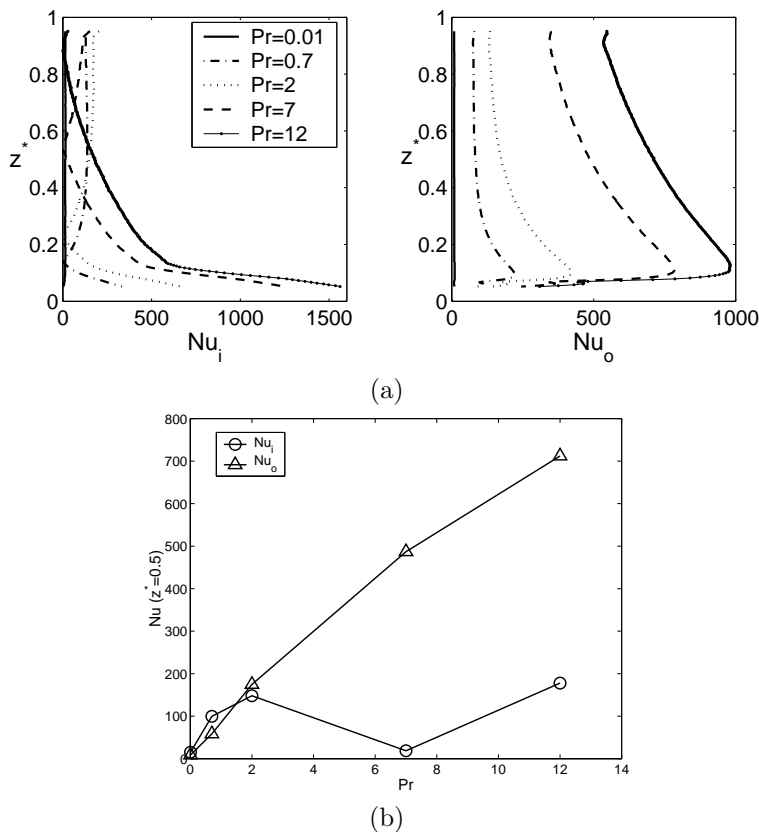


Figure 12.13: Local Nusselt numbers along both cylinders for $Re_i = 10216$, $C_w = 14858$ and different Prandtl numbers Pr : (a) Axial profiles; (b) Variations at mid-height $z^* = 0.5$ against Pr . Results obtained by the in-house RSM for $\Gamma = 77$ and $\eta = 0.961$.

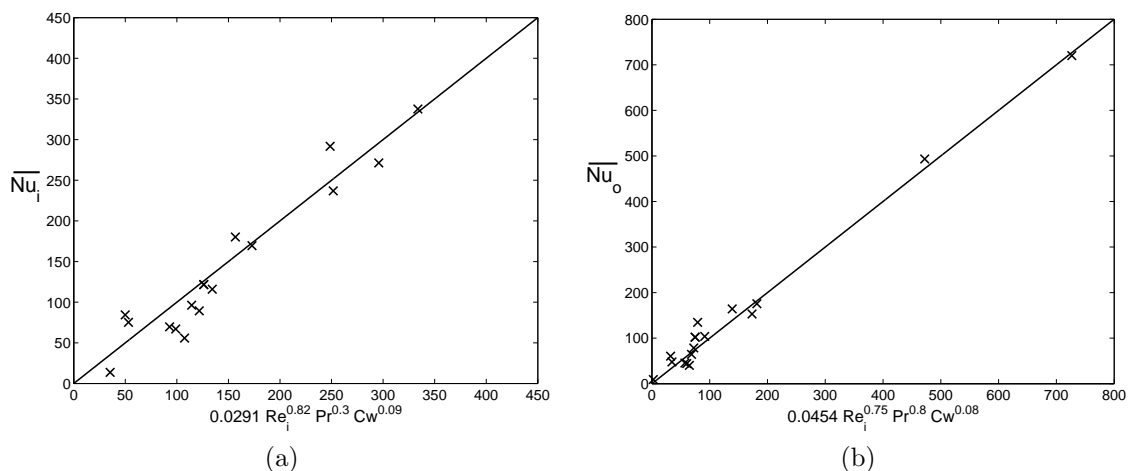


Figure 12.14: Correlations for the averaged Nusselt numbers along the: (a) inner cylinder and (b) the outer cylinder for all the considered cases. Results obtained by the in-house RSM for $\Gamma = 77$ and $\eta = 0.961$.

cavities, the exponent varies between 0.7 [260] and 0.89 [281], which confirms the relevance of the present results.

In the present case, one found that $\overline{Nu}_i \propto C_w^{0.09}$ and $\overline{Nu}_o \propto C_w^{0.08}$. To our knowledge, the only previous work providing a correlation with the flowrate coefficient is the one of Poncet and Schiestel [258] obtained using the same RSM model in the case of a rotor-stator interdisk cavity. These

authors gave indeed the following correlation for the averaged Nusselt number along the stationary disk: $\overline{Nu} \propto Re^{0.8} Pr^{0.5} C_w^{0.11}$ for a wide range of the parameters $5 \times 10^5 \leq Re = \Omega b^2/\nu \leq 1.44 \times 10^6$, $0 \leq C_w \leq 12082$ and $1 \leq Pr \leq 12$. The present results appear then to be in good agreement with this previous study in an other rotating flow system.

The dependence of \overline{Nu}_i and \overline{Nu}_o on the Prandtl number is quite different between the two cylinders. In Taylor-Couette systems, \overline{Nu} is usually known to be proportional to Pr^β , with β equal or close to 0.3, which is characteristic of forced convective heat transfer over a rotating cylinder. Aoki et al. [12] proposed $\beta = 0.3$ for $360 \leq Re_i \leq 2274$ and Tachibana and Fukui [333] found $\beta = 1/3$. The present results along the inner cylinder match quite well with these previous results as $\overline{Nu}_i \propto Pr^{0.3}$ here. But there is also a large variability in the values of β depending especially on the temperature distributions imposed at the walls (effect of the Grashof number Gr or of the heating factors κ_i and κ_o) and on the geometry (ratio $\Delta R/a$). Aoki et al. [12] showed indeed that $Nu \propto Gr^{0.29}$. Among other things, one can cite the numerical work of Kuosa et al. [164] and the experimental one of Lee and Minkowycz [175], who proposed $\beta = 0.4$ or the work of Simmers and Coney [322], who obtained $\overline{Nu} \propto f(Pr) \times Pr$. In the case of a turbulent rotor-stator flow, Owen and Haynes [232] found $\beta = 0.6$. Thus, it appears difficult to provide definitive conclusions concerning the correlation between the averaged Nusselt number and the Prandtl number along the outer cylinder. Nevertheless, the value $\beta = 0.8$ found here, remains in the range $[0.4 - 1]$. The reader can refer to the PhD theses of Fasquelle [92] and Giret [110] and to the review paper of F enot et al. [94], who performed a large review of previous works in Taylor-Couette systems with or without axial throughflow, grooved or ungrooved cylinders and, who provided numerous correlations for the Nusselt number against all flow parameters.

Some calculations have been performed using a classical RSM and a $k-\omega$ model available within StarCCM+ by Liebherr Aerospace for $Re_i = 10216$, $C_w = 14858$ and $Pr = 0.7$ in the same configuration. The computations are 3D with a mesh grid composed of 1.7×10^5 cells ($N_z = 30$). The $k-\omega$ and the RSM predict almost the same values for the averaged Nusselt numbers: $\overline{Nu}_i = 144$ and $\overline{Nu}_o = 190$ for the $k-\omega$ and $\overline{Nu}_i = 162$ and $\overline{Nu}_o = 214$ for the RSM. It means that the difference between the two RSM (StarCCM+ and the one of Elena and Schiestel [85]) is larger than 100% for the averaged Nusselt number on the stator, for example. This discrepancy may be explained either by the choice of the turbulence model or by the presence of 3D effects close to the walls. This question will be clarified in the following section by some LES calculations.

To validate the correlation law (12.7) along the rotor and to highlight the influence of both the rotation rate Ω and the flowrate coefficient C_w on the heat transfer coefficient, our results are compared to previous experimental [30, 110, 115] and numerical [240] data for a given Prandtl number $Pr = 0.7$ and three values of the flowrate coefficient (see Figure 12.15). For these parameters, the law (12.7) reduces to the form:

$$\overline{Nu}_i = \overline{Nu}_{i0} + \alpha \times \Omega^{0.82} \quad (12.9)$$

where the averaged Nusselt number \overline{Nu}_{i0} has been obtained in the configuration of Giret [110] ($\eta = 0.99$ and $\Gamma = 333$) without rotation ($\Omega = 0$). The coefficient α depends on $C_w^{0.09}$. The values of \overline{Nu}_{i0} and α are given in Table 12.3 for the three flowrates considered by Giret [110].

mass flowrate (g/s)	C_w	α	\overline{Nu}_{i0}
30	10684	0.533	6.03
60	21368	0.568	9.85
90	32052	0.589	14.17

Table 12.3: Coefficients involved in the empirical law (12.9) for the three flowrates considered by Giret [110].

A relatively good agreement is observed between the present results and the experimental data of Giret [110] for Ω up to 1500 rpm whatever the value of C_w . The better agreement is obtained for the intermediate value of the flowrate coefficient $C_w = 21368$. This new correlation (12.9) improves the correlation of Grosgeorges [115] and most of all the one of Bouafia et al. [30], which overestimates \overline{Nu}_i whatever the value of the rotation rate. The numerical results of Peres [240] fail to predict the good tendency as the averaged Nusselt number varies slightly against the rotation rate. For all correlations, the main discrepancy for the heat transfer coefficient along the rotor is observed for very

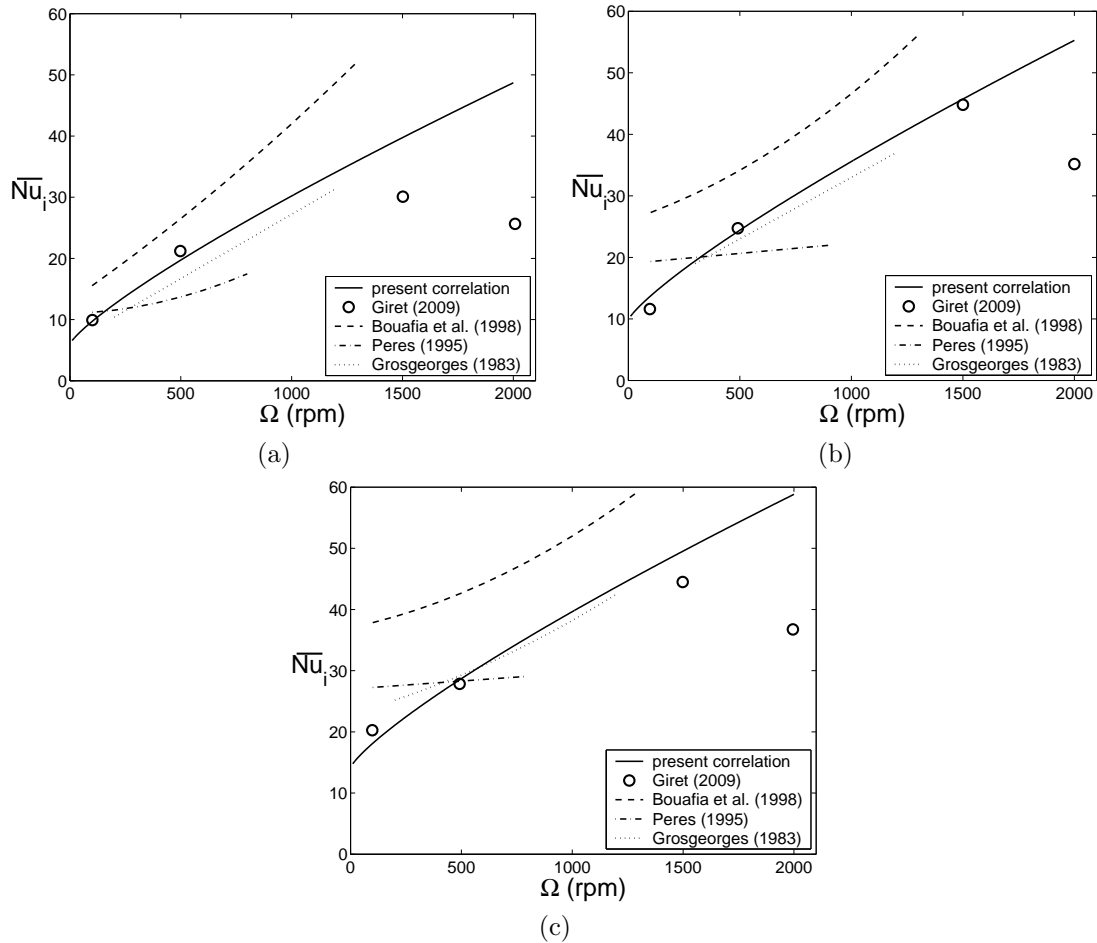


Figure 12.15: Variations of the averaged Nusselt number along the rotor \overline{Nu}_i against the rotation rate Ω for $Pr = 0.7$ and three values of the flowrate coefficient: (a) $C_w = 10684$ (mass flowrate of 30 g/s), (b) $C_w = 21368$ (mass flowrate of 60 g/s), (c) $C_w = 32052$ (mass flowrate of 90 g/s). Comparisons between Eq.(12.9) and previous results [30, 110, 115, 240].

high rotation rates ($\Omega = 2000 \text{ rpm}$). Giret [110] did not provide any explanation for the weak values of \overline{Nu}_i obtained for $\Omega = 2000 \text{ rpm}$. Note that the same experimental results are not available along the stator.

12.4 Towards the LES of Taylor-Couette-Poiseuille in real operating flow conditions

Turbulent flows in an open Taylor-Couette system with an axial throughflow is studied here by the means of large eddy simulations. The ultimate industrial application is the effective cooling of the rotor-stator gap of an electrical motor. The recent review of F enot *et al.* [94] pointed out the lack of reliable data in such configurations for the hydrodynamic field and most of all for the thermal one. The main objective of the first subsection is to validate the present LES approach against reliable data available in the literature [54, 226], which can be seen as a first step towards the simulation of the real flow conditions. Then, LES results in the configuration corresponding to the real machinery developed by Liebherr Aerospace Toulouse will be compared to velocity and temperature measurements performed at IRPHE using a new experimental set-up.

	[54]	present	[54]	present	[54]	present
N	0.2145	0.2145	0.429	0.429	0.858	0.858
Δz_i^+	22.95	21.36	16.8	15.87	9.93	9.31
Δz_o^+	–	19.4	–	13.41	–	7.05
Δr_i^+	0.27	0.47	0.3	0.33	0.35	0.63
Δr_o^+	0.23	0.43	0.24	0.45	0.26	0.47
$(a\Delta\theta)^+$	8.01	7.34	8.8	8.22	10.4	9.7
$(b\Delta\theta)^+$	13.86	13.33	14.34	13.9	15.8	14.7
(N_θ, N_z)	(128, 128)	(128, 130)	(128, 192)	(128, 194)	(128, 384)	(128, 386)
$\delta t(s)$	–	9×10^{-3}	–	7×10^{-3}	–	4×10^{-3}
CFL	–	0.2	–	0.22	–	0.25
CPU time	–	5.2 (s/it)	–	9 (s/it)	–	25.5 (s/it)
$C_{f,i}$	8.91×10^{-3}	8.91×10^{-3}	9.86×10^{-3}	1.08×10^{-2}	1.2×10^{-2}	1.58×10^{-2}
$C_{f,o}$	–	7.44×10^{-3}	–	8.05×10^{-3}	–	9.05×10^{-3}
$Re_{\tau,i}$	163.21	149.53	179.24	167.52	211.85	197.51
$Re_{\tau,o}$	141.19	135.8	146.1	141.6	160.91	149.71

Table 12.4: Numerical details and mean flow parameters. The number of mesh points N_r in the radial direction is fixed to 65 in all calculations. Comparisons with the LES of Chung and Sung [54].

12.4.1 Configuration of Nouri and Whitelaw [226]

The present LES results are compared to the velocity measurements of Nouri and Whitelaw [226] and to the LES of Chung and Sung [54] and discussed in terms of the rotation parameter N , which will take the values 0.2145, 0.429 and 0.858. The axial Reynolds number Re_Q is fixed to 8900 and the rotational Reynolds number will vary. All flow parameters are summed up in Table 12.1.

12.4.1.1 Numerical details

The numerical method is fully described in Chapter 3 and is the same as the one used in the two previous Chapters 10 and 11. It is only recalled that the derivatives are approximated using fourth-order compact formula in the radial and axial directions. A dynamic Smagorinsky model is used as subgrid-scale modeling.

Periodic boundary conditions are applied in the axial and circumferential directions and no-slip boundary conditions are imposed on the walls. All the numerical details used are summed in Table 12.4 and compared to the LES calculations of Chung and Sung [54]. The domain is here decomposed into 2 subdomains in the axial direction. In order to save computational resources, the solution is calculated by assuming a π -periodicity to enable direct comparisons with Chung and Sung [54]. After reaching the statistical convergence (about 2000 s of computed physical time), the mean and rms quantities are sampled during the last 80 s in each case and averaged both in the tangential and axial directions. All the calculations have been performed on the M2P2 cluster.

It is noticeable that Chung and Sung [54] discretized the different equations in time using the Crank-Nicholson method, and then the coupled velocity components in the convection terms are decoupled using the implicit velocity decoupling procedure. All the terms are resolved using a second-order central difference scheme in space with a staggered mesh. They used also a dynamic Smagorinsky model as subgrid-scale modeling.

12.4.1.2 Flow structures

To highlight the presence of near-wall structures, Figures 12.16 present isovalues of the Q-criterion colored by the radial position. Whatever the value of the rotation parameter N , coherent structures are well aligned with the axial flow along the stator. Rotation of the inner cylinder tilts the coherent structures appearing as spiral rolls and forming a negative angle (as they roll up in the opposite sense of the rotor) with the axial direction. These spirals are not observed in the LES results of Chung and Sung [54] for $N = 0.429$.

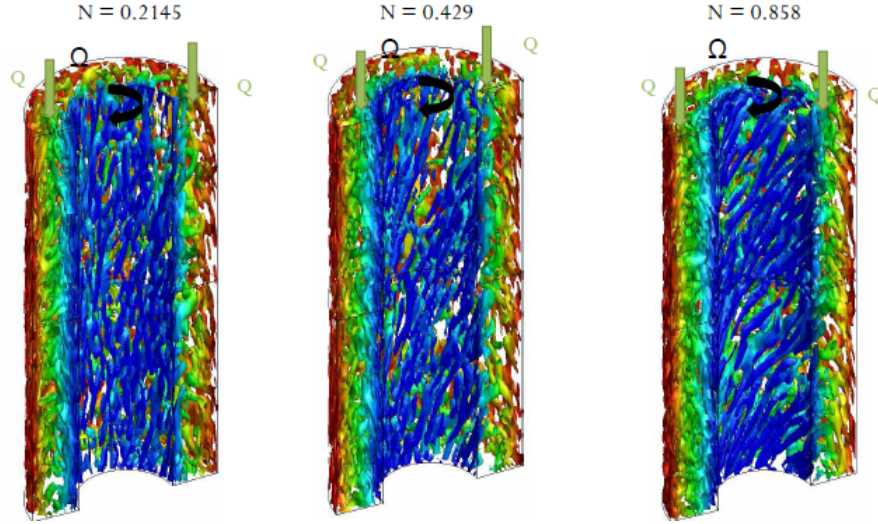


Figure 12.16: Isosurfaces of the Q-criterion ($Q = 0.5$) colored by the radial position for $\Gamma = 9$, $\eta = 0.5$ and three values of the rotation parameter N obtained by LES.

12.4.1.3 Mean and turbulent flow fields

Figure 12.17 shows the radial distributions of the mean axial and tangential velocity components normalized respectively by \bar{V}_z and Ωa . The axial velocity is weakly influenced by the rotation parameter N and the profile resembles the turbulent Poiseuille profile usually observed in pipe flows. The tangential velocity profile varies with $1/r$ for $0.35 \leq r^* \leq 0.9$ for $N = 0.429$ and $N = 0.858$, which means that the mean angular momentum is almost constant in the center region. On the contrary, it varies abruptly near the walls. The present results are in good agreement with the experimental data of Nouri and Whitelaw [226] for $N = 0.429$ and improve the previous ones of Chung and Sung [54]. The averaged friction coefficients C_f and the friction Reynolds numbers Re_τ obtained along both cylinders compare very favorably to the LES results of Chung and Sung [54] as listed in Table 12.4.

The radial variations of the $R_{\theta\theta}$ and R_{rz} components of the Reynolds stress tensor normalized by \bar{V}_z^2 are also displayed in Figure 12.17. Velocity fluctuations are particularly higher for the tangential component with very intense peak values close to the walls. For the two other normal components (not shown here), the same behavior is observed with almost constant turbulence intensities within the gap, which vanish towards the cylinders. As expected, increasing the rotation parameter N induces higher turbulence levels especially for the radial and tangential components. Furthermore, the distributions of the normal components are asymmetric, which may be attributed to the destabilizing effect of the centrifugal force. The R_{rz} shear component of the Reynolds stress tensor is shown in Figure 12.17. When N increases, the shear stresses increase in strength too. A good quantitative agreement has been obtained between the present LES results and the data of Nouri and Whitelaw [226]. It slightly improves the LES results of Chung and Sung [54] based on second-order spatial numerical schemes. It highlights then the importance of the high order schemes. The improvements are quite similar to those obtained by Jung and Sung [141] using a DNS with $65 \times 256 \times 256$ mesh points in the radial, tangential and axial directions respectively.

Figure 12.18 presents the anisotropy invariant map for the Reynolds stress tensor. It is noticeable that the present LES results respect the realizability diagram of Lumley [192]. As expected, turbulence is mainly at two-component close to the cylinders and tends to the isotropic state within the center of the gap. There is only a weak effect of the rotation parameter, the flow getting more isotropic in the center region for high N values. The present results and the ones of Chung and Sung [54] do not support their conclusions about a “disk-like” state at mid-radius. Even if the third invariant gets weakly negative, all the normal components of the Reynolds stress tensor are indeed all of the same order.

As a partial conclusion, this new LES approach has been fully validated against the velocity measurements of Nouri and Whitelaw [226] in an open Taylor-Couette system with an axial throughflow.

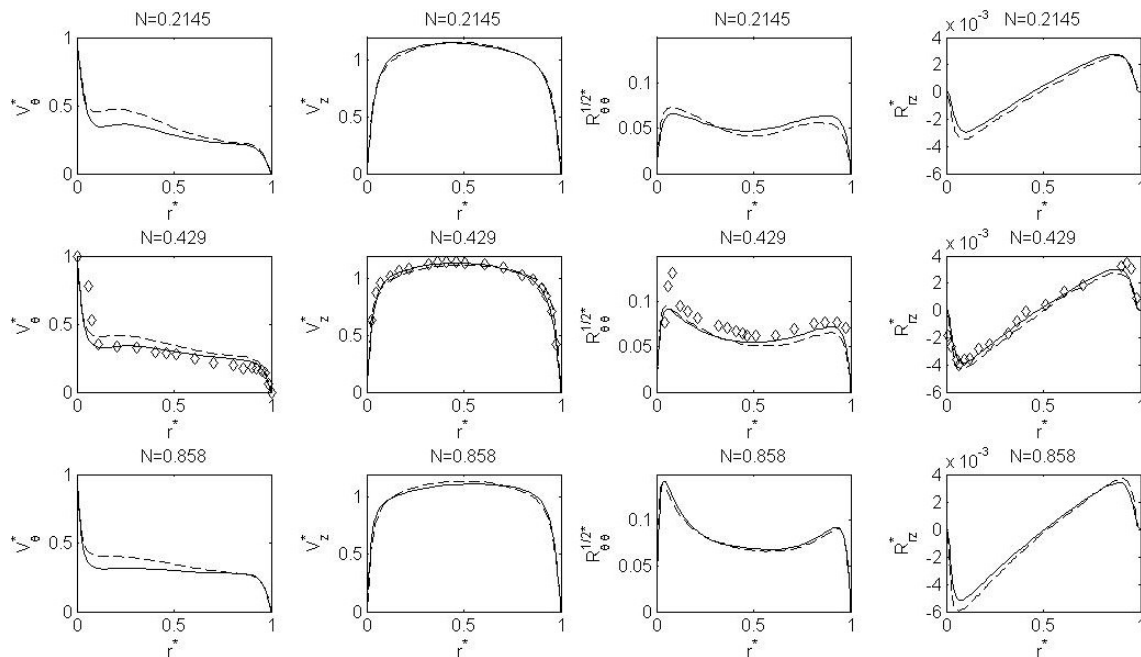


Figure 12.17: Radial distributions of the mean tangential and axial velocity components and of two components of the Reynolds stress tensor for $\Gamma = 9$, $\eta = 0.5$ and three values of N . Comparisons between the present LES (straight lines), the LES of Chung and Sung [54] (dashed lines) and the measurements of Nouri and Whitelaw [226] (symbols).

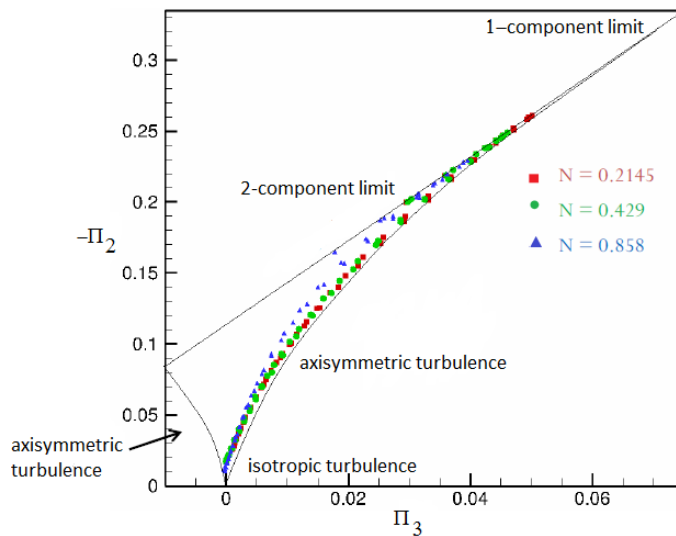


Figure 12.18: Anisotropy invariant map for the Reynolds stress tensor for $\Gamma = 9$, $\eta = 0.5$ and three values of N obtained by LES.

Near-wall structures appearing as elongated spiral rolls are observed along the inner cylinder. A very good agreement has been obtained for both the mean and turbulent fields and for the three values of the rotation parameter considered. More important, the present results improve the LES of Chung and Sung [54] highlighting the importance of the order of the spatial schemes. The present LES results can be now extended confidently to include heat transfer effects.

12.4.2 Configuration of the “Entrefer” project

In this section, one considers the fluid flow and the heat transfer in the gap between the rotor of an Air Cycle Machine and the stator of the electrical motor contained in an air conditioning pack developed by Liebherr Aerospace Toulouse. This configuration is very close to the one previously considered in Section 12.3.2 using the RSM. LES calculations will be compared to velocity and temperature measurements performed at IRPHE on a new experimental set-up.

12.4.2.1 Experimental facility developed at IRPHE

Two successive postdoctorate students developed a new Taylor-Couette facility at IRPHE to investigate the fluid flow and the heat transfer in a rotor-stator gap cooled by an axial throughflow.

General description and flow parameters The system (Fig.12.19) is composed of two concentric cylinders of length $h = 0.5$ m. The inner cylinder of radius $a = 8$ cm rotates around its axis at the rate Ω . The outer cylinder of radius $b = 9$ cm is stationary. The cavity may be thus defined by an aspect ratio equal to $\Gamma = 50$ and a radius ratio equal to $\eta = 0.89$ (narrow-gap cavity). The outer cylinder is made of PMMA to allow optical velocimetry techniques. Both cylinders are located in a tank made of PMMA that is regulated in temperature by a refrigerated circulator. The axial volumetric flowrate Q is imposed within the gap $\Delta R = b - a = 1$ cm by a centrifugal pump from the top to the bottom. All flow parameters are summarized in Table 12.1 and ensure that the similarity in terms of the Rossby number (ratio between the rotation velocity and the axial flow) and in terms of the geometry is preserved between the present experiment and the real turbomachinery. Using water as the working fluid (instead of air or freon) enables to consider weaker values of the rotation rate compared to the real rotating machinery.

Before entering the rotor-stator cavity, the water flow coming from 6 pipes is collected in a small cavity. When leaving the gap, water is gathered in an open tank which is also regulated in temperature. Water temperature is measured at the entrance and at the outlet of the gap through a set of 2 PT 100 probes located at mid-gap ($r = 0.85$ cm). The Prandtl number is fixed to 7 in most of the experiments but may be varied by changing the fluid temperature at the inlet.

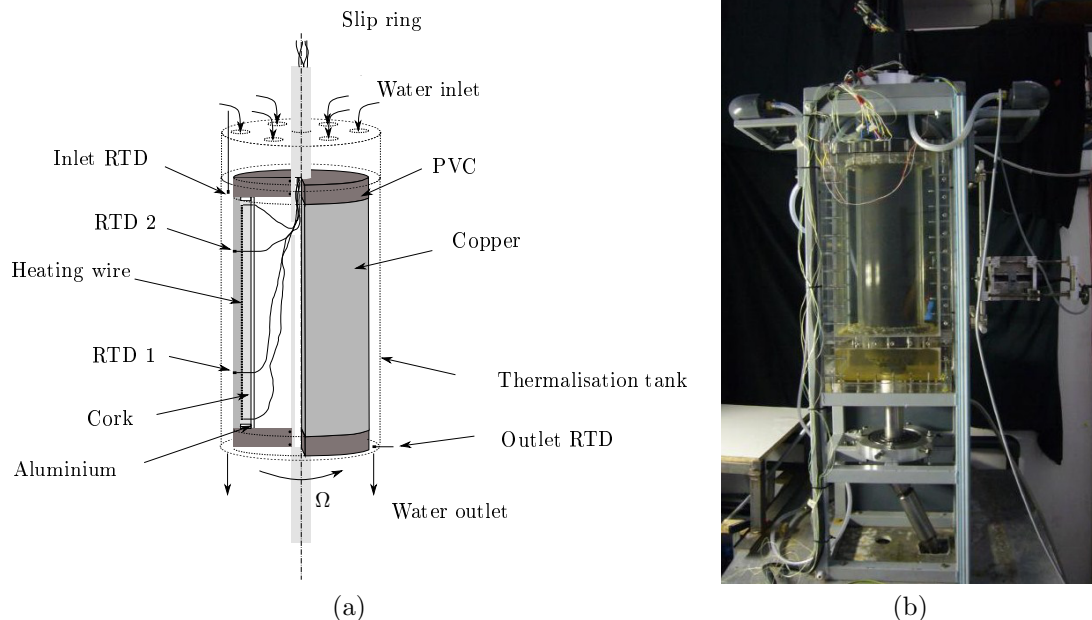


Figure 12.19: (a) Schematic representation and (b) photograph of the experimental facility developed at IRPHE.

Details about the rotor The rotor, which is also dedicated to supply a heat flux of $\varphi = 5.4 \text{ kW/m}^2$ to the fluid, is itself made of two concentric cylinders. The inner one is a 6 cm radius tube in aluminium. A 1 cm layer of cork was stuck on it to reduce heat losses. Then 60 m of a 4 mm diameter heating wire ($1 \Omega/\text{m}$) was wound on the cork layer. Conductive silver paste was added to fill the gap between the rings. A 8 cm radius tube in copper (5 mm thickness) was threaded on this assembly. In order to close the rotor, two PVC endcaps (5 cm thickness) were assembled on both sides. The motor shaft is a 3 cm radius tube in stainless steel metal. A small hole was drilled in it to take out every wires (probes and heating resistance) from the inner part of the rotor to a slip ring located at the top of the shaft. The shaft was passed through the endcaps of the rotor and sealing was achieved by two O-rings on both sides. Pressure screws on the end caps allow a proper alignment ($\pm 0.15 \text{ mm}$) and positioning of the cylinders respectively to the shaft. The rotor is mounted on 2 bearings. Atop, a lip seal is used for sealing between the shaft and the cavity as well as for the bottom.

To perform parietal temperature measurements, 4 RTD probes (PT100) were carefully mounted flush in the rotor. They were arranged in pairs symmetrically opposite respectively located at 16.7 and 33.3 cm from the top of the cylinder. Data were acquired using a 4 channel analog module.

Experimental procedure and data treatment The axial and azimuthal components of the velocity vector are measured by a two-component LDV system arranged as shown in Figure 12.20. Seeding was achieved with $5 \mu\text{m}$ polyamide particles. Each sample was conducted during 2 minutes in order to obtain a statistical convergence of the velocity.

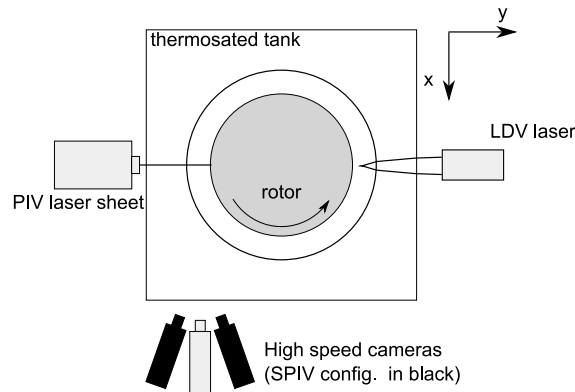


Figure 12.20: Arrangement of the different velocity measurement systems.

PIV and SPIV (Stereo-PIV) measurements were also performed by using a 5 W continuous laser and two high-speed cameras. Data acquisition frequency is set at 1500 Hz for a 512×1024 pixels resolution. The camera buffer limits the acquisition time at 2.6 s. Polyamide particles of $30 \mu\text{m}$ in diameter were used to seed the flow. Cross-correlations between the different frames are performed with the software DPIVSoft [209]. First interrogation windows are composed of 64×64 pixels with 50% overlapping. They are then translated and deformed according to the velocity field estimation. Smaller windows (32×32 pixels with 50% overlapping) are then chosen to enhance the spatial resolution.

The experimental procedure for the temperature measurements is described as follows. At first, the different temperature regulation systems are switched on. The pump is also turned on and the gap is filled with water before starting the rotation of the inner cylinder. When the whole system reaches the thermal equilibrium, data acquisition is triggered. Finally, the heating wire is powered. Different experiments showed that around 2h30 are necessary for the system to reach the steady state. The temperature of the incoming fluid is then close to 25°C . A 2D axisymmetric model developed with COMSOL allowed to estimate the heat loss in the system considering mainly conductive heat transfers. The wall heat flux is found to be equal to 90% of the flux provided by the heating wire.

12.4.2.2 Numerical modeling

One of the main conclusions drawn by F enot et al. [94] in their review paper is that *the multiplication of influential factors renders open cylindrical gap (Taylor-Couette-Poiseuille) far less widely understood,*

Q (l/s)	2	2	2	3	3	3
Ω (rpm)	100	200	300	100	200	300
Re_Q	7490	7490	7490	11200	11200	11200
Ta	8.8×10^6	3.5×10^7	7.9×10^7	8.8×10^6	3.5×10^7	7.9×10^7
N	2.24	4.47	6.71	1.49	2.98	4.47
Δz_i^+	26.95	37.6	48.82	22	29.99	36.15
Δz_o^+	24.4	33.88	43.38	19.68	27.29	32.57
Δr_i^+	0.47	0.66	0.86	0.38	0.52	0.62
Δr_o^+	0.43	0.6	0.76	0.34	0.47	0.56
$(a\Delta\theta)^+$	44.45	62.	80.51	57.66	78.62	94.76
$(b\Delta\theta)^+$	45.27	62.86	80.49	58.01	80.48	96.05
(N_r, N_θ, N_z)	(65, 144, 130)	(65, 144, 130)	(65, 144, 130)	(91, 128, 182)	(91, 128, 182)	(91, 128, 182)
δt (s)	1.5×10^{-4}	10^{-4}	8×10^{-5}	3×10^{-5}	7×10^{-5}	5×10^{-5}
CFL	0.21	0.22	0.24	0.07	0.23	0.22
CPU (s/it)	16.25	17.12	16.09	32.77	32.32	31.54
$C_{f,i}$	1.65×10^{-2}	3.2×10^{-2}	5.4×10^{-2}	9.72×10^{-3}	1.81×10^{-2}	2.63×10^{-2}
$C_{f,o}$	1.35×10^{-2}	2.6×10^{-2}	4.26×10^{-2}	7.77×10^{-3}	1.5×10^{-2}	2.13×10^{-2}
$Re_{\tau,i}$	169.8	236.86	307.54	195.79	266.93	321.74
$Re_{\tau,o}$	153.71	213.44	273.29	175.11	242.9	289.88

Table 12.5: Numerical details and mean flow parameters for the LES in the ‘‘Entrefer’’ configuration.

and it leads to contradictory conclusions among the authors. This state of affairs would seem to be essentially due to the entrance or input conditions for axial flow, whether it be dynamic or thermal. To overcome this problem, one chose to simulate a well-established hydrodynamic flow regime by rendering the flow in the axial direction periodic. To save computational time without any influence on the velocity field, the length of the cavity has been reduced such that $\Gamma = 10$ (i.e. 5 times smaller than in the experiment). It is noticeable that the boundary conditions for the thermal field remain the same as in the experiments. The consequence is that the thermal field is not established. The geometrical configuration simulated here is represented in Figure 12.21. The cavity is decomposed into 2 subdomains in the axial direction and to reduce computational time, a periodicity of $3\pi/4$ is assumed in the tangential direction. In this configuration, the WALE model has been used as the subgrid scale model. All the numerical details for the LES calculations are summed up in Table 12.5.

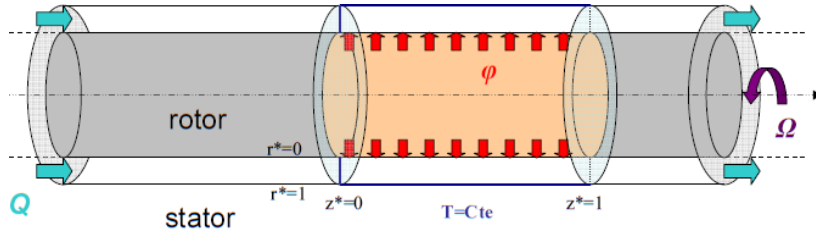


Figure 12.21: Sketch of the simulated cavity with boundary conditions for the thermal field.

In the present case, one considers only very small temperature differences between the incoming fluid and the rotor wall. Moreover, one has shown previously in a similar flow arrangement that the heat transfer process is dominated by forced convection and so that considering temperature as a passive scalar may lead to very satisfactory results. One supposes that density is not significantly affected by temperature differences, which allows to dissociate the dynamical effects from the heat transfer process.

Some calculations for $Pr = 7$ have also been performed using the RSM (Fluent) in its low Reynolds number formulation. Calculations are steady axisymmetric with a $(N_r = 81 \times N_z = 500)$ mesh grid. The geometrical parameters of the cavity are strictly the same as in the experiments. The Reynolds and energy equations are coupled through the Boussinesq approximation without the term of viscous dissipation. It has been checked that the inlet boundary conditions (turbulence intensities, velocity profiles) have only a weak influence on the velocity profiles and on the Nusselt distributions.

12.4.2.3 Hydrodynamic field

Figure 12.22 presents the iso-values of the Q criterion obtained by LES for four sets of parameters (Re_Q, Ta) . It highlights the presence of 3D unsteady coherent structures within the two boundary layers. They appear as thin negative spiral patterns along the rotor as they roll up in the opposite

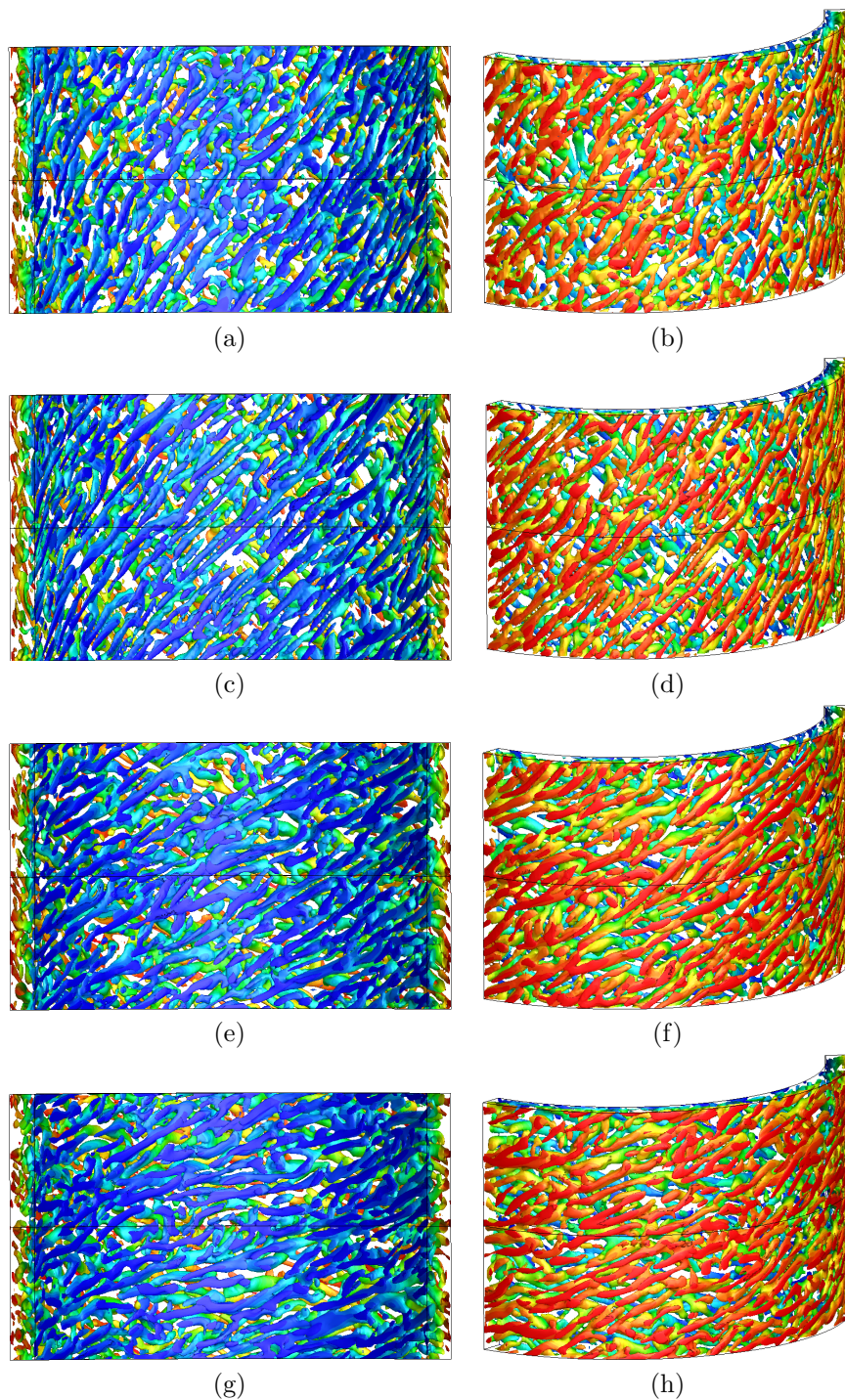


Figure 12.22: Iso-values of the Q criterion colored by the radial position along the rotor (a,c,e,g) and along the stator (b,d,f,h) obtained by LES for $\Gamma = 10$, $\eta = 0.89$ and: $N = 1.49$ ($Ta = 8.8 \times 10^6$ & $Re_Q = 11200$; a,b), $N = 2.24$ ($Ta = 8.8 \times 10^6$ & $Re_Q = 7490$; c,d), $N = 4.47$ ($Ta = 3.5 \times 10^7$ & $Re_Q = 7490$; e,f), $N = 6.71$ ($Ta = 7.9 \times 10^7$ & $Re_Q = 7490$; g,h).

sense of the inner cylinder rotation. They are very similar to those obtained in the previous section for a middle-gap cavity. The same spiral network is obtained along the stator with a positive angle. When the axial throughflow dominates rotation effects, these structures are aligned with the axial direction. They get progressively inclined with the tangential direction when the rotation rate increases. As examples, along the rotor, the angle formed by the spirals with the tangential direction is equal to

45° for $N = 1.49$ ($Ta = 8.8 \times 10^6$, $Re_Q = 11200$), to 22° for $N = 4.47$ ($Ta = 3.5 \times 10^7$, $Re_Q = 7490$) and to 16° for $N = 6.71$ ($Ta = 7.9 \times 10^7$, $Re_Q = 7490$). From this figure, one can draw two main conclusions:

- from a numerical point of view, there is no evidence of structures at the interface between the two subdomains produced by a numerical artifact, which validates one more time the multidomain approach.
- 3D unsteady structures appear as spiral rolls along both walls at a relatively small scale. They may play a key role in the wall heat transfer process. They could explain why most of the RANS models, which assume the base flow as being stationary and axisymmetric, fail to predict the right distributions of the heat transfer coefficient [231].

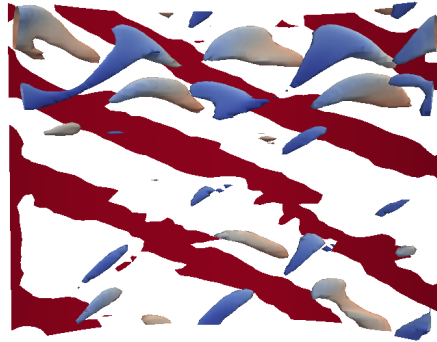


Figure 12.23: Iso-values of the Q criterion obtained by a hybrid RANS/LES method for $\Gamma = 10$, $\eta = 0.89$ and $N = 2.24$ (see in Reference [99]).

Some calculations have also been performed using the Code Saturne developed by EDF using both the elliptic blending RSM and a hybrid RANS/LES approach. The comparisons with the present LES have been published in Reference [99] for two sets of parameters. The computational cost is certainly about 2 – 3 times lower than in the present LES but the hybrid RANS/LES computation does not improve even the predictions of the RANS model and completely fails to predict the mean and turbulent flow fields, especially close to the walls. Figure 12.23 exhibits the iso-values of the Q criterion obtained by the hybrid RANS/LES method for $N = 2.24$ ($Ta = 8.8 \times 10^6$ & $Re_Q = 7490$). Some streaks are obtained within the boundary layers but it is clear that this approach does not capture so well the thin coherent 3D structures obtained by the pure LES.

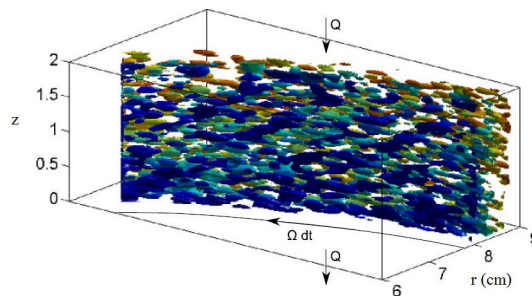


Figure 12.24: Iso-values of the λ_2 criterion ($\lambda_2 = 10^3$) obtained experimentally from SPIV measurements for $\Gamma = 50$, $\eta = 0.89$, $Re_Q = 7490$ and $Ta = 8.7 \times 10^6$.

The SPIV measurements have been performed at a sufficiently high frequency (1500 Hz) to be resolved in time and to make the Taylor hypothesis valid. By considering also that the flow is mainly in solid body rotation, one can calculate the λ_2 criterion, which is the second proper value of the $S^2 + A^2$ tensor, where S and A are the symmetric and antisymmetric parts of the velocity gradient tensor approximated using second-order finite difference schemes. The iso-values of λ_2 enable to

highlight the presence of coherent structures within the flow. One example is given in Figure 12.24 for $Re_Q = 7490$ and $Ta = 8.7 \times 10^6$. The axial fluid flows from the top to the bottom and time is increasing from the right to the left. Coherent structures along the rotor side can be observed with a given inclination angle. There is no apparent 3D large scale vortices within the core of the flow. These results are in qualitative good agreement with the iso-values of the Q criterion obtained numerically (Fig.12.22c & d).

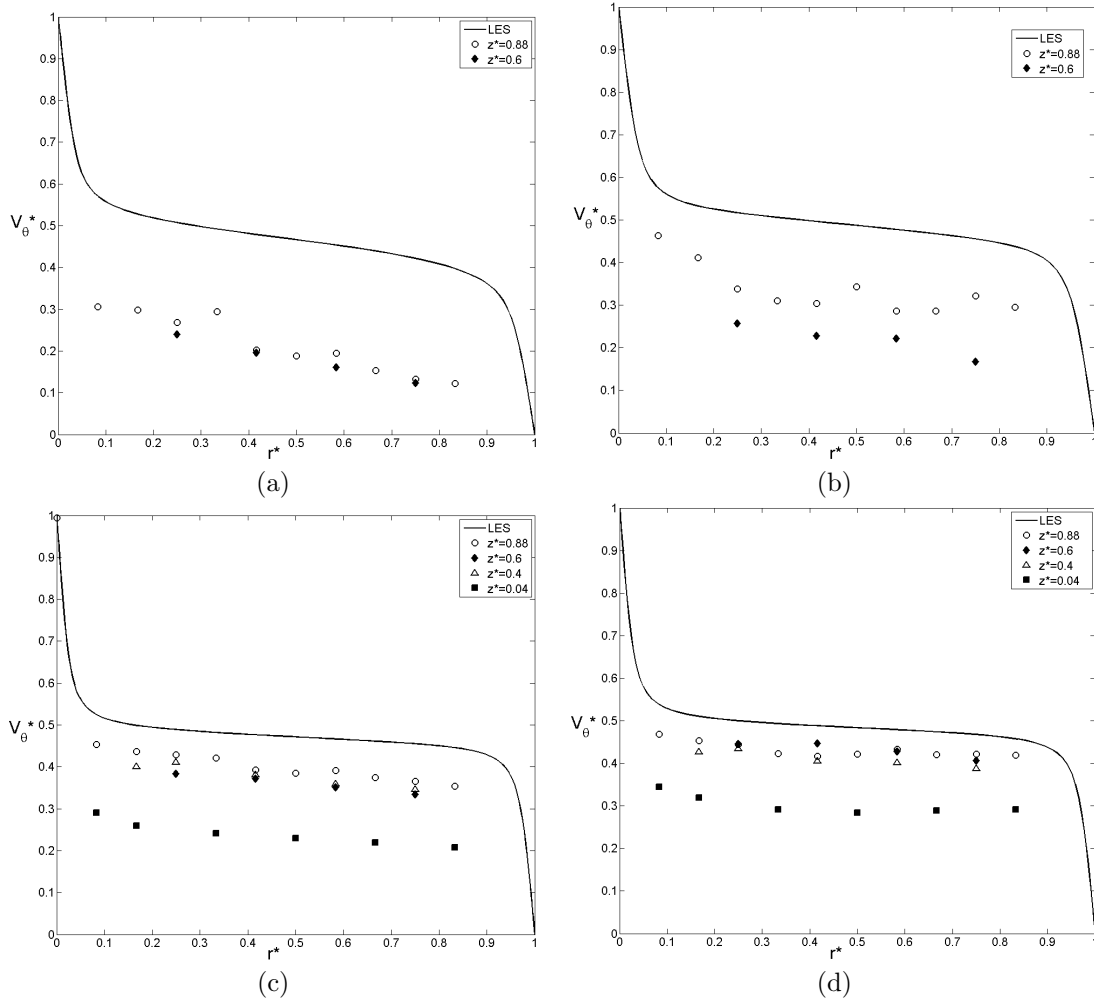


Figure 12.25: Axial variations of the mean tangential velocity V_θ^* for $\eta = 0.89$ and: (a) $N = 1.49$ ($Ta = 8.8 \times 10^6$, $Re_Q = 11200$), (b) $N = 2.24$ ($Ta = 8.8 \times 10^6$, $Re_Q = 7490$), (c) $N = 4.47$ ($Ta = 7.9 \times 10^7$, $Re_Q = 11200$), (d) $N = 6.71$ ($Ta = 7.9 \times 10^7$, $Re_Q = 7490$). Comparisons between the LES (lines) and the LDV measurements (symbols).

To go a little bit in more details, the LES results are compared first to the velocity measurements in terms of the mean velocity profiles. The axial and azimuthal velocity components are made dimensionless by the mean inlet axial velocity $\overline{V_z}$ and the rotor wall velocity Ωa respectively. Note that the value of $\overline{V_z}$ is the one read on the flowmeter, which slightly fluctuates. Thus, the integration of the normalized experimental axial velocity profiles in the radial direction does not yield a value of unity. The experimental profiles should be then rescaled to get the conservation of mass as was done by Chung and Sung [54] for the experimental data of Nouri & Whitelaw [226].

First of all, it has been checked whether the flow field is well established in the experiment or not. For that, Figure 12.25 compares the LES results with the velocity measurements performed by LDV at various axial positions and for four sets of parameters. First of all, the tangential velocity profiles vary very weakly with the rotation parameter N such that $V_\theta^*(r^* = 0.5)$ at mid-gap remains close to 0.5 in the simulations. One can just notice that, at low N values, V_θ^* varies with $1/r$ in the

gap and gets constant at high N . In that case, the profile resembles the Batchelor profile obtained in unmerged boundary layer interdisk flows. Experimentally, for $N = 1.49$ and $N = 2.24$, the axial flow pilots the hydrodynamic field and the tangential velocity remains very low even close to the cavity outlet at $z^* = 0.88$, corresponding to $22D_h$ (where $D_h = 2\Delta R$ is the hydraulic diameter). It means that the flow is not hydrodynamically established. When one increases the rotation rate, the experimental profiles get closer to the numerical ones as rotation effects dominate the axial flow. In the experiments, one can suppose that the flow is not perfectly established even if the axial dependence of the velocity profiles is weak for $0.4 \leq z^* \leq 0.88$ (between 10 and $22 D_h$). The main conclusion is that, even if the length of the cavity is relatively short in the experiments, for large values of the rotation parameter $N \geq 4$, the flow field may be considered as hydrodynamically established at the cavity outlet. On the contrary, the axial dependence of the tangential velocity profile is strong for $N \leq 2.3$.

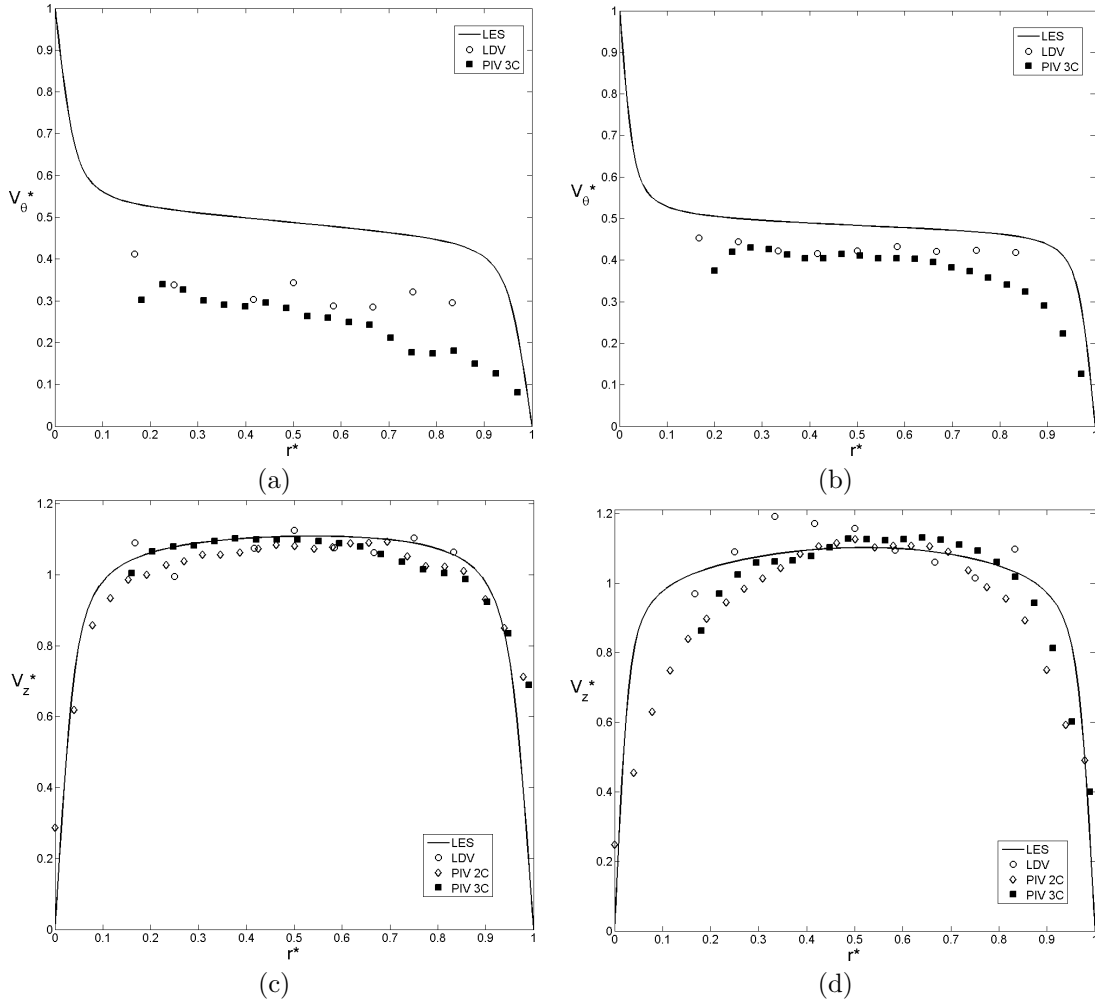


Figure 12.26: Comparisons of the different experimental approaches (symbols) plotted at $z^* = 0.9$ in terms of the mean (a,b) tangential V_θ^* and (c,d) axial V_z^* velocity components for $\eta = 0.89$, $Re_Q = 7490$ and two Taylor numbers: $Ta = 8.8 \times 10^6$, $N = 2.24$ (a,c) and $Ta = 7.9 \times 10^7$, $N = 6.71$ (b,d). Comparisons with the LES (lines).

Figure 12.26 compares the three velocity measurement techniques (LDV, PIV et SPIV) for two very different values of N close to the cavity outlet at $z^* = 0.9$ ($22.5D_h$). One recalls that all techniques do not provide the same informations. The results obtained by LDV and PIV 3C (at three components) are very similar. The PIV 3C gives an access to the velocity field closer to the walls, especially on the stator side. Close to the rotor, laser reflexions induce a loss of information within the boundary layer. The radial distribution of the mean axial velocity component computed by LES resembles a typical Poiseuille profile usually encountered in well established turbulent pipe flows and is not so

sensitive to the value of N . Experimentally, one recalls that by integration over the radius of the velocity profile, one does not obtain the flowrate corresponding to Re_Q and all profiles should be then rescaled. It is a quite classical result in such experiments already observed by Nouri and Whitelaw [226]. For $N = 2.24$, the experimental profiles are close to a turbulent Poiseuille profile, whereas for a larger value of $N = 6.71$ (same flowrate Q but a higher rotation rate Ω), the profiles look more like a laminar Poiseuille profile with a parabolic shape.

The corresponding profiles of the normal components of the Reynolds stress tensor are plotted in Figure 12.27 for the same parameters and at the same axial position $z^* = 0.9$. The tangential component $R_{\theta\theta}$ has been normalized by $(\Omega a)^2$ and the two others R_{rr} and R_{zz} by $\overline{V_z}^2$. It is noticeable that the cross-components of the Reynolds stress tensor are not shown here for three main reasons: they are at least one order weaker than the normal components, their behavior is very similar to that obtained in the previous section for a middle-gap cavity and it is particularly difficult to get a good statistical convergence of these quantities in the experiments. As shown on Figure 12.27, turbulence is mainly concentrated within the boundary layers, where peak values for $R_{\theta\theta}^*$ and R_{zz}^* are observed. On the contrary, the radial normal component is maximum at mid-gap. A weak asymmetry may be observed from the numerical profiles with higher turbulence levels close to the rotor. For a given axial Reynolds number, turbulence intensities increase, as expected, with increasing values of the Taylor number. The main interesting result is the very high levels of the $R_{\theta\theta}^*$ and R_{zz}^* components for $N = 6.71$, which have never been observed in any of the previous experimental or numerical studies published on that configuration [54, 226, 256]. A relatively good agreement has been obtained between the numerics and the experimental methods, especially for the radial and axial normal components. On the contrary, large discrepancies between the LDV and the PIV 3C techniques are observed for the tangential normal component.

The influence of the flow parameters (Re_Q , Ta) on the mean and turbulent flow fields is now investigated. The LES results and the LDV measurements are compared at $z^* = 0.9$ ($22.5D_h$) in terms of the two mean velocity components V_θ^* and V_z^* for two axial Reynolds numbers and three Taylor numbers (Fig.12.28 & 12.29). Note that the different quantities can not be measured by LDV in the boundary layers due to technical constraints. Figure 12.28 confirms the previous results already discussed. The numerical profiles for the mean velocity components are weakly dependent on the flow parameters, which can be mainly explained by the axial periodicity of the cavity. The axial mean velocity remains the same whatever the values of Re_Q and Ta . For large Ta values, the normalized tangential velocity remains constant within the gap and equal to 0.5. Fluid rotates as a solid body in the region located outside the boundary layers. For weaker values of Ta , V_θ^* varies linearly with $1/r$ such that the angular momentum is conserved. In the experiments, the effect of Re_Q remains weak. An asymmetry in the V_z profile is observed for all sets of parameters but it is not always along the same wall depending on the parameters. The flowrate has contrariwise a large influence on the tangential velocity profile and especially outside the boundary layers. High flowrates induce low tangential velocities in the gap. The discrepancies observed between the LES and the LDV measurements may be fully attributed to the different hydrodynamic flow regimes.

Figure 12.29 highlights the influence of the parameters on the turbulent field. As expected, higher values of the Taylor number induce higher turbulence levels within the gap and in the boundary layers whatever the value of Re_Q . This result is not so intuitive for the tangential normal component due to the normalization by $(\Omega a)^2$. It means that the tangential turbulence intensities increase more rapidly than the rotation rate of the inner cylinder, which can not be attributed to the axial flowrate fixed at a constant value. The same trends have been obtained both experimentally and numerically with a relatively good agreement between the two approaches. The LDV measurements seem to be less sensitive to the rotation rate. By comparisons between Figure 12.29a,c and 12.29b,d, it can be seen that the effect of the axial flowrate remains weak. Once again, as the normal axial component R_{zz}^* is normalized by $\overline{V_z}^2$, it means that this component R_{zz} increases with increasing values of Re_Q . It is also noticeable here that the peak values observed within the boundary layers, and especially along the rotor side, are particularly high compared to those published in previous papers [54, 226, 256].

A large numerical and experimental database has been established for 6 sets of parameters (Re_Q , Ta). The three measurement techniques have been compared favorably for most of the mean and turbulent quantities. Some important results are gained from this study. The axial variation of the velocity profiles does not depend only on the length of the cavity but also on the value of the rotation parameter N . For high values of $N \geq 4$, i.e. rotation effects are strong compared to the axial flowrate,

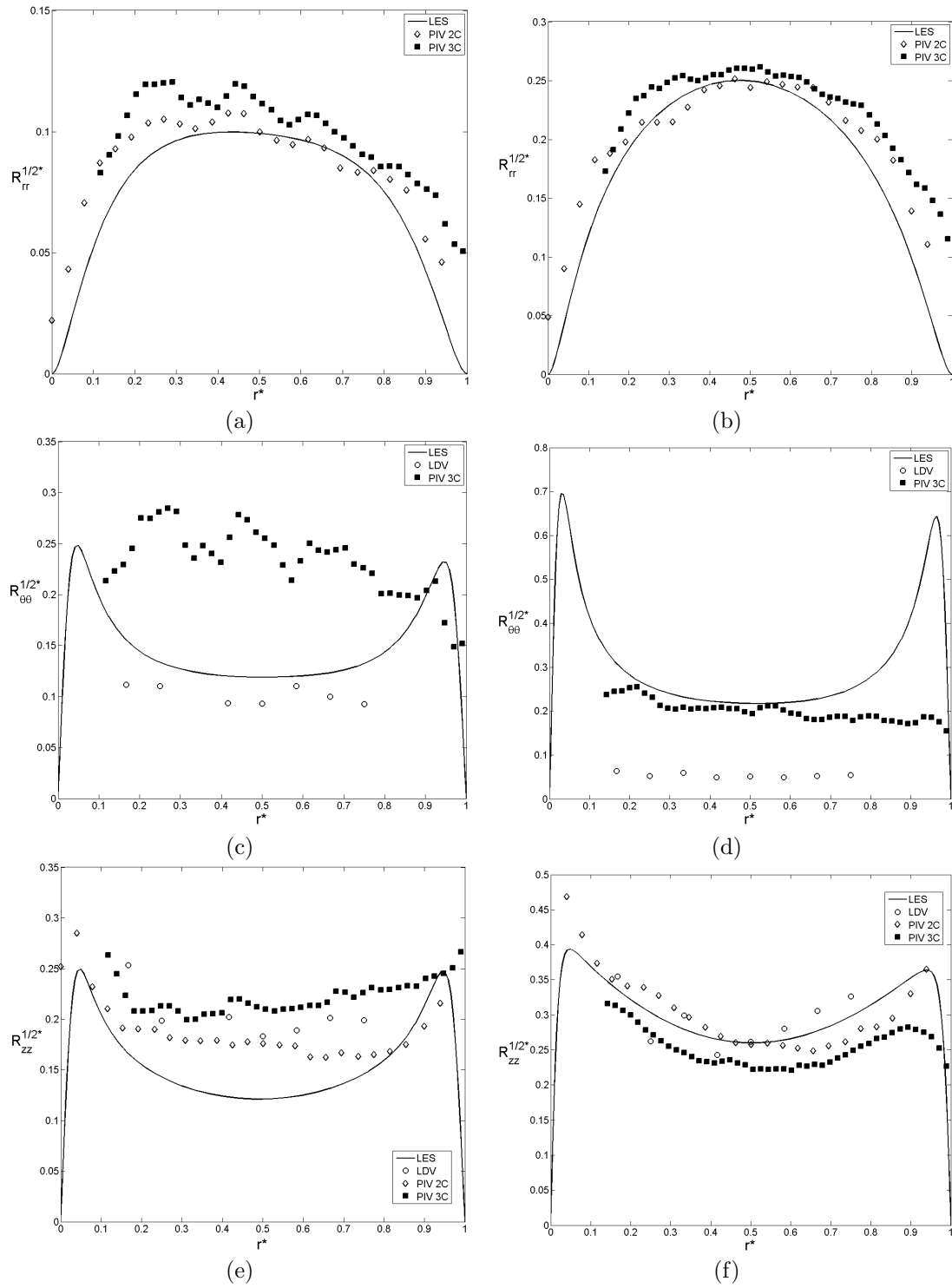


Figure 12.27: Comparisons of the different experimental approaches (symbols) plotted at $z^* = 0.9$ in terms of the normal components (a,b) $R_{rr}^* = \overline{v_r^2}/\overline{V_z^2}$, (c,d) $R_{\theta\theta}^* = \overline{v_\theta^2}/(\Omega a)^2$ and (e,f) $R_{zz}^* = \overline{v_z^2}/\overline{V_z^2}$ of the Reynolds stress tensor for $\eta = 0.89$, $Re_Q = 7490$ and two Taylor numbers: (a,c,e) $Ta = 8.8 \times 10^6$, $N = 2.24$ and (b,d,f) $Ta = 7.9 \times 10^7$, $N = 6.71$. Comparisons with the LES (lines).

similarity profiles are obtained for $z^* \geq 0.4$. In that case, LES results and velocity measurements compare quite favorably. On the contrary, for $N \leq 2.4$, all mean velocity profiles strongly depend on the axial position such that the experimental profiles remain far from the computed ones. In all cases,

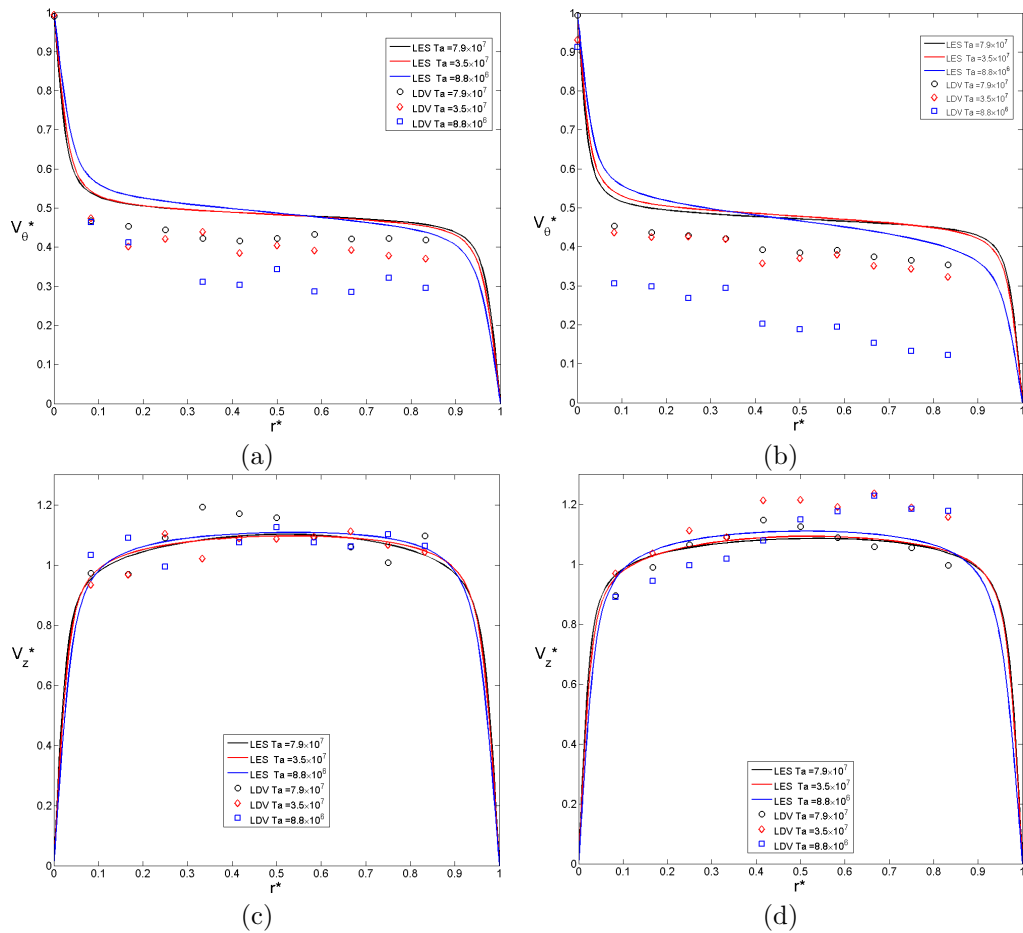


Figure 12.28: Influence of the Taylor number on the mean (a,b) tangential V_θ^* and (c,d) axial V_z^* velocity components for $Re_Q = 7490$ (a,c) and $Re_Q = 11200$ (b,d). Comparisons between the LES (lines) and the LDV measurements (symbols) obtained at $z^* = 0.9$ for $\eta = 0.89$.

the flow is highly turbulent with peak values in the boundary layers, where 3D coherent unsteady structures are observed in the simulations along both cylinders.

12.4.2.4 Heat transfer coefficient

From an engineering point of view, the main goal is to establish correlations for the heat transfer coefficient on the rotor wall according to the flow parameters: Re_Q , Ta and the Prandtl number Pr . In the ‘‘Liebherr 1’’ configuration, correlation laws have been established using the RSM for both cylinders. Equations under the form $Nu \propto Re_Q^m Ta^n Pr^\gamma$ have been obtained in the case of imposed temperatures on the walls. If the coefficients m , n and γ were in good agreement with data available in the literature on the rotor side, it has been found that $\gamma = 0.8$ on the stator, which was somewhat an unexpected result. Moreover, there were large discrepancies between the RSM results and calculations performed using StarCCM+ on the same configuration. It appeared then crucial to develop a LES approach to investigate possible 3D structures embedded in the flow before trying to establish more precise correlations for the Nusselt number in the case of an imposed heat flux on the inner surface of the rotor. In the following, the LES results will be compared to temperature measurements performed using the new IRPHE’s experiment.

As a shorter cavity is considered in the simulations and to enable direct comparisons with the experiments in which the Nusselt number measurements are performed at $z = 16$ cm and $z = 33$ cm, the LES results are extended to larger axial positions z using the following law:

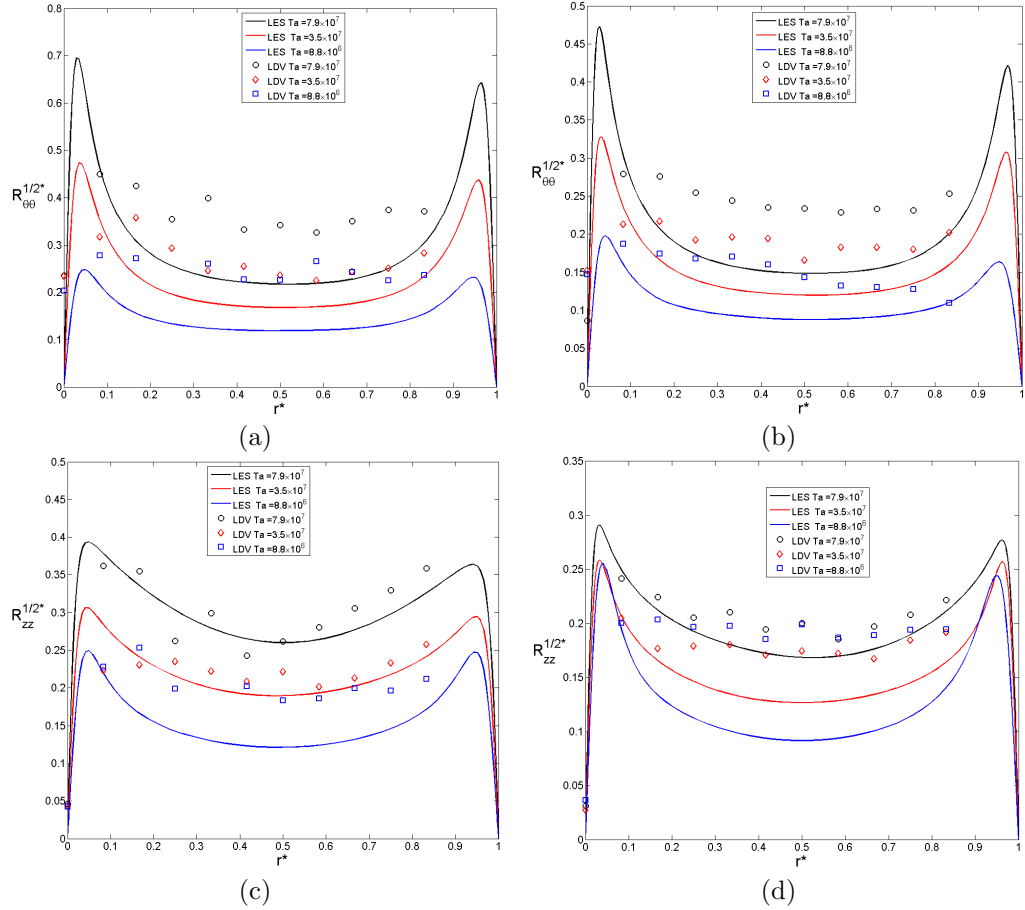


Figure 12.29: Influence of the Taylor number on the normal components (a,b) $R_{\theta\theta}^*$ and (c,d) R_{zz}^* of the Reynolds stress tensor for $Re_Q = 7490$ (a,c) and $Re_Q = 11200$ (b,d). Comparisons between the LES (lines) and the LDV measurements (symbols) obtained at $z^* = 0.9$ for $\eta = 0.89$.

$$Nu(z) = \frac{\varphi \Delta R}{\lambda \left[\frac{2\pi a \varphi}{c_p q_m} (z - z_0) \right] - T_p(z) + T_f(z_0)} \quad (12.10)$$

where $T_p(z)$ and $T_f(z_0)$ are the wall and fluid temperatures deduced from the simulations, $z_0 = 0$ the inlet axial location, λ the fluid thermal conductivity, q_m the mass flowrate and c_p the fluid thermal capacity. Equation (12.10) is deduced from an energy balance in an annulus of gap ΔR subjected to a heat flux φ imposed on the inner cylinder and a superimposed throughflow Q . It does not take into account the growth of the rotor boundary layer.

Figure 12.30 shows the temperature distribution $T_p(\theta, z)$ on the rotor wall for $Re_Q = 11200$ and $Ta = 8.8 \times 10^6$. It can be noticed that a small buffer region with adiabatic thermal conditions has been used in the numerics at the bottom of the system for numerical stability purpose. Streaks in the wall temperature distribution can be clearly seen due to the presence of the coherent structures within the rotor boundary layer, already evoked in the previous section. To evaluate the local Nusselt number distribution using Equation (12.10), the wall temperature has been then averaged along the azimuthal direction.

Figure 12.31 shows that the local Nusselt number decreases from the inlet of the gap and then tends to reach a constant value around $z \simeq 0.05$ cm (for $Ta = 7.9 \times 10^7$), which is well fitted by Equation (12.10). The higher the Taylor number is, more rapidly Nu tends to reach its limit. This behavior is in agreement with the precedent findings of Hirai *et al.* [128] or Poncet *et al.* [256] in Taylor-Couette-Poiseuille flows, which corresponds also to the thermal development of flow in pipes or ducts. As Nu tends to an asymptotical limit, the LES can be extended using Equation (12.10) and simulated Nusselt numbers will be given in the following at an axial position $z = 33$ cm ($z^* = z/h = 0.66$),

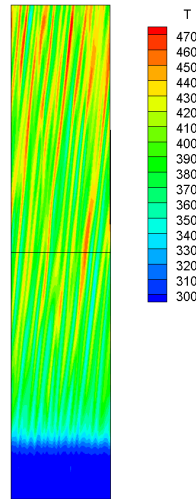


Figure 12.30: Outspread view in a (r, z) plane of the temperature map on the rotating inner cylinder surface for $Re_Q = 11200$, $Ta = 8.8 \times 10^6$ ($N = 1.49$) and $Pr = 7$ obtained by LES.

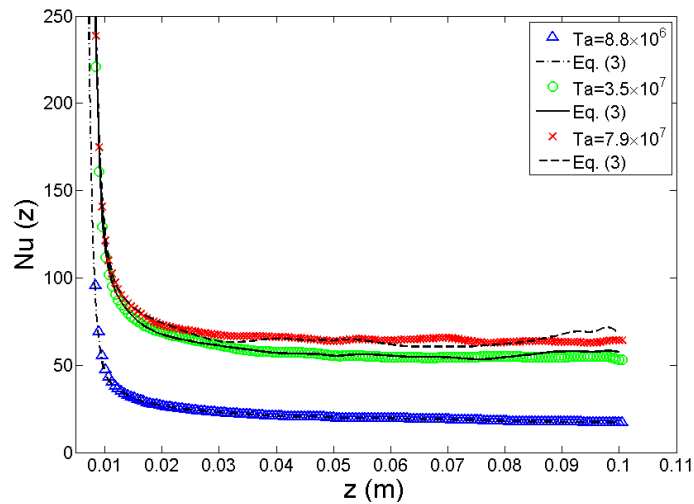


Figure 12.31: Axial variations of the local Nusselt number for $Re_Q = 11200$, $Pr = 7$ and three Taylor numbers. Comparisons between the present LES and Eq.(12.10).

corresponding to the lowest temperature probe in the experiment, thus giving the measurements as close as possible to the established regime.

The computational cost to get a good convergence of the statistics being relatively expensive, only 9 different cases for two Prandtl numbers have been considered, which is not enough to establish valuable correlations for the Nusselt number. So, let's start by presenting the experimental results. Figure 12.32 shows the evolution of the Nusselt number $Nu = h\Delta R/\lambda$ (λ the thermal conductivity of water) on the rotor as a function of the Taylor number for various axial Reynolds numbers Re_Q . There is a noticeable difference between the values obtained with the two probes (at $z^* = 0.32$ and 0.66) due to the transient nature of the heat transfer process. Nu is clearly an increasing function of Ta with more important variations for weak rotation rates. It may be attributed to the coherent structures observed within the rotor boundary layer, which would prevent the axial flow to cool the rotor at high rotation rates. The same tendency is obtained whatever the axial Reynolds number Re_Q . The present results are also compared to the experimental data of Gilchrist *et al.* [109] performed for $950 \leq Re_Q \leq 2080$. The agreement is particularly good at high Ta values.

The experimental data plotted in Figure 12.32 have also been fitted by correlation laws under the form: $Nu = B\Delta R \left(\frac{\Omega}{\nu}\right)^{2/7}$, with B an adjusting coefficient equal to 26 for the probe at $z^* = 0.32$

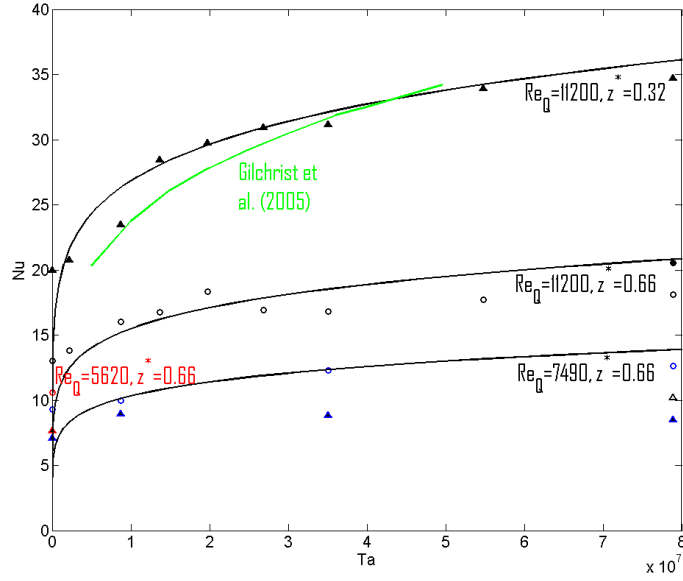


Figure 12.32: Variations of the Nusselt number according to the Taylor number for various axial Reynolds numbers. Comparisons between the present measurements and the previous results of Gilchrist et al. [109]. The lines correspond to the scalings deduced from Equation (12.14).

and $Re_Q = 11200$ as example. It is based on both the boundary theory in the turbulent regime and the assumption that heat transfer is purely conductive as it will be shown in the following. It works quite well especially for $Ta > 2 \times 10^7$. Thus, Nu scales like $Ta^{1/7}$ ($\Omega^{2/7}$) in the present experiments, whereas Gilchrist et al. [109] found an exponent equal to 0.226 but for a narrower range of Ta values.

Let's come back to the form of the correlation law for Nu . It was inspired by the work of Aoki et al. [12] on laminar Taylor-Couette flows. If one assumes that the flow may be divided into two flow regions, the inviscid region where the mixing effect of disturbance is very large and the viscous dominant region near the wall, the boundary theory in the turbulent regime gives the following relation:

$$\frac{\delta}{\Delta R} \sim \left(\frac{V_{ef} \Delta R}{\nu} \right)^{-1/5} \quad (12.11)$$

where V_{ef} represents the velocity at the boundary of the two regions. The balance between the centrifugal and viscous forces in the boundary layer region is:

$$\Omega^2 a \sim \frac{V_{ef} \nu}{\delta^2} \quad (12.12)$$

Then, the expression for $\delta/\Delta R$ representing the velocity gradient at the wall is:

$$\frac{\delta}{\Delta R} \sim \left(\frac{\Omega^2 a \Delta R^3}{\nu^2} \right)^{-1/7} \quad (12.13)$$

Assuming that the heat transfer is purely conductive $h = \lambda/\delta$, one finally gets:

$$Nu \sim Ta^{1/7} \quad (12.14)$$

By removing the thermalization of the external tank, the temperature of water can vary and the Prandtl number as well. It has been done for four sets of parameters (Ω , Q). Thus, 4×15000 measurements have been performed. An error minimization by the least square method provides the following correlation law:

$$Nu = 1.5294 \times 10^{-5} Re_Q^{1.0831} Ta^{0.1218} Pr^{0.9204} \quad (12.15)$$

It confirms, in particular, that the Nusselt number depends on the Taylor number with an exponent close to $1/7$ ($\simeq 0.1438$) as found by Equation (12.14). On the contrary, the exponent for the axial

Reynolds number 1.0831 is higher than the classical one found in the literature 0.8 [51]. The exponent for the Prandtl number 0.9 is also much higher than the classical value 0.3. The reader can refer to the section 12.3.2.3 for the discussion about the values of the different exponents and to the review of Fénot *et al.* [94].

One can also try to gather the results and express the Nusselt number under the form:

$$Nu = A(Pr)Re_{eff}^{\beta} \quad (12.16)$$

$$Re_{eff} = \frac{V_{eff} \times D_h}{\nu}, \quad V_{eff} = \left(\overline{V_z}^2 + \alpha(\Omega a)^2 \right)^{1/2} \quad (12.17)$$

where Re_{eff} and V_{eff} are the effective Reynolds number and velocity respectively, $D_h = 2\Delta R$ the hydraulic diameter and α a coefficient representing the relative importance of rotation compared to the axial flowrate. Figure 12.33a shows the evolution of Nu against Re_{eff} for $\alpha = 0.5$. α is usually arbitrarily fixed to 0.5 (see in [94]). It will be shown in the following that its value can also be optimized. The results obtained for three values of the axial Reynolds number are well scaled by a linear interpolation with $A = 0.92$ and $\beta = 0.27$.

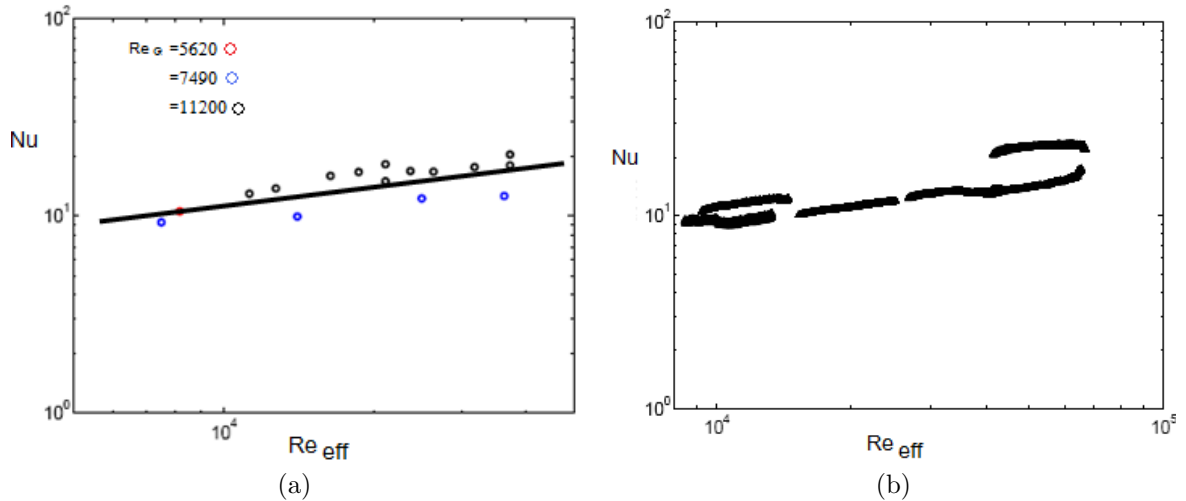


Figure 12.33: Evolution of the experimental Nusselt number at $z^* = 0.66$ according to the effective Reynolds number: (a) for three values of the axial Reynolds number and $Pr = 6$ (the linear interpolation has been obtained using $\alpha = 0.5$, $A = 0.92$ and $\beta = 0.27$); (b) for various Prandtl numbers with $\alpha = 0.5$.

If the Prandtl number varies, the experimental data may be correlated under the form:

$$Nu = ARe_{eff}^{\beta}Pr^{\gamma} \quad (12.18)$$

Using the least square method, the coefficients A , β and γ can be deduced for different values of α used in the literature [94] (see Table 12.6). The usual value for β found in the literature is 0.8 far from the one obtained here around 0.3. The same remark can be done for γ lower than 0.1 in the present case and far from the usual value 0.3. It can be partly explained by the fact that usual averaged values for the Nusselt number are obtained by an average along the axial direction and so integrates some edge effects as shown in Figure 12.11 for example.

Figure 12.33b reports the evolution of the Nusselt number against the effective Reynolds number for $\alpha = 0.5$ and various Prandtl numbers. Each segment corresponds to a given temperature drift due to the stop of the thermalization. The experimental values follow a linear behavior with the same slope when Re_{eff} increases.

Figure 12.34 shows the main results of this section. The LES and RSM results are compared to the temperature measurements in terms of the Nusselt number on the rotor side at $z^* = 0.66$. Nu is plotted against Equation (12.15). Some typical values are also reported in Table 12.7. What first meets the eyes is the large discrepancy between the different approaches, with an overestimation of

α	A	β	γ
0.25	0.28	0.37	0.1
0.5	0.499	0.31	0.05
0.6	0.667	0.28	0.026
0.8	0.56	0.3	0.04

Table 12.6: Values of A , β and γ for different values of α .

the Nusselt number by the numerics. There is no apparent reason, which could explain such a large overestimation by the RSM (Fluent) compared to the experiment, as the same boundary conditions and flow parameters have been considered. F enot *et al.* [94] tried, in their review paper, to provide some explanations for that: *It should be added that important data such as entry velocity profile and turbulence rate are generally not given consideration by the authors, and this omission no doubt partially explains to striking disparities in their reported results.* The influence of these parameters has been then tested for some particular cases, keeping in mind that the inlet boundary conditions are unknown in the experiments. Changing the turbulence intensities at the inlet or the type of velocity profile does not modify significantly the averaged value for the Nusselt number on the rotor. For example, Nu is 15% lower if the turbulence intensities imposed at the inlet decrease from 10% to 1%, which is not enough to explain the difference with the experiments. It may be attributed to both the presence of 3D structures within the boundary layers not captured by the RSM (Fluent) and to the turbulence modeling, which is not adapted to confined rotating flows with heat transfer.

Ta	Re_Q	$Pr = 0.7$	$Pr = 7$
8.8×10^6	7490	15.65 (LES)	–
8.8×10^6	11200	17.23 (LES)	19.25 (LES) 16.01 (exp.) 73.4 (RSM)
3.5×10^7	7490	20.89 (LES)	–
3.5×10^7	11200	24.9 (LES)	51.6 (LES) 16.81 (exp.) 125.4 (RSM)
7.9×10^7	7490	22.25 (LES)	–
7.9×10^7	11200	26.7 (LES)	64.65 (LES) 18.09 (exp.) 156.3 (RSM)

Table 12.7: Values of the Nusselt number at $z^* = 0.66$ for various flow parameters. Comparisons between the LES, the RSM (Fluent) and the experimental data.

The circles on Figure 12.34 represent the LES results, whose magnitude is roughly the same as in the experiments. The symbols confined closed to the origin of the axis correspond to the values obtained for $Pr = 0.7$ and the other group of three circles represent computations for $Pr = 7$. For $N = 1.49$ and $Pr = 7$, the LES is in close agreement with the experimental data: $Nu = 16.01$ in the experiment and $Nu = 19.25$ by LES (see Table 12.7). The general overestimation of the Nusselt number by the LES is mainly due to the periodicity of the flow in the axial direction, whereas the flow is in a transient state in the experiments. It would be risky to identify some correlations with such few numerical points but it seems that the Nusselt number is much more dependent on the Taylor number in the LES than in the experiments. On the contrary, its dependence on the Prandtl number is much weaker and close to $Pr^{1/3}$. Nevertheless, the LES improves significantly the predictions of the RSM.

In order to explain the difference remaining between the experiments and the LES or RSM predictions, the influence of the viscous dissipation term on the Nusselt number has been checked in the particular case where one is in perfect similarity with the real turbomachinery: an air flow at $Re_Q = 7490$ and $Ta = 7.8 \times 10^7$ using the RSM model of Fluent. In all simulations, the viscous dissipation term has been indeed not taken into account in the energy equation. With the viscous dissipation term, the Nusselt number is slightly lower. The maximum difference is 1.25 at a given

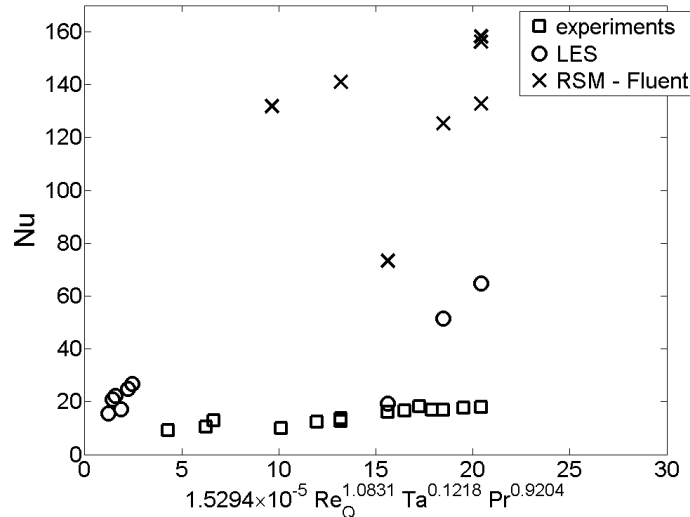


Figure 12.34: Comparisons in terms of the Nusselt number at $z^* = 0.66$ between the LES (circles), the RSM (Fluent, crosses) and the measurements (squares).

axial position, such that the difference is less than 1% on the mean value, which does not explain the discrepancies observed in Figure 12.34.

The measure of this heat source by viscous dissipation has also been performed in the experiments with no axial flow and for both fluids: water and air. For a water flow at a Taylor number equal to 7.9×10^7 , an increase of 0.085 K per hour has been registered. For an air flow at the same Ta , one has estimated the dissipated power being equal to 0.26 W, which would correspond to an increase in temperature of 300 K per hour. This last value is, of course, not negligible but one recalls that no axial flow is here imposed. The power injected in the fluid by viscous dissipation remains weak in all cases except for long time experiments using air as the working fluid. Nevertheless, when an axial flow is imposed, the increase in temperature is much lower. By supposing that the dissipated power due to viscosity remains the same (denoted here P_{inj}), one can also estimate the increase in temperature ΔT as a function of the axial mass flowrate q_m : $\Delta T = P_{inj}/(c_p q_m)$. Thus, for a flowrate equal to $0.01 \text{ m}^3/\text{s}$, the increase in ΔT is reduced to 79.2 K per hour.

12.5 Conclusion

In this Chapter, the turbulent flow between two concentric cylinders, where only the inner cylinder is rotating, has been considered numerically in the isothermal and non isothermal cases and the influence of the flow parameters (rotation rate, axial flowrate, geometry, working fluid) has been discussed in details. Four configurations have been studied: two using the RSM of Elena and Schiestel [85, 298] and the two others by LES. The numerical predictions have been compared either to data available in the literature or to measurements performed using a new experimental set-up recently developed at IRPHE for that occasion.

Even if the RSM has been widely validated in various rotating cavities [85, 253, 258, 298], it has been first favorably compared to the velocity measurements of Escudier and Gouldson [89] for a turbulent isothermal flow in a very elongated Taylor-Couette system with an axial flow. In particular, it improves significantly the predictions of the $k - \varepsilon$ model of Naser [217] in the same configuration. The RSM model has then been used in a Taylor-Couette-Poiseuille system defined by a radius ratio $\eta = 0.961$ and an aspect ratio $\Gamma = 77$ close to the real electric motor developed by Liebherr Aerospace Toulouse. The results showed that the flow is established quite rapidly. For axial positions larger than 20% of the cavity height, the radial profiles of the mean velocity components and also of the Reynolds stress tensor components do not depend any more on the axial position. The mean flow is helical with a turbulent Poiseuille-like profile for the mean axial velocity component and a torsional Couette-like profile for the mean tangential velocity component. Turbulence is mainly concentrated in the middle of the gap between the two cylinders and vanishes towards the walls. The thermal

field is also independent of the axial position for $z \geq 0.2h$. The dominating influence of the outer cylinder on the thermal field has been shown. Finally, new correlations have been provided for the averaged Nusselt numbers along both cylinders. On the rotor side, the Nusselt number depends on the voluminal flowrate Q to the power 0.09, on the rotation rate Ω to the power 0.82 and on the Prandtl number to the power 0.3. These coefficients are in relatively good agreement with other experimental data but large discrepancies remain with other RANS models available within StarCCM+ in the same configuration.

The calculations using the RSM were a first step towards the modeling of the real flow conditions. To go a little further, LES computations have been then compared to the velocity and temperature measurements performed on a new experimental set-up developed at IRPHE. To validate the LES approach, some comparisons have been first performed with the experimental data of Nouri and Whitelaw [226] and the LES of Chung and Sung [54] in the isothermal case and for a middle-gap cavity. The present LES improves the former one of Chung and Sung [54]. It shows, in particular, that high order spatial schemes (4th order here) are necessary to predict more accurately the turbulence intensities within the thin boundary layers. The second main result is the appearance of 3D coherent structures along both cylinders under the form of spiral rolls, which can not be captured by RANS models assuming the axisymmetry of the flow. In the framework of the "Entrefer moteur" project financially supported by Liebherr Aerospace Toulouse, a last configuration characterized by an aspect ratio $\Gamma = 50$ and a radius ratio $\eta = 8/9$ has been considered both numerically and experimentally. An axial water flow is superimposed on the base Taylor-Couette flow. The inner cylinder is rotating and heated by a constant heat flux, while the outer one is stationary and insulated. Spiral rolls have been also highlighted by LES in this configuration. Turbulence levels are remarkably high within the gap and especially in the boundary layers. A correlation for the Nusselt number measured at $z^* = 0.66$ has been established from 60000 measurements. On the rotor side, the Nusselt number depends on the voluminal flowrate Q to the power 1.08, on the rotation rate Ω to the power 0.24 and on the Prandtl number to the power 0.92, coefficients quite far from those previously found by the RSM in a slightly different configuration. A good agreement is obtained with the LES for some particular values of the rotation parameter $N \geq 4$. The hydrodynamic flow is then established in the experiments and the two approaches compare quite well in terms of the mean and turbulent velocity fields. For $N \leq 2.4$, the two methods show larger discrepancies even for the mean tangential flow. The flow is in a transient state in the experiments and all quantities are strongly dependent on the axial position, whereas the flow is assumed to be periodic in the axial direction in the LES. Nevertheless, the LES strongly improves the predictions of classical RANS models. Other calculations are now required to both cover a wider range of the flow parameters and to simulate also a non-periodic flow in the LES to get closer to the experimental conditions.

Part V

Research outlooks

Part V: Research outlooks

Summary: This final part presents some research outlooks, which will be undertaken within the next few years. The main topic is on the turbulent impinging jet flow onto a rotating disk with heat transfer (Chapter 13) used for the effective cooling of rotating machineries. This project is one part of the HYDREX action of the Labex MEC (ANR-11-LABX-0092). Other projects are briefly presented in the last Chapter 14 of this habilitation thesis and have absolutely nothing to deal with rotating disk flows: simulation of the mucus flow in the human respiratory system and its interaction with the cilia, and three projects on refrigeration technologies in the framework of an industrial chair on energy efficiency.

Impinging jet flow onto a rotating disk

Rotating flows remain an alive topic of research. Some future issues have already been evoked through the previous Chapters. One can add also the ones pointed out, in the review paper of Launder, Poncet & Serre [170]:

- the knowledge of the different scenarii for the transition to turbulence must be further extended. In particular, the role of the crossflow instability on turbulence breakdown needs to be clarified.
- efficient control strategies to delay or promote the transition to turbulence in the disk boundary layers remain to be developed.
- an urgent question to resolve is whether, in turbulent flow, the failure to reproduce numerically the permanent large-scale structures (see section 8.6) results from inadequate numerical modeling or whether the so-called failure arises from relatively small departures of the actual experiments from the idealized test-case configurations.
- numerical modeling must be improved to facilitate the exploration via LES of more complex flows addressing, in particular, higher rotation rates, appreciable density variations associated with large temperature differences, and finally actual industrial disk flow configuration geometries.

The last point will be my quest for the Holy Grail for the next few years. It falls perfectly within the framework of the HYDREX (“Extreme hydrodynamics in rotating machineries”) project (Labex “Mechanics & Complexity” MEC, 2011-2021, ANR-11-LABX-0092) coordinated by P. Le Gal (IRPHE). The goal is to consider industrial flows in real operating conditions. Two configurations will be considered:

1. the turbulent impinging jet flow over a rotating disk with heat transfer. This project will be my main one for the next few years and is discussed in the following;
2. the flow around a cluster of river current turbines (not evoked here). This work is part of the Federative Research and Development program *Urabaila* recently granted by the FUI14 in the frame of the Energy Climate program of the french government. In this large project coordinated by Bertin Technologies, the aim is to perform LES with the objective to achieve an accurate description of the physical mechanisms and thereby to provide reliable reference databases using the CFD code of the k-epsilon society, member also of the consortium.

The project on the impinging jet flow is in close collaboration with some members of the D2FT team (“Fluid dynamics and heat transfer”), Dr J. Pellé and Prof. S. Harmand, from the TEMPO laboratory in Valenciennes. They established a huge experimental database for both the heat transfer [237, 238] (by infrared thermography) and the hydrodynamic field [220] (using PIV) for a wide range of the flow parameters. This project is in the framework of the theme V entitled “Heat transfer in one- and two-phase jet flows” of the AMETH research group coordinated by Prof. Harmand. Dr. R. Da Soghe and Dr. C. Bianchini from the University of Florence are also involved in this work for their expertise in CFD using the softwares CFX and OpenFOAM. Dr A. Meslem and Pr. V. Sobolik from LaSIE in La Rochelle will perform mass transfer measurements using an innovative electrodiffusionnal method coupled to a voluminal PIV system. This project called *EASIJET* has been submitted to the 2014 call for project of the french National Research Agency (ANR blanche).

13.1 Motivation

In rotating machineries, an effective cooling system is nearly always required to remove heat due to the high rotation rates reached in very small clearances. The specific engineering application of this study is an alternator, which can be found in a wind generator (3 m radius, maximum rotational speed of 25 rpm, delivered power of 750 kW) established in the North of France (see Fig.13.1). It consists of a discoidal rotor-stator system, which does not use gears allowing the generators to operate at low rotational speeds while reducing energy losses. The main technological lock consists in solving the ineffective cooling due to high electrical losses dissipated for a relative low rotational speed. An improvement on the cooling of discoidal rotor-stator alternators could be obtained by using air jet impingement. The turbulent impinging jet is also of great importance in many other engineering problems, such as the drying of textiles and paper products, the cooling of gas turbine components and microelectronic equipments or the freezing of tissue in cryosurgery, among other things. One is particularly interested here in the optimization of the cooling process in gas turbine engine or electrical wind generator (see Fig.13.1) to increase their efficiency.

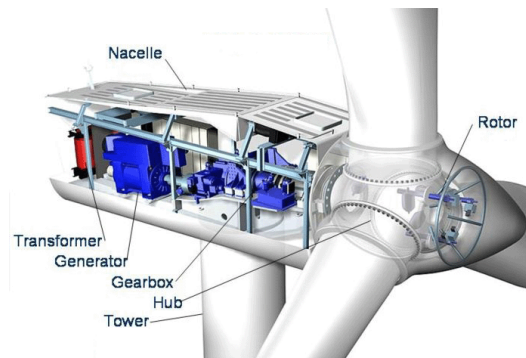


Figure 13.1: Illustration of an alternator wind generator after Diamond Industrial Ltd.

In the literature, a huge amount of heat transfer data is available but it is often restricted to the cooling of a stationary disk by jet impingement. Rotating disks have been considered more recently in the framework of the 13th ERCOFTAC/IAHR Workshop on Refined Turbulence Modeling (Graz, 2008) in open configurations. Its workshop has summarized the main works dedicated to the round jet impinging perpendicularly onto a rotating heated disk. Numerical results have been compared to the experimental data of Popiel and Boguslawski [263] and Minagawa and Obi [211] for a single rotating disk. As far as unshrouded rotor-stator systems with impinging jet are concerned, there is a lack of information available in the literature as pointed out by the recent review of Harmand *et al.* [123]. Only few groups of researchers have concentrated their efforts to investigate the problem of a jet impinging onto a rotating disk with confinement effects. Sara *et al.* [291] have experimentally investigated the mass transfer between an impinging jet and a rotating disk in a confined system by naphthalene sublimation. These authors concluded that the mass/heat transfers increase by increasing both rotation and impinging flowrate even if for their low rotational Reynolds numbers, the jet is dominant. One can cite also Minagawa and Obi [211], who have been interested in the turbulence development in this configuration. In fact, in all available studies about convective heat transfer in configuration where effects of a rotating disk and jet impingement are coupled, authors [50, 263] have distinguished three regions (Fig.13.2):

- Region 1: the area of the disk where the jet influence on the heat transfer is the greatest near the impingement point;
- Region 2: a mixed region between regions 1 and 3;
- Region 3: the area where rotation has the greatest effect far from the impingement point at high radii.

Chen *et al.* [50] have also concluded that the location of those three zones depends on the ratio between the jet and the rotation mass flowrates. They have also noted that the heat transfer on the rotating

disk is modified by the jet for rotational Reynolds numbers lower than 2×10^5 . For greater values of Re , the jet does not affect so much the local heat transfer distribution.

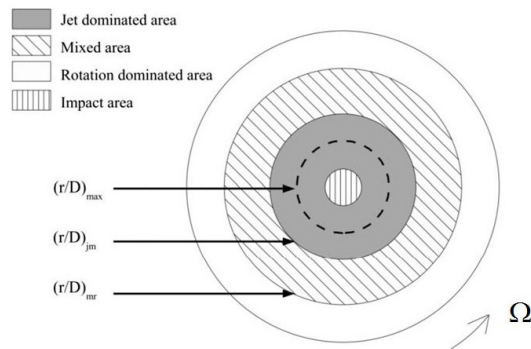


Figure 13.2: Three characteristic flow regions after Pellé and Harmand [238] for a rotor-stator flow with impinging jet and heat transfer.

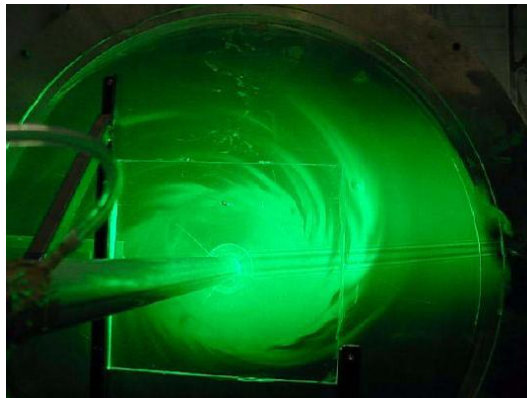


Figure 13.3: Flow structure due to the interaction of the impinging jet with the base rotor-stator flow, after Owen (unpublished).

Numerical simulations are complex due to the superimposition of complex elementary phenomena (impinging jet, high rotation rates, confinement effects, unshrouded cavity ...). The effect of an unshrouded cavity on the hydrodynamic field is that the flow pumped from the rotor leaves the cavity to the external surroundings and ingress may then occur to supply the entrainment demands of the rotating flow. At the periphery of the cavity, there can therefore be both inflow along the stator and outflow on the rotor, which is very challenging for numerical methods for the choice of appropriate outlet boundary conditions.

13.2 Experimental facility developed at the TEMPO laboratory

The experimental set-up (Fig.13.4) is the same than previously detailed in [237, 238]. The rotor has a $b = 310$ mm radius and its rotational velocity could be changed with a frequency variator. Rotor is made with aluminum, chosen for its high thermal conductivity and its low density. A $p = 2.5$ mm layer of zircon whose thermal conductivity is $\lambda_{zir} = 0.7$ W/mK was deposited on the cooled side of the rotor by plasma projection. Four infrared emitters are placed on the bottom of the disk in order to heat it until cooled surface reached about 80°C . A stationary disk faces the rotor at a distance $h = 6.2$ mm for which the dimensionless spacing interval is $G = h/b = 0.02$. It guarantees that the stator clearly affects the fluid flow within the cavity, as G remains far below the limiting value $G = 0.0752$ for the maximum Reynolds number considered here [51, 233]. The stationary disk has the

same diameter as the rotating disk and a central opening ($D = 26$ mm) was pierced at the stator to allow passage of a long pipe linked to a centrifugal blower, which is used to impose an axial flow. The jet aspect ratio is then $h/D = 0.25$. The jet mass flowrate is controlled by pressure loss measurements, which were previously correlated to the mass flow rate, and adjusted by creating a pressure loss at the blower suction.

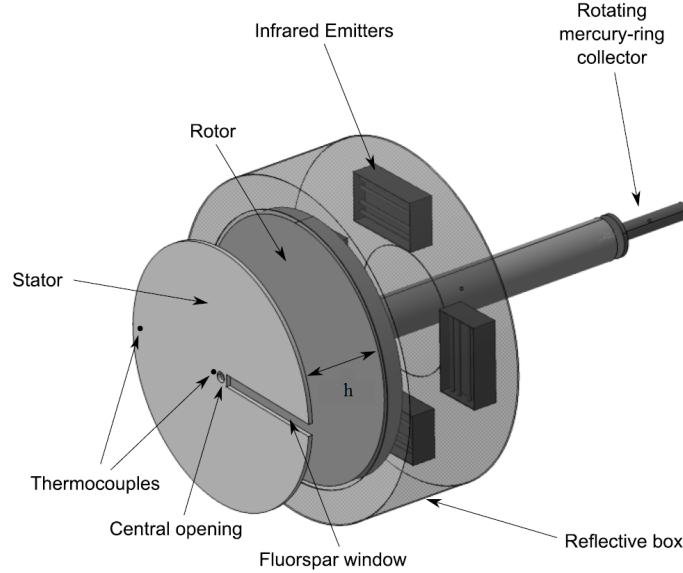


Figure 13.4: Experimental set-up for the impinging jet flow developed at the TEMPO laboratory.

Apart from the two geometrical parameters h/D and G , the base flow depends also on the jet and rotational Reynolds numbers defined respectively by:

$$Re_j = \frac{VD}{\nu} \quad Re = \frac{\Omega b^2}{\nu} \quad (13.1)$$

with ν the fluid kinematic viscosity and V the jet axial flow velocity imposed at the inlet. For numerical investigations, it is also convenient to use a nondimensional flowrate $C_w = \frac{Q}{\nu b}$ (Q the voluminal flowrate) instead of Re_j and which can be combined with Re to form the turbulent flow parameter λ_t . To enable direct comparisons between the axial flow due to the impinging jet and the tangential flow due to the rotation of the disk, one can define also the rotation parameter N :

$$\lambda_t = C_w Re^{-0.8} \quad N = \frac{\Omega b}{V} \quad (13.2)$$

All the values considered for these parameters are summed up in Table 13.1.

Fluid velocity is measured by PIV, whose system is fully described in Nguyen *et al.* [220]. It consists of a double-pulsed Nd:YAG laser, a CCD camera mounted with a Nikkor lens of 105 mm and $f/5.6$ aperture and a synchronizer. The laser sheet thickness is about 1 mm created by a cylindrical and a spherical lens. An olive oil droplet generator (TSI 9307) generates particles with a mean diameter of $1 \mu\text{m}$ to seed the inlet of the centrifugal blower. PIV images are captured by the TSI PowerView Plus 4 MP camera with a resolution of 2048×2048 pixels and a pixel size of $7.4 \times 7.4 \mu\text{m}^2$. The time interval between the first and second exposures is chosen to yield maximum particle displacements of 6 pixels. PIV measurements are performed at three (r, θ) planes and for each axial plane, images are separately captured at three different regions. For the values of Re and Re_j considered here, 500 image pairs are recorded for each run at a sampling rate of 1 Hz to ensure that the velocity fields obtained from the image pairs are statistically independent. Image acquisition and processing are performed with TSI Insight TM 3G software. The PIV images are analysed by a recursive Nyquist rectangular grid algorithm with two iterations and 50% window overlap. The first and second-pass interrogation windows are square interrogation spots of 64×64 pixels and 32×32 pixels, respectively. The final

Test case	Ωb (m/s)	Re ($\times 10^{-5}$)	V (m/s)	Re_j ($\times 10^{-3}$)	C_w	λ_t	N
1	1.623	0.33	10	17.2	1133	0.275	0.162
2	1.623	0.33	15	25.8	1700	0.413	0.108
3	1.623	0.33	25	43	2833	0.688	0.065
4	12.985	2.66	10	17.2	1133	0.052	1.299
5	12.985	2.66	15	25.8	1700	0.078	0.866
6	12.985	2.66	25	43	2833	0.13	0.519
7	25.971	5.32	10	17.2	1133	0.03	2.597
8	25.971	5.32	15	25.8	1700	0.045	1.731
9	25.971	5.32	25	43	2833	0.074	1.039

Table 13.1: Values of the flow parameters for the impinging jet flow over a rotating disk.

number of velocity vectors was 110×110 vectors. In the velocity computation, 2D displacement fields are computed from the correlation map with a Gaussian peak fit [158] for sub-pixel accuracy and are validated by a signal-to-noise ratio of 1.5. Statistical validation tools using a median filter [355] and a standard deviation filter are performed between the iterations to remove erroneous vectors, and then fill in the blanks by interpolation. The uncertainty in the PIV measurements, calculated using the error analysis developed by Coleman and Steele [57], are estimated to be less than 9% of the mean jet velocity near the rotation axis and typically less than 6% at the periphery.

The wall heat flux on the rotor surface can be obtained by solving the heat equation in the zircon layer using a finite-difference method. The boundary conditions applied are the surface temperatures recorded by an infrared camera (watching the rotor through a fluorspar window placed inside the stator) and the interface (aluminum/zircon) temperatures recorded by thermocouples. The convective heat flux can be then deduced by solving a thermal balance equation for each point on the disk surface and the local heat transfer coefficient is then obtained. The best choice of the reference temperature for the Nusselt number calculation in such a discoidal system [233] is the adiabatic wall temperature T_{ad} , which can be either measured or calculated by: $T_{ad} = T_{\infty} + \frac{Pr^{1/3}(\omega r)^2}{2C_p}$, where T_{∞} is the ambient temperature of the test room. An estimation of the maximum reached by $\frac{Pr^{1/3}(\omega r)^2}{2C_p}$ (C_p the mass thermal capacity) shows that the temperature increase due to friction effects is under $0.3K$. So it is assumed that friction effects are negligible for our operating conditions and T_{∞} can be taken as the reference temperature. An AGEMA 900 infrared camera is situated one meter above the rotor and records the rotor surface temperatures with a frequency of 35 Hz. Two T-type thermocouples, located at two different radii $r = 0$ and $r = 0.3$ m, are used to measure temperatures at the bottom of the disk at the aluminium/zircon interface. Measurements are realized using a Graphtec GL 200 acquisition system whose uncertainty on the temperature is ± 0.5 K for T-type thermocouples. The thickness of the aluminium layer is such that the temperature at the zircon/aluminum interface is homogeneous for our operating conditions. Thermocouples give a difference temperature less than $1K$. The reference air temperature T_{∞} is measured by a K-type thermocouple placed outside the test-rig, far enough from the heating system but near from the backside of the stator, in order to measure the temperature of the air which will enter in the air-gap. That temperature is assumed constant during a test, due to the placement of the experimental apparatus in a very large room. The absolute error for the air temperature is estimated at ± 1 K. Two special T-type thermocouples located at the bottom of the stator to put them in constant contact with the stator surface inside the air-gap are directly linked to the acquisition system. They are placed at radii of 0.05 m and 0.3 m. As for the measurements at the zircon/aluminium interface, the absolute error for the stator temperature T_{stator} is ± 0.5 K according to the data acquisition system's specifications. Due to the high conductivity material which is used for the stator, temperature difference between the thermocouples is under 1 K. The reader can refer to the previous paper of Pellé and Harmand [237, 238] for more details about the temperature measurement set-up. Taking into account all uncertainties, Pellé and Harmand [239] showed that the Nusselt numbers can be determined with an uncertainty under 30%.

13.3 Preliminary results

Preliminary results have been obtained using the RSM model described in Chapter 4 and compared to the experimental data of Nguyen *et al.* [220] and to the predictions of a $k-\omega$ SST model available within the CFX solver performed by R. Da Soghe and C. Bianchini from the University of Florence. The results have been published recently in *Int. J. Heat Fluid Flow* (see Ref.[257]). For both models, a 200×80 mesh grid in the (r, z) frame is sufficient to get grid independent solutions with 20 elements in the tangential direction for the $k-\omega$ SST model.

13.3.1 Hydrodynamic fields

Figures 13.5a,b present the mean streamline patterns obtained by the RSM and $k-\omega$ SST models in a meridian (r, z) plane for $G = 0.02$, $h/D = 0.25$ and test case 5. The air jet squirts from the center of the stator and impinges the rotor. After the impingement, the fluid is deflected and flows radially along the rotor. This radial outflow, which is enhanced due to the combination of the jet flow and centrifugal effects, is confined by a large recirculation zone appearing along the stationary disk. Poncet [249] showed that the size of this recirculation bubble depends mainly on the aspect ratio G of the cavity, which could explain why it is almost constant in the present study. Whatever the flow parameters, this jet-dominated area (Region 1) observed close to the rotation axis extends to a dimensionless radius $r/b \simeq 0.14$. For larger radii, the flow is purely centrifugal with streamlines parallel to the disks. In that case, this flow structure is sometimes called a Stewartson flow structure by abuse of language. Its denomination is used to mention that looking at the tangential velocity profile, there is only one boundary layer on the rotating disk. For some particular test cases (4, 5, 7, 8, 9), a recirculation zone is observed on the stator side. Qualitatively, the same results are obtained by the $k-\omega$ SST model. Nevertheless, one can notice that the recirculation along the stator at low radii after the jet impingement is much larger than the one observed by the RSM. Its size is besides not so sensitive to the value of the jet Reynolds number Re_j . Similar deficiencies have already pointed out by Da Soghe *et al.* [66]. Secondly, some backflow was observed along the stator by the RSM for a given set of parameters. For such cases, there may be some convective transport of turbulence close to the rotation axis as reported by Cheah *et al.* [49] in an enclosed rotor-stator system.

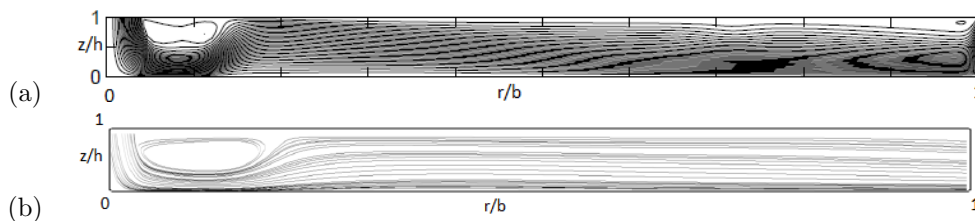


Figure 13.5: Streamline patterns obtained for $G = 0.02$, $h/D = 0.25$ and test case 5 by: (a) the RSM; (b) the $k-\omega$ SST model.

One interesting mean quantity for engineers is the radial distribution of the core-swirl ratio β known also in the literature as the entrainment coefficient K . It is defined as the ratio of the time-averaged tangential velocity at mid-gap ($z/h = 0.5$) and the local tangential velocity of the rotor Ωr at the same radius. For flows with unmerged boundary layers, referred as Batchelor flows in the literature, β can be indeed directly linked to the radial pressure gradient within the cavity and thus to the axial thrusts applied on the rotor [251], which can be useful in real turbines. Figure 13.6 shows the distribution of the core-swirl ratio β along the dimensionless radius for the 9 test cases. The experimental results and those obtained by the RSM and $k-\omega$ SST models are compared to the analytical law of Daily *et al.* [68] and to the ones obtained by Poncet *et al.* [251, 253] for Batchelor and Stewartson flows.

In test cases 1 – 3, the RSM model predicts Stewartson flows with a core-swirl ratio close to zero even if a small increase can be noticed towards the periphery of the cavity. It is in good agreement with the two analytical laws dedicated to this flow regime. The mean flow is thus clearly dominated by the impinging jet ($0.065 \leq N \leq 0.162$) and rotation effects remain weak. For these test cases and in certain flow regions, measured velocities are of the same order than the measurement uncertainty

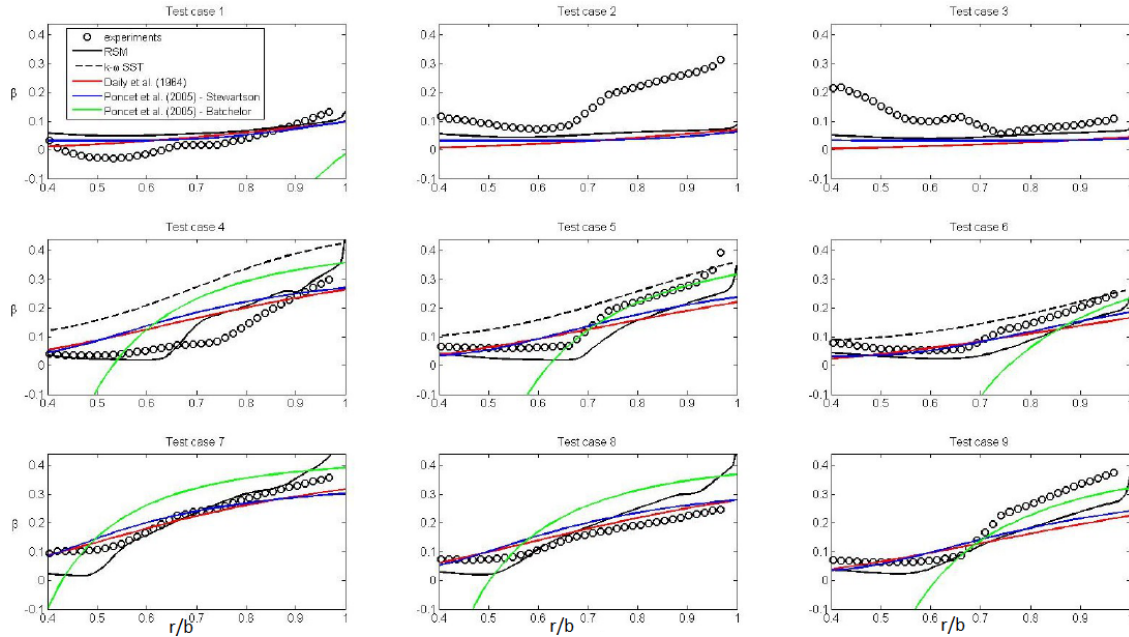


Figure 13.6: Radial variations of the core-swirl ratio β obtained by the RSM for $G = 0.02$ and $h/D = 0.25$ and the 9 test cases. Comparisons with the analytical laws of Daily *et al.* [68] and Poncet *et al.* [251, 253], the experimental data and the predictions of the $k-\omega$ SST model.

and are very fluctuating when non-dimensionalized so the analysis is biased. The relative high values reached by β for test case 2 and $r/b > 0.7$ may be attributed to peripheral effects and some possible ingress of fluid. By increasing the rotation rate (and so N and Re), the core-swirl ratio increases as expected. For test cases 4 to 6, one can observe from the radial distributions of β the transition from the Stewartson flow structure obtained for $r < r_c$, where the predominant effect is due to the impinging jet, to a Batchelor flow structure at $r > r_c$ where rotation effects become not negligible. For example, for test case 5, it is found that $r_c = 0.66b$ from the PIV measurements, which is in good agreement with [251]. A quite good agreement between the experiments and the numerics is here obtained with the same radial evolution of β . It was indeed expected that the RSM performs better for higher rotational Reynolds numbers Re . At low Re , such that for test cases 1-3, the RSM may have the tendency to relaminarize the flow and predicts laminar flows, which are known to exhibit smaller values of the core-swirl coefficient than in the turbulent regime (see for example in [233, 249]). On the contrary, the $k-\omega$ SST overpredicts the core-swirl ratio especially for test case 4 and for low radii in the two other cases. If one increases further Re up to 5.32×10^5 (Test cases 7-9), the flow structure switches to a Batchelor flow at lower radii than in the previous cases, at around $r_c \simeq 0.5b$ in test case 7 for example. This critical radius for the transition from the Stewartson to the Batchelor flow regime increases when one increases the jet Reynolds number Re_j to reach $r_c \simeq 0.65b$ in test case 9. The experimental data appear to be in particular good agreement with the values predicted by the analytical laws of Daily *et al.* [68] and Poncet *et al.* [253].

Figure 13.7 shows the mean radial velocity distributions, normalized by the jet velocity V , along the dimensionless radius r/b for test case 5 ($N = 0.866$, see Table 13.1) at three axial positions. One position is located close to the rotor ($z/h = 0.23$), one is around mid-gap ($z/h = 0.53$) and one is near the stator ($z/h = 0.84$). The present results are compared to the LDA measurements of Mingawa and Obi [211] and the numerical results of Manceau *et al.* [197] obtained by an EB-RSM model in the case of a jet impinging onto a rotating disk. Whatever the axial position, the present measurements provide negative radial velocities for $r/b \leq 0.16$ ($r/D \leq 2$), meaning that the flow is mainly centripetal. It was thought that the flow should be centrifugal due to the presence of the jet, so it is identified as a recirculation area. Its thickness is very large because negative radial velocities are observed near the stator but also near the rotor. It must involve very high radial velocities in the rotor boundary layer. At larger radii ($r/b \geq 0.16$ or $r/D \geq 2$), radial velocities increase and reach a maximum at around $r/b \simeq 0.26$ ($r/D \approx 3$) before a slow decrease until the air gap outlet. As expected, the radial velocities

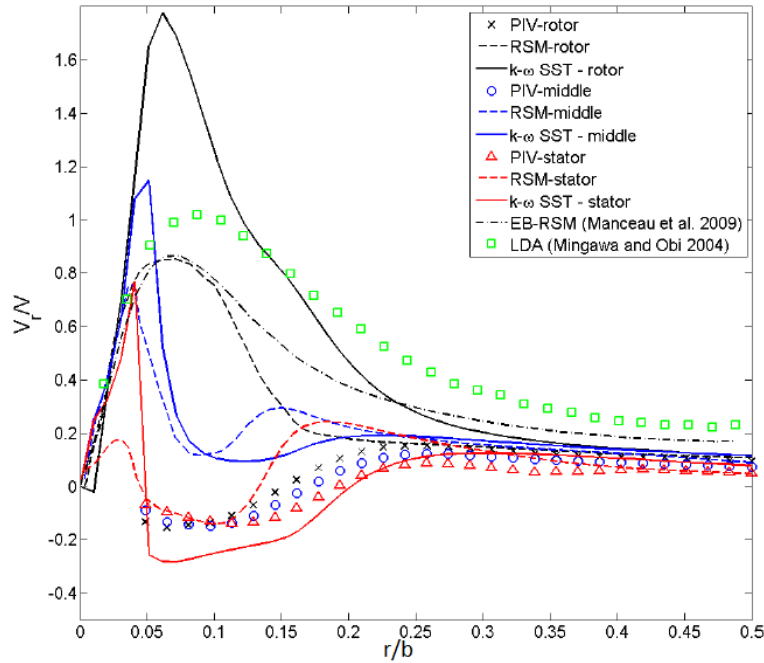


Figure 13.7: Radial variation of the averaged mean radial velocity V_r/V for $G = 0.02$, $h/D = 0.25$ and test case 5 at three axial positions: one near the rotor ($z/h = 0.23$), at mid-gap ($z/h = 0.53$) and one close to the stator ($z/h = 0.84$). Comparisons between the experiments (symbols), the RSM (dashed lines), the $k - \omega$ SST (solid lines), the LDA measurements of Mingawa and Obi [211] (green squares) and the EB-RSM model of Manceau *et al.* [197] (dash-dotted line).

near the rotor are higher than near the stator.

A good agreement is obtained between the PIV measurements and the RANS results at large radii $r/b \geq 0.25$, where V_r remains quite weak. On the other hand, large differences can be observed in the jet dominated area. These discrepancies may be explained as following. After impinging on the rotor, the jet deflects in radial direction. A radial wall jet begins to form and creates a thin wall boundary layer. Hadžiabdić and Hanjalić [120] showed the existence of vortical structures formed at the wall-jet edge and counter-rotating secondary vortices created near the impinging plane (rotor plane in our case). The secondary vortices rolled up between the impinging plane and the vortical structures at the wall-jet edge. Footprints of these structures were displayed in the POD analysis of Nguyen *et al.* [220]. However, in the PIV measurements, the laser thickness was 1 mm, which is not small enough compared to the boundary layer thickness and the small gap between the rotor and the stator. Velocity measurements on the laser planes could be the volume-averaged values of particle displacements that displaying the entrainment of the vortical structures around the stagnation point in the radial direction. An investigation of the flow structures near the impinging jet in the (r, z) plane using stereo PIV is arranged for a further study and validation of the numerical simulation.

The RSM profiles very close to the impinging zone ($r/b \leq 0.05$, on the rotor side) are thus in better agreement with the previous results of [197, 211] obtained without the stator. The RSM predicts the centripetal flow along the stator but the size of this recirculation is much weaker than the measured one. When one approaches the rotating disk, the values of the mean radial velocity increase to reach the peak value obtained previously by the EB-RSM model of Manceau *et al.* [197] at $r/b \simeq 0.075$ ($r/D \simeq 0.9$). It is noticeable that almost the same distributions (not shown here) have been obtained for the other sets of parameters. The $k - \omega$ SST predicts rather the same profiles as the ones obtained by the RSM. The radial velocity is positive at low radii after the jet impingement with peak values much higher than those obtained by the RSM. Then, V_r tends to zero along the rotor, also around $r/b \simeq 0.25$. The discrepancies may be explained by the larger recirculation areas previously evoked in Figure 13.5. It is noticeable that it reproduces quite well the radial velocity profile on the stator side.

Those observations about radial and tangential mean velocity components are concordant with those by Poncet *et al.* [251]. The flow is at very low radii, near the jet impingement, mainly centrifugal.

Thus, when increasing radius, radial velocities tend to decrease and rotation effects become dominant inside the air-gap. If the jet Reynolds number is too low compared to the rotational Reynolds number, a centripetal flow can occur near the stator at outer radii and the flow tends to become a Batchelor type flow. Nevertheless, in this case, the rotating core rotates at a lower speed than in the rotor-stator configuration without superposed flow ($\beta = 0.438$), as expected in unshrouded system [38].

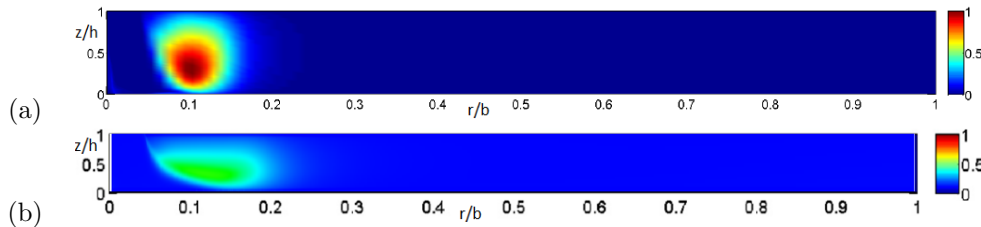


Figure 13.8: Maps of the normalized turbulence kinetic energy k^* obtained for $G = 0.02$, $h/D = 0.25$ and test case 6 by: (a) the RSM; (b) the $k-\omega$ SST model.

Figure 13.8 presents some maps of the turbulence kinetic energy k^* (normalized by its maximum) in a meridional plane for test case 6 obtained by the RSM and the $k-\omega$ SST models. Both models exhibit the same behavior. Turbulence is mainly produced by the impinging jet at low radii, where the lowest values of the local Reynolds number Re_r are observed. Rotation has then only a weak effect on the turbulence production. Not surprisingly, turbulence kinetic energy increases for increasing values of Re_j (not shown here). The cavity being opened to atmosphere, the fluid at the periphery does not flow inwards along the stationary disk and then, there is no convective transport of turbulence close to the rotation axis as reported by Cheah *et al.* [49] in an enclosed rotor-stator system.

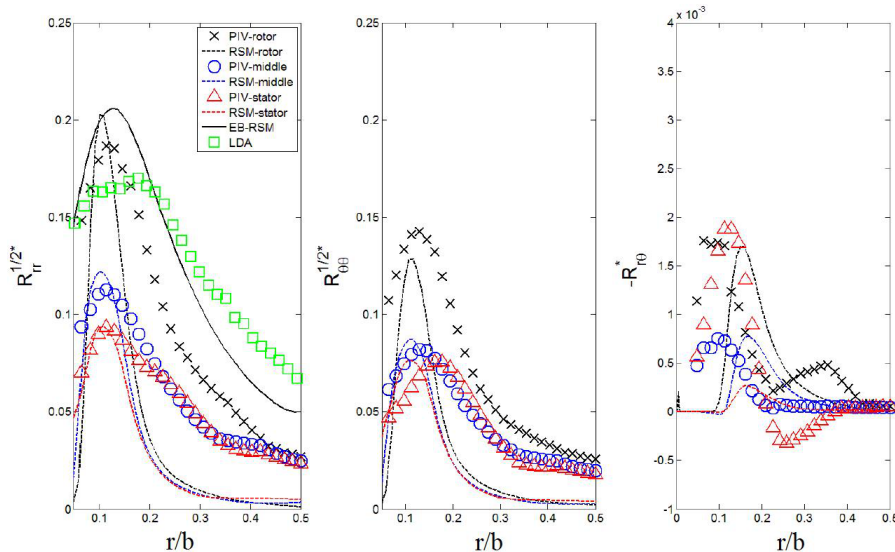


Figure 13.9: Radial variation of three components of the Reynolds stress tensor for test case 5 ($Re = 2.66 \times 10^5$, $C_w = 1700$), $G = 0.02$ and $h/D = 0.25$ and at three axial positions: one near the rotor ($z/h = 0.23$), at mid-gap ($z/h = 0.53$) and one close to the stator ($z/h = 0.84$). Comparisons between the experiments (symbols), the RSM (dashed lines), the $k-\omega$ SST model (solid lines), the LDA measurements of Mingawa and Obi [211] (green squares) and the EB-RSM model of Manceau *et al.* [197] (dash-dotted line). Note that the Reynolds stress tensor components are here normalized as follows: $R_{rr}^* = v_r'^2/V^2$, $R_{\theta\theta}^* = v_\theta'^2/V^2$ and $R_{r\theta}^* = v_r v_\theta/V^2$.

To have a more precise view of the turbulent intensities for test case 5, the radial distributions of the three Reynolds stress tensor components available in the experiments are plotted in Figure 13.9 at three axial positions and compared to the LDA measurements of Mingawa and Obi [211] and the numerical results of Manceau *et al.* [197] obtained by an EB-RSM model in the case of a jet impinging

onto a rotating disk. The two normal components increase up to a peak value reached at around $r/b \simeq 0.12$ ($r/D \simeq 1.4$). Then, they decrease towards the periphery of the cavity. The peak values are particularly well predicted by the RSM. On the other hand, the RSM seems to relaminarize the flow more rapidly than expected in the experiments. Compared to the former results [197, 211], the stator does not affect so much the behavior of the radial normal Reynolds stress tensor component. The cross component has a more singular behavior: after reaching a maximum around $r/b \simeq 0.15$, it decreases with the radius but can become negative close to the stator, which is not predicted here by the RSM. It is important to note that, for the three Reynolds stress tensor components considered here, turbulent intensities are more important on the rotor side and at given radius, decrease when one approaches the stationary disk. The same tendencies have been obtained for the other test cases (not shown here), Re and Re_j having only a slight effect on the distributions of the turbulent intensities. Comparing the two RANS modelings, the tendencies are rather the same with higher turbulence intensities close to the jet and peak values observed along the rotor. Nevertheless, the $k-\omega$ SST strongly overpredicts the turbulence intensities in the jet impingement zone.

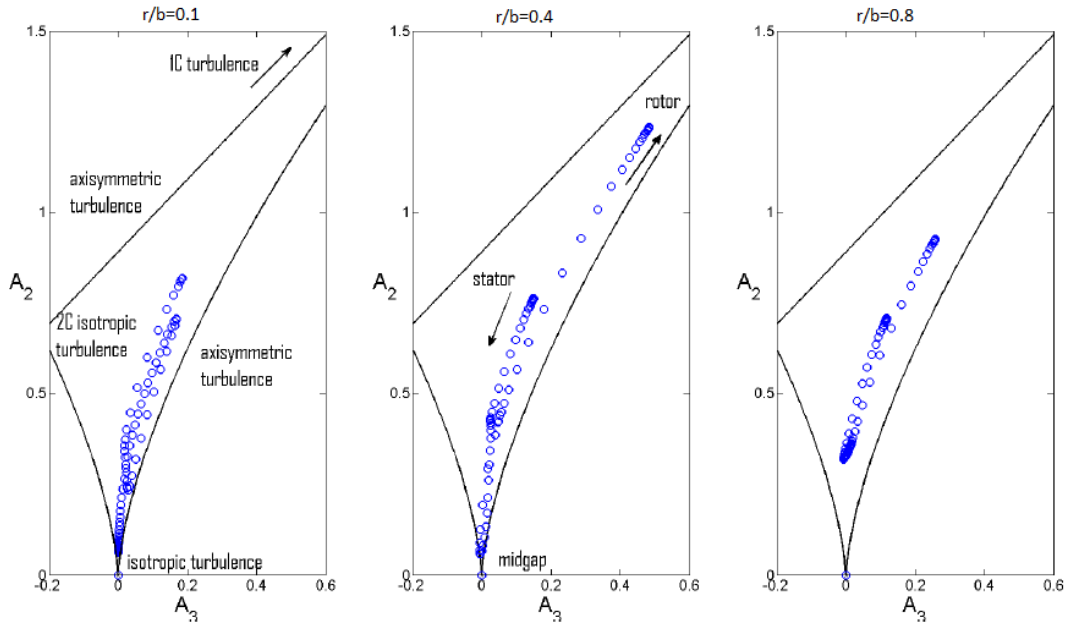


Figure 13.10: Anisotropy invariant maps obtained by the RSM for $G = 0.02$, $h/D = 0.25$ and test case 5 at three characteristic radial positions: (a) $r/b = 0.1$, (b) $r/b = 0.4$ and (c) $r/b = 0.8$.

Figure 13.10 shows the anisotropy invariant map for the Reynolds stress tensor at three radial positions for test case 5. At $r/b = 0.1$ (Fig.13.10a), the flow is dominated by the impinging jet and exhibits a Stewartson flow structure. In that flow region, turbulence exhibits a three-component behavior. At mid-gap, it tends to the isotropic limit ($A_2 = A_3 = 0$). It confirms the previous results of Haddadi and Poncet [119] for torsional Couette flows in a shrouded rotor-stator cavity. At $r/b = 0.8$ (Fig.13.10c), where the flow has switched to the Batchelor flow structure ($\beta > 0.1$) and is mainly dominated by rotation, turbulence remains at three components. At $r/b = 0.4$ (Fig.13.10b), both effects, rotation and jet impingement, live together. In that case, turbulence is isotropic at mid-gap and tends to the one-component limit (high values of A_2 and A_3) close to the rotor. Similar behaviors are observed whatever the test case, which means that the flow anisotropy depends only weakly on the rotational and jet Reynolds numbers in this range of parameters. Note that the structural anisotropy is axisymmetric whatever the flow conditions, which is inherent to the choice of the dimensionality tensor in the RSM model [249].

13.3.2 Thermal field

Some calculations have been performed for an air ($Pr = 0.7$) flow entering the cavity at the same temperature as the one imposed on the stator surface: $T_\infty = T_{stator} = 20^\circ C$. The temperature

of the rotor is fixed to $T_{rotor} = 80^\circ C$. At the periphery of the cavity, if ingress occurs, the fluid reenters the cavity at T_∞ . Results are discussed in terms of the local Nusselt number defined as: $Nu = \frac{DJ_w}{\rho C_p \alpha (T_{rotor} - T_\infty)}$, where D is the jet diameter, ρ the density of air and C_p its specific heat capacity. J_w is the wall heat flux given by: $J_w = -\rho C_p \alpha \frac{\partial T}{\partial z}|_w$, where the index w denotes a value evaluated at the wall. Figure 13.11 shows the local Nusselt number along the dimensionless radius r/b for 3 rotational Reynolds numbers and 2 jet Reynolds numbers. In all cases, Nu is a decreasing function with r/b , the highest values being observed near the jet. Experimental data for $r/b < 0.1$ are not available due to the fact that the pipe which brings the jet does not allow an optical access to this area.

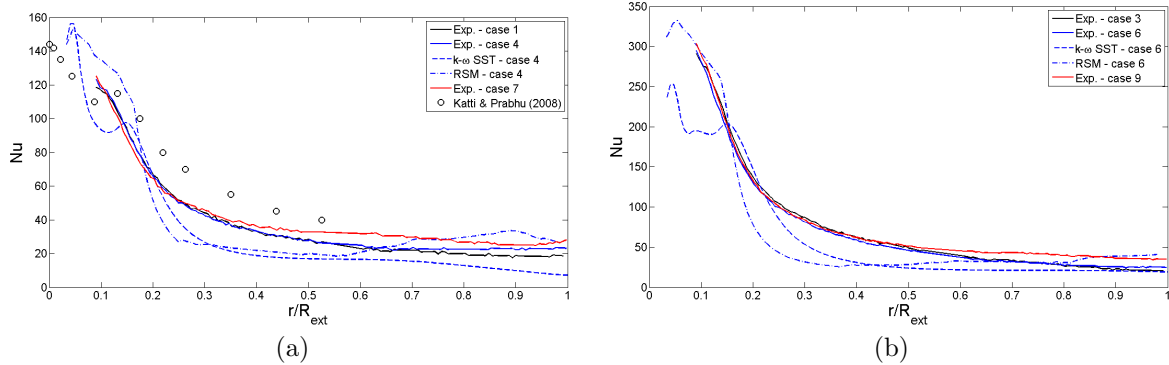


Figure 13.11: Radial profiles of the local Nusselt number for $G = 0.02$, $h/D = 0.25$: (a) $Re_j = 16000$, (b) $Re_j = 42000$. Comparisons between the experiments (solid lines), the RSM (dash-dotted lines), the k- ω SST model (dashed lines) and the experimental data of Katti and Prabhu [148] (circles).

For a fixed jet Reynolds number Re_j , considering Figures 13.11a and b, the 3 profiles relative to the 3 rotational Reynolds numbers show that the local Nusselt number does not depend on Re for $r/b \leq (r/b)_0$. $(r/b)_0$ is equal to around 0.34 for $Re_j = 1.6 \times 10^4$ and 0.5 for $Re_j = 4.2 \times 10^4$. In this region, it is assumed that the convective heat transfer are the same as if there was no rotation. By comparing the two figures, it can be seen also that the local Nusselt number increases with the jet Reynolds number. Thus, when $r/b \leq (r/b)_0$ and for all tested Re and Re_j values, radial velocities are very high in a very thin rotor boundary layer because the flow is centripetal everywhere outside. In this area, the flow is not rotating so the rotational Reynolds number Re is not an influent parameter. Those high centrifugal velocities involve strong shear stresses and so high heat transfer. As the size of this area is the same for all Re_j , increasing the jet velocity results in an increase in the convective heat transfer.

After that, one can detect another critical radius $(r/b)_1$ where the curves relative to $Re = 3 \times 10^4$ and $Re = 2.58 \times 10^5$ separate. It occurs at $(r/b)_1 = 0.67$ for $Re_j = 1.6 \times 10^4$ and at $(r/b)_1 = 0.77$ for $Re_j = 4.2 \times 10^4$. The influence of rotation on the convective heat transfer appears after a critical radius which is lower when increasing Re and higher when increasing Re_j . The decrease of the local Nusselt number when r/b is increasing is due to the thickening of the rotor boundary layer associated with lower radial and higher tangential velocities. After $(r/b)_1$, the local Nusselt number continues to decrease but more slowly than near the center of the rotor. One can observe that it remains quite constant in the case where $Re_j = 1.6 \times 10^4$ and $Re = 2.58 \times 10^5$. Local Nusselt numbers, which are reached at outer radii are higher for higher rotational speed.

On Figure 13.11a, results from Katti and Prabhu [148] are also reported. They have been established for $Re_j = 16000$, $h/D = 0.5$ and without rotation nor confinement. They are available for $r/b \leq 0.5$ where one proved before that the rotation has no high effect. The present results are concordant with those of Katti and Prabhu [148] with slightly lower values. This difference may be attributed to confinement effects as already demonstrated by Gao and Ewing [103].

The local Nusselt number also increases with the jet Reynolds number, which can be seen by comparing Figures 13.11a and b. However, at the same value of Re , the difference between both Re_j is large near the impingement point and decreases as the radius increases, meaning that the influence of the jet Reynolds number seems to disappear at the periphery of the cavity (large r/b).

The RSM and k- ω SST models provide very satisfactory results for test cases 4 and 6 in terms of

the distribution of the local Nusselt number. Whatever the jet Reynolds number, similar behaviors are observed: Nu decreases more rapidly with the local radius in the computations before being rather constant at large radii where rotation effects dominate. The RSM seems to offer the best results, especially for the peak value in case 6, where the $k-\omega$ SST slightly underestimates the heat transfer coefficient.

For engineering applications, it can be also useful to consider the averaged Nusselt number Nu_{av}^D based on the jet diameter D . Experimental results are typically correlated under the form [368]:

$$Nu_{av} = aRe_j^n Pr^l f(e/D) \quad (13.3)$$

where $f(e/D)$ is an empirically determined function and a , n and l are constants determined by experiments. Additional dimensionless parameters may be added to the correlation to account for other effects (angle of incidence, surface curvature, pressure loss ...). When rotation effects are superimposed on the jet flow problem, one can also suppose that Nu_{av} depends also on the rotational Reynolds number Re to a power m . For turbulent rotor-stator flows without jet, it is quite classical to obtain $m = 0.8$ [233].

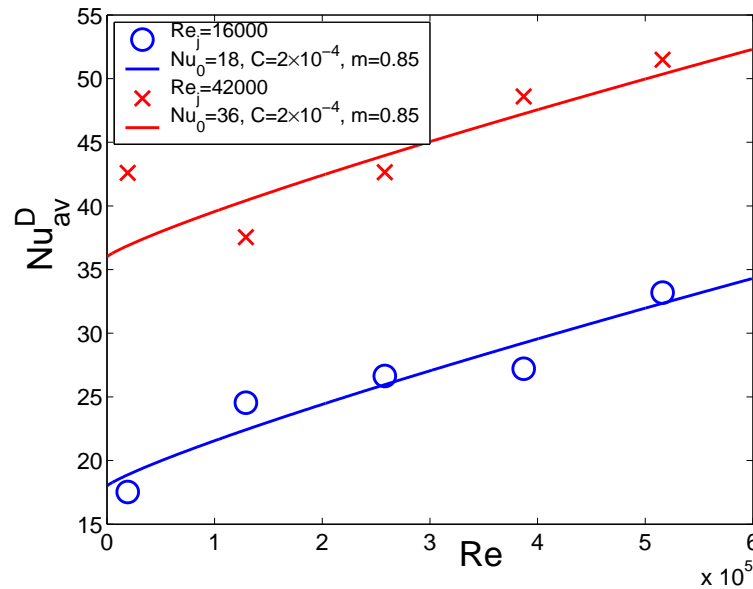


Figure 13.12: Variations of the averaged Nusselt number Nu_{av}^D (based on the jet diameter D) along the rotor against the rotational Reynolds number for $G = 0.02$, $h/D = 0.25$ and two values of the jet Reynolds number $Re_j = 16000$ and $Re_j = 42000$. Comparison between the experimental data (symbols) and correlation laws (lines).

Figure 13.12 presents the dependence of Nu_{av}^D on Re for two values of the jet Reynolds number Re_j . The averaged Nusselt number is so an increasing function with Re and Re_j , which is concordant with the observations by Sara *et al.* [291] obtained for lower Re and larger jet aspect ratios. The present experiments can be correlated under the form:

$$Nu_{av} = Nu_0 + C \times Re^m \quad (13.4)$$

where $C = 2 \times 10^{-4}$ and Nu_0 is the averaged Nusselt number obtained without rotation. This value can be deduced from the experiments performed by Sagot *et al.* [282] in the case of a round jet impinging a circular flat stationary plate at constant temperature. They provided the following correlation valid for $10^4 < Re_j < 3 \times 10^4$, $2 < h/D < 6$ and $3 < b/D < 10$:

$$Nu_{av} = 0.0622Re_j^{0.8} \left(1 - 0.168 \frac{b}{D} + 0.008 \left(\frac{b}{D} \right)^2 \right) \left(\frac{h}{D} \right)^{-0.037} \quad (13.5)$$

From the present measurements, Nu_0 is equal to 18 and 36 for $Re_j = 1.6 \times 10^4$ and 4.2×10^4 respectively to be compared with the values 20.3 and 44 deduced from Equation (13.5). The weak

discrepancies may be attributed to the very small value of $h/D = 0.24$ (not in the validity domain $2 < h/D < 6$) and due to the difference of boundary conditions applied on the rotor (wall heat flux against imposed wall temperature). The exponent $m = 0.85$ highlighting the dependance of Nu_{av} on the rotational Reynolds number is in good agreement with the common value $m = 0.8$ found in many rotating disk systems [233]. It is more adventurous to get the coefficient n as only two values of the jet Reynolds number Re_j are considered here. Nevertheless, one can propose $n = 0.72$, which falls between the values obtained by Wen and Jang [353] ($n = 0.696$) or Tawfek [335] ($n = 0.691$) for a round jet impinging a flat surface and the value ($n = 0.8$) from Equation (13.5). It is noteworthy that Nu_{av}^D does not scale neither with the turbulent flow parameter λ_t nor with the rotation parameter N .

Test case	Experiments	RSM	k- ω SST
4	26.64	29.79	18.5
6	42.65	40.54	32.8

Table 13.2: Comparisons for the averaged Nusselt number over the rotating disk subjected to an impinging jet for test cases 4 and 6.

The averaged Nusselt numbers have also been computed by the RSM and k- ω SST models for test cases 4 and 6. As it can be seen in Table 13.2, the RSM results are in excellent agreement with the values obtained experimentally, whereas the k- ω SST slightly underpredicts the averaged Nusselt number in both cases. Calculations have also been performed with a modified version of the k- ω SST model including a curvature correction term. The model correction results in a multiplicative factor of the transport equation production term, expressed as a complex function of the stress and vorticity tensors. This version does not improve the predictions of the former model in terms of velocity and thermal fields.

13.4 Future works

As shown previously, the RSM of Elena & Schiestel [85] provided very satisfactory overall results for the hydrodynamic and thermal fields if one compares it to the predictions of a classical k- ω SST model. But it showed also some limits in predicting the interaction of the impinging jet with the base rotor-stator flow and in particular, the spreading of the jet and the size of the recirculation area along the stator. This may be attributed to the 3D unsteady structures highlighted by Owen (Fig.13.3), which can not be captured by steady axisymmetric calculations. Thus, from a numerical point of view, 3D simulations are now required to investigate the presence and the role of these structures but also the three-dimensional nature of the turbulent boundary layers developed along both disks. To improve our knowledge, it would be very interesting to investigate the flow field and the turbulence levels inside the rotor boundary layer. It will be next realized with stereo-PIV measurements performed in a (r, z) plane at TEMPO and compared to LES calculations.

A new PhD thesis just starts under the guidance of Dr S. Viazzo and myself on that topic. The PhD student, R. Oguic, will investigate the fluid flow and the heat transfer in the case sketched on Figure 13.13. It gathers many numerical difficulties (the $r = 0$ -singularity evoked in Chapter 3, the choice of the outlet boundary conditions, very elongated cavity in the radial direction, fluid/solid thermal coupling) as well as several physical complexities (highly turbulent flow, 3D unsteady flow, thin boundary layers, interaction of the jet with the rotor-stator flow ...), which are very challenging for numerical methods.

Investigations using LES, which have not yet received much attention up to now, will be performed using the code based on fourth-order compact schemes. Two configurations have been already successfully simulated: the plane jet impinging onto a flat plate [19] and onto a cubical pedestal without thermal effect [3]. Recently, the code in its mono-domain version has been extended to cylindrical coordinate in annular configurations and validated against velocity measurements for turbulent rotor-stator flows [345].

Some important numerical developments are still required before simulating the full problem:

1. The $r = 0$ -singularity: the numerical method has to deal efficiently with the axis singularity. Grid stretching being required close to the nozzle of the jet, one can not use the same approach

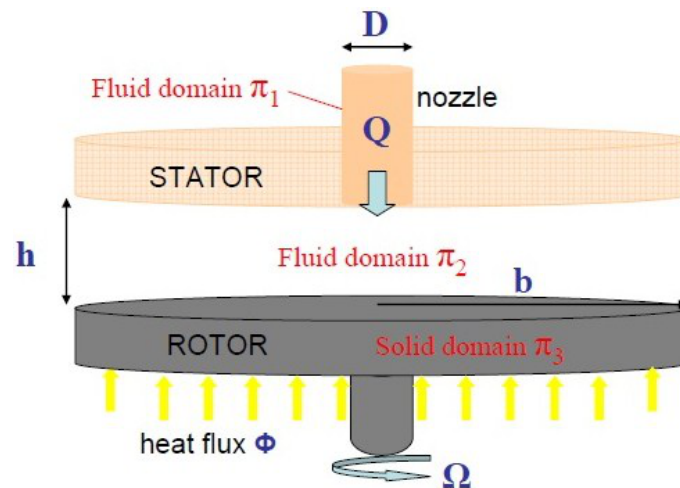


Figure 13.13: Sketch of the impinging jet flow onto a rotating disk confined by a stationary disk and opened to atmosphere, highlighting the presence of three distinct domains to simulate.

as the one developed by Peres [241] (see Chapter 3) but one will consider techniques based on regularity properties along the axis.

2. Necessity of a multidomain approach: it is now well known that such flow is very sensitive to inlet boundary conditions imposed for the jet. It seems then crucial to simulate also the turbulent Poiseuille flow in the inlet nozzle (fluid domain Π_1). For the heat transfer, both in the real system and in the TEMPO experiment, the heat flux is imposed on the lower surface of the rotor and the energy equation is then solved to estimate the heat transfer by conduction and so the temperature distribution on the disk surface. To do that numerically, it is important to solve also the energy equation in the solid part. It justifies the choice to decompose the calculation domain into, at least 3 subdomains, 2 fluid domains and 1 solid domain (Fig.13.13). According to the radial extension of the cavity, the fluid domain Π_2 should be also divided into several subdomains. The multidomain decomposition method used will be the same as the one previously used in various rotating flow configurations (Chapters 10 to 12).
3. Choice of the inlet and outlet boundary conditions. For the inlet conditions, several cases could be considered including pre-swirled flow or not. The choice of the outlet boundary conditions is more crucial for both the stability and accuracy of the calculation. Advective boundary conditions are usually considered in such configuration. A renormalization should be applied to ensure mass conservation between the inlet and the outlet.
4. Simulations of eccentric single or multiple jets. It will require the treatment of the inlet boundary conditions. The multidomain decomposition technique being incompatible with the use of Fourier series according to the azimuthal direction, a voluminal penalization technique will be implemented making it possible for the code to keep its structure.

When the first 3 steps will be achieved, one will try to increase the performance of the new code by changing first the Fast Fourier Transforms using the FFTW (Fastest Fourier Transform in the West) library. One will refer to the previous work of Mercader *et al.* [208] to do so. The FFTW package provides very interesting features such as its speed or the opportunity to have a parallelized code for platforms with SMP machines using an OpenMP implementation. A MPI version for distributed-memory transforms is also available in FFTW version 3.3. It is also portable to any platform with a C compiler. Finally, to increase the spatial resolution of the simulation and in association with the multidomain approach, one will make a parallel computing using a MPI implementation.

In the framework of the EASIJET project, one will approach the experimental and numerical analysis of heat transfers, wall frictions and flow structures in the following cases: single jet impinging a stationary disk for the calibration of the experimental methods and the validation of the numerical codes, single jet impinging a rotating disk in order to establish a detailed cartography of the flow

regimes according to the parameters, single and multiple eccentric jets, configurations making it possible to increase the wall heat transfers. The numerical part performed at M2P2 will cover all levels of turbulence modeling. Simulations by DNS/LES will be based on the in-house research code using high-order finite-difference compact schemes and some RANS and hybrid RANS/LES (with continuous transition) calculations will be done using the open-source code developed by EDF, Code Saturne. It will be also a good opportunity to implement the RSM version developed by Elena and Schiestel [85] into the standard version available within Code Saturne to have a 3D version of this model associated with more efficient algorithms, while keeping the innovative modeling. The numerical simulations will be compared to dynamic and thermal measurements. For the dynamic measurements, LaSIE developed a polarographic method already applied to the study of a jet impinging a stationary surface, which allows the measurement of the local friction coefficient. It will be coupled to a voluminal PIV using three cameras. For the thermal measurements, the DF2T team of the TEMPO laboratory will perform temperature measurements by infrared thermography, associated to an inverse technique of resolution of the energy equation. One will be able at the end of this project to propose correlations for the heat transfer coefficients according to the flow parameters (jet arrangements, jet and rotation speeds, interdisk spacing).

Other projects for the next five years

The following projects have absolutely nothing to do with rotating flows. They are all closely linked to industrial applications and thus are classified as being confidential.

14.1 SIMEOX project

SIMEOX is an apparatus of assistance to the bronchial drainage, developed by Physio-Assist, which makes it possible to facilitate the mucus clearance from the bronchi for patients suffering from obstructive disorders, cystic fibrosis . . . The main advantage is a gain of autonomy as it would replace daily physiotherapy sessions. The electronic device is composed of a generating turbine of depressions, a generator of vibrations, and a microcontroller allowing the control of the vibration frequency. SIMEOX produces successive pressure troughs during the exhalation phase (Fig.14.1). Between each oscillation, the pulmonary pressure returns to the atmospheric pressure. The generated signal is transmitted to the tracheo-bronchial air.

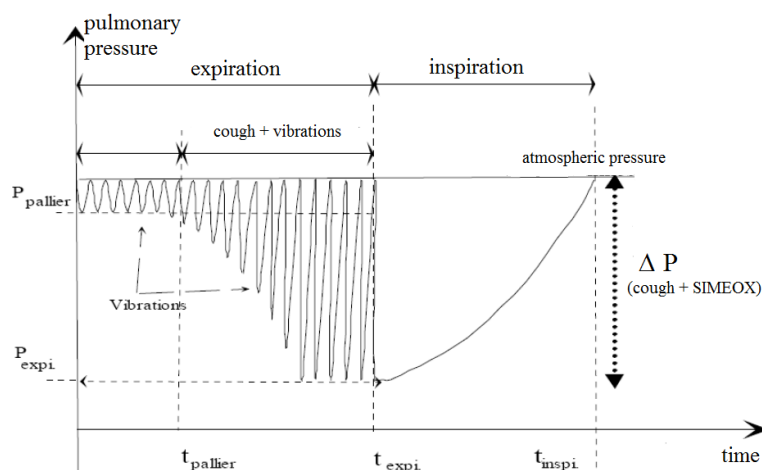


Figure 14.1: Pressure signal imposed by the SIMEOX during the respiratory cycle.

Mucus is a complex biological material that lubricates and protects the human lungs, gastrointestinal tract, vagina, eyes, and other moist mucosal surfaces. Mucus serves as a physical barrier against foreign particles, including toxins and environmental ultrafine particles, while allowing rapid passage of selected gases, ions, nutrients, or proteins. Its selective barrier properties are precisely regulated at the biochemical level across vastly different length scales. Though it is mostly composed of water (98%), bronchial mucus is a chemically and rheologically complex fluid secreted by the respiratory epithelium. A variety of glycol-sylated proteins, called mucins, gives it its intriguing mechanical properties while various additional constituents provide its immunological character. At the macroscale, mucus behaves as a non-Newtonian gel, distinguished from classical solids and liquids by its response to shear rate and shear stress, while, at the nanoscale, it behaves as a low viscosity fluid. Mucus is a non-Newtonian fluid that exhibits a plethora of phenomena such as stress relaxation, tensile stresses, shear-thinning, and yielding behavior.

Since the first description of cystic fibrosis, it has been known that these patients eventually succumb to severe lung disease associated with chronic infection. In persons with cystic fibrosis, there

is extensive and progressive bronchiectasis associated with accumulation of large amounts of purulent secretions. This toxic soup of pro-inflammatory cytokines, neutrophil breakdown products and bacteria leads to progressive damage to the airways and lungs. Clinical wisdom has suggested that patients with cystic fibrosis have thick secretions in their airway that make it difficult to clear bacteria, and that promote the development of bronchiectasis. The difficult mucus clearance in that case is not yet fully understood. Some researchers consider that patients with cystic fibrosis initially have normal functioning cilia and an efficient cough and that poor mucus clearance in airways results from abnormal mucus adhesiveness and tenacity. For others, mucus suffers from a default in the active ion transport mechanisms through the epithelium resulting in thick secretions due to a low water and low salt content of airway surface fluid. It has also been recently suggested that in cystic fibrosis, there is no rheological abnormality of airway secretions other than that associated with purulence, and that the apparent inhibition in the mucociliary transport rate might be partly due to a ciliary inhibitor present in these secretions. The second problem is that the small peripheral airways can be completely obstructed by mucus leading to pulmonary obstruction. Promoting airway clearance using a variety of medications and chest physical therapy or airway clearance techniques and devices has long been a mainstay of cystic fibrosis therapy.

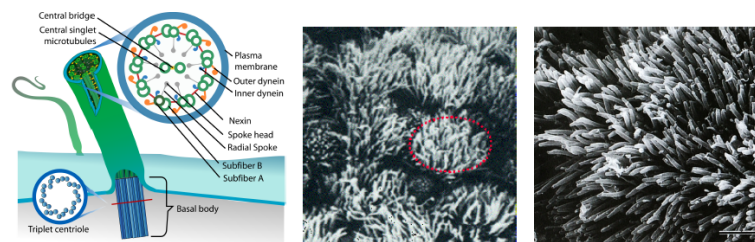


Figure 14.2: Polymer structure of a cilium (left picture, M.R.Villareal), cilia cluster over an epithelium cell (middle picture), and cilia details in straight state (right picture from [361]).

For healthy people, airway mucus is cleared by two major mechanisms: mucociliary clearance and airflow interaction (cough). As shown in Figure 14.2, human respiratory ducts are coated by epithelial cells that yield a carpet of cilia vibrating at a frequency between 8 and 15 Hz in the airway surface fluid to propulse the mucus stratum with entrapped particles outside the ventilatory system. Cilia are small hairlike projections ($7\mu\text{m}$ in length) on the epithelial cells lined all along the bronchial respiratory tract, the inner lining of which is covered by mucus blanket. By momentum transfer, their beating induces a forward velocity of the mucus layer (Fig.14.3). If mucus is too viscous, the cilia will not be able to move very well within it, and the decreased ciliary tip velocity will lead to a reduction of the mucociliary clearance. The efficient transfer of momentum between the cilia and the mucus layer requires that the cilia firmly contact the mucus during their forward stroke while minimally interacting with it during the return stroke. If the serous fluid is too deep or too shallow, the mucociliary clearance will also decrease. When the mucus layer is too thick and clearance by the cilia is hindered, clearance by coughing takes over. Mucus needs to be both viscous and elastic. The elasticity of mucus is important for clearance by cilia because it efficiently transmits energy, with little energy losses. The viscosity of mucus results in energy loss, but this is necessary for mucus to be displaced and either expectorated or swallowed. A balance between these factors must be maintained for optimal mucociliary clearance.

When disruption of normal secretory or mucociliary clearance processes occurs, respiratory secretions can accumulate and impair pulmonary function, reduce lung defenses, and increase the risk for infection and possibly neoplasia. Infections may then induce the disappearance of cilia at the epithelium surface. Cough assumes thus increasing importance as lung disease develops. Cough induces high velocities of the airflow with typical values around 200 m/s in the trachea. During a forced expiration, the airways are compressed by the transmural pressure. Airway narrowing increases airflow velocity, which increases mucus transport. Using the former version of the SIMEOX, Zahm *et al.* [366] found that the displacement of artificial mucus after a single simulated cough was higher when the airway diameter was narrower due to higher shear stresses between the mucus layer and the air flow. Mucus viscosity in a given sample may vary by a factor of up to 10^3 , depending on the applied shear. This decrease in viscosity can be explained by a temporary realignment of the macromolecular

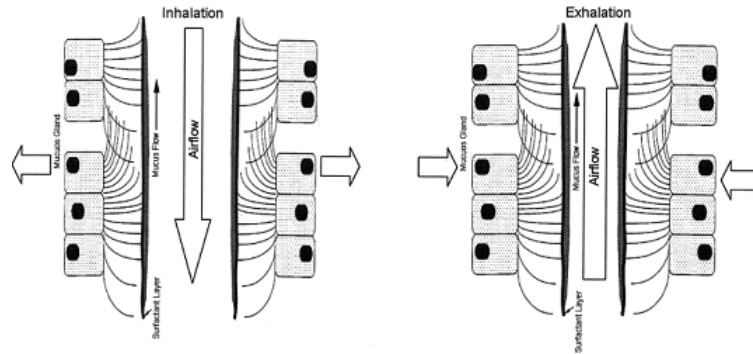


Figure 14.3: Two mechanisms of mucus clearance during breathing, after Fink [96].

glycoproteins by the applied force, so repeated forced exhalations with short intervals between the exhalations may reduce viscosity and improve mucus transport more than cough with longer intervals, which is supported by the findings of Zahm *et al.* [366]. The reader can refer to the monograph of Rogers and Lethem [277] and to the report by Poncet and Seyssiecq-Guarente [262] for more details about the state of art on bronchial mucus.

In the first part of the SIMEOX project, one has characterized the macrorheological properties of artificial mucus (actigum and viscogum) by measurements using a plate-plate rheometer. The choice of working with artificial mucus is imposed by the fact that real mucus contains antibiotic-resistant bacteria. The main result is that for the highest concentration in actigum (2 g for 100 mL), the rheological properties can follow a Herschel-Bulkley law:

$$\tau = \tau_0 + K\dot{\gamma}^n \quad (14.1)$$

where the threshold shear constraint is equal to $\tau_0 = 18$ Pa, the consistency index to $K = 23.3$ Pa.s^{-0.312} and the flow index $n = 0.312$. The threshold viscosity μ_0 for a shear rate $\dot{\gamma}$ close to 0 is equal to 900 Pa.s [317]. This law has been used to perform numerical simulations using the software ANSYS Fluent. Different calculations have been performed in the upper bronchial tree (the trachea) by R. Ngwong [221] and in the acinus (generation 20) by V. Hoarau [129] during their Master 1 internship in 2013. One assumes, in all calculations, rigid walls, laminar and isothermal flows and one considers in most of them only the effect of the SIMEOX without air flow. Note that, for patients suffering from cystic fibrosis, infections have generally completely destroyed the cilia, that is why they do not have been taken into account here. The duration of the numerical experiments is fixed to the exhalation time $T = 2.33$ s. The pressure signal imposed at the inlet is as follows:

$$P(t) = P_m + A \sin(2\pi ft) \quad (14.2)$$

It allows to represent the established regime of the SIMEOX (Fig.14.1) with a return to the atmospheric pressure after each oscillation. The values for the amplitude A of the signal is more or less imposed by the tolerance of patients. Amplitudes larger than 30 mbar can be painful and induce respiratory discomfort. V. Hoarau [129] performed calculations in the 20th generation of the bronchial tree (acini), characterized by a small radius (0.225 mm) quite comparable to the mucus thickness. The mucus thickness is besides very difficult to know accurately as it strongly varies from one patient to another, as it depends on the disease progression and on many other factors (location in the bronchial tree, period of the day, if the patients smoke or not ...). Thus, one simulated a rigid tube full of bronchial mucus. He established for various values of the amplitude A between 15 and 150 mbar, that the optimal frequency is 12 Hz with small differences between 6 and 20 Hz. Two criteria have been used to identify the optimal frequency: the maximum decrease in dynamic viscosity induced by pressure oscillations after one expiratory period and the flow regions where the dynamic viscosity of mucus remains equal to $\mu_0 = 900$ Pa.s. It is noticeable that the value for the optimal frequency of 12 Hz confirms the previous results of Zahm [365]. However, he speculated that this value is due to the beating frequency of the cilia equal also to 12 Hz. The present results show that the reason is somewhere else as there is no cilia in the present case.

Ngwong [221] performed similar calculations within Fluent but for the air/mucus flow in the

trachea considering a mucus thickness of 0.5 mm to be compared to the trachea radius of 8 mm. Some results are shown in Figure 14.4 for $A = 30$ mbar and $f = 12$ Hz. After $t = 2.33$ s, there is both a strong decrease for the maximum of the dynamic viscosity from 900 to 249 Pa.s but also an effective transport of mucus with a noticeable decrease in the thickness of the mucus layer. The frequency still does not have a major influence on the mucus clearance in the range [6 – 20] Hz, whereas, as expected, increasing the amplitude of the signal increases significantly the mucus clearance.

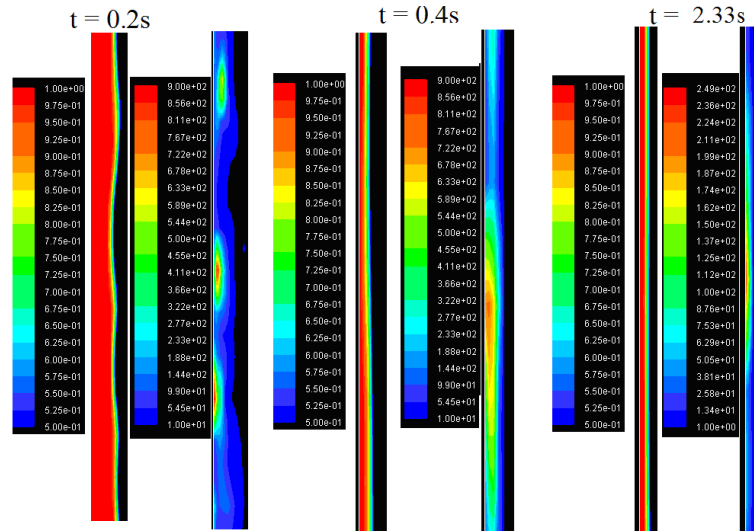


Figure 14.4: Maps of the dynamic viscosity and the presence rate of the mucus in the trachea (zoom on the wall region) for $A = 30$ mbar and $f = 12$ Hz at different times, after Ngwong [221].

Experimentally, future works include the development of an experimental set-up to establish correlations between the mucus properties and its effective transport by the SIMEOX. The main difficulty is due to the recovery thixotropic time of the mucus, which is shorter than the time required to collect the mucus from the tube after the use of the SIMEOX and adjust the rheometer for the measurement of the mucus dynamic viscosity. Some efforts to characterize the surface properties of the mucus, such as its surface tension and its adhesivity, has to be done.

Numerically, one will work on the form of the signal imposed by the SIMEOX. The sinusoidal pressure signal could be replaced by Heavyside functions to see if sharper gradients induce larger decrease in viscosity. A second overview is to introduce the thixotropy of the mucus in its rheological constitutive equation. A third step will be to take into account the air flow using a simplified model for the cilia motion as done by Enault *et al.* [87], who imposed unsteady velocity profiles as boundary conditions on the top and bottom sides of the mucus layer. Finally, the key point will be to be able to simulate the whole respiratory system, from the trachea to the acini, to see if the SIMEOX has also an influence on the mucus transport in the acini, where respiration acts.

In a close future, one will turn our attention also to the interaction between cilia and mucus for patients suffering from severe asthma. Asthma is characterized by sudden episodes of dyspnea and bronchospasm. The hypersecretion that is usually present during asthma episodes is a result of mediator release after antigen exposure. Even with resolution of dyspnea and pulmonary dysfunction, there is ongoing airway inflammation and hyperplasia of the mucus glands and cells. Bronchodilation probably has no effect on mucus transport in these patients. It has been postulated that during an asthma episode, a cilia-inhibiting factor reduces cilia activity, disorganizes ciliary beating, and thereby reduces ciliary efficiency but the cilia inhibition may be caused by abnormal physical properties of the mucus rather than an intrinsic ciliary inhibitor. Mucus hypersecretion and changes in the flow or surface properties of mucus may also reduce ciliary activity. Mucociliary transport, therefore, can be severely reduced in patients with asthma, and there is a further reduction during sleep. This project, called MUCIL, will be a collaboration with the Physio-Assist company and the “Laboratoire Adh sion & Inflammation” (Inserm U1067 / CNRS UMR 7333) in Marseilles. They are two main goals. The fundamental objective is to understand the interaction between cilia beating and mucus in the case of patients suffering from severe asthma and how the dynamics of the cilia is modified by a change

in the rheological properties of mucus. The team of A. Viallat at INSERM is able to recreate a full epithelium with cilia and mucus production starting from cells taken on corpses. Then, they investigate the rheological properties of mucus by microrheology and the interaction of cilia with the mucus layer. With J. Favier and U. D’Ortona from the M2P2, one will perform numerical simulations based on the lattice Boltzmann method. Cilia will be taken into account using the immersed boundary method developed by Dauplain *et al.* [70] in the case of the ctenophore *Pleurobrachia pileus*. An “one-way” coupling will be considered between cilia and the surrounding fluids. The second objective concerns the performance of the SIMEOX in the case of severe asthma: are the form, the frequency and the amplitude of the signals the same for cystic fibrosis and asthma? In a far future, one will be able to consider other complex effects such as mass injection through the epithelium and the solid deformation of the walls. A postdoctoral student funded by the Institut Carnot STAR will start to work on that project in February 2014.

14.2 Industrial chair CRSNG-Hydro-Québec on energy efficiency

I recently obtained an industrial chair CRSNG-Hydro-Québec on energy efficiency together with a position of associate professor at the University of Sherbrooke (Faculté de Génie). This chair, which should start in September 2014 and last 5 years, is directly linked to the RDC project of Prof. M. Sorin (Univ. Sherbrooke) as it can be seen in Figure 14.5. The main objective is to develop CFD tools to investigate the heat and mass transfers in three base components of refrigeration systems: two-phase ejectors, cold transportation by ice slurries and magnetic refrigeration. Most of the experimental set-ups are developed by the partners, the “Laboratoire des technologies de l’énergie” (LTE-Hydro-Québec, Shawinigan) and CanmetEnergie (Varenes). It is financially supported by the CRSNG and three companies: Hydro-Québec, CanmetEnergie and Rio Tinto Alcan for a total budget of 1 million Canadian dollars over the next 5 years. It will finance, among others, 5 PhD and 3 Master theses.

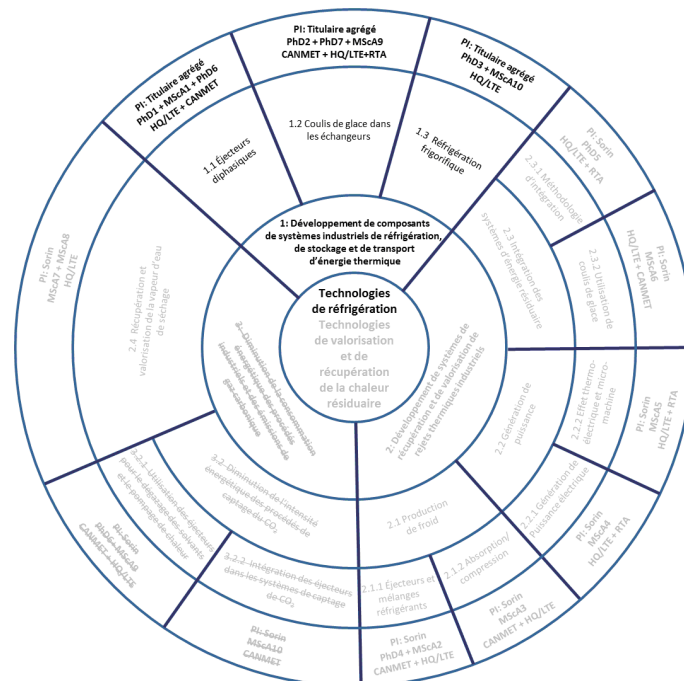


Figure 14.5: Structure of the CRSNG-Hydro-Québec industrial chair on energy efficiency.

14.2.1 Two-phase ejectors

The objective is here to develop CFD tools to analyze the fluid flow and the heat transfer in two-phase ejectors. A sketch of a typical ejector is shown in Figure 14.6. Three experimental set-ups are available for comparisons, two at CanmetEnergie and one at the University of Sherbrooke. This project, which will imply one Master and two PhD students, is a close collaboration with M. Dostie (LTE, Hydro-Québec) and Z. Aidoun (CanmetEnergie).

Refrigeration systems using an ejector offer some advantages compared to traditional systems using vapor compression. They are cheaper and have a very simple form without moving part. This simplicity of construction reduces the needs for maintenance and the associated costs. Contrary to a classical compressor, ejectors can function with liquids, gases or a combination of both. An ejector can be built-in in a system of refrigeration in several ways. One-phase ejector can easily replace the compressor or at least decrease its load. There are systems which use two-phase ejectors to replace partially or completely the relaxation valve in a conventional system with compressor. In an industrial context where great quantities of thermal energy of low quality are rejected into the environment and where requirements in refrigeration are simultaneously needed, the use of ejectors becomes an attractive option. Another application of the ejectors is the pumping of heat (revalorization of the thermal discharges).

One of the greatest disadvantages of the ejectors is their low thermodynamic effectiveness. To understand the principal cause of this phenomenon and to design more efficient ejectors, it is necessary to study the fundamental mechanisms governing the heat and mass transfers. Several phenomena must be taken into account: interaction between the boundary layers and the shock waves, phase change, transfer of momentum between phases, mixture process between the primary and secondary flows . . . CFD is a powerful tool making it possible to reproduce the physics of the flow for a better geometrical and operational design of the ejector. One finds many CFD studies on single-phase ejectors in the literature [15, 307], but they are especially focused on the shock waves in the vapour phase. The presence of droplets in the vapour phase is a current phenomenon, which has a strong impact on the performance of the single-phase ejectors and, which does not receive until now any attention. It will be studied within the framework of this chair. To our knowledge, there are no CFD studies on two-phase ejectors, because of the very complex flow structure. Experimental work was already completed at CanmetEnergie and at the University of Sherbrooke with this type of ejector [274] within the framework of the research programme of the previous CRSNG-Hydro-Quebec chair. This set-up will be used for optimization purposes.

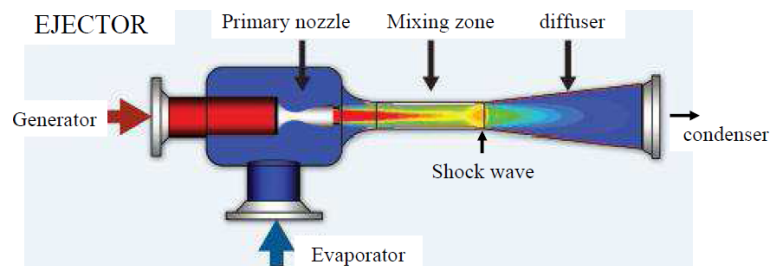


Figure 14.6: Operating principle of an ejector (CanmetEnergie).

A combined numerical and experimental approach will be considered to evaluate the exergetic losses in two types of ejector and to try to minimize them. This project is split into two parts:

- single-phase ejector with liquid droplets;
- two-phase ejector with liquid as the secondary fluid and vapour phase as the primary fluid.

From a methodological point of view, it is unthinkable to develop an in-house code being able to take into account the complexity of all the phenomena involved in this problem: two-phase flow with phase change, intense thermal transfers, turbulence, shock waves, interactions shock waves - boundary layers, complex geometry . . . For the flow with liquid droplets in the vapour phase, one proposes to consider, as a first step, an homogeneous model, which simulates the flow and the heat transfer for only one phase with physical (density, dynamic and kinematic viscosities) and thermodynamic (specific

heat, speed of sound, ...) properties expressed as a single formulation balanced by the presence rate of the least dense phase. This model is perfectly relevant when the presence rate of the liquid phase, represents less than 5% of the total. This model is proposed in all commercial softwares. The goal being to carry out here a parametric study of the flow and heat transfer in an ejector, while varying its geometry, the pressures and the temperatures at the generator and the evaporator, the compression and entrainment ratios ..., one will use the software ANSYS Fluent. This software offers, moreover, a broad range of turbulence models, which could be compared. One will also be interested in the impact of the mixture properties on the performance of the ejector.

Experimentally, global measurements of flowrates, pressures, temperatures (at the inlet, along the mixing zone, at the outlet), heat fluxes, and of the pump power will be performed on the experimental set-up developed at CanmetEnergie. These measurements will serve as entry data for the CFD model in terms of initial and boundary conditions. Some local optical measurements are also planned to study in more details the flow structure. A new transparent ejector will be designed. For the measurement technique, one will consider the former work of Porcar *et al.* [264], who used the diffusion of light in a two-phase ejector with liquid droplets or the more recent ones by Humble *et al.* [133] by PIV or Dvorak & Safarik [81] by Schlieren diffraction.

Two-phase ejectors (here the primary flow is liquid and the secondary one is vapour) are systems being able, in particular, to replace partially or completely the relaxation valve in a conventional system of heat pump with compressor. Experimental work was already completed at CanmetEnergie on this type of ejector by Reddick *et al.* [273, 274] in the framework of the research programme of the previous CRSNG-Hydro-Québec chair. They showed in particular that the use of such ejector using the R134a coolant can increase up to 11% the performance coefficient compared to the conventional system with the relaxation valve. On the other hand, to our knowledge, there is no CFD study on two-phase ejectors.

In this study, the CFD code considered will be the AVBP code developed by the CERFACS for the study of the 3D unsteady turbulent flows of compressible fluids on unstructured or hybrid grids. This code has been validated on many applications concerning reactive flows, flows in gas turbines, piston engines or in industrial furnaces. New modules are also under constant development. It includes many numerical ingredients: various numerical methods and turbulence models. The initial version of the code is limited to gas flows but an extension to two-phase flows by an Euler-Euler or Euler-Lagrange formulation is implemented in collaboration with the IMFT. AVBP is a parallel code under MPI making it possible to perform calculations with a high space resolution.

Numerically, a particular effort will be related to the turbulence modeling by a more elaborate approach than classical two-equation models in order to study the local interactions between the shock waves, turbulence and the boundary layers in the mixing and recompression areas. To model the two-phase character of the flow, it is rather complicated to predict, at this stage of the project, the flow structure in the ejector, which should vary drastically according to the different pressures and the entrainment ratio. Very simple experiments are thus necessary first to know even coarsely the flow structure. It could be very simple numerical experiments starting from 2D calculations using Fluent. After this preliminary step, one will consider more precise calculations with AVBP. If the liquid phase is dispersed in the gas phase, which occurs for important rates of vacuum and high speeds of gas compared to that of the liquid, the Euler-Euler mesoscopic model available in AVBP seems completely suitable. It makes it possible to obtain the local properties of the dispersed phase (liquid) by solving an evolution equation of Boltzmann type for the probability density of the liquid phase. For certain ranges of parameters (typically 50% of gas and 50% of liquid with similar speeds), one will switch to another method like the VOF (Volume of Fluid) method.

Experimentally, one will consider, in a second time, some modifications of the test bench already available at the University of Sherbrooke to add an optical access in the divergent part of the nozzle in order to make local measurements by laser tomography. Bouhanguel *et al.* [33] applied this technique to study the flow structure in the mixing zone, the shock waves ... by playing with the illumination source, the polarization direction of the incident light and the type of tracers.

A combined numerical (AVBP code) and experimental approach (3 experiments at CanmetEnergie and at the University of Sherbrooke) will thus be undertaken to evaluate the origin of the energy and exergetic losses in a two-phase ejector with phase change and thus to make it possible to minimize them. One will test several geometries of ejectors as well as mixtures of natural or synthetic cooling agents under various operating conditions (geometry of the mixing chamber, operating conditions in terms of primary and secondary flows, inlet pressures and temperatures, entrainment and compression

ratios). The goal is to propose technical solutions (several entries of secondary fluid, control strategy of the boundary layer ...) to decrease the sources of exergetic losses.

14.2.2 Storage and transport of ice slurry coolants

The objective is here to develop CFD tools able to simulate the formation, the storage and the transport of ice slurry coolants. A new experimental set-up will be designed at the University of Sherbrooke for the storage of ice slurry and the detailed analysis of its physical properties, while an experiment is already available at CanmetEnergie for the transport part (see Fig.14.7a). This project, which will imply one Master and two PhD students, is a close collaboration with Prof. N. Galanis (Univ. Sherbrooke) and M. Poirier (CanmetEnergie).

Ice slurries (Fig.14.7b) constitute a substitution solution of the one-phase secondary fluids in conventional systems of refrigeration. Ice slurry is a mixture composed of a liquid phase (water), of a solid phase (ice crystals) and of an additive such as glycol for example. By its constitution, it makes it possible to evacuate more heat than water alone for the same mass flowrate. Moreover, the heat transfer is done at a relatively stable temperature (phase change), which improves the quality of the produced cold. Its use as a coolant allows the reduction and the containment of the refrigerants, the reduction in the size of the cold store thanks to the storage of cold, the reduction in the bore of distribution and a fall in the electric demand [149].

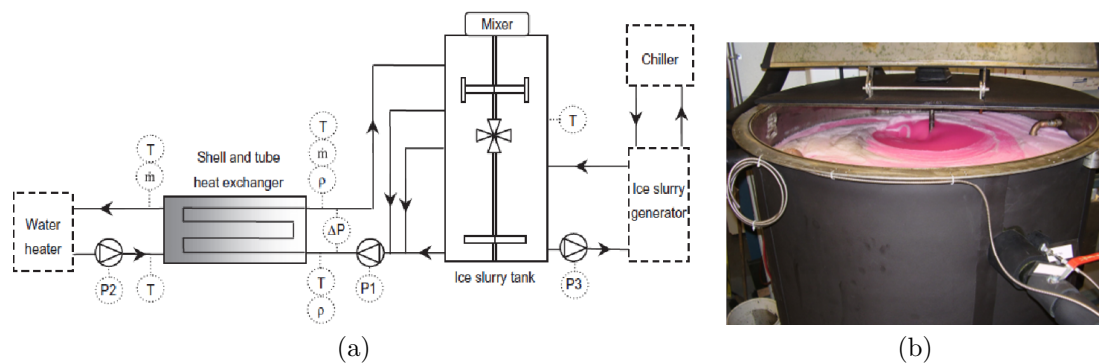


Figure 14.7: (a) Experimental set-up developed by Renaud-Boivin *et al.* [275] at CanmetEnergie (Varenes) for the storage and transport of ice slurries; (b) Storage and mixing tank with ice slurries (CanmetEnergie).

There exists only very few studies in the literature on the effectiveness of heat exchangers using ice slurries. Indeed, although one notes a significant improvement of the effectiveness of such exchangers, the structure of ice slurry flows inside the exchanger remains relatively unknown. Several cross effects can influence the flow of the slurry inside the exchanger. The inlet mass flowrate of the fluid, the concentration of the solid phase, the temperature of the mixture, the heat flux to be evacuated and the geometry of the exchanger are indeed important parameters, which have to be considered. Another key parameter is the change of ice concentration (in solid phase) during its transport in the exchanger, which can involve a modification of the type of flow and, consequently, of the heat transfer. A fundamental study is thus necessary in order to improve the understanding of the thermal and hydraulic behaviors of this coolant. One will also be interested in the microscopic properties of the slurry during its formation, its storage and its transport, to include/understand how they affect its macroscopic behaviour.

This project is split into 2 parts: the development of a CFD tool to estimate the heat transfer and the pressure losses of an ice slurry flow and the installation of an experimental set-up for the production and storage of ice slurry to investigate in details its physical properties.

Ice slurry is a complex fluid, exhibiting various dynamical behaviours depending on its precise composition [203]. Small differences in density can induce some stratification due to the competition between the gravity and diffusion phenomena. One proposes here to extend the CFD model developed under the ANSYS Fluent software during the previous chair. The main objectives are as followed:

- to investigate the heat and mass transfer mechanisms for a laminar circular pipe flow and the influence of the stratification; A comparative study of the various multiphase flow methods as

was made by Akbari *et al.* [6] for nanofluid flows will be performed. The authors concluded that all the models provide similar results for the hydrodynamic and thermal fields, whereas the VOF model is less computationally expensive;

- to perform a parametric study in the laminar regime and quantify the influence of the boundary conditions on the thermal field (cold or hot walls), the influence of the heat exchanger geometry (circular or rectangular channel) and of various other parameters (ice slurry concentration, flowrate . . .) on the flow characteristics (friction coefficient, Nusselt number, . . .);
- to perform the same analysis in the turbulent regime. To our knowledge, there are few studies on turbulent ice-slurry flows [349]. In the turbulent regime, the mechanisms are even more complex and the benchmark done in the laminar regime for the choice of the two-phase flow model has to be made once again. Turbulence increases mixing, which reduces the inhomogeneities in the flow while being able to cause the formation of aggregates of ice particles. The choice of the two-phase flow model can be thus completely different from the laminar case. The choice of the turbulence model is also crucial and a numerical benchmark of the different turbulence models available within Fluent will be performed. The wall heat transfers being increased by the turbulent nature of the flow, a low-Reynolds number model seems to be more appropriate. The objective is to highlight the model providing the best compromise between accuracy and computational cost.

CFD calculations will be systematically compared to the measurements carried out at CanmetEnergie (measurements of the pressure losses, of the temperature and density of the slurry at both the entry and the exit of the pipe, measurements of the axial temperature distribution along the lower and upper walls of the tube to check the importance of the natural convection and/or the ice stratification).

Another objective is the development of an experimental device of production, storage and transport of ice slurry of low dimensions at the University of Sherbrooke for the optimization of both the ice slurry generator and the storage tank (reduction of its size, minimization of the energy used for agitation). It appears indeed crucial to understand how the characteristics at a microscopic scale of the ice crystals affect the behaviour of the slurry at the macroscopic scale. This can be done only by a well-controlled experiment allowing to act on all the chain links: additive (glycol, salts . . .), type of mixer . . . The size of the crystals and their form strongly influence the flow and the heat transfer, mainly at low Reynolds numbers. One will study the size and the shape of the particles during the storage phase by measurements using an electronic microscope. The goal is to understand the growth of the crystals (maturation, agglomeration . . .) and to obtain ideal characteristics for the slurry (spherical form, fluidity . . .) for a better storage without agglomeration and a better extraction even for high values of ice mass fraction without stopper effect. The storage tank will be connected to a capillary rheometer allowing the measurements of the rheological behavior of the slurry. Mellari *et al.* [203] showed that according to the concentration in additive, the slurry has a shear-thinning, Newtonian or shear-thickening behaviour but always exhibits a shear stress threshold. In most of the CFD approaches, the slurry is considered as a Newtonian fluid for more simplicity. This assumption is valid only for ice mass fraction between 6 and 15% depending on the type of additive and the rheometer used. It appears necessary to develop more complete rheological models taking into account the ice solid fraction, the temperature of the slurry . . . The possible thixotropic character of the slurry should have also to be considered. Previous studies showed that it is necessary to have two rheological models: one for weak shearing and one for strong shearing. Measurements by a second rheometer with a vibrating membrane are planned to cover a broad range of shearing. Lastly, the device will be supplemented by a circular heat exchanger designed in metaplex to allow flow visualizations. That will allow moreover local velocity measurements by optical methods (PIV). The influence of the storage time on the pressure gradient and on the heat transfer coefficients will be studied in details for various sets of parameters (flow, ice mass fraction . . .).

CFD calculations on the dynamic modeling of the progressive fusion of ice slurry in the storage tank could be also carried out using the enthalpic method. This model will be validated from temperature measurements made by thermocouples laid out on the interior wall of the tank. One proposes to extend the study of Kouskou *et al.* [159] by taking into account the axisymmetric real geometry of the tank and by considering the fusion phase of the ice. The Lattice Boltzmann methods seem completely adapted to this type of problems.

14.2.3 Magnetic refrigeration

The objective is here to develop a 3D modeling of a porous multi-layer regenerator used in magnetic refrigeration (MR). This project will imply one Master and one PhD students in collaboration with J. Bouchard (LTE, Hydro-Québec).

The MR is based on the magnetocaloric effect, which consists of the reversible heating of a magnetic material as soon as it is subjected to a magnetic field (Fig.14.8). The magnetic material warms up during magnetization (2) and cools during demagnetization (5). Between the 2 processes, heat transfers take place between material and the heat and cold sources via coolants (3). The MR is recognized as being more effective than the mechanical compression of gases to reach cryogenic temperatures. The interest for the MR at ambient temperatures is induced by the recent discovery of the magnetocaloric effect at these temperatures for certain magnetic materials such as gadolinium. A vaster range of applications is thus accessible. The MR appears among technologies of cold production with a strong potential in energy effectiveness. According to optimal conditions, the output associated with the MR is considered as being 20% higher than that of the most powerful systems of refrigeration with compression. Moreover, the solid state of the cooling agent allows to avoid the harmful gas emission for the ozone layer such as CFC (chlorofluorocarbons) or HCFC (hydrochlorofluorocarbons). That has other advantages: a system of MR can be compact because of its high density of energy and the absence of compressor makes MR a relatively quiet technology.

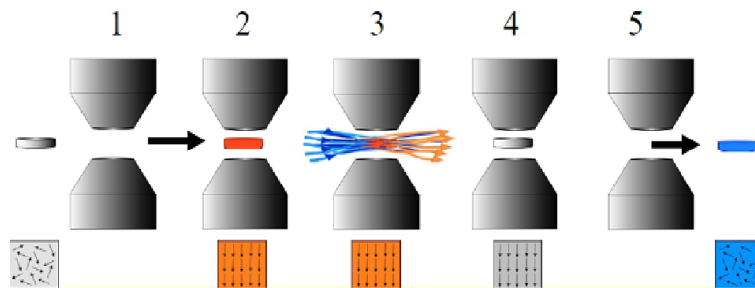


Figure 14.8: Principle of the magneto-caloric effect.

A system of MR is composed of pumps, magnets, heat exchangers and a regenerator. The geometry and the composition of the latter impose a limit on the fall of temperature, which is thermodynamically possible to reach. Magnetic materials with a magneto-caloric effect at ambient temperature are constantly required and can be found under the form of thin plates or of granules compacted in order to obtain a dense regenerator but allowing an effective heat transfer with the coolant. As it is difficult to measure this exchange inside the regenerator of an experimental prototype, a CFD tool is more adapted to study the heat transfer and the capacity of refrigeration. Because of important approximations, the available models do not generate realistic quantitative results. Generally, the regenerator is modeled like a 1D and one-phase flow [320, 321]. At best, one models a restricted volume made up of ordered granules. It is now necessary to design a CFD tool able to simulate a porous regenerator made up of a random three-dimensional arrangement of magnetic granules.

As a first step, it will be necessary to develop a new experimental set-up of porous regenerator in LTE-Shawinigan since that developed during the previous chair has been dismantled. The device will allow global measurements of the vacuum magnetic field, coolant flowrate, and pressures upstream and downstream from the regenerator, temperatures at the entry, the exit and along the regenerator for comparisons with the CFD model. Local measurements of the velocity profiles at the entry of the regenerator are also planned to be used as boundary conditions for the model. According to the aptitudes of the candidates, other developments will be considered on the three components of the regenerator (magnet, coolant and active material) and in particular on the last two with the use of nanofluids as coolant [6], and the use of alloys containing manganese [88], which have a large magneto-caloric effect close of the ambient temperature for weak magnetic fields.

The only unsteady 3D model of porous regenerator is still to date that developed by Bouchard et al. [31] during the previous chair. The two principal limitations of this model raised by the authors themselves are: the limited size of the calculation domain because of the memory and computation time required, which quickly become prohibitive if one wishes to reproduce several magnetic cycles

of refrigeration; the incapacity to numerically reproduce the pressure loss in the porous regenerator compared with the experiments made at LTE. This may be attributed to the ordered fitting of the magneto-caloric material granules. The porous regenerator will be thus modeled like a three-dimensional random fitting of the magnetic solid granules. Thus, the regenerating fluid will circulate through the tortuous channels formed by the interstices between the granules. For that, one proposes to use the Palabos library as CFD tool. It is an open-source library, developed in C++ and based on the Lattice-Boltzmann method. Palabos is associated with the MPI library. It is thus easy to carry out calculations massively parallel on suitable platforms and thus to reach calculation domains over the full regenerator. Algorithms of sequential addition or reorganization will be used to pile up randomly the magnetic granules [319]. The coupled resolution of the Navier-Stokes (fluid) and energy (fluid and granules) equations will make it possible to determine the distributions of velocity (fluid) and temperature (fluid and granules). These granules will be simulated by a immersed boundary method [246]. The inclusion of a source term, which depends on the intensity of the magnetic field in the energy equation for the granules will make it possible to model the magneto-caloric effect. Also, the variation of the physical properties of the magnetic granules with the temperature and the intensity of the magnetic field will be taken into account.

Bibliography

- [1] K. Abe, T. Kondoh, and Y. Nagano. A two-equation heat transfer model reflecting second-moment closures for wall and free turbulent flows. *Int. Heat Fluid Flow*, 17:228–237, 1996.
- [2] S. Abide. *Une méthode de décomposition de domaine pour la simulation numérique directe. Contribution à l'étude de jets plans en impact*. PhD thesis, École Nationale Supérieure des Techniques Industrielles et des Mines de Nantes, 2005.
- [3] S. Abide and S. Viazzo. A 2D compact fourth-order projection decomposition method. *J. Comp. Phys.*, 206:252–276, 2005.
- [4] S. C. Abrahamson, J. K. Eaton, and D. J. Koga. The flow between shrouded co-rotating disks. *Phys. Fluids A*, 1:241–251, 1989.
- [5] J.A.D. Ackroyd. On the steady flow produced by a rotating disc with either surface suction or injection. *J. Engng. Maths.*, 12(3):207–220, 1978.
- [6] M. Akbari, N. Galanis, and A. Behzadmehr. Comparative analysis of single and two-phase models for CFD studies of nanofluid heat transfer. *Int. J. Thermal Sci.*, (50):1343–1354, 2011.
- [7] M.E. Ali and P.D. Weidman. On the stability of circular Couette flow with radial heating. *J. Fluid Mech.*, 220:53–84, 1990.
- [8] M. Amaouche, H. Ait Abderrahmane, and G.H. Vatistas. Nonlinear modes in the hollow-cores of liquid vortices. *Eur. J. Mech. B/Fluids*, 41:133–137, 2013.
- [9] C.D. Andereck, S.S. Liu, and H.L. Swinney. Flow regimes in a circular Couette system with independently rotating cylinders. *J. Fluid Mech.*, 164:155–183, 1986.
- [10] H.I. Andersson, E. de Korte, and R. Meland. Flow of a power-law fluid over a rotating disk revisited. *Fluid Dyn. Res.*, 28:75–88, 2001.
- [11] H.I. Andersson and M. Lygren. LES of open rotor-stator flow. *Int. J. Heat Fluid Flow*, 27(4):551–557, 2006.
- [12] H. Aoki, H. Nohira, and H. Arai. Convective heat transfer in an annulus with an inner rotating cylinder. *Bulletin JSME*, 10(39):523–532, 1967.
- [13] H.A. Attia. Numerical study of flow and heat transfer of a non-Newtonian fluid on a rotating porous disk. *Appl. Math. Comp.*, 163:327–342, 2005.
- [14] K.S. Ball, B. Farouk, and V.C. Dixit. An experimental study of heat transfer in a vertical annulus with a rotating inner cylinder. *Int. J. Heat Mass Transfer*, 32:1517–1527, 1989.
- [15] Y. Bartosiewicz, Z. Aidoun, and Y. Mercadier. Numerical assessment of ejector operation for refrigerant applications based on CFD. *Appl. Thermal Eng.*, 26:604–612, 2006.
- [16] G.K. Batchelor. Note on a class of solutions of the Navier-Stokes equations representing steady non rotationally symmetric flow. *Quart. J. Mech. Appl. Math.*, 4:29–41, 1951.
- [17] Y. Bazilevs and I. Akkerman. Large eddy simulation of turbulent Taylor-Couette flow using isogeometric analysis and the residual-based variational multiscale method. *J. Comp. Phys.*, 229:3402–3414, 2010.
- [18] F. Beaubert. *Simulation des grandes échelles turbulentes d'un jet plan en impact*. PhD thesis, École Nationale Supérieure des Techniques Industrielles et des Mines de Nantes, 2002.
- [19] F. Beaubert and S. Viazzo. Large eddy simulations of plane turbulent impinging jets at moderate Reynolds numbers. *Int. J. Heat Fluid Flow*, 24(4):512–519, 2003.
- [20] K. M. Becker and J. Kaye. Measurement of diabatic flow in an annulus with an inner rotating cylinder. *Trans. ASME, J. Heat Transfer*, 84:97–105, 1962.
- [21] K. Bergeron, E.A. Coutias, J.P. Lynov, and A.H. Nielsen. Self-organization in circular shear layers. *Physica Scripta*, 67:33–37, 1996.
- [22] K. Bergeron, E.A. Coutias, J.P. Lynov, and A.H. Nielsen. Dynamical properties of forced shear layers in an annular geometry. *J. Fluid Mech.*, 402:255–289, 2000.
- [23] M. Biage and J.C.C. Campos. Visualization study and quantitative velocity measurements in turbulent Taylor-Couette flow tagging: a description of the transition to turbulence. *J. Braz. Soc. Mech. Sci. Eng.*, 25(4):378–390, 2003.

- [24] E. Bilgen and R. Boulos. Functional dependence of torque coefficient of coaxial cylinders on gap width and Reynolds numbers. *Trans. ASME, J. Fluids Eng.*, 95(1):122–126, 1973.
- [25] R.D. Blevins. *Applied fluid dynamics handbook*. Ed. Van Nostrand Reinhold Company Inc., New-York, 1984.
- [26] U.T. Bödewadt. Die Drehströmung über festem Grunde. *Z. Angew. Math. Mech.*, 20:241–253, 1940.
- [27] D. Bohn, J. Ren, and C. Tuemmers. Investigation of the unstable flow structure in a rotating cavity. In *Proc. of the ASME Turbo Expo 2006: Power for Land, Sea and Air*, Barcelona, 2006.
- [28] P. Boroński. *Méthode des potentiels poloïdal-toroïdal appliquée à l'écoulement de Von Kármán en cylindre fini*. PhD thesis, École Polytechnique, 2005.
- [29] D. Borrero-Echeverry, M.F. Schatz, and R. Tagg. Transient turbulence in Taylor-Couette flow. *Phys. Rev. E*, 81:025301, 2010.
- [30] M. Bouafia, Y. Bertin, J.B. Saulnier, and P. Ropert. Analyse expérimentale des transferts de chaleur en espace annulaire étroit et rainuré avec cylindre intérieur tournant. *Int. J. Heat Mass Transfer*, 41(10):1279–1291, 1998.
- [31] J. Bouchard, H. Nesreddine, and N. Galanis. Model of porous regenerator used for magnetic refrigeration at room temperature. *Int. J. Heat Mass Transfer*, 52(5-6):1223–1229, 2009.
- [32] R. Bouffanais and D. Lo Jacono. Unsteady transitional swirling flow in the presence of a moving free surface. *Phys. Fluids*, 21:064107, 2009.
- [33] A. Bouhanguel, P. Desevaux, and E. Gavignet. Flow visualization in supersonic ejectors using laser tomography techniques. *Int. J. Refrigeration*, 34:1633–1640, 2011.
- [34] M. Bourgoïn, L. Marié, F. Pétrélis, C. Gasquet, A. Guigon, J.-B. Luciani, M. Moulin, F. Namer, J. Burguete, A. Chiffaudel, F. Daviaud, S. Fauve, P. Odier, and J.-F. Pinton. Magnetohydrodynamics measurements in the Von Kármán sodium experiment. *Phys. Fluids*, 14(9):3046–3058, 2002.
- [35] M. Bourgoïn, P. Odier, J.-F. Pinton, and Y. Ricard. An iterative study of time independent induction effects in magnetohydrodynamics. *Phys. Fluids*, 16(7):2529–2547, 2004.
- [36] J.P. Boyd. *Chebyshev and Fourier Spectral Methods, 2th Edition*. Dover Publications, New-York, 2001.
- [37] P. Bradshaw. Effects of streamline curvature on turbulence. *AGARDograph.*, 169, 1973.
- [38] J.F. Brady and L. Durlafsky. On rotating disk flow. *J. Fluid Mech.*, 175:363–94, 1987.
- [39] D. Buisine, F. Oble, and H. Andrianarahinjaka. Etude numérique des structures spirales tridimensionnelles à la périphérie d'une cavité interdisque. *C.R. Acad. Sci. Paris, série IIb*, 328:237–246, 2000.
- [40] M.J. Burin, E. Schartman, and H. Ji. Local measurements of turbulent angular momentum transport in circular Couette flow. *Exp. Fluids*, 48:763–769, 2010.
- [41] O. Cadot, Y. Couder, A. Daerr, S. Douady, and A. Tsinober. Energy injection in closed turbulent flows: stirring through boundary layers versus inertial stirring. *Phys. Rev. E*, 56(1):427–433, 1997.
- [42] O. Cadot and O. Le Maître. The turbulent flow between two rotating stirrers: similarity laws and transitions for the driving torques fluctuations. *Eur. J. Mech. B/Fluids*, 26(2):258–270, 2007.
- [43] C. Cambon. Turbulence and vortex structures in rotating and stratified flows. *Eur. J. Mech. B/Fluids*, 20:489–510, 2001.
- [44] C. Cambon and L. Jacquin. Spectral approach to non-isotropic turbulence subjected to rotation. *J. Fluid Mech.*, 202(1):295–317, 1989.
- [45] T. Cebeci and P. Bradshaw. *Physical and Computational Aspects of Convective Heat Transfer*. Springer, New-York, 1988.
- [46] M. I. Char and Y. H. Hsu. Numerical prediction of turbulent mixed convection in a concentric horizontal rotating annulus with low-Re two-equation models. *Int. J. Heat Mass Transfer*, 41(12):1633–1643, 1998.
- [47] S.S. Chawla and R. Purushothaman. Spin-up in the Bödewadt flow. *J. Math. Anal. Appl.*, 71:463–481, 1979.
- [48] S.S. Chawla and P.K. Srivastva. On the Bödewadt-Rosenblat flow. *Z. Angew. Math. Phys.*, 57:793–814, 2006.
- [49] S.C. Cheah, H. Iacovides, D.C. Jackson, H. Ji, and B.E. Launder. Experimental investigation of enclosed rotor-stator disk flows. *Exp. Therm. Fluid Sci.*, 9:445–455, 1994.
- [50] Y.M. Chen, W.T. Lee, and S.J. Wu. Heat (mass) transfer between an impinging jet and a rotating disk. *Heat Mass Transfer*, 34(2):195–201, 1998.
- [51] P.R.N. Childs. *Rotating Flow*. Butterworth-Heinemann, Oxford, 2011.

- [52] F. Chillá, S. Ciliberto, C. Innocenti, and E. Pampaloni. Boundary layers and scaling properties in turbulent thermal convection. *Nuovo Cimento D*, 15:1229–1249, 1993.
- [53] J.M. Chomaz, M. Rabaud, C. Basdevant, and Y. Couder. Experimental and numerical investigation of a forced circular shear layer. *J. Fluid Mech.*, 187:115–140, 1988.
- [54] S. Y. Chung and H. J. Sung. Large-eddy simulation of turbulent flow in a concentric annulus with rotation of an inner cylinder. *Int. J. Heat Fluid Flow*, 26:191–203, 2005.
- [55] W.G. Cochran. The flow due to a rotating disk. *Proc. Camb. Phil. Soc.*, 30:365–375, 1934.
- [56] G.N. Coleman, J. Kim, and J.R. Spalart. A numerical study of strained three-dimensional wall-bounded turbulence. *J. Fluid Mech.*, 416:75–116, 2000.
- [57] H.W. Coleman and W.G. Steele. Engineering application of experimental uncertainty analysis. *AIAA journal*, 33(10):1888–1896, 1995.
- [58] D. Coles. Transition in circular Couette flow. *J. Fluid Mech.*, 21(3):385–425, 1965.
- [59] M. Couette. Etude sur le frottement des liquides. *Ann. Chim. Phys.*, 21:433, 1890.
- [60] T. Craft, H. Iacovides, B. E. Launder, and A. Zacharos. Some swirling-flow challenges for turbulent CFD. *Flow, Turbulence & Combustion*, 80:419–434, 2008.
- [61] A. Cros, E. Floriani, P. Le Gal, and R. Lima. Transition to turbulence of the Batchelor flow in a rotor/stator device. *Eur. J. Mech. B/Fluids*, 24:409–424, 2005.
- [62] A. Cros and P. Le Gal. Spatiotemporal intermittency in the torsional Couette flow between a rotating and a stationary disk. *Phys. Fluids*, 14:3755–3765, 2002.
- [63] O. Czarny, H. Iacovides, and B. E. Launder. Precessing vortex structures in turbulent flow within rotor-stator disc cavities. *Flow, Turbulence & Combustion*, 69:51–61, 2002.
- [64] O. Czarny, E. Serre, and P. Bontoux. Interaction between Ekman pumping and the centrifugal instability in Taylor-Couette flow. *Phys. Fluids*, 15(2):467–477, 2003.
- [65] O. Czarny, E. Serre, P. Bontoux, and R. Lueptow. Interaction of wavy cylindrical Couette flow with endwalls. *Phys. Fluids*, 16(4):1140–1148, 2004.
- [66] R. Da Soghe, B. Facchini, L. Innocenti, A. Andreini, and S. Poncet. Numerical benchmark of turbulence modeling in gas turbine rotor-stator system. *ASME TurboExpo Power for Land, Sea & Air*, GT2010-22627, 2010.
- [67] J. W. Daily and R. E. Nece. Chamber dimension effects on induced flow and frictional resistance of enclosed rotating disks. *ASME J. Basic Eng.*, 82:217–232, 1960.
- [68] J.W. Daily, W.D. Ernst, and V.V. Asbedian. *Enclosed rotating disks with superposed throughflow*. Hydrodynamics Laboratory Report 64, M.I.T, Department of Civil Engineering, 1964.
- [69] B.J. Daly and F.H. Harlow. Transport equation for turbulence. *Phys. Fluids A*, 13(11):2634–2649, 1970.
- [70] A. Dauptain, J. Favier, and A. Bottaro. Hydrodynamics of ciliary propulsion. *J. Fluids & Structures*, 24:1156–1165, 2008.
- [71] R.C. Di Prima and H. Swinney. Instabilities and transition in flow between concentric rotating cylinders. In H. Swinney & J.P. Gollub, editor, *Hydrodynamic instabilities and the transition to turbulence*, pages 139–180. Springer, 1981.
- [72] D. Dijkstra and G.J.F. Van Heijst. The flow between two finite rotating disks enclosed by a cylinder. *J. Fluid Mech.*, 128:123–154, 1983.
- [73] M. Djaoui and R. Debuchy. Heat transfer in a rotor-stator system with a radial inflow. *C.R. Acad. Sci. Paris IIb*, 326:309–314, 1998.
- [74] M. Djaoui, A. Dymont, and R. Debuchy. Heat transfer in a rotor-stator system with a radial inflow. *Eur. J. Mech. B - Fluids*, 20:371–398, 2001.
- [75] F.V. Dolzhanskii, V.A. Krymov, and D.Y. Manin. Stability and vortex structures of quasi-two-dimensional shear flows. *Sov. Phys. Usp.*, 33(7):495–520, 1990.
- [76] F.V. Dolzhanskii, V.A. Krymov, and D.Y. Manin. An advanced experimental investigation of quasi-two-dimensional shear flows. *J. Fluid Mech.*, 241:705–722, 1992.
- [77] S. Dong. Turbulent flow between counter-rotating concentric cylinders: a direct numerical simulation study. *J. Fluid Mech.*, 615:371–399, 2008.

- [78] L.A. Dorfman. *Hydrodynamic Resistance and Heat Loss from Rotating Solids*. Oliver & Boyd, Edinburgh and London, 1963.
- [79] B. Dubrulle and F. Hersant. Momentum transport and torque scaling in Taylor-Couette flow from an analogy with turbulent convection. *Eur. Phys. J. B*, 26:379–386, 2002.
- [80] G. Dufour, N. Gourdain, F. Duchaine, O. Vermorel, L.Y.M. Gicquel, J.-F. Boussuge, and T. Poinso. Numerical investigations in turbomachinery: A state of the art. large eddy simulation applications. In *VKI Lecture Series*, the von Kármán Institute for Fluid Dynamics, 2009.
- [81] V. Dvorak and P. Safarik. Transonic instability in entrance part of mixing chamber of high-speed ejector. *J. Thermal Science*, 14(3):258–264, 2005.
- [82] B. Eckhardt, S. Grossmann, and D. Lohse. Torque scaling in turbulent Taylor-Couette flow between independently rotating cylinders. *J. Fluid Mech.*, 581:221–250, 2007.
- [83] L. Elena. *Modélisation de la turbulence inhomogène en présence de rotation*. PhD thesis, Université Aix-Marseille I-II, 1994.
- [84] L. Elena and R. Schiestel. Turbulence modeling of confined flow in rotating disk systems. *AIAA J.*, 33(5):812–821, 1995.
- [85] L. Elena and R. Schiestel. Turbulence modeling of rotating confined flows. *Int. J. Heat Fluid Flow*, 17:283–289, 1996.
- [86] C.J. Elkins and J.K. Eaton. Turbulent heat and momentum transport on a rotating disk. *J. Fluid Mech.*, 402:225–253, 2000.
- [87] S. Enault, D. Lombardi, P. Poncet, and M. Thiriet. Mucus dynamics subject to air and wall motion. *ESAIM Proc.*, 30:125–141, 2010.
- [88] K. Engelbrecht, J.B. Jensen, and C.R. Haffenden Bahl. Experiments on a modular magnetic refrigeration device. *J. Mech. Eng.*, 58:3–8, 2012.
- [89] M. P. Escudier and I. W. Gouldson. Concentric annular flow with centerbody rotation of a Newtonian and a shear-thinning liquid. *Int. J. Heat Fluid Flow*, 16:156–162, 1995.
- [90] M. P. Escudier, I. W. Gouldson, and D.M. Jones. Flow of shear-thinning fluids in a concentric annulus. *Exp. Fluids*, 18:225–238, 1995.
- [91] A.J. Faller. Instability and transition of disturbed flow over a rotating disk. *J. Fluid Mech.*, 230:245–269, 1991.
- [92] A. Fasquelle. *Contribution à la modélisation multi-physique: électro-vibro-acoustique et aérothermique de machines de traction*. PhD thesis, École Centrale de Lille, 2007.
- [93] S. Fauve, C. Laroche, and B. Castaing. Pressure fluctuations in swirling turbulent flows. *J. Phys. II France*, 3:271–278, 1993.
- [94] M. Fénot, Y. Bertin, E. Dorignac, and G. Lalizel. A review of heat transfer between concentric rotating cylinders with or without axial flow. *Int. J. Thermal Sci.*, 50:1138–1155, 2011.
- [95] H.E. Fettis. On the integration of a class of differential equations occurring in boundary layer and other hydrodynamic problems. In *Proc. Fourth Midwest Conf. on Fluid Mech.*, pages 93–114, Purdue, 1955.
- [96] J.B. Fink. Forced expiratory technique, directed cough, and autogenic drainage. In *39th Respiratory Care Journal Conference; Airway Clearance: Physiology, Pharmacology, Techniques, and Practice*, Cancun, Mexico, 2007.
- [97] G. Fontaine. *Développement d'un solveur pseudospectral multidomaine parallèle pour la résolution des équations de Navier-Stokes tridimensionnelles en coordonnées cylindriques*. PhD thesis, Aix-Marseille Université, 2012.
- [98] G. Fontaine, S. Poncet, and E. Serre. Multidomain extension of a divergence-free pseudo-spectral algorithm for the direct numerical simulation of wall-confined rotating flows. *Lecture Notes Comput. Sci. Eng.*, 95:261–271, 2014.
- [99] C. Friess, S. Poncet, and S. Viazzo. Taylor-Couette-Poiseuille flows: from RANS to LES. In *Int. Symp. Turb. Shear Flow Phenomena, TSFP8*, Poitiers, 2013.
- [100] W.G. Früh and P.L. Read. Experiments on a barotropic rotating shear layer. Part 1. instability and steady vortices. *J. Fluid Mech.*, 383:143–173, 1999.
- [101] N. Fukushima, T. Fushimi, M. Shimura, M. Tanahashi, and T. Miyauchi. Dynamics of large- and small-scale vortical structures in turbulent Taylor-Couette flow. In *Int. Symp. Turb. Shear Flow Phenomena, TSFP7*, Ottawa, 2011.
- [102] X. Gan, M. Kilic, and J.M. Owen. Superposed flow between two discs contrarotating at differential speeds. *Int. J. Heat Fluid Flow*, 15(6):438–446, 1994.

- [103] N. Gao and D. Ewing. Investigation of the effect of confinement on the heat transfer to round impinging jets exiting a long pipe. *Int. J. Heat Fluid Flow*, 27(1):33–41, 2006.
- [104] G. Gauthier, P. Gondret, F. Moisy, and M. Rabaud. Instabilities in the flow between co- and counter-rotating disks. *J. Fluid Mech.*, 473:1–21, 2002.
- [105] G. Gauthier, P. Gondret, and M. Rabaud. Axisymmetric propagating vortices in the flow between a stationary and a rotating disk enclosed by a cylinder. *J. Fluid. Mech.*, 386:105–126, 1999.
- [106] M. Germano, U. Piomelli, P. Moin, and W. Cabot. A dynamic subgrid-scale eddy viscosity model. *Phys. Fluids A*, 3 (7):1760–1765, 1991.
- [107] A.V. Getling. Rayleigh-Bénard convection: structure and dynamics. In *Advances in Nonlinear Dynamics, Vol.11*, Singapore, 1998.
- [108] M. Gibson and B.E. Launder. Ground effects on pressure fluctuations in the atmospheric boundary layer. *J. Fluid. Mech.*, 86(3):491–511, 1978.
- [109] S. Gilchrist, C.Y. Ching, and D. Ewing. Heat transfer enhancement in axial Taylor-Couette flow. *ASME Conference Proceedings*, pages 227–233, 2005.
- [110] A. Giret. *Transferts thermiques convectifs dans le cadre de machines tournantes*. PhD thesis, Université de Poitiers, 2009.
- [111] K. Goda. A multistep technique with implicit difference schemes for calculating two or three dimensional cavity flows. *J. Comp. Phys.*, 30:76–95, 1979.
- [112] A. Goharzadeh and I. Mutabazi. Experimental characterization of intermittency regimes in the Couette-Taylor system. *Eur. Phys. J. B*, 19:157–162, 2001.
- [113] D.D. Gray and A. Giorgini. The validity of the Boussinesq approximation for liquids and gases. *Int. J. Heat Mass Transfer*, 19:545–551, 1976.
- [114] H.P. Greenspan. *The Theory of Rotating Fluids*. Cambridge University Press, 1968.
- [115] M. Grosgeorges. *Contribution à l'étude du refroidissement d'une paroi tournante par air chargé d'huile*. PhD thesis, Université de Nancy, 1983.
- [116] J.L. Guermond, J.T. Oden, and S. Prudhomme. Mathematical perspectives on large eddy simulation models for turbulent flows. *J. Math. Fluid Mech.*, 6:194–248, 2004.
- [117] R. Guillerm. *Étude expérimentale des instabilités thermo-hydrodynamiques dans un système de Couette-Taylor*. PhD thesis, Université du Havre, 2010.
- [118] R. Guillerm, R. Da Soghe, C. Bianchini, S. Poncet, and S. Viazzo. Numerical predictions of flow field in closed and opened Taylor-Couette cavities. In *4th European Conference for Aerospace Sciences*, Saint-Petersburg, 2011.
- [119] S. Haddadi and S. Poncet. Turbulence modeling of torsional Couette flows. *Int. J. Rotating Machinery*, (Article ID 635138), 2008.
- [120] M. Hadžiabdić and K. Hanjalić. Vortical structures and heat transfer in a round impinging jet. *J. Fluid Mech.*, 596:221–260, 2008.
- [121] K. Hanjalic and B. E. Launder. Contribution towards a Reynolds-stress closure for low-Reynolds number turbulence. *J. Fluid Mech.*, 74:583–610, 1976.
- [122] D.M. Hannah. Forced flow against a rotating disc. *ARC-RM-2772*, 1952.
- [123] S. Harmand, J. Pellé, S. Poncet, and I. Shevchuk. Review of fluid flow and convective heat transfer within rotating disk cavities with impinging jet. *Int. J. Therm. Sci.*, 67:1–30, 2013.
- [124] S. Harmand, B. Watel, and B. Desmet. Local convective heat exchanges from a rotor facing a stator. *Int. J. Therm. Sci.*, 11(1):404–413, 2000.
- [125] W. Heinrichs. Spectral collocation schemes on the unit disc. *J. Comp. Phys.*, 199:66–86, 2004.
- [126] J. Herrero, F. Giralt, and J.A.C. Humphrey. Influence of the geometry on the structure of the flow between a pair of corotating disks. *Phys. Fluids*, 11(1):88–96, 1999.
- [127] R. Hide and C.W. Titman. Detached shear layers in a rotating fluid. *J. Fluid. Mech.*, 29(1):39–60, 1967.
- [128] S. Hirai, K. Takagi, K. Tanaka, and T. Higashiya. Turbulent heat transfer to the flow in a concentric annulus with a rotating inner cylinder. In *Proc. of the 8th Int. Heat Transfer Conf.*, San Francisco, 1986.
- [129] V. Hoarau. *Simulation de l'écoulement du mucus dans les bronchioles respirantes et influence du SIMEOX*. École de l'Air de Salon, Master 1 report, 2013.

- [130] R. Hollerbach and A. Fournier. End-effects in rapidly rotating cylindrical Taylor-Couette flow. In *AIP Conference proceedings*, volume 733, pages 114–121, New-York, 2004. Ed. Rosner et al., AIP Press.
- [131] M. Holodniok, M. Kubicek, and V. Hlavacek. Computation of the flow between two rotating coaxial disks: multiplicity of steady-state solutions. *J. Fluid. Mech.*, 108:227–240, 1981.
- [132] R.F. Huang and M.K. Hsieh. Phase-resolved flow characteristics between two shrouded co-rotating disks. *Exp. Fluids*, 51:1529–1547, 2011.
- [133] R.A. Humble, G.E. Elsinga, F. Scarano, and D.B.W. Van Oudheusden. Three-dimensional instantaneous structure of a shock wave/turbulent boundary layer interaction. *J. Fluid Mech.*, 622:33–62, 2009.
- [134] H. Iacovides and J. W. Chew. The computation of convective heat transfer in rotating cavities. *Int. J. Heat Fluid Flow*, 14(2):146–154, 1992.
- [135] M. Itoh. Experiments on the turbulent flow in the narrow clearance between a rotating and a stationary disk. In T. Kobayashi B.F. Carroll and M.J. Morris, editors, *Turbulent flows*, pages 27–32. ASME-FED Vol.208, 1995.
- [136] M. Itoh, Y. Yamada, S. Imao, and M. Gonda. Experiments on turbulent flow due to an enclosed rotating disk. In W. Rodi and E.N. Ganic, editors, *Engineering Turbulence Modeling and Experiments*, pages 659–668, New-York, 1990. Elsevier.
- [137] M. Itoh, Y. Yamada, S. Imao, and M. Gonda. Experiments on turbulent flow due to an enclosed rotating disk. *Exp. Thermal Fluid Sci.*, 5:359–368, 1992.
- [138] M. Itoh, Y. Yamada, and K. Nishioka. Transition of the flow around an enclosed rotating disk. *Trans. Jpn Soc. Mech. Eng.*, 51:452–460, 1985.
- [139] R. Jakoby, T. Zierer, K. Lindblad, J. Larsson, L. de Vito, D. E. Bohn, J. Funcke, and A. Decker. Numerical simulation of the unsteady flow field in an axial gas turbine rim seal configuration. In *ASME Paper GT2004-53829, ASME Turbo Expo 2004*, Vienna, 2004.
- [140] H. Ji, M. Burin, E. Schartman, and J. Goodman. Hydrodynamic turbulence cannot transport angular momentum effectively in astrophysical disks. *Nature*, 444:343–346, 2006.
- [141] S.Y. Jung and H.J. Sung. Characterization of the three-dimensional turbulent boundary layer in a concentric annulus with a rotating inner cylinder. *Phys. Fluids*, 18(115102):1–11, 2006.
- [142] A. Kageyama, H. Ji, J. Goodman, F. Chen, and E. Shoshan. Numerical and experimental investigation of circulation in short cylinders. *J. Phys. Soc. Japan*, 73(9):2424–2437, 2004.
- [143] L. Kahouadji. *Analyse de stabilité linéaire d'écoulements tournants en présence de surface libre*. PhD thesis, Université Pierre et Marie Curie - Paris VI, 2011.
- [144] L. Kahouadji, L. Martin-Witkowski, and P. Le Quéré. Seuils de stabilité pour un écoulement à surface libre engendré dans une cavité cylindrique à petit rapport de forme. *Mécanique & Industries*, 11(5):339–344, 2010.
- [145] H.S. Kang, H. Choi, and J.Y. Yoo. On the modification of the near-wall coherent structure in a three-dimensional turbulent boundary layer on a free rotating disk. *Phys. Fluids*, 10(9):2315–2322, 1998.
- [146] G.S. Karamanos and G.E. Karniadakis. A spectral vanishing viscosity method for large eddy simulation. *J. Comp. Phys.*, 163:22–50, 2000.
- [147] G.E. Karniadakis, M. Israeli, and S.A. Orszag. High-order splitting methods for the incompressible Navier-Stokes equations. *J. Comp. Phys.*, 97:414–443, 1991.
- [148] V. Katti and SV Prabhu. Experimental study and theoretical analysis of local heat transfer distribution between smooth flat surface and impinging air jet from a circular straight pipe nozzle. *Int. J. Heat Mass Transfer*, 51(17-18):4480–4495, 2008.
- [149] M. Kauffeld, M. Kawaji, and P. Egolf. *Handbook on Ice Slurries Fundamentals and Engineering*. IIF/IIR, 2005.
- [150] J. Kaye and E. C. Elgar. Modes of adiabatic and diabatic fluid flow in an annulus with an inner rotating cylinder. *Trans. ASME*, 80:753–765, 1958.
- [151] W.M. Kays. Turbulent Prandtl number - where are we ? *Trans. ASME*, 116:284–295, 1994.
- [152] R. Kedia, M.L. Hunt, and T. Colonius. Numerical simulations of heat transfer in Taylor-Couette flow. *J. Heat Transfer*, 120:65–71, 1998.
- [153] H.B. Keller. A new difference scheme for parabolic problems. in numerical solution of partial differential equations II. In *Proc. Sympos. of SYNSPADE 1970*, pages 327–350, New-York, 1971. Academic Press.
- [154] M. Kilic, X. Gan, and J.M. Owen. Transitional flow between contra-rotating disks. *J. Fluid Mech.*, 281:119–135, 1994.

- [155] G.P. King, Y. Li, W. Lee, H.L. Swinney, and P.S. Marcus. Wave speeds in wavy Taylor-vortex flow. *J. Fluid Mech.*, 141:365–390, 1984.
- [156] C.W. Kitchens and T.S. Chang. Newtonian and non-Newtonian liquids rotating adjacent to a stationary surface. *Appl. Sci. Res.*, 27:283–296, 1973.
- [157] K. Koal, J. Stiller, and H.M. Blackburn. Adapting the spectral vanishing viscosity method for large-eddy simulations in cylindrical configurations. *J. Comput. Phys.*, 231:3389–3405, 2012.
- [158] J. Kompenhans, M. Raffel, S.T. Wereley, and C.E. Willert. *Particle image velocimetry: a practical guide; with 42 tables*. Springer, 2007.
- [159] T. Kousksou, J.P. Bédécarrats, F. Strub, and J. Castaing-Lasvignottes. Numerical simulation of fluid flow and heat transfer in a phase change thermal energy storage. *Int. J. Energy Technology Policy*, 6(1-2):143–158, 2008.
- [160] R.H. Kraichnan. Eddy viscosity in two and three dimensions. *J. Atmos. Sci.*, 33:1521, 1976.
- [161] H.O. Kreiss and S.V. Parter. On the swirling flow between rotating coaxial disks: existence and uniqueness. *Commun. Pure Appl. Math.*, 36:55–84, 1983.
- [162] R.P.J. Kunnen, H.J.H. Clercx, B.J. Geurts, L.J.A. Van Bokhoven, R.A.D. Akkermans, and R. Verzicco. Numerical and experimental investigation of structure function scaling in turbulent Rayleigh-Bénard convection. *Phys. Rev. E*, 77:016302, 2008.
- [163] D.C. Kuo and K.S. Ball. Taylor-Couette flow with buoyancy: onset of spiral flow. *Phys. Fluids*, 9(10):2872–2884, 1997.
- [164] M. Kuosa, P. Sallinen, and J. Larjola. Numerical and experimental modelling of gas flow and heat transfer in the air gap of an electric machine. *J. Thermal Science*, 13(3):264–278, 2004.
- [165] T. M. Kuzay and C. J. Scott. Turbulent heat transfer studies in annulus with inner cylinder rotation. *J. Heat Transfer*, 99:12–19, 1977.
- [166] R. Laguerre, C. Nore, A. Ribeiro, J. Léorat, J.L. Guermond, and F. Plunian. Impact of impellers on the axisymmetric magnetic mode in the VKS2 dynamo experiment. *Phys. Rev. Lett.*, 101:104501, 2008.
- [167] G.N. Lance and M.H. Rogers. The axially symmetric flow of a viscous fluid between two infinite rotating disks. *Proc. R. Soc. London A*, 266:109–121, 1962.
- [168] D. Lathrop, J. Fineberg, and H.L. Swinney. Transition to shear-driven turbulence in Taylor-Couette flow. *Phys. Rev. A*, 46:6390–6408, 1992.
- [169] B. E. Launder, W. C. Reynolds, W. Rodi, J. Mathieu, and D. Jeandel. *Turbulence models and their applications*. Ed. Eyrolles, Paris, 1984.
- [170] B.E. Launder, S. Poncet, and E. Serre. Laminar, transitional, and turbulent flows in rotor-stator cavities. *Annu. Rev. Fluid Mech.*, 42:229–248, 2010.
- [171] B.E. Launder and W.C. Reynolds. Asymptotic near-wall stress dissipation rates in a turbulent flow. *Phys. Fluids A*, 26(5):1157–1158, 1983.
- [172] B.E. Launder and B.I. Sharma. Application of the energy dissipation model of turbulence to the calculation of flow near a spinning disc. *Lett. Heat Mass Transfer*, 1:131–138, 1974.
- [173] B.E. Launder and D.P. Tselepidakis. Application of a new second-moment closure to turbulent channel flow rotating in orthogonal mode. *Int. J. Heat Fluid Flow*, 15(1):2–10, 1994.
- [174] M. Le Bars and P. Le Gal. Experimental analysis of the stratorotational instability in a cylindrical Couette flow. *Phys. Rev. Lett.*, 99:064502, 2007.
- [175] Y. N. Lee and W. J. Minkowycz. Heat transfer characteristics of the annulus of two-coaxial cylinders with one cylinder rotating. *Int. J. Heat Mass Transfer*, 32(4):711–722, 1989.
- [176] S. Leibovich and K. Stewartson. A sufficient condition for the instability of columnar vortices. *J. Fluid Mech.*, 126:335–356, 1983.
- [177] S.K. Lele. Compact finite difference schemes with spectral-like resolution. *J. Comp. Phys.*, 103:16–42, 1992.
- [178] J. Léorat and C. Nore. Interplay between experimental and numerical approaches in the fluid dynamo problem. *C. R. Phys.*, 9:741–748, 2008.
- [179] V. Lepiller. *Etude expérimentale des instabilités hydro-thermiques dans un anneau cylindrique vertical de Couette-Taylor soumis à un gradient radial de température*. PhD thesis, Université du Havre, 2006.
- [180] V. Lepiller, A. Goharzadeh, A. Prigent, and I. Mutabazi. Weak temperature gradient effect on the stability of the circular Couette flow. *Eur. Phys. J. B*, 61:445–455, 2008.

- [181] N. Leprovost, B. Dubrulle, and P.-H. Chavanis. Dynamics and thermodynamics of axisymmetric flows: Theory. *Phys. Rev. E*, 73:046308, 2006.
- [182] G.S. Lewis and H.L. Swinney. Velocity structure functions, scaling, and transitions in high Reynolds number Couette-Taylor flow. *Phys. Rev. E*, 59(5):5457–5467, 1999.
- [183] D.K. Lilly. A proposed modification of the Germano subgrid-scale closure method. *Phys. Fluids A*, 4:633–635, 1992.
- [184] R.J. Lingwood. Absolute instability of the Ekman layer and related rotating flows. *J. Fluid. Mech.*, 331:405–428, 1997.
- [185] H.S. Littell and J.K. Eaton. Turbulence characteristics of the boundary layer on a rotating disk. *J. Fluid. Mech.*, 266:175–207, 1994.
- [186] D. Liu, S.H. Choi, and H.B. Kim. Experiments on the stability of Taylor-Couette flow with radial temperature gradient. Moscow, 2009. FLUCOME.
- [187] J.M. Lopez, J.E. Hart, F. Marques, S. Kittelman, and J. Shen. Instability and mode interactions in a differentially-driven rotating cylinder. *J. Fluid Mech.*, 462:383–409, 2002.
- [188] J.M. Lopez, F. Marques, and M. Avila. The Boussinesq approximation in rapidly rotating flows. *J. Fluid Mech.*, 737:56–77, 2013.
- [189] J.M. Lopez, F. Marques, A.M. Rubio, and M. Avila. Crossflow instability of finite Bödewadt flows: transient and spiral waves. *Phys. Fluids*, 21:114107, 2009.
- [190] J.M. Lopez and P.D. Weidman. Stability of stationary endwall boundary layers during spin-down. *J. Fluid Mech.*, 326:373–398, 1996.
- [191] R. Lueptow. Taylor-Couette flow. *Scholarpedia*, 4(11):6389, 2009.
- [192] J.L. Lumley. Computational modeling of turbulent flows. *Adv. Appl. Mech.*, 18:123–176, 1978.
- [193] M. Lygren and H. I. Andersson. Turbulent flow between a rotating and a stationary disk. *J. Fluid. Mech.*, 426:297–326, 2001.
- [194] M. Lygren and H. I. Andersson. Large eddy simulations of the turbulent flow between a rotating and a stationary disk. *Z. Angew. Math. Phys.*, 55:268–281, 2004.
- [195] H. Ma. Chebyshev-Legendre super spectral viscosity method for nonlinear conservation laws. *SIAM J. Numer. Anal.*, 35:893–908, 1998.
- [196] Y. Maday, S. Ould-Kaber, and E. Tadmor. Legendre pseudospectral viscosity method for nonlinear conservation laws. *SIAM J. Numer. Anal.*, 30:321–342, 1993.
- [197] R. Manceau, R. Perrin, M. Hadziabdic, P. Fourment, and S. Benhamadouche. Turbulent jet impinging onto a rotating disc: a collaborative evaluation of RANS models. *Turbulence, Heat and Mass Transfer 6*, Begell House, 2009.
- [198] D.Y. Manin. Characteristics size of vortices in developed quasi-two-dimensional flows. *Izvestiya, Atmospheric and Oceanic Physics*, 26(6):426–429, 1990.
- [199] L. Marié and F. Daviaud. Experimental measurement of the scale-by-scale momentum transport budget in a turbulent shear flow. *Phys. Fluids*, 16(2):457–461, 2004.
- [200] M.T. Matthews and J.M. Hill. Newtonian flow with nonlinear Navier boundary condition. *Acta Mech.*, 191(3-4):195–217, 2007.
- [201] J. Maurer, P. Tabeling, and G. Zocchi. Statistics of turbulence between two counterrotating disks in low-temperature helium gas. *Europhys. Lett.*, 26(1):31–36, 1994.
- [202] J.B. McLeod and S.V. Parter. On the flow between two counter-rotating infinite plane disks. *Arch. Ration. Mech. Anal.*, 54:301–327, 1974.
- [203] S. Mellari, M. Boumaza, and P.W. Egolf. Physical modeling, numerical simulations and experimental investigations of non-Newtonian ice slurry flows. *Int. J. Refrigeration*, 35:1284–1291, 2012.
- [204] C. Meneveau, T.S. Lund, and W.H. Cabot. A Lagrangian dynamic subgrid-scale model of turbulence. *J. Fluid Mech.*, 319:353–385, 1996.
- [205] S. Menon, P.K. Yeung, and W.W. Kim. Effect of subgrid models on the computed interscale energy transfer in isotropic turbulence. *Comput. Fluids*, 25(2):165–180, 1996.
- [206] F.R. Menter and Y. Egorov. A scale-adaptive simulation model using two-equation models. In *AIAA paper 2005-1095*, Reno/NV, 2005.

- [207] F.R. Menter and Y. Egorov. The scale-adaptive simulation method for unsteady flow predictions. In *Aerodynamic noise from wall-bounded flows*. Von Kármán lecture series 03, 2009.
- [208] I. Mercader, O. Batiste, and A. Alonso. An efficient spectral code for incompressible flows in cylindrical geometries. *Comput. Fluids*, 39:215–224, 2010.
- [209] P. Meunier and T. Leweke. Analysis and minimization of errors due to high gradients in particle image velocimetry. *Exp. Fluids*, 35:408–421, 2003.
- [210] M. Miklavčič and C.Y. Wang. The flow due to a rough rotating disk. *Z. Angew. Math. Phys.*, 55:235–246, 2004.
- [211] Y. Minagawa and S. Obi. Development of turbulent impinging jet on a rotating disk. *Int. J. Heat Fluid Flow*, 25:759–766, 2004.
- [212] F. Moisy, O. Doaré, T. Pasutto, O. Daube, and M. Rabaud. Experimental and numerical study of the shear-layer instability between two-counter-rotating disks. *J. Fluid Mech.*, 507:175–202, 2004.
- [213] R. Monchaux, F. Ravelet, B. Dubrulle, A. Chiffaudel, and F. Daviaud. Properties of steady states in turbulent axisymmetric flows. *Phys. Rev. Lett.*, 96(12):124502, 2006.
- [214] N. Mordant, J.-F. Pinton, and F. Chillà. Characterization of turbulence in a closed flow. *J. Phys. II France*, 7:1729–1742, 1997.
- [215] K. Nakabayashi, O. Kitoh, and Y. Katoh. Similarity laws of velocity profiles and turbulence characteristics of Couette-Poiseuille turbulent flows. *J. Fluid Mech.*, 507:43–69, 2004.
- [216] R.S. Nanda. Revolving flow of an incompressible fluid past a porous flat plate. *J. Sci. Engng. Res.*, 5:59–64, 1960.
- [217] J. A. Naser. Prediction of Newtonian and non-Newtonian flow through concentric annulus with centerbody rotation. CSIRO, 1997. Int. Conf. on CFS in Mineral and Metal Processing and Power Generation.
- [218] C.L.M. Navier. Sur les lois du mouvement des fluides. *Comp. Rend. Acad. Sci.*, 6:389–440, 1827.
- [219] N. Nguyen, J.P. Ribault, and P. Florent. Multiple solutions for flow between coaxial disks. *J. Fluid Mech.*, 68(2):369–388, 1975.
- [220] T.D. Nguyen, J. Pellé, S. Harmand, and S. Poncet. PIV measurements of an air jet impinging on an open rotor-stator system. *Exp. Fluids*, 53:401–412, 2012.
- [221] R. Ngwong. *Étude sur la caractérisation rhéologique du mucus bronchique: simulation numérique de l'écoulement air/mucus dans la trachée*. Aix-Marseille Université, Master 1 report, 2013.
- [222] F. Nicoud and F. Ducros. Subgrid-scale stress modelling based on the square of the velocity gradient tensor. *Flow, Turbulence & Combustion*, 62(3):183–200, 1999.
- [223] H. Niino and N. Misawa. An experimental and theoretical study of barotropic instability. *J. Atmos. Sci.*, 41:1992–2011, 1984.
- [224] C. Nore, L. Martin Witkowski, E. Foucault, J. Pécheux, O. Daube, and P. Le Quéré. Competition between axisymmetric and three-dimensional patterns between exactly counter-rotating disks. *Phys. Fluids*, 18:054102, 2006.
- [225] C. Nore, F. Moisy, and L. Quartier. Experimental observation of near-heteroclinic cycles in the von Kármán swirling flow. *Phys. Fluids*, 17:064103, 2005.
- [226] J. M. Nouri and J. H. Whitelaw. Flow of Newtonian and non-Newtonian fluids in a concentric annulus with rotation of the inner cylinder. *J. Fluid Eng.*, 116:821–827, 1994.
- [227] J. M. Nouri and J. H. Whitelaw. Flow of Newtonian and non-Newtonian fluids in an eccentric annulus with rotation of the inner cylinder. *Int. J. Heat Fluid Flow*, 18:236–246, 1997.
- [228] J.E. Nydahl. *Heat transfer for the Bödewadt problem*. PhD thesis, Colorado State University, 1971.
- [229] C. L. Ong. *Computation of fluid flow and heat transfer in rotating disc systems*. PhD thesis, University of Sussex, 1988.
- [230] S.A. Orszag and A.T. Patera. Secondary instability of wall-bounded shear flows. *J. Fluid Mech.*, 128:347–385, 1983.
- [231] J. M. Owen. Flow and heat transfer in rotating disc systems. In *CHT01 Turbulence heat and mass transfer*, pages 33–58. Ed. Y. Nagano, K. Hanjalic, T. Tsuji, Aichi Shuppan Press, 2000.
- [232] J. M. Owen and C. M. Haynes. Design formulae for the heat loss and frictional resistance of air-cooled rotating discs - vol.4. In *Improvements in fluid mechanics and systems for energy conversion*, Milan, 1976.

- [233] J.M. Owen and R.H. Rogers. *Flow and heat transfer in rotating disk systems. Vol. 1: Rotor-Stator Systems*. Ed. Morris, W.D. John Wiley and Sons Inc., New-York, 1989.
- [234] R. Pasquetti and C.J. Xu. High-order algorithms for large-eddy simulation of incompressible flows. *J. Sci. Comp.*, 17(1-4):273–284, 2002.
- [235] S.V. Patankar. *Numerical heat transfer and fluid flow*. Mac Graw Hill, New-York, 1980.
- [236] C.E. Pearson. Numerical solutions for time-dependent viscous flow between rotating coaxial disks. *J. Fluid Mech.*, 21(4):623–633, 1965.
- [237] J. Pellé and S. Harmand. Heat transfer measurements in an open rotor-stator system air-gap. *Exp. Therm. Fluid Sci.*, 31:165–180, 2007.
- [238] J. Pellé and S. Harmand. Heat transfer study in a rotor-stator system air-gap with an axial inflow. *Appl. Therm. Eng.*, 29:1532–1543, 2009.
- [239] J. Pellé and S. Harmand. Convective heat transfer in a rotor stator system air gap with multiple suctions of fluid through the stator. *J. Heat Transfer*, 133:071707, 2011.
- [240] I. Peres. *Contribution à l'analyse de l'écoulement et des transferts convectifs dans un espace annulaire lisse ou encoché par voie de simulations numériques. Application à un transfert de moteur électrique rapide*. PhD thesis, Université de Poitiers, 1995.
- [241] N. Peres. *A 3D pseudospectral method for cylindrical coordinates. Application to the simulations of rotating cavity flows*. PhD thesis, Aix-Marseille Université, 2012.
- [242] N. Peres, S. Poncet, and E. Serre. A 3D pseudospectral method for cylindrical coordinates. Application to the simulations of rotating cavity flows. *J. Comput. Phys.*, 231:6290–6305, 2012.
- [243] H.J. Pesch and P. Rentrop. Numerical solution of the flow between two counter-rotating infinite plane disks by multiple shooting. *Z. Angew. Math. Mech.*, 58:23–28, 1978.
- [244] R. Peyret. *Spectral methods for incompressible viscous flow*. Springer-Verlag, New-York, 2002.
- [245] B. Pier. Finite amplitude crossflow vortices, secondary instability and transition in the rotating-disk boundary layer. *J. Fluid Mech.*, 487:315–343, 2003.
- [246] A. Pinelli, I.Z. Naqavi, U. Piomelli, and J. Favier. Immersed-boundary methods for general finite-difference and finite-volume Navier-Stokes solvers. *J. Comp. Phys.*, 229(24):9073–9091, 2010.
- [247] J.-F. Pinton, P.C.W. Holdsworth, and R. Labbé. Power fluctuations in a closed turbulent shear flow. *Phys. Rev. E*, 60(3):2452–2455, 1999.
- [248] J. W. Polkowski. Turbulent flow between coaxial cylinders with inner cylinder rotating. *Trans. ASME, Journal for Gas Turbines and Power*, 106(1):128–135, 1984.
- [249] S. Poncet. *Écoulements de type rotor-stator soumis à un flux axial: de Batchelor à Stewartson*. PhD thesis, Université de Provence (Aix-Marseille I), 2005.
- [250] S. Poncet and M. P. Chauve. Shear-layer instability in a rotating system. *J. Flow Visualization & Image Processing*, 14(1):85–105, 2007.
- [251] S. Poncet, M. P. Chauve, and P. Le Gal. Turbulent rotating disk with inward throughflow. *J. Fluid. Mech.*, 522:253–262, 2005.
- [252] S. Poncet and M.P. Chauve. Crossflow instability in a rotor-stator cavity with axial inward throughflow. *J. Fluid Mech.*, 545:281–289, 2005.
- [253] S. Poncet, M.P. Chauve, and R. Schiestel. Batchelor versus Stewartson flow structures in a rotor-stator cavity with throughflow. *Phys. Fluids*, 17(075110), 2005.
- [254] S. Poncet, R. Da Soghe, C. Bianchini, S. Viazzo, and A. Aubert. Turbulent Couette-Taylor flows with endwall effects: a numerical benchmark. *Int. J. Heat Fluid Flow*, 44:229–238, 2013.
- [255] S. Poncet, R. Da Soghe, and B. Facchini. RANS modelings of flows in rotating disk systems. In *Eccomas CFD 2010*, Lisbon, 2010.
- [256] S. Poncet, S. Haddadi, and S. Viazzo. Numerical modeling of fluid flow and heat transfer in a narrow Taylor-Couette-Poiseuille system. *Int. J. Heat Fluid Flow*, 32:128–144, 2011.
- [257] S. Poncet, T.D. Nguyen, J. Pellé, S. Harmand, R. Da Soghe, C. Bianchini, and S. Viazzo. Turbulent impinging jet flow into an unshrouded rotor-stator system: hydrodynamics and heat transfer. *Int. J. Heat Fluid Flow*, 44:719–734, 2013.

- [258] S. Poncet and R. Schiestel. Numerical modeling of heat transfer and fluid flow in rotor-stator cavities with throughflow. *Int. J. Heat Mass Transfer*, 50(7-8):1528–1544, 2007.
- [259] S. Poncet, R. Schiestel, and R. Monchaux. Turbulence modeling of the Von Kármán flow: viscous and inertial stirrings. *Int. J. Heat Fluid Flow*, 29(1):62–74, 2008.
- [260] S. Poncet and E. Serre. High-order LES of turbulent heat transfers in a rotor-stator cavity. *Int. J. Heat Fluid Flow*, 30(4):590–601, 2009.
- [261] S. Poncet, E. Serre, and P. Le Gal. Revisiting the two first instabilities of the flow in an annular rotor-stator cavity. *Phys. Fluids*, 21(6):064106, 2009.
- [262] S. Poncet and I. Seyssiecq-Guarente. *Étude sur la caractérisation rhéologique du mucus bronchique - Étude bibliographique*. Physio-Assist, Contract 080931, 2012.
- [263] C.O. Popiel and L. Boguslawski. Local heat transfer from a rotating disk in an impinging round jet. *ASME J. Heat Transfer*, 108:357–364, 1986.
- [264] R. Porcar, J.P. Prenel, and C. Robert. Visualisation des ondes de choc dans un éjecteur supersonique. *Optics Communications*, 14(1):104–107, 1975.
- [265] M. Rabaud and Y. Couder. A shear-flow instability in a circular geometry. *J. Fluid Mech.*, 136:291–319, 1983.
- [266] A. Randriamampianina and S. Poncet. Turbulence characteristics of the Bödewadt layer in a large enclosed rotor-stator system. *Phys. Fluids*, 18:055104, 2008.
- [267] A. Randriamampianina, R. Schiestel, and M. Wilson. Spatio-temporal behaviour in an enclosed corotating disk pair. *J. Fluid Mech.*, 434:39–64, 2001.
- [268] I. Raspo. A direct spectral domain decomposition method for the computation of rotating flows in a T-shape geometry. *Comput. Fluids*, 32:431–456, 2003.
- [269] I. Raspo, S. Hugues, E. Serre, A. Randriamampianina, and P. Bontoux. A spectral projection method for the simulation of complex three-dimensional rotating flows. *Comput. Fluids*, 31:745–767, 2002.
- [270] F. Ravelet. *Bifurcations globales hydrodynamiques et magnétohydrodynamiques dans un écoulement de Von Kármán turbulent*. PhD thesis, Ecole Polytechnique, 2005.
- [271] F. Ravelet, A. Chiffaudel, F. Daviaud, and J. Léorat. Toward an experimental Von Kármán dynamo: numerical studies for an optimized design. *Phys. Fluids*, 17(11):117104, 2005.
- [272] F. Ravelet, L. Marié, A. Chiffaudel, and F. Daviaud. Multistability and memory effect in a highly turbulent flow: experimental evidence for a global bifurcation. *Phys. Rev. Letters*, 93(16), 2004.
- [273] C. Reddick, Y. Mercadier, and M. Ouzzane. Experimental study of an ejector refrigeration system. In *Int. Refrig. & Air Conditioning Conf.*, Purdue, USA, 2012.
- [274] J.C. Reddick. *Conception, construction et analyse d'un système de réfrigération à éjecteur*. PhD thesis, Université de Sherbrooke, 2011.
- [275] S. Renaud-Boivin, M. Poirier, and N. Galanis. Experimental study of hydraulic and thermal behavior of an ice slurry in a shell and tube heat exchanger. *Exp. Ther. Fluid Sci.*, 37:130–141, 2012.
- [276] W.C. Reynolds. Towards a structure-based turbulence model. In T.B. Gatski, S. Sarkar, and C.G. Speziale, editors, *Studies in Turbulence*. Springer-Verlag, 1991.
- [277] D.F. Rogers and M.I. Lethem. *Airway Mucus: Basic Mechanisms and Clinical Perspectives (Respiratory Pharmacology and Pharmacotherapy)*. Stuttgart, 1997.
- [278] M.H. Rogers and G.N. Lance. The rotationally symmetric flow of a viscous fluid in the presence of an infinite rotating disk. *J. Fluid Mech.*, 7:617–631, 1960.
- [279] M.H. Rogers and G.N. Lance. The boundary layer on a disk of finite radius in a rotating fluid. *Quart. J. Mech. Appl. Math.*, 17:319–330, 1964.
- [280] J.C. Rotta. *Turbulente Strömungen*. Teubner, Stuttgart, 1972.
- [281] R. P. Roy, G. Xu, and J. Feng. A study of convective heat transfer in a model rotor-stator disk cavity. *ASME J. Turbomach.*, 123:621–632, 2001.
- [282] B. Sagot, G. Antonini, A. Christgen, and F. Buron. Jet impingement heat transfer on a flat plate at a constant wall temperature. *Int. J. Thermal Sci.*, 47(12):1610–1619, 2008.
- [283] B. Sahoo. Effects of partial slip, viscous dissipation, Joule heating on Von Kármán flow and heat transfer of an electrically conducting non-Newtonian fluid. *Comm. Nonlin. Sci. Num. Sim.*, 14(23-24):2982–2998, 2009.

- [284] B. Sahoo. Flow and heat transfer of an electrically conducting third grade fluid past an infinite plate with partial slip. *Meccanica*, 45:319–330, 2010.
- [285] B. Sahoo and S. Poncet. Flow and heat transfer of a third grade fluid past an exponentially stretching sheet with partial slip boundary condition. *Int. J. Heat Mass Transfer*, 54(23-24):5010–5019, 2011.
- [286] B. Sahoo and S. Poncet. Effects of slip on steady Bödewadt flow of a non-Newtonian fluid. *Comm. Nonlinear Sci. Num. Sim.*, 17:4181–4191, 2012.
- [287] B. Sahoo and S. Poncet. Blasius flow and heat transfer of a fourth grade fluid with slip. *Appl. Math. Mech.*, 34(12):1465–1480, 2013.
- [288] B. Sahoo and H.G. Sharma. Effects of partial slip on the steady Von Kármán flow and heat transfer of a non-Newtonian fluid. *Bull. Braz. Math. Soc.*, 38:595–609, 2007.
- [289] D.K. Salkuyeh. Generalized Jacobi and Gauss-Seidel methods for solving linear system of equations. *Numer. Math. J. Chinese Univ. (English Ser.)*, 16:164–170, 2007.
- [290] P.I. San'kov and E.M. Smirnov. Stability of viscous flow between rotating and stationary disks. *Mekhanika Zhidkoshi i gaza*, 6:79–87, 1991.
- [291] O.N. Sara, J. Erkmén, S. Yapıcı, and M. Çopur. Electrochemical mass transfer between an impinging jet and a rotating disk in a confined system. *Int. Comm. Heat Mass Transfer*, 35(3):289–298, 2008.
- [292] W.S. Saric, H.L. Reed, and E.B. White. Stability and transition of three-dimensional boundary layers. *Ann. Rev. Fluid Mech.*, 35:413–440, 2003.
- [293] O. Savas. Circular waves on a stationary disk in rotating flow. *Phys. Fluids*, 26:3445–3448, 1983.
- [294] O. Savas. Stability of Bödewadt flow. *J. Fluid. Mech.*, 183:77–94, 1987.
- [295] N. Schaeffer and P. Cardin. Quasigeostrophic model of the instabilities of the Stewartson layer in flat and depth-varying containers. *Phys. Fluids*, 17, 2005.
- [296] E. Schartman, H. Ji, Burin M.J., and J. Goodman. Stability of quasi-Keplerian shear flow in a laboratory experiment. *Astronomy & Astrophysics*, 543(A94):1–13, 2012.
- [297] R. Schiestel. *Les écoulements turbulents: modélisation et simulation*. Hermès, Paris, 1998.
- [298] R. Schiestel and L. Elena. Modeling of anisotropic turbulence in rapid rotation. *Aerospace Science and Technology*, 7:441–451, 1997.
- [299] R. Schiestel, L. Elena, and T. Rezoug. Numerical modeling of turbulent flow and heat transfer in rotating cavities. *Numer. Heat Transfer A*, 24:45–65, 1993.
- [300] R. Schiestel and S. Viazzo. A Hermitian-Fourier numerical method for solving the incompressible Navier-Stokes equations. *Comput. Fluids*, 24:739–752, 1995.
- [301] H. Schlichting. *Boundary layer theory (7th Edition)*. McGraw-Hill, New-York, 1979.
- [302] L. Schouveiler, P. Le Gal, and M.P. Chauve. Stability of a traveling roll system in a rotating disk flow. *Phys. Fluids*, 10(11):2695–2697, 1998.
- [303] L. Schouveiler, P. Le Gal, and M.P. Chauve. Instabilities of the flow between a rotating and a stationary disk. *J. Fluid. Mech.*, 443:329–350, 2001.
- [304] L. Schouveiler, P. Le Gal, M.P. Chauve, and Y. Takeda. Spiral and circular waves in the flow between a rotating and a stationary disk. *Exp. Fluids*, 26:179–187, 1999.
- [305] E.W. Schwiderski and H.J. Lugt. Rotating flows of Von Kármán and Bödewadt type. *Phys. Fluids*, 7:867–872, 1964.
- [306] E.W. Schwiderski and H.J. Lugt. Rotating flows over a rotating disk. *Ing. Archiv*, 34:198–206, 1965.
- [307] D. Scott, Z. Aidoun, O. Bellache, and M. Ouzzane. CFD simulations of a supersonic ejector for use in refrigeration applications. In *Int. Refrig. & Air Conditioning Conf.*, pages 1–8, Purdue, USA, 2008.
- [308] A. Scotti, C. Meneveau, and D.K. Lilly. Generalized Smagorinsky model for anisotropic grids. *Phys. Fluids*, A5:2306–2308, 1993.
- [309] E. Serre, P. Bontoux, and B. E. Launder. Direct numerical simulation of transitional turbulent flow in an enclosed rotor-stator cavity. *Flow, Turbulence & Combustion*, 69:35–50, 2002.
- [310] E. Serre, P. Bontoux, and B. E. Launder. Transitional-turbulent flow with heat transfer in a closed rotor-stator cavity. *J. Turbulence*, 5:008, 2004.

- [311] E. Serre, E. Crespo Del Arco, and P. Bontoux. Annular and spiral patterns in flows between rotating and stationary discs. *J. Fluid. Mech.*, 434:65–100, 2001.
- [312] E. Serre, O. Czarny, H. Iacovides, P. Bontoux, and B. E. Launder. *Precessing vortex structures in flow within rotor-stator disc cavities: DNS and Visualization Studies*. Eds I.P. Castro, P.E. Hancock and T.G. Thomas, CIMNE, Barcelona, 2002.
- [313] E. Serre and J.P. Pulicani. 3D pseudo-spectral method for convection in rotating cylinder. *Int. J. Comp. Fluids*, 30(4):491–519, 2001.
- [314] E. Serre, E. Tuliska-Sznitko, and P. Bontoux. Coupled numerical and theoretical study of the flow transition between a rotating and stationary disk. *Phys. Fluids*, 16(3):688–706, 2004.
- [315] E. Séverac, S. Poncet, E. Serre, and M. P. Chauve. Large eddy simulation and measurements of turbulent enclosed rotor-stator flows. *Phys. Fluids*, 19:085113, 2007.
- [316] E. Séverac and E. Serre. A spectral vanishing viscosity LES model for the simulation of turbulent flows within rotating cavities. *J. Comp. Phys.*, 226(2):1234–1255, 2007.
- [317] I. Seyssiecq-Guarente and S. Poncet. *Étude sur la caractérisation rhéologique du mucus bronchique - Premiers résultats sur fluides modèles*. Physio-Assist, Contract 080931, 2012.
- [318] J.D. Sherwood. Resistance coefficients for Stokes flow around a disk with a Navier slip condition. *Phys. Fluids*, 24:093103, 2012.
- [319] Y. Shi and Y. Zhang. Simulation of random packing of spherical particles with different size distributions. *Appl. Phys. A.*, 92:621–626, 2008.
- [320] F. Shir, E. Della Torre, L.H. Bennett, C. Mavriplis, and R.D. Shull. Modeling of magnetization and demagnetization in magnetic regenerative refrigeration. *IEEE Transactions on Magnetics*, 40(4):2098–2100, 2004.
- [321] B.M. Siddikov. Numerical simulation of the passive regenerator. *Int. J. App. Sci. Comp.*, 9(2):89–97, 2002.
- [322] D. A. Simmers and J. E. R. Coney. A Reynolds analogy solution for the heat transfer characteristics of combined Taylor vortex and axial flows. *Int. J. Heat Mass Transfer*, 22:679–689, 1979.
- [323] J. Smagorinsky. General circulation experiments with the primitive equations. *Monthly Weather Review*, 91(3):99–164, 1963.
- [324] G.P. Smith and A.A. Townsend. Turbulent Couette flow between concentric cylinders at large Taylor numbers. *J. Fluid Mech.*, 123:187–217, 1982.
- [325] H.A. Snyder and S.K.F. Karlsson. Experiments on the stability of Couette motion with a radial thermal gradient. *Phys. Fluids*, 7(10):1696–1706, 1964.
- [326] V. Sobolik, B. Izrarb, F. Lusseyran, and S. Skali. Interaction between the Ekman layer and the Couette-Taylor instability. *Int. J. Heat Mass Transfer*, 43:4381–4393, 2000.
- [327] J. Sommeria. La Tache Rouge de Jupiter: une clé pour la turbulence? *Le courrier du CNRS*, 77:97–102, 1991.
- [328] M.M. Sorour and J.E.R. Coney. The effect of temperature gradient on the stability of flow between vertical, concentric, rotating cylinders. *J. Mech. Eng. Sci.*, 21:403–409, 1979.
- [329] A.C. Srivastava and G.C. Sarma. Forced flow of a second-order fluid against a rotating disk. *Int. J. Non-Linear Mech.*, 5:525–532, 1970.
- [330] K. Stewartson. On the flow between two rotating coaxial disks. *Proc. Camb. Phil. Soc.*, 49:333–341, 1953.
- [331] K. Stewartson. On almost rigid rotations. *J. Fluid Mech.*, 3:17–26, 1957.
- [332] A. Syed and W.G. Früh. Modelling of mixing in a Taylor-Couette reactor with axial flow. *Chem. Technol. Biotechnol.*, 78:227–235, 2003.
- [333] F. Tachibana and S. Fukui. Convective heat transfer of the rotational and axial flow between two concentric cylinders. *Bulletin JSME*, 7(26):385–391, 1964.
- [334] E. Tadmor. Convergence of spectral methods for nonlinear conservation laws. *SIAM J. Numer. Anal.*, 26(1):30–44, 1989.
- [335] A. A. Tawfek. Heat transfer and pressure distributions of an impinging jet on a flat surface. *Heat Mass Transfer*, 32:49–54, 1996.
- [336] G. I. Taylor. Distribution of velocity and temperature between concentric rotating cylinders. *Proc. Roy. Soc. A*, 265:494–512, 1935.

- [337] G.I. Taylor. Stability of a viscous liquid contained between rotating cylinders. *Phil. Trans. Roy. Soc. Lond.*, 223:289–343, 1923.
- [338] N. Tilton, D. Martinand, E. Serre, and R.M. Lueptow. Pressure-driven radial flow in a Taylor-Couette cell. *J. Fluid Mech.*, 660:527–537, 2010.
- [339] P. Tong, W.J. Goldburg, J.S. Huang, and T.A. Witten. Anisotropy in turbulent drag reduction. *Phys. Rev. Lett.*, 65:2780–2783, 1990.
- [340] P. G. Tucker. Temporal behaviour of flow in rotating cavities. *Numerical Heat Transfer - Part A*, 41(6-7):611–627, 2002.
- [341] J.A. Van de Konijnenberg, A.H. Nielsen, J.J. Rasmussen, and B. Stenum. Shear-flow instability in a rotating fluid. *J. Fluid Mech.*, 387:177–204, 1999.
- [342] A.I. Van de Vooren. The connection between Ekman and Stewartson layers for a rotating disk. *J. Eng. Math.*, 27:189–207, 1993.
- [343] G. Verhille, T. Séon, and P. Le Gal. Résonances d’une cavité rotor-stator au voisinage du point critique du SF6. In *20e Congrès Français de Mécanique*, Besançon, 2011.
- [344] B. Viaud, E. Serre, and J.M. Chomaz. Transition to turbulence through steep global-modes cascade in an open rotating cavity. *J. Fluid Mech.*, 688:493–506, 2011.
- [345] S. Viazzo, S. Poncet, E. Serre, A. Randriamampianina, and P. Bontoux. High-order LES of confined rotor-stator flows. *Flow, Turbulence & Combustion*, 88(1-2):63–75, 2012.
- [346] M.R. Visbal and D.V. Gaitonde. On the use of higher-order finite-difference schemes on curvilinear and deforming meshes. *J. Comp. Phys.*, 181:155–185, 2002.
- [347] R. Volk, P. Odier, and J.-F. Pinton. Fluctuation of magnetic induction in Von Kármán swirling flows. *Phys. Fluids*, 18(085105), 2006.
- [348] Th. Von Kármán. Über laminare und turbulente Reibung. *Z. Angew. Math. Mech.*, 1:233–252, 1921.
- [349] J. Wang, S. Wang, T. Zhang, and Y. Liang. Numerical investigation of ice slurry isothermal flow in various pipes. *Int. J. Refrigeration*, 36:70–80, 2013.
- [350] P.D. Weidman. On the spin-up and spin-down of a rotating fluid. Part 1. Extending the Wedemeyer model. *J. Fluid Mech.*, 77(4):685–708, 1976.
- [351] J.E. Welch, F.H. Harlow, J.P. Shannon, and B.J. Daly. *The MAC method, a computing technique for solving viscous, incompressible, transient fluid flow problems involving free surfaces*. Los Alamos scientific Laboratory Report LA3425, UC32, University of California, 1966.
- [352] H.G. Weller, G. Tabor, H. Jasak, and C. Fureby. A tensorial approach to computational continuum mechanics using object-oriented techniques. *Computers in Physics*, 12(6):620–631, 1998.
- [353] M.-Y. Wen and K.-J. Jang. An impingement cooling on a flat surface by using circular jet with longitudinal swirling strips. *Int. J. Heat Mass Transfer*, 46:4657–4667, 2003.
- [354] F. Wendt. Turbulente Strömungen zwischen zwei rotierenden konaxialen Zylindern. *Ing. Arch.*, 4:577–595, 1933.
- [355] J. Westerweel. Efficient detection of spurious vectors in particle image velocimetry data. *Exp. Fluids*, 16(3):236–247, 1994.
- [356] D.E. Wroblewski. *An experimental investigation of turbulent heat transport in a boundary layer with an embedded streamwise vortex*. PhD thesis, University of California, Berkeley, 1990.
- [357] X. Wu and K.D. Squires. Prediction and investigation of the turbulent flow over a rotating disk. *J. Fluid. Mech.*, 418:231–264, 2000.
- [358] C. Xu and R. Pasquetti. Stabilized spectral element computations of high Reynolds number incompressible flows. *J. Comput. Phys.*, 196:680–704, 2004.
- [359] C. Yang and S. Liao. On the explicit, purely analytic solution of Von Kármán swirling viscous flow. *Comm. Nonlinear Sci. Num. Sim.*, 11:83–93, 2006.
- [360] H.N. Yoshikawa, M. Nagata, and I. Mutabazi. Instability of the vertical annular flow with a radial heating and rotating inner cylinder. *Phys. Fluids*, 25:114104, 2013.
- [361] M. Yoshitsugu, Y. Hanamure, S. Furuta, F. Deguchi, K. Ueno, and M. Rautiainen. Ciliary mobility and surface morphology of cultured human respiratory epithelial cells during ciliogenesis. *Biol. Cell.*, 82:211–216, 1994.
- [362] A. Yoshizawa. Bridging between eddy-viscosity-type and second-order models using a two-scale dia. In *9th Symposium on Turbulent Shear Flows*, Kyoto, Japan, 1993.

- [363] J.P. Yu, E.M. Sparrow, and E.R.G. Eckert. Experiments on a shrouded, parallel disk system with rotation and coolant throughflow. *Int. J. Heat Mass Transfer*, 16:311–328, 1973.
- [364] A. Zacharos. *The use of unsteady RANS in the computation of three-dimensional flows in rotating cavities*. PhD thesis, School of Mechanical, Aerospace & Civil Engineering, University of Manchester, 2009.
- [365] J.M. Zahm. *Rapport : tests effectués avec l'appareil SIMEOX (Mucoviscidose - Innovation)*. INSERM U514, 2007.
- [366] J.M. Zahm, H. Kaplan, A.L. Herard, F. Doriot, D. Pierrot, P. Somelette, and E. Puchelle. Cell migration and proliferation during the in vitro wound repair of the respiratory epithelium. *Cell. Motil. Cytoskel.*, 37:33–43, 1997.
- [367] P.J. Zandbergen and D. Dijkstra. Von Kármán swirling flows. *Ann. Rev. Fluid Mech.*, 19:465–491, 1987.
- [368] N. Zuckerman and N. Lior. Jet impingement heat transfer: Physics, correlations, and numerical modeling. *Advances in Heat Transfer*, 39:565–631, 2006.

Instabilities, turbulence and heat transfer in confined rotating flows

This habilitation thesis sums up 8 years of experimental and numerical investigations in the fields of fluid mechanics and heat transfer. It is directly in line with my PhD thesis on the stability and turbulence of rotor-stator interdisk flows with throughflow. It gave place to 12 publications in international journals of rank A. The following 9 flow arrangements divided into two main parts have been thus considered and studied in details in this monograph:

1. Part 1: Rotating disk flows:
 - Similarity solutions of the flow of a non-Newtonian fluid over an infinite stationary rough disk;
 - Stability of the flow over a finite rotating disk with a free surface;
 - Stability and transition to turbulence of enclosed rotor-stator disk flows;
 - Fully turbulent regime of enclosed rotor-stator disk flows under isothermal and non-isothermal conditions;
 - Turbulent Von Kármán swirling flows between two rotating disks equipped or not with straight blades;
 - Impinging jet flow over a rotating disk with heat transfer.
2. Part 2: Flows induced by the differential rotation of concentric cylinders:
 - Stability of Taylor-Couette flows with radial thermal gradients;
 - Transitional and turbulent flows in a Taylor-Couette apparatus with atypical boundary conditions;
 - Turbulent Taylor-Couette-Poiseuille flows with or without heat transfer.

These works are either fundamental or find some applications in geophysics (Earth's mantle convection, zonal winds, ocean currents . . .) and in the turbomachinery industry. Almost all rotating machineries are indeed composed of rotor-stator cavities, where high rotation rates are reached in very small clearances, which may induce large overheatings. The first Part of this thesis has been mainly motivated by some industrial contracts with the SNECMA Moteurs group, which develops the liquid hydrogen turbopump of the Vulcain engine (Ariane V) with the goal to better predict the axial thrusts applied on the rotor. The final goal of the second Part was to improve the cooling of an electrical motor developed by Liebherr Aerospace Toulouse.

High-order numerical tools have been then developed for these specific applications. Two codes based on the same projection and temporal schemes have been used with different spatial schemes: code 1 is based on Chebyshev polynomials for the spatial discretization in the non homogeneous directions, whereas code 2 is based on 4th order compact finite-difference schemes. Both codes have been extended to Large Eddy Simulation using either the SVV technique for code 1 or more classical subgrid scale modelings for code 2. They are both available in their multidomain approach using the matrix influence technique, which enables to take into account either complex geometries, high aspect ratio cavities or atypical boundary conditions. An innovative Reynolds Stress Model sensitized to rotation effects has also been widely used to cover high turbulent flow regimes.

These in-house numerical tools have been compared also to other numerical approaches available within commercial or open source CFD codes through different numerical benchmarks. They have been systematically validated against experimental data obtained either by flow visualizations or by velocity measurements performed by Laser Doppler Velocimetry or Particle Image Velocimetry.

Rotating flows in confined systems are still an alive topic of research. The route to turbulence in some specific cases is not yet fully understood and there is clearly a lack of numerical and experimental studies of non-Newtonian rotating fluid flows for applications in process or food engineering.

Keywords: interdisk flows, Taylor-Couette system, turbulence modeling, high-order numerical methods, flow visualizations, laser Doppler velocimetry, instability, heat transfer.